
**METALS
AND SUPERCONDUCTORS**

Formation of Dissipative Structures in Crystals during Heat and Electron Transport

I. A. Zel'tser, A. S. Karabanov, and E. N. Moos

Esenin State Pedagogical University, ul. Svobody 46, Ryazan, 390000 Russia

e-mail: eugen@moos.pptus.ru

Received January 11, 2005

Abstract—The surface restructuring (faceting) of solids subjected to longitudinal electric-field and temperature gradients has been studied experimentally and theoretically. Tungsten crystals and wires preheated with a direct current in vacuum or a hydrogen atmosphere to a temperature higher than half the melting temperature are studied by electron microscopy and metallography. The processes of formation of bulk defects and of a regular surface structure are found to correlate. For the first time, these processes are analyzed in terms of synergetics. © 2005 Pleiades Publishing, Inc.

1. INTRODUCTION

A specific steplike surface structure is developed in refractory-metal crystals heated to a temperature higher than half the melting temperature if the crystal is subjected to an electric or thermal macroscopic field whose gradient exceeds 0.4–0.5 V/cm or 500 K/cm, respectively [1–6]. The step shape depends on the surface orientation, and the step size along the field varies from 4 to 15 μm .

Although the causes of the restructuring of the crystal surfaces were discussed in [1–6], the models proposed in those papers are not exhaustive and are often conflicting. In particular, the authors of [1–3] believe that this phenomenon is caused by volume processes. Later, the authors of [4–6] took into account the specific features of only surface diffusion on an anisotropic surface and ignored volume processes. The purpose of this work is to reveal the essence and role of these processes using the fluctuation–dissipative principle.

2. RESULTS OF MICROSCOPIC STUDIES

We studied epitaxial tungsten foils 5–10 μm thick evaporated on molybdenum single-crystal substrates in a fluoride process. The foils were annealed with a direct current at 2100–2200 K for 10–30 h at a pressure of 10^{-8} – 10^{-9} Torr. The small thickness of the foils (crystals) was an important factor. During dc heating, the electric-field strength in foils is relatively high (3–5 V/cm), which accelerates the formation of a wave surface (Fig. 1). As the current is switched off, the crystals cool rapidly and nonequilibrium structural defects in them are quenched. The foils were thinned from one side by electropolishing in a 3% NaOH solution and were then studied with an electron microscope.

We found that the crystal volume near the wave surface (Fig. 1) contains defects that manifest themselves

in the form of triangles and other more complex structures (Fig. 2a). In terms of their contrast, the defects correspond to stacking faults and are located in the $\{112\}$ planes. The electron diffraction pattern of a crystal area (Fig. 2a) with the (111) plane parallel to the surface is shown in Fig. 2b. Figure 2c shows the magnified (110) reflection, which has the shape of a three-rayed star. This shape indicates lattice distortions in the crystal volume.

The formation of stacking faults in a pure metal can only be related to an excess vacancy concentration and vacancy-complex formation. Therefore, dc heating disturbs thermodynamic equilibrium in the vacancy subsystem of the crystal. The fact that there is a correlation between the processes of formation of bulk defects and of a regular surface structure was supported by a metallographic study (in an optical microscope) of tungsten wires 120 μm in diameter preheated with an electric current in a hydrogen atmosphere. A high hydrogen

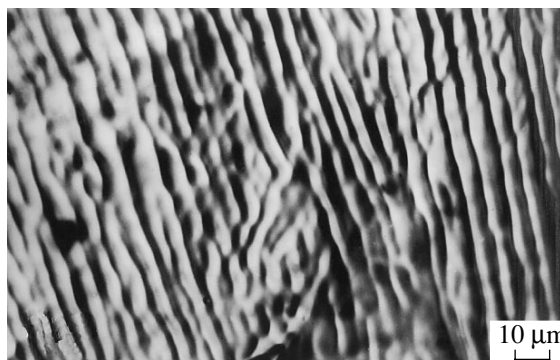


Fig. 1. Optical micrograph of a single-crystal tungsten foil dc-heated in vacuum ($P = 10^{-8}$ – 10^{-9} Torr, $T = 2100$ K, $t = 10$ h).

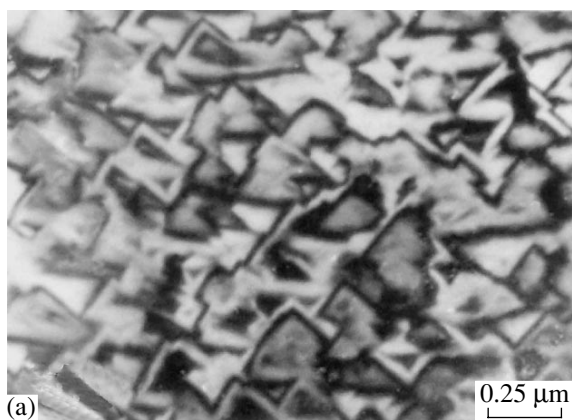


Fig. 2. Single-crystal tungsten foil dc-heated in vacuum ($P = 10^{-8}$ – 10^{-9} Torr, $T = 2100$ K, $t = 10$ h), observed in an electron microscope. (a) Defects near a surface structure, (b) the electron diffraction pattern of this region, and (c) the shape of the (110) reflection.

pressure (760–1520 Torr) provided intense heat removal from the wires and rather high fields (3–4 V/cm) in them; these fields are three to four times higher than the fields that can be created in vacuum at a pressure of 10^{-8} – 10^{-9} Torr at the same temperature (2800 K). Therefore, a surface structure in the wires heated in a hydrogen atmosphere develops within 10–20 h (in contrast to 100–200 h for the samples heated to

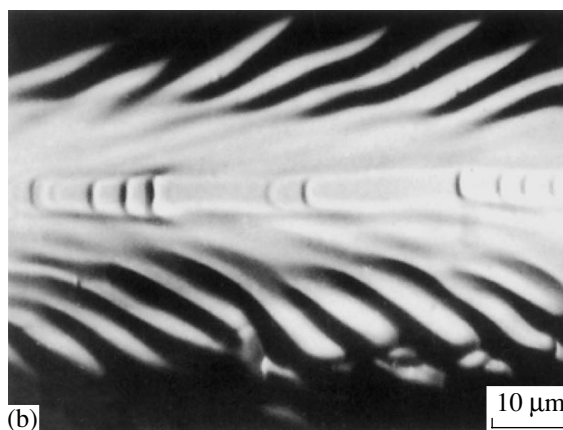
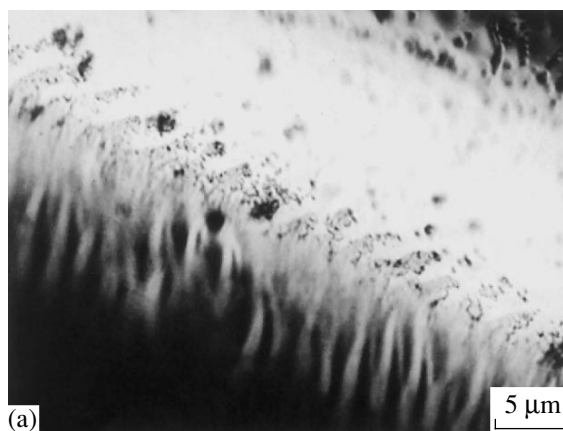


Fig. 3. Optical micrographs of the surface of a tungsten wire dc-heated in a hydrogen atmosphere ($P = 760$ – 1520 Torr, $T = 2800$ K). (a) The wire surface after 1-h annealing followed by electrochemical etching and (b) the wire surface after annealing for 10–15 h.

the same temperature in vacuum). The wires heated in a hydrogen atmosphere at 2800 K for 1–2 h are almost smooth when analyzed with an optical microscope. However, after etching in an ammonia solution, ridges appear on the wire surfaces because of the contact potential difference in the Ni–W pair (Fig. 3a); the size and arrangement of ridges correspond to those after longer heat treatments (Fig. 3b). Therefore, we can conclude that the distribution of structural defects in the crystal volume correlates with the crystal shape and that excess vacancies appear at the very beginning of the formation of the steplike structures. Hence, surface restructuring can be conjectured to be related unambiguously to a significant deviation of the vacancy concentration from its equilibrium value in a crystal carrying an electric or a heat flow and to effective mass transfer between its surface and volume. This finding cannot be explained by the models of this phenomenon proposed in [4, 5], in which the concentration of diffusion carriers (atoms or vacancies) is taken to be equal to a thermodynamically equilibrium value. Steplike structures are detected in fields that only slightly exceed the criti-

cal fields (according to the data of many authors). Structural defects in such samples have not been clearly revealed by the methods of metallography and electron microscopy. In the former method, it is difficult to separate them from the shape effect during chemical etching, and, in the latter method, the character of contrast indicates a high density of vacancy–impurity clusters.

Thus, the main features that characterize the restructuring of the crystal surface are the following:

(i) Surface restructuring occurs only in the presence of gradients of an electric or heat field of the same direction. When subjected to ac heating or uniform heating, the steps lose their stability and disappear [1–3].

(ii) The step growth rate is nonlinear in time; in the first heating stage, the surface shape does not change (a latent period); in the intermediate stage, the step growth rate is maximum; and, at the final stage, the rates of changes in the step size and height become stable in time [1–3].

(iii) This phenomenon has a threshold; that is, certain critical field gradients must be exceeded [1–3].

(iv) The vacancy concentration in the crystal volume is not a thermodynamically equilibrium value. The period of changes in the excess vacancy concentration is correlated with the surface-relief period. This conclusion is supported by the results given in this section. The experimental data indicate a correlation between the processes of formation of bulk defects and of a regular surface structure.

These features demonstrate that the restructuring of polycrystalline and single-crystal surfaces has a fluctuation–dissipative character.

3. THERMODYNAMIC CONSIDERATION OF THE RESULTS

The features given above correspond to the necessary conditions for the formation of dissipative structures [7, 8]. According to the theory of self-organization in nonequilibrium systems [7, 8], such structures can form only when the following four conditions are simultaneously satisfied:

(i) The system is thermodynamically open; i.e., it exchanges energy and matter with its environment.

(ii) The system is substantially nonlinear (it is described by nonlinear equations).

(iii) The deviation from equilibrium exceeds a critical value.

(iv) Microscopic processes correlate.

In this case, the regular structures that form in a crystal carrying an electric or a heat flow should be attributed to the class of dissipative structures. These structures are ordered configurations appearing beyond the stable region of a thermodynamic branch (the states that appear from an equilibrium state via continuous deformation) [7, 8]. If a deviation of a nonlinear system from equilibrium exceeds a certain critical value, these

states can become unstable and the system passes to a new mode and becomes a dissipative structure. Dissipative processes are characterized by nonzero entropy production. The first condition of structure formation is related to the second law of thermodynamics.

Let us show that, although the transition from a smooth defectless crystal to a stepped crystal with bulk defects that occurs in the system under study is related to a decrease in its entropy S , the second law of thermodynamics is not violated and that it manifests itself in a more general form. The system is open for flows of electricity, heat, and matter. Its entropy can decrease under specific external and internal conditions, more specifically, if the loss of entropy S per unit time ($d_e S/dt$) exceeds the entropy production inside the system ($d_i S/dt$). Thus, we have

$$\frac{dS}{dt} = \frac{d_e S}{dt} + \frac{d_i S}{dt} < 0, \quad (1)$$

if

$$\left| \frac{d_e S}{dt} \right| > \frac{d_i S}{dt} \geq 0, \quad (2)$$

where

$$\frac{d_e S}{dt} = -\int I_s n d\Sigma, \quad (3)$$

$$\frac{d_i S}{dt} = \int \sigma dV. \quad (4)$$

Here, Σ and V are the surface area and volume of the crystal, respectively; I_s is the local entropy flux on the crystal surface; n is a unit vector normal to the surface; and σ is the local entropy production.

It can be shown that the total entropy flux $(d_e S/dt)_{12}$ through two rectangular sections 1–1 and 2–2 chosen arbitrarily and located normal to the crystal axis is negative.

According to [9], the local entropy flux can be written in the form

$$I_s = \frac{I_f - \sum_k^m \mu_k I_k}{T}, \quad (5)$$

where μ_k and I_k are the electrochemical potential and the flux of the k th component, respectively; I_f is the heat flow; and T is the temperature.

For the vacancy mechanism of electrodiffusion, Eq. (5) can be rewritten as

$$I_s = \frac{I_f - \mu_e I_e - \mu_a I_a - \mu_v I_v}{T}, \quad (6)$$

or, using the equality $I_V = -I_a$, as

$$I_s = \frac{I_f - \mu_e I_e - (\mu_V - \mu_a) I_V}{T}, \quad (7)$$

where μ_e , μ_a , and μ_V are the electrochemical potentials and I_e , I_a , and I_V are the fluxes of electrons, atoms, and vacancies, respectively.

Using the approximation $\mu_{V2} = \mu_{V1}$ and taking into account the equalities $\mu_{e2} - \mu_{e1} = -e\phi$ and $\mu_{a2} - \mu_{a1} = Ze\phi$, we obtain

$$\left(\frac{d_e S}{dt}\right)_{12} = \frac{-e\phi I_e - Ze\phi I_V}{T} \Sigma_{12} < 0, \quad (8)$$

where e and Ze are the electron and ion charges, respectively; ϕ is the potential difference between the second and first cross sections; and Σ_{12} is the cross-sectional area of the crystal.

As the electric field increases, the loss of entropy $(d_e S/dt)_{12}$ increases. When it exceeds a certain critical value, the smooth defectless crystal begins to transform into a stepped crystal with bulk defects.

Thus, a direct current passing through the crystal ensures that inequality (1) is satisfied (the same result is obtained for a heat flow). The second and third conditions for the formation of dissipative structures require a transition from ordinary linear to nonlinear approaches, where ordering occurs spontaneously under certain conditions. We can assume that crystal surface shape fluctuations decrease in amplitude and disappear if the field gradient is less than a certain critical value. However, when the field gradient exceeds the critical value, some fluctuations grow and result in the formation of macroscopic order in the crystal surface. The fourth condition (the cooperative character of behavior) reflects the causality (at a microscopic level) of the processes resulting in structure formation. When these processes are cooperative due to specific interactions, spontaneous structure formation is observed.

As follows from the experiment, the vacancy concentration in crystals under valleys between steps can substantially exceed the equilibrium concentration during dc heating even for a steady-state shape of the surface (Fig. 1). This fact can be related to a substantial contribution of the flux of surface vacancies to the surface diffusion flux. The diffusion coefficient of these vacancies is anisotropic (it is dependent on the local surface orientation). Therefore, the deceleration of the surface flux in a region with a low diffusion coefficient can lead to two limiting effects: (i) the fixation of vacancies directly on the surface with the formation of valleys or (ii) the appearance of a bulk diffusion flux, when the electrochemical potential of the vacancies providing the diffusion flux is equal to the electrochemical potential of vacancies on the surface of a given curvature. According to the decomposition phenomenon observed, the supersaturation can be as high as a fraction of one percent; however, for distances of several

microns, this value can cause rather intense diffusion fluxes through the crystal volume at relatively low temperatures.

It follows that an electric field on the surface creates a steady-state excess vacancy concentration in valleys and that the portion of a step facing the output minus terminal of the power supply is a barrier to surface diffusion flux, since this portion contains loose faces having a relatively high surface energy. We can state that the structure formation on crystals that are subjected to electric or heat fields is related to cooperative surface-volume diffusion.

The interrelation between the surface shape and the redistribution of surface and volume diffusion fluxes reflects specific couplings that cause the cooperative character of this microscopic process. The operation of these couplings obeys the principle of macroscopic surface restructuring, according to which the crystal surface takes a shape for which the output total entropy flux is maximum.

Let us introduce a coordinate system xy in the plane of the crystal under study. Let $y = y(x)$ be an equation of its surface (in our two-dimensional case, this is the equation of its boundary line). The function $y(x)$ is determined from the condition of the maximum loss of entropy, i.e., the maximum of the curvilinear integral

$\int I_s n d\Sigma$ or $\int I_{sn} \sqrt{1 + y'^2} dx$ at a given crystal volume or, in the two-dimensional case, at a given area $\int y dx$. If I_{sn}

is a function of the direction of the line tangent to the sought curve (i.e., a function of y'), then, following the Lagrange method, we seek the maximum of the integral

$$\int (I_{sn} \sqrt{1 + y'^2} + \lambda y) dx \quad (9)$$

with the undetermined multiplier λ .

Then, the Euler equation gives

$$\frac{I_{sn}}{\sqrt{1 + y'^2}} - y' \sqrt{1 + y'^2} \frac{dI_{sn}}{dy'} + \lambda y = \text{const.} \quad (10)$$

Given an explicit expression for the entropy flux I_{sn} , we can determine the crystal surface shape from Eq. (10).

4. RESULTS OF THE CONSIDERATION OF TRANSPORT PROCESSES

The formation of a stacking fault in a pure metal can only be related to the presence of excess vacancies in the crystal. Direct-current heating of the crystal causes supersaturation. Therefore, apart from the development of a periodic surface structure, a mathematical model describing surface restructuring in a crystal with macroscopic fields must also explain the appearance of excess vacancies and the possible correlation of these phenomena.

The formation of nonequilibrium vacancies in solids as a result of the action of external fields is described by the phenomenological diffusion theory [9] developed in terms of the thermodynamics of irreversible processes. Therefore, a model of this phenomenon should be based on this theory. It can be shown that, when foils are heated by passing a direct current through them, there appear fluxes of vacancies and of current and heat carriers:

$$I_V = -D_V \left(\text{grad } C_V - \frac{C_V Ze \text{ grad } \phi}{kT} + \frac{C_V Q_V \text{ grad } T}{kT^2} \right), \quad (11)$$

$$I_e = -\frac{\text{grad } \phi}{\rho}, \quad (12)$$

$$I_f = -\kappa \text{ grad } T, \quad (13)$$

where $C_V = C_V^p + g$ is the vacancy concentration (C_V^p and g are its equilibrium and nonequilibrium components, respectively), D_V is the vacancy diffusion coefficient, Ze is the effective vacancy charge, Q_V is the heat for vacancy transfer, ϕ is the electric potential, T is the absolute temperature, ρ is the electrical resistivity, κ is the thermal conductivity, and k is the Boltzmann constant.

Here, the subscripts V , e , and f stand for vacancies and current and heat carriers, respectively. As is known [10], defects contribute to the electrical resistivity (thermal conductivity) of pure metals. In the approximation of a low defect concentration, an increase in the residual resistance should be proportional to this concentration. For vacancies, the additional resistivity is [10]

$$\rho_V = -\frac{mwC_V A}{n_e e^2}, \quad (14)$$

where m is the electron mass, w is the electron velocity near the upper boundary of the Fermi distribution, n_e is the number of free electrons per atom, e is the electron charge, and A is the effective scattering area (from scattering theory).

Thus, vacancies interact with electric and temperature fields. In this case, the problem of calculating the electric and temperature fields and the vacancy concentration can be reduced to the solution of a set of continuity equations for vacancies and current and heat carriers. For a steady state, this set of equations has the form

$$\begin{cases} -\text{div } I_V + \sigma_V = 0 \\ -\text{div } I_e = 0 \\ -\text{div } I_f + \sigma_f = 0, \end{cases} \quad (15)$$

where

$$\sigma_V = \frac{g}{t_V},$$

$$\sigma_f = \frac{(\text{grad } \phi)^2}{\rho}.$$

Here, σ_V is the rate of formation or disappearance of vacancies at relatively low supersaturations [11], σ_f is the density of heat sources, and t_V is the average lifetime of nonequilibrium vacancies. For the corresponding boundary conditions, set (15) can numerically be solved with a computer.

Here, we restrict ourselves to the approximation $\text{grad } \phi = E$, $E = \text{const}$, and $T = \text{const}$. Then, for the one-dimensional case, the vacancy-concentration distribution along the sample surface (with the electric field directed along the surface) can be determined from the continuity equation for vacancies

$$\frac{d^2 g}{dx^2} - \frac{ZeE}{kT} \frac{dg}{dx} + \frac{g}{l^2} = 0 \quad (16)$$

and has the form

$$g = \left\{ C_1 \sin \left[\frac{1}{l^2} - \left(\frac{ZeE}{kT} \right)^2 \right]^{\frac{1}{2}} x + C_2 \cos \left[\frac{1}{l^2} - \left(\frac{ZeE}{kT} \right)^2 \right]^{\frac{1}{2}} x \right\} \exp \frac{ZeEx}{kT}, \quad (17)$$

where C_1 and C_2 are constants of integration and $l = (t_V D_V)^{1/2}$ is the vacancy mean free path [9, 11]. In gold at high temperatures, $l = 4 \mu\text{m}$ [12]; at $Z = 1$, $E = 1 \text{ V/cm}$, $T = 2400 \text{ K}$, and $l = 10^{-4} \text{ cm}$ (which corresponds to the experimental conditions), we have $(ZeEl/kT)^2 = 25 \times 10^{-8}$. Thus, in the rather wide range of $l = 10^{-4} - 10^{-2} \text{ cm}$, we have $(ZeEl/kT) \ll 1$ and Eq. (17) can be significantly simplified:

$$g = \left(C_1 \sin \frac{2\pi}{\lambda} x + C_2 \cos \frac{2\pi}{\lambda} x \right) \exp \frac{ZeEx}{kT}, \quad (18)$$

where the surface structure period is

$$\lambda = 2\pi l. \quad (19)$$

If $E = 0$, then $\sigma_V = 0$ and, instead of Eq. (16), we obtain a version of the second Fick law from the continuity equation for vacancies. In this case, in contrast to Eq. (16), there are no periodic solutions for the vacancy concentration. Therefore, the formation of a periodic structure of the nonequilibrium component of the vacancy concentration is caused by an electric field. Obviously, a periodic surface structure can correlate with the volume-vacancy distribution.

Since a vacancy exchange between the volume and surface in a steady state must not lead to a further change in the surface, the properties of the surface (the vacancy concentration in the surface layer) should change for a period λ identical to that of the volume-vacancy concentration. Changes in the properties of a

local surface region can only be related to a change in its crystallographic orientation (hkl); hence, the surface should have a relief of the same period.

Thus, within the framework of this model, the surface structure period is specified by the state of the volume vacancy subsystem.

A more complete solution to the problem that simultaneously takes into account volume and surface diffusion can substantially correct the surface structure period in Eq. (19). However, even in the approximation used above, the solution agrees well with the experimental data on l and λ at high temperatures. In particular, in dc-heated tungsten ($T = 2400$ K, $E = 1\text{--}2$ V/cm), a surface structure with a period $\lambda \approx 12$ μm forms. In this case, the model proposed gives $l = 2$ μm , which agrees well with the value of l determined in gold at high temperatures ($l = 4$ μm) [12].

In our calculations, we did not take into account the interaction of vacancies with a temperature field ($T = \text{const}$). However, depending on the sign of the heat for vacancy transfer, this interaction can result in either an increase or decrease in the distribution amplitude of nonequilibrium vacancies.

In metals with $Q_V < 0$ (vacancies move from a cold to hot region), hot and cold regions alternating at a period λ should form as a result of the effect of vacancies on electrical resistivity (14) along the surface. Vacancies can move from cold to hot regions due to thermal diffusion, which would lead to an increase in the distribution amplitude of nonequilibrium vacancies and to a subsequent increase in the amplitudes of the nonequilibrium components of the electrical resistivity and temperature and so on (a fluctuation process).

To date, a "dc structure" has only been detected in metals (W, Mo, Ta, Nb, Pt) of this type ($Q_V < 0$), which supports this assumption.

Thus, our analysis indicates that an important role is played by volume processes in the dc-structure formation and that it is necessary to simultaneously consider volume and surface diffusion processes in developing a model based on the fluctuation–dissipative principle.

5. CONCLUSIONS

Electron-microscopic and metallographic studies of tungsten single crystals and wires heated to high temperatures in vacuum or a hydrogen atmosphere through the passing of a direct current have shown that the appearance of a steplike surface structure is related to the interaction of the surface and volume diffusion subsystems when the system strongly deviates from equilibrium.

It has been experimentally and theoretically shown that the structure under study belongs to the class of dissipative structures; therefore, the development of a model to describe this phenomenon requires a synergistic approach [7, 8]. As a result of the surface macroscopic restructuring of a crystal subjected to a supercritical electric or temperature gradient, the crystal surface takes a shape for which the total entropy flux passing through the surface into the environment is maximum.

Note that the results obtained and the technique developed can be used to study surface restructuring not only in metals but also in semiconductors (e.g., in gallium arsenide, where the process of surface faceting [13] is similar to that observed in metals [1–6] and is used in molecular-beam epitaxy to grow structures with a one-dimensional electron gas [14]).

REFERENCES

1. R. W. Schmidt, *Z. Phys.* **120**, 69 (1942).
2. D. N. Vasil'kovskii, Candidate's Dissertation (Tashkent. Univ., Tashkent, 1963).
3. G. M. Neumann, W. Hirschwald, and I. N. Stranski, *J. Phys. Chem. Solids* **1**, 619 (1967).
4. G. Froberg and P. Adam, *Acta Metall.* **23**, 365 (1975).
5. I. V. Zakurdaev and E. Ya. Chernyak, *Fiz. Met. Metall-oved.* **43**, 574 (1977).
6. E. Ya. Chernyak, G. N. Shuppe, and V. N. Yakovlev, *Fiz. Tverd. Tela (Leningrad)* **14**, 3640 (1972) [*Sov. Phys. Solid State* **14**, 2977 (1972)].
7. G. Nicolis and I. Prigogine, *Self-Organization in Non-equilibrium Systems* (Wiley, New York, 1977; Mir, Moscow, 1979).
8. W. Ebeling, *Struktur- und Prozessbildung bei irreversiblen Prozessen* (Teubner, Leipzig, 1976; Mir, Moscow, 1979).
9. Y. Adda and I. Philibert, *La diffusion dans les solides* (Saclay, France, 1966), Vols. 1, 2.
10. A. Damask and G. Dienes, *Point Defects in Metals* (Gordon and Breach, New York, 1963; Mir, Moscow, 1966).
11. B. S. Bokshtein, S. Z. Bokshtein, and A. A. Zhukhovitskii, *Thermodynamics and Kinetics of Diffusion in Solids* (Metallurgiya, Moscow, 1974; Oxonian, New Delhi, 1985).
12. C. P. Flynn, J. Bass, and D. Lazarus, *Philos. Mag.* **11**, 521 (1965).
13. M. V. Baizer, V. Yu. Vitukhin, I. V. Zakurdaev, and A. I. Rudenko, *Fiz. Tekh. Poluprovodn. (St. Petersburg)* **32**, 527 (1998) [*Semiconductors* **32**, 469 (1998)].
14. V. I. Kadushkin, V. A. Kul'bachinskii, E. V. Bogdanov, and A. P. Senichkin, *Fiz. Tekh. Poluprovodn. (St. Petersburg)* **28**, 1889 (1994) [*Semiconductors* **28**, 1042 (1994)].

Translated by K. Shakhlevich

**METALS
AND SUPERCONDUCTORS**

Electrical Conductivity and Superconductivity of Ordered Indium–Opal Nanocomposites

D. V. Shamshur, A. V. Chernyaev, A. V. Fokin, and S. G. Romanov

Ioffe Physicotechnical Institute, Russian Academy of Sciences, Politekhnikeskaya ul. 26, St. Petersburg, 194021 Russia

e-mail: a.chernyaev@mail.ioffe.ru

Received December 23, 2004

Abstract—The electrical conductivity is measured experimentally and the parameters of the superconducting transition are determined in a regular spatial network of multiply connected submicron-sized indium grains embedded in voids of an ordered opal dielectric matrix. The In–opal nanocomposite was prepared by pressure injection of the molten metal into voids of opal samples. Arrays of In grains of different sizes were produced by properly varying the characteristic geometric sizes of the opal voids, which offered the possibility of observing quantitative and qualitative changes in the temperature dependence of electrical resistance and studying the size effects on the critical temperature and critical magnetic field in the In–opal nanocomposites. It was found that, as the coherence length becomes comparable to the size of the superconducting grains, the parameters of the superconducting transition in the nanocomposite increase sharply. © 2005 Pleiades Publishing, Inc.

1. INTRODUCTION

The conductivity and superconductivity of ensembles of low-dimensional conductors have been attracting considerable research interest, because they offer the possibility of observing size effects originating from a substantial decrease of a conductor or superconductor in size, which entails a change in the basic carrier scattering mechanisms and, accordingly, an increase in the critical temperature T_c [1] and critical magnetic field H_c [2]. The superconducting (SC) state becomes more stable in nanostructured systems, because their inherent inhomogeneities pin magnetic vortices and, thus, change the magnetic flux dynamics. This feature is well known to be typical of thin films (see, e.g., [3]). If the size of the SC nanoparticles is comparable to the coherence length ξ , the behavior of such structures becomes still more complicated. In this case, a magnetic field penetrates deep into a sample because of the field being incompletely screened [4] and the superconductivity in ensembles of nanoparticles becomes spatially inhomogeneous. Coexistence of the normal and SC phases becomes possible, and resistive anomalies [5, 6] associated with the presence of interfaces, as well as topological effects of the type of resistance oscillations, may occur [7].

The electrical conductivity of three-dimensional (3D) regular ensembles of SC nanoparticles has been studied much less comprehensively than that of 2D lattices [8] because of the technological difficulties encountered in the course of sample preparation. Initially, artificial ensembles of millimeter-sized metallic spheres were obtained [4]. As far as we know, direct extension to micron- and submicron-sized spheres proved impossible because of a lack of suitable tech-

nology for the preparation of such objects. The behavior of 3D structures with particles of submicron size has been investigated for the particular case of granular superconductors [4], superconductors embedded in voids of porous glasses [9–11], and synthetic opals [12].

It must be remembered that most of the granular conductors studied thus far have percolation-type conduction, because a uniform current distribution in a system of contacting particles is impossible to ensure due to the uncontrollable quality of the intergrain contacts. The method of stabilizing SC nanoparticle ensembles in voids of a regular porous dielectric opal matrix that is employed in the present work provides a good approach to a spatially uniform current distribution [12]. This approach permits one to attain periodic modulation of the properties of a nanocomposite with a crystalline dielectric matrix [13]. A liquid metal injected under pressure into a 3D matrix occupies all accessible free space, forming grains and intergrain bridges in interviod windows. The bridges replacing point contacts between grains impart stability to the intergrain conductivity. On the whole, the lattice opal-pore topology confers a regular structure to the metal spatial network.

Increasing the nanoparticle ensemble dimensionality makes interpretation of the electrical conductivity and superconductivity of the ensemble complicated. In the case where the size of the nanoparticles is less than the London penetration depth, magnetic vortices cannot form in the grains via the Abrikosov mechanism. Therefore, in [14], the results obtained in studying the magnetoresistance and current–voltage characteristics of metal–opal nanocomposites were interpreted in terms of magnetic field transport by topological vorti-

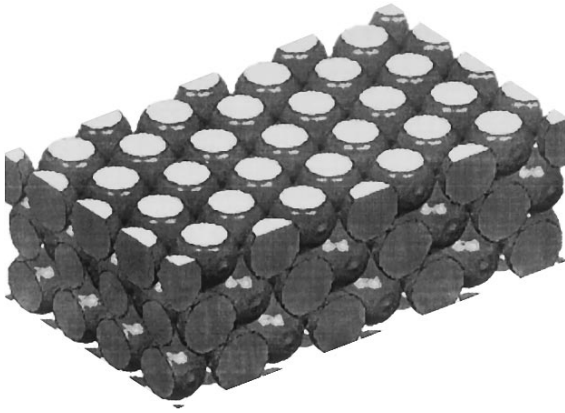


Fig. 1. Close packing of spheres forming a face-centered cubic lattice (model of the opal structure).

ces that correspond to screening currents flowing along the lattice contours. It was assumed also that magnetic field penetration into a sample is actually a stepwise process giving rise to the formation of a 3D current lattice of a multisized architecture.

The present communication reports on a study of the dependence of the electrical conductivity and SC properties of an In–opal nanocomposite on the indium nanoparticle size. The size of nanoparticles was varied by (i) using opals with silicate spheres of different size; (ii) deposition of silicon oxide from a polysilicate solution to attain a sufficiently large geometric-modulation depth of the current flow channel, i.e., the ratio of the maximum to minimum cross section of the channel; and (iii) deposition of a given number of titanium dioxide monolayers on the inner opal surface for high-precision controllable variation of void size.

2. SAMPLES AND EXPERIMENTAL TECHNIQUE

Opal is a densely packed, face-centered cubic array of identical silicate spheres [15] with voids between contacting spheres (Fig. 1). The fcc packing of spheres of diameter D has voids of two types, namely, octahedral (O voids) with a characteristic size $d_O = 0.41D$ and tetrahedral (T voids) with $d_T = 0.23D$, interconnected by channels of varying cross section with the smallest size $d_b = 0.15D$. Voids in the opal form, in turn, a regular lattice. In the present work, we used opals with spheres of different size (Table 1), with the scatter in diameter not exceeding 5% for each sample. The method of molecular layer-by-layer deposition of oxides on the inner surface of the silica gel (“overgrowth”) [16] makes it possible, as applied to opal [17], to vary the void dimensions to within the thickness of one molecular layer of the deposited oxide. One operational cycle including several chemical reactions applies one monatomic TiO_2 layer [16]. Opals with different numbers of titanium oxide monolayers N_{TiO_2} (up to 60) were prepared. To prepare nanocomposites 1.4 and 1.5, the free volume fraction of opal voids f was reduced considerably, from 26% in an ideal fcc lattice to 13%, by predeposition on the inner opal surface of a thick SiO_2 layer from a polysilicate solution. To prepare an In–opal nanocomposite, molten metal was pressure injected into the voids of the opal samples [12]. The samples measured about $5 \times 2 \times 0.4$ mm.

Electron-microscope images (Fig. 2) showed the metal to form in the opal a regular continuous three-dimensional network between the dielectric spheres. Viewed in cross section, the metal network is a regular array of closed contours that include metal grains interconnected by bridges of a smaller cross section than

Table 1. Geometric characteristics and superconducting transition parameters of the In–opal nanocomposites studied

Sample no.	f_{in}	N_{TiO_2}	δ , nm	D , nm	d_O , nm	d_T , nm	d_b , nm	T_c , K	$H_c(0)$, Oe
1.1	0.26	0	0	230	95	52	36	3.57	2200
1.2	0.23	23	3.1	230	89	46	30	3.61	2900
1.3	0.17	54	7.2	230	81	37	21	3.66	3850
1.5	0.13	0	8.2	230	79	35	19	4.15	15000
1.4	0.08	34	13	230	69	26	10	3.72–4.17	18900–22200
2.1	0.26	0	0	290	120	66	45	3.49	940
2.2	0.22	20	2.7	290	115	60	40	3.495	1250
2.3	0.19	40	5.3	290	109	55	34	3.51	1750
2.4	0.16	60	8.0	290	104	49	29	3–5	2200–5000
3.1	0.26	0	0	190	79	43	30	3.46	2260
3.2	0.20	20	2.7	190	73	37	24	3.47	1740
3.3	0.16	40	5.3	190	68	32	19	3.55	2300
3.4	0.12	60	8.0	190	63	27	14	3.58	2650

Note: The void volume fraction of samples 1.4 and 1.5 was preliminarily reduced to 13% through the deposition of SiO_2 (for sample 1.5, $\delta = \delta_{\text{SiO}_2}$; for sample 1.4, $\delta = \delta_{\text{SiO}_2} + \delta_{\text{TiO}_2}$). The error of δ determination was 2 nm, and that for sample 1.4, 4 nm.

that of a grain. The metal used to fill the voids by this method [18] occupies the entire opal free space [19], and, therefore, the metal network is a spatial replica of the sphere array.

To preclude the manifestation of surface conduction, indium was removed from the thin near-surface region of the opal by etching it in a 20% solution of nitric acid for 20 min, with subsequent checking for the absence of surface conductivity of the sample. Next, contact pads less than 0.3 mm wide were prepared by grinding and a current-conducting glue-based silver paste was applied to them.

Experimental studies were conducted on In–opal samples of three lots differing in terms of the diameter of the silicate spheres making up the opal matrix. The characteristic geometric dimensions of the opal voids and the superconducting transition parameters of the nanocomposite samples studied are listed in Table 1. Also given in Table 1 are the number of TiO₂ layer deposition cycles, the oxide thickness δ , and the indium volume fraction f_{In} .

The geometric dimensions of In grains were determined in the following way. The shape of each grain was approximated by a sphere inscribed into the void, with the diameter reduced by 2δ to account for the thickness of the TiO₂ film:

$$d_o = D(\sqrt{2} - 1) - 2\delta, \quad (1)$$

$$d_T = D\left(\sqrt{\frac{3}{2}} - 1\right) - 2\delta, \quad (2)$$

$$d_b = D\left(\frac{2}{\sqrt{3}} - 1\right) - 2\delta. \quad (3)$$

The TiO₂ overgrowing procedure lengthens the channels interconnecting the opal voids; therefore, cylinders provide a good approximation to the In bridges filling intervoid opal windows in samples with a large number of deposited TiO₂ monolayers. The cylinder axis length is

$$L = D\left(1 - \frac{\sqrt{2}}{2}\right) + 2\delta. \quad (4)$$

The dimensions of indium nanoparticles d_o , d_T , and d_b were determined by two different methods, depending on the approach employed to calculate the total TiO₂ layer thickness. In one method, we used the relation $\delta = N_{\text{TiO}_2} \delta_1$, where $\delta_1 \approx 0.13$ nm is the monolayer thickness derived with due account of the anatase structure. The other method is based on optical measurements providing the fraction of empty space in the opal volume. Optical measurements yielded the position of the maximum of the reflectance band produced by diffraction from the (111) planes of the fcc lattice of an unloaded opal. As follows from the Bragg law, $\lambda = 2n_{\text{eff}}d$ in the case of normal incidence of light on the sample surface. The effective refractive index was

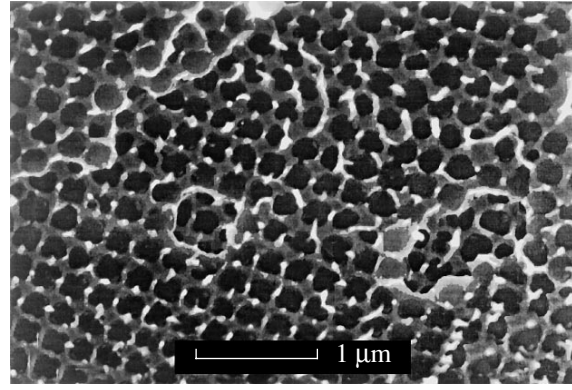


Fig. 2. Electron microscope image of In–opal nanocomposite sample 1.1.

found as $n_{\text{eff}}^2 = n_{\text{SiO}_2}^2 f_{\text{SiO}_2} + n_{\text{TiO}_2}^2 f_{\text{TiO}_2} + f_{\text{air}}$, where n_{SiO_2} , n_{TiO_2} , and f_{SiO_2} , f_{TiO_2} are the refractive indices and volume fractions of silica and anatase, respectively. The replacement of air in the opal voids by optical oil with a known refractive index produces a red shift of the diffraction maximum. Knowing the refractive indices of silica and anatase (1.43 and 2.3, respectively) and assuming that the lattice constant remains unchanged and that the volume fraction of silica is equal to 0.74, one can readily solve the two equations for the volume fraction of anatase and air in the opal matrix.

Next, the TiO₂ layer thickness was derived from the expression

$$\delta = cD\left(1 - \frac{f_{\text{overgrown}}}{f_{\text{origin}}}\right), \quad (5)$$

where $f_{\text{overgrown}}$ and f_{origin} are the free volume fractions of the “overgrown” and “original” (without the oxide layers) opal, respectively, and $c = \left(\frac{1}{\pi\sqrt{2}} - \frac{1}{6}\right) \approx 0.0584$.

Equation (5) is valid in the case of spheres contacting at one point and can be derived¹ from the obvious

¹ To derive Eq. (5), consider a sample of cubic shape with N_{cell}^3 elementary opal cells, bearing in mind that each cell has a lattice constant $a = D\sqrt{2}$ and contains $n = 4$ silicate spheres. Introducing the notations S_{sph} for the sphere surface area and V_{sph} for the sphere volume, we obtain $V_{\text{origin}} = (N_{\text{cell}}a)^3 - N_{\text{cell}}^3 nV_{\text{sph}}$ for the total free volume and $S_{\text{inner}} = N_{\text{cell}}^3 nS_{\text{sph}} - 6N_{\text{cell}}^2 n \times 0.5S_{\text{sph}}$ for the opal inner surface area; note that the outer opal surface area (the second term) may be neglected because of its relative smallness. For samples 1.4 and 1.5 featuring a large change in the free volume (i.e., $\delta \sim d_b$), δ was calculated accounting for the change in the inner opal surface area, with S_{inner} assumed to be a linear function of the variable δ . In this particular case, in place of Eq. (5), we obtain $5\delta^2 - D\delta + cD^2\left(1 - \frac{f_{\text{overgrown}}}{f_{\text{origin}}}\right) = 0$.

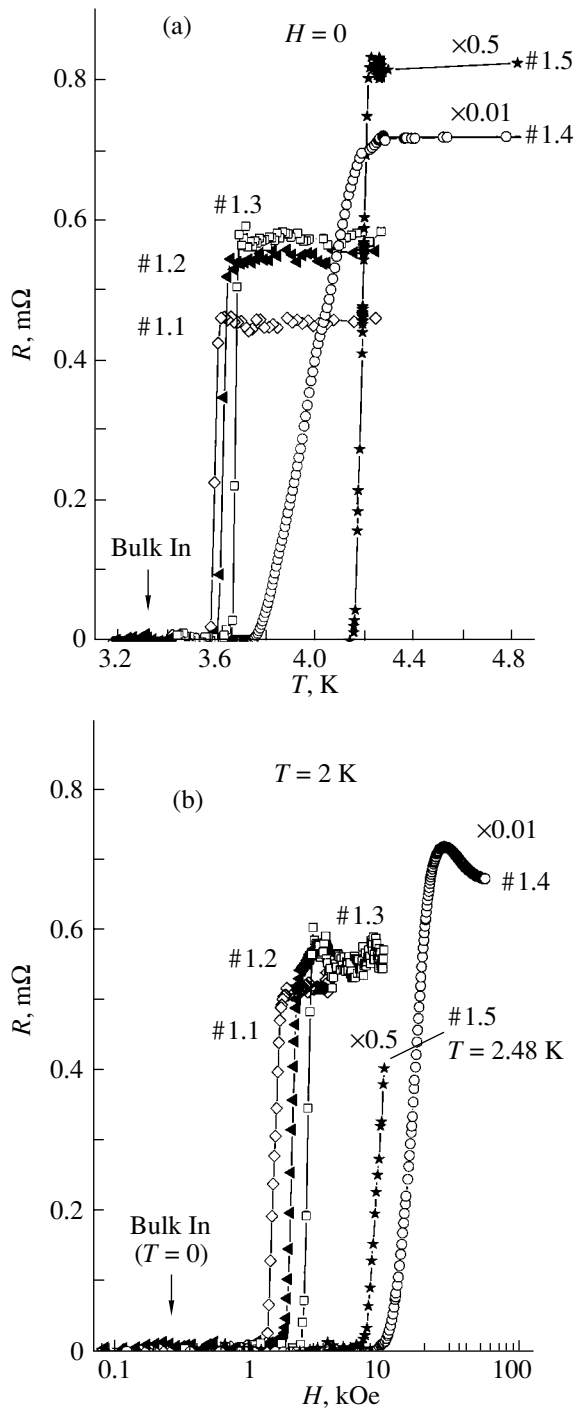


Fig. 3. Superconducting transition in In–opal nanocomposite samples. (a) Temperature dependences of resistance $R(T)$ and (b) magnetic-field dependences of resistance $R(H)$. The volume fraction of In is 0.26 (5), 0.23 (5), 0.17 (5), 0.08 (1), and 0.13 (5) in samples 1.1, 1.2, 1.3, 1.4, and 1.5, respectively. The figures in parentheses are currents (in milliamperes) through the samples.

relation

$$\frac{f_{\text{overgrown}}}{f_{\text{origin}}} = \frac{V_{\text{origin}} - S_{\text{inner}} \delta}{V_{\text{origin}}}, \quad (6)$$

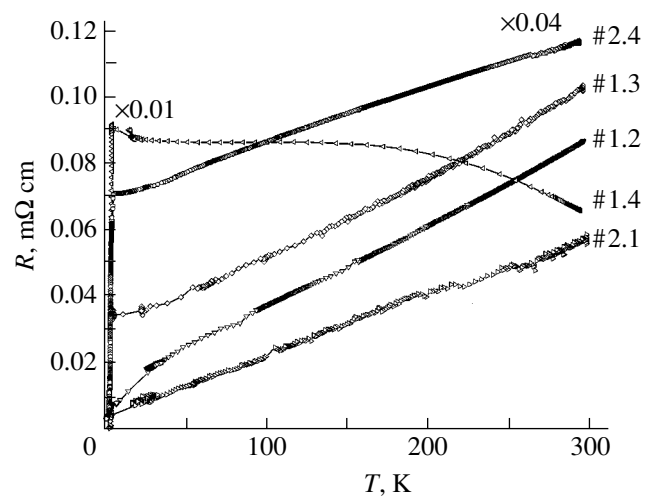


Fig. 4. Temperature dependences of the effective electrical resistivity of In–opal samples. The currents flowing through the samples of lot 1 are the same as in Fig. 3, and the currents for lot 2 are 5 and 0.1 mA for samples 2.1 and 2.4, respectively.

where V_{origin} is the volume of the original opal and S_{inner} is the total inner opal surface area.

The total layer thicknesses δ calculated by the above methods differed by less than $\Delta\delta = 2$ nm for all samples except for sample 1.4 (the difference for this sample is about 4 nm due to the fact that the void size was modified using two different methods, namely, SiO_2 deposition and subsequent TiO_2 layer-by-layer overgrowth).

The electrical resistance of the samples was measured in the temperature range 300–0.4 K and in magnetic fields of up to 70 kOe by the dc four-probe technique.

3. EXPERIMENTAL RESULTS

All the samples of the In–opal nanocomposite studied undergo the SC transition. cursory examination of Fig. 3 and Table 1 reveals that the critical temperatures and critical magnetic fields of the SC transition noticeably exceed those of bulk indium ($T_c^{\text{bulk}} = 3.41$ K and $H_c^{\text{bulk}}(0) = 280$ Oe at $T = 0$). Below the critical temperature T_c , the application of a magnetic field restores the sample resistivity to its normal-state value, $\rho = \rho_N$. One can see that T_c and H_c (Fig. 3, Table 1) correlate with the indium grain size within the same lot. Samples with a larger number of TiO_2 layering cycles exhibit higher T_c and H_c . Note that the decrease in the indium grain size is accompanied by an increase in the “effective” electrical resistivity of a sample $\rho_S = (S_S/l_S)R$ in the normal phase directly before the SC transition and by the slope of the temperature dependence of $R(T)$ becoming smoother (Fig. 4). The $\rho_S(T)$ dependence measured on a sample with the smallest In bridge

diameter ($d_b \approx 10$ nm) takes on a nonmetallic character: $\rho_S(300\text{ K})/\rho_S(4.2\text{ K}) \approx 0.7$ (Fig. 4).

The SC transition widths in temperature, ΔT_c , and in magnetic field, ΔH_c , were determined from the resistance jump as the difference in temperature (or magnetic field) between the $0.9\rho_N$ and $0.1\rho_N$ levels, and T_c and H_c were derived at the $\rho = 0.5\rho_N$ level.

Samples with a comparatively high volume fraction of indium ($f_{\text{In}} = 0.17\text{--}0.26$) exhibit a narrow SC transition, $\Delta T_c < 0.1$ K and $\Delta H_c < 100$ Oe (Fig. 3). The SC transition in samples characterized by a relatively small volume fraction of the conducting part, $f_{\text{In}} < 17\%$ (samples 1.4 and 2.4), is broad both in temperature and in magnetic field, with the $R(T)$ and $R(H)$ curves (for $T < T_c$) featuring a stepwise character [20]. For these samples, Table 1 lists two values of T_c and $H_c(0)$, namely, the boundaries of the interval within which the parameters vary between the $0.9\rho_N$ and $0.1\rho_N$ levels. Sample 1.5 occupies an intermediate position: one observes a sharp SC transition which splits into two transitions with critical temperatures that are close in magnitude.

Note that our results are consistent with the data reported in [18], where the SC transition width in temperature measured in In–opal nanocomposite samples increases with the depth of geometric modulation, i.e., with increasing ratios $d_o : d_b$ and $d_T : d_b$. Also, the critical magnetic field in sample 1.4 extrapolated to $T = 0$ exceeds $H_c^{\text{bulk}}(0)$ by about 70 times [20].

4. DISCUSSION OF THE RESULTS

4.1. Size Dependence of the Critical Superconducting Transition Temperature

The strong-coupling theory of Éliashberg [21, 22], which takes into account the delayed nature of electron–phonon interaction and provides a consistent interpretation of excitation decay, was used by McMillan [23] to derive the relation

$$T_c = \frac{\Theta}{1.45} \exp\left(-\frac{1.04(1 + \lambda_{\text{e-ph}})}{\lambda_{\text{e-ph}} - \mu^*(1 + 0.62\lambda_{\text{e-ph}})}\right), \quad (7)$$

which contains as parameters the Debye temperature Θ , the electron–phonon coupling constant $\lambda_{\text{e-ph}}$, and the Coulomb pseudopotential μ^* , whose exact value is known fairly well for polyvalent metals: $\mu^* = 0.1$. This relation does not contain any fitting parameters.

The relation $\lambda \sim 1/\langle\omega^2\rangle$ [23] was employed in [1] to calculate the ratios $\langle\omega\rangle/\langle\omega_{\text{bulk}}\rangle$ and $\langle\omega^2\rangle/\langle\omega_{\text{bulk}}^2\rangle$ for a particle of spherical shape having an fcc lattice and, using

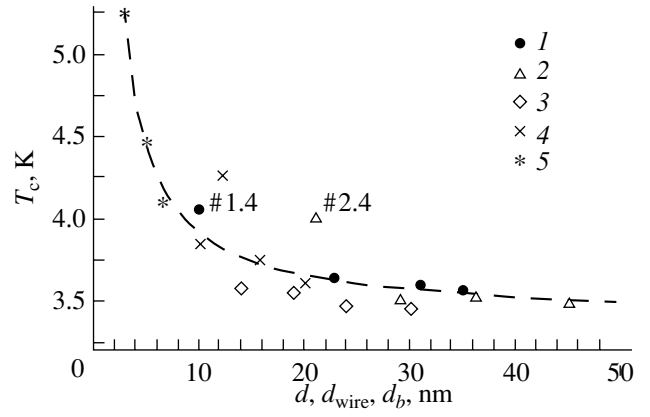


Fig. 5. Critical superconducting transition temperature plotted vs characteristic sample dimension: indium film thickness d , In wire diameter d_{wire} for indium in asbestos pores, or the smallest dimension of the In network in opal, d_b (1) In–opal nanocomposite, lot 1; (2) In–opal, lot 2; (3) In–opal, lot 3; (4) thin films [1]; and (5) In–asbestos nanocomposite [24]. The dashed line is a plot of Eq. (8).

Eq. (7), to derive an expression relating the T_c/T_c^{bulk} ratio to the particle radius r [23]:

$$\begin{aligned} & T_c/T_c^{\text{bulk}} \\ &= \frac{1}{1 + 0.674(a_0/r)} \exp\left(\frac{1.04(1 + \lambda_{\text{e-ph}}^{\text{bulk}})}{\lambda_{\text{e-ph}}^{\text{bulk}} - 0.1(1 + 0.62\lambda_{\text{e-ph}}^{\text{bulk}})}\right. \\ & \quad \left. - \frac{1.04(1 + k\lambda_{\text{e-ph}}^{\text{bulk}})}{k\lambda_{\text{e-ph}}^{\text{bulk}} - 0.1(1 + 0.62k\lambda_{\text{e-ph}}^{\text{bulk}})}\right), \quad (8) \\ & k = \frac{1 + 0.674(a_0/r)}{1 - 0.551(a_0/r)}, \end{aligned}$$

where $\lambda_{\text{e-ph}}^{\text{bulk}}$ is the electron–phonon coupling constant of the bulk material and a_0 is the lattice constant (for In, $a_0 = 0.33$ nm, $\lambda_{\text{e-ph}}^{\text{bulk}} = 0.71$ [1]).

The critical temperatures observed in In–opal samples are fitted satisfactorily (except for T_c of sample 2.4) by Eq. (8). This is illustrated by Fig. 5, which presents, in addition to the In–opal data, the results obtained with films [1] and with In loaded in asbestos voids [24].

The decrease in the coordination number, i.e., in the number of nearest neighbors, for surface atoms was found [1] to reduce the force constants, with the elasticity tensor components responsible for the shear strain decreasing to a greater extent, and this is why the average phonon frequency decreases. This gives rise to an increase in the electron–phonon coupling constant (inversely proportional to the mean squared phonon frequency) [23]. On the whole, despite a certain decrease of the Debye temperature ($\Theta \sim \langle\omega\rangle$), the critical SC transition temperature increases.

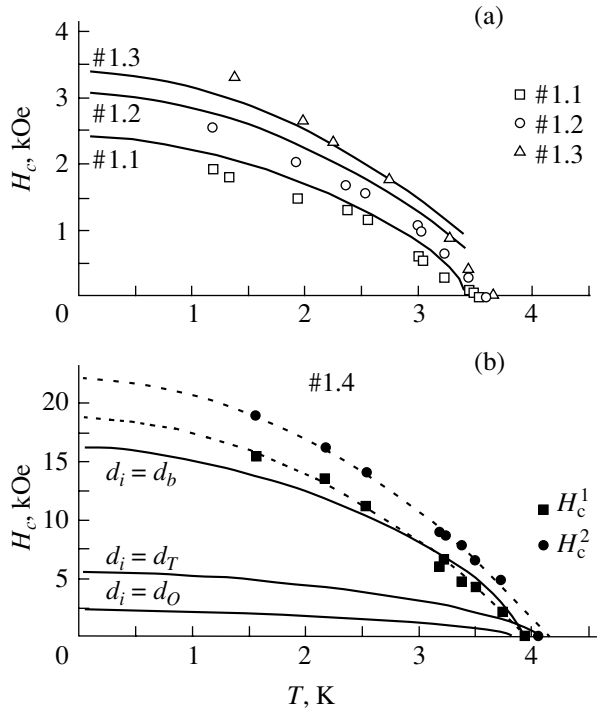


Fig. 6. Temperature dependences of critical magnetic fields for In-opal nanocomposite samples. Solid lines are calculated dependences, and symbols refer to experimental data. (a) Samples 1.1, 1.2, and 1.3 with $f_{\text{In}} = 0.17\text{--}0.26$; the average thermodynamic critical magnetic fields were calculated from Eqs. (9) and (10), and the experimental values of H_c were determined from the condition $\rho(H) = 0.5\rho_N$. (b) Sample 1.4 ($f_{\text{In}} = 0.08$); the calculated critical magnetic fields were identified with H_c of the superconducting transition of spherical In particles with diameters d_O , d_T , and d_b ; the experimental values of H_c^1 and H_c^2 were derived from the corresponding maxima of the $dR(H)/dH$ derivative. Dotted lines are the fitting of experimental data with the relation $H_c(T) = H_c(0)(1 - (T/T_c)^2)$.

4.2. Size Dependence of the Critical Magnetic Field

Samples with $f_{\text{In}} \geq 0.17$ exhibited a sharp SC transition without steps. In such samples, In grains differing in size become superconducting apparently at the same value of H_c . One may therefore introduce an average thermodynamic critical magnetic field $\langle H_c \rangle$. To find this quantity, we represent the energy of SC state destruction by the magnetic field, $\Delta\varepsilon = \varepsilon_N - \varepsilon_S$, as the sum of the energies $\Delta\varepsilon_i = (1/8\pi)(H_c^i)^2 V_i$ corresponding to different In grains (i.e. the sum over all voids) $\Delta\varepsilon = \sum_i \Delta\varepsilon_i$. Therefore, we can write

$$\langle H_c \rangle = \sqrt{(1/V) \sum_i (H_c^i)^2 V_i}, \quad (9)$$

where V is the sample volume. In grains embedded in a nanocomposite are typically of three characteristic

sizes corresponding to the different sizes of the voids in an opal, namely, d_O , d_T , and d_b . Each of the critical magnetic fields H_c^i can be identified with the characteristic grain size d_i and grain volume V_i and is calculated separately for each grain type from the relation [2]

$$H_c^i(T) = kH_c^{\text{bulk}}(T)\lambda(T)/d_i \quad (10)$$

in the limit $d_i \ll \lambda(T)$, where $H_c^{\text{bulk}}(T) = H_c^{\text{bulk}}(0)[(1 - (T/T_c)^2)]$, $\lambda(T) = \lambda(0)[1 - (T/T_c)^4]^{-1/2}$, and $\lambda(0) = 64$ nm for bulk indium at $T = 0$. The coefficient k depends on the actual sample shape; we used the value $k = 4\sqrt{5}$ for particles of spherical shape.

From examining Fig. 6a, it is evident that the experimentally measured critical magnetic field for samples with a comparatively high volume fraction of indium $f_{\text{In}} = 0.17\text{--}0.26$ is satisfactorily described by the average thermodynamic critical magnetic field $\langle H_c \rangle$. This quantitative agreement implies “classical” behavior (i.e., a pattern consistent with the Landau–Ginzburg theory) of the superconductor network in the opal.

For samples with $f_{\text{In}} < 0.17$ (samples 1.4 and 2.4), which exhibit a broad stepwise SC transition [20], one can isolate two critical magnetic fields, H_c^1 and H_c^2 . For sample 1.4, Fig. 6b shows the experimentally observed critical magnetic fields $H_c^1(T)$ and $H_c^2(T)$, as well as the critical magnetic fields $H_c^i(T)$ as calculated from Eq. (10), for In grains with the characteristic sizes specified in Table 1. We readily see that the experimentally observed critical magnetic fields range up to $H_c(0) = 22$ kOe and are noticeably higher than the predicted values. Thus, they do not fit into the classical pattern, even with the small transverse bridge dimension $d_b \approx 10$ nm taken into account.

4.3. Estimation of the Electrical Resistivity of the Indium Network in Opals

In order to explain the observed qualitative and quantitative differences in the SC properties between samples with a relatively high ($f_{\text{In}} = 0.17\text{--}0.26$) and a relatively low ($f_{\text{In}} < 0.17$) indium volume fraction, it appears reasonable to estimate the coherence length of SC electrons. To do this, one needs to know the effective carrier mean free path l_{eff} (here, “effective” means sample-averaged, because the scattering in grains with different characteristic indium nanograin sizes d_O , d_T , and d_b may differ considerably). This would require, in turn, knowledge of the electrical resistivity of the In network in the opal.

The electrical resistivity of the In network in the opal, ρ_{net} , can be estimated from the experimentally measured sample resistance R , linear sample dimensions, and indium grain dimensions d_O , d_T , and d_b . In general, ρ_{net} depends on the ratio of the effective cross-

Table 2. Electrical resistivity of the In network, effective carrier mean free path, and coherence length calculated for In–opal samples

Sample no.	$\rho_s(300 \text{ K}), \text{ m}\Omega \text{ cm}$	$\frac{\rho_s(300 \text{ K})}{\rho_s(4.2 \text{ K})}$	$\rho_{\text{net}}(4.2 \text{ K}), \mu\Omega \text{ cm}$	$l_{\text{eff}}(4.2 \text{ K}), \text{ nm}$	$\xi_{\text{eff}}(0 \text{ K}), \text{ nm}$
1.1	0.066	7.41	1.11	49	150
1.2	0.086	12.36	0.663	81	194
1.3	0.101	2.9	2.82	19	94
1.5	0.455	1.77	4.64	12	73
1.4	>0.102	0.74	>11	<5	<48
2.1	0.058	14.32	0.573	94	208
2.2	0.057	7.11	1.15	47	147
2.3	0.065	5.54	1.48	36	130
2.4	>0.08	1.91	>4.31	<13	<76
3.1	0.064	5.22	1.57	34	126
3.2	0.076	13.71	0.598	90	204
3.3	0.101	43.64	0.188	287	364
3.4	0.097	66.67	0.123	438	450

Note: The entries for samples 1.4 and 2.4 are corrected parameters.

sectional area of the conducting component in the nanocomposite to the effective length of the current-carrying path

$$\rho_{\text{net}} = R(S_{\text{eff}}/l_{\text{eff}}). \quad (11)$$

Because the fairly complex shape of the opal voids makes exact calculation of ρ_{net} difficult, let us take a simple model.

Consider a sample in which all indium making up the network is molten and forms a rectangular parallelepiped-shaped rod of length $l_{\text{eff}} = l_s$ and cross-sectional area $S_{\text{eff}} = f_{\text{In}}S_s$; the In volume fraction $f_{\text{In}} = V_{\text{In}}/V_s$ remains unchanged. This model neglects completely carrier scattering from the superconductor–matrix interface. In this case, we can write

$$\rho_{\text{model}} = f_{\text{In}}(S_s/l_s)R. \quad (12)$$

The 300-K electrical resistivities of the In network in opals calculated by the above method and listed in Table 2 demonstrate the validity of this model, $\rho_{\text{model}} \approx \rho_{\text{net}}$. As seen from Table 2, the values of ρ_{net} are close to those of ρ_{bulk} and there is no clear-cut trend toward a change in ρ_{net} with a variation in grain size. This reflects apparently that there is no noticeable carrier scattering by the interface with opal at 300 K. Indeed, the mean free path of carriers in bulk indium at 300 K as estimated from the Drude relation

$$l_{\text{eff}} = \frac{\hbar k_F}{N_0 e^2 \rho_{\text{net}}}, \quad (13)$$

$l_{\text{bulk}}(300 \text{ K}) \approx 7 \text{ nm}$, turns out to be smaller than the In grain size (here, the electron wave vector k_F is calcu-

lated by the Sommerfeld theory of metals: $k_F = \sqrt{3\pi^2 N_0}$, where N_0 is the electron concentration in a metal). The above reasoning suggests that the electrical resistivity of the In network in opal at 300 K may be reasonably accepted as equal to that of bulk indium: $\rho_{\text{net}}(300 \text{ K}) = \rho_{\text{bulk}}(300 \text{ K})$.

At low temperatures, the electrical resistivity of the In network is substantially higher than ρ_{bulk} . Indeed, the observed values of $R(300 \text{ K})/R(4.2 \text{ K})$ exceed the ratios for bulk indium by one to two orders of magnitude (Table 2): $\rho_{\text{bulk}}(300 \text{ K})/\rho_{\text{bulk}}(4.2 \text{ K}) = 256$ [25]. Obviously enough, as the temperature decreases, scattering from boundaries plays an ever increasing role and the relative decrease in the sample resistance observed experimentally reflects in the same measure the decrease in ρ_{net} :

$$R(300 \text{ K})/R(T) = \rho_{\text{net}}(300 \text{ K})/\rho_{\text{net}}(T). \quad (14)$$

Table 2 contains the electrical resistivities of the In network in opal calculated for 4.2 K. The resistivity $\rho_{\text{net}}(4.2 \text{ K})$ is seen to grow with decreasing In grain size. Figure 7 displays the temperature dependence of the electrical resistivity of the In network, $\rho_{\text{net}}(T)$, as calculated for two samples with the maximum (sample 2.1) and minimum (sample 1.4) variation in electrical resistivity (between room and liquid-helium temperatures). The calculated temperature dependence of electrical resistivity for bulk indium (dashed line) was derived

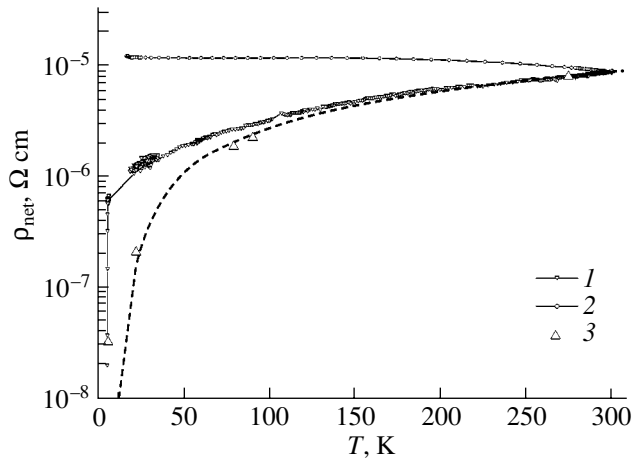


Fig. 7. Temperature dependences of the electrical resistivity of the In network in opal. (1) In–opal nanocomposite sample 2.1 (with the largest In grains), (2) In–opal sample 1.4 (with the smallest In grains), and (3) bulk indium [25, 26]. The dashed line is a plot of Eq. (15) for bulk indium.

from that of pure indium at 273 K ($\rho_{\text{bulk}}(273) = 8.2 \times 10^{-6} \Omega \text{ cm}$) using the relation [26]

$$\rho(T) = \rho(273)(\Theta/273)F(\Theta/T)/F(\Theta/273), \quad (15)$$

where $F(\Theta/T)$ is a tabulated function [27]. Relation (15) is valid for any pure metal and follows from the Bloch–Grüneisen expression for the electrical resistivity of an ideal metal lattice.

The above reasoning is valid for any In–opal sample except for samples 1.4 and 2.4, whose experimental electrical resistivity was found to be approximately two orders of magnitude higher than that of the other In–opal samples (Fig. 4). This should apparently be assigned to a substantial number of bridges breaking in the course of thermal cycling. Therefore, we introduced corrections to the electrical resistivity by plotting for all samples the dependence of the effective electrical resistivity of a sample $\rho_S = (S_S/l_S)R$ at 300 K on the minimum characteristic In grain size d_b . The results obtained by extrapolating the linear relation are presented in Table 2. This procedure disregards carrier scattering from boundaries, which can play a significant role in these samples even at 300 K; therefore, the corrected quantity R_{correct} and the function $\rho_{\text{net}}(T)$ calculated using this quantity yield underestimated values.

4.4. Properties of the In–Opal Nanocomposite in the Normal State

As already mentioned, the electrical conductivity of the indium present in an In–opal nanocomposite is considerably affected by electron scattering of two types, namely, from phonons and from the opal matrix interfaces. Scattering from point defects may be neglected because the experimental value of the ratio $\rho_S(300 \text{ K})/\rho_S(4.2 \text{ K}) \leq 14$ is small in all the In–opal samples studied as compared to that of bulk indium

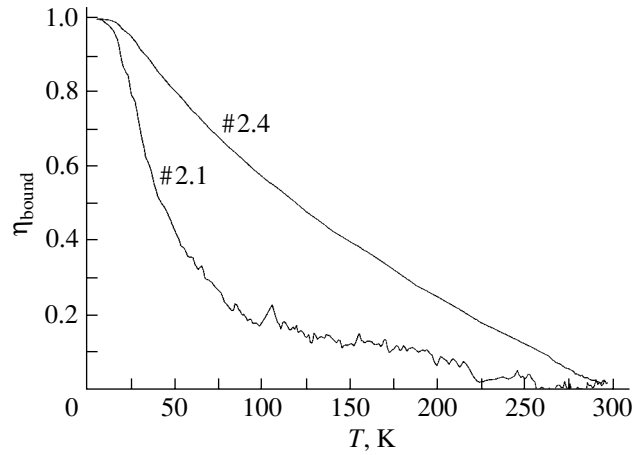


Fig. 8. Calculated temperature dependences of the quantities characterizing the relative role of boundaries in carrier scattering in In–opal nanocomposite samples.

(Table 2). Assuming the number of electron collisions with boundaries to be temperature independent, one can estimate the fraction of such collisions in relation to the total number of collisions per unit time from the temperature dependence of the resistivity. The function

$$\begin{aligned} \eta_{\text{ph}}(T) &= \rho_{\text{ph}}(T)/(\rho_{\text{ph}}(T) + \rho_{\text{bound}}(T)) \\ &= \rho_{\text{bulk}}(T)/\rho_S \end{aligned} \quad (16)$$

is the relative number of scattering events by phonons in In–opal samples under temperature variation, and $\eta_{\text{bound}}(T) = 1 - \eta_{\text{ph}}(T)$ is the relative number of scattering events by the interfaces. Figure 8 displays the temperature dependence of $\eta_{\text{bound}}(T)$ as calculated for two

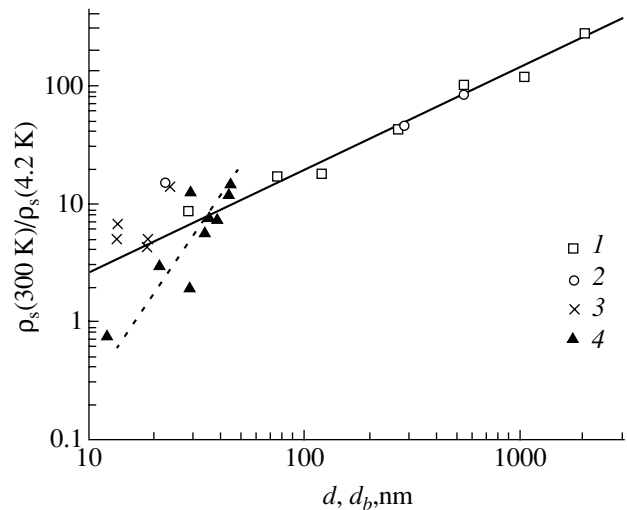


Fig. 9. Ratio $\rho_S(300 \text{ K})/\rho_S(4.2 \text{ K})$ plotted vs minimal characteristic size: bridge size d_b (for In–opal nanocomposite samples) or film thickness d (for thin films). (1) Thin films [28]; (2) thin films [29]; (3) In–opal samples, lot 3; and (4) In–opal samples, lots 1 and 2.

samples (2.1 and 2.4) with markedly different modulation of the current-carrying channel.

Figure 9 compares the size dependences of the ratio $\rho_S(300\text{ K})/\rho_S(4.2\text{ K})$ for the In network in the opal measured in the present work with those for thin indium films taken from [28, 29]. Note the good correlation of this quantity between films and the In–opal nanocomposite at close values of the characteristic size. The deviation observed for In–opal samples from the linear relation typical of films toward a decreasing $\rho_S(300\text{ K})/\rho_S(4.2\text{ K})$ ratio should apparently be assigned to the effective dimension of In grains being less than that of the film. Another point to mention is that samples of lot 3, which have the highest concentration of grain array defects and, accordingly, contain a substantial portion of In grains of macroscopic size, exhibit a deviation in the opposite sense.

It is worth noting that, in sample 1.4 with the smallest size of the In network, we have $\rho_S(300\text{ K})/\rho_S(4.2\text{ K}) \approx 0.7 < 1$ (this sample has a nonmetallic behavior of resistivity; see Fig. 4). The smallest characteristic bridge size in this sample, $d_b \sim 10\text{ nm}$ (Table 1), is close to the mean free path of carriers in bulk indium at 300 K, which implies that scattering from the In–TiO₂ interface becomes significant even at room temperature. While the dimensions of the octahedral and tetrahedral voids for this sample substantially exceed $l_{\text{bulk}}(300\text{ K})$, their resistivity is hardly noticeable against the background of the high bridge resistance (Fig. 4).

4.5. Coherence Length

We made an estimate of the SC electron coherence length in order to account for the quantitative variation of the SC transition parameters observed to occur in In–opal samples at In volume fractions $f_{\text{In}} < 0.17$.

The coherence length was calculated using the Gor'kov equation [30] in the dirty limit:

$$\xi_d(T) = 0.855 \left(\frac{\xi_0 l_{\text{eff}} T_c}{T_c - T} \right)^{1/2}, \quad l_{\text{eff}} \ll \xi_0, \quad (17)$$

where $\xi_0 = \frac{0.18 \hbar v_F}{k_0 T_c} \approx 640\text{ nm}$ is the BCS coherence length in the pure material at $T=0$ and l_{eff} is the electron mean free path. As follows from the estimates of the carrier mean free path at 4.2 K presented in Table 2, the condition $l_{\text{eff}} \ll \xi_0$ for a dirty superconductor is satisfied for all the In–opal samples studied.

The effective electron mean free paths in In–opal samples were estimated using the values of $\rho_{\text{net}}(4.2\text{ K})$ [calculated from Eq. (14)] and the Drude relation (13).

The values of the coherence length at $T=0$ calculated from Eq. (17) are presented in Table 2 and Fig. 10. We readily see that, in samples with a relatively high In volume fraction, $f_{\text{In}} = 0.17\text{--}0.26$, which exhibit a comparatively narrow SC transition ($\Delta T_c < 0.1\text{ K}$, $\Delta H_c <$

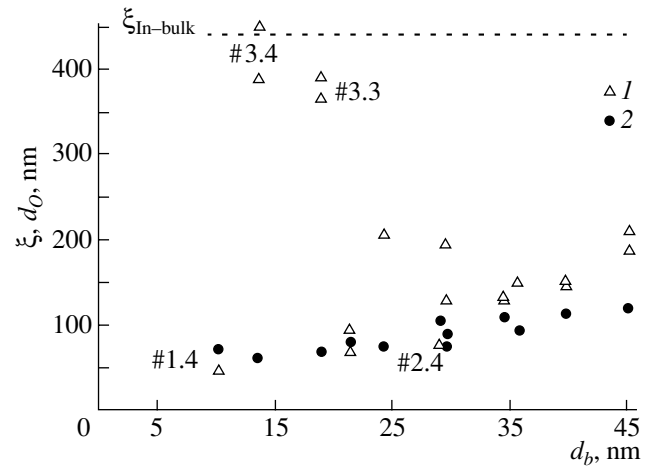


Fig. 10. (1) Calculated coherence length at $T=0$ correlated with the grain size d_O (2) for In–opal nanocomposite samples. The dashed line shows the coherence length in the pure material at $T=0$.

100 Oe), the coherence length is in excess of the In grain size. A trend is also seen toward ξ decreasing with decreasing grain size. As is evident from Table 2, for samples with $f_{\text{In}} < 0.17$, which exhibit a broad stepped SC transition [20], the calculated coherence length turns out to be of about In grain size and in all cases less than the largest dimension d_O of the grains occupying octahedral opal voids. In–opal samples of lot 3 have typically large values of ξ because of the presence of macroscopic In inclusions accounted for by a high defect concentration in the opal void network.

5. CONCLUSIONS

Synthetic opal samples with a volume fraction of indium-loaded voids $8\% < f_{\text{In}} < 26\%$ have been employed to systematically study the dependence of the electrical conductivity and SC transition parameters in a multiply connected array of indium grains on their size. The grain size was changed (with the maximum variation of the channel dimension in samples of lot 1 being $10 \leq d_b \leq 36\text{ nm}$) through proper variation of the free volume of the opal by layer-by-layer deposition on its inner surface of a given number of titanium dioxide monolayers, with the grain array parameter of the superconductor remaining unchanged. It has been shown that the characteristic pattern of the magnetic-field and temperature dependences of electrical resistivity in the SC transition region varies with decreasing indium grain size. The observed effect is treated as implying that the coherence length becomes comparable to the In grain size in the opal.

ACKNOWLEDGMENTS

The authors are indebted to M.S. Kononchuk for carrying out the low-temperature experiments and data

analysis. The authors are also grateful to R. V. Parfen'ev for his continual interest in this work and valuable discussions.

Support of the Russian Foundation for Basic Research (project no. 02-02-17685), the Presidium of the Russian Academy of Sciences, and the Foundation for Support of Leading Scientific Schools (project no. NSh-2200.2003.2) is gratefully acknowledged.

REFERENCES

1. S. Matsuo, H. Sugiura, and S. Noguchi, *J. Low Temp. Phys.* **15**, 481 (1974).
2. V. L. Ginzburg, *Zh. Éksp. Teor. Fiz.* **34**, 113 (1958) [*Sov. Phys. JETP* **7**, 78 (1958)].
3. V. V. Moshchalkov, Y. Bruynseraede, L. van Look, M. J. van Bael, and A. Tonomura, in *Handbook of Nanostructured Materials and Nanotechnology*, Ed. by H. S. Nalwa (Academic, San Diego, 2000), Vol. 3, p. 451.
4. T. D. Clark, *Phys. Rev. B: Solid State* **8**, 137 (1973).
5. P. Santhanam, C. C. Chi, S. J. Wind, M. S. Brady, and J. J. Bucchignano, *Phys. Rev. Lett.* **66**, 2254 (1991).
6. Y. K. Kwong, K. Lin, P. J. Hakonen, M. S. Isaacson, and J. M. Parpia, *Phys. Rev. B: Condens. Matter* **44**, 462 (1991).
7. W. A. Little and R. D. Parks, *Phys. Rev. Lett.* **9**, 9 (1962).
8. E. V. Charnaya, C. Tein, K. J. Lin, C. S. Wur, and Yu. A. Kumzerov, *Phys. Rev. B: Condens. Matter* **58**, 467 (1998).
9. J. H. P. Watson, *J. Appl. Phys.* **37**, 516 (1966).
10. N. K. Hindley and J. H. P. Watson, *Phys. Rev.* **183**, 525 (1969).
11. J. H. P. Watson, *Phys. Rev. B: Solid State* **2**, 1282 (1970).
12. V. N. Bogomolov, V. V. Zhuravlev, A. I. Zadorozhniĭ, E. V. Kolla, and Yu. A. Kumzerov, *Pis'ma Zh. Éksp. Teor. Fiz.* **36**, 298 (1982) [*JETP Lett.* **36**, 365 (1982)].
13. S. G. Romanov and D. V. Shamsur, *Fiz. Tverd. Tela (St. Petersburg)* **42**, 581 (2000) [*Phys. Solid State* **42**, 594 (2000)].
14. S. G. Romanov, *Pis'ma Zh. Éksp. Teor. Fiz.* **59**, 778 (1994) [*JETP Lett.* **59**, 809 (1994)].
15. V. N. Bogomolov, L. K. Kazantseva, E. V. Kolla, and Yu. A. Kumzerov, *Fiz. Tverd. Tela (Leningrad)* **29**, 622 (1987) [*Sov. Phys. Solid State* **29**, 359 (1987)].
16. V. B. Aleskovskii, *Chemistry of the Solid State (Vysshaya Shkola, Moscow, 1978)* [in Russian].
17. S. G. Romanov, A. V. Fokin, and K. Kh. Babamuratov, *Pis'ma Zh. Éksp. Teor. Fiz.* **58**, 883 (1993) [*JETP Lett.* **58**, 824 (1993)].
18. V. V. Tretyakov, S. G. Romanov, A. V. Fokin, and V. I. Alperovich, *Mikrochim. Acta, Suppl.* **15**, 211 (1998).
19. V. G. Balakirev, V. N. Bogomolov, V. V. Zhuravlev, Yu. A. Kumzerov, V. P. Petranovskii, S. G. Romanov, and L. A. Samoĭlovich, *Kristallografiya* **38**, 111 (1993) [*Crystallogr. Rep.* **38**, 348 (1993)].
20. D. V. Shamsur, A. V. Chernyaev, A. V. Fokin, and S. G. Romanov, *Nanostructures: Physics and Technology* (Ioffe Institute, St. Petersburg, 2000), p. 311.
21. Zh. M. Éliashberg, *Zh. Éksp. Teor. Fiz.* **38**, 996 (1960) [*Sov. Phys. JETP* **11**, 716 (1960)].
22. Zh. M. Éliashberg, *Zh. Éksp. Teor. Fiz.* **39**, 1437 (1960) [*Sov. Phys. JETP* **12**, 1000 (1960)].
23. W. L. McMillan, *Phys. Rev.* **167**, 331 (1968).
24. Yu. A. Kumzerov, in *Nanostructured Films and Coatings*, Ed. by G. M. Chow, I. A. Ovid'ko, and T. Tsakalakos (Kluwer Academic, Dordrecht, 2000), NATO Sci. Ser., 3, Vol. 78, p. 63.
25. *Encyclopedia of Physics*, Ed. by S. Flugge (Springer, Berlin, 1956), Vol. XIX, p. 173.
26. *Tables of Physical Quantities* (Atomizdat, Moscow, 1976) [in Russian].
27. J. McDonald, in *Low Temperature Physics*, Ed. by C. DeWitt (Springer, Berlin, 1956; *Inostrannaya Literatura, Moscow, 1959*).
28. G. J. Dolan, *J. Low Temp. Phys.* **15**, 133 (1974).
29. B. L. Brandt, R. D. Parks, and R. D. Chaudhari, *J. Low Temp. Phys.* **4**, 41 (1971).
30. L. P. Gor'kov, *Zh. Éksp. Teor. Fiz.* **36**, 1918 (1959) [*Sov. Phys. JETP* **9**, 1364 (1959)].

Translated by G. Skrebtsov

SEMICONDUCTORS
AND DIELECTRICS

Photoelectric and X-ray Dosimetric Properties of $\text{TlGaS}_2\langle\text{Yb}\rangle$ Single Crystals

S. N. Mustafaeva

Institute of Physics, National Academy of Sciences of Azerbaijan, pr. Dzshavida 33, Baku, 1143 Azerbaijan

e-mail: itpcht@itpcht.ab.az

Received November 25, 2004

Abstract—The photoelectric properties of $\text{TlGa}_{1-x}\text{Yb}_x\text{S}_2$ ($x = 0, 0.01$) single crystals are investigated. It is established that partial substitution of ytterbium for gallium leads to (i) an increase in the electrical resistivity of the samples, (ii) a shift in the maximum of the intrinsic photocurrent toward the long-wavelength range of the spectrum, (iii) a considerable broadening of the spectral sensitivity range, and (iv) an increase in the amplitude of the extrinsic photocurrent. Analysis of the x-ray dosimetric characteristics of the $\text{TlGa}_{1-x}\text{Yb}_x\text{S}_2$ single crystals demonstrates that, upon partial substitution of ytterbium for gallium in TlGaS_2 , the x-ray sensitivity coefficient increases significantly and the current–dose characteristics $\Delta I_{E,0} \sim E^\alpha$ tend to linearity ($\alpha = 1$) at low dose rates ($E, \text{R/min}$) of soft x rays. At high dose rates of hard x rays, α tends to 0.5 for both undoped and ytterbium-doped TlGaS_2 single crystals. © 2005 Pleiades Publishing, Inc.

1. INTRODUCTION

Single crystals of the TlGaS_2 compound belong to the class of wide-band-gap semiconductors with a layered structure and a high sensitivity to electromagnetic radiation in the visible spectral range. In our previous works [1, 2], we investigated dc and ac hopping conduction of TlGaS_2 single crystals. The influence of gamma radiation on the ac conductivity of TlGaS_2 single crystals was analyzed in [3]. As was shown in [4], the physical properties of TlGaS_2 single crystals can be controlled by doping with metallic impurities.

The purpose of this work was to investigate how the ytterbium doping of TlGaS_2 single crystals affects their photoelectric and x-ray dosimetric characteristics.

2. SAMPLE PREPARATION AND EXPERIMENTAL TECHNIQUE

Homogenous samples of TlGaS_2 and $\text{TlGaS}_2\langle\text{Yb}\rangle$ single crystals at an ytterbium content of 0.1 mol % were synthesized directly from the initial components. Single crystals of the TlGaS_2 and $\text{TlGa}_{0.999}\text{Yb}_{0.001}\text{S}_2$ compounds were grown by the Bridgman method. The samples synthesized were ground and placed in quartz

ampules, which were then evacuated to a residual pressure of 10^{-3} Pa and placed in a two-zone furnace. The velocity of travel of the ampule in the furnace was equal to 0.3 cm/h. The crystallographic data obtained from analyzing the x-ray diffraction patterns of the single crystals under investigation are presented in the table.

Samples of TlGaS_2 and $\text{TlGaS}_2\langle\text{Yb}\rangle$ single crystals were prepared in the form of plates in such a way that the dc electric field applied to the sample would be directed parallel to the natural layers of the single crystal and the light (x rays) would be incident along the C axis. Indium was used as a contact material. The distance between the contacts in all the samples studied was varied in the range 0.10–0.15 cm. After the ytterbium doping of the TlGaS_2 crystals, the dark resistance along the layers increased by a factor of ~ 70 .

As an x-ray source, we used a URS-55a instrument with a BSV-2 (Cu) tube. The x-ray intensity was controlled by varying the electric current in the tube at each specified value of the accelerating voltage. The absolute values of the x-ray dose were measured on a DRGZ-02 dosimeter. The change in the electrical conductivity of the samples under exposure to x rays was measured at a low-load resistance ($R_l \ll R_{cr}$).

Crystallographic data for TlGaS_2 and $\text{TlGa}_{0.999}\text{Yb}_{0.001}\text{S}_2$ single crystals

Composition of the crystal	Crystal system	Unit cell parameters					Space group	$\rho_x, \text{g/cm}^3$
		$a, \text{Å}$	$b, \text{Å}$	$c, \text{Å}$	β, deg	z		
TlGaS_2	Monoclinic	10.772	10.772	15.638	100.06	16	$C2/c$	5.560
$\text{TlGaS}_2 \langle 0.1 \text{ mol \% Yb} \rangle$	Monoclinic	10.776	10.776	15.646	100.06	16	$C2/c$	5.022

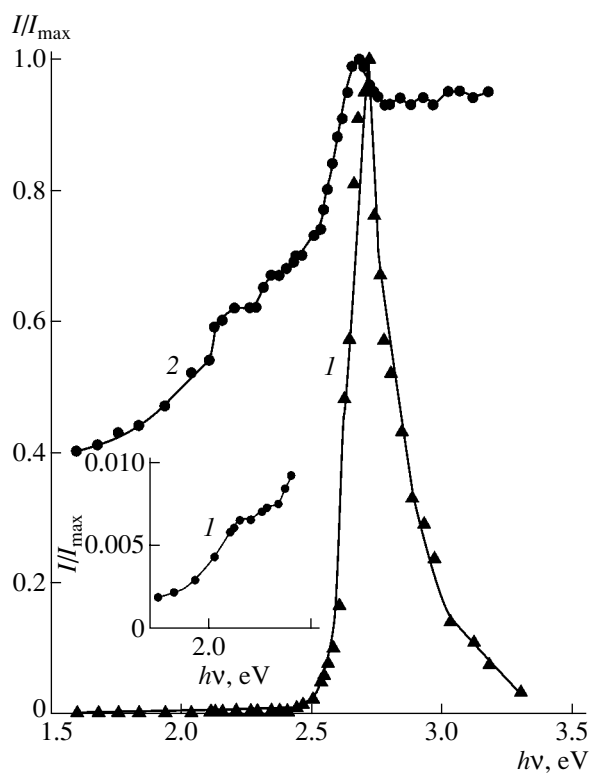


Fig. 1. Photocurrent spectra (normalized to unity): (1) TiGaS_2 and (2) $\text{TiGaS}_2\langle\text{Yb}\rangle$ single crystals. $T = 300$ K.

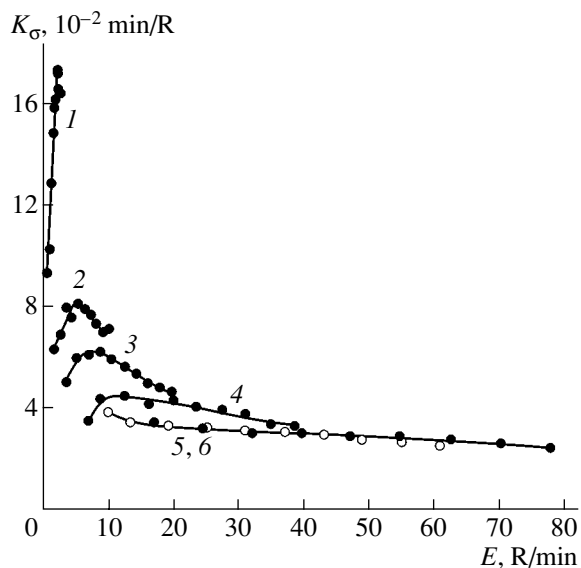


Fig. 2. Dependences of the characteristic x-ray conductivity coefficient K_σ on the dose rate E for the TiGaS_2 single crystal ($F = 80$ V/cm) at different accelerating voltages across the tube. $V_a =$ (1) 25, (2) 30, (3) 35, (4) 40, (5) 45, and (6) 50 keV.

The results of the investigations into the photoelectric and x-ray dosimetric properties of TiGaS_2 and $\text{TiGaS}_2\langle\text{Yb}\rangle$ single crystals are given below. All measurements were carried out at temperature $T = 300$ K.

3. RESULTS AND DISCUSSION

Figure 1 shows the photocurrent spectra measured (and then normalized to unity) for TiGaS_2 (curve 1) and $\text{TiGaS}_2\langle\text{Yb}\rangle$ (curve 2) single crystals. The strengths F of the dc electric fields applied to the TiGaS_2 and $\text{TiGaS}_2\langle\text{Yb}\rangle$ single crystals are equal to 200 and 300 V/cm, respectively. The photocurrent reaches a maximum at an energy $h\nu_{\text{max}} = 2.72$ eV for the undoped TiGaS_2 single crystal and at an energy $h\nu_{\text{max}} = 2.68$ eV for the ytterbium-doped single crystal. Furthermore, the ytterbium doping of the TiGaS_2 single crystals leads to a considerable broadening of the spectral sensitivity range. At energies $h\nu = 2.15$ and 2.30 eV, the photocurrent spectra of the TiGaS_2 and $\text{TiGaS}_2\langle\text{Yb}\rangle$ single crystals display two peaks corresponding to the extrinsic photocurrent (for the TiGaS_2 single crystal, the extrinsic photocurrent spectrum is plotted on an enlarged vertical scale in the inset to Fig. 1). A distinguishing feature is the extrinsic-to-intrinsic photocurrent ratio being less than 0.01 for the TiGaS_2 single crystals and exceeding 0.6 for the $\text{TiGaS}_2\langle\text{Yb}\rangle$ single crystals; i.e., after the ytterbium doping of the single crystals, the amplitude of the extrinsic photocurrent increases significantly.

Moreover, the single crystals of the TiGaS_2 and $\text{TiGaS}_2\langle\text{Yb}\rangle$ compounds are sensitive to x rays. The x-ray conductivity coefficient (K_σ), which characterizes the x-ray sensitivity of the crystals under investigation, can be defined as the relative change in the conductivity due to x rays per unit dose:

$$K_\sigma = \frac{\sigma_E - \sigma_0}{\sigma_0 E} = \frac{\Delta\sigma_{E,0}}{\sigma_0 E}, \quad (1)$$

where σ_0 is the dark conductivity and σ_E is the conductivity under exposure to x rays at a dose rate E (R/min). The characteristic x-ray conductivity coefficients were determined for undoped and ytterbium-doped TiGaS_2 single crystals at different accelerating voltages V_a across the tube and at corresponding x-ray dose rates. Figure 2 shows the dependences of the x-ray conductivity coefficient K_σ on the x-ray dose rate for the TiGaS_2 single crystal at temperature $T = 300$ K with a dc electric field strength $F = 80$ V/cm (the ohmic portion of the current-voltage characteristic). Figure 3 depicts the dependences $K_\sigma(E)$ for the $\text{TiGaS}_2\langle\text{Yb}\rangle$ single crystal at an operating voltage $U = 7$ V ($F = 80$ V/cm). As can be seen from these figures, the x-ray sensitivity of the TiGaS_2 single crystal varies in the range 0.025–0.174 min/R, whereas the x-ray conductivity coefficient K_σ of the $\text{TiGaS}_2\langle\text{Yb}\rangle$ single crystal falls in the

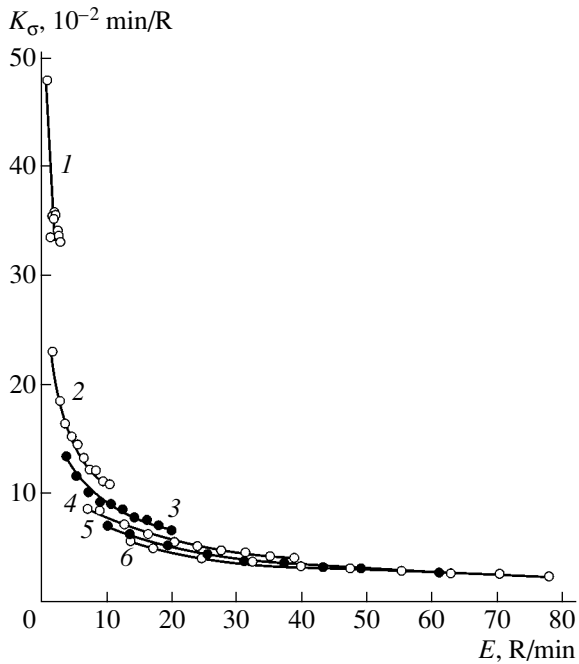


Fig. 3. Dependences of the x-ray conductivity coefficient K_G on the dose rate E for the $\text{TiGaS}_2\langle\text{Yb}\rangle$ single crystal ($F = 70$ V/cm) at different accelerating voltages $V_a = (1)$ 25, (2) 30, (3) 35, (4) 40, (5) 45, and (6) 50 keV.

range 0.024–0.480 min/R; i.e., the x-ray conductivity coefficient of the $\text{TiGaS}_2\langle\text{Yb}\rangle$ single crystal is approximately 3 times greater than the coefficient K_G of the TiGaS_2 crystal. The analysis of the experimental results demonstrated that the x-ray conductivity coefficient K_G of the $\text{TiGaS}_2\langle\text{Yb}\rangle$ single crystals regularly decreases with an increase in the dose rate and the accelerating voltage V_a . For $V_a > 30$ –35 keV and $E > 20$ R/min, the variation in the x-ray conductivity coefficient $K_G(E, V_a)$ of the TiGaS_2 and $\text{TiGaS}_2\langle\text{Yb}\rangle$ single crystals becomes very insignificant.

One of the possible reasons for this behavior of the x-ray conductivity coefficient $K_G(E, V_a)$ is as follows. At relatively low accelerating voltages, the x-ray conduction is predominantly caused by the absorption of x rays in the surface layer of the crystal. In this case, as the x-ray intensity increases, the mechanism of quadratic surface recombination becomes dominant, which leads to the observed decrease in the x-ray conductivity. An increase in the accelerating voltage leads to an increase in the effective x-ray hardness. As a result, the depth of penetration of x rays into the crystal increases; i.e., the absorption of x rays and the generation of x-ray free carriers occur predominantly in the bulk, and the fraction of x rays penetrating through the crystal increases. Consequently, as the accelerating voltage increases, the x-ray conductivity coefficient decreases and becomes less dependent on the dose rate.

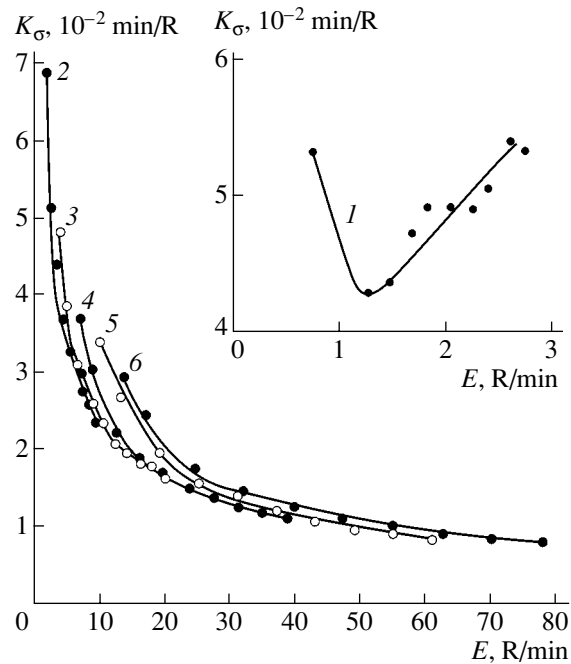


Fig. 4. Dependences of the x-ray conductivity coefficient K_G on the dose rate E for the $\text{TiGaS}_2\langle\text{Yb}\rangle$ single crystal in a dc electric field $F = 1.5 \times 10^3$ V/cm at different accelerating voltages $V_a = (1)$ 25, (2) 30, (3) 35, (4) 40, (5) 45, and (6) 50 keV.

The x-ray conductivity coefficient K_G as a function of the dose rate E was also measured at operating voltages lying in the quadratic portion of the current–voltage characteristics of the TiGaS_2 and $\text{TiGaS}_2\langle\text{Yb}\rangle$ sin-

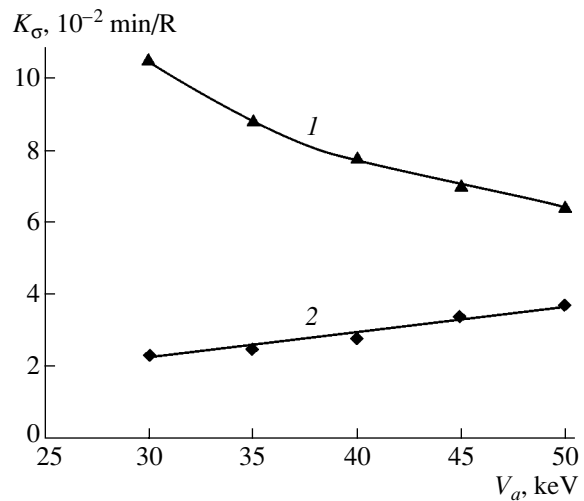


Fig. 5. Dependences of the x-ray conductivity coefficient K_G of the $\text{TiGaS}_2\langle\text{Yb}\rangle$ single crystal on the x-ray hardness at the dose rate $E = 10$ R/min in dc electric fields $F = (1)$ 70 and (2) 1.5×10^3 V/cm.

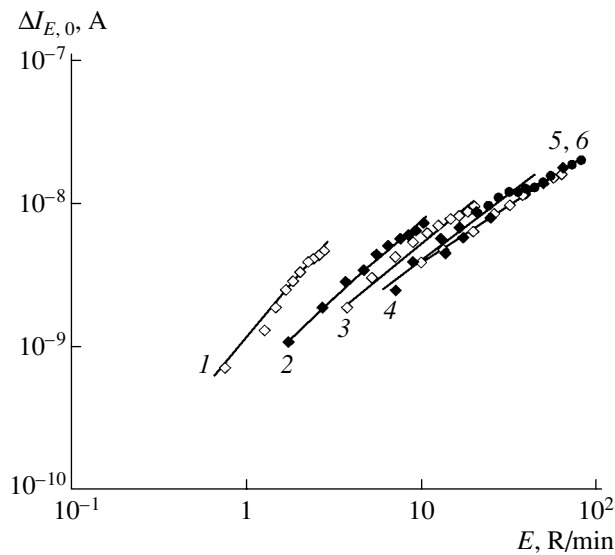


Fig. 6. Current–dose characteristics of the TI GaS₂ single crystal at different x-ray hardnesses: (1) 25, (2) 30, (3) 35, (4) 40, (5) 45, and (6) 50 keV.

gle crystals. Figure 4 displays the dependence $K_{\sigma}(E)$ for the TI GaS₂(Yb) single crystals at a dc electric field strength $F = 1.5 \times 10^3$ V/cm. It can be seen from Fig. 4 that these values of K_{σ} are several times smaller than those measured at operating voltages in the ohmic portion of the current–voltage characteristic. A similar situation is observed for the TI GaS₂ single crystals. These experimental results indicate that, in strong electric fields, the concentration of charge carriers injected from the contact is considerably higher than the con-

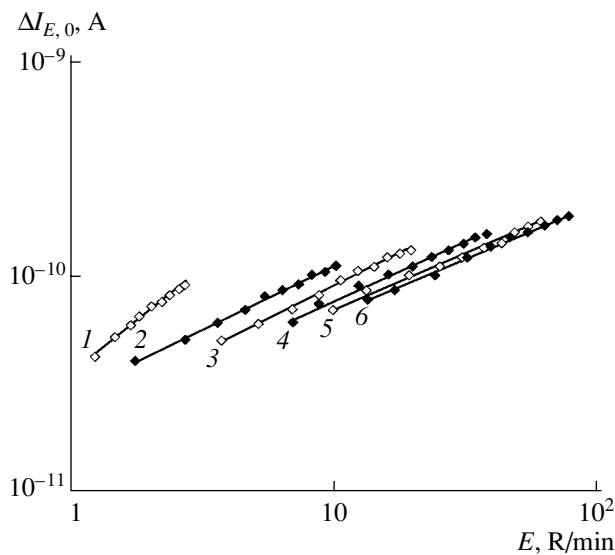


Fig. 7. Dependences of $\Delta I_{E,0}$ on the dose rate E for the TI GaS₂(Yb) single crystal at accelerating voltages $V_a =$ (1) 25, (2) 30, (3) 35, (4) 40, (5) 45, and (6) 50 keV.

centration of carriers generated under exposure to x rays. In other words, the dark conductivity σ_0 in relationship (1) increases as a result of the injection and, hence, the x-ray conductivity coefficient K_{σ} decreases. From a comparison of Figs. 3 and 4, we can see that, as the accelerating voltage V_a increases, the x-ray conductivity coefficient K_{σ} decreases at operating voltages lying in the ohmic portion of the current–voltage characteristic and increases linearly at operating voltages in the quadratic portion of the current–voltage characteristic. Figure 5 illustrates these features of the variation in the x-ray conductivity coefficient $K_{\sigma}(V_a)$ for the TI GaS₂(Yb) single crystal.

From analyzing the current–dose characteristics of the TI GaS₂ and TI GaS₂(Yb) single crystals (Figs. 6, 7), it follows that the dependence of the steady-state x-ray current on the dose rate can be adequately described by a power law:

$$\Delta I_{E,0} = I_E - I_0 \sim E^{\alpha}. \quad (2)$$

The exponent α is plotted in Fig. 8 as a function of the effective x-ray hardness V_a for the TI GaS₂ and TI GaS₂(Yb) single crystals. It follows from Fig. 8 that, upon partial substitution of ytterbium for gallium in the TI GaS₂ single crystals, the current–dose characteristics tend to linearity ($\alpha = 1$) at low dose rates of soft x rays (at low voltages V_a). At relatively high dose rates of hard x rays (at high voltages V_a), the exponent α tends to 0.5 for undoped and ytterbium-doped TI GaS₂ single crystals.

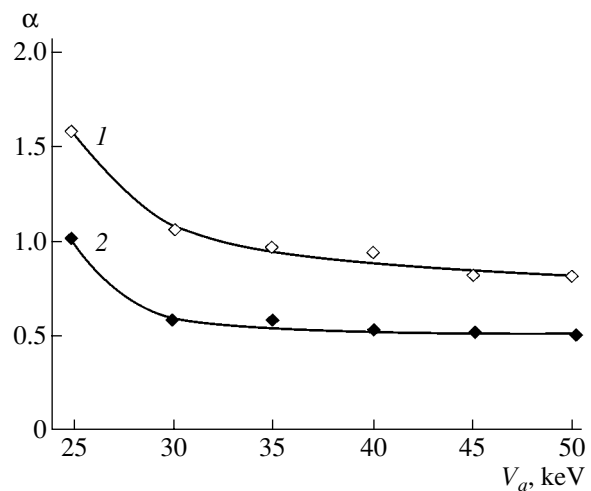


Fig. 8. Dependences $\alpha(V_a)$ for (1) TI GaS₂ and (2) TI GaS₂(Yb) single crystals.

4. CONCLUSIONS

The results obtained have demonstrated that $\text{TlGaS}_2(\text{Yb})$ single crystals are characterized by a high x-ray sensitivity and can be used in the design of uncooled (operable at room temperature) x-ray detectors.

REFERENCES

1. S. N. Mustafaeva, V. A. Aliev, and M. M. Asadov, *Fiz. Tverd. Tela (St. Petersburg)* **40** (4), 612 (1998) [*Phys. Solid State* **40** (4), 561 (1998)].
2. S. N. Mustafaeva, *Fiz. Tverd. Tela (St. Petersburg)* **46** (6), 979 (2004) [*Phys. Solid State* **46** (6), 1008 (2004)].
3. A. U. Sheleg, K. V. Iodkovskaya, and N. F. Kurilovich, *Fiz. Tverd. Tela (St. Petersburg)* **45** (1), 68 (2003) [*Phys. Solid State* **45** (1), 69 (2003)].
4. S. N. Mustafaeva, É. M. Kerimova, and N. Z. Gasanov, *Fiz. Tverd. Tela (St. Petersburg)* **43** (3), 427 (2001) [*Phys. Solid State* **43** (3), 443 (2001)].

Translated by V. Artyukhov

SEMICONDUCTORS
AND DIELECTRICS

Electronic Properties of Silicon with Ultrasmall Germanium Clusters

V. N. Brudnyi*, S. N. Grinyaev*, and A. V. Dvurechenskii**

* Kuznetsov Siberian Physicotechnical Institute, pl. Revolyutsii 1, Tomsk, 634050 Russia
e-mail: brudnyi@ic.tsu.ru

** Institute of Semiconductor Physics, Siberian Division, Russian Academy of Sciences,
pr. Akademika Lavrent'eva 13, Novosibirsk, 630090 Russia

Received December 30, 2004

Abstract—The electronic states of silicon with a periodic array of spherical germanium clusters are studied within the pseudopotential approach. The effects of quantum confinement in the energies and wave functions of the localized cluster states are analyzed. It is demonstrated that clusters up to 2.4 nm in size produce one localized s state whose energy monotonically shifts deep into the silicon band gap as the cluster size increases. The wave function of the cluster level corresponds to the single-valley approximation of the effective-mass method. In the approximation of an abruptly discontinuous potential at the heterointerface, the quantities calculated using the effective-mass method for clusters containing more than 200 Ge atoms are close to those obtained by the pseudopotential method. For smaller clusters, it is necessary to take into account the smooth potential at the interface. © 2005 Pleiades Publishing, Inc.

1. INTRODUCTION

Silicon structures with germanium quantum dots that self-assemble during molecular-beam epitaxial growth have attracted particular research attention as promising materials for use in microelectronics and optoelectronics [1]. Dense arrays of ultrasmall germanium clusters that are characterized by a high photoluminescence intensity at room temperature and, hence, can be used for lasing are of special interest [2, 3]. In a recent work [4], nearly spherical germanium islands less than 10 nm in size on silicon oxide films were prepared by low-temperature synthesis. These quantum dots are intermediate in terms of their characteristics between point defects (or small-sized aggregates of defects) and large-sized clusters (crystal fragments) with bulk properties. In order to describe adequately the electronic states of ultrasmall clusters, it is necessary to elaborate appropriate models whose parameters, depending on the number of atoms in clusters, would gradually transform from atomic parameters of deep-lying levels to band parameters of the envelope wave function method.

A reliable basis for the description and development of correct models for cluster materials can be gained from fundamental methods accounting for the actual microscopic potential in the structure as a whole. These methods, as applied to cluster materials, make it possible to determine all of the most important parameters of the electronic and crystal structures of a particular material and to reveal regularities in their variation as the cluster size changes. A number of regularities, for example, pinning of Schottky barriers by metallic clus-

ters, have been revealed for clusters containing only a few hundred atoms [5]. Such a situation occurs in the case where the states of a defect correspond to strongly localized wave functions. In Si/Ge strained structures, this condition is satisfied for hole states owing to the large values of the valence-band discontinuity and the effective mass of the holes.

In this work, we investigated the specific features of the electronic structure of silicon with dense periodic arrays of ultrasmall spherical germanium clusters. The electronic states were calculated using the pseudopotential method, as was done in our previous study [6]. However, in the present work, we considered clusters containing a substantially larger number of germanium atoms as compared to that of the clusters studied in [6]. This enabled us to analyze the quantum confinement effects more thoroughly and to determine the range of applicability of the standard effective-mass method within the approximation of an abruptly discontinuous potential at the cluster–matrix heterointerface.

2. COMPUTATIONAL TECHNIQUE

The electronic states of silicon with cluster defects composed of germanium atoms were calculated using two methods, namely, the model pseudopotential method and the method of a $(10 \times 10 \times 10)$ extended unit cell. The local pseudopotentials of silicon and germanium ions were chosen in the form of a parabolic function that has an effective depth $V_0 = V(0)$ inside a sphere of radius R_m and continuously transforms into the Coulomb potential outside this sphere. The potential of valence electrons was taken into account through

Calculated band energies of silicon and germanium crystals at symmetric points of the Brillouin zone (with respect to the top of the valence band $\Gamma_{25'v}$, eV)

Γ			L		X		$\Delta(0, 0, 3/4)$	
Γ_{1v}	Si	-12.6 (-12.4)	$L_{2'v}$	-10.2 (-9.3)	X_{1v}	-8.3	Δ_{1v}	-10.13
	Ge	-12.1 (-12.6)		-10.1 (-10.6)		-8.3		
$\Gamma_{25'v}$	Si	0.00	L_{1v}	-7.2 (-6.8)	X_{4v}	-3.0 (-2.9)	Δ_{2c}	-6.17
	Ge	0.00		-7.0 (-7.7)		-2.8		
Γ_{15c}	Si	3.36 (3.37)	$L_{3'v}$	-1.2 (-1.2)	X_{1c}	1.35	Δ_{5v}	-2.75
	Ge	3.25 (3.2)		-1.1 (-1.4)		1.23		
Γ_{2c}	Si	4.26 (4.2)	L_{1c}	2.23 (2.10)			Δ_{1c}	1.26 (1.30)
	Ge	1.06 (1.0)		0.90 (0.84)				

Note: The experimental values of the corresponding quantities [7] are given in parentheses. The spin-split levels are averaged.

the screening of the pseudopotentials of the ions by the permittivity function with corrections for exchange interaction and correlation in the Hubbard–Sham approximation. The crystal potential was represented as a superposition of the pseudopotentials of individual atoms. The band spectrum of an ideal crystal was calculated using the Löwdin method in the basis set consisting of plane waves (approximately 65 waves were exactly taken into account, and approximately 100 waves were included in terms of perturbation theory). The parameters of the pseudopotentials were determined by fitting the band spectra to the energies of the optical transitions in ideal crystals. The parameters of the pseudopotentials (in atomic units $\hbar = m_e = c = 1$) are as follows: $V_0(\text{Si}) = -1.83$, $R_m(\text{Si}) = 3.41$, $V_0(\text{Ge}) = -2.01$, and $R_m(\text{Ge}) = 3.18$.

The calculated band energies of the silicon and germanium ideal crystals at symmetric points of the Brillouin zone are listed in the table. The minimum of the conduction band for the silicon crystal is located on the line Δ with wave vector $k = 2\pi/a(0, 0, 3/4)$ ($a = 5.43 \text{ \AA}$). To this minimum there corresponds the indirect band gap $E_{g, \text{ind}}(\Delta_{1c} - \Gamma_{25'v}) = 1.26 \text{ eV}$. The irreducible representations of the space group O_h^7 are given in the notation proposed by Bouckaert *et al.* [8]. A comparison shows that the band energies of the silicon and germanium crystals are in good agreement with experimental data on the optical and photoemission spectra of these materials.

We considered spherical germanium clusters containing up to 329 germanium atoms located in sequential coordination spheres with a maximum radius $r_{\text{cl}} = a\sqrt{18}/2 \approx 1.2 \text{ nm}$. The levels of the clusters were identified with the states of the superlattice with a wave vector equal to zero. The wave functions were determined in the basis set consisting of symmetrized combinations of Bloch functions for 15 lower bands of the silicon ideal crystal. Since the lattice constants of the silicon and germanium crystals differ from each other, the ger-

manium clusters are in a strained state. Taking into account that the strain that arose in ultrasmall germanium clusters was close to a uniform strain, the germanium atoms were located at sites of the ideal lattice of the silicon crystal. This corresponds to uniform compression of the clusters. The potential of the Ge_{Si} heterostructural defect was assumed to be equal to the difference between the pseudopotentials of the germanium and silicon ions $\Delta V = V_{\text{Ge}} - V_{\text{Si}}$, which is screened by the Thomas–Fermi function with corrections for exchange interaction [5]. The density of the electron gas was taken equal to that in the silicon ideal crystal. Owing to the compensation for the Coulomb tails of the potentials of the Si^{+4} and Ge^{+4} ions, the potential ΔV was localized inside the sphere with a model radius $R_m(\text{Si})$ and had an amplitude that was one order of magnitude smaller than the amplitude of the pseudopotential of silicon. The relatively weak potential of the Ge_{Si} single defect produced only a resonant state near the top of the silicon valence band.

3. RESULTS OF THE CALCULATIONS WITHIN THE PSEUDOPOTENTIAL APPROACH

For all the germanium clusters under consideration, one deep-lying level that is completely filled with electrons and has symmetry Γ_{15} is displaced by the perturbation potential into the silicon band gap. This state arises as a result of the interaction between the resonant states of the Ge_{Si} single heterostructural defects. The energy of the cluster level E_{cl} , which is reckoned from the top of the valence band of the silicon ideal crystal, increases monotonically as the number of atoms N_{cl} in the cluster increases (Fig. 1). The germanium cluster produces a substantial effect on the states in the vicinity of the top of the silicon valence band but has virtually no effect on the states of the conduction band edge. This is associated with the fact that the strained germanium clusters serve as sufficiently deep quantum wells for holes ($\Delta E_v \sim 0.8 \text{ eV}$) and, simultaneously, act as low barriers for electrons ($\Delta E_c \sim 0.2 \text{ eV}$). However, the con-

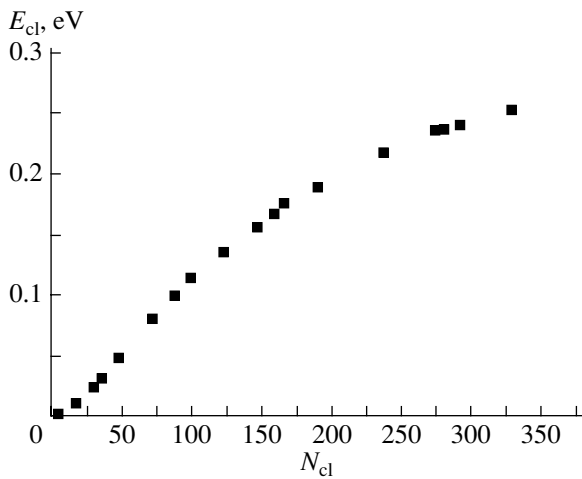


Fig. 1. Dependence of the energy E_{cl} of the deep-lying level on the number N_{cl} of germanium atoms in the cluster.

tribution of the cluster states increases in the upper conduction bands of silicon. An increase in the cluster size leads to a slower change in the position of the corresponding deep-lying level. A comparison between the results of our previous calculations performed in [6] for an $(8 \times 8 \times 8)$ extended unit cell (corresponding to the surface density of clusters $N_{cl} = 2.63 \times 10^{12} \text{ cm}^{-2}$) and the data obtained in this work for a $(10 \times 10 \times 10)$ extended unit cell (corresponding to the surface density of clusters $N_{cl} = 2.23 \times 10^{12} \text{ cm}^{-2}$) shows that, when the germanium fraction in the cluster material increases by a factor of approximately 2, the deep-lying levels E_{cl} are shifted deep into the band gap by a nearly identical energy of $\sim 0.03 \text{ eV}$ for clusters consisting of 99, 123, 147, and 159 Ge atoms. These shifts are caused by the enhancement of the hybridization of the states in the nearest neighbor clusters as they approach each other. The same shift for different clusters means that the effects associated with the delocalization of the function due to both the increase in the geometric size of the clusters and the decrease in the energy of the level equally affect the hybridization of the states.

We analyzed the wave functions of the deep-lying levels for different cluster sizes. It was revealed that the wave function is predominantly localized within the geometric boundaries of the cluster. Figure 2 shows the distribution of the total charge density for three states of the deep-lying level for a cluster consisting of 191 Ge atoms in the cross section of the $(10 \times 10 \times 10)$ extended unit cell by the (111) plane. It can be seen from this figure that, for the most part, the charge density is localized within the cluster.

In the expansion of the localized cluster functions in the basis set of the symmetrized Bloch functions for the silicon ideal crystal, the largest coefficients C_{nk} correspond to the states near the top of the valence band. This is illustrated in Fig. 3 for a cluster consisting of

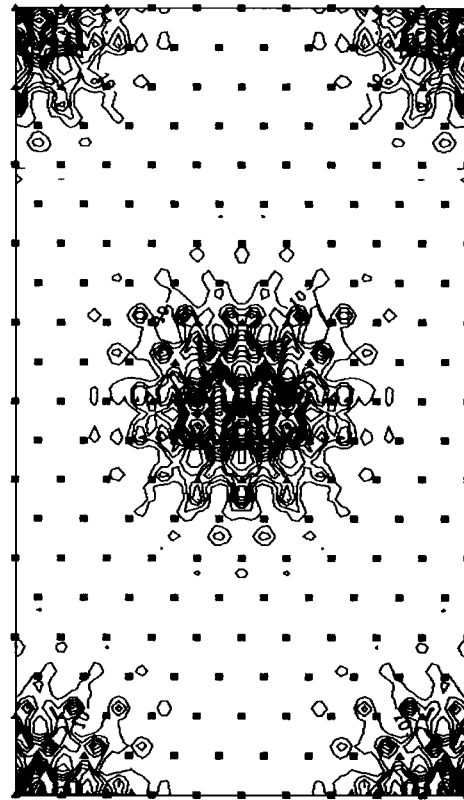


Fig. 2. Charge density distribution of the localized state for silicon with clusters consisting of 191 Ge atoms ($E_{cl} = 0.19 \text{ eV}$) in the (111) plane. Triangles and squares indicate germanium and silicon atoms, respectively. Contour interval of $10 e/\Omega_0$, where Ω_0 is the volume of the extended unit cell.

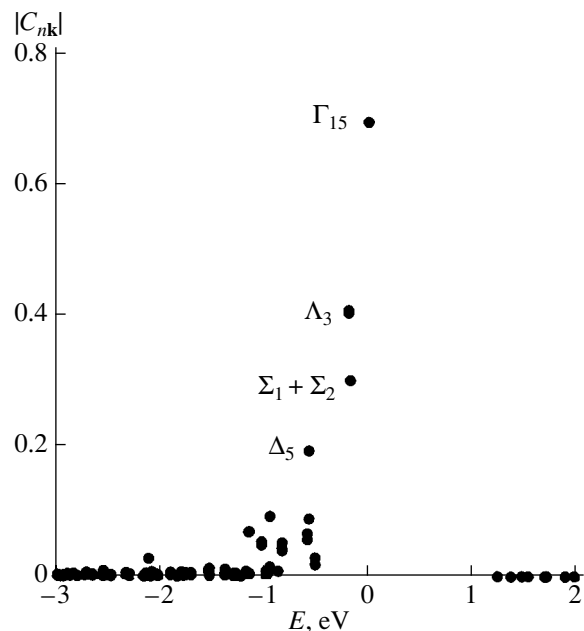


Fig. 3. Dependence of the expansion coefficients C_{nk} of the cluster wave function ($N_{cl} = 191$, $E_{cl} = 0.19 \text{ eV}$) on the energy of the included states (reckoned from the top of the valence band of the silicon ideal crystal).

191 Ge atoms. The state located immediately at the top of the valence band Γ_{15v} has the maximum weight ($|C_{nk}| \sim 0.7$). Other states in the vicinity of the extremum are characterized by considerably smaller weights. As the sizes of the germanium clusters decrease, the deep-lying levels shift toward the top of the valence band and the weight of the Γ state becomes close to unity. Therefore, the wave function of the deep-lying level corresponds to the single-valley (Γ_{15v}) approximation of the effective-mass method.

4. CALCULATION OF THE CLUSTER STATES WITHIN THE EFFECTIVE-MASS APPROACH

In order to describe the hole quantum-well states in the framework of the envelope wave function method, the clusters were represented in the form of spherical quantum dots, whose radii r_{cl} , in accordance with the approximation of an abruptly discontinuous potential at the heterointerface, were chosen equal to the mean radius of the last coordination sphere of the cluster and the subsequent sphere filled with silicon atoms. The matching conditions for the envelope wave functions on a sphere lead to the following equation for determining the energy of the s states in the germanium quantum

well (w): $kr_{cl}\cot(kr_{cl}) = 1 - \frac{m_w}{m_b}(1 + \lambda r_{cl})$, where $k =$

$(2m_w E)^{1/2}/\hbar$ is the wave vector in the quantum well and $\lambda = [2m_b(\Delta E_v - E)]^{1/2}/\hbar$ is the damping decrement in the silicon barrier (b). The radial part $R(r)$ of the envelope wave function has the form

$$R(r) = \begin{cases} C \sin(kr)/r, & r \leq r_{cl} \\ C \sin(kr_{cl}) \exp[\lambda(r_{cl} - r)], & r > r_{cl} \end{cases}$$

where C is the normalization factor. In this case, we used the calculated effective masses (averaged over directions) of heavy holes $m_b(\text{Si}) = 0.45$ and $m_w(\text{Ge}) = 0.35$ (expressed in terms of a free electron mass). The valence-band discontinuity $\Delta E_v = 0.63$ eV was determined as the difference between the energies at the top of the valence band of the strained germanium crystal and the unstrained silicon crystal. The inclusion of the strain in the calculation leads to a radical change in the mutual arrangement of the band edges of these two materials. When the strain is disregarded, the germanium quantum dot acts as a quantum barrier for holes, whereas the surrounding silicon matrix serves as a quantum well. The calculated energies of the deep-lying level E_{cl} are presented in Fig. 4. It can be seen from this figure that, as the cluster size increases, the values obtained using the effective-mass method rapidly approach the data calculated by the pseudopotential method. For clusters in which the number of atoms exceeds 200 and the radius is larger than ~ 2 nm, the energies of the deep-lying level E_{cl} calculated by the two methods almost coincide with each other. This

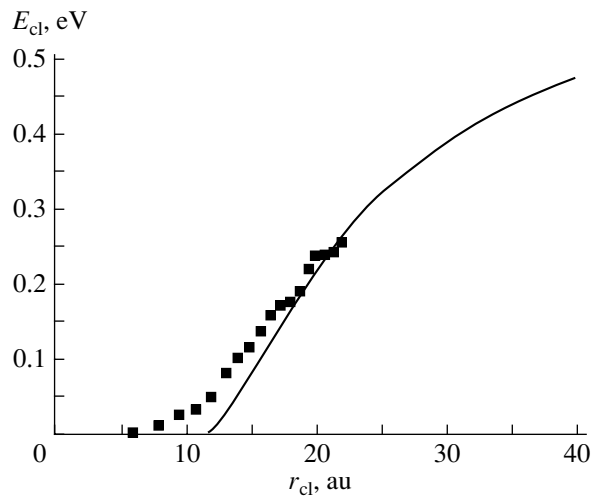


Fig. 4. Dependence of the energy of the deep-lying level on the cluster radius r_{cl} according to the calculations performed by the pseudopotential method (points) and the effective-mass method (solid line).

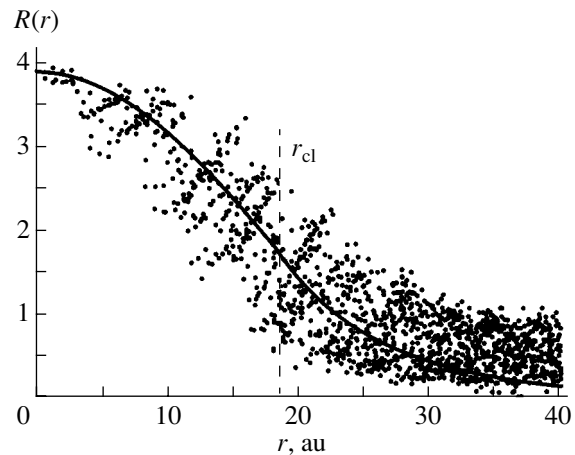


Fig. 5. Model radial part $R(r)$ (solid line) of the envelope wave function for a quantum dot inside the silicon crystal and the function $(\rho_{cl}/\rho_{Si})^{1/2}$ (points) calculated using the pseudopotential method.

rather rapid convergence of the results is associated with the strong localization of the wave function of the deep-lying level due to the large values of the valence-band discontinuity and the effective mass of the holes. The observed nonmonotonic dependence of the energy of the deep-lying level on the cluster radius (calculated by the pseudopotential method) is explained by the nonmonotonic change in the number of atoms in the sequential coordination spheres. Figure 5 shows the model radial function $R(r)$ and the corresponding function $(\rho_{cl}/\rho_{Si})^{1/2}$ calculated using the pseudopotential method for a cluster consisting of 191 Ge atoms on a uniform grid of points inside a sphere with a volume

equal to the volume of the $(10 \times 10 \times 10)$ extended unit cell. Here, ρ_{cl} and ρ_{Si} are the total densities $\rho(r) = |\Psi_{\Gamma_{15}}(r)|^2$ for three degenerate states of the cluster level with energy E_{cl} and the top of the valence band of the silicon ideal crystal, respectively. For convenience of comparison, the radial function $R(r)$ is multiplied by a factor that brings the value of this function at the center of the cluster into coincidence with the corresponding value of the function $(\rho_{\text{cl}}/\rho_{\text{Si}})^{1/2}$. Close agreement between the results obtained by the two methods demonstrates the validity of the single-valley model of the effective-mass method for calculating the cluster states. The discrepancy observed outside the cluster is associated with the fact that the tails of the functions of the nearest neighbor clusters overlap.

However, the energy levels calculated by the effective-mass method for clusters containing less than 150 atoms are considerably shallower than those obtained from the exact calculation. This can be explained by two main factors. First, the actual potential, which is smooth in the vicinity of the heterointerface, differs from the discontinuous potential used in the model calculation. Second, since the states of the band spectrum of bulk germanium are still not formed in clusters containing a small number of atoms, the use of the effective-mass method with band parameters of the crystal for the calculation of these states is not justified.

5. CONCLUSIONS

Thus, it was demonstrated that, as the size of ultrasmall spherical germanium clusters increases, the hole quantum-well level monotonically shifts deep into the silicon band gap. This should lead to a red shift in the edge of the impurity absorption due to optical transitions from localized levels of the germanium cluster to the lower conduction band of the silicon matrix [6]. The wave function of the cluster level corresponds to the single-valley approximation of the effective-mass method. This makes it possible to use the effective-mass method for calculating the electronic states of large-sized germanium clusters of arbitrary shape. In the approximation with an abruptly discontinuous potential at the cluster–matrix heterointerface, the quantities calculated by the effective-mass method for

clusters larger than ~ 2 nm in size are close to those obtained by the pseudopotential method. For smaller sized clusters, it is necessary to take into account the smooth potential at the interface and to elaborate new correct models in terms of atomic parameters.

ACKNOWLEDGMENTS

This work was performed within the framework of the state scientific program “Universities of Russia” (project no. UR 01.01.055) and was supported by the Ministry of Education and Science of the Russian Federation within the program “Basic Research in the Field of Natural and Exact Sciences in 2003–2004” (project no. E02-3.4-365).

REFERENCES

1. O. P. Pchelyakov, Yu. B. Bolkhovityanov, A. V. Dvurechenskiĭ, L. V. Sokolov, A. I. Nikiforov, A. I. Yakimov, and B. Voigtländer, *Fiz. Tekh. Poluprovodn. (St. Petersburg)* **34**, 1281 (2000) [*Semiconductors* **34**, 1229 (2000)].
2. A. G. Makarov, N. N. Ledentsov, A. F. Tsatsul’nikov, G. É. Tsyrlin, V. A. Egorov, V. M. Ustinov, N. D. Zakharov, and P. Werner, *Fiz. Tekh. Poluprovodn. (St. Petersburg)* **37**, 219 (2003) [*Semiconductors* **37**, 210 (2003)]; Yu. B. Bolkhovityanov, S. Ts. Krivoshchapov, A. I. Nikiforov, B. Z. Ol’shanskiĭ, O. P. Pchelyakov, L. V. Sokolov, and S. A. Teys, *Fiz. Tverd. Tela (St. Petersburg)* **46**, 67 (2004) [*Phys. Solid State* **46**, 64 (2004)].
3. A. I. Nikiforov, V. V. Ul’yanov, O. P. Pchelyakov, S. A. Teys, and A. K. Gutakovskiy, *Fiz. Tverd. Tela (St. Petersburg)* **47**, 67 (2005) [*Phys. Solid State* **47**, 67 (2005)].
4. S. N. Grinyaev and V. A. Cheldyshev, *Fiz. Tekh. Poluprovodn. (St. Petersburg)* **35**, 84 (2001) [*Semiconductors* **35**, 86 (2001)].
5. A. V. Dvurechenskiĭ, A. V. Nenashev, and A. I. Yakimov, *Izv. Akad. Nauk, Ser. Fiz.* **66**, 157 (2002).
6. V. N. Brudnyĭ and S. N. Grinyaev, *Izv. Vyssh. Uchebn. Zaved., Fiz., No. 6*, 59 (2004).
7. *Landolt–Börnstein: Zahlenwerte und Funktionen aus Naturwissenschaften und Technik*, Ed. by O. Madelung (Springer, Berlin, 1987), Vol. 22.
8. L. P. Bouckaert, R. Smoluchowski, and E. Wigner, *Phys. Rev.* **50**, 58 (1936).

Translated by O. Borovik-Romanova

On the Possibility of Determining the Diffusion Length of Excitons in Semiconductors from Photomagnetic Measurement Data

I. G. Atabaev, N. A. Matchanov, M. U. Khazhiev, and D. Saidov

Physicotechnical Institute, Physics–Sun Scientific Production Association,
Uzbek Academy of Sciences, ul. Mavlanova 2B, Tashkent, 700084 Uzbekistan

e-mail: sirnornur@uzsci.net

Received March 21, 2005

Abstract—The effect of a magnetic field on the photocurrent I_{ph} in Si and GaAs solar cells is investigated. It is shown that the observed change in the photocurrent I_{ph} of the solar cells in response to a magnetic field can be caused by a decrease in the diffusion length of excitons L_{exc} . A simplified model of the photomagnetic experiment is proposed to estimate the diffusion length of excitons L_{exc} and the contribution made by excitons to the photocurrent of the solar cells. © 2005 Pleiades Publishing, Inc.

1. INTRODUCTION

Research into semiconductor solar cells has demonstrated that excitons can make a significant contribution to the photocurrent of solar cells [1–3]. In particular, Corkish *et al.* [4] revealed a relatively high density of excitons in silicon at room temperature. In this respect, excitons should be taken into account in the theories describing diodes and solar cells. Although excitons are neutral particles, they can make a noticeable contribution to the electric current of devices owing to their diffusion into a junction region in which these particles can decay into free charge carriers under the action of the field. Corkish *et al.* [4] also developed a generalized three-particle theory of charge carrier transfer in semiconductors. The results obtained within this theory as applied to silicon-based devices indicate that the inclusion of excitons in the theory leads to a decrease in the dark saturation current and to an increase in the photo-generated current, because the diffusion length of excitons exceeds the diffusion length of minority carriers. Moreover, those authors proposed a method for experimental verification of the contribution from excitons to the electric current and made estimates of the exciton parameters by measuring the spectral photoresponse of solar cells.

It is obvious that correct estimate of the contribution made by excitons to the efficiency of a solar cell requires experimental data on the lifetime and the diffusion length of excitons in different semiconductor materials. The particular interest expressed by researchers in these characteristics stems from the possibility of producing an exciton condensate in semiconductors, because both the lifetime and the diffusion

length of excitons are important parameters that determine the conditions providing the formation of an exciton condensate in solids.

As a rule, these parameters can be estimated from the results of optical measurements of semiconductor samples with a low density of impurities. Semiconductor solar cells are characterized by a relatively high density of shallow impurities. However, to the best of our knowledge, there are no experimental data in the literature on the lifetime and the diffusion length of excitons that could be obtained by optical methods for such structures.

It is known that an exciton has a zero electric charge. Hence, the lifetime and the diffusion length of excitons cannot be directly determined from electrical measurements. Nonetheless, the possibility exists of estimating these characteristics from the photoelectric parameters of solar cells and other semiconductor devices (see [4]).

In this work, we proposed a possible method for estimating the diffusion length of excitons in semiconductors. It is well known that, when excitons reach a p – n junction region, they decay into free charge carriers and make a contribution to the photocurrent I_{ph} .

In a magnetic field, the energy of formation of an exciton changes insignificantly. However, the magnetic field can lead to a substantial decrease in the lifetime and the diffusion length of the excitons. In the case where the diffusion length considerably decreases in response to a magnetic field, this effect opens up new possibilities for correctly determining the diffusion length of excitons in semiconductors.

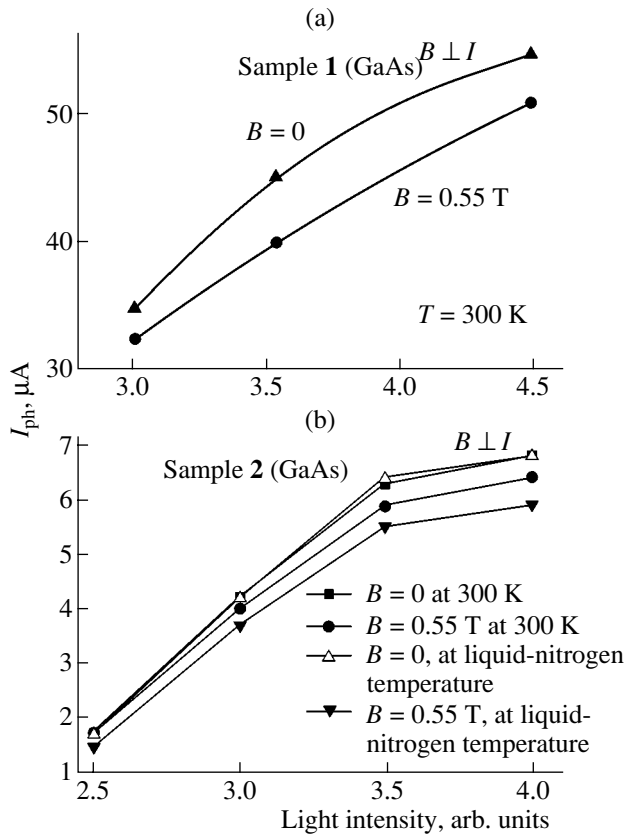


Fig. 1. Dependences of the photocurrent on the light intensity upon illumination of GaAs solar cells with (a) shallow and (b) deep p - n junctions.

2. SIMPLIFIED MODEL OF THE EXPERIMENT

Let us consider a simplified model of the experiment. It is assumed that, in a magnetic field, all excitons decay into free charge carriers and that the photocurrent I_{ph} passing through a p - n junction is determined only by the lifetime and the diffusion length of free charge carriers, i.e., electrons and holes. It should be noted that the above assumption is a rather rough approximation. The assumption that the diffusion length of excitons should decrease in response to a magnetic field would be more realistic. However, the main objective of the present work is to demonstrate that the diffusion length of excitons L_{exc} in semiconductors can, in principle, be determined experimentally.

We also assume that excitons are generated only at the surface of a semiconductor (this can be easily achieved by appropriately choosing the wavelength of photons to be used in illumination).

It is easy to show that, in the stationary case, the change in the photocurrent after the magnetic field is

switched on can be adequately described by the relationship

$$\Delta I = [I_{ph} - I_{ph}(H)] \sim N_{exc}(0) [\exp(-L_{pn}/L_{exc}) - \exp(-L_{pn}/L_{e,h})]. \quad (1)$$

As follows from relationship (1), the change in the photocurrent ΔI depends primarily on (i) the ratio between the diffusion length of charge carriers $L_{e,h}$ and the diffusion length of excitons L_{exc} , (ii) the depth of the p - n junction L_{pn} , and (iii) the exciton density N_{exc} near the surface of the semiconductor. The photocurrent I_{ph} should remain unchanged at $L_{exc} = L_{e,h}$, should increase at $L_{exc} < L_{e,h}$, and should decrease at $L_{exc} > L_{e,h}$. It can also be seen from relationship (1) that the diffusion length of excitons can be determined more precisely from the experiments with samples characterized by different depths of the p - n junctions.

Of course, our assumption that the diffusion length of excitons drastically decreases in response to a magnetic field significantly simplifies the model of the experiment. However, as was already mentioned, the purpose of this work is to demonstrate that it is possible, in principle, to determine experimentally the diffusion length of excitons.

3. EXPERIMENTAL TECHNIQUE AND RESULTS

The experiments were performed using Si- and GaAs-based solar cells (with different areas) in a magnetic field of 0.55 T [5]. The solar cells were exposed to light from an incandescent lamp and a semiconductor laser (1 mW, $\lambda = 0.63$ – 0.68 μm). It should be noted that the photocurrent in the experiments with the semiconductor laser was of the order of 1 μA because of the small exposure area (the diameter of the laser beam was approximately 3 mm). Moreover, the design of the solar cells corresponded to the solar spectrum.

Figure 1 shows the dependences of the photocurrent on the light intensity upon exposure of the GaAs solar cells (Fig. 1a, sample 1 (GaAs) with an efficiency of 23%; Fig. 1b, sample 2 (GaAs) with an efficiency of 18%) to light from a semiconductor laser. The light intensity was controlled by varying the voltage applied to the laser in the range from 2.5 to 4.5 V, in which the light intensity depends linearly on the applied voltage. The diffusion length of charge carriers in the base region of the solar cell was approximately equal to 3–4 μm , and the depth of the p - n junction in the heavily doped surface region was approximately 1 μm (according to the data sheet for the solar cells).

The results of the measurements demonstrated that, at room temperature, the change in the photocurrent $\Delta I = [I_{ph} - I_{ph}(H)] < 0$ amounts to 6–8%. Consequently, the inequality $L_{exc} > L_{e,h} \sim 1$ μm holds for the surface region of the solar cell and the contribution made by the

excitons reaches 6–8%. The photocurrent I_{ph} increases linearly with an increase in the light intensity. At liquid-nitrogen temperature, the contribution of the excitons increases to 10–15% (Fig. 1b). Therefore, the condition $L_{exc} > L_{e,h}$ is satisfied for all the GaAs solar cells under investigation.

Figure 2 shows the dependences of the photocurrent on the light intensity upon illumination of silicon solar cells (Fig. 2a, sample 1 (Si) with an efficiency of 15%; Fig. 2b, sample 2 (Si) with an efficiency of 11%) in a magnetic field. The diffusion length of charge carriers in the base region of the solar cells lies in the range 60–80 μm . In the heavily doped surface p region, the diffusion length of charge carriers $L_{e,h}$ is approximately equal to 0.6–0.9 μm and the depth of the p – n junction L_{pn} is approximately 1 μm . According to the measurements of the spectral sensitivity, the junction depth of silicon solar cell 1 with an efficiency of 15% is smaller than that of silicon solar cell 2 with an efficiency of 11%.

It can be seen from Fig. 2 that the photocurrent of the silicon solar cells exhibit a behavior different from that of the GaAs solar cells: in the former case, the change in the photocurrent ΔI amounts to approximately 3% at room temperature and has the opposite sign. In our opinion, the above features of the change in the photocurrent are associated with the mechanism of generation and accumulation of photoinduced charge carriers in these cells.

In the GaAs solar cells, photocarriers are generated near the surface of the crystal, as was assumed in [3]. However, the generation and drift of photocarriers and excitons in silicon occur not only near the surface of the crystals but also in their bulk, because the quantity $1/\alpha$ for $\lambda = 0.63$ – 0.68 μm is approximately equal to 3 μm [6]. Therefore, the photocurrent in silicon solar cells with a sufficiently deep p – n junction is predominantly generated in the diffusion region and the diffusion length of excitons L_{exc} in this region should be compared with the diffusion length of charge carriers $L_{e,h}$ ($L_{exc} > L_{e,h}$) and $\Delta I < 0$ (Fig. 2b, silicon solar cell 2).

In the case of shallower p – n junctions, the generation and accumulation of charge carriers predominantly occur in the base region of the solar cell. In this region, we have $L_{e,h} \sim 60$ – 80 μm , $L_{exc} < L_{e,h}$, and $\Delta I > 0$ (Fig. 2a, silicon solar cell 1).

When the solar cells were exposed to light from an incandescent lamp, the light intensity was controlled by varying the distance between the light source and the solar cell, because the variation in the filament voltage of the lamp leads to a change in the optical spectrum. The experimental results demonstrated that, in this case also, the photocurrent of the solar cells under investigation changes in the magnetic field.

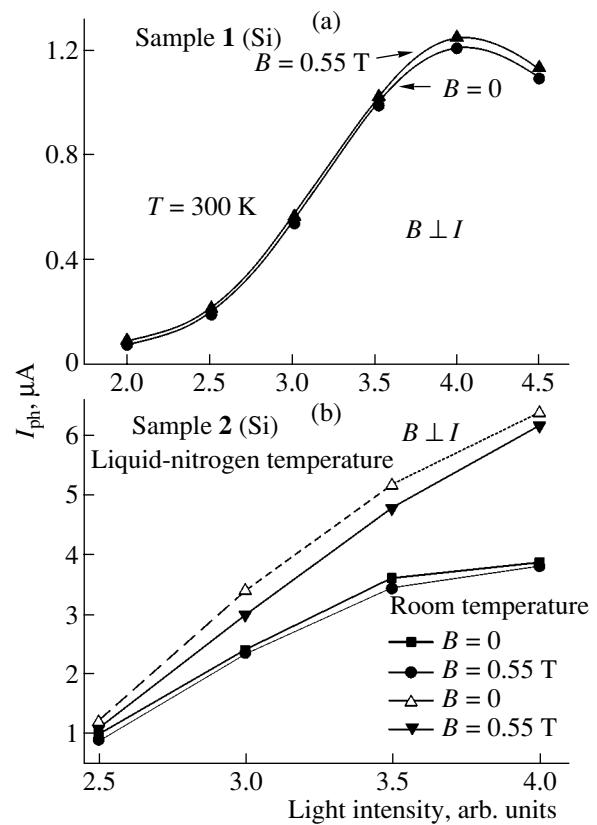


Fig. 2. Dependences of the photocurrent on the light intensity upon illumination of silicon solar cells with (a) shallow and (b) deep p – n junctions.

4. DISCUSSION

The model proposed is based on the assumption that the diffusion length of excitons drastically decreases in a magnetic field. First and foremost, we consider the possibility of excitons decaying in semiconductors due to the influence of the magnetic field on the exciton binding energy. The exciton binding energy is equal to 7.5 meV in Si and 3.2–4.4 meV in GaAs [7]. It is well known that the exciton binding energy in semiconductors decreases in response to a magnetic field [8, 9]. The change in the exciton binding energy $\Delta\epsilon_{bind}$ due to the interaction of the spin of charge carriers with the magnetic field can be written in the form

$$\Delta\epsilon_{bind} \sim g_e \mu_B S, \quad (2)$$

where g_e is the electronic Landé factor (equal to 2.0–2.5 for Si, 1.5–1.8 for Ge, and 0.44 for GaAs), $\mu_B = 58 \mu\text{eV/T}$ is the Bohr magneton, and S is the magnetic induction. In our experiments, the magnetic field was 0.55 T. In this case, the change in the exciton binding energy $\Delta\epsilon_{bind}$ should be approximately 0.05 meV. It is clear that this change is too small and, hence, the magnetic field used in our experiments cannot substantially affect the diffusion length of excitons through the binding energy.

According to Zeeger [10], the magnetic field brings about the Zeeman splitting of exciton states and changes the character of the exciton recombination. It is known that the interaction of excitons with charged shallow impurities is the main channel of exciton decay in semiconductors [11–13]. As follows from the estimates made by Trlifaj [12, 13], the probability of exciton decay in direct-band-gap and indirect-band-gap semiconductors through this channel is five or six orders of magnitude higher than that through the other recombination channels. The probability of decay P of an exciton due to the interaction with a shallow impurity is proportional to the impurity density. According to Singh and Landsberg [11], the probabilities of exciton decay in Si, Ge, and GaP semiconductors are as follows:

$$P_{\text{Si}} \sim 0.48 \times 10^{-5} n_d^+ \text{ s}^{-1},$$

$$P_{\text{Ge}} \sim 0.17 \times 10^{-4} n_d^+ \text{ s}^{-1},$$

$$P_{\text{GaP}} \sim 0.45 \times 10^{-5} n_d^+ \text{ s}^{-1}.$$

Here, n_d^+ is the density of charged shallow impurities in the crystal.

It is evident that the splitting of exciton states in the magnetic field leads to a sharp increase in the probability of interaction of excitons with charged shallow impurities and to a decrease in the exciton diffusion length. Therefore, the change in the photocurrent $\Delta I = [I_{\text{ph}} - I_{\text{ph}}(H)]$ of the solar cells in our experiments can be associated with the decrease in the diffusion length of excitons in the magnetic field.

Another possible factor that can be responsible for the observed change in the photocurrent $\Delta I = [I_{\text{ph}} - I_{\text{ph}}(H)]$ is the decrease in the diffusion length of free charge carriers $L_{e,h}$. As is known, the change in the diffusion length $\Delta L_{e,h}$ of free charge carriers in a magnetic field is small and lies in the range 0.5–1.5%. Hence, the change in the photocurrent ΔI for all semiconductor solar cells should be only negative in sign. However, the change in the photocurrent ΔI for silicon is positive in sign; consequently, the revealed effect cannot be caused by the change in the diffusion length $\Delta L_{e,h}$ of charge carriers.

The photoelectromagnetic effect cannot manifest itself in our experiments, because the electromotive force induced in this case is aligned parallel to the surface of the solar cell.

One more possible factor that can affect the photocurrent is associated with the influence of the magnetic field on the transfer of charge carriers in the solar cells. In order to check this effect, an electric current (from an external power supply) equal to the photocurrent induced under exposure to light was passed through the

sample in the dark. It turned out that, in this case, the electric current remained unchanged after the magnetic field was switched on.

Thus, the observed change in the photocurrent can be explained by the change in the exciton diffusion length due to the increase in the probability of exciton recombination through charged shallow impurities in response to a magnetic field.

Gorban' *et al.* [14] theoretically calculated the photoconversion efficiency for silicon solar cells with a high efficiency under air-mass-zero conditions [6] with due regard for the excitonic effects. It was found that the total contribution of all excitonic effects to the photocurrent in silicon solar cells leads to a decrease in the limiting photoconversion efficiency by 5–10%. Consequently, the photocurrent of the silicon solar cells in our case should increase by ~5–10%. In our experiments, the corresponding increase in the photocurrent reached 3%. Therefore, the results obtained in the present work are in agreement with the theoretical model proposed in [14].

5. CONCLUSIONS

The results obtained in this study have demonstrated that the observed change in the photocurrent of semiconductor solar cells in response to a magnetic field can be associated with the decrease in the exciton diffusion length. This effect can be used to estimate both the exciton diffusion length in semiconductors and the contribution made by excitons to the photocurrent of solar cells.

ACKNOWLEDGMENTS

We would like to thank M.N. Tursunov and S. Dadamukhamedov (Physicotechnical Institute, Tashkent, Uzbekistan) for supplying the solar cells and S.Zh. Karazhanov (Physicotechnical Institute, Tashkent, Uzbekistan), Paul H.M. van Loosdrecht (University of Groningen, The Netherlands), S.S. Saxena (Cavendish Laboratory, University of Cambridge, United Kingdom), and M. Fiebig (MBI, Berlin, Germany) for their participation in discussions of the results and helpful remarks.

REFERENCES

1. M. J. Keevers and M. A. Green, *J. Appl. Phys.* **75**, 4022 (1994).
2. S. Zh. Karazhanov, *J. Appl. Phys.* **82** (10), 5807 (1997).
3. P. P. Altermatt, J. Schmidt, G. Heiser, and A. G. Aberle, *J. Appl. Phys.* **82**, 4938 (1997).
4. R. Corkish, D. S.-P. Chan, and M. A. Green, *J. Appl. Phys.* **79** (1), 195 (1996).

5. I. G. Atabaev, N. A. Matchanov, E. N. Bakhranov, T. M. Saliev, and M. Khojiev, in *Proceedings of the International Conference on Quantum Complexities in Condensed Matter, Bukhara, Uzbekistan, 2003* (Bukhara, 2003), p. 17.
6. M. M. Koltun, *Solar Cells* (Nauka, Moscow, 1987), p. 66 [in Russian].
7. T. Someya, H. Akiyama, and H. Sakaki, *Phys. Rev. Lett.* **76** (16), 2965 (1996).
8. M. Z. Maialle and M. H. Degani, *Semicond. Sci. Technol.* **16**, 982 (2001).
9. A. N. Reznitskiĭ, A. V. Kornievskiĭ, A. A. Kisilev, S. A. Permogorov, L. N. Tenishev, A. A. Klochikhin, S. Yu. Verbin, H. Gerlach, M. Hetterich, M. Grün, and C. Klingshirn, *Fiz. Tverd. Tela* (St. Petersburg) **40** (5), 900 (1998) [*Phys. Solid State* **40** (5), 829 (1998)].
10. K. Zeeger, *Semiconductor Physics* (Springer, Wien, 1973).
11. J. Singh and P. T. Landsberg, *J. Phys. C: Solid State Phys.* **9**, 3627 (1976).
12. M. Trlifaj, *Czech. J. Phys. B* **15**, 780 (1965).
13. M. Trlifaj, *Czech. J. Phys. B* **14**, 227 (1964).
14. A. P. Gorban', A. V. Sachenko, V. P. Kostylyov, and N. A. Prima, *Semicond. Phys., Quantum Electron. Optoelectron.* **3** (3), 322 (2000).

Translated by O. Borovik-Romanova

SEMICONDUCTORS
AND DIELECTRICS

First-Principles Calculations of the Electronic Structure and Plastic Properties of CsCl, CsBr, and CsI Crystals

A. Yu. Kuznetsov, A. B. Sobolev, A. S. Makarov, and A. N. Velichko

Ural State Technical University, ul. Mira 19, Yekaterinburg, 620002 Russia

e-mail: kay@dpt.ustu.ru

Received October 28, 2004

Abstract—The electronic structure and plastic properties are investigated for a number of alkali halide crystals (CsCl, CsBr, CsI). First-principles calculations are carried out within the Hartree–Fock and density-functional theory approximations using several variants of the exchange–correlation functional, including the hybrid exchange technique. The results obtained with the use of five methods are compared with the available experimental data. The tendencies revealed in the variations in the band parameters and plastic properties of the crystals under investigation are analyzed. © 2005 Pleiades Publishing, Inc.

1. INTRODUCTION

Alkali halide crystals are of particular interest because they occupy a special place in solid-state physics as model objects. The most significant feature of the electronic structure of crystals with a CsCl-type lattice is the energy gap E_{g2} between the occupied states of the anions and cations, which is considerably narrower than the “main” band gap E_{g1} . It is this circumstance that makes it possible to observe core–valence band transitions or cross luminescence. A necessary condition for the excitation of cross luminescence is the occurrence of a hole in the core band, and the cross luminescence spectrum itself is determined by radiative transitions of electrons from the valence band formed predominantly by the p states of the halide ions to the highest lying cation core band in which the hole is located [1]. In order to describe the mechanism of cross luminescence quantitatively, it is expedient to calculate the electronic structure of the crystals under investigation. Owing to the recent progress in the development of the electronic structure theory, it has become possible to obtain more reliable information on the band structure of insulators as compared to previous data [2, 3].

This paper reports on the results of investigations into the band structure and plastic properties of CsCl, CsBr, and CsI crystals.

2. COMPUTATIONAL TECHNIQUE

The calculations were performed within the framework of the *ab initio* linear combinations of atomic orbitals (LCAO) method in the Hartree–Fock (HF) approximation with the CRYSTAL98 program package [4, 5]. We also used the Wien2k program package, which provides for calculations within the approximations of augmented plane waves and linearized aug-

mented plane waves (LAPW/APW + lo) on the basis of the density functional theory (DFT) [6].

One of the advantages of the CRYSTAL98 program package is that the calculations of the electronic structure can be carried out both in the framework of the Hartree–Fock approximation and on the basis of the density functional theory. Moreover, the program package includes a variant of the hybrid method in which the DFT exchange and correlation are superposed on the exact Hartree–Fock solution. In this case, the calculations are performed using identical basis sets (BS) and other computational parameters. These features of the CRYSTAL98 program package are unique because they provide a means for analyzing different aspects of the microscopic and macroscopic characteristics of the objects under investigation in the framework of a single program code with the use of several methods [7]. When describing the electronic subsystem of atoms (or ions), we used basis sets of Gaussian-type functions (GTFs) with the appropriate exponents and contraction coefficients [4]. For heavy ions, we used the effective core potentials (ECP), because, in this case, the exact description of the wave functions of the core electrons can be replaced by the effective potentials in order to decrease the computational time [8].

The Wien2k computer code employs a mixed (LAPW/APW + lo) basis set. Here, LAPW is the main basis set and APW + lo is the basis set used for calculating states that are “heavy” for LAPW (for example, the d and f valence states and the states in atoms with a muffin-tin (MT) sphere that is considerably smaller than the other spheres in the cell). This technique substantially increases the efficiency of the calculation (accuracy/computational time) [6].

Crystals of CsCl, CsBr, and CsI have a simple cubic lattice with space group $Pm3m$. The primitive cell consists of two atoms, namely, the cesium atom with coor-

dinates (0,0,0) and the halogen atom with coordinates (1,1,1)($a/2$), where a is the lattice parameter.

In the calculations with the CRYSTAL98 program package for cesium, we used the effective core potentials with a valence basis set of six functions (4, 1, and 1 GTFs for the $5sp$, $6sp$, and $7sp$ shells, respectively) for all the crystals under investigation. For bromine and iodine, we also used the effective core potentials and a basis set with four functions (3 and 1 GTFs for the valence sp shell and one unoccupied sp shell, respectively). For chlorine, we employed the complete basis set of 19 functions (8, 6, 3, 1, and 1 GTFs for the $1s$, $2sp$, $3sp$, $4sp$, and $5sp$ shells, respectively) [9]. Using these basis sets, we calculated the total energies and electronic structures for all three crystals in the framework of several approximations, namely, the Hartree–Fock approximation, the density functional theory approximation, and the hybrid scheme with the above algorithm. In the density functional theory calculations, we used the local density approximation (LDA) with the Dirac–Slater exchange [10] and the Vosko–Wilk–Nusair correlation [11], as well as the gradient approximation to the exchange and correlation in the variant of the generalized gradient approximation (GGA), which was proposed by Perdew and Wang (PWGGA) [12]. For the calculations with the hybrid method, we applied the gradient correction of the exchange functional proposed by Becke [13] in the framework of the Hartree–Fock exchange formalism. In this case, the hybrid exchange potential was used together with the gradient correction of the correlation potential proposed by Perdew and Wang (B3PW). For the density functional theory calculations, the exchange and correlation potentials were augmented in terms of the auxiliary Gaussian basis sets [5].

In the calculations with the Wien2k program package, the radii of the muffin-tin atomic spheres were chosen to be equal to each other. Their values were determined from the condition of coincidence of the lattice constant with the experimental value after minimizing the total energy. We used the exchange–correlation potential in the Perdew–Burke–Ernzerhof generalized gradient approximation [14] with an energy separation of -8.16 eV between the ground and valence states.

The bulk elastic modulus was calculated from the curves describing the dependence of the total energy on the strain of the unit cell. These curves were obtained from the calculated dependence $E(a)$, where a is the calculated lattice constant.

Both the CRYSTAL98 and Wien2k program packages provide a means for determining the elastic constants, which characterize the plastic properties of the

crystals upon deformation of the unit cell, with the use of the strain tensor:

$$\varepsilon = \begin{pmatrix} \varepsilon_{11} & \varepsilon_{12} & \varepsilon_{13} \\ \varepsilon_{21} & \varepsilon_{22} & \varepsilon_{23} \\ \varepsilon_{31} & \varepsilon_{32} & \varepsilon_{33} \end{pmatrix}.$$

The elastic constants of the crystals can be determined by approximating the obtained dependences of the total energy on the strain.

For a simple cubic lattice, there exist only three independent components of the tensor of the elastic constants: C_{11} , C_{12} , and C_{44} . For the cubic crystal system, it is convenient to use a combination of elastic constants, for example, the bulk elastic modulus, which was calculated for the crystals under consideration according to the following relationship [5]:

$$B = \frac{C_{11} + 2C_{12}}{3}.$$

The calculations of the electronic structure and elastic properties were carried out for the equilibrium lattice parameter obtained by minimizing the total energy for each computational algorithm (see table).

3. RESULTS OF CALCULATIONS

The band structures and model densities of states (DOS), which were obtained within the framework of all the computational algorithms used in this work, are qualitatively identical for all the crystals under investigation.

For brevity, the graphic data on the electronic structure are presented only for the B3PW hybrid algorithm. The band structure of the CsCl, CsBr, and CsI crystals is shown in Fig. 1. The model densities of states for the valence band and quasi-core subbands are presented in Fig. 2.

The valence band is formed by the Cl $3p$ shell for the CsCl crystals, the Br $4p$ shell for the CsBr crystals, and the I $5p$ shell for the CsI crystals (i.e., by the p shells of the halogens). The core band top for all the studied crystals is formed by the Cs $5p$ shell.

The table presents the effective charges determined from the Mulliken charge density distribution, the integrated data on the band parameters calculated within different approximations, and the corresponding experimental data obtained using ultraviolet photoelectron spectroscopy [16].

It can be seen from the table that the Hartree–Fock calculations, without invoking additional approximations, lead to a substantial overestimation of the band gap E_{g1} for all three crystals, whereas the calculations performed within the density functional theory give an underestimation of this quantity. These tendencies are characteristic of the methods used for modeling the electronic structure of wide-band-gap insulators. The

Equilibrium lattice parameters a (Å); bulk elastic moduli B (GPa); band parameters E_{g1} , ΔE_v , and E_{g2} (eV); and effective ion charges Q (e) for CsCl, CsBr, and CsI crystals according to calculations in the framework of the Hartree–Fock and density-functional theory approximations

Crystal	Parameter	HF	B3PW	LDA	PWGGA	Wien2k	Experiment
CsCl	a	4.437	4.360	4.180	4.390	4.160	4.120 [2]
	B	14.6	13.0	23.7	11.6	19.2	19.8 [15]
	E_{g1}	12.4	6.2	4.6	4.4	5.5	7.9 [16]
	ΔE_v	0.93	0.90	1.17	0.85	1.3	1.8 [16]
	E_{g2}	5.5	5.3	4.4	5.4	4.3	4.0 [16]
	Q_{Cs^+}	+0.994	+1.054	+1.074	+1.071	–	–
	Q_{Cl^-}	–0.1006	–0.946	–0.926	–0.929	–	–
CsBr	a	4.713	4.615	4.400	4.619	4.330	4.295 [2]
	B	12.9	10.4	17.5	10.7	14.5	18.0 [15]
	E_{g1}	12.3	6.3	4.5	4.8	4.6	7.3 [16]
	ΔE_v	1.04	0.99	1.31	0.93	1.4	2.1 [16]
	E_{g2}	6.5	5.9	4.9	5.8	4.9	4.5 [16]
	Q_{Cs^+}	+1.007	+1.035	+1.076	+1.054	–	–
	Q_{Br^-}	–0.993	–0.965	–0.924	–0.946	–	–
CsI	a	5.018	4.840	4.630	4.860	4.610	4.567 [2]
	B	12.1	9.5	16.3	9.6	13.7	14.4 [15]
	E_{g1}	11.6	6.1	4.3	4.7	3.8	6.5 [16]
	ΔE_v	1.24	1.24	1.58	1.14	2.1	2.4 [16]
	E_{g2}	7.6	6.3	5.3	6.2	4.5	5.2 [16]
	Q_{Cs^+}	+1.006	+1.027	+1.064	+1.044	–	–
	Q_{I^-}	–0.994	–0.973	–0.936	–0.956	–	–

most realistic band gaps were obtained using the B3PW hybrid functional. This is consistent with the results obtained for other objects [17, 18].

4. DISCUSSION

The analysis of the data given in the table and the densities of states presented in Fig. 2 demonstrates that the results obtained by the methods used in this study adequately reflect the tendencies revealed in the variations in the band parameters of the CsCl, CsBr, and CsI crystals. Specifically, the band gap E_{g1} decreases, the valence band width ΔE_v increases, the width of the second energy gap of the crystal E_{g2} increases, and the core band width $\Delta C_s 5p$ decreases.

The characteristic variation in the valence band width ΔE_v in the series of crystals under consideration is associated with the increase in the degree of overlap of the wave functions of the anions with an increase in their ionic radii as the lattice constant increases. The opposite situation is observed for the cation. In this

series of compounds, an increase in the lattice constant leads to a decrease in the core band width $\Delta C_s 5p$ due to the decrease in the degree of overlap of the wave functions.

The effective charges Q obtained from the Mulliken charge density distribution indicate that the chemical bond in these compounds exhibits purely ionic nature (see table).

The calculated data on the plastic properties of the crystals under investigation are important from the standpoint of the possibility of correctly describing the macroscopic physical properties from first principles. Moreover, in this case, the discrepancy between the calculated data and the experimental values characterizes the correctness of the basis sets used. The results of calculations of the bulk elastic moduli (see table) reflect well the experimentally observed tendencies in the variations in the elastic moduli upon changing over from the CsCl crystals to the CsI crystals.

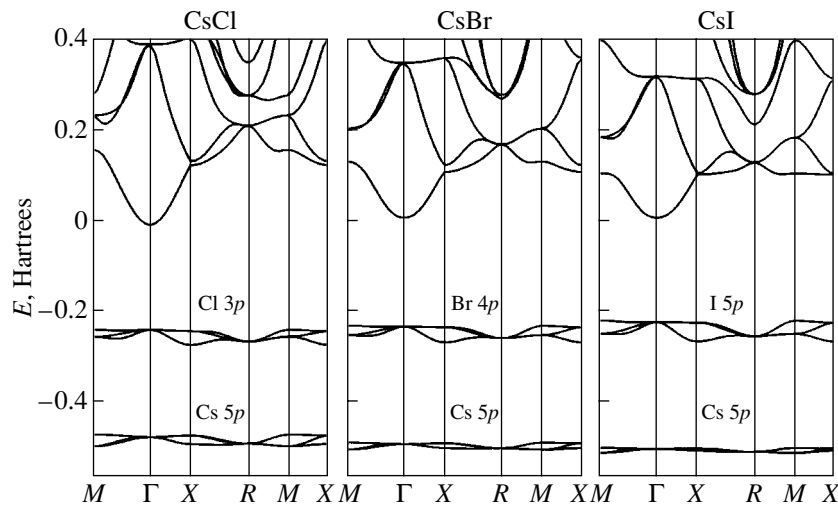


Fig. 1. Band structure of the CsCl, CsBr, and CsI crystals (calculations according to the B3PW hybrid algorithm). The states in the ranges of negative and positive energies correspond to the valence and quasi-core bands and the conduction band, respectively.

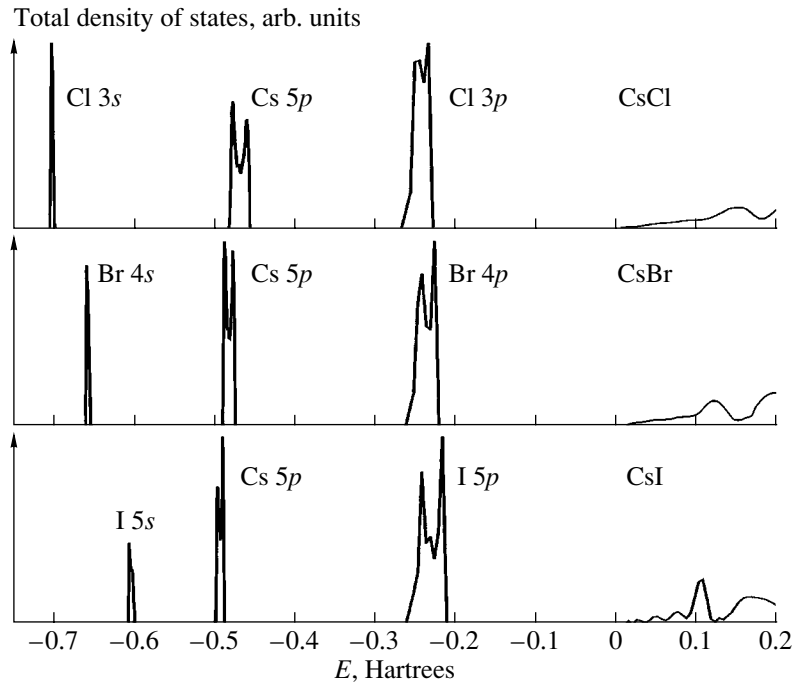


Fig. 2. Model densities of states for the valence band and quasi-core subbands of the CsCl, CsBr, and CsI crystals (calculations according to the B3PW hybrid algorithm). The states in the ranges of negative and positive energies correspond to the valence and quasi-core bands and the conduction band, respectively.

In general, the results obtained are in satisfactory agreement with the experimental data. It should be noted that the “pure” Hartree–Fock calculations, as a rule, give substantially overestimated band gaps but are in excellent agreement with the experimental data on the total energy of the system. The hybrid algorithm leads to more realistic results from the standpoint of the optical experiment.

5. CONCLUSIONS

The above calculations demonstrated that the transitions from the Cs 5*p* band to the valence band correspond to the transparent region of the CsCl, CsBr, and CsI crystals and initiate cross luminescence in the course of the effective generation of core holes in the Cs 5*p* band.

ACKNOWLEDGMENTS

This work was supported by the Russian Foundation for Basic Research, project no. 03-02-16463a.

REFERENCES

1. P. A. Rodnyĭ, *Fiz. Tverd. Tela (Leningrad)* **34** (7), 1975 (1992) [*Sov. Phys. Solid State* **34** (7), 1053 (1992)].
2. S. Satpathy, *Phys. Rev. B: Condens. Matter* **33** (12), 8706 (1986).
3. I. F. Bikmetov and A. B. Sobolev, *Fiz. Tverd. Tela (Leningrad)* **33** (1), 268 (1991) [*Sov. Phys. Solid State* **33** (1), 155 (1991)].
4. R. Dovesi, R. Orlando, C. Roetti, C. Pisani, and V. R. Saunders, *Phys. Status Solidi B* **217** (1), 63 (2000).
5. V. R. Saunders, R. Dovesi, C. Roetti, M. Causa, N. M. Harrison, R. Orlando, and C. M. Zicovich-Wilson, *CRYSTAL98 User's Manual* (University of Torino, Torino, Italy, 1998).
6. P. Blaha, K. Schwarz, G. K. H. Madsen, D. Kvasnicka, and J. Luitz, *Computer Code Wien2k* (Technische Universität, Wien, Austria, 2001).
7. R. A. Evarestov, S. Piskunov, E. A. Kotomin, and G. Borstel, *Phys. Rev. B: Condens. Matter* **67** (6), 064101 (2003).
8. P. J. Hay and W. R. Wadt, *J. Chem. Phys.* **82** (1), 270 (1985).
9. http://www.crystal.unito.it/basis_sets/ptable.html.
10. J. Slater, *The Self-Consistent Field for Molecules and Solids* (McGraw-Hill, New York, 1975; Mir, Moscow, 1978).
11. S. H. Vosko, L. Wilk, and M. Nusair, *Can. J. Phys.* **58** (8), 1200 (1980).
12. J. P. Perdew and Y. Wang, *Phys. Rev. B: Condens. Matter* **45** (23), 13244 (1992).
13. A. D. Becke, *Phys. Rev. A: At., Mol., Opt. Phys.* **38** (6), 3098 (1988).
14. J. P. Perdew, K. Burke, and M. Ernzerhof, *Phys. Rev. Lett.* **77** (18), 3865 (1996).
15. W. N. Mei, L. L. Boyer, M. J. Mehl, M. M. Ossowski, and H. T. Stokes, *Phys. Rev. B: Condens. Matter* **61** (17), 11425 (2000).
16. J. A. Smith and W. Pong, *Phys. Rev. B: Solid State* **12**, 5931 (1975).
17. J. Muscat, A. Wander, and N. M. Harrison, *Chem. Phys. Lett.* **342** (3–4), 397 (2001).
18. S. Piskunov, E. Heifets, R. I. Eglitis, and G. Borstel, *Comput. Mater. Sci.* **29** (2), 165 (2004).

Translated by N. Korovin

SEMICONDUCTORS
AND DIELECTRICS

On the Theory of Diffraction of Light in Photonic Crystals with Allowance for Interlayer Disordering

V. A. Kosobukin

*Ioffe Physicotechnical Institute, Russian Academy of Sciences,
Politekhnicheskaya ul. 26, St. Petersburg, 194021 Russia*

e-mail: Vladimir.Kosobukin@mail.ioffe.ru

Received January 13, 2005

Abstract—Electrodynamic Green’s functions are used to construct an analytical theory of the Bragg diffraction of polarized light in photonic crystals having a close-packed structure. For opal-based photonic crystals, the Bragg diffraction intensity is calculated with allowance for permittivity periodic modulation and for the presence of an optical crystal boundary and interlayer disordering, which usually appears during sample growth. A comprehensive study is made of the effect of the structure disorder caused by the random packing of growth layers on diffraction. For a random constructed twinned fcc structure, the average structure factor and the scattering (diffraction) cross sections (which are dependent on the linear polarization of the incident and scattered waves) are calculated. Numerical examples are used to show that the theory developed can be applied to analyze and process experimental diffraction patterns of real photonic crystals having a close-packed structure disordered in one direction. © 2005 Pleiades Publishing, Inc.

1. INTRODUCTION

The diffraction of waves of different physical nature (x rays, neutrons, electrons) serves as a basis for the methods of studying the atomic structures of crystals [1] and disordered solids [2]. However, the Bragg diffraction of waves in periodic structures (crystals) causes the formation of band gaps in their energy spectra [1, 3]. The main feature of periodic dielectric structures, which are called photonic crystals, is the presence of stop bands, i.e., band gaps in an electromagnetic spectrum for certain directions in a crystal or a total band gap for all directions [4]. These circumstances have attracted particular interest in the creation and study of photonic crystals, which have band gaps in various spectral regions, from the microwave [5, 6] to the visible [6–9] range.

In an x-ray spectrum, stop bands are extremely narrow and a total band gap cannot form, since the permittivity spatial-modulation depth, which specifies the stop-band width, is $\sim 10^{-5}$ [3]. As a consequence, x-ray studies of crystals deal with the angular (directional) measurement of diffraction patterns [1] rather than with the spectroscopy of stop bands. Conversely, primary interest in photonic crystals is provoked by the presence of rather wide band gaps in the visible and long-wavelength regions of an energy spectrum. Such band gaps are analyzed by spectroscopic methods, predominantly by reflection and transmission methods (see, e.g., [6–8, 10, 11]).

Studies of the Bragg diffraction of light in photonic crystals, which began only recently [12–14], have revealed qualitatively new effects as compared to x-ray

diffraction analysis of atomic crystals. In particular, it has been demonstrated [14] that Bragg reflections in visible light not only carry direct information on the spatial structure of a photonic crystal but also serve as indicators of the formation of energy stop bands for certain directions in the crystal. Therefore, a diffraction experiment allows one to empirically distinguish Bragg diffraction channels responsible for the formation of certain stop bands. Hence, it becomes important to analyze the main specific features of the diffraction of light in a real photonic crystal, which are affected by refraction of light, structure disordering, etc.

The purpose of this work is to develop a theory of the Bragg diffraction of visible light for real photonic crystals and to calculate observable quantities of practical importance. The theory is formulated in an analytical form and is based on electrodynamic Green’s functions; the effects of refraction of light by a crystal boundary and diffraction of light by Bragg planes in the crystal are separated. Using photonic crystals based on opals, we also consider the effect of growth interlayer disorder on Bragg diffraction. The article consists of the following sections. In Section 2, we consider the general formulation of the problem. In Section 3, we calculate the diffraction intensity of linearly polarized waves in a photonic crystal. The structure factor is analyzed for individual layers and fcc lattices in Section 4 and for random layer packing in Section 5.

2. GENERAL RELATIONSHIPS

The permittivity of an ideal photonic crystal is taken to be

$$\boldsymbol{\varepsilon}(\mathbf{r}) = \boldsymbol{\varepsilon}_0 + \Delta\boldsymbol{\varepsilon}(\mathbf{r}). \quad (1)$$

Here, the background constant

$$\boldsymbol{\varepsilon}_0 = \frac{1}{V} \int_V d\mathbf{r} \cdot \boldsymbol{\varepsilon}(\mathbf{r}) \quad (2)$$

is obtained by averaging over the crystal volume V . The contribution $\Delta\boldsymbol{\varepsilon}(\mathbf{r}) = \Delta\boldsymbol{\varepsilon}(\mathbf{r} + \hat{\mathbf{a}}_i)$ is periodic with periods equal to the vectors $\hat{\mathbf{a}}_i$ of the basic crystal lattice translations and is responsible for the processes of Bragg diffraction. It can be expanded in a Fourier series,

$$\begin{aligned} \Delta\boldsymbol{\varepsilon}(\mathbf{r}) &= \sum_{\mathbf{b}(\neq 0)} \Delta\boldsymbol{\varepsilon}_{\mathbf{b}} e^{i\mathbf{b} \cdot \mathbf{r}}, \\ \Delta\boldsymbol{\varepsilon}_{\mathbf{b}} &= \frac{1}{v_0} \int_{v_0} d\mathbf{r} \cdot e^{-i\mathbf{b} \cdot \mathbf{r}} \Delta\boldsymbol{\varepsilon}(\mathbf{r}) = \Delta\boldsymbol{\varepsilon}_{-\mathbf{b}}^*, \end{aligned} \quad (3)$$

where v_0 is the unit cell volume, \mathbf{b} is a reciprocal lattice vector, and $\Delta\boldsymbol{\varepsilon}_{\mathbf{b}=0} = 0$. The kinematics of diffraction is specified by the orientation of the crystallographic (Bragg) planes, each of which is perpendicular to the corresponding vector \mathbf{b} . Equation (3) implies the presence of long-range order and becomes invalid for a disordered crystal; however, the short-range order and specific features related to it remain the same, which finds application in the structural analysis of noncrystalline solids [2].

Let the half-space $z > 0$ be occupied by a photonic crystal whose dielectric function is described by Eq. (1) with the background constant expressed by Eq. (2). In a zero approximation ($\Delta\boldsymbol{\varepsilon} = 0$), we only take into account the background permittivity using a function $\varepsilon^0(z)$ that is equal to ε_1 if $z < 0$ and to ε_0 if $z > 0$. A jump in the background permittivity $\varepsilon^0(z)$ defines the optical boundary of the photonic crystal $z = 0$, which provides a mirror reflection of light irrespective of the orientation of the crystallographic planes. For monochromatic light (with frequency ω), the electric field \mathbf{E}^0 , the tensor Green's function \hat{G}^0 of the zero approximation, and the total field \mathbf{E} are defined by the following electrodynamic equations:

$$\begin{aligned} [\text{curl curl} - k_0^2 \varepsilon^0(z) \hat{I}] \{ \mathbf{E}^0(\mathbf{r}), \hat{G}^0(\mathbf{r}, \mathbf{r}'), \mathbf{E}(\mathbf{r}) \} \\ = \{ 0, \hat{I} \delta(\mathbf{r} - \mathbf{r}'), k_0^2 \Delta\boldsymbol{\varepsilon}(\mathbf{r}) \mathbf{E}(\mathbf{r}) \}. \end{aligned} \quad (4)$$

Here, $k_0 = \omega/c$, c is the velocity of light in vacuum, \hat{I} is the unit matrix with the elements $I_{\alpha\beta} = \delta_{\alpha\beta}$, α and β are Cartesian indices, $\delta_{\alpha\beta}$ is the Kronecker delta, and $\Delta\boldsymbol{\varepsilon}(\mathbf{r}) = 0$ outside the crystal. Solutions to Eq. (4), $\mathbf{E}^0(\mathbf{r})$ and $\hat{G}^0(\mathbf{r}, \mathbf{r}')$, satisfying the Maxwell boundary conditions in z at the $z = 0$ plane are given in Appendix I.

When a perturbation $\Delta\boldsymbol{\varepsilon}(\mathbf{r})$ exists, the total electric field outside the photonic crystal (at $z < 0$) is expressed by the relation

$$\begin{aligned} E_{\alpha}(\mathbf{r}) &= E_{\alpha}^0(\mathbf{r}) \\ &+ k_0^2 \sum_{\beta} \int d\mathbf{r}' \cdot G_{\alpha\beta}^0(\mathbf{r}, \mathbf{r}') \Delta\boldsymbol{\varepsilon}(\mathbf{r}') \tilde{E}_{\beta}(\mathbf{r}'); \end{aligned} \quad (5)$$

hereafter, a tilde labels the field in the crystal (at $z' > 0$). The total field taking into account the diffraction of light by the $\Delta\boldsymbol{\varepsilon}(\mathbf{r})$ relief is determined from the integral equation

$$\begin{aligned} \tilde{E}_{\beta}(\mathbf{r}) &= \tilde{E}_{\beta}^0(\mathbf{r}) \\ &+ k_0^2 \sum_{\gamma} \int d\mathbf{r}' \cdot \tilde{G}_{\beta\gamma}^0(\mathbf{r}, \mathbf{r}') \Delta\boldsymbol{\varepsilon}(\mathbf{r}') \tilde{E}_{\gamma}(\mathbf{r}'). \end{aligned} \quad (6)$$

When solving the set of equations (4)–(6), we assume that a wave with linear polarization σ (p or s), an amplitude E_{σ}^{inc} , and a wave vector

$$\begin{aligned} \mathbf{K} &= \boldsymbol{\kappa} + \mathbf{e}_z k_1, \quad \boldsymbol{\kappa} = \sqrt{\varepsilon_1} k_0 \sin\theta (\mathbf{e}_x \cos\varphi + \mathbf{e}_y \sin\varphi), \\ k_1 &= \sqrt{\varepsilon_1} k_0 \cos\theta \end{aligned} \quad (7)$$

is incident from the medium occupying the half-space $z < 0$ on the crystal surface $z = 0$ at an angle θ (Fig. 1a). Hereafter, \mathbf{e}_{α} are the Cartesian unit vectors of the “optical” coordinate system, θ is the polar angle, and φ is the azimuthal angle. At $z < 0$, the first of Eqs. (4) has the solution

$$\begin{aligned} E_{\alpha}^0(\mathbf{r}) &= E_{\sigma}^{\text{inc}} e_{\alpha}^{\sigma}(\mathbf{K}) \exp(i\boldsymbol{\kappa} \cdot \boldsymbol{\rho}) \\ &\times [\exp(ik_1 z) + r_{\sigma}^0(\boldsymbol{\kappa}) \exp(-ik_1 z)] \end{aligned} \quad (8)$$

for the tangential ($\alpha = x, y$) field components and $E_z^0(\mathbf{r}) = (i/k_1^2) d(\boldsymbol{\kappa} \cdot \mathbf{E}^0)/dz$ for the normal component, where $\mathbf{r} = (\boldsymbol{\rho}, z)$, with $\boldsymbol{\rho} = (x, y)$. The polarization unit vectors of field (8) can be expressed as

$$\begin{aligned} \mathbf{e}^p(\mathbf{K}) &= (\mathbf{e}_x \cos\varphi + \mathbf{e}_y \sin\varphi) \cos\theta - \mathbf{e}_z \sin\theta, \\ \mathbf{e}^s(\mathbf{K}) &= -\mathbf{e}_x \sin\varphi + \mathbf{e}_y \cos\varphi \end{aligned} \quad (9)$$

for the p - and s -polarized waves, respectively. The coefficients of reflection r_{σ}^0 of these waves for the boundary $z = 0$ have the form

$$r_p^0 = \frac{\varepsilon_1 k - \varepsilon_0 k_1}{\varepsilon_1 k + \varepsilon_0 k_1}, \quad r_s^0 = \frac{k_1 - k}{k_1 + k}, \quad (10)$$

where $k(\boldsymbol{\kappa}) = \sqrt{\varepsilon_0 k_0^2 - \boldsymbol{\kappa}^2}$. In the crystal ($z > 0$), the tangential components of the external field in Eq. (6) are

$$\tilde{E}_{\alpha}^0(\mathbf{r}) = E_{\sigma}^{\text{inc}} t_{\sigma}^0(\boldsymbol{\kappa}) e_{\alpha}^{\sigma}(\mathbf{Q}) \exp(i\mathbf{Q} \cdot \mathbf{r}), \quad (11)$$

where $t_{\sigma}^0 = 1 + r_{\sigma}^0$. The relation between the vectors

$$\mathbf{Q} = \boldsymbol{\kappa} + \mathbf{e}_z k, \quad k = \sqrt{\varepsilon_0} k_0 \cos \vartheta \quad (12)$$

and \mathbf{K} defined in Eq. (7) is determined from the law of refraction of light $\sqrt{\varepsilon_1} \sin \theta = \sqrt{\varepsilon_0} \sin \vartheta = \kappa/k_0$ (the condition of conservation of vector $\boldsymbol{\kappa}$) at the boundary $z = 0$ (Fig. 1a). Here, the unit vectors $\mathbf{e}^{\sigma}(\mathbf{Q})$ are obtained from Eq. (9) through the substitution of $\theta \rightarrow \vartheta$. The wave vectors of the scattered wave \mathbf{Q}' inside the crystal and \mathbf{K}' outside it are obtained by substituting $\varphi \rightarrow \varphi'$, $\vartheta \rightarrow \pi - \vartheta'$, and $\theta \rightarrow \pi - \theta'$ into Eqs. (7) and (9) for \mathbf{K} and into Eq. (12) for \mathbf{Q} , where the angles ϑ' and θ' are reckoned from the negative direction of the unit vector \mathbf{e}_z . For elastic diffraction, we have $|\mathbf{Q}'| = |\mathbf{Q}| = \sqrt{\varepsilon_0} k_0$ and $|\mathbf{K}'| = |\mathbf{K}| = \sqrt{\varepsilon_1} k_0$.

3. OBSERVABLE OPTICAL QUANTITIES

The Bragg diffraction of waves is coherent elastic scattering and manifests itself at wavelengths comparable to the spatial period of a scattering medium. When an atomic structure is analyzed, the Born approximation of the theory of diffraction (scattering) is usually sufficient [2]. This is also true of opal-like photonic crystals having a small optical contrast, $|\Delta\varepsilon|/\varepsilon_0 \ll 1$. Let us calculate the observable characteristics of diffraction in the Born approximation (in the lowest order in $\Delta\varepsilon$) by putting $\tilde{\mathbf{E}} \approx \tilde{\mathbf{E}}^0(\mathbf{r}) = \tilde{\mathbf{E}}^0(\mathbf{Q}) \exp(i\mathbf{Q} \cdot \mathbf{r})$ in Eqs. (5) and (6) and using Eq. (11). In this case, $\tilde{\mathbf{E}}$ has the same polarization σ as that of the external field \mathbf{E}^0 . The field outside the crystal $\mathbf{E}' = \mathbf{E} - \mathbf{E}^0$ can be found from Eq. (5) using representation (I.1) [see Appendix I] for the Green's function $\hat{G}^0(\mathbf{r}, \mathbf{r}')$. Evaluating the integral with respect to $\boldsymbol{\kappa}$ in representation (I.1) by the method of stationary phase [15, 16] results in the following asymptotic expression for the field radiated into the back hemisphere ($z < 0$, $\sqrt{\varepsilon_1} k_0 r \gg 1$):

$$E'_{\alpha}(\mathbf{r}) = -\frac{i\sqrt{\varepsilon_1} k_0^3 \cos \theta' e^{i\sqrt{\varepsilon_1} k_0 r}}{2\pi r} \times \sum_{\beta} D_{\alpha\beta}^0(0^-, 0^+; \boldsymbol{\kappa}') \left(\int_V d\mathbf{r}' \cdot \Delta\varepsilon(\mathbf{r}') e^{-i\mathbf{q} \cdot \mathbf{r}'} \right) \tilde{E}_{\beta}^0(\mathbf{Q}). \quad (13)$$

For the problem of radiation from the crystal, the tensor Green's function $\hat{D}^0(z, z'; \boldsymbol{\kappa})$ in a mixed $(z, \boldsymbol{\kappa})$ representation is given by Eqs. (I.3), (I.4), (I.6), and (I.7). The vector $\boldsymbol{\kappa}'$ is expressed by Eq. (7) through the angles θ' and φ' of the vector \mathbf{K}' directed to the point of observation $\mathbf{r} = (\boldsymbol{\rho}, z) = r[(\mathbf{e}_x \cos \varphi' + \mathbf{e}_y \sin \varphi') \sin \theta' - \mathbf{e}_z \cos \theta']$

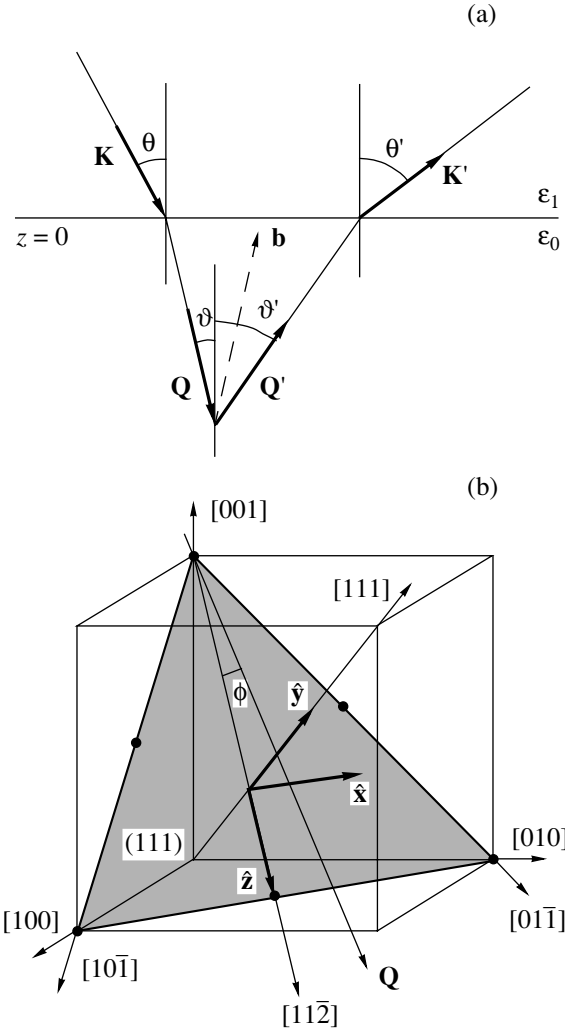


Fig. 1. Geometry of the problem. (a) Wave transformation during diffraction of light in a crystal. The wave vector $\mathbf{K}(\mathbf{K}')$ of the incident (secondary) wave corresponds to the vector $\mathbf{Q}(\mathbf{Q}')$ inside the crystal; $\mathbf{Q} + \mathbf{b} = \mathbf{Q}'$, where \mathbf{b} is a reciprocal-lattice vector. (b) Main directions and planes used to analyze the diffraction of light in an opal fcc lattice.

outside the crystal. In Eq. (13), we introduced a light scattering vector in the crystal,

$$\mathbf{q} = \mathbf{Q}' - \mathbf{Q}. \quad (14)$$

Using Eq. (12) for the wave vectors \mathbf{Q} and \mathbf{Q}' , we find the dimensionless quantities

$$\zeta_{\alpha} = \frac{1}{k_0 \sqrt{\varepsilon_0}} q_{\alpha} \quad (15)$$

in the optical coordinate system with the \mathbf{e}_{α} unit vectors:

$$\begin{aligned} \zeta_x &= \sin \vartheta' \cos \varphi' - \sin \vartheta \cos \varphi, \\ \zeta_y &= \sin \vartheta' \sin \varphi' - \sin \vartheta \sin \varphi, \\ \zeta_z &= -(\cos \vartheta' + \cos \vartheta). \end{aligned} \quad (16)$$

Let us calculate the Poynting vector $S_{\sigma}^{\text{inc}} = c\sqrt{\epsilon_1}|\mathbf{E}_{\sigma}^{\text{inc}}|^2/8\pi$ of incident wave (8) with polarization σ and the Poynting vector $S_{\sigma'} = c\sqrt{\epsilon_1}|\mathbf{E}_{\sigma'}|^2/8\pi$ of scattered wave (13) with polarization σ' outside the crystal (at $z \rightarrow -\infty$). Their ratio $S_{\sigma'}/S_{\sigma}^{\text{inc}}$ specifies the scattering (diffraction) cross section

$$\frac{dW(\sigma \rightarrow \sigma')}{d\Omega'} = \frac{k_0^4}{16\pi^2} \left| \int_V d\mathbf{r} \cdot \Delta\epsilon(\mathbf{r}) e^{-i\mathbf{q} \cdot \mathbf{r}} \right|^2 \cdot |t_{\sigma}^0(\mathbf{\kappa})|^2 \times w_{\sigma\sigma'}(\mathbf{Q}, \mathbf{Q}') \cdot |t_{\sigma'}^0(\mathbf{\kappa}')|^2 \quad (17)$$

in all channels $(\mathbf{K}, \sigma) \rightarrow (\mathbf{K}', \sigma')$ controlled by the polarizations of the incident (σ) and diffracted (σ') waves.

In Eq. (17), $d\Omega' = \sin\theta'd\theta'd\varphi'$ is an element of the solid angle and the quantities

$$\begin{aligned} w_{ss} &= \cos^2(\varphi' - \varphi), \\ w_{pp} &= \cos^2\theta' [\cos\vartheta \cos(\varphi' - \varphi) - \sin\vartheta \tan\vartheta']^2, \\ w_{sp} &= \cos^2\theta' \sin^2(\varphi' - \varphi), \\ w_{ps} &= \cos^2\vartheta \sin^2(\varphi' - \varphi) \end{aligned} \quad (18)$$

are calculated using functions (I.4), (I.6), and (I.7). According to Eqs. (17) and (18), when light is diffracted in the plane of incidence on the crystal ($\varphi' = \varphi$, $w_{sp} = w_{ps} = 0$), depolarization is absent.

According to Eq. (17), the basic specific features of diffraction depend on the quantity

$$\left| \int_V d\mathbf{r} \cdot \Delta\epsilon(\mathbf{r}) e^{-i\mathbf{q} \cdot \mathbf{r}} \right|^2 = v_0 V |\Delta\epsilon_{\mathbf{q}}|^2 S(\mathbf{q}), \quad (19)$$

which includes the structure factor

$$S(\mathbf{q}) = \left| \frac{1}{\sqrt{N}} \sum_{\mathbf{n}} e^{-i\mathbf{q} \cdot \mathbf{R}_{\mathbf{n}}} \right|^2 = \frac{1}{N} \sum_{\mathbf{n}, \mathbf{n}'} e^{-i\mathbf{q} \cdot (\mathbf{R}_{\mathbf{n}} - \mathbf{R}_{\mathbf{n}'})}, \quad (20)$$

where N is the number of unit cells in the crystal volume $V = v_0 N$.

The formfactor

$$\Delta\epsilon_{\mathbf{q}} = \frac{1}{v_0} \int_V d\mathbf{r} \cdot \Delta\epsilon(\mathbf{r}) e^{-i\mathbf{q} \cdot \mathbf{r}} \quad (21)$$

is obtained upon integration over the Wigner–Seitz cell volume v_0 centered at $\mathbf{R}_{\mathbf{n}} = 0$. For an fcc lattice constructed from close-packed dielectric balls of the same size, from Eq. (2) we have $\epsilon_0 = \epsilon_i f + \epsilon_e (1 - f)$, where ϵ_i and ϵ_e are the dielectric constants inside and outside

the balls, respectively, and $f = \pi\sqrt{2}/6 \approx 0.74$ is the packing factor.

The angular and frequency dependences of the scattering intensity are defined by quantities (17). We use them to discuss the Bragg diffraction of light in the case of randomly packed growth layers, which is typical of self-organizing systems, such as synthetic opals [12–14, 17] and the photonic crystals related to them [18]. When opals grow, monodisperse $a\text{-SiO}_2$ balls of a sub-micron diameter a form close-packed (hexagonal) layers. Such two-dimensional crystals form close packing in the growth direction of a three-dimensional structure. The hexagonal layers can occupy the A , B , or C positions known for fcc lattices [1]. In the close-packed structure obtained, the positions of adjacent layers are different and the shift of a layer from one position (e.g., A) to the next position B or C is controlled by a translation vector \mathbf{u}_I or \mathbf{u}_{II} , respectively. In the ideal fcc lattice, only one of these vectors is realized, whereas in real opal crystals the choice of the translation vector \mathbf{u}_I or \mathbf{u}_{II} is a probabilistic event.

The random character of alternation of the A , B , and C layers implies that observable quantities (17) should be averaged and, in the case of close packing of identical balls, only structure factor (20) is averaged. In Eq. (20), we divide the summation over sites $\mathbf{n} = (\mathbf{n}_{||}, l)$ into intralayer (over $\mathbf{n}_{||}$) and interlayer (over l) summation and use the representation $\mathbf{R}_{\mathbf{n}' - \mathbf{n}} \equiv \mathbf{R}_{\mathbf{n}_{||} - \mathbf{n}_{||}, 0} + \mathbf{R}_{0, l' - l}$ where $l(l')$ is the layer number. The random vector $\mathbf{R}_{0, l=1}$ can take two values, \mathbf{u}_I or \mathbf{u}_{II} . In the case of random packing, the averaging of structure factor (20) gives

$$\langle S(\mathbf{q}) \rangle = S_{||}(\mathbf{q}) \langle S_{\perp}(\mathbf{q}) \rangle = S_{||}(\mathbf{q}) \left\langle \frac{1}{L} \sum_{l, l'=1}^L e^{-i\mathbf{q} \cdot \mathbf{R}_{0, l-l'}} \right\rangle. \quad (22)$$

Here, $S_{||}(\mathbf{q})$ is a sum of type (20) relating to a regular layer and L is the number of layers along the structure growth axis.

4. DIFFRACTION BY A REGULAR STRUCTURE

Our next problem is to calculate the quantities that are observed during the diffraction of light in opals with allowance for disordering and to analyze them as applied to the experimental data from [12–14]. First, we discuss the Bragg diffraction of light by two possible regular fcc lattices, namely, $\dots ABCABC\dots$ and $\dots ACBACB\dots$, which are called fcc-I and fcc-II in what follows. The fcc-I lattice is taken to be basic, and all crystallographic planes and directions shown in Fig. 1b are referenced to it. The fcc-I and fcc-II lattices have a common hexagonal layer and are constructed by the translation of this layer by a vector \mathbf{a}_3 , which is equal to \mathbf{u}_I or \mathbf{u}_{II} , respectively.

Close-packed (hexagonal) layers serve as building blocks for constructing both ideal fcc lattices and ran-

dom close-packed structures. Therefore, we first consider the structure factor $S_{\parallel}(\mathbf{q})$, involved in Eq. (22), for a two-dimensional lattice specified by two intralayer basis vectors $\hat{\mathbf{a}}_i$ (with $i = 1, 2$). Summation over layer sites \mathbf{n}_{\parallel} in Eq. (20) gives

$$S_{\parallel}(\mathbf{q}) = \prod_{i=1,2} S_i(\mathbf{q}) = \prod_{i=1,2} \frac{1}{N_i} \frac{\sin^2(N_i \mathbf{q} \cdot \hat{\mathbf{a}}_i/2)}{\sin^2(\mathbf{q} \cdot \hat{\mathbf{a}}_i/2)}, \quad (23)$$

where N_i is the number of sites in the $\hat{\mathbf{a}}_i$ direction. At $N_i \rightarrow \infty$, each multiplier in Eq. (23) transforms into a 2π -periodic delta function

$$S_i(\mathbf{q}) = 2\pi \sum_{m_i} \delta(\mathbf{q} \cdot \hat{\mathbf{a}}_i - 2\pi m_i), \quad (24)$$

where m_i are integers. For a regular packing of hexagonal layers (fcc structure), layer-by-layer summation over l in Eq. (22) gives

$$S_{\perp}(\mathbf{q}) = \frac{1}{L} \frac{\sin^2(L\mathbf{q} \cdot \hat{\mathbf{a}}_3/2)}{\sin^2(\mathbf{q} \cdot \hat{\mathbf{a}}_3/2)} \xrightarrow{L \rightarrow \infty} 2\pi \sum_{m_3} \delta(\mathbf{q} \cdot \hat{\mathbf{a}}_3 - 2\pi m_3), \quad (25)$$

where m_3 are integers.

In the case of a three-dimensional ideal lattice, the maxima of structure factor (22) correspond to the zeros of the delta functions entering into Eqs. (24) and (25), i.e., to the Laue equations $\mathbf{q} \cdot \hat{\mathbf{a}}_i = 2\pi m_i$ with $i = 1, 2, 3$. These equations are used to make a kinematic analysis of diffraction processes in the ideal crystal lattice. For this lattice, we define the reciprocal lattice with basis vectors $\hat{\mathbf{b}}_i$ and expand scattering vector (14) in terms of this basis. Taking into account the identity $(\hat{\mathbf{a}}_i \cdot \hat{\mathbf{b}}_j) = 2\pi\delta_{ij}$, we can verify that the three equations $\mathbf{q} \cdot \hat{\mathbf{a}}_i = 2\pi m_i$ are equivalent to the diffraction conditions

$$\mathbf{q} = \mathbf{b} \equiv \sum_i m_i \cdot \hat{\mathbf{b}}_i \quad (26)$$

or $\mathbf{Q}' - \mathbf{Q} = \mathbf{b}$, which depend on the set of indices (m_1, m_2, m_3) . In terms of the dimensionless quantities of Eq. (15) and $\boldsymbol{\beta} = \mathbf{b}a/(2\pi)$ Eq. (26) takes the form

$$\boldsymbol{\zeta} = \Lambda \boldsymbol{\beta} = \Lambda \sum_i m_i \boldsymbol{\beta}_i, \quad (27)$$

where $\Lambda = \lambda/(a\sqrt{\epsilon_0})$, $\lambda = 2\pi/k_0$ is the light wavelength in vacuum, and a is the fixed distance between the hexagonal-layer sites. At $m_1 = m_2 = m_3 = 0$, diffraction is

absent: $\mathbf{Q}' = \mathbf{Q}$ ($\vartheta' = \vartheta$, $\varphi' = \varphi$), according to Eq. (26). A set of (m_1, m_2, m_3) with at least one nonzero index determines a possible intensity maximum (reflection) caused by diffraction from a system of crystallographic planes normal to the vector \mathbf{b} given by Eq. (26). It is important that m_i are not the (hkl) Miller indices characterizing a diffracting plane and the vector $\mathbf{b}(hkl)$ normal to it.¹ At given values of ϑ and φ , the solutions to Eq. (26) or (27) specify the angles ϑ' and φ' for the propagation direction of diffracted light in the crystal.

Due to the constraint $|\zeta_{\alpha}| \leq 2$ the quantity $\lambda/(a\sqrt{\epsilon_0})$ at which this reflection can appear decreases with increasing indices (m_1, m_2, m_3) in Eq. (27).

To comprehensively analyze the kinematics of diffraction of light in opals, it is sufficient to consider two geometries of light incidence (we call them *A* and *B*). In geometry *A*, light is incident in the (111) plane of the fcc lattice; that is, $\mathbf{Q} \parallel (111)$ (Fig. 1b). In this geometry, recently studied experimentally in [12–14], we can reveal specific features characteristic of the diffraction of light by layers with a two-dimensional hexagonal lattice. In geometry *B*, light is obliquely incident on the (111) plane. In this geometry, which is used in most studies dealing with the optics of opals, the diffraction of light from the one-dimensional lattice formed by the (111) planes become pronounced.

4.1. Geometry A

Let the wave vector of the incident wave $\mathbf{Q} \parallel (111)$ make an angle ϕ with the $[11\bar{2}]$ direction in the fcc lattice (Fig. 1b). By expressing basis vectors (II.1) [see Appendix II] in terms of the optical coordinate system

¹ To describe Bragg diffraction in this work, we use the following coordinate systems: (i) An optical system with unit vectors \mathbf{e}_{α} , in terms of which wave vectors (7) and (12) are specified (Fig. 1a). (ii) A crystallographic system with unit vectors $\hat{\mathbf{X}} \parallel [100]$, $\hat{\mathbf{Y}} \parallel [010]$, and $\hat{\mathbf{Z}} \parallel [001]$, with respect to which the Miller indices of the basic fcc lattice are determined (Fig. 1b). (iii) A system with $\hat{\mathbf{x}}$, $\hat{\mathbf{y}}$, and $\hat{\mathbf{z}}$ unit vectors, in which the contributions from diffraction by hexagonal layers and diffraction by their packed structure are separated using representation (22). Miller indices, which are used to determine systems of (hkl) crystallographic planes and the direction of the wave vector \mathbf{Q} in the crystal, are related to the basic fcc lattice; the relation between the indices (hkl) and the indices $\{m_i\}$ involved in Eq. (26) is given by Eq. (II.4) [see Appendix II]. For the fcc-II lattice, which is obtained by mirror reflection of the basic fcc-I lattice through the (111) plane, it is convenient to consider Eq. (26) using the coordinate system whose unit vectors are obtained by inverting the unit vectors $\hat{\mathbf{x}}$, $\hat{\mathbf{y}}$, and $\hat{\mathbf{z}}$. Then, for a given direction of \mathbf{Q} , the parameters $\{m_i\}$ and the Miller indices (hkl) of the planes responsible for diffraction in the fcc-I and fcc-II lattices would be different in sign.

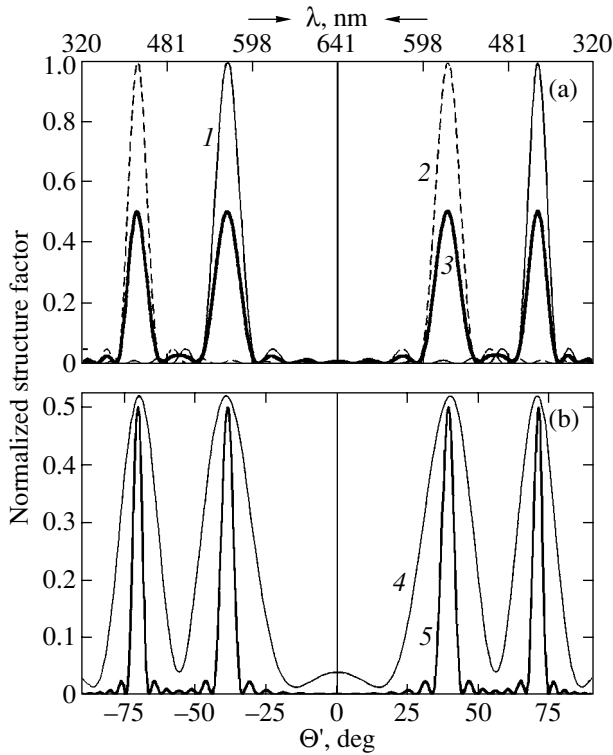


Fig. 2. Dependences of the normalized structure factors $S_{\perp}^{I,II}/L$ on the angle Θ' at $\mathbf{Q} \parallel [11\bar{2}]$ for the fcc-I and fcc-II structures consisting of L hexagonal layers. (a) The values of (1) S_{\perp}^I/L , (2) S_{\perp}^{II}/L , and (3) $(S_{\perp}^I + S_{\perp}^{II})/(2L)$ at $L = 10$. (b) The values of $(S_{\perp}^I + S_{\perp}^{II})/(2L)$ at L equal to (4) 5 and (5) 20. The calculations were performed from Eq. (25) at $a\sqrt{\epsilon_0} = 370$ nm, which corresponds to the radius $a/2 = 135$ nm of a -SiO₂ spheres in an opal with $\sqrt{\epsilon_0} = 1.37$. The dependence of the Bragg wavelength λ on the Θ' angle, which is equal to $\Theta' = \vartheta'$ at $\varphi' = \pi/2$ and to $\Theta' = -\vartheta'$ at $\varphi' = 3\pi/2$, is specified by Eq. (29).

with basis vectors $\mathbf{e}_z = \mathbf{Q}/Q$, we find the vector $\boldsymbol{\beta}$ in Eq. (27) to be

$$\begin{aligned} \boldsymbol{\beta} = & -\mathbf{e}_x \frac{2}{\sqrt{3}} \left[m_1 \sin\left(\phi + \frac{\pi}{3}\right) + m_2 \sin\left(\phi - \frac{\pi}{3}\right) \right] \\ & + \mathbf{e}_z \frac{2}{\sqrt{3}} \left[m_1 \cos\left(\phi + \frac{\pi}{3}\right) + m_2 \cos\left(\phi - \frac{\pi}{3}\right) \right] \\ & + \mathbf{e}_y \alpha \left(m_3 - \frac{m_1 + m_2}{3} \right). \end{aligned} \quad (28)$$

Here, $\alpha = a/A$, where A is the interlayer distance ($\alpha = \sqrt{3}/2$ for the fcc lattice). Substituting Eqs. (16) and (28) into Eq. (27), we find that the x and z components of vector equation (27) are independent of α ; that is, their form is formally identical to that in the case of a single layer ($\alpha \rightarrow 0$). This pair of equations is invari-

ant with respect to rotations of the vector \mathbf{Q} through angles ϕ that are multiples of $\pi/3$ if the indices m_1 and m_2 are properly chosen for each of the equivalent positions of the hexagonal layer. In the case of $\mathbf{Q} \parallel [11\bar{2}]$ ($\phi = 0$), these equations $\zeta_x = \Lambda(m_2 - m_1)$ and $\zeta_z = \Lambda(m_1 + m_2)/\sqrt{3}$ with $m_1 = m_2 = -1$ have solutions $\varphi'_1 = \pi/2$ and $\varphi'_2 = 3\pi/2$. The corresponding condition for Bragg diffraction by the layer is

$$\lambda_{[11\bar{2}]}(\vartheta') = \frac{a\sqrt{3\epsilon_0}}{2}(1 + \cos\vartheta'). \quad (29)$$

Expression (29) describes the dispersion of light in the angle $0 < \vartheta' < \pi/2$ made in the back hemisphere by the diffraction direction in the $(\bar{1}10)$ plane with the (111) plane; here, $a\sqrt{3\epsilon_0}/2 < \lambda < a\sqrt{3\epsilon_0}$.

In order to analyze the diffraction of light by three-dimensional fcc lattices, we take into account the third of equations (27), $\zeta_y = \Lambda\alpha(3m_3 - m_1 - m_2)$. With allowance for Eq. (29) at $m_1 = m_2 = -1$, we obtain

$$\tan \frac{\vartheta'}{2} = \frac{\sqrt{3}\alpha}{2 \sin\varphi'_{1,2}} \left(m_3 + \frac{2}{3} \right). \quad (30)$$

For the fcc-I lattice, Eq. (30) has two solutions: $\vartheta'_1 = 70.5^\circ$ at $\varphi'_1 = \pi/2$ and $m_3 = 0$ and $\vartheta'_2 = 39^\circ$ at $\varphi'_2 = 3\pi/2$ and $m_3 = -1$. Relation (II.4) shows that these solutions correspond to diffraction of light by the (002) and $(\bar{1}\bar{1}1)$ planes, respectively. At other values of m_3 , it follows from Eq. (30) that $\vartheta' > \pi/2$; that is, the light is diffracted into the forward hemisphere. Similarly, for the fcc-II lattice, there exist two solutions in the back hemisphere; they are mirror-symmetric with respect to the previous solutions about the (111) plane: $\vartheta'_1 = 39^\circ$ at $\varphi'_1 = \pi/2$ and $m_3 = 1$ and $\vartheta'_2 = 70.5^\circ$ at $\varphi'_2 = 3\pi/2$ and $m_3 = 0$.

Figure 2 shows the angular dependences of the normalized structure factors for the fcc-I and fcc-II lattices consisting of a small number L of hexagonal layers. The quantities $S_{\perp}^{I,II}(\mathbf{q})/L$ are calculated from Eq. (25) as functions of the angle $\Theta' = \vartheta'$ at $\varphi' = \pi/2$, i.e., above the (111) plane, and of the angle $\Theta' = -\vartheta'$ at $\varphi' = 3\pi/2$, i.e., below the (111) plane. The $\lambda(\Theta')$ scale corresponds to Eq. (29). As follows from Fig. 2a, S_{\perp}^I/L is maximum at the angles calculated from Eq. (30) ($\Theta' = -39^\circ$ and 70.5°) and S_{\perp}^{II}/L is maximum at $\Theta' = -70.5^\circ$ and 39° .

Figure 2 also shows the quantity $(S_{\perp}^I + S_{\perp}^{II})/(2L)$, which is the form factor of a mixture of the fcc-I and fcc-II structures having a common growth axis and the same number of layers L . As is seen from Fig. 2b, the broadening of all diffraction maxima $|\Delta\Theta'| \sim 1/L$ is related to

a small number of layers in the fcc structures. According to Eq. (25), $S_{\perp}^{I,II}(\mathbf{q})/L = 1$ at $L = 1$.

4.2. Geometry B

To consider the case where light is incident at an angle $\vartheta \neq \pi/2$ to the $[\bar{1}\bar{1}\bar{1}]$ direction in the plane that makes an angle ϕ with the $[11\bar{2}]$ direction, we express quantity (28) in terms of the unit vectors $\mathbf{e}'_x = \mathbf{e}_x$, $\mathbf{e}'_y = \mathbf{e}_y$, and $\mathbf{e}'_z = -\mathbf{e}_z$:

$$\begin{aligned} \boldsymbol{\beta} = & -\mathbf{e}'_x \frac{2}{\sqrt{3}} \left[m'_1 \sin\left(\phi + \frac{\pi}{3}\right) + m'_2 \sin\left(\phi - \frac{\pi}{3}\right) \right] \\ & + \mathbf{e}'_y \frac{2}{\sqrt{3}} \left[m'_1 \cos\left(\phi + \frac{\pi}{3}\right) + m'_2 \cos\left(\phi - \frac{\pi}{3}\right) \right] \\ & + \mathbf{e}'_z \alpha \left(\frac{m'_1 + m'_2}{3} - m'_3 \right). \end{aligned} \quad (31)$$

It follows that diffraction is independent of ϕ at $m'_1 = m'_2 = 0$. In this case, at $m'_3 \geq 1$, Eq. (27) with $\boldsymbol{\beta} = -m'_3 \alpha \mathbf{e}'_z$ describes diffraction from a one-dimensional chain of structureless planes with specular reflection of light from them ($\vartheta' = \vartheta$ and $\varphi' = \varphi$). The Bragg wavelengths

$$\lambda(\vartheta) = \frac{2}{m'_3} \frac{a\sqrt{\epsilon_0}}{\alpha} \cos \vartheta \quad (32)$$

correspond to the period a/α of this chain in a homogeneous medium with dielectric constant ϵ_0 . At $m'_3 = 1$, from Eq. (32) we find the long-wavelength limit $\lambda(0) = 2a\sqrt{2\epsilon_0/3}$ for diffraction by a system of planes with $\mathbf{b} \parallel [111]$ in the fcc lattice. At $m'_3 \geq 2$, we find the upper boundaries $\lambda(0)/m'_3$ for higher order diffraction. These results are identical for the fcc-I and fcc-II lattices. Note that diffraction of the type $m'_1 = m'_2 = 0$ and $m'_3 = 1$ manifests itself in the spectra of light reflection (transmission) by the (111) growth plane of opals, which have been studied in most works. The diffraction pattern becomes much more complex as the wavelength decreases when $m'_1 \neq 0$ or $m'_2 \neq 0$ in Eq. (31).

According to Eq. (17), the maximum of the structure factor specified by the vector \mathbf{b} can be observed if the corresponding quantity $|\Delta\epsilon_{\mathbf{b}}|^2$ is sufficiently large. The simplest estimate of the form factor $\Delta\epsilon_{\mathbf{b}}$ can be obtained from Eq. (21) in the isotropic approximation, where the

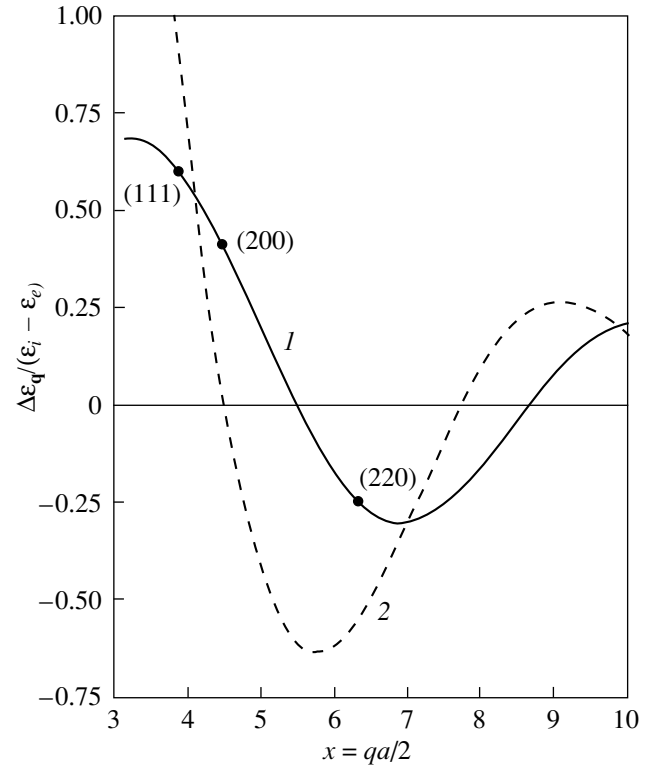


Fig. 3. Dependence of $\Delta\epsilon_{\mathbf{q}}/(\epsilon_i - \epsilon_e)$ on $x = |\mathbf{q}|a/2$ as calculated from Eq. (33) (curve 1) and the function $F(x) = (\pi/\sqrt{2})(\sin x - x \cos x)/x^3$ (curve 2). The computations were carried out for an fcc lattice ($f = 0.74$). The (hkl) points in curve 1 correspond to the conditions $|\mathbf{q}| = |\mathbf{b}(hkl)|$ with reciprocal lattice vectors $\mathbf{b}(hkl)$ related to the (111), (200), and (220) planes.

polyhedral Wigner–Seitz cell of the fcc lattice is replaced by a sphere of the same volume ($v_0 = a^3/\sqrt{2}$). Evaluating integral (21) gives

$$\Delta\epsilon_{\mathbf{q}} = (\epsilon_i - \epsilon_e) \left[F\left(\frac{qa}{2}\right) - F\left(\frac{qa}{2f^{1/3}}\right) \right]. \quad (33)$$

Here, $F(x) = (\pi/\sqrt{2})(\sin x - x \cos x)/x^3$; f is the packing factor for balls forming an fcc lattice; and ϵ_i and ϵ_e are the permittivities inside and outside the balls, respectively. In Fig. 3, curve 1 shows the normalized form factor $F(x) - F(x/f^{1/3})$ as compared to the form factor $F(x)$ of an individual ball (Fig. 3, curve 2). The (hkl) points in curve 1 give the values of $\Delta\epsilon_{\mathbf{b}}/(\epsilon_i - \epsilon_e)$ calculated from Eq. (33) at $\mathbf{q} = \mathbf{b}(hkl)$ for the (111), (200), and (220) planes. Below, we consider how the specific features of the diffraction of light described above for an fcc lattice are modified when we take into account the growth disordering of opals.

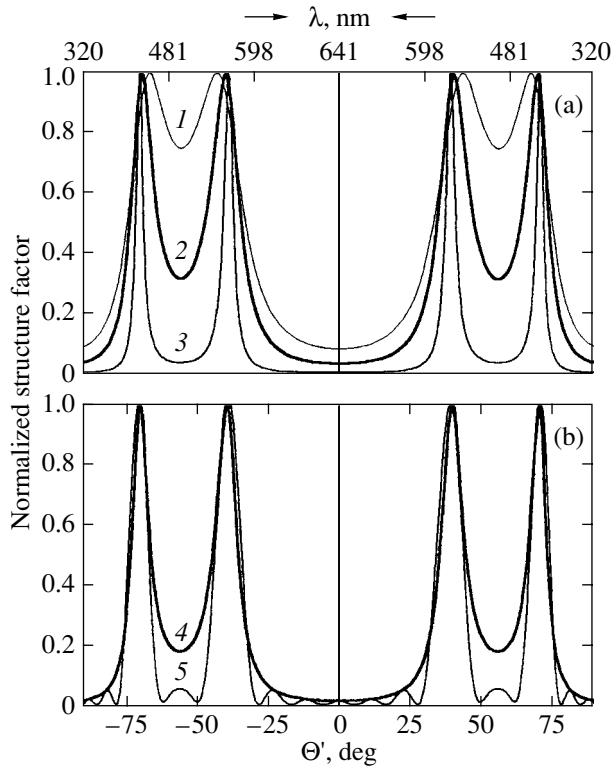


Fig. 4. Dependence of the average structure factor on Θ' at $\mathbf{Q} \parallel [11\bar{2}]$. (a) Normalized functions $\langle S_{\perp} \rangle$ given by Eq. (41) for randomly packed hexagonal layers with various values of p : (1) 0.65, (2) 0.75, and (3) 0.9. (b) Normalized function $\langle S_{\perp} \rangle$ given by Eq. (41) for randomly packed hexagonal layers with $p = 0.8$ and (5) the function $(S_{\perp}^I + S_{\perp}^{II})/L$ given by Eq. (25) for a mixture of the fcc-I and fcc-II structures with $L = 10$. The calculations were performed at $\alpha = \sqrt{3}/2$ with the same parameters as those in Fig. 2. The Bragg wavelength λ is related to the angle Θ' through Eq. (29).

5. DIFFRACTION BY RANDOM CLOSE-PACKED LAYERS

For randomly packed L hexagonal layers, the average value of the structure factor entering into Eq. (22) can be written as [19]

$$\langle S_{\perp}(\mathbf{q}) \rangle = \sum_{l=-L+1}^{L-1} \left(1 - \frac{|l|}{L}\right) \langle e^{-i\mathbf{q} \cdot \mathbf{R}_{0,l}} \rangle. \quad (34)$$

As noted above, for close-packed hexagonal layers, each subsequent layer is obtained through translation of the previous layer by the vector \mathbf{u}_I or \mathbf{u}_{II} . We introduce a stacking correlation coefficient p , which is equal to the probability of the vectors of two sequential layer translations being the same. At $p = 0$, we have a three-dimensional hexagonal close-packed (hcp) lattice. Upon translation by the vector $\mathbf{u}_I(\mathbf{u}_{II})$, we have $p = 1$ and the fcc-I (fcc-II) structure is formed. If $0 < p < 1$, we have a statistical mixture of the fcc-I and fcc-II

structures with stacking faults. In the last case, the matrix

$$\hat{M}(\mathbf{q}) = \begin{pmatrix} p e^{-i\mathbf{q} \cdot \mathbf{u}_I} & (1-p) e^{-i\mathbf{q} \cdot \mathbf{u}_{II}} \\ (1-p) e^{-i\mathbf{q} \cdot \mathbf{u}_I} & p e^{-i\mathbf{q} \cdot \mathbf{u}_{II}} \end{pmatrix} \quad (35)$$

specifies the average value of the phase factor $\langle e^{-i\mathbf{q} \cdot \mathbf{R}_{0,l}} \rangle = (1/2) \mathbf{e}^T \cdot \hat{M}(\mathbf{q}) \cdot \mathbf{e}$, where \mathbf{e} is a matrix vector whose transposition gives $\mathbf{e}^T = (1, 1)$; therefore, $\mathbf{e}^T \cdot \mathbf{e} = 2$. Taking into account the fact that, at $l > 0$,

$$\langle e^{-i\mathbf{q} \cdot \mathbf{R}_{0,l}} \rangle = \frac{1}{2} \mathbf{e}^T \cdot \hat{M}^l(\mathbf{q}) \cdot \mathbf{e}, \quad (36)$$

from Eq. (34) we obtain

$$\langle S_{\perp}(\mathbf{q}) \rangle = \frac{1}{2} \mathbf{e}^T \cdot \left\{ \hat{I} + \sum_{l=1}^{L-1} \left(1 - \frac{l}{L}\right) [\hat{M}^l + (\hat{M}^*)^l] \right\} \cdot \mathbf{e}. \quad (37)$$

Summation in this formula to an accuracy of terms of the order $1/L \ll 1$ ($L \rightarrow \infty$) gives

$$\langle S_{\perp}(\mathbf{q}) \rangle = \frac{1}{2} \mathbf{e}^T \cdot [(\hat{I} - \hat{M})^{-1} + (\hat{I} - \hat{M}^*)^{-1} - \hat{I}] \cdot \mathbf{e}, \quad (38)$$

where \hat{I} is the unit matrix. Using the elements of matrix (35), we obtain

$$\langle S_{\perp}(\mathbf{q}) \rangle = \frac{p(1-p) \sin^2 \Delta\psi}{(1-2p) \sin^2 \psi_0 + p^2 (1 - 2 \cos \psi_0 \cos \Delta\psi + \cos^2 \Delta\psi)}, \quad (39)$$

where

$$\Delta\psi = \frac{1}{2} \mathbf{q} \cdot (\mathbf{u}_I - \mathbf{u}_{II}), \quad \psi_0 = \frac{1}{2} \mathbf{q} \cdot (\mathbf{u}_I + \mathbf{u}_{II}). \quad (40)$$

In geometry A, where $\mathbf{Q} \parallel [11\bar{2}]$ and $\mathbf{u}_{I,II} = a(\hat{\mathbf{y}}/\alpha \pm \hat{\mathbf{z}}/\sqrt{3})$, we can use Eqs. (39) and (40) to find the average structure factor

$$\langle S_{\perp}(\mathbf{q}) \rangle = \frac{3}{2} \frac{p(1-p)}{(2p-1)(\cos 2\psi_0 - 1) + p^2(2\cos \psi_0 + 5/2)} \quad (41)$$

at wavelength (29); here, $\psi_0 = 4\pi \tan(\vartheta'/2)/(\alpha\sqrt{3})$. Note that, according to this derivation, in Eq. (13) from [12], which is a particular case of Eq. (41), the cotangent should be replaced by the tangent.

Structure factor (41) normalized to unity in its maxima is shown in Fig. 4a for random close-packed ($\alpha = \sqrt{3}/2$) layers having different correlation coefficients p . Curves 1–3 show the dependence of structure factor (41) on angle Θ' (which is equal to ϑ' at $\varphi' = \pi/2$ and to

$-\partial'$ at $\varphi' = 3\pi/2$) and on wavelength (29). It is seen that, as p increases in the range $p > 0.5$, the function $\langle S_{\perp} \rangle$ changes substantially and, at $1 - p \ll 1$, approaches the sum of the angular dependences characteristic of the fcc-I and fcc-II lattices with limited thicknesses. This conclusion follows from Fig. 4b, where the normalized value of $\langle S_{\perp} \rangle$ calculated for a random packing with $p = 0.8$ (curve 4) is compared with the structure factor $(S_{\perp}^I + S_{\perp}^{II})/L$ corresponding to a mixture of the fcc-I and fcc-II structures with the number of layers $L = 10$ (Fig. 4b, curve 5). Near maxima, these dependences are seen to be rather close to each other. If we take into account the good agreement between the angular dependence of $\langle S_{\perp} \rangle$ with $p = 0.8$ and experimental data [12] and the similarity between this dependence and the angular dependence of $(S_{\perp}^I + S_{\perp}^{II})/(2L)$ with $L = 10$, we can conclude that the latter dependence also agrees with experiment. Therefore, the characteristic number of hexagonal layers in fcc domains in the opals experimentally studied in [12] is $\bar{L} \cong 10$.

Thus, in random close-packed hexagonal layers, regular regions (domain) $ABCABC$ and $ACBACB$ of fcc structures alternate with each other. The alternation of these domains means the formation of a twin structure [12]. The length of domains forming twins is random because of random breaks in the regular packing. For stacking correlation coefficients p close to unity, there exist domains with a fairly large number of layers L ; these domains can generate specific features characteristic of fcc lattices in the diffraction patterns. As shown above, this behavior allows us to use the angular dependences of the diffraction intensity to estimate both the correlation coefficient p [12] and the characteristic fcc domain size. Therefore, it seems interesting to theoretically find the length distribution of fcc domains at a given p and to calculate the average length and its dispersion with allowance for the coexistence of fcc and hcp domains, stacking faults, etc.

In concluding this section, we note that the effects of interlayer disordering discussed above will not manifest themselves in the standard geometry of mirror reflection of light by the (111) planes, that is, for diffraction with $m'_1 = m'_2 = 0$ at wavelengths (32). Indeed, in this case, we have $\mathbf{u}'_I = \mathbf{u}'_{II}$ and $\langle e^{-iq \cdot \mathbf{R}_{0,\nu}} \rangle = e^{-iq \cdot \mathbf{u}'_{I,II}}$ in Eq. (34); that is, the contribution of this diffraction process to structure factor (34) is independent of random layer packing if the layers are equally spaced. However, the effects of a twin structure should manifest themselves in nonspecular diffraction processes with $m'_1 \neq 0$ or $m'_2 \neq 0$.

6. CONCLUSIONS

In this work, we have developed a theory of the Bragg diffraction of linearly polarized light in photonic

crystals with allowance for its refraction by a dielectric interface and for the effects of interlayer disordering in a sample. The quantities that can be observed using diffraction (as a function of the scattering direction) and spectroscopy (as a function of the probing-light frequency) methods have been calculated. The theory can be applied to analyze the crystal structure of opals and to refine the quantitative characteristics of the visualized patterns of stop bands in photonic crystals [14]. The results of analyzing the intensities of diffraction maxima agree well with the diffraction experimental data from [12], which demonstrate the existence of a random fcc twin structure in synthetic opals. By comparing the theoretic results obtained for two models of domains having an fcc lattice with the experimental data from [12], we have estimated the characteristic domain size along the sample growth direction. To develop the theory, we used the Born approximation for light scattering; that is, strictly speaking, the theory can only be applied to describe the effects of simple diffraction in photonic crystals with relatively weak permittivity modulation (such as opals). However, this theory can be directly generalized using self-consistent solutions to the equations for an electromagnetic field in a crystal. This generalization is necessary in relatively rare cases of multiple Bragg diffraction [20] or in the case of diffraction in photonic crystals with very strong permittivity modulation.

APPENDIX I

Solution of the Electrodynamical Problem

In the case where the dielectric tensor has the form $\epsilon^0(z, \omega)\delta_{\alpha\beta}$, with the function $\epsilon^0(z, \omega)$ being equal to ϵ_1 at $z < 0$ and to ϵ_0 at $z > 0$, the components of the Green's function that is the solution to the second of Eqs. (4) are given by the integral Fourier representation

$$G_{\alpha\beta}^0(\mathbf{r}, \mathbf{r}'; \omega) = \int \frac{d^2\kappa}{(2\pi)^2} \exp[i\kappa \cdot (\boldsymbol{\rho} - \boldsymbol{\rho}')] D_{\alpha\beta}^0(z, z'; \kappa, \omega). \quad (\text{I.1})$$

Here, $\mathbf{r} = (\boldsymbol{\rho}, z)$, $\boldsymbol{\rho} = \rho(\mathbf{e}_x \cos\phi + \mathbf{e}_y \sin\phi)$, $\kappa = \kappa(\mathbf{e}_x \cos\varphi + \mathbf{e}_y \sin\varphi)$, and

$$D_{\alpha\beta}^0(z, z'; \kappa, \omega) = \sum_{\mu, \nu} T_{\alpha\mu}(\varphi) d_{\mu\nu}^0(z, z'; \kappa, \omega) T_{\beta\nu}(\varphi) \quad (\text{I.2})$$

for a given direction of the wave vector κ . The nonzero elements of the angle φ rotation matrix are $T_{xx} = T_{yy} = \cos\varphi$, $-T_{xy} = T_{yx} = \sin\varphi$, and $T_{zz} = 1$. Tensor (I.2) has the form

$$\hat{D}^0 = \begin{pmatrix} d_{xx}^0 \cos^2 \varphi + d_{yy}^0 \sin^2 \varphi & (d_{xx}^0 - d_{yy}^0) \sin \varphi \cos \varphi & d_{xz}^0 \cos \varphi \\ (d_{xx}^0 - d_{yy}^0) \sin \varphi \cos \varphi & d_{xx}^0 \sin^2 \varphi + d_{yy}^0 \cos^2 \varphi & d_{xz}^0 \sin \varphi \\ d_{zx}^0 \cos \varphi & d_{zx}^0 \sin \varphi & d_{zz}^0 \end{pmatrix}. \quad (\text{I.3})$$

The components $d_{\alpha\beta}^0(z, z'; \kappa, \omega)$ are obtained from the second of Eqs. (4) with the wave vector $\kappa = \mathbf{e}_x \kappa$ ($\varphi = 0$) and with the operator $\{\partial/\partial \mathbf{r}\} = \{i\kappa, 0, d/dz\}$. These components are separated for indices x and z in the case of p polarization and for index y in the case of s polarization. The functions $d_{\alpha\beta}^0(z, z')$ at $z = 0$ satisfy the Maxwellian boundary conditions for z and can be expressed in terms of the reflectivities r_σ^0 given by Eq. (10) and of $t_\sigma^0 = 1 + r_\sigma^0$.

We now give expressions for the components of the Green's function $d_{\alpha\beta}^0(z, z'; \kappa, \omega)$ by writing them in the form $d_{\alpha\beta}^0(m, m')$, where m and m' are the number of media (1 or 2) that contain the point of observation (z) and the source (z'), respectively; that is, $m = 1$ at $z < 0$ and $m' = 2$ at $z' > 0$. For s -polarized waves, we have

$$d_{yy}^0(1, 2') = \frac{i}{2k_1} t_s^0 \exp(-ik_1 z + ikz'), \quad (\text{I.4})$$

$$d_{yy}^0(2, 2') = \frac{i}{2k} \{ \exp[ik|z - z'|] - r_s^0 \exp[ik(z + z')] \}, \quad (\text{I.5})$$

and, for p -polarized waves, we have

$$d_{xx}^0(1, 2') = \frac{ik_1}{2k_0^2 \varepsilon_1} t_p^0 \exp(-ik_1 z + ikz'), \quad (\text{I.6})$$

$$d_{zz}^0(1, 2') = \frac{\kappa}{k_1} d_{xz}^0(1, 2') = \frac{\kappa}{k} d_{zx}^0(1, 2') = \frac{\kappa^2}{k_1 k} d_{xx}^0(1, 2'), \quad (\text{I.7})$$

$$d_{xx}^0(2, 2') = \frac{ik}{2k_0^2 \varepsilon_0} \{ \exp[ik|z - z'|] - r_p^0 \exp[ik(z + z')] \}, \quad (\text{I.8})$$

$$d_{zx}^0(2, 2') = -\frac{i\kappa}{2k_0^2 \varepsilon_0} \{ \text{sgn}(z - z') \exp[ik|z - z'|] + r_p^0 \exp[ik(z + z')] \}, \quad (\text{I.9})$$

$$d_{xz}^0(2, 2') = -\frac{i\kappa}{2k_0^2 \varepsilon_0} \{ \text{sgn}(z - z') \exp[ik|z - z'|] - r_p^0 \exp[ik(z + z')] \}, \quad (\text{I.10})$$

$$d_{zz}^0(2, 2') = \frac{ik}{2k_0^2 \varepsilon_0} \left(\frac{\kappa}{k} \right)^2 \{ \exp[ik|z - z'|] + r_p^0 \exp[ik(z + z')] \} - \frac{\delta(z - z')}{\varepsilon_0 k_0^2}. \quad (\text{I.11})$$

APPENDIX II

In this work, we use the basis vectors

$$\hat{\mathbf{a}}_1 = \frac{a}{2}(-\hat{\mathbf{x}} + \sqrt{3}\hat{\mathbf{z}}), \quad \hat{\mathbf{a}}_2 = \frac{a}{2}(\hat{\mathbf{x}} + \sqrt{3}\hat{\mathbf{z}}), \quad (\text{II.1})$$

$$\hat{\mathbf{a}}_3 = a\left(\frac{1}{\sqrt{3}}\hat{\mathbf{z}} + \frac{1}{\alpha}\hat{\mathbf{y}}\right),$$

where the following unit vectors of an fcc lattice are involved: $\hat{\mathbf{x}} \parallel [\bar{1}10]$, $\hat{\mathbf{y}} \parallel [111]$, and $\hat{\mathbf{z}} \parallel [11\bar{2}]$ (Fig. 1b). The vectors $\hat{\mathbf{a}}_1$ and $\hat{\mathbf{a}}_2$ specify the lattice sites of a hexagonal layer with an intersite distance a . The introduction of the basis translation vector $\hat{\mathbf{a}}_3$, which depends on the parameter $\alpha = a/A$, allows us to consider a set of lattices that are topologically equivalent to the fcc lattice but have different distances A between the hexagonal layers. The limiting cases of these structures are the fcc lattice at $A = a\sqrt{2/3}$ ($\alpha = \alpha_{\max} = \sqrt{3/2}$) and individual layers at $A \rightarrow \infty$, $\alpha \rightarrow 0$.

Based on Eqs. (II.1), the basis vectors of the reciprocal lattice can be found to be

$$\hat{\mathbf{b}}_1 = \frac{2\pi}{a} \left(-\hat{\mathbf{x}} + \frac{1}{\sqrt{3}}\hat{\mathbf{z}} - \frac{\alpha}{3}\hat{\mathbf{y}} \right), \quad (\text{II.2})$$

$$\hat{\mathbf{b}}_2 = \frac{2\pi}{a} \left(\hat{\mathbf{x}} + \frac{1}{\sqrt{3}}\hat{\mathbf{z}} - \frac{\alpha}{3}\hat{\mathbf{y}} \right), \quad \hat{\mathbf{b}}_3 = \frac{2\pi}{a} \alpha \hat{\mathbf{y}}.$$

At $\alpha \rightarrow 0$, basis vectors (II.2) transform into the vectors

$$\hat{\mathbf{b}}_1^0 = \frac{2\pi}{a} \left(-\hat{\mathbf{x}} + \frac{1}{\sqrt{3}}\hat{\mathbf{z}} \right), \quad (\text{II.3})$$

$$\hat{\mathbf{b}}_2^0 = \frac{2\pi}{a} \left(\hat{\mathbf{x}} + \frac{1}{\sqrt{3}}\hat{\mathbf{z}} \right), \quad \hat{\mathbf{b}}_3^0 = 0,$$

which correspond to the individual-layer model. The indices m_i in expansion (26) of the reciprocal lattice vector \mathbf{b} in terms of basis vectors (II.2) are related to the Miller indices (hkl) of the plane normal to the vector \mathbf{b} :

$$\begin{aligned} h : k : l \\ = (m_1 - m_2 + m_3) : (-m_1 + m_2 + m_3) : (-m_1 - m_2 + m_3). \end{aligned} \quad (\text{II.4})$$

ACKNOWLEDGMENTS

The author is grateful to M.F. Limonov and A.V. Sel'kin for helpful discussions.

This work was supported by the Russian Foundation for Basic Research, project no. 04-02-17592.

REFERENCES

1. C. Kittel, *Introduction to Solid State Physics*, 5th ed. (Wiley, New York, 1976; Nauka, Moscow, 1978).
2. J. Ziman, *Models of Disorder* (Cambridge University Press, Cambridge, 1979; Mir, Moscow, 1982).
3. J. C. Slater, *Insulators, Semiconductors, and Metals* (McGraw-Hill, New York, 1967; Mir, Moscow, 1969), Chap. 6.
4. J. D. Joannopoulos, R. D. Meade, and J. N. Winn, *Photonic Crystals: Molding of Flow of Light* (Princeton University Press, Princeton, 1995).
5. E. Yablonovitch, Phys. Rev. Lett. **58** (20), 2059 (1987); E. Yablonovitch, T. J. Gmitter, and K. M. Leung, Phys. Rev. Lett. **67** (17), 2295 (1991); E. Yablonovitch, T. J. Gmitter, R. D. Meade, A. M. Rappe, K. D. Brommer, and J. A. Joannopoulos, Phys. Rev. Lett. **67** (24), 3380 (1991).
6. *Confined Electrons and Photons: New Physics and Applications*, Ed. by E. Burstein and C. Weisbuch (Plenum, New York, 1995).
7. A. Blanco, E. Chomski, S. Grachtak, M. Ibisate, S. John, S. Leonard, C. Lopez, F. Mesegure, H. Miguez, J. Mondia, G. A. Ozin, O. Toader, and H. M. van Driel, Nature (London) **405**, 437 (2000).
8. V. N. Astratov, V. N. Bogomolov, A. A. Kaplyanskii, A. V. Prokofiev, L. A. Samilovich, S. M. Samoilovich, and Y. A. Vlasov, Nuovo Cimento Soc. Ital. Fis., D **17**, 1349 (1995).
9. K. Buch and S. John, Phys. Rev. B: Condens. Matter **58** (3), 3896 (1998).
10. A. V. Baryshev, A. V. Ankudinov, A. A. Kaplyanskiĭ, V. A. Kosobukin, M. F. Limonov, K. B. Samusev, and D. E. Usvyat, Fiz. Tverd. Tela (St. Petersburg) **44** (9), 1573 (2002) [Phys. Solid State **44** (9), 1648 (2002)].
11. A. V. Baryshev, A. A. Kaplyanskiĭ, V. A. Kosobukin, M. F. Limonov, and A. P. Skvortsov, Fiz. Tverd. Tela (St. Petersburg) **46** (7), 1291 (2004) [Phys. Solid State **46** (7), 1331 (2004)].
12. A. V. Baryshev, A. A. Kaplyanskiĭ, V. A. Kosobukin, M. F. Limonov, K. B. Samusev, and D. E. Usvyat, Fiz. Tverd. Tela (St. Petersburg) **45** (3), 434 (2003) [Phys. Solid State **45** (3), 459 (2003)].
13. A. V. Baryshev, A. A. Kaplyanskii, V. A. Kosobukin, M. F. Limonov, K. B. Samusev, and D. E. Usvyat, Physica E (Amsterdam) **17**, 426 (2003).
14. A. V. Baryshev, A. A. Kaplyanskii, V. A. Kosobukin, K. B. Samusev, D. E. Usvyat, and M. F. Limonov, Phys. Rev. B: Condens. Matter **70** (11), 113 104 (2004).
15. H. Jeffreys and B. Swirles, *Methods of Mathematical Physics* (Cambridge University Press, Cambridge, 1966; Mir, Moscow, 1969), Vol. 3.
16. V. A. Kosobukin, Fiz. Tverd. Tela (St. Petersburg) **39** (3), 560 (1997) [Phys. Solid State **39** (3), 488 (1997)].
17. V. N. Astratov, A. M. Adavi, S. Fricker, M. S. Skolnick, D. M. Whittacker, and P. N. Pusey, Phys. Rev. B: Condens. Matter **66** (16), 165 215 (2002).
18. R. M. Amos, J. G. Rarity, P. R. Tapster, T. J. Shepherd, and S. C. Kitson, Phys. Rev. B: Condens. Matter **61** (3), 2929 (2000).
19. W. Loose and B. J. Ackerson, J. Chem. Phys. **101** (9), 7211 (1994).
20. H. M. van Driel and W. L. Vos, Phys. Rev. B: Condens. Matter **62** (15), 9872 (2000).

Translated by K. Shakhlevich

**DEFECTS, DISLOCATIONS,
AND PHYSICS OF STRENGTH**

Bulk Elastic Energy of Bismuth Crystal Twins and the Surface Energy of the Twin–Matrix Interface in a Magnetic Field

A. I. Pinchuk and S. D. Shavreĭ

Mozyr' State Pedagogical University, Mozyr', 247760 Belarus

e-mail: apinchook@tut.by

Received December 28, 2004

Abstract—Partial suppression of twinning in bismuth crystals in a static magnetic field is found not to be accompanied by a change in the bulk elastic energy stored in wedge twins. Application of a magnetic field decreases the surface energy of the twin–matrix interface. © 2005 Pleiades Publishing, Inc.

1. INTRODUCTION

Earlier [1], we established that twinning in bismuth crystals is partially suppressed under long-term concentrated loading in a static magnetic field. This manifests itself in a decrease in the number and size of wedge twins. As a result, the volume of the twins and the area of the twin–matrix interfaces decrease [2]. In this connection, it is important to answer the question as to whether the application of a magnetic field leads to a decrease in the bulk elastic energy of twins and in the surface energy of the twin–matrix interface.

2. SPECIMEN PREPARATION AND EXPERIMENTAL TECHNIQUE

Bismuth single crystals were grown by the Bridgman method from raw materials of chemical purity. Specimens in the form of a rectangular prism ($10 \times 5 \times 5$ mm in size) were prepared by cleaving a bismuth single crystal along the cleavage plane. The wedge twins belonging to the $\{110\}\langle 001\rangle$ system were produced by pressing a standard diamond pyramid into the (111) cleavage plane of the bismuth crystals. The measurements were carried out using a PMT-3 microhardness tester and a special device fabricated from nonferromagnetic metals for applying a load to a specimen in a magnetic field. The magnetic induction vector lay in the (111) cleavage plane of the bismuth crystals. Some precautions were taken to eliminate effects from the instruments. Special control tests showed that switching the magnetic field on and off during loading of the specimen did not result in an increase in the size of the indentation made by the diamond pyramid. The relative change in the magnetic field at the geometric center of the gap in the electromagnet limb into which the specimen was placed did not exceed 2%.

The concentrated load P amounted to 0.14 N. In the first series of measurements, the magnetic field induc-

tion B was constant and equal to 0.2 T and the time of loading of the crystal with the indenter was varied in the range $t = 0\text{--}5$ h. In the second series of measurements, the magnetic field induction was varied in the range $B = 0\text{--}0.9$ T, whereas the time t of loading of the crystal with the indenter was constant and equal to 5 min.

During the experiments, the length and width of the wedge twins, as well as their number in the vicinity of the indentation produced by the diamond pyramid, were directly measured with an eyepiece micrometer in the PMT-3 instrument. Points in the experimental curves were obtained by averaging over the results of measuring the sizes of twin interlayers wedged around 20 or more indentations. The experimental error did not exceed 3%.

The bulk elastic energy of a twin was estimated from the relationship $W_V = w_V VN$, where w_V is the bulk elastic energy density, V is the average volume of the twin, and N is the average number of mechanical twins wedged around the indentation after the load is removed and the magnetic field is switched off.

On each side of the “twin–parent crystal” interphase boundary in the crystal, there occur displacements of the same order of magnitude as the width of the wedge twin. Since the displacements at the end of the wedge twin are equal to zero, elastic strains arise around the twin. These strains are of the order of sh/L , where h is the width of the wedge twin at the twin mouth, L is the length of the wedge twin, and $s = 0.694$ is a multiplier [3]. Consequently, the bulk elastic energy density can be estimated in order of magnitude as

$$w_V = \frac{G(sh)^2}{L^2}. \quad (1)$$

Then, the bulk elastic energy of the wedge twin can be obtained from the relationship

$$W_V = \frac{G(sh)^2}{L^2} VN. \quad (2)$$

Since the shape of twin interlayers formed under point loading can be approximated by a lens, the volume of a twin can be calculated according to the expression for the volume of a spherical segment. The radius of the base of the spherical segment was taken to be equal to the average length of the wedge twin, and the thickness of the spherical segment was assumed to be equal to the average thickness of the wedge twin at the mouth [4, 5].

The surface energy of the twin–parent crystal interphase boundary can be estimated according to the expression $W_s = w_s SN$, where w_s is the specific surface energy of the twin–matrix interphase boundary and S is the surface area of the twin–matrix interphase boundary. In the monograph by Klassen-Neklyudova [3], the specific surface energy of the twin boundary was estimated from the relationship $w_s = Ga$, where G is the shear modulus and a is the lattice parameter of the bismuth crystal. Therefore, the surface energy of the twin–matrix interfaces can be determined as

$$W_s = GaSN. \quad (3)$$

The area of the twin–matrix interfaces S was calculated as half the area of the spherical segment with the base radius taken equal to the average length of the wedge twin [4, 5].

3. RESULTS AND DISCUSSION

The experimental dependences $W_V(t)$ and $W_s(t)$ obtained in the first series of experiments are shown in Figs. 1 and 2, respectively. It can be seen from the curves depicted in Figs. 1 and 2 that the energies W_V and W_s increase both in the presence and in the absence of the magnetic field and exhibit a tendency toward saturation as the time t of loading of the crystal with the indenter increases. It can be concluded that, within the limits of experimental error, the application of the magnetic field does not lead to a change in the bulk elastic energy of the wedge twins for the same time t .

The magnetic field decreases the average distance between the dislocations L/h , which is expressed in terms of the lattice parameters of the bismuth crystal (Fig. 3). As can be seen from relationship (1), this leads to an increase in the density of the bulk elastic energy w_v , which is stored in the wedge twin during concentrated loading of the crystal with the indenter in the magnetic field. Therefore, although application of the magnetic field to the bismuth crystals results in the suppression of twinning, the bulk elastic energy of the wedge twins remains unchanged for equal times t .

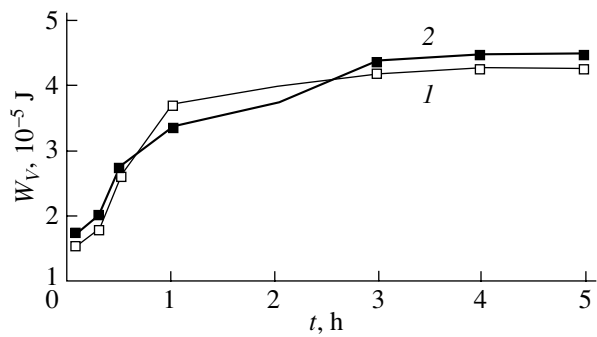


Fig. 1. Dependences of the bulk elastic energy W_V of wedge twins in bismuth crystals on the time t of loading of the crystal with an indenter (1) without a magnetic field and (2) in a magnetic field of 0.2 T.

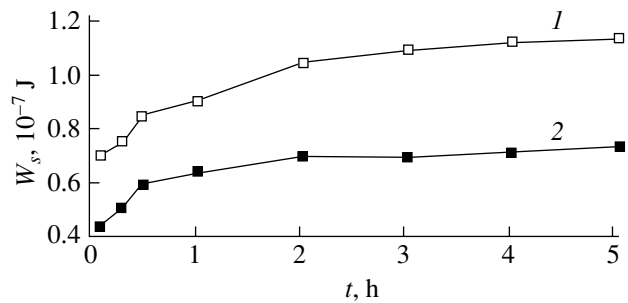


Fig. 2. Dependences of the surface energy W_s of twin–matrix interfaces of wedge twins in bismuth crystals on the time t of loading of the crystal with an indenter (1) without a magnetic field and (2) in a magnetic field of 0.2 T.

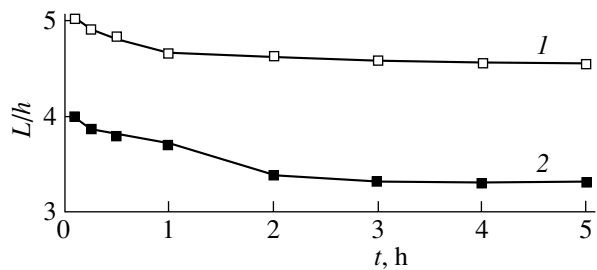


Fig. 3. Dependences of the ratio L/h on the time t of concentrated loading (1) without a magnetic field and (2) in a magnetic field of 0.2 T.

The magnetic field does not suppress the generation of twinning dislocations in the mouth of the twin. As is known, the number of twinning dislocations located at a twin–matrix interface is equal to the ratio h/a . As the time t of concentrated loading increases, the twin thickness h increases both in the presence and in the absence of a magnetic field [1]. An increase of the twin thickness h brings about an increase in the twin volume V and the interfacial area S and, as follows from relation-

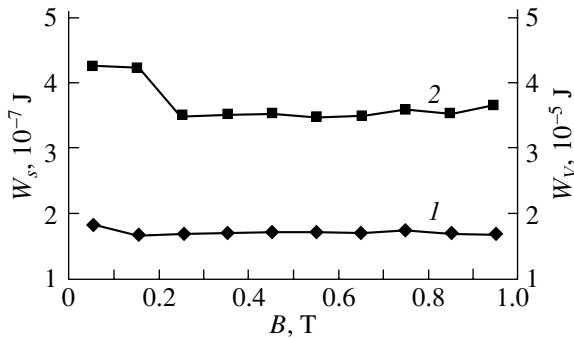


Fig. 4. Dependences of (1) the bulk elastic energy W_V and (2) the surface energy W_s of wedge twins on the magnetic field induction B upon loading of the crystal with an indenter for $t = 5$ min.

ships (2) and (3), an increase in the bulk energy W_V and the surface energy W_s , respectively.

For equal times t , the surface energy of the twin boundary W_s in the presence of the magnetic field is considerably less than that in the absence of the magnetic field (Fig. 2). Apparently, application of the magnetic field disables magnetosensitive (paramagnetic) stoppers and the unlocked twin boundary takes on a thermodynamically equilibrium length. As a consequence, the area S of the twin–matrix interfaces in the magnetic field decreases [5], which, according to relationship (3), leads to a decrease in the surface energy of the twin boundary W_s .

In the second series of experiments, the bulk elastic energy and the surface energy of the twins were investigated as functions of the magnetic field induction. As was shown in our previous study [6], the length of wedge twins abruptly decreases as the magnetic field induction reaches a threshold value $B = 0.2$ T. Although

the total volume of the twins also decreases in a similar manner at $B = 0.2$ T, the bulk elastic energy of the wedge twins W_V remains virtually constant (Fig. 4, curve 1). The latter circumstance can be explained by the shortening of the distance between the dislocations L/h at $B = 0.2$ T. This leads to an increase in the bulk elastic energy density w_V , which is localized in the twin. Since the area of the twin–matrix interfaces S at $B = 0.2$ T decreases abruptly (primarily due to the shortening of the average length of the wedge twins L), the surface energy of the twin boundary W_s also decreases in a similar manner (Fig. 4, curve 2).

ACKNOWLEDGMENTS

This work was supported in part by the Belarussian Republic Foundation for Basic Research, project no. F03-105.

REFERENCES

1. A. I. Pinchuk and S. D. Shavreĭ, *Fiz. Tverd. Tela* (St. Petersburg) **43** (1), 39 (2001) [*Phys. Solid State* **43** (1), 39 (2001)].
2. S. D. Shavreĭ and A. I. Pinchuk, *Pis'ma Zh. Tekh. Fiz.* **29** (15), 35 (2003) [*Tech. Phys. Lett.* **29** (8), 632 (2003)].
3. M. V. Klassen-Neklyudova, *Mechanical Twinning of Crystals* (USSR Academy of Sciences, Moscow, 1960; Consultants Bureau, New York, 1962).
4. A. I. Pinchuk, *Metallofiz. Noveĭshie Tekhnol.* **22** (3), 88 (2000).
5. A. I. Pinchuk and S. D. Shavreĭ, *Metallofiz. Noveĭshie Tekhnol.* **22** (12), 43 (2000).
6. A. I. Pinchuk and C. D. Shavreĭ, *Fiz. Tverd. Tela* (St. Petersburg) **46** (9), 1603 (2004) [*Phys. Solid State* **46** (9), 1655 (2004)].

Translated by V. Artyukhov

**DEFECTS, DISLOCATIONS,
AND PHYSICS OF STRENGTH**

Redistribution of Dislocations in Silicon near Stress Concentrators

A. M. Orlov, A. A. Solov'ev, A. A. Skvortsov, and I. O. Yavtushenko

Ul'yanovsk State University, Ul'yanovsk, 432979 Russia

e-mail: OrlovAM@ulsu.ru

Received December 16, 2004; in final form, March 11, 2005

Abstract—The distribution of defects in dislocation tracks in silicon plates was studied for various indentation angles. The regularities of variations in the linear density and maximum path of dislocations in slip bands are established. A model is proposed to describe the distribution of dislocations in the dislocation tracks. By fitting the theory to the experimental data, the dependence of this distribution on the energy relaxation time is determined. © 2005 Pleiades Publishing, Inc.

1. INTRODUCTION

Studying the dislocation mobility in semiconductor crystals in fields of various nature is one of the main problems in solid-state physics [1–9]. The objects of research are usually dislocations introduced into a crystal through indentation or scratching. As a result of the action of external forces, dislocation motion develops in slip planes, which causes a linear arrangement of dislocation pits (rows, chains, tracks) along the corresponding crystal directions. In the literature, this process is analyzed, for the most part, in terms of both the maximum distances passed by dislocations from a stress concentrator [1, 4–8] and the variations in dislocation density with penetration depth [9]. However, the reasons for the dissociation of dislocation tracks in crystals and the character of the dislocation redistribution between their localized and scattered states have not actually been studied. There is virtually no information on the mechanism of dislocation redistribution caused by a change in the direction of indentation. The character of the dislocation distribution in chains during their expansion in the corresponding directions likewise has not yet been considered. This study is an attempt to fill this gap.

2. EXPERIMENTAL

Standard 76-mm dislocation-free phosphorus-doped silicon plates with a resistivity $\rho = 0.01 \Omega \text{ cm}$ were used to make the samples ($\sim 3 \times 1 \times 0.04 \text{ cm}$) for the experiment. The plates were prepared, using the conventional technology, from a single crystal grown in the [111] direction by the Czochralski technique. Scratches 5 to 10 mm long served as dislocation sources (stress concentrators) on the working (111) surface, which were produced under a load $P = (0.78\text{--}2.45) \text{ N}$ using a tetrahedral diamond pyramid (indenter) with a vertex angle of 90° . Scratches were scribed at

various angles ($0^\circ, 10^\circ, 20^\circ, 30^\circ, 40^\circ$) with respect to the [110] crystal direction. The motion of dislocations in the field of introduced internal stresses was stimulated by isothermal annealing of samples at 923 K for $t = 150 \text{ min}$. Over this time t , the internal stresses relaxed almost completely and dislocation transport stopped [9]. The arrangement of dislocations in the plates was studied using etching pits, which were produced by immersing the plates in a standard SR-4 selective etching solution [3, 9].

3. EXPERIMENTAL RESULTS AND DISCUSSION

It is known [10] that in silicon the main slip planes coincide with the $\langle 110 \rangle$ directions. Our results are fully consistent with this assertion. However, the orientation of the etch figure rows is unambiguously determined by the indentation direction with respect to the [110] crystal axis. Let us consider this result in more detail.

When a scratch is scribed in the [110] direction (Fig. 1a), dislocations are observed to run away in the [011] and $[10\bar{1}]$ directions. On the other hand, when a plate is indented in the $[\bar{1}\bar{1}0]$ direction, opposite to the [110] direction, the predominant running tracks are $[\bar{1}01]$ and $[0\bar{1}\bar{1}]$. Such a distribution of dislocations indicates the special nature of the stresses created by microcracks caused by scribing. Apparently, the projection of the leading vector of microcrack propagation onto a scratch always coincides in sign with the direction of the introduced concentrator of stresses. That is why the angle α between the [110] direction and the direction of indentation of the crystal surface (Fig. 1b) was measured carefully in our experiments as reckoned counterclockwise from the basic direction. The precise determination of α was checked with etching of the fig-

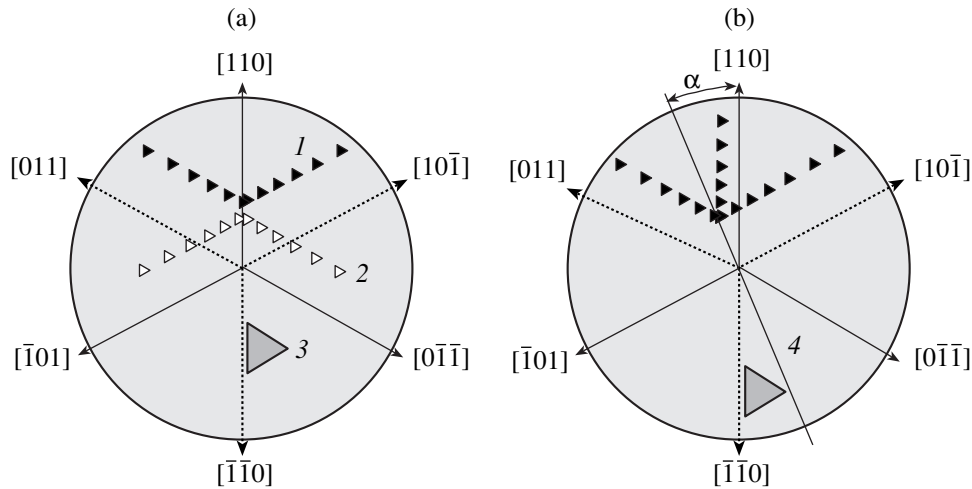


Fig. 1. The main directions of dislocation motion in the crystal under study. (a) The indentation direction coincides with the crystal direction (1) $[110]$ and (2) $[\bar{1}\bar{1}0]$. (b) The direction of scratching does not coincide with the $[110]$ direction; a scratch is drawn at an angle α to the $[110]$ direction. (1, 2) Dislocation etch pits; (3) a stacking fault; and (4) a stress concentrator.

ures, whose orientation was the same throughout the crystal surface due to the specific crystal features.

If $0^\circ < \alpha < 15^\circ$, the direction of dislocation motion is identical to that in the case considered above. However, as α approaches 15° , the dislocation etch pits are rearranged gradually from well-defined rows along the direction of running away, $[10\bar{1}]$, to randomly scattered individual dislocations located on the right-hand side of a scratch.

For higher angles, $15^\circ < \alpha < 30^\circ$, the scattered dislocation etch pits begin to group again into rows of etch figures oriented along a new direction, $[110]$. However, when $\alpha = 30^\circ$, only two predominant directions remain,

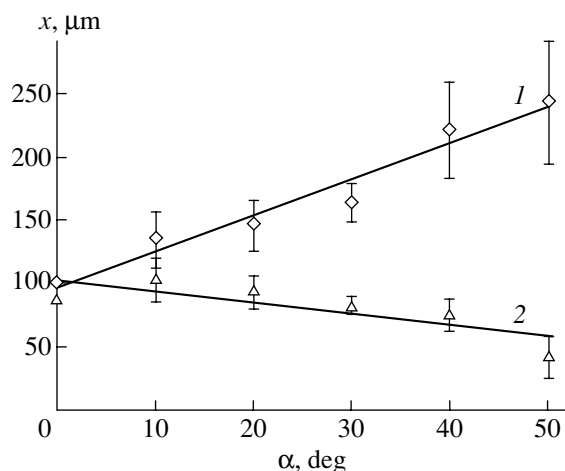


Fig. 2. Displacements of the leading dislocations from the edge of a scratch (drawn at various angles α to the $[110]$ direction; $P = 1.0$ N) measured after 150 min of isothermal annealing at 923 K. Measurements were carried out (1) along dislocation rows coinciding with the $[011]$ direction and (2) in the direction normal to the scratch.

$[011]$ and $[110]$, which make an angle of 60° between them.

As the angle α increases further from 30° to 60° , the pattern of the dislocation distribution repeats itself, but the orientation of the slip lines on the left-hand side of the scratch changes: the rows of etch figures in the $[011]$ direction disappear but appear in the $[\bar{1}01]$ direction. The angle between the observed rows (along $[\bar{1}01]$ and $[110]$) in this case is 120° , as in the first case. The general pattern of dislocation redistribution over the slip planes is given in Table 1.

Thus, the angle between the observed rows, as well as their orientations, is always determined by the nearest allowed slip directions on both sides of the scratch and the dissociation of dislocation tracks into individual dislocations in an indented crystal always becomes more intense as α approaches angles $15^\circ \pm n \times 30^\circ$, where $n = 0, 1, 2, 3, \dots$. Therefore, taking into account this periodicity, we will consider only the motion of dislocations associated with scratches whose angle with respect to any of the $\langle 110 \rangle$ crystal directions does not exceed 30° .

According to the experimental results, not only the topography of the dislocation distribution but also the character of their motion along the corresponding chains depend on α (Fig. 2). It is seen from Fig. 2 that, as the angle between a scratch and the $[110]$ direction increases, the dislocation path length $x(\alpha)$ along the $[011]$ dislocation rows increases (curve 1 in Fig. 2), while their distance from the scratch decreases (curve 2 in Fig. 2).

The most unexpected result was obtained when analyzing the character of the dislocation distribution in dislocation rows arranged along the corresponding crystal directions. It was established that the linear dis-

Table 1. Directions of dislocation paths starting from a stress concentrator at different angles α

Number	Angle between a scratch and the [110] direction	Indentation direction	Crystallographic orientation of dislocation rows	Comments
1	$\alpha = 0^\circ$	[110] 	[011] and [10 $\bar{1}$]	
	$\alpha = 180^\circ$	$[\bar{1}\bar{1}0]$ 	$[\bar{1}01]$ and $[0\bar{1}\bar{1}]$	
2	$0^\circ \leq \alpha < 15^\circ$		[011] and [10 $\bar{1}$]	Gradual transition to scattered dislocations on the right-hand side of a scratch
	$180^\circ \leq \alpha < 195^\circ$		$[\bar{1}01]$ and $[0\bar{1}\bar{1}]$	Gradual transition to scattered dislocations on the left-hand side of a scratch
3	$\alpha = 15^\circ$		[011]	Scattered dislocations on the right side of a scratch
	$\alpha = 195^\circ$		$[0\bar{1}\bar{1}]$	Scattered dislocations on the left-hand side of a scratch
4	$15^\circ < \alpha \leq 30^\circ$		[110], [011]	Gradual redistribution of dislocations into rows on the right-hand side of a scratch
	$195^\circ < \alpha \leq 210^\circ$		$[\bar{1}\bar{1}0]$, $[0\bar{1}\bar{1}]$	Gradual redistribution of scattered dislocations into rows on the left-hand side of a scratch
5	$\alpha = 30^\circ$		[011], [110]	
	$\alpha = 210^\circ$		$[\bar{1}\bar{1}0]$, $[0\bar{1}\bar{1}]$	
6	$30^\circ < \alpha < 45^\circ$		[110], [011]	Gradual transition to scattered dislocations on the left-hand side of a scratch
	$210^\circ < \alpha < 225^\circ$		$[\bar{1}\bar{1}0]$, $[0\bar{1}\bar{1}]$	Gradual transition to scattered dislocations on the right-hand side of a scratch
7	$\alpha = 45^\circ$		[110]	Scattered dislocations on the left-hand side of a scratch
	$\alpha = 225^\circ$		$[\bar{1}\bar{1}0]$	Scattered dislocations on the right side of a scratch
8	$45^\circ < \alpha < 60^\circ$		$[\bar{1}01]$, [110]	Gradual redistribution of scattered dislocations into rows on the left-hand side of a scratch
	$225^\circ < \alpha < 240^\circ$		$[\bar{1}\bar{1}0]$, [10 $\bar{1}$]	Gradual redistribution of dislocations into rows on the right-hand side of a scratch
9	$\alpha = 60^\circ$		$[\bar{1}01]$, [110]	
	$\alpha = 240^\circ$		$[\bar{1}\bar{1}0]$, [10 $\bar{1}$]	

location density in the direction of migration [011] shows a steady tendency toward a decrease (for $0^\circ \leq \alpha < 30^\circ$), is constant (for $\alpha = 30^\circ$), or increases (for $30^\circ < \alpha \leq 60^\circ$), changing smoothly from one state to another with an increase in α . Furthermore, regardless of the azimuth angle α of a scratch, there are almost always one or more clusters of etch pits in dislocation chains that produce high peaks in the dislocation density.

This feature is observed most clearly at high values of α , where, in addition to the main peak, a significant number of smaller peaks are observed, which distort the general pattern of the dislocation distribution (Fig. 3). Optical microscopy studies showed that the main reason for the appearance of these small peaks is the presence of areas of intersection of dislocation tracks with different crystallographic orientation involved in the dislocation redistribution described above. The con-

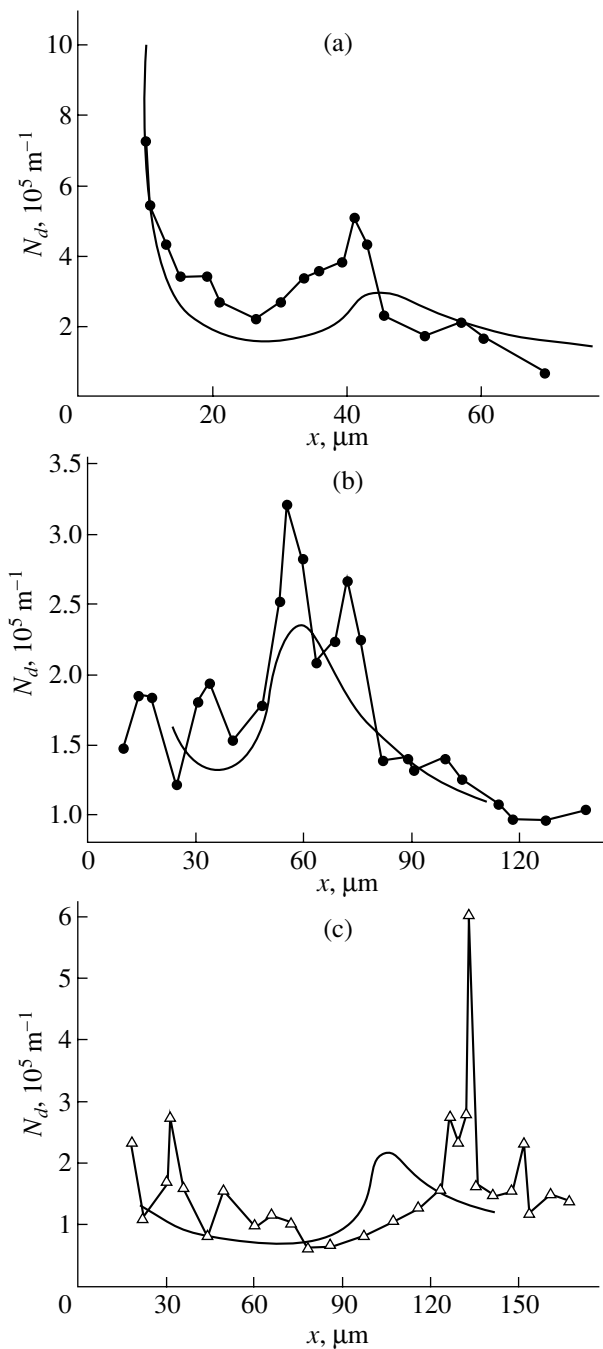


Fig. 3. Measured linear dislocation density in the [011] slip line as a function of distance at various values of α : (a) 0° , (b) 30° , and (c) 40° . Curves calculated from Eq. (8) are superimposed on the experimental points. The load on the pyramid during scratching is 0.98 N.

vincing reproducibility of these results excludes the possibility of any procedural error and calls for clarification of the physical reasons for the observed phenomena.

We carried out such an analysis with allowance for the periodical distribution of microcracks along certain crystal directions and their redistribution caused by a

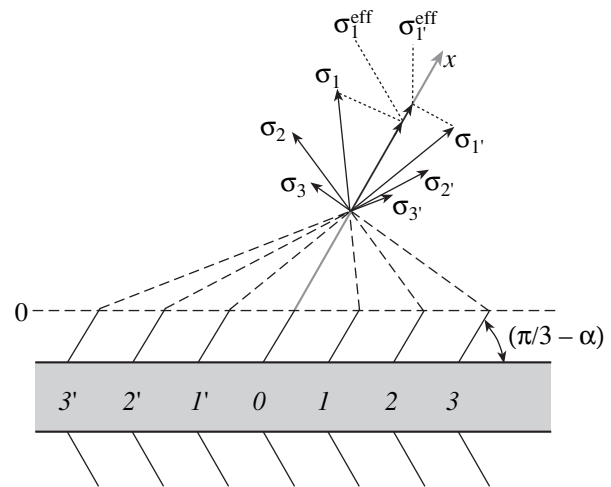


Fig. 4. Distribution of stresses that are caused by microcracks 3', 2', 1', 0, 1, 2, 3 introduced into a crystal during indentation of the surface and act on a chosen dislocation slip line.

change in the azimuth position of a scratch, as well as for the fact that the rate of dislocation nucleation varies due to relaxation processes.

Our conclusion will be based on the velocity of dislocation motion over the slip planes, which is determined, above all, by the internal stresses σ_{int} [6] caused by indentation of a crystal:

$$V = \frac{dx}{dt} = V_0 \left(\frac{\sigma_{\text{int}}}{\sigma_0} \right)^m \exp\left(-\frac{E}{kT}\right), \quad (1)$$

where V_0 and σ_0 are constants, $m = 1$ for silicon, E is the activation energy for dislocation motion, k is the Boltzmann constant, and T is temperature.

Indeed [11], when a scratch is produced, there appear a great number of microcracks (Fig. 4) with linear density $f(m^{-1})$, which expand predominantly over the "leading" slip planes. At the tip of each (i th) microcrack, stress is induced, which decreases with distance x according to the law [9, 12]

$$\sigma_i(x) = -\frac{bGN_d^0}{2\pi(1-\nu)} \ln\left(1 - \frac{a'}{x}\right), \quad (2)$$

where σ_i is the stress at the dislocation site, $G = 1.5 \times 10^{11}$ Pa is the shear modulus, $\nu = 0.3$ is Poisson's ratio, b is the Burgers vector, and N_d^0 is the linear dislocation density in a region a' near the microcrack.

The elastic stress field created by an ensemble of microcracks with linear density f relaxes during high-temperature annealing, spending its energy on dislocation nucleation and on the motion of microcracks over favorable slip bands.

Assuming f to be constant and taking into account the various distances of a dislocation from stress con-

centrators (crack tips, Fig. 4), it is easy to estimate the resulting stress σ_{eff} that pushes this dislocation in a slip plane as a sum of the corresponding components.

The intermediate results of the calculations are shown in Fig. 5. They are obtained with allowance for the redistribution of microcracks (by analogy with dislocations) between different (for example, [011] and $[\bar{1}01]$) crystal directions, depending on the azimuth angle of the scratch:

$$f_{\bar{1}01}(\alpha) = \frac{f}{60^\circ}\alpha, \quad f_{011}(\alpha) = f\left(1 - \frac{\alpha}{60^\circ}\right), \quad (3)$$

$$f = f_{011} + f_{\bar{1}01}.$$

It is seen that the higher α , the larger the areas with localized dislocations that are subjected to the effective action of stresses. This has a direct influence on the penetration depth of dislocations into the crystal along the chosen slip direction.

The stresses considered are not constant but rather rapidly relax during high-temperature annealing, which favors dislocation nucleation and motion. Taking this into account, we can write [13]

$$\sigma_{\text{int}}(x, t) = \sigma_{\text{eff}}(x) \left(\xi_1 \exp\left(-\frac{t}{\tau_1}\right) + \xi_2 \exp\left(-\frac{t}{\tau_2}\right) \right), \quad (4)$$

where τ_1 and τ_2 are the characteristic relaxation times of dislocation nucleation and motion, respectively, and ξ_1 and ξ_2 are dimensionless coefficients satisfying the condition $\xi_1 + \xi_2 = 1$. It should be noted that the energy of a single microcrack prevails in the generation of dislocations forming a track, whereas the energy of an ensemble of microcracks prevails in the dislocation motion.

When t is specified, expression (4) describes the relaxing stress acting only on the leading dislocation in a slip chain. In order to describe all the following dislocations, it is necessary to introduce the appropriate correction that accounts for the dislocation generation rate. This rate is related to σ_{int} through a simple relation,

$$v(t) = dn/dt = \chi \sigma_{\text{int}}(t, x_0), \quad (5)$$

where n is the number of generated dislocations, χ is a dimensional function, and x_0 is the coordinate of a dislocation source.

Thus, taking into account Eq. (4), we get

$$\frac{dn}{dt} = v_0 \left(\xi_1 \exp\left(-\frac{t}{\tau_1}\right) + \xi_2 \exp\left(-\frac{t}{\tau_2}\right) \right). \quad (6)$$

Here, v_0 is the dislocation generation rate at $t = 0$.

Solving this equation makes it possible to determine both the time $t = t_i$ at which any dislocation $i = 1, 2, 3 \dots$

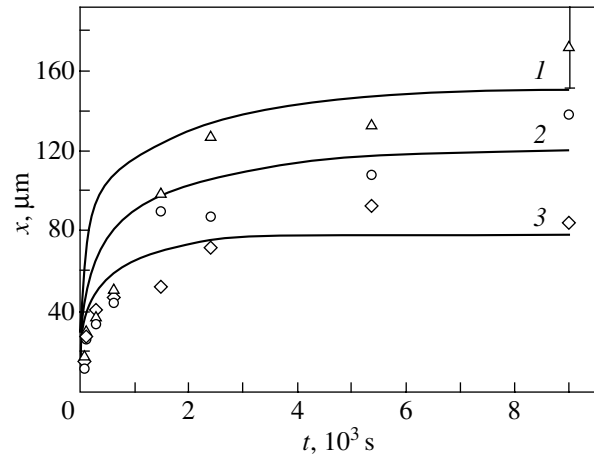


Fig. 5. Distances traveled by the leading dislocations from a stress concentrator plotted vs annealing time. The points are experimental data, and the lines are the results calculated using Eq. (8). (1) $\alpha = 40^\circ$, (2) 30° , and (3) 0° .

appears and the total number n of dislocations generated during the annealing time t :

$$n_i = v_0 (\xi_1 \tau_1 + \xi_2 \tau_2) - v_0 \left(\xi_1 \tau_1 \exp\left(-\frac{t_i}{\tau_1}\right) + \xi_2 \tau_2 \exp\left(-\frac{t_i}{\tau_2}\right) \right). \quad (7)$$

Substituting Eqs. (4) and (7) into Eq. (1), we obtain

$$\frac{dx_i}{dt} = \frac{V_0 \sigma_{\text{int}}(x_i, t) \left(\xi_1 \exp\left(-\frac{t-t_i}{\tau_1}\right) + \xi_2 \exp\left(-\frac{t-t_i}{\tau_2}\right) \right)}{\sigma_0} \times \exp\left(-\frac{E_a}{kT}\right). \quad (8)$$

Equation (8) makes it possible to follow the kinetics of each dislocation with stress, which relaxes continually during isothermal annealing beginning from the moment of its nucleation $t - t_i$, and the redistribution of dislocations¹ in slip lines at an arbitrary moment t .

Using Eq. (8) and the experimentally determined distribution of dislocations in dislocation tracks for various angles of indentation of silicon plates (Fig. 3), it is possible not only to estimate the relaxation parameters (τ_1 , τ_2) and the coefficients ξ_1 and ξ_2 but also to establish the basic mechanism responsible for variations in the linear dislocation density in dislocation tracks at various α .

The calculated results for α values correlated with the experiment are shown in Figs. 3 and 5. It should be

¹The linear dislocation density was determined, taking into account Eq. (8), from the equation $N_d = \frac{dn_d}{dx} \approx \frac{2}{x_{i+1} - x_i}$, where dn_d is the number of dislocations within section dx .

Table 2. Numerical data correlated with the experiment for $T = 923$ K

Parameters	Azimuth angle α between the [110] crystal direction and a scratch		
	0°	30°	40°
τ_1, s	75	150	200
τ_2, s	1000	2000	2700
ξ_1	0.93	0.94	0.91
$N_d^0, 10^9 \text{ m}^{-1}$	2.308	2.308	2.308
v_0, s^{-1}	0.128	0.077	0.045
E, eV		2.2	
σ_0, Pa		1×10^6	
$V_0, \text{m/s}$		1×10^3	

noted that coincidence of the experimental and calculated data (including the paths of the leading dislocations (Fig. 5), their distribution over the slip lines (Fig. 3), and the presence and position of the main peaks in the $N_d(x)$ curves) occurs for each value of α only at certain values of τ_1 and τ_2 listed in Table 2.

Consequently, the above-described, experimentally determined transformation of the linear dislocation density with a variation in the azimuth angle of a scratch is unambiguously determined by the relaxation time of the energy needed for the dislocation generation and motion. We do not have independent data on these parameters and cannot compare the results of these calculations with the experiment, which is of interest. We will accomplish this in practice in the near future.

REFERENCES

1. Yu. S. Boyarskaya, D. Z. Grabko, M. I. Medinskaya, and N. A. Palistrant, *Fiz. Tekh. Poluprovodn. (St. Petersburg)* **31** (2), 179 (1997) [*Semiconductors* **31** (2), 139 (1997)].
2. N. I. Tarbaev, *Fiz. Tverd. Tela (St. Petersburg)* **40** (10), 1845 (1998) [*Phys. Solid State* **40** (10), 1672 (1998)].
3. A. A. Skvortsov, A. M. Orlov, V. A. Frolov, and A. A. Solov'ev, *Fiz. Tverd. Tela (St. Petersburg)* **42** (11), 1998 (2000) [*Phys. Solid State* **42** (11), 2054 (2000)].
4. I. V. Ostrovskii, L. P. Steblenko, and A. B. Nadtochiĭ, *Fiz. Tekh. Poluprovodn. (St. Petersburg)* **34** (3), 257 (2000) [*Semiconductors* **34** (3), 251 (2000)].
5. M. V. Mezhenyĭ, M. G. Mil'vidskii, V. F. Pavlov, and V. Ya. Reznik, *Fiz. Tverd. Tela (St. Petersburg)* **43** (1), 47 (2001) [*Phys. Solid State* **43** (1), 47 (2001)].
6. V. A. Makara, L. P. Steblenko, N. Ya. Gorid'ko, V. M. Kravchenko, and A. N. Kolomiets, *Fiz. Tverd. Tela (St. Petersburg)* **43** (3), 462 (2001) [*Phys. Solid State* **43** (3), 480 (2001)].
7. V. I. Alekseenko, *Zh. Tekh. Fiz.* **70** (6), 63 (2000) [*Tech. Phys.* **45** (6), 732 (2000)].
8. Y. Yamashita, F. Jyobe, Y. Kamiura, and K. Maeda, *Phys. Status Solidi A* **171**, 27 (1999).
9. A. M. Orlov, A. A. Skvortsov, and A. A. Solov'ev, *Zh. Éksp. Teor. Fiz.* **123** (3), 590 (2003) [*JETP* **96** (3), 523 (2003)].
10. M. P. Shaskol'skaya, *Crystallography (Vysshaya Shkola, Moscow, 1984)* [in Russian].
11. V. P. Alekhin, *Physics of Strength and Plasticity of Surface Layers of Materials (Nauka, Moscow, 1983)* [in Russian].
12. L. D. Landau and E. M. Lifshitz, *Theory of Elasticity (Nauka, Moscow, 1965; Pergamon, Oxford, 1970)*.
13. A. S. Azheganov, D. A. Gorinov, K. A. Senik, and N. K. Shestakova, *Struct. Dyn. Mol. Syst.* **10** (1), 97 (2003).

Translated by E. Borisenko

DEFECTS, DISLOCATIONS, AND PHYSICS OF STRENGTH

Mechanical Properties of Thin Ag Films on a Silicon Substrate Studied Using the Nanoindentation Technique

A. V. Panin¹, A. R. Shugurov^{1,2}, and K. V. Oskomov^{2,3}

¹ Institute of Strength Physics and Materials Science, Siberian Division, Russian Academy of Sciences, Akademicheskii pr. 2/1, Tomsk, 634021 Russia
e-mail: pav@ms.tsc.ru

² Tomsk State University, pr. Lenina 36, Tomsk, 634050 Russia

³ Institute of High-Current Electronics, Siberian Division, Russian Academy of Sciences, Akademicheskii pr. 2/3, Tomsk, 634021 Russia

Received February 22, 2005

Abstract—The mechanical properties of thin Ag films of equal thickness containing grains of various sizes were studied. The film hardness was measured using the Oliver–Pharr techniques based on indentation work calculations or on direct measurements of the area of pyramid imprints in AFM images. In order to avoid the influence of a substrate on the measured hardness, a technique was developed to determine the true values of the film hardness. It was established that the hardness of Ag films decreases with an increase in mean grain size, whereas the elastic modulus remains almost unchanged. It was shown that the dependence of the yield stress of Ag films on grain size does not obey the classical Hall–Petch law. © 2005 Pleiades Publishing, Inc.

1. INTRODUCTION

Thin metallic films are widely used in the production of integrated circuits, magnetic and optical devices, microsensors, etc. Though the electrical properties of thin-filmed materials draw the most attention, their mechanical properties also play an important role, because when films are being deposited and operated on strong internal stresses can be created in them, which can cause deformation and fracture during relaxation [1–3].

Among the techniques developed for studying the mechanical properties of thin films is nanoindentation, which makes it possible to analyze the processes of elastic and plastic deformation in very small volumes. This is very important, because the thickness and grain size of films are very small. However, some difficulties arise caused by the fact that the results of measurements are not always in one-to-one correspondence with the actual characteristics of a film [4–6]. The reason for this is, above all, the influence of a substrate under the deposited film, which, as a rule, has absolutely different mechanical properties. Furthermore, there is the problem of material pile-up or, on the contrary, sink-in over the faces of the indenting pyramid, which causes inaccuracies in determining the contact area between the indenter and a sample and, thus, results in data distortions. Finally, the measurement results depend on the method used to process the indentation curves. Despite there being a great number of studies in this area [4–11], the problem of measuring the mechanical properties of thin films by using the nanoindentation technique has not been solved yet.

In the present work, the accuracies and reliabilities of various techniques developed for analyzing nanoindentation data are compared in order to accurately determine the hardness of Ag thin films and to study the influence of grain size on their mechanical properties.

2. EXPERIMENTAL

Ag films $t = 460$ nm thick were deposited on SiO₂/Si substrates using the magnetron sputtering technique at room temperature. The grain size d in the films was varied using one-hour isothermal air annealing at temperatures of 150 and 200°C. This made it possible to obtain films of equal thickness with various grain sizes.

Atomic-force microscopy (AFM) studies of the surface morphology of the Ag films showed that the as-deposited film surface is characterized by a fine grained structure with a mean grain size of 100 nm. The surface roughness of the films does not exceed 50 nm. Annealings at 150 and 200°C cause the mean grain size to increase to 250 and 400 nm, respectively. In this case, the maximum roughness height of the sample surface is 100 nm.

The mechanical properties of the films were studied using the nanoindentation technique and a NanoTest 600 setup. Tests were carried out using a Berkovich trihedral pyramid. The film hardness was determined using three different methods.

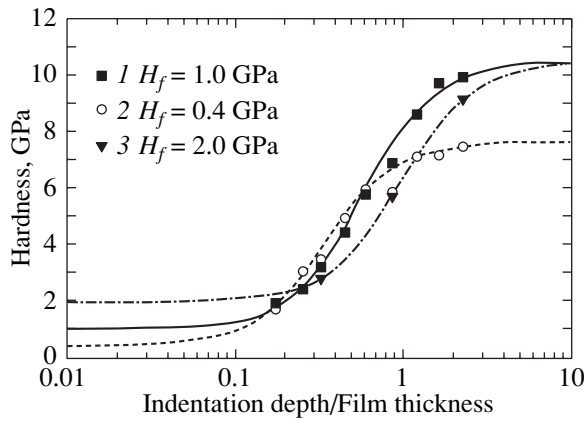


Fig. 1. Dependence of the hardness of an Ag film with a mean grain size of 250 nm on the relative penetration depth of the indenter. (1) The hardness as calculated using the OP technique; (2) the hardness as calculated from the work done during indentation; and (3) the hardness obtained from AFM measurements of an indenter imprint. Lines show the fitting of Eq. (7) to the experimental data.

Using the technique proposed by Oliver and Pharr [12], the hardness H was calculated from the expression

$$H = \frac{P_{\max}}{A}, \quad (1)$$

where P_{\max} is the maximum applied load and A is the contact area between the indenter and a sample,

$$A = 24.5h_c^2 + C_1h_c. \quad (2)$$

Here, $C_1 = 1.65 \times 10^{-6}$ is a constant, which describes the deviation from an ideal Berkovich pyramid caused by the tip curvature, and

$$h_c = h_{\max} - 0.75 \frac{P_{\max}}{S} \quad (3)$$

is the contact depth between the indenter and a sample, where h_{\max} is the maximum penetration depth of the indenter and S is the contact rigidity of a material.

Another method used to calculate the film hardness is based on determining the work that is done during indentation. According to this approach, the hardness is determined as [5]

$$H = \frac{kP_{\max}^3}{9W^2}, \quad (4)$$

where k is a constant, which depends on the indenter geometry (for a Berkovich pyramid, $k = 0.0408$), and W is the work done in the indentation process.

Finally, direct measurements of the contact area between the indenter and a sample were carried out using the AFM images of indentations on the surface of the films. The measured area of a pyramid imprint includes the contact area between the indenter and the

piled-up material. The value of H was calculated from Eq. (1).

Usually, in order to avoid the influence of a substrate on the results of nanoindentation of thin films, the penetration depth of the indenter is limited so that it does not exceed 10% of the film thickness. However, calculations of the contact area between the indenter and a sample using formula (2) imply that the sample surface is ideally smooth. If a film has a rough surface and the penetration depth of the indenter is smaller than the roughness height, then the real contact area can differ significantly from the calculated value, which will result in considerable inaccuracies in determining the hardness and elastic modulus. Taking into account that in the studied Ag films the maximum roughness height on a surface reaches 20% of the film thickness, the maximum load was chosen so as to make the penetration depth of the indenter more than the roughness heights. Consequently, the maximum load was from 0.5 to 200 mN.

The elastic modulus of the samples was determined from the relaxation curve slope using the following relationships [12]:

$$E^* = \frac{\sqrt{\pi} S}{2 \sqrt{A}}, \quad (5)$$

$$E^* = \left(\frac{1 - \nu^2}{E} + \frac{1 - \nu_{\text{ind}}^2}{E_{\text{ind}}} \right)^{-1}, \quad (6)$$

where E^* is the effective elastic modulus of the film-indenter system and E , E_{ind} and ν , ν_{ind} are the elastic moduli and Poisson's ratios of the materials of the film and the indenter, respectively.

3. RESULTS AND DISCUSSION

Measurements of the hardness were carried out with the abovementioned techniques taking the Ag film with a mean grain size $d = 250$ nm as an example. Figure 1 shows the measured hardness as a function of the penetration depth h of the indenter normalized by the film thickness t . It follows from Fig. 1 that, regardless of the calculating technique, H increases with h/t . When $h/t = 0.2$ – 0.5 , all techniques give similar results. However, when $h/t > 1.0$, the hardness as determined from the indentation work (IW) is far lower than the hardness determined using the Oliver–Pharr (OP) technique or AFM images.

There can be several reasons for the observed dependence of the hardness on the penetration depth. First, when indenting a film–substrate system, the response to indentation is determined by the mechanical properties of both the film and the substrate and the contribution made by the substrate becomes more considerable as the penetration depth increases. Second, the increase in film hardness can be due to the actual contact area broadening in comparison with the calcu-

lated value because of the extrusion of the material over the indenter faces and its piling-up on the film surface (Fig. 2).

However, as is seen from Fig. 1, the inclusion of the increase in the contact area between the indenter and the sample in the case where A is determined from AFM images actually has no effect on the character of H increasing with h/t . Moreover, the hardness of the film–substrate composition increases only until it reaches the hardness of the substrate (Fig. 3). Thus, it is the Si substrate that causes the increase in H .

Recently, several models have been suggested which allow one to exclude the contribution of a substrate to the measured hardness of the film–substrate composition and determine the true hardness of the film. According to [6], the variation in the composition hardness with an increase in the indenter penetration depth can be described by the expression

$$H_c = H_s + \frac{H_f - H_s}{1 + \frac{h^2}{\alpha t}}, \quad (7)$$

where H_c , H_s , and H_f are the hardnesses of the composition, the substrate, and the film, respectively, and α is a parameter with dimensions of length that mainly depends on the film thickness in the case of plastic materials. Expression (7) makes it possible to estimate the real hardness of a film by fitting the experimental data for the film–substrate composition to Eq. (7) and determining the values of H_f and α .

Figure 1 shows the dependence of the film–substrate composition hardness on the indenter penetration depth as determined by fitting the experimental data and the actual hardness of the Ag film found from this dependence. The fitting was performed using the following parameter values: $H_s = 10.5$ GPa and $\alpha = 1.55 \times 10^{-7}$ m (OP), $H_s = 7.7$ GPa and $\alpha = 0.56 \times 10^{-7}$ m (IW), and $H_s = 10.5$ GPa and $\alpha = 4.42 \times 10^{-7}$ m (AFM). As is seen from Fig. 1, all three methods give different values for H_f .

In order to verify the results obtained by the various techniques, H_f was used to calculate the elastic modulus of the films. Combining Eqs. (1) and (5), the effective elastic modulus was found to be

$$E^* = \sqrt{\frac{\pi H S}{P_{\max}}} \cdot 2. \quad (8)$$

Substitution of the calculated values of the true hardness of the film into Eq. (8) gives $E^* = 93$ GPa (OP), $E^* = 59$ GPa (IW), and $E^* = 132$ GPa (AFM). Using these values and the parameters $\nu = 0.37$, $\nu_{\text{ind}} = 0.07$, and $E_{\text{ind}} = 1000$ GPa, we get from Eq. (6) that $E = 88$ GPa (OP), $E = 54$ GPa (IW), and $E = 130$ GPa (AFM). A direct analysis of the nanoindentation curves carried out using Eqs. (5) and (6) shows that, when $h/t \leq 0.5$, the elastic modulus of a film is 80–89 GPa,

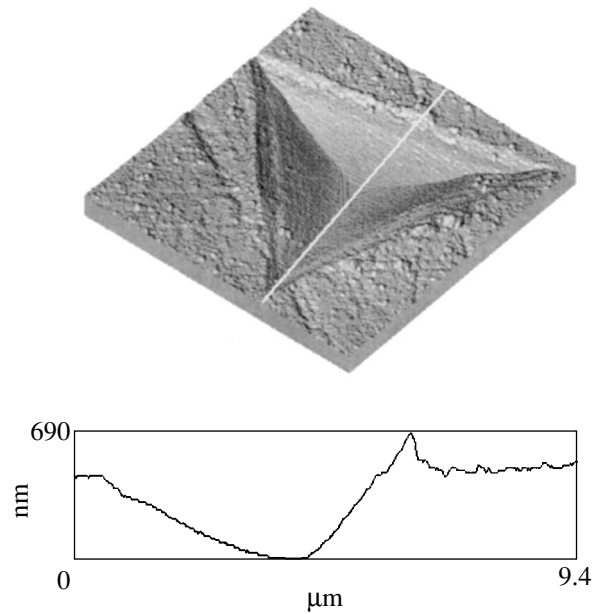


Fig. 2. AFM image and profilogram of an indenter imprint on the surface of an Ag film. $P_{\max} = 200$ mN.

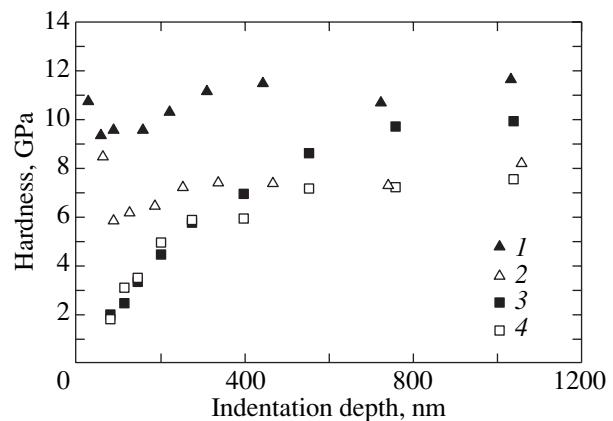


Fig. 3. Dependence of the hardness of (1, 2) a Si substrate and (3, 4) an Ag film with a grain size of 250 nm on the penetration depth of the indenter. (1, 3) The hardness as determined using the OP technique and (2, 4) the hardness calculated from the work done during indentation.

which agrees well with the elastic modulus of bulk silver. Since these results coincide only with the value of E obtained by the OP method, we conclude that this technique gives the most reliable results. That is why the OP technique in combination with the method for calculating the true hardness is further used to study the dependence of the mechanical properties of the Ag films on grain size.

The measured values of the hardness of the films with grains 100 and 400 nm in size are presented in Fig. 4. In calculating H_f , we used $H_s = 10.5$ GPa and $\alpha =$

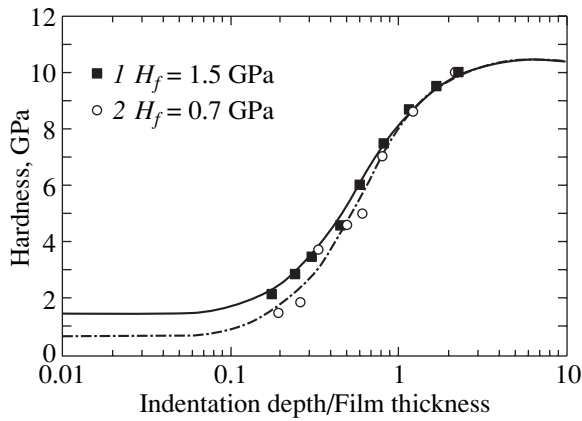


Fig. 4. Hardness of Ag films with a mean grain size of (1) 100 and (2) 400 nm plotted vs the relative penetration depth of the indenter. Lines show the fitting of Eq. (7) to the experimental data.

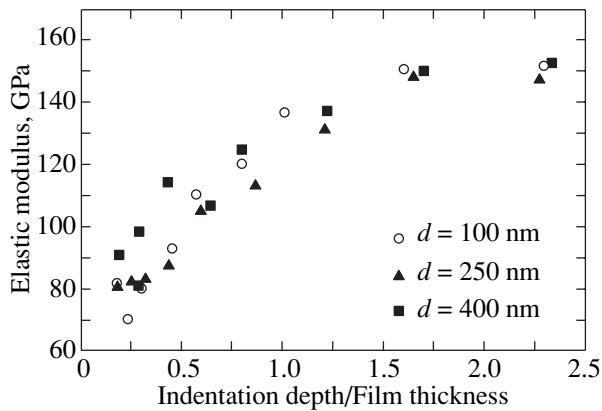


Fig. 5. Dependence of the elastic modulus of Ag films with various grain sizes on the relative penetration depth of the indenter.

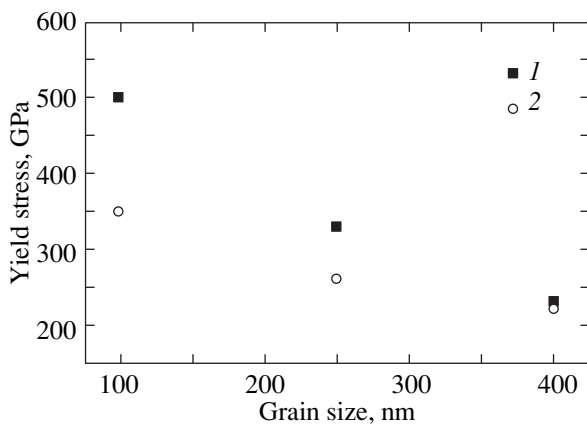


Fig. 6. Dependence of the yield stress of Ag films on the mean grain size. (1) The experimental data and (2) calculations based on the Nix-Freund model and the Hall-Petch relationship.

1.55×10^{-7} m. An analysis of the results obtained shows that, as the grain size decreases from 400 to 100 nm, the true hardness of the Ag films increases from 0.7 to 1.5 GPa.

The values of the elastic modulus of the films studied are shown in Fig. 5. The E value is practically independent of grain size and, for the indenter penetration depth not exceeding $\sim 30\%$ of the film thickness, it is ~ 80 GPa. As h increases further, E asymptotically approaches the elastic modulus of the silicon substrate.

The nanoindentation technique does not make it possible to directly measure the precise yield stress σ_y of the samples studied. However, this quantity can be estimated using the Tabor technique [13], according to which $\sigma^y \approx H/3$. Figure 6 shows the $\sigma_y(d)$ dependence for Ag films. It should be noted that the values obtained are one order of magnitude higher than the yield stress of bulk silver.

The primary factors that cause the hardness of thin films to be higher than that of the corresponding bulk materials are small grain sizes and restrictions imposed by a substrate on the dislocation motion in a film. The latter factor causes the strength characteristics of thin films to be dependent on the film thickness. To describe this dependence, the Nix-Freund model is usually used [1, 14]. According to this model, the minimum stress that should be applied in order to cause dislocation motion in a single-crystal film deposited on a substrate is given by

$$\sigma_y = 3.464 \frac{b}{2\pi(1-\nu)t\mu_f + \mu_s} \ln\left(\frac{\beta t}{b}\right), \quad (9)$$

where b is the Burgers vector of the film; μ_f and μ_s are the shear moduli of the film and substrate, respectively; and β is a constant. For polycrystalline materials, the effect of grain size on the strength properties is traditionally described by the Hall-Petch relationship

$$\sigma_y = \sigma_{y0} + k_{HP}d^{-1/2}, \quad (10)$$

where σ_{y0} is the yield stress component independent of grain size [i.e., the yield stress of a single crystal, which can be determined, e.g., from Eq. (9)] and k_{HP} is the Hall-Petch coefficient.

The values of σ_y of the Ag films calculated from Eqs. (9) and (10) are presented in Fig. 6. In the calculations, the following parameter values of the film and substrate were used: $\mu_{Ag} = 27$ GPa, $\mu_{Si} = 66.5$ GPa, $b = 2.89$ Å, $\nu = 0.37$, $\beta = 2.6$, and $k_{HP} = 0.083$ MN/m $^{-3/2}$ [15]. It is seen that the yield stress as estimated from the nanoindentation data agrees well with the calculated value only for the Ag films with a grain size of 400 nm. For the films with $d = 100$ and 250 nm, discordance is observed between the experimental and calculated data, which increases as the grain size decreases.

It is known that, when the grain size in bulk materials decreases from 1 μm to 30 nm, the Hall-Petch rela-

tionship differs from the classical relation in that the exponent d changes from -0.5 to almost zero [16, 17]. The observed increase in the yield stress of the Ag films studied is, on the contrary, faster than the $\sigma_y \sim d^{-1/2}$ dependence. A similar effect of more intense strengthening with a decrease in grain size ($\sigma_y \sim d^{-1}$) in comparison with that of bulk materials was observed earlier in thin Al films [18].

4. CONCLUSIONS

The nanoindentation technique has been used to measure the hardness and elastic modulus of thin Ag films on Si substrates. It has been shown that, when the surface roughness of films is high, it is possible to use a load which causes the penetration depth of the indenter to be deeper than 10% of the film depth. In this case, the OP technique in combination with the method for calculating the true hardness makes it possible to correctly determine the mechanical properties of thin films deposited on a substrate. The studies performed have shown that the Ag film hardness decreases as the mean grain size increases, whereas the elastic modulus remains constant.

The data on nanoindentation have been used to determine the yield stress of the films. It has been shown that, for Ag films with a grain size of 400 nm, the experimentally estimated yield stress agrees well with the value obtained from the Nix–Freud model and the Hall–Petch relationship. For films with smaller grain sizes, significant discordance is observed between the experimental and calculated data.

ACKNOWLEDGMENTS

This work was supported by the Russian Science Support Foundation, the Ministry of Education of the Russian Federation, and CRDF in the framework of the BRHE program (project no. 016-02).

REFERENCES

1. W. D. Nix, *Metall. Trans. A* **20**, 2217 (1989).
2. R. P. Vinci, E. M. Zielinski, and J. C. Bravman, *Thin Solid Films* **262**, 142 (1995).
3. T. L. Alford, L. Chen, and K. S. Gadre, *Thin Solid Films* **429**, 248 (2003).
4. R. Saha and W. D. Nix, *Acta Mater.* **50**, 23 (2002).
5. J. R. Tuck, A. M. Korsunsky, S. J. Bull, and R. I. Davidson, *Surf. Coat. Technol.* **137**, 217 (2001).
6. A. M. Korsunsky, M. R. McGurk, S. J. Bull, and T. F. Page, *Surf. Coat. Technol.* **99**, 171 (1998).
7. T. Y. Tsui, C. A. Ross, and G. M. Pharr, *Mater. Res. Soc. Symp. Proc.* **473**, 57 (1997).
8. R. A. Andrievskiĭ, G. V. Kalinnikov, N. Hellgren, P. Sandstom, and D. V. Shtanskiĭ, *Fiz. Tverd. Tela (St. Petersburg)* **42** (9), 1624 (2000) [*Phys. Solid State* **42** (9), 1671 (2000)].
9. Yu. I. Golovin, A. I. Tyurin, and V. V. Khlebnikov, *Zh. Tekh. Fiz.* **75** (4), 91 (2005) [*Tech. Phys.* **50** (4), 479 (2005)].
10. Ya. M. Soifer and A. Verdyan, *Fiz. Tverd. Tela (St. Petersburg)* **45** (9), 1621 (2003) [*Phys. Solid State* **45** (9), 1701 (2003)].
11. R. Saha, Z. Xue, Y. Huang, and W. D. Nix, *J. Mech. Phys. Solids* **49**, 1997 (2001).
12. W. Oliver and G. Pharr, *J. Mater. Res.* **7** (6), 1564 (1992).
13. D. Tabor, *The Hardness of Metals* (Clarendon, London, 1951).
14. L. B. Freund, *J. Appl. Mech.* **54**, 553 (1987).
15. T. H. Courtney, *Mechanical Behavior of Materials* (McGraw-Hill, New York, 1990).
16. M. Yu. Gutkin and I. A. Ovid'ko, *Usp. Mekh.* **2** (1), 68 (2003).
17. V. A. Pozdnyakov, *Fiz. Met. Metalloved.* **96** (1), 114 (2003).
18. R. Venkatraman and J. C. Bravman, *J. Mater. Res.* **7** (8), 2040 (1992).

Translated by E. Borisenko

**DEFECTS, DISLOCATIONS,
AND PHYSICS OF STRENGTH**

Influence of the Composition of the Tetragonal Phase in the Surface Layers of Zirconia-Based Ceramics on Their Strength

G. Ya. Akimov, G. A. Marinin, and V. M. Timchenko

Donetsk Physicotechnical Institute, National Academy of Sciences of Ukraine, Donetsk, 83114 Ukraine

e-mail: akimov@host.dipt.donetsk.ua

Received January 13, 2005; in final form, March 10, 2005

Abstract—The strength of partially stabilized zirconia-based ceramics is analyzed as a function of the porosity, the grain size, and the degree of tetragonality of the tetragonal phase. It is found that the strength of the studied ceramics, unlike conventional materials, is virtually independent of the porosity and the average grain size and is determined primarily by the content of the easily transformed tetragonal phase. © 2005 Pleiades Publishing, Inc.

1. INTRODUCTION

It is known that the flexural strength σ_f of polycrystalline ceramic materials can be most adequately described by the formula proposed by Knudsen [1]:

$$\sigma_f = B\bar{d}^{-a} \exp(-kP), \quad (1)$$

where B is a constant; \bar{d} is the average grain size; a is the numerical coefficient, which is approximately equal to 0.5; k is the numerical coefficient ranging from 4 to 9; and P is the relative porosity. As can be seen, relationship (1) does not account for possible phase transformations that can occur during fracture of the material. The influence of phase transformations on the strength of ceramic materials has been comprehensively discussed in papers concerned with investigating the cracking resistance K_{Ic} . In particular, McMeeking and Evans [2] and Lange [3] derived expressions relating the cracking resistance K_{Ic} to the mechanically activated phase transformation of the tetragonal (T) phase into the monoclinic (M) phase in partially stabilized zirconia (PSZ) ceramics. However, it is known that mechanical stresses can also bring about the $T \rightarrow M$ transformation on the surface of the PSZ ceramics. This transformation is accompanied by an increase in the volume and, hence, should give rise to compressive stresses at the surface, thus affecting the flexural strength σ_f [4]. As a rule, the flexural strength σ_f is determined primarily by the surface condition of the ceramic material. It is well known that the strength of ceramic materials can be substantially enhanced by increasing the smoothness of their surface, i.e., by eliminating stress concentrators from the surface. Moreover, stress concentrators existing on the surface and under the surface can be blocked (rather than eliminated), for example, by compressive stresses.

In this work, we carried out an additional analysis of the results reported earlier in [5, 6], with due regard for the new data obtained after the publication of those papers.

2. SAMPLE PREPARATION AND EXPERIMENTAL TECHNIQUE

Ceramic samples were prepared under cold isostatic pressing (CIP) from a powder of partially stabilized $ZrO_2 + 3 \text{ mol } \% Y_2O_3$ zirconia ceramics [5] (series 1) and a powder of $ZrO_2 + 4 \text{ mol } \% Y_2O_3$ [6] (series 2). Powders of series 1 were compacted under a pressure of 0.1 GPa and were then sintered in air at temperatures of 1623 and 1773 K. Powders of series 2 were also compacted under a pressure of 0.1 GPa and were then sintered at a temperature of 1773 K. After sintering in air, some of the samples of series 2 were subjected to hot isostatic pressing (HIP) in an argon atmosphere under a pressure of 0.2 GPa at a temperature of 1723 K [6].

The density ρ_{exp} for all the samples studied was determined by hydrostatic weighing, and the porosity was calculated according to the formula $P = 1 - \frac{\rho_{\text{exp}}}{\rho_{\text{theor}}}$. The theoretical density ρ_{theor} was calculated from the x-ray powder diffraction data.

After grinding, all samples were tested for strength by three-point bending. The base length of the gauge was equal to 14.5 mm, and the velocity of the movable crosspiece of the testing machine was 0.5 mm/min.

The phase composition was determined using x-ray powder diffraction at room temperature on a DRON-3M diffractometer (CoK_{α} radiation) with computer recording and plotting of the x-ray powder diffraction patterns. The calculation of the phase composition was performed according to the procedure described earlier

Influence of the composition of the tetragonal phase in the surface layers of zirconia-based ceramics on their strength

Parameters	Ceramics		Ceramics	
	ZrO ₂ + 3 mol % Y ₂ O ₃	(series 1)	ZrO ₂ + 4 mol % Y ₂ O ₃	(series 2)
	sintering temperature * <i>T_s</i> , K		sintering conditions	
	1623	1773	<i>T_s</i> , K	<i>T_s</i> , K + <i>T_{HIP}</i> , K
ρ, g/cm ³	5.99	5.99	5.98	6.13
<i>P</i> , %	1.5	1.5	1.64	Not determined**
σ _{<i>f</i>} , MPa	720 ± 20	720 ± 20	1026 ± 30	1400 ± 20
<i>d</i> , μm	0.20 ± 0.05	0.6 ± 0.1	0.6 ± 0.3	1.6 ± 0.3
<i>c/a</i> for the tetragonal phase	1.0080 (43)	1.0100 (30)	1.0170 (71)	1.0170 (61)
(%)***	1.0155 (57)	1.0157 (70)		1.0350 (14)
Content of the other phase (%)	Not found	Not found	<i>M</i> (4) **** <i>F</i> (25)	<i>M</i> (8) <i>F</i> (17)

* *T_s* is the sintering temperature.

** Since there were no data on the theoretical density of the PSZ ceramics subjected to hot isostatic pressing, it was impossible to calculate the porosity. The value of ρ_{theor} for the PSZ ceramics is equal to 6.1 g/cm³.

*** Content of the tetragonal phase.

**** *F* stands for the cubic phase (fluorite).

in [7]. In our calculations, we used x-ray powder diffraction patterns for the (111) reflections in the angle range 33° ≤ 2θ ≤ 39° and x-ray powder diffraction patterns for the (400) reflections in the angle range 85° ≤ 2θ ≤ 90°. The data were averaged over five points.

The degree of tetragonality *c/a* for the tetragonal phase was determined according to the procedure described in [6].

The average grain size was estimated by analyzing the micrographs obtained using scanning electron microscopy (SEM). For samples of series 1 and 2, we examined the SEM micrographs of the microsections and cleavages, respectively. The results obtained are given in the table.

3. RESULTS AND DISCUSSION

It can be easily verified that the Knudsen relationship (1) does not hold upon substitution of the parameters listed in the table. This can be clearly seen from a thorough analysis of the results presented in the table. For example, the average grain sizes in ceramic samples of series 1, which were sintered at two different temperatures, differ by a factor of 3, with the porosity and strength of the samples being equal. For ceramic samples of series 2, the grain size after hot isostatic pressing is larger than that prior to hot isostatic pressing by a factor of almost 3. In this case, the strength of the ceramic samples subjected to hot isostatic pressing does not decrease but rather increases by 30%. The porosity of 1.64% does not provide an explanation for the above findings: in the case when the strength most

strongly depends on the porosity in terms of relationship (1), i.e., when the coefficient *k* takes on a value of 9, the decrease in the porosity by 1.64% should lead to an increase in the strength by only 14%.

The above-described circumstance forced us to analyze the main characteristic of the tetragonal phase, namely, the ratio of the lattice parameter *c* to the lattice parameter *a*, i.e., the degree of tetragonality *c/a*. Since only the tetragonal phase can transform into the monoclinic phase under tensile stresses and the maximum stresses arising upon three-point bending are localized on a stretched surface of the sample, it is on this surface that the aforementioned phase transformation occurs first of all and is accompanied by compressive stresses that block stress concentrators. In turn, this leads to an increase in the flexural strength σ_{*f*}.

In ceramic samples of series 1, the surface layer down to a depth of 20 μm (which corresponds to the penetration depth of x rays at the given wavelength) consists of grains of the tetragonal phase. This result holds good within the accuracy of the x-ray powder diffraction analysis. In this case, there exist two modifications of the tetragonal phase with degrees of tetragonality *c/a* in the ranges 1.008–1.010 and 1.0155–1.0157.

Ceramic samples of series 1 sintered at a temperature of 1623 K have smaller grains, which should lead to an increase in strength. However, the degree of tetragonality *c/a* is also somewhat smaller, which makes the *T* → *M* transformation difficult. At this point, it should be remembered that the degree of tetragonality *c/a* for the tetragonal phase can vary over a wide range from 1.005 to 1.035. The former value corresponds to

the so-called T' phase, which does not transform under external stresses, and the latter value is characteristic of the easily transformed phase [6, 8]. As regards ceramic samples of series **1** sintered at a temperature of 1773 K, an increase in the grain size is compensated for by an increase in the degree of tetragonality c/a .

This effect of the degree of tetragonality is especially pronounced in ceramic samples of series **2**.

Ceramic samples of series **2** subjected to hot isostatic pressing have very large grains and consist of several phases. This should lead to an abrupt decrease in the flexural strength σ_f . However, we observed quite the reverse: the flexural strength σ_f reached 1400 MPa. This value of σ_f is apparently provided by only 14% of the easily transformed tetragonal phase with the degree of tetragonality $c/a = 1.035$. It is worth noting that, for ceramic samples of series **2** not subjected to hot isostatic pressing, the grain size is smaller by a factor of more than 2 and the strength is considerably lower, even though these samples contain 71% of the tetragonal phase with a relatively high degree of tetragonality $c/a = 1.017$. In closing the analysis of the experimental results, we should note one more very strong effect. For ceramic samples of series **1**, which were sintered at a temperature of 1623 K and had grain sizes $\sim 0.2 \mu\text{m}$, we observed the flexural strength $\sigma_f = 720 \text{ MPa}$. For ceramic samples of series **2**, which were sintered at a temperature of 1773 K and had grain sizes $\sim 0.6 \mu\text{m}$, we obtained $\sigma_f = 1026 \text{ MPa}$. The degrees of tetragonality of these materials differ by no more than 0.0015, whereas the flexural strengths σ_f differ by 306 MPa.

If the above analysis of the experimental results adequately reflects reality, we can argue that, at a sufficiently high density (98–99% of the theoretical value), the degree of tetragonality of the tetragonal phase, rather than its amount, is primarily responsible for the strength of the PSZ ceramics. The higher the degree of tetragonality c/a , the greater the strength of the PSZ ceramics. The observed increase in the strength of the ceramic samples can be explained by the presence of the easily transformed tetragonal phase with a high degree of tetragonality c/a . According to the data obtained by Nikol'skiĭ *et al.* [8], the high degree of tetragonality c/a can be associated with the decreased content of yttrium ions in the crystal lattice of zirconia. In this case, even weak elastic tensile stresses bring about the $T \rightarrow M$ transformation, which naturally occurs at the strongest stress concentrators, thus hampering the nucleation of cracks.

When the amount of the easily transformed tetragonal phase is exhausted, the applied stress becomes relatively strong and the tetragonal phase with a lower degree of tetragonality makes a significant contribution. This leads to a high strength of the ceramic material.

4. CONCLUSIONS

Thus, the results reported in this paper and their analysis allowed us to draw the following conclusions. The strength of PSZ ceramics at a relatively high density (~ 98 – 99% of the theoretical value) substantially depends on the presence (or absence) of a modification of the tetragonal phase with a high degree of tetragonality in the structure. It seems likely that the presence (or absence) of structural elements in the monoclinic or cubic (fluorite) phase does not play a decisive role. The grain size is also of little importance, at least for grain sizes ranging from 0.2 to 1.9 μm . Possibly, the same is also true for larger sized grains, because, according to Jue and Vikar [9], such grains contain morphological elements (twins or domains) with a size of $\sim 0.3 \mu\text{m}$ in the tetragonal phase.

REFERENCES

1. F. P. Knudsen, *J. Am. Ceram. Soc.* **42** (8), 376 (1959).
2. R. M. McMeeking and A. G. Evans, *J. Am. Ceram. Soc.* **65** (5), 242 (1982).
3. F. F. Lange, *J. Mater. Sci.* **17**, 235 (1982).
4. N. Claussen, in *Advances in Ceramics*, Ed. by N. Claussen, M. Rühle, and A. H. Heuer (American Ceramic Society, Columbus, Ohio, 1984), Vol. 12, Part II, p. 325.
5. G. Ya. Akimov and V. M. Timchenko, *Ogneupory Tekh. Keram.*, No. 10, 6 (2003).
6. G. Ya. Akimov, G. A. Marinin, and V. Yu. Kameneva, *Fiz. Tverd. Tela (St. Petersburg)* **46** (2), 250 (2004) [*Phys. Solid State* **46** (2), 254 (2004)].
7. M. I. Kabanova and V. A. Dubok, *Poroshk. Metall. (Kiev)*, No. 5, 85 (1992).
8. V. Yu. Nikol'skiĭ, S. K. Filatov, T. A. Zhuravina, and V. A. Frank-Kamenetskiĭ, *Izv. Akad. Nauk SSSR, Neorg. Mater.* **8** (8), 1500 (1972).
9. J. F. Jue and A. V. Vikar, *J. Am. Ceram. Soc.* **73** (12), 3650 (1990).

Translated by N. Korovin

MAGNETISM AND FERROELECTRICITY

Magnetic Moments and Hyperfine Magnetic Fields in Ordered and Disordered Quasi-Binary $\text{Fe}_{75}(\text{Si}_{1-x}\text{Ge}_x)_{25}$ Alloys

A. K. Arzhnikov, L. V. Dobysheva, G. N. Konygin, and E. P. Elsukov

Physicotechnical Institute, Ural Division, Russian Academy of Sciences, ul. Kirova 132, Izhevsk, 426001 Russia

e-mail: arzhnikov@otf.pti.udm.ru

Received October 22, 2004

Abstract—Disordered and DO_3 type-ordered $\text{Fe}_{75}(\text{Si}_{1-x}\text{Ge}_x)_{25}$ alloys are fabricated and investigated using x-ray diffraction, Mössbauer spectroscopy, and magnetic measurements. The variations in the magnetic and Mössbauer characteristics are interpreted using *ab initio* calculations of the electronic structure, magnetic moments, hyperfine magnetic fields, and isomer shifts. The main differences in the properties are related to the increase in the crystal lattice parameter when Si is replaced by Ge in ordered alloys and to a different behavior of the correlations in the Si and Ge positions in disordered alloys. © 2005 Pleiades Publishing, Inc.

1. INTRODUCTION

Binary $\text{Fe}_{1-x}M_x$ ($M = \text{Si}, \text{Sn}, \text{Ge}$) alloys are classical model objects for analyzing magnetic properties that are dependent on the type and concentration of the *sp* element and on the parameters and type of the crystal lattice [1–6]. By studying quasi-binary $\text{Fe}_{75}(\text{Si}_{1-x}\text{Sn}_x)_{25}$ and $\text{Fe}_{75}(\text{Si}_{1-x}\text{Ge}_x)_{25}$ alloys, it is possible to compare the effect of different *sp* elements. Disordered $\text{Fe}_{75}(\text{Si}_{1-x}\text{Sn}_x)_{25}$ alloys were prepared and studied in [7]. To date, $\text{Fe}_{75}(\text{Si}_{1-x}\text{Ge}_x)_{25}$ alloys have not been fabricated in the entire range of values of the parameter x . Based on earlier data [3, 8], we assumed that $\text{Fe}_{75}(\text{Si}_{1-x}\text{Ge}_x)_{25}$ alloys could be obtained not only in a disordered state but also in the ordered phase of type DO_3 (Fig. 1; in what follows, samples of this type are referred to as $\text{Fe}_3\text{Si}_{1-x}\text{Ge}_x$). The preparation of the ordered phase would extend the possibilities for studying the relation between the magnetic properties and the local characteristics of the crystalline structure.

In this work, we fabricated disordered samples $\text{Fe}_{75}(\text{Si}_{1-x}\text{Ge}_x)_{25}$ in the entire range of values of the parameter x using the method of mechanical alloying; then, the samples were DO_3 -type ordered by thermal treatment. Disordered and ordered samples were studied using x-ray diffraction, Mössbauer spectroscopy, and magnetic measurements.

To explain the main laws of the variation of the magnetic and Mössbauer characteristics, we performed *ab initio* calculations of the electronic structure, magnetic moments, hyperfine magnetic fields (HFMFs), and isomer shifts of ordered Fe_3Si , $\text{Fe}_{12}\text{Si}_3\text{Ge}$, $\text{Fe}_{24}\text{Si}_4\text{Ge}_4$, $\text{Fe}_{12}\text{SiGe}_3$, Fe_3Ge , $\text{Fe}_{25}\text{Si}_7$, $\text{Fe}_{25}\text{Si}_3\text{Ge}_4$, and $\text{Fe}_{25}\text{Ge}_7$ alloys and disordered Fe_3Si and Fe_3Ge alloys.

2. EXPERIMENTAL METHODS AND RESULTS

Disordered $\text{Fe}_{75}(\text{Si}_{1-x}\text{Ge}_x)_{25}$ samples ($x = 0, 0.2, 0.4, 0.6, 0.8, 1.0$) were fabricated by mechanical alloying in a “Pulverizette-7” planetary ball mill from high-purity components of appropriate composition. Grinding was performed in an argon atmosphere over 16 h using bowls and balls of ShKh-15 steel. The mass of the originally loaded powder was 10 g. Possible penetration of the grinder materials into the sample under study was monitored by gravimetric measurements of the bowls, balls, and powder before and after grinding. The weight

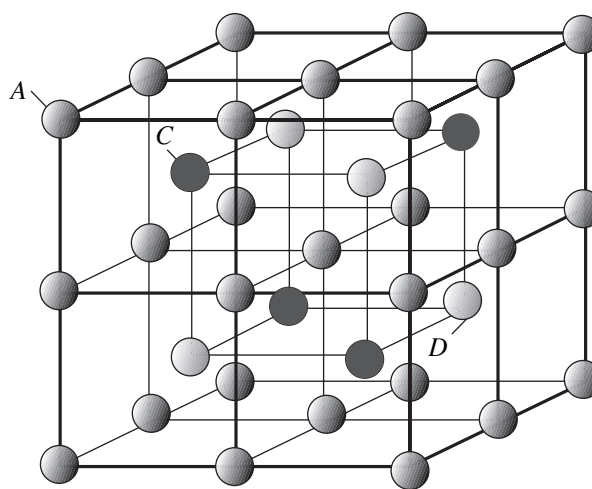


Fig. 1. The DO_3 -type ordered phase. Sites D are occupied by atoms of *sp* elements, and sites A and C are occupied by iron atoms and have nonequivalent environments.

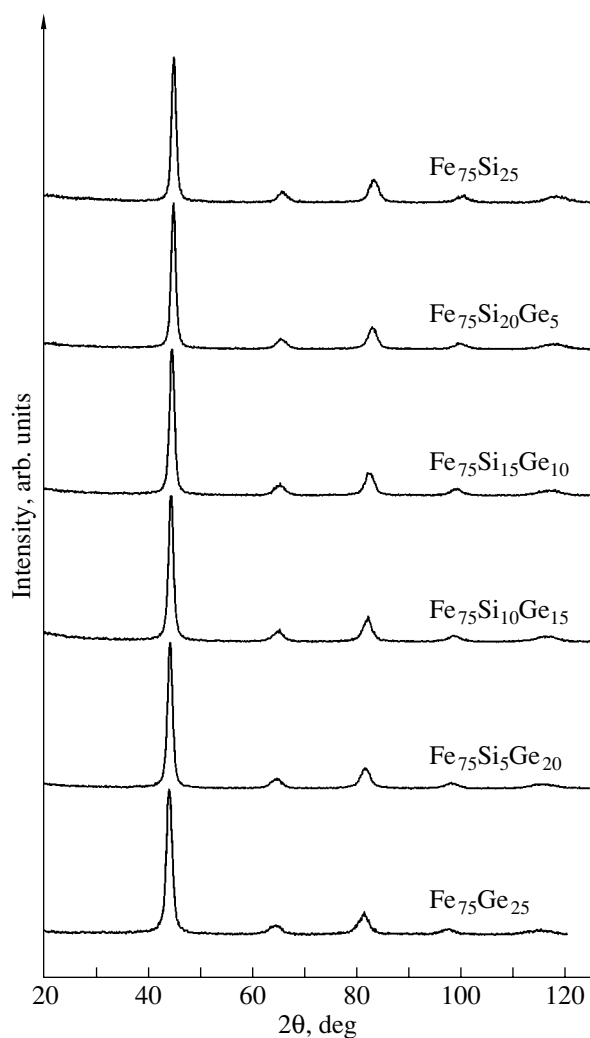


Fig. 2. X-ray diffraction patterns ($\text{CuK}\alpha$ radiation) of mechanically alloyed $\text{Fe}_{75}(\text{Si}_{1-x}\text{Ge}_x)_{25}$ powders. The grinding time is $t_{\text{grind}} = 16$ h.

increase after grinding was less than 1% for all samples.

To obtain an ordered state, the ground samples were annealed over 4 h in a vacuum furnace at temperatures of 723 K ($\text{Fe}_{75}\text{Ge}_{25}$) and 773 K (for $x < 1$).

Earlier published data [1, 7, 9] on a disordered $\text{Fe}_{75}\text{Si}_{25}$ solid solution and the Fe_3Si DO_3 -type ordered phase were used.

X-ray powder diffraction patterns were obtained at room temperature using a DRON-3 diffractometer (monochromated $\text{CuK}\alpha$ radiation). Mössbauer spectra were recorded using a YaGRS-4M spectrometer with a ^{57}Co source in a Cr matrix at a temperature of 77 K. Mathematical processing of Mössbauer spectra was performed using a continuous (based on a generalized regular algorithm for solving inverse problems [10]) and a discrete representation. Data on the saturation magnetization were obtained using a vibrating-sample

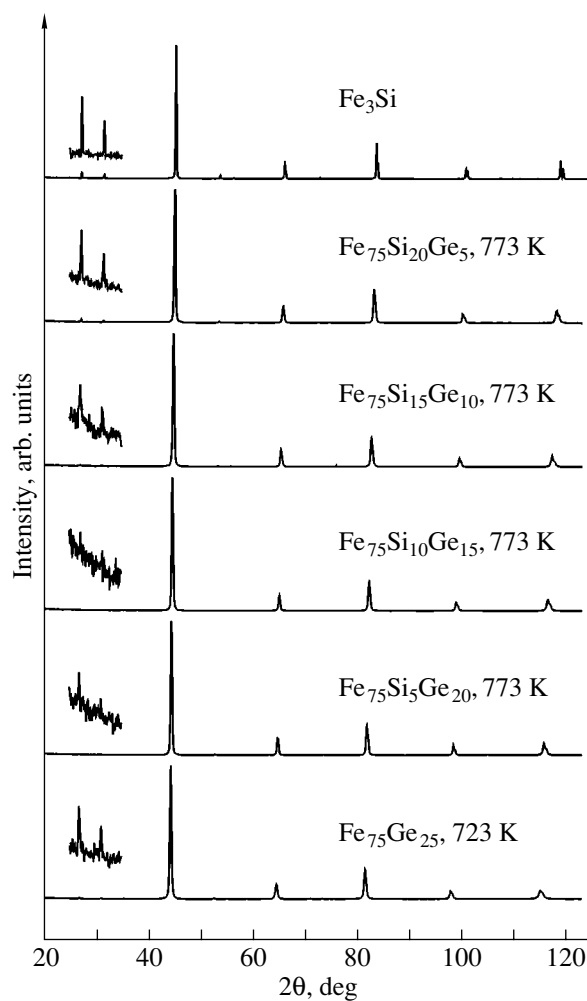


Fig. 3. X-ray diffraction patterns ($\text{CuK}\alpha$ radiation) of $\text{Fe}_3(\text{Si}_{1-x}\text{Ge}_x)$ powders annealed at various temperatures over $t_{\text{ann}} = 4$ h.

magnetometer at 77 K in an external magnetic field of $1.27 \times 10^6 \text{ A m}^{-1}$. From these data, the average magnetic moments per iron atom \bar{m}_{Fe} were calculated.

In the x-ray diffraction patterns of all ground samples, only broadened bcc reflections were observed, without any additional lines from possible pure components of the loaded mixture and their compounds (Fig. 2). This fact confirms the single-phase nature of the nanocrystalline state of the alloys obtained. In the diffraction patterns of the annealed samples (Fig. 3), a set of bcc reflections and (111) and (200) superstructural reflections corresponding to the DO_3 -ordered structure was observed. Reflections that would indicate phase decomposition of the samples during annealing were not observed. The lattice corresponding to the DO_3 ordering in Fe_3Si is shown schematically in Fig. 1. When ordered, Si and Ge atoms randomly occupy D sites. At small deviations from the stoichiometric com-

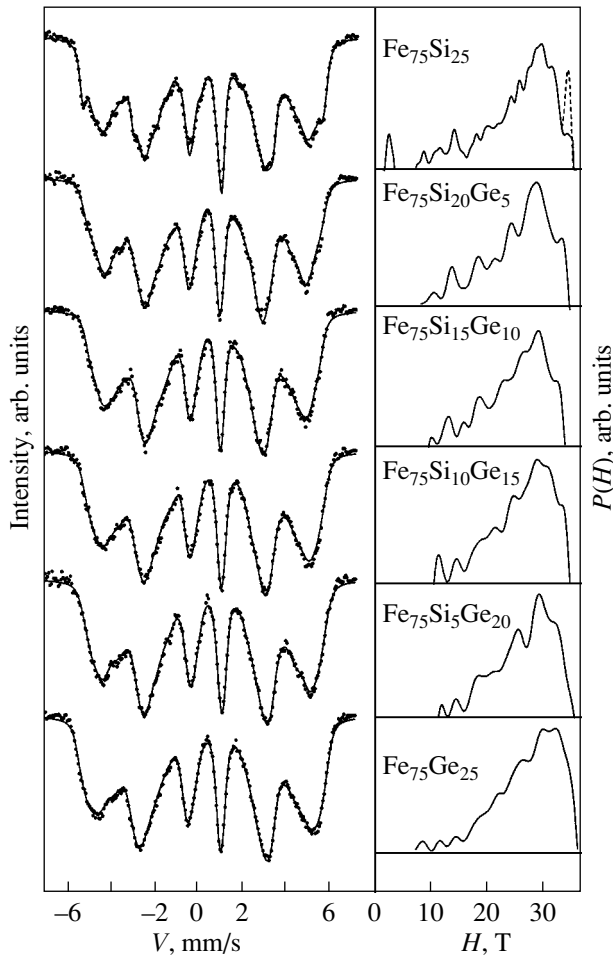


Fig. 4. Mössbauer spectra and hyperfine magnetic field distribution functions $P(H)$ for mechanically alloyed $\text{Fe}_{75}(\text{Si}_{1-x}\text{Ge}_x)_{25}$ powders. $t_{\text{grind}} = 16$ h, and the measurement temperature is $T_{\text{measur}} = 77$ K.

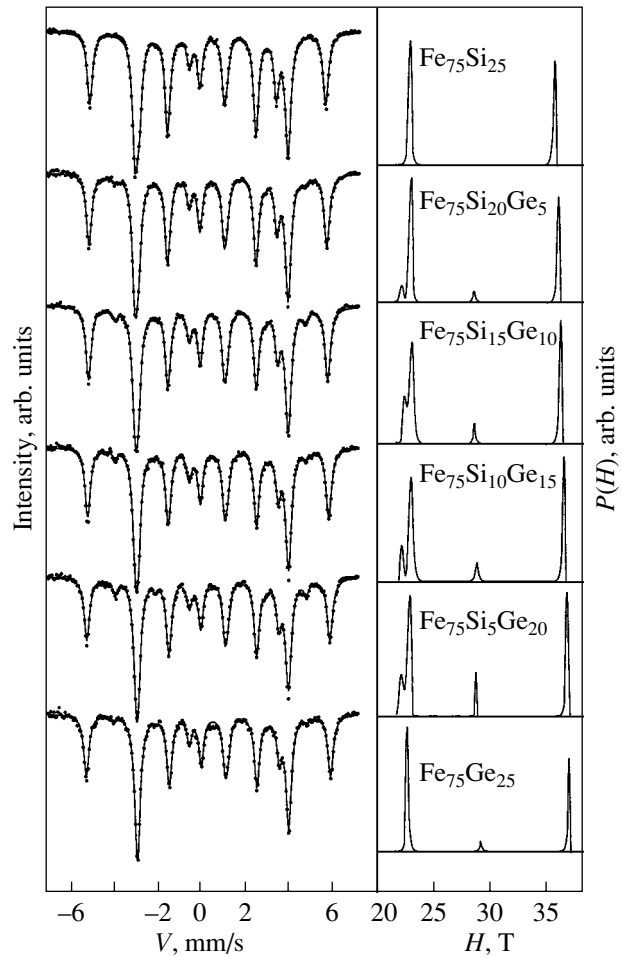


Fig. 5. Mössbauer spectra and hyperfine magnetic field distribution functions $P(H)$ for $\text{Fe}_3\text{Si}_{1-x}\text{Ge}_x$ powders annealed over $t_{\text{ann}} = 4$ h.

position, in alloys with a lower content of sp elements, additional iron atoms replace Si or Ge. In alloys with a Si and Ge content exceeding 25 at. %, excess sp atoms replace iron atoms without forming nearest neighbor pairs; i.e., they occupy C sites (Fig. 1).

Mössbauer spectra and the corresponding HFMF distribution functions $P(H)$ for mechanically alloyed $\text{Fe}_{75}(\text{Si}_{1-x}\text{Ge}_x)_{25}$ powders are shown in Fig. 4. The spectra have a shape (characteristic of disordered crystalline systems) corresponding to a set of different local atomic configurations of the environment of iron atoms, with smooth lines, without any components from the possible phases, and with smooth functions $P(H)$. With increasing germanium concentration, the function $P(H)$ shifts to a higher field region.

The Mössbauer spectra and the functions $P(H)$ of the samples that were ground and subsequently ordered by annealing (Fig. 5) agree with the results of the x-ray studies and confirm that the heat treatment indeed converted the alloys under study to the DO_3 -ordered state.

There are two nonequivalent positions of iron atoms (Fig. 1): position C , where all eight neighboring sites are occupied by iron atoms and the magnitude of the HFMF is $H_0 \approx 33.3\text{--}34.7$ T, and position A , where there are four (Si, Ge) atoms and four iron atoms in the first coordination sphere and $H_4 \approx 21.5$ T. The additional low-intensity component in the Mössbauer spectra and in the $P(H)$ curve in the region of 27.0 T belongs to iron atoms with three atoms of an sp element in their nearest environment (H_3), thus indicating a deviation from the stoichiometric composition to a lower impurity concentration. The relative intensities of the components of the Mössbauer spectra with three (I_3) and four (I_4) (Si, Ge) atoms in the nearest environment of an iron atom and the calculated concentration dependences of the probabilities of the corresponding local atomic configurations $P_3^{DO_3}$ and $P_4^{DO_3}$ show that the maximum deviation from the stoichiometric composition (75 at. % Fe) is 0.7 at. % in the $\text{Fe}_{75}\text{Si}_5\text{Ge}_{20}$ sample (Fig. 6). The probabilities P_k of the formation of local atomic configura-

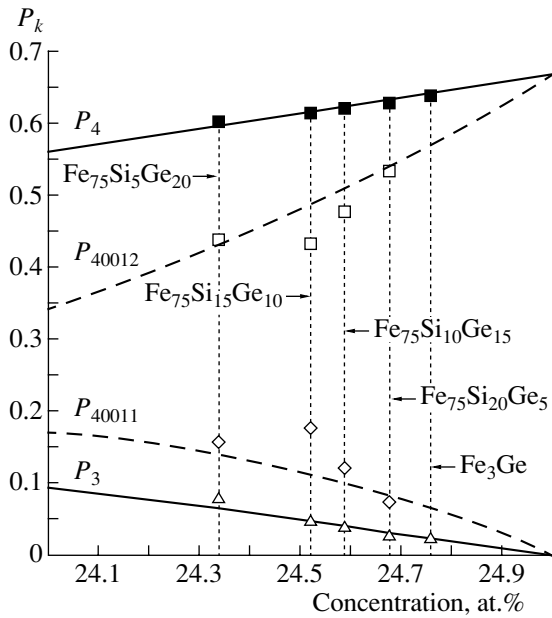


Fig. 6. Probabilities $P_3^{DO_3}$ and $P_4^{DO_3}$ (solid lines), the contributions of the [4 0 0 1 1] and [4 0 0 1 2] configurations to $P_4^{DO_3}$ (dashed lines), and the intensities of separate components of the Mössbauer spectra of annealed samples, which are superimposed on these curves for estimating the real composition of an alloy. The intensities I_3 are shown by triangles, I_4 by open squares, and I_{4s} by diamonds; closed squares correspond to the sum of I_4 and I_{4s} .

tions with a fixed number k of atoms of the sp elements in the nearest environment of an Fe atom were calculated from the conditions for atoms of the sp elements to be replaced randomly by iron atoms:

$$\begin{aligned} P_3^{DO_3} &= \frac{2}{3+4y} 4y(1-y)^3, \\ P_4^{DO_3} &= \frac{2}{3+4y} (1-y)^4. \end{aligned} \quad (1)$$

Here, y is the deviation of the iron concentration from its stoichiometric value to higher concentrations.

Figure 5 shows that the shape of the function $P(H)$ in the region corresponding the H_4 component varies with the relative content of silicon and germanium. For binary intermetallic compounds, the distribution $P(H)$ is narrow and symmetric (Fig. 5), whereas for $0 < x < 1$ the distribution is broadened and asymmetric. In discrete processing, this asymmetry was taken into account as an additional satellite line, which we denote by H_{4s} . The results of processing the spectra using discrete and continuous representations (the values of HFMFs and isomer shifts) are shown in Fig. 7. These two sets of the experimental data obtained using differ-

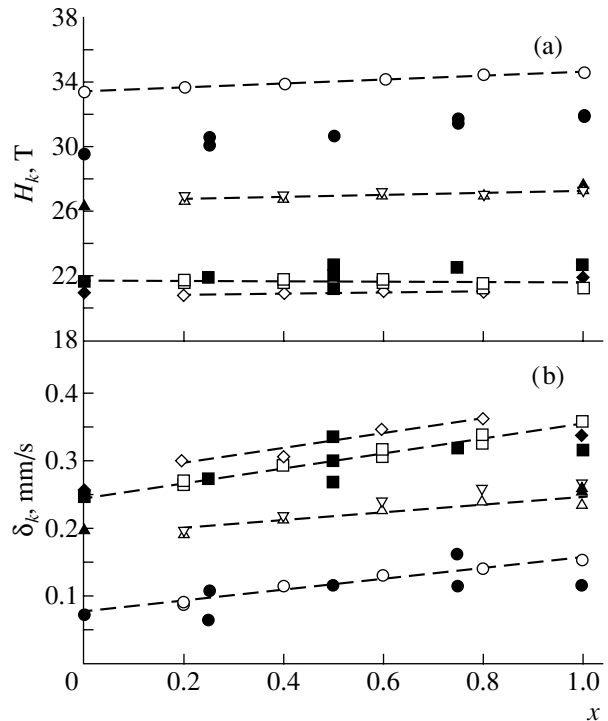


Fig. 7. Concentration dependence of (a) hyperfine magnetic fields H_k and (b) isomer shifts δ_k (k is the number of (Si, Ge) atoms in the nearest environment of an iron atom) for annealed $\text{Fe}_3\text{Si}_{1-x}\text{Ge}_x$ powders. H_0 and δ_0 are shown by circles, H_3 and δ_3 by triangles, H_4 and δ_4 by squares, and H_{4s} and δ_{4s} by diamonds. Open symbols correspond to experimental data, and solid symbols indicate theoretical data.

ent methods of spectrum processing, except for a satellite component, virtually coincide and therefore are shown in Fig. 7 by the same symbols. With increasing germanium content, the HFMFs H_0 and H_3 increase from 33.4 to 34.7 T and from 26.8 up to 27.4 T, respectively. The hyperfine fields corresponding to four impurity atoms remain practically unchanged both for the main component $H_4 = 21.5$ T and for the satellite component $H_{4s} = 21.0$ T. The intensity of the latter component, I_{4s} , as determined by discrete processing varies from 8% at $x = 0.2$ to 18% at $x = 0.6$. The isomer shifts δ corresponding to the above local atomic configurations increase linearly with x (Fig. 7). It should be noted that in Fig. 7 the hyperfine interaction parameters H_4 and δ_4 calculated from $P(H)$ are obtained without separating the main and satellite components in $P(H)$.

The quantitative results of the study of the behavior of the average characteristics are shown in Fig. 8. With increasing germanium concentration, the bcc lattice parameter increases linearly from 0.2838 to 0.2896 nm for disordered alloys and from 0.2826 to 0.2882 nm for ordered alloys (Fig. 8a). The average magnetic moment of an iron atom \bar{m}_{Fe} calculated from the saturation

magnetization increases with x from 1.64 to 2.03 μ_B for disordered alloys, whereas in the ordered state the variation of \bar{m}_{Fe} is weak (Fig. 8b). The average hyperfine magnetic field at an iron atomic nucleus \bar{H}_{Fe} increases from 24.6 to 27.4 T for the disordered state and remains practically unchanged (26.2 T) for the ordered state. The average isomer shift $\bar{\delta}_{Fe}$ changes from 0.13 to 0.24 mm s⁻¹ and from 0.18 to 0.29 mm s⁻¹ for ground and annealed powders, respectively. The ratio $\bar{H}_{Fe}/\bar{m}_{Fe}$ also changes, decreasing from 14.8 to 13.4 T/ μ_B for disordered alloys and from 16.4 to 15.8 T/ μ_B for ordered systems.

It should be noted that, first, in contrast to the non-linear relations for Fe₇₅(Si_{1-x}Sn_x)₂₅ alloys [7], in this case all concentration dependences are almost linear and, second, during ordering, the magnetic moment at high Ge concentrations undergoes more significant changes than at low concentrations (Fig. 8b).

3. THEORETICAL CALCULATIONS: METHODS AND RESULTS

In this study, we performed quantum-mechanical calculations of the electronic structure, magnetic moments, hyperfine magnetic fields, and isomer shifts using the spin-polarized density-functional theory. The exchange-correlation potential was described in the local density approximation (LDA) [11]. As shown in [12], the LDA and the generalized gradient approximation (GGA) [13] yield the same results in many cases if they are scaled by the magnitude of the magnetic moment.

Since the experimental data indicate that the lattice remains bcc in the entire concentration range, the systems were simulated using a bcc lattice. The values of the lattice parameters were chosen to be equal to the experimental ones.

Calculations were performed by two methods. The method of linearized plane waves FP LAPW (WIEN2k software package [14]) was used to perform simulation for the Fe₃Si, Fe₁₂Si₃Ge, Fe₂₄Si₄Ge₄, Fe₁₂SiGe₃, Fe₃Ge, Fe₂₅Si₇, Fe₂₅Si₃Ge₄, and Fe₂₅Ge₇ periodic systems. Calculations for ordered and disordered Fe₃Si and Fe₃Ge systems were performed using the Korringa-Kohn-Rostoker (KKR) method and the software package from [15].

Fully relativistic KKR calculations were performed using the parametrization of the exchange-correlation potential suggested in [16]. The conventional values of the main parameters for this software package were chosen in the calculations. The number of points on the energy scale from $E_{min} = -0.3$ Ry to the Fermi level was equal to 250. Expansions in angular momentum were performed up to $l_{max} = 4$. The number of created k vectors was 834. Calculations for disordered systems were

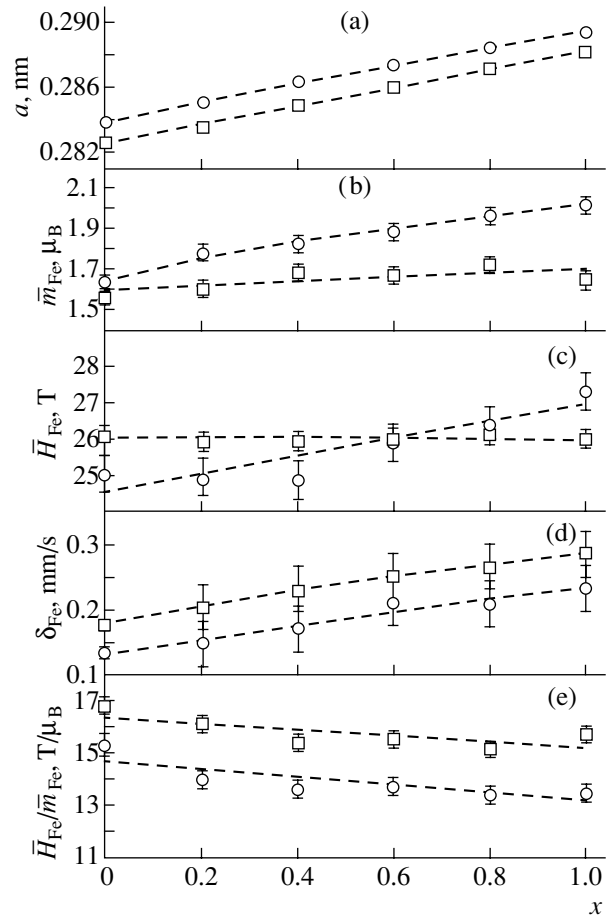


Fig. 8. Concentration dependence of (a) the bcc lattice parameter, (b) average magnetic moment \bar{m}_{Fe} , (c) average hyperfine magnetic field \bar{H}_{Fe} at a ^{57}Fe nucleus site, (d) average isomer shift $\bar{\delta}_{Fe}$ (α_{Fe}), and (e) $\bar{H}_{Fe}/\bar{m}_{Fe}$ ratio for mechanically alloyed (circles) and annealed (squares) Fe₇₅(Si_{1-x}Sn_x)₂₅ powders.

performed in the coherent potential approximation (CPA).

When using the FP LAPW method, we expanded the wave functions, charge density, and potential in terms of spherical harmonics in nonoverlapping atomic spheres of radius R_{MT} and in terms of plane waves in the remaining part of the unit cell. The basis set of functions was divided into valence and core (for electrons at the inner levels) parts. The core levels we took to be the 1s, 2s, 2p, and 3s levels for iron; the 1s, 2s, 2p, 3s, and 3p levels for germanium; and the 1s, 2s, and 2p levels for silicon. These states were calculated using a spherical potential and were assumed to have a spherically symmetric charge density and to be almost completely confined inside the muffin-tin spheres of radius R_{MT} . The radius of spheres was chosen to be $R_{MT} = 2.3$ au for all atoms. The valence electron wave functions inside the atomic spheres were expanded up to $l_{max} = 10$ and

Table 1. The average magnetic moment per iron atom, magnetic moments (measured in Bohr magnetons μ_B), HFMFs (in teslas), and isomer shifts (in millimeters per second) for nonequivalent iron atoms in ordered alloys

	x	a_{lat} , nm	$\bar{m}_{\text{Fe}}^{\text{ord}}$	Config-uration	m_0	H_0	δ_0	Configuration	m_4	H_4	δ_4
Fe ₃ Si	0	0.2815	1.65	[0 6 0 0]	2.52	-26.9	0.074	[4 0 0 12]	1.28	-19.6	0.246
Fe ₂₅ Si ₇ *		0.2815						[4 0 0 11]	1.26	-19.1	0.257
Fe ₁₂ Si ₃ Ge	0.25	0.2838	1.69	[0 6 0 0]	2.48	-27.5	0.065	[4 0 0 12]	1.32	-19.9	0.273
				[0 6 0 0]	2.57	-27.8	0.109	[4 0 0 12]			
Fe ₂₄ Si ₄ Ge ₄	0.5	0.28575	1.68	[0 6 0 0]	2.56	-27.9	0.116	[4 0 0 12]**	1.38	-20.6	0.270
								[4 0 0 12]***	1.31	-20.0	0.301
								[4 0 0 12]****	1.23	-19.4	0.339
Fe ₁₂ SiGe ₃	0.75	0.2866	1.73	[0 6 0 0]	2.64	-28.9	0.164	[4 0 0 12]	1.37	-20.5	0.320
				[0 6 0 0]	2.56	-28.7	0.117	[4 0 0 12]			
Fe ₃ Ge	1.0	0.2880	1.74	[0 6 0 0]	2.60	-29.1	0.119	[4 0 0 12]	1.37	-20.7	0.319
Fe ₂₅ Ge ₇ *		0.2880						[4 0 0 11]	1.39	-20.0	0.341
Fe ₃ Si	0	0.2880	1.74	[0 6 0 0]	2.60	-28.6	0.142	[4 0 0 12]	1.39	-20.9	0.304

* Simulation of this system was performed in order to determine the configuration that arises in a non stoichiometric compound.

** Configuration with four Si atoms in the nearest environment.

*** Configuration with two Si atoms and two Ge atoms in the nearest environment.

**** Configuration with four Ge atoms in the nearest environment.

Table 2. Magnetic moments (measured in Bohr magnetons μ_B), HFMFs (in teslas), and isomer shifts (in millimeters per second) for iron atoms with different configurations of the nearest environment

	a_{lat} , nm	Configura-tion	m_0	H_0	δ_0	Configura-tion	m_k	H_k	δ_k			
Fe ₁₅ Si	0.2838	[0 2 0 0]	2.22	-27.4	0.036	[1 0 0 3]	2.04	-27.8	0.080			
		[0 0 4 0]	2.23	-26.7	0.016							
		[0 0 0 0]	2.37	-29.2	0.050							
Fe ₁₄ Si ₂	0.2838	[0 2 4 0]	2.34	-24.8	0.026	[2 0 0 6]	1.75	-25.5	0.143			
Fe ₂₅ Si ₃ Ge ₄	0.2880	[0 5 0 0]	2.56	-29.4	0.126	[3 0 0 10]	1.74	-25.3	0.260			
		[0 4 0 0]	2.55	-29.5	0.115	[4 0 0 11]				1.39	-20.3	0.320
		[0 6 0 0]	2.52	-29.6	0.141							
		[0 6 0 0]	2.58	-28.9	0.141							
		[0 0 12 0]	2.55	-23.7	0.056							

calculated with the potential expanded in spherical harmonics up to $l = 4$. We used the APW + lo basis [17] with additional local orbitals for the Fe $3p$ and Ge $3d$ states. The wave functions in the interstitial region were expanded in plane waves with a cutoff vector K_{max} defined by the relation $R_{\text{MT}} K_{\text{max}} = 7$. The charge density was expanded in a Fourier series up to $G_{\text{max}} = 20$. A grid of 35 k points was chosen in the irreducible part of the Brillouin zone. Practice shows that such a choice of the parameters ensures the accuracy of calculations required for the systems under study.

The results of simulations are listed in Tables 1–3. In these tables and further in the text, we denote various

atomic configurations of the environment by the symbol $[nmk\dots]$, where n is the number of atoms of the sp elements in the first coordination sphere, m is the number of these atoms in the second coordination sphere, etc. For all systems, except for Fe₃Si and Fe₃Ge having a symmetric structure, the relaxation of atoms inside the unit cell was simulated under the condition that the forces acting on the atoms be zero. For the Fe₂₄Si₄Ge₄ system, simulations were performed in an extended cell in order to generate nonequivalent configurations of the nearest environment with four Ge atoms, with four Si atoms, and with two Ge atoms and two Si atoms. Likewise, to interpret the lines related to a nonstoichiomet-

Table 3. Hyperfine magnetic fields (in teslas) and the average magnetic moment (in Bohr magnetons μ_B) for an iron atom in ordered and disordered alloys

	a_{lat} , nm	H_0	H_4	$m_{\text{Fe}}^{\text{ord}}$	a_{lat} , nm	H_0	H_4	$\bar{m}_{\text{Fe}}^{\text{ord}}$	$\bar{m}_{\text{Fe}}^{\text{disord}}$
Fe ₃ Si(KKR)	0.2815	-26.7	-19.0	1.71	0.2838	-27.3	-19.6	1.74	2.08
Fe ₃ Si(WIEN)	0.2815	-26.9	-19.6	1.65	0.2838	-27.5	-20.1	1.68	-
Fe ₃ Ge(KKR)	0.2880	-28.5	-20.3	1.80	0.2896	-29.9	-20.0	1.91	2.27
Fe ₃ Ge(WIEN)	0.2880	-29.1	-20.7	1.74	0.2896	-29.7	-21.0	1.77	-

ric composition, an extended cell was used to simulate the Fe₂₅Si₃Ge₄, Fe₂₅Si₇, and Fe₂₅Ge₇ systems, in which there are cluster configurations with three *sp* atoms in the nearest environment. To study the effect of the lattice parameter on the magnetic properties, calculations were performed for the Fe₃Si and Fe₃Ge systems with the same lattice constant equal to 0.2880 nm (Table 1).

We note that the calculated values of the HFMFs differ from the experimental values. However, this difference has a regular character. This type of disagreement between theory and experiment for HFMFs is customary. We believe that the deviations from the experimental data arise because the approximations of the exchange-correlation potential are not sufficiently good. Therefore, it is more reasonable to compare the calculated HFMFs with the experimental data using relative units (for example, reducing them to one of the values of the field in a given series of samples). Indeed, a comparison of relative results shows quite good agreement with experiment (Fig. 7).

Using the KKR method, we performed simulations for ordered and disordered Fe₃Si and Fe₃Ge alloys (Table 3). In the table, the data are listed for ordered systems with lattice parameters characteristic of the ordered and disordered alloys and for disordered systems with the corresponding parameters. For comparison, the results of the FP LAPW (WIEN) calculations are also shown. In the proposed realization of the KKR method in the coherent potential approximation, there is no possibility of calculating the HFMFs as a function of the nearest environment. Moreover, in a one-site approximation such as CPA, calculations of the HFMFs in the disordered case are generally problematic [18, 19]. Earlier in our calculations [20, 21], we were repeatedly convinced that the changes in the HFMFs in binary alloys of iron with *sp* elements are mainly related to the changes in the spin polarization of the core electrons at the nucleus site, which, in turn, is proportional to the magnetic moment of the atom to a high accuracy. Calculations performed for ordered quasi-binary alloys also confirm this proportionality and the predominance of the contribution of polarization of the core electrons to the HFMFs. Judging by experiment (Fig. 8e), this trend is also observed for disordered quasi-binary alloys. Therefore, we can estimate the average HFMFs in disordered samples from the average magnetic moment calculated in the CPA.

The isomer shift was calculated using the formula

$$\delta_k = A - B\rho_k(0), \quad (2)$$

where $\rho_k(0)$ is the electron density at the nucleus site of an iron atom having k atoms of the *sp* elements in its nearest environment. The coefficients A and B ($A = 3240.3359$, $B = 0.21286470$) were chosen from the condition that, in the ordered Fe₃Si alloy, the calculated and experimental isomer shifts δ_0 and δ_4 are equal. We note that, both in experiment and in theory, the values obtained for the isomer shift should be treated with care. In experiment, the reason for this is related to the possible inevitable errors in absolute measurements, and in theory, to a low relative accuracy of calculating the quantities $\rho_k(0)$. When calculating the HFMFs, integration is performed over a sufficiently large sphere (which reduces the possible errors). As for δ_k , the quantities are calculated at one point lying very close to the center of the nucleus, i.e., in the most problematic region for approximations of the exchange-correlation potential. The isomer shifts calculated from Eq. (2) for ordered ternary alloys are shown in Fig. 7 and Table 1.

4. DISCUSSION

Above all, we consider the HFMFs in *DO*₃-ordered systems. By comparing the experimental and theoretical data (Figs. 7, 8), we can conclude that the changes in the HFMFs with increasing germanium concentration are related to the increase in the local magnetic moments and, accordingly, to a greater contribution of the polarization of core electrons to the HFMFs (Table 1). In turn, the increase in the local magnetic moment is due to the increase in the crystal lattice parameter. In these systems, just as in the binary systems [20], the increase in the local moment with the lattice constant is due to a decrease in the overlap of the wave functions of the *d* electrons located at different sites and to the concomitant narrowing of the *d* band. To find additional justification for this statement, we performed calculations for the Fe₃Si and Fe₃Ge systems with the same lattice constant (Table 1). From Table 1, it can be seen that, in this case, the magnetic moments and HFMFs for both systems virtually coincide.

A comparison of the intensities of the H_3 and H_4 components with the probabilities of formation of the

configurations with three and four atoms (Fig. 6) and the results of *ab initio* calculations (Table 2) confirm the assumption regarding the reason for the value of the HFMF in the region of 2.7 T. This HFMF value is related to the nonstoichiometry of the composition and the appearance of configurations with three atoms of the *sp* elements in the nearest environment of an iron atom.

It is more difficult to explain the nature of the satellite H_{4s} appearing at intermediate concentrations, $x = 0.2, 0.4, 0.6,$ and 0.8 (Fig. 5). The assumption that the satellite is related to local crystal distortions of asymmetrical configurations of atoms of different types in the nearest environment is not confirmed by the calculations. It should be noted that the satellite appears simultaneously with the component H_3 associated with a nonstoichiometric composition (Fig. 5). At deviations from the stoichiometric composition to higher iron concentrations, there appear not only iron atoms with three atoms of the *sp* elements in the nearest environment but also nonequivalent positions of iron atoms with four atoms of the *sp* elements in the nearest environment; they differ in terms of the number of atoms of the *sp* elements in the fourth coordination sphere: [4 0 0 1 2], [4 0 0 1 1], etc. The probabilities of the most probable [4 0 0 1 2] and [40011] configurations are determined by the expressions

$$\begin{aligned} P_{40012}^{DO_3} &= \frac{2}{3+4y}(1-y)^4(1-y)^{12}, \\ P_{40011}^{DO_3} &= \frac{2}{3+4y}(1-y)^4(1-y)^{11}12y, \end{aligned} \quad (3)$$

where, as in Eq. (1), y is a deviation from stoichiometry. The probabilities of configurations with ten or less *sp* atoms in the fourth coordination sphere, which are proportional to $o(y^2)$, are small at small deviations from stoichiometry, and we disregard them.

In Fig. 6, which shows these probabilities, we see that, at small deviations, the probability $P_{40011}^{DO_3}$ can be as high as 10–15%. The *ab initio* calculations show (Table 1) that the HFMF for the [4 0 0 1 1] configuration is 0.5 to 0.7 T lower than that for the [4 0 0 1 2] configuration. This result is in reasonable agreement with the position of the satellite with respect to the H_4 line. Thus, we can assert that the splitting of the H_4 line is due to the appearance of two configurations with different numbers of *sp* atoms in the fourth coordination sphere. The intensities of these lines depend on the deviation of the concentration from the stoichiometric composition and are determined by Eqs. (3). In Fig. 6, the line intensities are compared with the probabilities. It is seen that the experimental data are in reasonable agreement with the calculated values for the [4 0 0 1 1] and [4 0 0 1 2] configurations and $P_3^{DO_3}$.

Theoretical calculations explain the concentration changes in the magnetic moment and HFMFs in the DO_3 -ordered alloys. However, for disordered alloys, calculations of the magnetic moment do not agree with the changes observed experimentally. The calculations show that, for Fe_3Ge and Fe_3Si , the relative changes in the magnetic moment caused by the transition from the disordered to the DO_3 -ordered phase are approximately the same (Table 3). The fact that the value of the magnetic moment is larger in the disordered phase is partially due to the larger lattice parameter, but mainly it is caused by the formation of configurations with one, two, and three *sp* atoms in the nearest environment and by the decrease in the number of configurations with four atoms. Studies of disordered binary alloys have shown that the magnetic moment of iron in the configurations with one and two *sp* atoms in the nearest environment is close to the magnetic moment of pure iron [5]. In a disordered state, these configurations are most probable at an Fe concentration of 75 at. %. Therefore, the average magnetic moment increases at the expense of a decrease in the number of iron atoms with four *sp* atoms in the nearest environment and with a rather low magnetic moment. This conclusion is easily verified by calculating the average number of *sp* atoms in the nearest environment:

$$\bar{k} = \sum_{k=0}^8 kP_k,$$

where k is the number of *sp* atoms in the nearest environment and P_k is the probability of the formation of configurations with k atoms of the *sp* elements. In the case of complete disorder (in the absence of correlations in the positions of *sp* atoms), we have

$$P_k = \frac{8!}{k!(8-k)!}(0.25-y)^k(0.75+y)^{8-k}, \quad (4)$$

where y is the deviation of the iron concentration from a stoichiometric value of 75 at. %. For $y = 0$, we have $\bar{k} = 2$, whereas for a DO_3 -ordered alloy, $P_0 = 1/3$, $P_4 = 2/3$, and $\bar{k} \approx 2.7$.

From the experimental data (Fig. 8b), we see that the change in the magnetic moment under ordering in the $Fe_{75}Ge_{25}$ alloy is much greater than that in the $Fe_{75}Si_{25}$ alloy. Therefore, the ordering and disordering processes in these alloys are different. Deconvolution of the Mössbauer spectra of disordered $Fe_{75}Si_{25}$ alloys into elementary spectra of separate configurations and EXAFS measurements show that the average number of Si atoms in the nearest environment differs strongly from 2 (the figure corresponding to complete disorder) and is equal to $\bar{k}_{\text{Mössb}} \approx 2.7$ [1] or $\bar{k}_{\text{EXAFS}} \approx 2.8$ [9]. On the contrary, for a disordered $Fe_{75}Ge_{25}$ alloy, this number is close to 2 ($\bar{k}_{\text{Mössb}} \approx 2.2$ [4]); therefore, this alloy can be considered to be virtually disordered. Obviously,

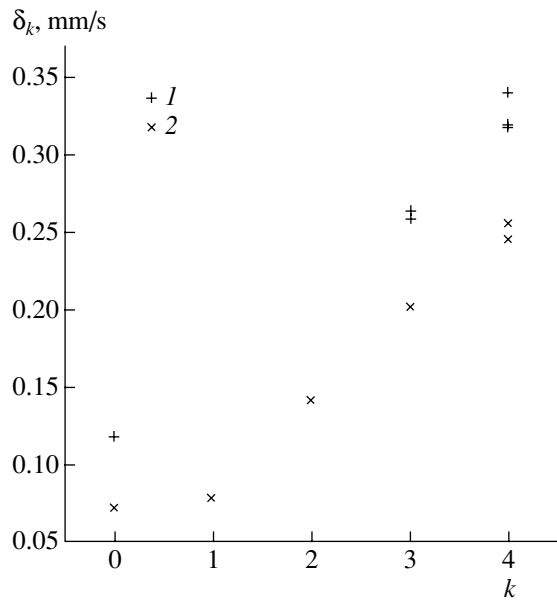


Fig. 9. Dependence of the isomer shift δ_k on the number k of (Si, Ge) atoms in the nearest environment of an Fe atom for systems with a lattice parameter close to that of (1) Fe_3Ge and (2) Fe_3Si .

alloys with high Si concentrations are not completely disordered and exhibit significant correlations in the positions of silicon atoms at short distances, which are not detected by x-ray diffraction.

Variations in the isomer shift are related to the composition and ordering of alloys. The effect of an increase in germanium concentration is mainly determined by the induced increase in the lattice parameter and the corresponding decrease in the electron density at the nucleus site. The ordering-induced changes are associated with the disappearance of the configurations with one, two, and three atoms of the sp elements in the nearest environment and the appearance of the nearest environment configurations with four atoms, for which an iron nucleus has a higher isomer shift. Confirmation of the last conclusion can be found in Fig. 9, where the calculated values of the isomer shift are plotted as a function of the number of sp atoms in the nearest environment.

Thus, the main differences in properties between quasi-binary $\text{Fe}_{75}(\text{Si}_{1-x}\text{Ge}_x)_{25}$ alloys are related to the variation in the crystal lattice parameter when Si atoms are replaced by Ge atoms in ordered alloys and to the different behaviors of the correlations of Si and Ge positions in disordered alloys.

ACKNOWLEDGMENTS

This study was supported by INTAS (grant no. 03-51-4778) and the Russian Foundation for Basic Research (project no. 03-02-16139).

REFERENCES

1. E. P. Elsukov, G. N. Konygin, V. A. Barinov, and E. V. Voronina, *J. Phys.: Condens. Matter* **4**, 7597 (1992).
2. E. P. Elsukov, E. V. Voronina, V. M. Fomin, and G. N. Konygin, *Fiz. Met. Metalloved.* **85**, 307 (1998).
3. A. F. Cabrera and F. H. Sanchez, *Phys. Rev. B: Condens. Matter* **65** (9), 094 202 (2002).
4. G. N. Konygin, E. P. Elsukov, and V. E. Porsev, *Fiz. Met. Metalloved.* **96** (3), 59 (2003).
5. E. P. Elsukov, *Fiz. Met. Metalloved.* **76** (5), 5 (1993).
6. E. P. Elsukov, G. N. Konygin, E. V. Voronina, A. V. Korolev, A. I. Ulyanov, S. K. Godovikov, and A. V. Zagainov, *J. Magn. Magn. Mater.* **214**, 258 (2000).
7. G. N. Konygin, E. P. Elsukov, G. A. Dorofeev, and A. A. Opalenko, *Izv. Akad. Nauk, Ser. Fiz.* **65** (7), 1005 (2001).
8. S. Sarkar and C. Bansal, *J. Alloys Compd.* **366**, 107 (2004).
9. E. V. Voronina, V. M. Fomin, Yu. A. Babanov, and E. P. Elsukov, *Fiz. Met. Metalloved.* **89** (1), 75 (2000).
10. E. V. Voronina, N. V. Ershov, A. L. Ageev, and Yu. A. Babanov, *Phys. Status Solidi B* **160**, 625 (1990).
11. J. P. Perdew and Y. Wang, *Phys. Rev. B: Condens. Matter* **45** (23), 13 244 (1992).
12. S. Cottenier, B. de Vries, J. Meersschant, and M. Rots, *J. Phys.: Condens. Matter* **14**, 3275 (2002).
13. J. P. Perdew, S. Burke, and M. Ernzerhof, *Phys. Rev. Lett.* **77** (18), 3865 (1996).
14. P. Blaha, K. Schwarz, G. K. H. Madsen, D. Kvasnicka, and J. Luitz, *WIEN2k: An Augmented Plane Wave + Local Orbitals Program for Calculating Crystal Properties* (Karlheinz Schwarz Technische Universität, Wien, Austria, 2001).
15. H. Ebert, in *Lecture Notes in Physics*, Vol. 535: *Electronic Structure and Physical Properties of Solids*, Ed. by H. Dreysse (Springer, Berlin, 2000), p. 191.
16. S. H. Vosko, L. Wilk, and M. Nusair, *Can. J. Phys.* **58**, 1200 (1980).
17. G. K. H. Madsen, P. Blaha, K. Schwarz, E. Sjöstedt, and L. Nordström, *Phys. Rev. B: Condens. Matter* **64** (19), 195 134 (2001).
18. A. K. Arzhnikov, L. V. Dobysheva, and S. G. Novokshonov, *J. Phys.: Condens. Matter* **3**, 9025 (1991).
19. A. K. Arzhnikov, L. V. Dobysheva, and S. G. Novokshonov, *Fiz. Met. Metalloved.* **76** (5), 32 (1993).
20. A. K. Arzhnikov, L. V. Dobysheva, and F. Brauers, *Fiz. Tverd. Tela (St. Petersburg)* **42** (1), 86 (2000) [*Phys. Solid State* **42** (1), 89 (2000)].
21. A. K. Arzhnikov and L. V. Dobysheva, *Phys. Rev. B: Condens. Matter* **62** (9), 5324 (2000).

Translated by I. Zvyagin

MAGNETISM AND FERROELECTRICITY

Implementation of the Linear Augmented Slater-Type Orbital Method in the LDA + U Approximation

N. G. Yakutovich, N. N. Dorozhkin, and V. M. Anishchik

Belarussian State University, pr. Franziska Skaryny 4, Minsk, 220080 Belarus

e-mail: yakutovich@bsu.by

Received October 5, 2004

Abstract—The formalism of the linear augmented Slater-type orbital method in the LDA + U approximation is described. All the expressions necessary for the program implementation of this method are derived, and the electronic structure of the ferromagnetic compounds MeB_6 ($Me = La, Gd$) is calculated. The results obtained can be used in analyzing experimental data for rare-earth hexaborides. © 2005 Pleiades Publishing, Inc.

1. INTRODUCTION

Research in the $4f$ states of rare-earth metals and their compounds is a central problem in the study of these materials. Consideration of the f states is necessary for constructing a correct structure of the band spectrum. As is known, the use of the electron-density functional in the local density approximation (LDA) does not provide an adequate description of strongly correlated systems. The gradient corrections as applied to the exchange–correlation potential in the generalized gradient approximation (GGA) [1] substantially refine the description of the energy spectrum for systems with a rapidly varying electron density; however, in the case of strongly correlated systems containing $4f$ ($5f$) orbitals, description of their energy spectrum remains unsatisfactory.

In order to determine the exact location of the energy bands associated with the $4f$ ($5f$) orbitals, it is necessary to take into account strong intra-atomic correlation interactions in the f shell. The description of the electronic properties of strongly correlated systems can be refined by including the correlation effects in terms of the multiband Hubbard model. These interactions can be taken into account in the framework of the so-called LDA + U approximation [2].

In this paper, we use the LDA + U scheme based on the linear augmented Slater-type orbital (LASTO) method proposed by Davenport *et al.* [3, 4] for one atom in a unit cell and generalized in our previous work [5] for an arbitrary number of atoms in a unit cell. It should be noted that LASTO calculations in the LDA + U approximation have already been reported in the literature [6]; however, the formalism of this method has not been published before. This gap will be filled in the present paper.

2. COMPUTATIONAL TECHNIQUE

The starting point for the changeover from the LDA approximation to the LDA + U approximation is the consideration of the total energy of the system. In the LDA + U approximation, the total energy of the system can be represented in the following form [7]:

$$E^{\text{tot}}(\rho, \hat{n}) = E^{\text{LDA}}(\rho) + E^{ee}(\hat{n}) - E^{dc}(\hat{n}), \quad (1)$$

where $E^{\text{LDA}}(\rho)$ is the conventional functional of the local spin density $\rho^\sigma(\mathbf{r})$ ($\sigma = \uparrow, \downarrow$); $E^{ee}(\hat{n})$ is the electron–electron interaction energy for the f orbitals, which is taken into account in the framework of the multiband Hubbard model; and $E^{dc}(\hat{n})$ is the energy of interaction inside the f orbitals, which is already included in the local spin density functional $E^{\text{LDA}}(\rho)$. In order to calculate the total energy of the system, it is necessary to determine the density matrix \hat{n}^σ . The explicit form of the density matrix depends on the computational technique.

According to [3–5], the wave function in the LASTO approximation can be represented as a linear combination of so-called augmented Slater-type orbitals:

$$\Psi_{\mathbf{k}}(\mathbf{r}) = \sum_N c_N \Psi_N(\mathbf{r}), \quad (2)$$

where

$$\Psi_N(\mathbf{r}) = \frac{1}{\sqrt{N}} \sum_{\mathbf{R}_v} e^{i\mathbf{k}\mathbf{R}_v} \phi_N(\mathbf{r} - \boldsymbol{\tau}_i - \mathbf{R}_v). \quad (3)$$

In relationships (2) and (3), $N = \{i, n, lm\}$ is the position of the i th atom in the unit cell; \mathbf{R}_v is the lattice vector; and the functions $\phi_N(\mathbf{r})$ are the Slater-type orbitals outside the muffin-tin (MT) spheres and the exact solutions of the radial Schrödinger equation inside the muf-

fin-tin spheres, which are smoothly augmented to the Slater-type orbitals at the boundary of the muffin-tin spheres. The Slater-type orbital outside the muffin-tin spheres is conveniently represented as a series in vectors of the reciprocal lattice:

$$\Psi_N(\mathbf{r}) = \chi_N(\mathbf{r}) = \frac{1}{\sqrt{N_c \Omega}} \sum_{\mathbf{g}} e^{i(\mathbf{k}+\mathbf{g})\mathbf{r}} \tilde{\phi}_N(\mathbf{k}+\mathbf{g}) T_i(\mathbf{g}), \quad (4)$$

$$\mathbf{r} \in \Omega_2.$$

Here, $T_i(\mathbf{g}) = \exp(-i\mathbf{g}\boldsymbol{\tau}_i)$ and the basis function inside the muffin-tin spheres can be written in the following form:

$$\Psi_N(\mathbf{r}) = \phi_N(\mathbf{r}) = \frac{1}{\sqrt{N_c \Omega}} e^{i\mathbf{k}(\mathbf{R}+\boldsymbol{\tau}_i)}$$

$$\times \sum_{\Lambda} [\beta_{N, k\Lambda g_{k\lambda}}(\mathbf{r}_k) + \alpha_{N, k\Lambda \dot{g}_{k\lambda}}(\mathbf{r}_k)] Y_{\Lambda}(\mathbf{r}_k), \quad (5)$$

$$\mathbf{r} \in \Omega_1.$$

Here, N_c is the number of unit cells in the crystal; Ω is the volume of the unit cell; \mathbf{k} is the wave vector; \mathbf{g} is the vector of the reciprocal lattice; α and β are the coefficients in the expansion of the Slater-type orbital of the i th sphere in terms of solutions of the radial Schrödinger equation in the k th sphere, which are determined from the continuity condition of the basis wave function and its derivative with respect to the surface of the k th sphere and are given in [4]; $g_{k\lambda}$ and $\dot{g}_{k\lambda}$ are the solution of the Schrödinger equation and the corresponding energy derivative for the k th atom and the orbital quantum number λ ; $Y_{\Lambda}(\mathbf{r})$ are the spherical harmonics; Λ stands for the set of indices $\{\lambda\mu\}$; Ω_1 is the region inside the muffin-tin spheres or the first-type region; and Ω_2 is the region outside the muffin-tin spheres or the second-type region.

The electron density can be represented as

$$\rho^{\sigma}(\mathbf{r}) = \sum_{\mathbf{k}, b} f_{\mathbf{k}, b} |\Phi_{\mathbf{k}}^{b, \sigma}(\mathbf{r})|^2, \quad (6)$$

where $f_{\mathbf{k}, b}$ is the population of the band with index b . Then, following Shick *et al.* [7] and using the representation of the wave function (5) with due regard for relationship (6), we obtain the expression for the density matrix in the framework of the LASTO method:

$$n_{\mu\mu'}^{\sigma} = \sum_{\mathbf{k}, b} f_{\mathbf{k}, b} \sum_{k, N, N'} C_N^{*b, \sigma} C_{N'}^{b, \sigma}$$

$$\times [\beta_{N, k\lambda\mu}^* \beta_{N', k\lambda\mu} + \alpha_{N, k\lambda\mu}^* \alpha_{N', k\lambda\mu} \langle \dot{g}_{k\lambda} | \dot{g}_{k\lambda} \rangle]. \quad (7)$$

A possible changeover from the LDA approximation to the LDA + U approximation consists in implementing the so-called ‘‘second-variation’’-based procedure [7].

This procedure enables one to obtain the solution in the LDA + U approximation after only one iteration on the basis of the self-consistent LDA solution. The key idea in this procedure is that the LDA + U eigenfunctions of the problem $|\Phi^i\rangle$ are expanded in a set of functions obtained from the solution of the equation

$$(-\nabla^2 + V_{\text{LDA}}^{\sigma}(\mathbf{r})) \Psi^{b, \sigma}(\mathbf{r}) = e^{b, \sigma} \Psi^{b, \sigma}(\mathbf{r}). \quad (8)$$

Here, $\Psi^{b, \sigma}(\mathbf{r})$ is the LDA eigenfunction, because the potential V_{LDA}^{σ} is constructed using the LDA electron density.

In order to determine the coefficients of the expansion $|\Phi^i\rangle = \sum_j d_j^i |\Psi^j\rangle$, it is necessary to solve the secular equation $\sum_j H_{jj} d_j^i = e_i d_j^i$, where the Hamiltonian written in terms of the LASTO method has the form

$$H_{b'b}^{\sigma} = e_b \delta_{b'b} + \sum_{N, N'} C_N^{*b, \sigma} C_{N'}^{b, \sigma} \quad (9)$$

$$\times \sum_{\mu, \mu'} [\beta_{N, k\lambda\mu}^* V_{\mu\mu'}^{\sigma} \beta_{N', k\lambda\mu} + \alpha_{N, k\lambda\mu}^* V_{\mu\mu'}^{\sigma} \alpha_{N', k\lambda\mu} \langle \dot{g}_{k\lambda} | \dot{g}_{k\lambda} \rangle].$$

Here, $V_{\mu\mu'}^{\sigma}$ is the effective potential acting on the Y_{lm} subspace (d (f) states) [7].

The LASTO method in the LDA + U approximation was tested using ferromagnetic gadolinium. The energy location of the $4f$ bands is well reproduced for $U = 0.49$ Ry and $J = 0.05$ Ry [7]. These parameters can be calculated from first principles and in different approximations; however, here, they are used as adjustable parameters. This problem calls for further consideration and will not be discussed in the present paper.

3. RESULTS AND DISCUSSION

The results of calculating the electronic structure of LaB_6 and GdB_6 compounds in the LDA and LDA + U approximations are presented below. These compounds have a CaB_6 -type crystal lattice (space group $O_{h11}-Pm3m$). The unit cell of each compound contains seven atoms: one metal atom and six boron atoms forming an octahedron. The LaB_6 compound is a paramagnet in which the magnetic unit cell coincides with the crystallographic unit cell. In the ground state, the GdB_6 compound is a ferromagnet; hence, the magnetic unit cell of GdB_6 also coincides with the crystallographic unit cell. The lattice parameters of the LaB_6 and GdB_6 compounds are listed in the table. The radii of the muffin-tin spheres for boron atoms were calculated from the nearest distance between the boron atoms in the adjacent octahedra, whereas the radius R_{MT} of the metal atom was chosen from analyzing the $Me-Me$ distance.

Lattice constants of the MeB_6 ($Me = La, Gd$) compounds and the largest radii of the muffin-tin spheres

Compound	Lattice constant [8], au	R_{MT}^{Me} , au	R_M^B , au
LaB ₆	7.8593	3.9296	1.5954
GdB ₆	7.7751	3.8875	1.5783

The calculation in the LDA approximation was carried out for 85 k points in the irreducible part of the Brillouin zone, which corresponds to approximately 1600 k points in the whole Brillouin zone. In order to check the convergence of the results, the calculation was performed with 165 k points in the irreducible part of the Brillouin zone. A comparison of the densities of states did not reveal a substantial difference between them. The calculation was carried out using the von Barth–Hedin exchange–correlation potential [9]. The sets of basis functions for valence electrons of the atoms were chosen as follows: $2s2p$ for boron atoms and $5p5d4f6s$ for lanthanum and gadolinium atoms. For both compounds, the calculation was carried out in the spin-polarized version. After applying consistent procedure in the LDA approximation, we obtained the paramagnetic solution for the LaB₆ compound and the ferromagnetic solution for the GdB₆ compound, which is in complete agreement with the experiment. The total densities of states and the partial densities of f states as calculated in the LDA approximation for spins \uparrow and \downarrow of the LaB₆ and GdB₆ compounds are presented in

Figs. 1 and 3, respectively. The results of these calculations agree well with those obtained earlier, for example, by Kimura *et al.* [10]. However, in a number of experimental works concerned with the determination of the Fermi surface for rare-earth hexaborides (in particular, for the LaB₆ hexaboride), the conclusion was drawn that the frequencies of de Haas–van Alphen oscillations can be correctly reproduced from the band calculations in the LDA approximation. In order to describe the frequencies of de Haas–van Alphen oscillations correctly, Harima *et al.* [11] artificially displaced the empty $4f$ bands up to an energy of 0.1 Ry. This modified band structure of the LaB₆ compound allowed those authors to achieve good agreement between the theoretical calculation of the frequencies of de Haas–van Alphen oscillations and the experimental data. Therefore, it can be assumed that the energy location of the $4f$ bands in the LaB₆ compound is incorrectly described in the LDA approximation, even though these bands are not occupied. In the GdB₆ compound, the energy location of the $4f$ levels, as should be expected, coincides with that of pure gadolinium in the LDA calculation. The occupied $4f$ band has a width of the order of 0.04 Ry and lies at an energy approximately 0.3 Ry below the Fermi level, whereas the unoccupied $4f$ states are located at an energy 0.05 Ry above the Fermi level and have a width of approximately 0.08 Ry. The fact that the energy location of the $4f$ bands in the GdB₆ compound changes insignificantly as compared to pure gadolinium can be explained by a strong localization of the $4f$ orbitals (approximately

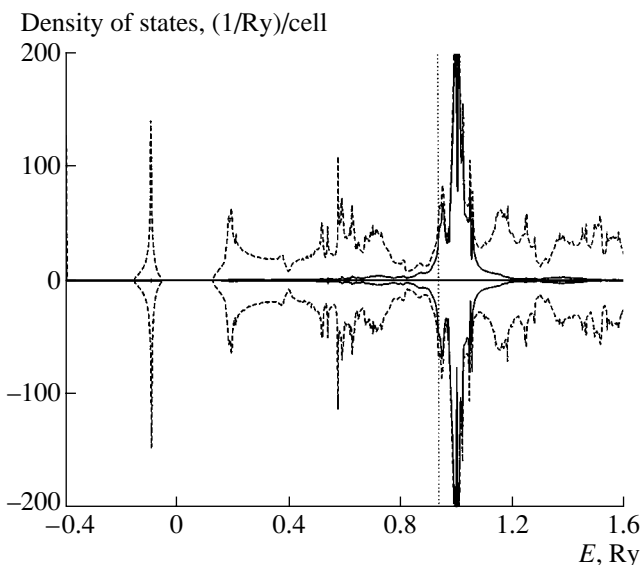


Fig. 1. Density of states for the LaB₆ compound according to the LASTO calculations in the LDA approximation for spins \uparrow and \downarrow . The Fermi level is located at an energy $E_{F(LDA)} = 0.929$ Ry. The dashed and solid lines represent the total density of states and the partial density of $4f$ states, respectively.

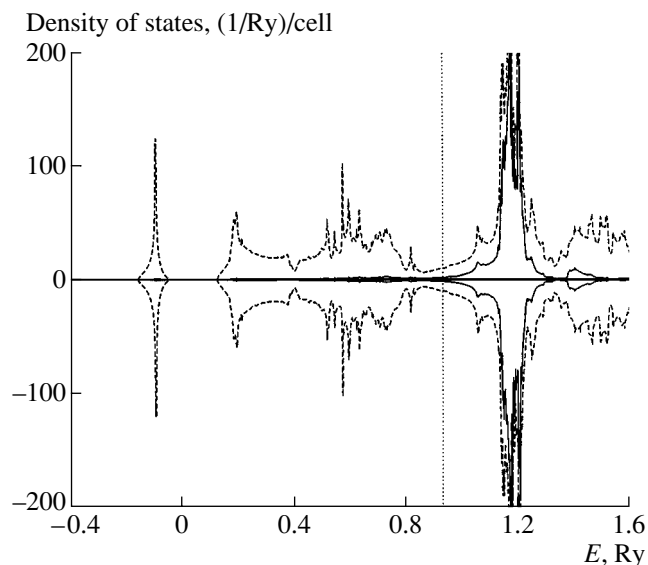


Fig. 2. Density of states for the LaB₆ compound according to the LASTO calculations in the LDA + U approximation for spins \uparrow and \downarrow . $E_{F(LDA)} = 0.929$ Ry. The dashed and solid lines represent the total density of states and the partial density of $4f$ states, respectively.

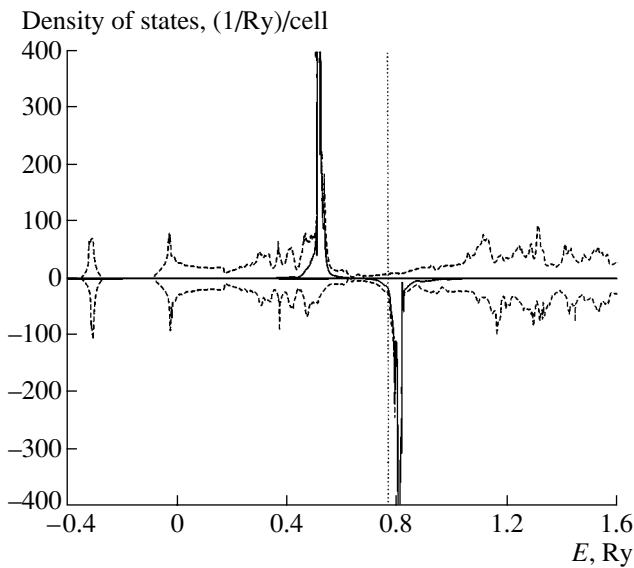


Fig. 3. Density of states for the GdB_6 compound according to the LASTO calculations in the LDA approximation for spins \uparrow and \downarrow . $E_{\text{F(LDA)}} = 0.758$ Ry. The dashed and solid lines represent the total density of states and the partial density of $4f$ states, respectively.

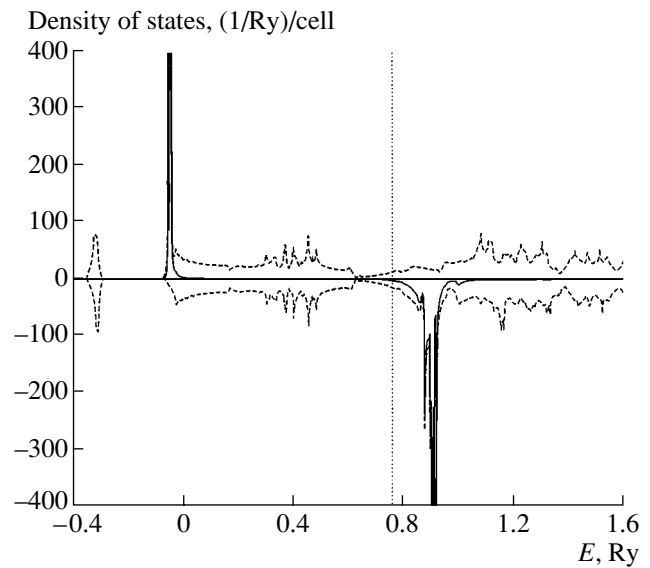


Fig. 4. Density of states for the GdB_6 compound according to the LASTO calculations in the LDA + U approximation for spins \uparrow and \downarrow . $E_{\text{F(LDA)}} = 0.758$ Ry. The dashed and solid lines represent the total density of states and the partial density of $4f$ states, respectively.

95% of the $4f$ electrons are located inside the muffin-tin sphere of the metal).

We attempted to correct this situation for the energy location of the $4f$ states and carried out the calculation of the band structure of the LaB_6 and GdB_6 compounds in the framework of the LASTO method in the LDA + U approximation. In the band calculations for the GdB_6 compound, we used the same parameters as for pure gadolinium, i.e., $U = 0.49$ Ry and $J = 0.051$ Ry, which were taken from Shick *et al.* [7]. Taking into account that the parameter U does not change significantly for all lanthanides, we used the same value of $U = 0.49$ Ry in the band calculation for the LaB_6 compound. The parameter J should decrease as the distance between the metal atoms increases; therefore, this parameter could be taken to be somewhat less than that for pure gadolinium both in the case of the GdB_6 compound and for the LaB_6 compound. However, the parameter J was chosen equal to its value for gadolinium. Figures 2 and 4 present the total densities of states and the partial densities of f states according to the LASTO calculation in the LDA + U approximation for the LaB_6 and GdB_6 compounds, respectively. It can be seen from these figures that, in the case of LaB_6 , the $4f$ bands are shifted to higher energies by approximately 0.17 Ry. For this compound, the density of states at the Fermi level is somewhat decreased. The result obtained confirms the assumption that the $4f$ bands in the LaB_6 compound are located at higher energies. For the LaB_6 compound, the density of states at the Fermi level is approximately equal to 10 (1/Ry)/cell [electronic specific heat coefficient $\gamma_e = 1.7$ mJ/(mol K²)]. For the GdB_6 compound,

the calculations demonstrated that the energy location of the f bands in the spectrum is similar to that of pure gadolinium [7]. The occupied $4f$ bands are shifted to lower energies by approximately 0.5 Ry and located at an energy 0.8 Ry below the Fermi level. This is confirmed by the results of the optical experiments reported in the paper by Kubo *et al.* [12]. The empty $4f$ bands are shifted to higher energies, and the energy splitting between $4f \uparrow$ and \downarrow is equal to 11.5 eV. The density of states at the Fermi level for the GdB_6 compound is approximately equal to 14 (1/Ry)/cell, which corresponds to the electronic specific heat coefficient $\gamma_e = 2.4$ mJ/(mol K²).

For comparison, the electronic specific heat coefficient for pure gadolinium, according to our calculation, is equal to 7.48 mJ/(mol K²), which is in good agreement with the experimental value of 6.38 mJ/(mol K²) [13].

REFERENCES

1. J. P. Perdew, S. Burke, and M. Ernzerhof, *Phys. Rev. Lett.* **77**, 3865 (1996).
2. V. I. Anisimov, F. Aryasetiawan, and A. I. Lichtenstein, *J. Phys.: Condens. Matter* **9**, 767 (1997).
3. J. W. Davenport, *Phys. Rev. B: Condens. Matter* **29** (6), 2896 (1984).
4. J. W. Davenport, M. Weinert, and R. E. Watson, *Phys. Rev. B: Condens. Matter* **32** (8), 4876 (1985).

5. N. G. Yakutovich, N. N. Dorozhkin, V. M. Anishchik, and B. V. Novysh, *Fiz. Tverd. Tela (St. Petersburg)* **42** (11), 1943 (2000) [*Phys. Solid State* **42** (11), 1995 (2000)].
6. G. W. Fernando, R. E. Watson, M. Weinert, A. N. Kocharian, A. Ratnaweera, and K. Tennakone, *Phys. Rev. B: Condens. Matter* **61**, 375 (2000).
7. A. B. Shick, A. I. Liechtenstein, and W. E. Pickett, *Phys. Rev. B: Condens. Matter* **60** (15), 10763 (1999).
8. N. N. Sirota, V. V. Novikov, and A. V. Novikov, *Fiz. Tverd. Tela (St. Petersburg)* **42** (11), 2033 (2000) [*Phys. Solid State* **42** (11), 2093 (2000)].
9. U. Barth and L. Hedin, *J. Phys. C.: Solid State Phys.* **5**, 1629 (1972).
10. S. Kimura, H. Harima, T. Nanba, S. Kunii, and T. Kasuya, *J. Phys. Soc. Jpn.* **60**, 745 (1991).
11. H. Harima, O. Sakai, T. Kasuya, and A. Yanase, *Solid State Commun.* **66**, 603 (1988).
12. Y. Kubo, S. Asano, H. Harima, and A. Yanase, *J. Phys. Soc. Jpn.* **62**, 205 (1993).
13. *Handbook of Physical Quantities*, Ed. by I. S. Grigor'ev and E. Z. Meilikhov (Énergoatomizdat, Moscow, 1991; CRC, Boca Raton, FL, 1997).

Translated by O. Moskalev

MAGNETISM AND FERROELECTRICITY

Single-Pulse Nuclear Echo Signals in Magnetically Ordered Media

V. S. Kuz'min* and V. M. Kolesenko**

* Sakharov International State Ecological University, Minsk, 220009 Belarus

e-mail: kuzmin@iftt.bas-net.by

** Institute of Solid-State and Semiconductor Physics, National Academy of Sciences of Belarus,
ul. Brovki 17, Minsk, 220072 Belarus

Received November 16, 2004

Abstract—An analytical expression for the amplitude of a single-pulse nuclear echo signal generated in magnetically ordered materials is obtained taking into account the inhomogeneous broadening of the spectroscopic transition and the inhomogeneous distribution of the gain with an average value of greater than unity. It is shown that, in this signal, summation of the oscillations of nuclear magnetic moments with equal amplitudes and phases occurs at each instant of time. The cause of the effective suppression of the nuclear magnetic moment oscillations in the initial portion of the free precession signal is revealed analytically. The dependence of the amplitude of the one-pulse echo signal on the strength of an external alternating magnetic field, the pulse duration, and the width of the gain distribution is determined. The results obtained are compared with the experimental data for a Co_2MnSi ferromagnetic polycrystalline sample. © 2005 Pleiades Publishing, Inc.

1. INTRODUCTION

It is known that, in magnetically ordered media, the generation of coherent nuclear magnetic resonance (NMR) responses is caused not only by inhomogeneous broadening but also by amplification of the radio-frequency (RF) field at nuclei arising upon a strong hyperfine interaction between the electronic and nuclear subsystems [1, 2]. Since ferromagnets have an extended domain structure, the corresponding coefficients of amplification of the radio-frequency field at nuclei inside the domains and at the domain boundaries differ significantly in magnitude [1, 2]. As a result, the frequencies of oscillations of the nuclear magnetic moments (Rabi frequencies) during exposure to an alternating radio-frequency field should have different values [3]. In magnetically ordered media, the superposition of these oscillations of the nuclear magnetic moments after the radio-frequency field is switched off leads to the generation of a ferromagnetic single-pulse echo signal [4, 5]. Although there are numerous studies [6–8] concerned with theoretical treatment of this phenomenon in which the inhomogeneous gain distribution and the inhomogeneous broadening are taken into account, the role played by the inhomogeneous gain distribution in the generation of a ferromagnetic single-pulse echo signal remains unclear. The mechanism proposed earlier in [9] for the formation of a single-pulse echo in conventional spin systems under nonresonant excitation conditions cannot be used to elucidate the nature of a ferromagnetic single-pulse echo signal, because, according to experimental data, this signal is generated not only under nonresonant but also under resonant excitation conditions [4, 5]. In the aforemen-

tioned works, the ferromagnetic single-pulse echo signals were calculated numerically. Hence, it is difficult to draw an unambiguous conclusion regarding the physical nature of this phenomenon. In order to elucidate the nature of the ferromagnetic single-pulse echo signal and the mechanism of its formation, it is necessary to obtain analytical expressions for the single-pulse echo response in magnetically ordered media with due regard for the inhomogeneous broadening of the spectroscopic transition and the inhomogeneous gain distribution. The purpose of the present work is to solve this problem.

2. ANALYTICAL CALCULATIONS

In magnetically ordered media, a free precession signal generated by a resonant radio-frequency pulse in a two-level nuclear spin system can be represented in the following form [7]:

$$\langle \langle v(t) \rangle \rangle = \int_1^{\eta_m} \eta F(\eta) d\eta \int_{-\infty}^{+\infty} v(\Delta, \eta, t) g(\Delta) d\Delta, \quad (1)$$

where $\Delta = \omega_n - \omega_0$ is the detuning of the precession frequency ω_n of a single spin packet from the central frequency ω_0 of the NMR line; $g(\Delta)$ and $F(\eta)$ are the functions of the distribution of the detuning of single spin packets Δ over the NMR frequencies and the distribution of the gain η of the radio-frequency field, respectively; η_m is the maximum gain; and $v(\Delta, \eta, t)$ is the v component of the magnetic moment of a single spin packet with gain η and detuning Δ . By ignoring the

relaxation processes, we can write this component in the following form [9]:

$$\begin{aligned} v(\Delta, \eta, t) &= v_0 \omega_1 \eta \left(\left[\frac{\beta - \Delta}{2\beta^2} \sin(\beta t_1 - \Delta t) \right. \right. \\ &\quad \left. \left. + \frac{\beta + \Delta}{2\beta^2} \sin(\beta t_1 + \Delta t) \right]_1 + \left[-\frac{\Delta \sin \Delta t}{\beta^2} \right]_2 \right) \\ &= v_1(\Delta, \eta, t) + v_2(\Delta, \eta, t). \end{aligned} \quad (2)$$

Here, v_0 is the equilibrium magnetization, $\omega_1 = \gamma H_1$ is the Rabi frequency (where γ is the gyromagnetic ratio and H_1 is the amplitude of the radio-frequency pulse), $\beta = (\eta^2 \omega_1^2 + \Delta^2)^{1/2}$ is the effective field (expressed in terms of frequency) acting on a spin packet with detuning Δ , and t is the time reckoned from the end of the radio-frequency pulse of duration t_1 .

Let us assume that the inhomogeneous broadening of the spectroscopic transition and the inhomogeneous gain distribution in a ferromagnetic material can be described by the normal distribution laws $g(\Delta)$ and $F(\eta)$:

$$g(\Delta) = \frac{1}{\sqrt{2\pi}\sigma} \exp\left(-\frac{\Delta^2}{2\sigma^2}\right), \quad (3)$$

$$F(\eta) = \frac{1}{\sqrt{2\pi}\eta_0} \exp\left(-\frac{(\eta - \bar{\eta})^2}{2\eta_0^2}\right), \quad (4)$$

where σ and η_0 are the quantities characterizing the half-widths of the corresponding distributions and $\bar{\eta}$ is the average gain. Then, relationship (1) can be rewritten as

$$\begin{aligned} \langle \langle v(t) \rangle \rangle &= \int_1^{\eta_m} \eta \langle v_1(\eta, t) \rangle F(\eta) d\eta \\ &\quad + \int_1^{\eta_m} \eta \langle v_2(\eta, t) \rangle F(\eta) d\eta, \end{aligned} \quad (5)$$

where

$$\langle v_i(\eta, t) \rangle = \int_{-\infty}^{+\infty} v_i(\Delta, \eta, t) g(\Delta) d\Delta. \quad (6)$$

In order to evaluate the integral $\langle v_1(\eta, t) \rangle$, we use the stationary phase approximation [10]. The area of the radio-frequency pulse $\omega_1 t_1 > 1$ is taken as a large parameter. Using the standard computational procedure in the framework of the method described in [10], we find the stationary points $\Delta_{1,2} = \pm \eta \omega_1 t / \sqrt{t_1^2 - t^2}$. As a

result, we obtain the following expression for this integral [11]:

$$\begin{aligned} \langle v_1(\eta, t) \rangle &= v_0 \frac{\sqrt{\omega_1 \eta} (t_1 - t)^{3/4}}{\sigma t_1 (t_1 + t)^{1/4}} \\ &\quad \times \exp\left(-\frac{\eta^2 \Delta_0^2}{2\sigma^2}\right) \sin \Phi(t), \end{aligned} \quad (7)$$

where $t \in [0, t_1)$, $\Delta_0 = \omega_1 t / \sqrt{t_1^2 - t^2}$ is the stationary point in the absence of amplification of the radio-frequency field, and $\Phi(t) = \eta \omega_1 \sqrt{t_1^2 - t^2} + \pi/4$ is the phase of magnetization oscillations of the nuclear subsystem under inhomogeneous broadening conditions.

It follows from relationship (7) that integral (6) with the subscript $i = 1$ describes damped oscillations of the magnetization at a variable frequency $d\Phi(t)/dt = \eta \omega_1 t / (t_1^2 - t^2)^{1/2}$. Since the analytical expression for integral (6) with the subscript $i = 2$ is cumbersome in form, we do not present it in this paper. Note only that the time dependence of this integral exhibits a maximum (in the vicinity of the instant at which the radio-frequency pulse is switched off) and then decays monotonically. In the saddle-point approximation [10], we calculated the first integral in relationship (5), which has the form

$$\langle \langle v_1(t) \rangle \rangle = v_0 \frac{\sqrt{\omega_1}}{4\sigma\eta_0} A(t) \exp(E(t)) \sin(P(t)), \quad (8)$$

where

$$A(t) = \frac{(t_1 - t)^{3/4} [\bar{\eta}^2 + \eta_0^4 \omega_1^2 (t_1^2 - t^2)]^{3/4}}{t_1 (t_1 + t)^{1/4} q^2(t)},$$

$$E(t) = \left(\frac{\bar{\eta}^2 / \eta_0^4 - \omega_1^2 (t_1^2 - t^2)}{4q(t)} - \frac{\bar{\eta}^2}{2\eta_0^2} \right),$$

$$P(t) = \frac{\bar{\eta} \omega_1 \sqrt{t_1^2 - t^2}}{2\eta_0^2 q(t)} + \frac{3}{2} \arctan \left\{ \frac{\eta_0^2 \omega_1 \sqrt{t_1^2 - t^2}}{\bar{\eta}} \right\} + \frac{\pi}{4},$$

$$q(t) = \frac{\Delta_0^2}{2\sigma^2} + \frac{1}{2\eta_0^2}.$$

The analysis of expression (8) for the first integral in relationship (5) demonstrated that this expression holds within the time interval $t \in [0; kt_1)$, where $k =$

$\sqrt{1 - \left[1 + \frac{\sigma^2}{\omega_1^2 \eta_0^2} (\bar{\eta} - 1) \right]^{-1}}$. In this interval, the magnetization of the nuclear subsystem [see relationship (8)] in ferromagnets oscillates at a variable frequency

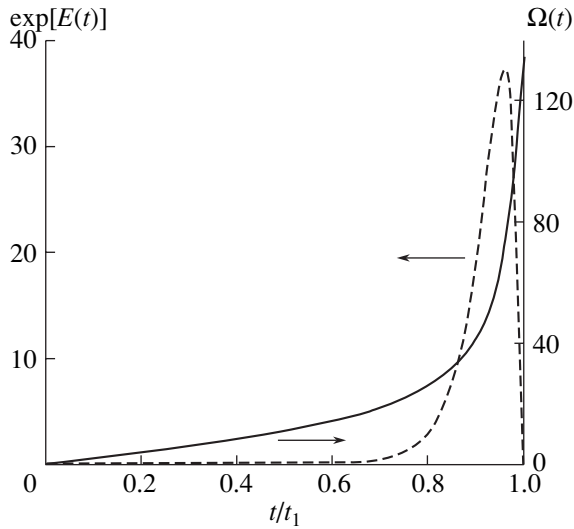


Fig. 1. Time dependences of the exponential function $\exp[E(t)]$ and the instantaneous frequency of magnetization oscillations $\Omega(t)$ at $\omega_1 t_1 = 2\pi$, $\sigma/\omega_1 = 5$, $\eta_0 = 0.8$, and $\bar{\eta} = 2.7$.

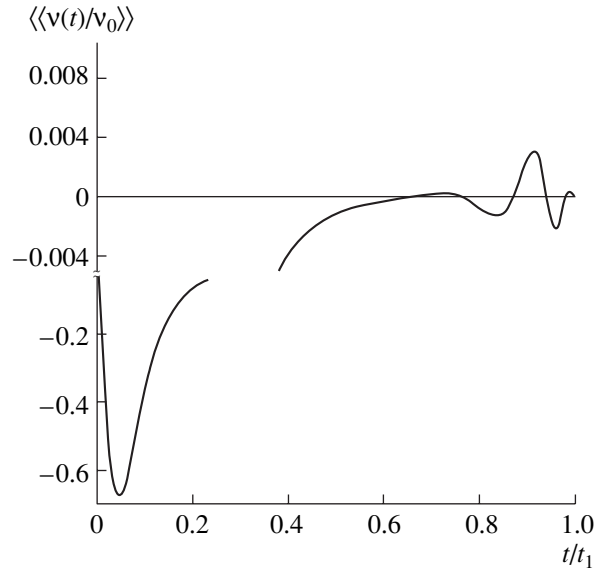


Fig. 2. Time dependence of the free precession signal generated in the ferromagnet at $\omega_1 t_1 = 2\pi$, $\sigma/\omega_1 = 5$, $\eta_0 = 0.8$, and $\bar{\eta} = 2.7$.

$\Omega(t) = dP(t)/dt$, with the amplitude being a composite function of time.

According to numerical calculations of the second integral in relationship (5), this integral, like the quantity $\langle v_2(\eta, t) \rangle$, passes through a maximum (in the vicinity of the instant at which the radio-frequency pulse is terminated) and then monotonically decreases to zero. Expression (8) contains the exponential function (Fig. 1) with an exponent capable of taking on extreme values. This indicates that the signal amplitude can take on a maximum value at a certain instant of time. Since this maximum is formed at the end of the time interval $[0; kt_1)$, it can be interpreted as the ferromagnetic single-pulse echo signal. Thus, the first term in relationship (5) describes the maximum of the signal amplitude at the end of the time interval $[0; kt_1)$ and the second term characterizes this maximum immediately after the termination of the pulse. The total free-precession signal described by relationship (5) is presented in Fig. 2. Therefore, a resonant pulsed field acting on the inhomogeneous broadened nuclear subsystem with an inhomogeneous gain distribution in ferromagnets leads to the generation of a ferromagnetic single-pulse echo signal in a free precession signal (Fig. 2). The time of generation of the ferromagnetic single-pulse echo signal t_m can be determined by analyzing the exponential factor in relationship (8) for extrema:

$$t_m = t_1 \sqrt{1 - \left[\frac{\omega_1^2 t_1^2 \eta_0^4}{\bar{\eta}^2} + \frac{\omega_1 t_1 \eta_0^2}{\bar{\eta}} \left(\frac{\omega_1^2 t_1^2 \eta_0^4}{\bar{\eta}^2} + \frac{\sigma^2}{\omega_1^2 \eta_0^2} - 1 \right) \right]^{1/2} - 1} \quad (9)$$

The instantaneous frequency $\Omega(t)$ of the magnetization oscillations [see relationship (8)] increases monotonically according to a linear law and, at the end of the time interval $[0; kt_1)$, i.e., at the instant of generation of a ferromagnetic single-pulse echo signal, exhibits an asymptotic behavior (Fig. 1). A comparison of the two curves depicted in Fig. 1 shows that the maximum contribution to the ferromagnetic single-pulse echo signal comes only from those oscillations of nuclear magnetic moments whose generalized Rabi frequencies $\eta\omega_1$ lie within the range of the linewidth of the function $\exp[E(t)]$, which is the envelope for this signal. Interestingly, the amplitude of the signal [relationship (8)] immediately after the termination of the pulse increases monotonically in a weak linear fashion and does not display oscillations with time. In other words, this portion of the time interval is characterized by effective suppression of the magnetization oscillations, which has been observed in many experiments with a single-pulse echo [1, 2].

3. RESULTS AND DISCUSSION

When calculating expression (8) in the saddle-point approximation, the first integral in relationship (5) is divided into the difference between two integrals with saddle points in such a way that, at each instant of time, their real parts are determined as $\eta_1 = \bar{\eta}/2q(t)\eta_0^2$ and the imaginary parts $\eta_2 = \pm\omega_1\sqrt{t_1^2 - t^2}/2q(t)$ differ only in sign. In this representation, at each instant of time, combinations of oscillations of nuclear magnetic moments are chosen from the response such that their

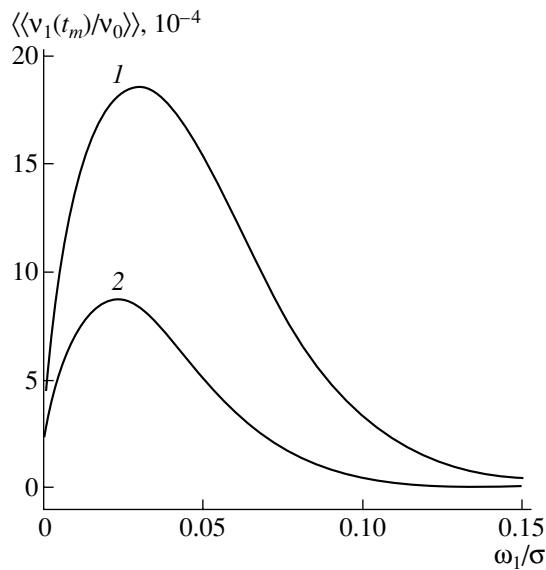


Fig. 3. Theoretical field dependences of the amplitude of the ferromagnetic single-pulse echo signal at $\eta_0 = 0.8$, $\bar{\eta} = 2.7$, and $\sigma t_1 = (1)$ 120 and (2) 200.

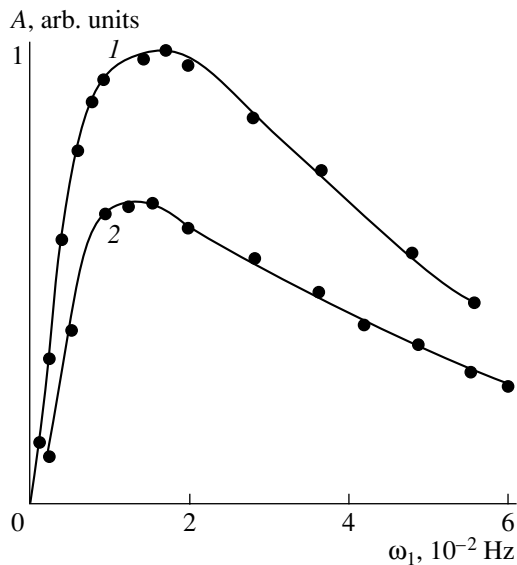


Fig. 4. Experimental field dependences (see [5]) of the amplitude of the ferromagnetic single-pulse echo signal at $t = (1)$ 10 and (2) 20 μs .

amplitudes are equal to each other and the phases are opposite in sign. The combinations of oscillations thus chosen make a nonzero contribution to the free precession signal: as the end point of the time interval $[0; kt_1)$ is approached, the amplitudes of these oscillations increase and, hence, the amplitude of the resultant oscillation increases, passes through a maximum, and then decreases to zero; i.e., the ferromagnetic single-pulse echo signal is formed. Thus, in the free precession

signal, there occurs effective summation of particular combinations of nuclear magnetic moment oscillations providing a dominant contribution to the response.

The time dependence of the resultant magnetization amplitude considered above reflects the time dependence of the function $\exp[E(t)]$, whose effective width changes with time, which leads to the asymmetric shape of the ferromagnetic single-pulse echo signal (Fig. 2). The time interval $[0; kt_1)$ in which the ferromagnetic single-pulse echo signal can be generated is determined by the Rabi frequency ω_1 , the width of the inhomogeneously broadened spectrum σ , the width of the inhomogeneous gain distribution η_0 , and the average gain $\bar{\eta}$ [see relationship (8)]. It follows from the expression kt_1 for the upper limit of this interval that its length is maximum and approximately equal to t_1 in the case where the relationship $\bar{\eta} > 1 + \omega_1^2 \eta_0^2 / \sigma^2$ holds. This relationship is one of the conditions for the observation of the ferromagnetic single-pulse echo signal.

In order to compare the theoretical description of the ferromagnetic single-pulse echo signal with experimental data [4, 5], we examine the amplitude of the ferromagnetic single-pulse echo signal [see relationship (8)] at the instant the signal is formed as a function of the Rabi frequency, the duration of the radio-frequency pulse, and the width of the gain distribution. As a result, we obtain

$$\begin{aligned} \langle\langle v_1(t_m) \rangle\rangle &= v_0 M \frac{c(2a + \sqrt{b})^{3/4}}{b(a + \sqrt{b})^{7/2}} \\ &\times \exp\left(-\frac{\bar{\eta}^2}{2\eta_0^2} \left[1 - \frac{\sigma^2/(\omega_1^2 \eta_0^2)}{a + \sqrt{b}}\right]\right), \end{aligned} \quad (10)$$

where

$$\begin{aligned} M &= \frac{\sigma^3 \bar{\eta}^2}{\omega_1^4 \eta_0^5 (t_1 + t_m)}, \quad a = \frac{\omega_1 t_1 \eta_0^2}{\bar{\eta}}, \\ b &= a^2 + \frac{\sigma^2}{\omega_1^2 \eta_0^2} - 1, \quad c = \frac{\bar{\eta}^{1/4}}{\omega_1^{1/4} t_1^{1/4} \eta_0^{1/2}}. \end{aligned}$$

Let us analyze relationship (10) for the two limiting cases $\sigma/\omega_1 \gg \eta_0$ and $\sigma/\omega_1 \ll \eta_0$, in which the amplitude of the ferromagnetic single-pulse echo signal is given, respectively, by the expressions

$$\langle\langle v_1(t_m) \rangle\rangle = v_0 \frac{\omega_1^{1/2} \bar{\eta}^{-2}}{2\sigma^{3/2} t_1 \eta_0}, \quad (11)$$

$$\langle\langle v_1(t_m) \rangle\rangle = v_0 \frac{\sigma^3 \bar{\eta}^7}{2\omega_1^6 t_1 \eta_0^{15}} \exp\left(-\frac{\bar{\eta}^2}{2\eta_0^2}\right). \quad (12)$$

It can be seen from these expressions that the amplitude of the ferromagnetic single-pulse echo signal

increases according to a fractional-power law at low Rabi frequencies (small strengths of the alternating magnetic field) and decreases hyperbolically at high Rabi frequencies. Consequently, as the strength of the radio-frequency field increases, the amplitude of the ferromagnetic single-pulse echo signal passes through a maximum (Fig. 3), which, in turn, shifts toward weaker fields and decreases monotonically in height as the duration of the radio-frequency pulse increases. This behavior of the ferromagnetic single-pulse echo signal agrees well with the experimental data [5] (Fig. 4). It follows from relationships (11) and (12) that the amplitude of the ferromagnetic single-pulse echo signal decreases with increasing width of the gain distribution η_0 and increases with increasing average gain $\bar{\eta}$.

4. CONCLUSIONS

Thus, the generation of a ferromagnetic single-pulse echo in magnetically ordered materials is caused by the inhomogeneous distribution of the gain with an average value of greater than unity. The absence of oscillations of the free precession signal is explained by the fact that the dominant contribution to the response is made by nuclear magnetic moment oscillations whose amplitudes at every instant are equal to each other and whose phases differ only in sign. The analytical description of the ferromagnetic single-pulse echo signal agrees well with experimental data [4, 5]: the dependence of the amplitude of the ferromagnetic single-pulse echo signal on the Rabi frequency exhibits a pronounced maximum, which, as the duration of the radio-frequency pulse increases, shifts toward lower frequencies and decreases in height.

ACKNOWLEDGMENTS

We would like to thank T.V. Smirnova for the computer processing of the results obtained in this study.

This work was supported in part by the Belarussian Republic Foundation for Basic Research, project no. F04M-028.

REFERENCES

1. A. S. Borovik-Romanov, Yu. M. Bun'kov, B. S. Dumesh, M. I. Kurkin, M. P. Petrov, and V. P. Chekmarev, *Usp. Fiz. Nauk* **142** (4), 537 (1984) [*Sov. Phys. Usp.* **27**, 235 (1984)].
2. M. I. Kurkin and E. A. Turov, *NMR in Magnetically Ordered Materials: Theory and Applications* (Nauka, Moscow, 1990) [in Russian].
3. I. G. Kilipari and V. I. Tsifrinovich, *Phys. Rev. B: Condens. Matter* **57** (18), 11554 (1998).
4. V. I. Tsifrinovich, É. S. Mushailov, N. V. Baksheev, A. M. Bessmertnyĭ, E. A. Glzman, V. K. Mal'tsev, O. V. Novoselov, and A. E. Reingardt, *Zh. Éksp. Teor. Fiz.* **88** (4), 1481 (1985) [*Sov. Phys. JETP* **61**, 886 (1985)].
5. V. I. Tsifrinovich, A. M. Akhalkatsi, and I. G. Kilipari, *Fiz. Tverd. Tela (Leningrad)* **32** (5), 1426 (1990) [*Sov. Phys. Solid State* **32** (5), 832 (1990)].
6. V. P. Chekmarev, M. I. Kurkin, and S. I. Goloshchapov, *Zh. Éksp. Teor. Fiz.* **76** (5), 1675 (1979) [*Sov. Phys. JETP* **49**, 851 (1979)].
7. I. G. Kilipari, *Fiz. Tverd. Tela (Leningrad)* **34** (8), 2512 (1992) [*Sov. Phys. Solid State* **34** (8), 1346 (1992)].
8. L. N. Shakhmuratova, D. K. Fowler, and D. H. Chaplin, *Phys. Rev. A: At., Mol., Opt. Phys.* **55** (4), 2955 (1997).
9. V. S. Kuz'min, I. Z. Rutkovskii, A. P. Saiko, A. D. Tarasevich, and G. G. Fedoruk, *Zh. Éksp. Teor. Fiz.* **97** (3), 880 (1990) [*Sov. Phys. JETP* **70**, 493 (1990)].
10. A. Nayfeh, *Introduction to Perturbation Techniques* (Wiley, New York, 1981; Mir, Moscow, 1984).
11. V. S. Kuz'min and G. G. Fedoruk, *Nonstationary Coherent Phenomena in Paramagnetic Spin Systems* (Belarus. Gos. Univ., Minsk, 2001) [in Russian].

Translated by V. Artyukhov

MAGNETISM AND FERROELECTRICITY

Band Structure and the Magnetic and Elastic Properties of SrFeO₃ and LaFeO₃ Perovskites

I. R. Shein, K. I. Shein, V. L. Kozhevnikov, and A. L. Ivanovskii

*Institute of Solid-State Chemistry, Ural Division, Russian Academy of Sciences,
Pervomaiskaya ul. 91, Yekaterinburg, 620219 Russia*

e-mail: shein@ihim.uran.ru

Received November 25, 2004

Abstract—The band structure and the magnetic and elastic characteristics of SrFeO₃ and LaFeO₃ perovskites with ferromagnetic and antiferromagnetic collinear spin configurations (of the *A*, *C*, and *G* types) are investigated using the *ab initio* pseudopotential method (the VASP program package) with the inclusion of the single-site Coulomb correlations (the LSDA + *U* formalism). It is shown that, in the pressure range 0–50 GPa, the most stable states are the ferromagnetic metal state for the SrFeO₃ compound and the antiferromagnetic insulator state of the *G* type for the LaFeO₃ compound. © 2005 Pleiades Publishing, Inc.

1. INTRODUCTION

Since the discovery of giant magnetoresistance in manganates [1], the spin and charge ordering effects and their role in the formation of the band structure and physical properties of complex transition metal oxides (i.e., systems with strong Coulomb correlations) have attracted considerable research attention. This class of compounds involves *M*FeO₃ perovskite-like ferrites, some of which possess a mixed electronic–ionic conductivity and hold promise as cathode and membrane materials (see, for example, review [2]).

As is known, the *M*FeO₃ phases can exhibit different properties depending on the type of *M* sublattice. In particular, LaFeO₃ is an antiferromagnetic (AFM) insulator [3], SrFeO₃ is a metal [4], and CaFeO₃ is a system with charge ordering (Fe^{IV} → Fe^{IV+x} + Fe^{IV-x}) [5]. It should be noted that the type of spin and charge states for *M*FeO₃ phases can radically change depending on many factors, such as the stoichiometry (the presence of oxygen vacancies in the lattice), temperature, and external pressure. For example, stoichiometric SrFeO_{*x*} (2.5 ≤ *x* ≤ 3.0) is characterized not only by different states of the charge and spin ordering but also by a combined state of the charge and spin ordering [6]. Pressure treatment of the CaFeO₃ compound brings about the suppression of charge ordering (at *P* > 20 GPa) and a substantial change in the temperature of the transition from the antiferromagnetic state to the spin-glass state [7]. Pressure treatment of the SrFeO₃ compound encourages the antiferromagnetic → ferromagnetic (FM) phase transition [8, 9].

The band structure of the SrFeO₃ and LaFeO₃ perovskites has been studied in a number of works. In particular, the energy bands and atomic interactions in the SrFeO₃ perovskite were investigated in the framework

of the density functional theory (DFT) in the local spin density approximation (LSDA) using the tight-binding linear muffin-tin orbital method within the atomic sphere approximation (TB LMTO–ASA) [10] and the augmented spherical wave (ASW) method [11, 12]. The band structure of the ferromagnetic and antiferromagnetic phases of the LaFeO₃ perovskite was investigated using the TB LMTO–ASA [13], linearized augmented plane wave (LAPW) [13], and full-potential linearized augmented plane wave and LMTO (within the generalized gradient approximation) (FLAPW–GGA, LMTO–GGA) [14] methods at the LSDA level. It turned out that the LSDA calculations lead to a systematic underestimation of the band gap and atomic magnetic moments of the ferrite. According to Sharma *et al.* [3], the band gap and the magnetic moment (Fe) for the LaFeO₃ compound are 0.2 eV and 3.7 μ_B, respectively, whereas the experimental values are approximately equal to 2.1 eV (optical measurements [15]) and 4.6 ± 0.2 μ_B [16]. The LMTO–ASA calculations in the LSDA + *U* approximation with the inclusion of the single-site correlations [17] demonstrated that, as the Coulomb parameter *U* increases from 0.5 to 10.0 (at a constant exchange parameter *J*), the theoretical band gap and magnetic moment (Fe) for the LaFeO₃ perovskite increase to 3.4 eV and 4.4 μ_B, respectively. The contribution of the correlation correction to the parameters of the band structure of the SrFeO₃ perovskite was not considered.

In this study, the LSDA + *U* scheme was used to make a comparative analysis of the band structures and atomic interactions in SrFeO₃ and LaFeO₃ perovskites with different types of collinear magnetic ordering, namely, ferromagnetic and antiferromagnetic ordering (of the *A*, *C*, and *G* types). Moreover, taking into account that ferrite-based phases are promising for use

as cathode materials, we calculated their elastic parameters (such as the bulk moduli B_0 and their first derivatives B'_0) for the first time and analyzed the changes in the energy and magnetic parameters of these phases under uniform compression.

2. MODELS AND CALCULATION TECHNIQUE

The comparative analysis of the band structures of the SrFeO_3 and LaFeO_3 perovskite-like phases was performed for a cubic structure (space group $Pm\bar{3}m$) with the following atomic positions (in the cell): O, $3d$ (0, 0, 1/2); Sr (La), $1b$ (1/2, 1/2, 1/2); and Fe, $1a$ (0, 0, 0). The coordination polyhedra of the oxygen and iron atoms are the $[\text{Fe}_2(\text{Sr,La})_4]$ and $[\text{O}_6]$ octahedra, respectively. The coordination polyhedra of the strontium or lanthanum atoms are the $[\text{O}_{12}]$ cubo-octahedra. The interatomic distances and the unit cell parameter a are related as follows: $\text{Fe-O} = a/2$, $\text{O-O} = (\text{Sr,La})\text{-O} = (a/\sqrt{2})$, and $\text{Fe-(Sr,La)} = a\sqrt{3}/2$. The number of formula units in the unit cell is assumed to be $Z = 1$.

We consider four types of collinear magnetic states of the ferrites: one ferromagnetic state and three types of antiferromagnetic configurations. In our case, the antiferromagnetic configurations correspond to the ferromagnetic ordering of spins in the planes and to the antiferromagnetic ordering between the adjacent planes of the iron atoms along the z axis ($\langle 001$, type A), along the diagonal of the cube base ($\langle 110$, type C), and along the diagonal of the cube itself ($\langle 111$, type G) (Fig. 1). All these types of magnetic ordering were described using computational supercells composed of eight unit cells ($Z = 8$).

The band structures of the SrFeO_3 and LaFeO_3 compounds were calculated by the *ab initio* pseudopotential method with the VASP program package [18–20]. The exchange–correlation energy was taken into account according to the scheme described in [21]. The *ab initio* pseudopotentials were generated with the use of the projector augmented wave method [22]. The single-site Coulomb correlations in the LSDA + U scheme were included in the representation proposed by Dudarev *et al.* [23], according to which the Coulomb (U) and exchange (J) parameters are expressed through the effective parameter $U_{\text{eff}} = U - J$. For both phases, the parameters used for the iron atoms $U = 6.0$ eV and $J = 0.6$ eV ($U_{\text{eff}} = 5.4$ eV) were taken from [17]. The results of the LSDA calculations of the LaFeO_3 (SrFeO_3) paramagnetic phases ($U = J = 0$) were used as the initial data in the discussion of the magnetic effects.

When constructing the densities of states, the integration over the Brillouin zone was performed by the tetrahedron method. The convergence criterion for the total energy of the systems was equal to 0.0001 eV. The pressure treatment (in the range 0–50 GPa) was simulated by isotropic compression of the cell. The bulk moduli B_0 and their first derivatives B' with respect to

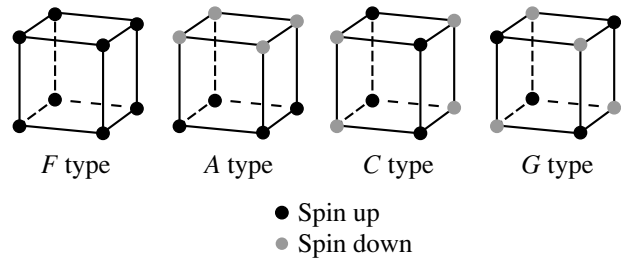


Fig. 1. Ferromagnetic (F) and antiferromagnetic (A , C , G) types of collinear spin ordering (in the iron sublattice) for the SrFeO_3 and LaFeO_3 phases.

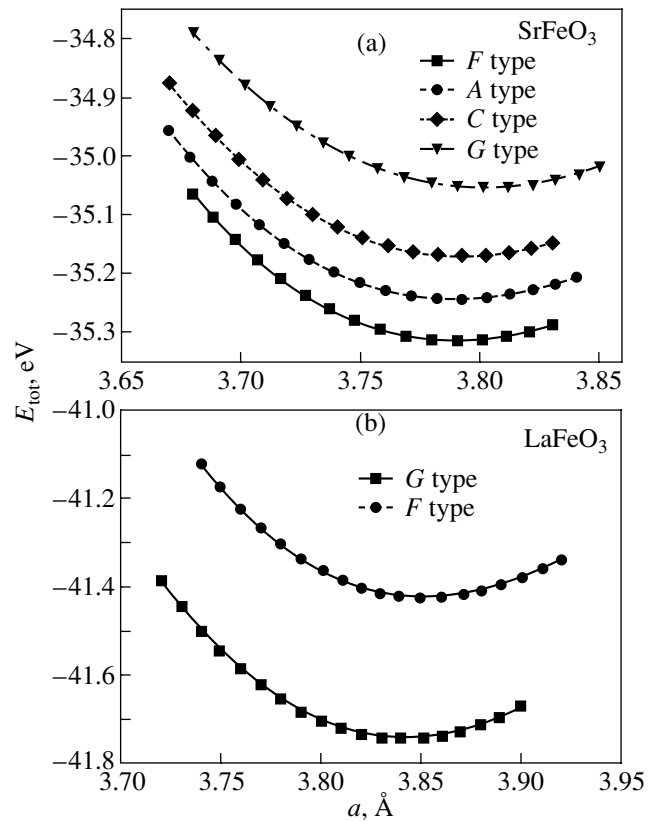


Fig. 2. Dependences of the total energy E_{tot} on the lattice parameter for the magnetic phases of the SrFeO_3 and LaFeO_3 perovskites.

pressure were determined by calculating the total energies of the crystals as functions of the cell volume with the use of the Birch equation [24].

The total and partial densities of states were obtained for the equilibrium states of the phases. In order to analyze the effects of interatomic interactions, we constructed the charge density maps (ρ) and the difference spin density maps ($\Delta\rho = \rho\uparrow - \rho\downarrow$).

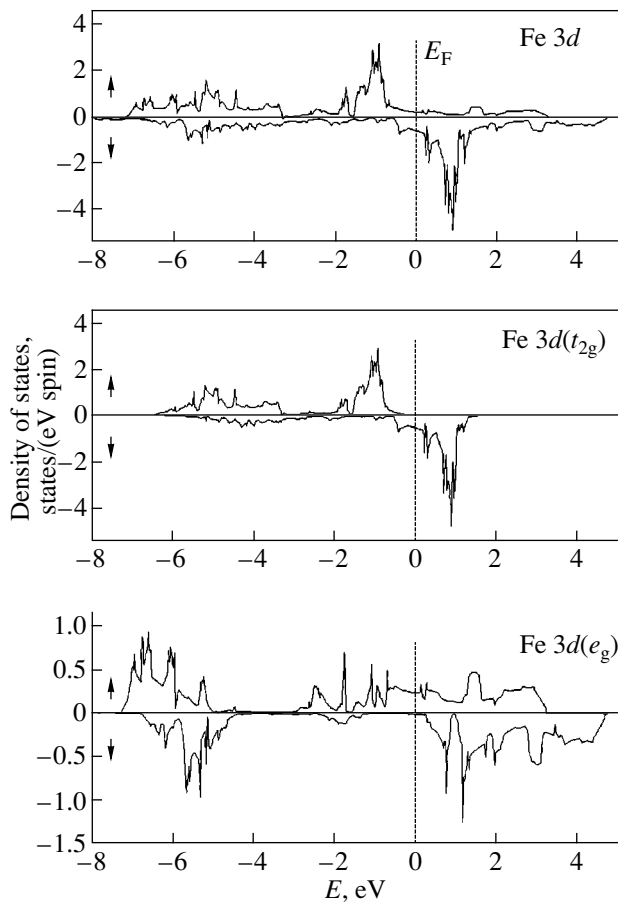


Fig. 3. Spin densities of Fe 3d states and their decomposition into the components t_{2g} and e_g for the ferromagnetic phase of the SrFeO₃ perovskite.

3. RESULTS AND DISCUSSION

At the first stage, the equilibrium states for all the magnetic phases of the SrFeO₃ and LaFeO₃ compounds

Calculated (within the LSDA + U formalism) and experimental characteristics for the ferromagnetic and antiferromagnetic (types A, C, G) phases of SrFeO₃ and LaFeO₃ perovskite-like oxides: the differences ΔE_{tot} (eV/cell) between the minimum energy for each magnetic phase under consideration and the energy of the stable phase, equilibrium lattice parameters a_0 (nm), bulk moduli B_0 (GPa) and their first derivatives B' , the density of states at the Fermi level $N(E_F)$ (states/eV cell) or the band gap (eV), and the magnetic moments of atoms (μ_B)

Parameter	LaFeO ₃			SrFeO ₃				
	experiment	FM	AFM(G)	experiment	FM	AFM(A)	AFM(C)	AFM(G)
ΔE_{tot}	–	0.318	0.000	–	0.000	0.072	0.146	0.262
a_0	0.3926 [16]	0.3852	0.3841	0.3850 [4]	0.3790	0.3789	0.3793	0.3801
B_0	–	197.9	198.4	–	171.3	162.0	159.0	147.5
B'	–	5.40	5.40	–	5.40	5.42	5.42	5.40
$N(E_F)$ /Band gap	2.1 [16]	2.78	2.52	–	0.84	0.76	0.83	0.64
Magnetic moment (Fe)	4.6 ± 0.2 [16]	4.23	4.06	3.1 ± 0.1 [4]	3.70	3.72	3.73	3.64
Magnetic moment (O)	–	0.21	0.00	0.1–0.3 [26, 27]	0.08	0.06	0.00	0.00
Magnetic moment (Sr, La)	–	0.00	0.00	–	0.01	0.02	0.00	0.00

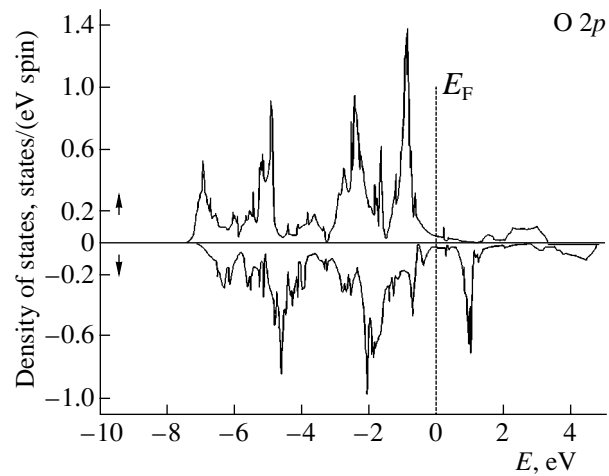


Fig. 4. Spin densities of O 2p states for the ferromagnetic phase of the SrFeO₃ perovskite.

were determined by minimizing the total energy E_{tot} (Fig. 2). For the SrFeO₃ compound, the equilibrium lattice parameters a_0 for the magnetic phases are close to each other. The lattice parameter for the most stable ferromagnetic phase was calculated to be $a_0 = 0.3790$ nm. This is in reasonable agreement with the experimental data (0.3851–0.3852 nm [25, 26]). The differences between the calculated and measured [25, 26] lattice parameters a_0 do not exceed 1.6% (see table). The lattice parameter a_0 varies by no more than 0.3% depending on the type of magnetic ordering. According to the recent measurements performed by Maljuk *et al.* [27], the lattice parameters of an annealed single crystal of the composition SrFeO_{2.96} are as follows: $a = 0.3864$ nm, $b = 0.3865$ nm, and $c = 0.3868$ nm. For the model cubic phase LaFeO₃, the lattice parameter a_0 is equal to 0.3841–0.3852 nm. This is in satisfactory

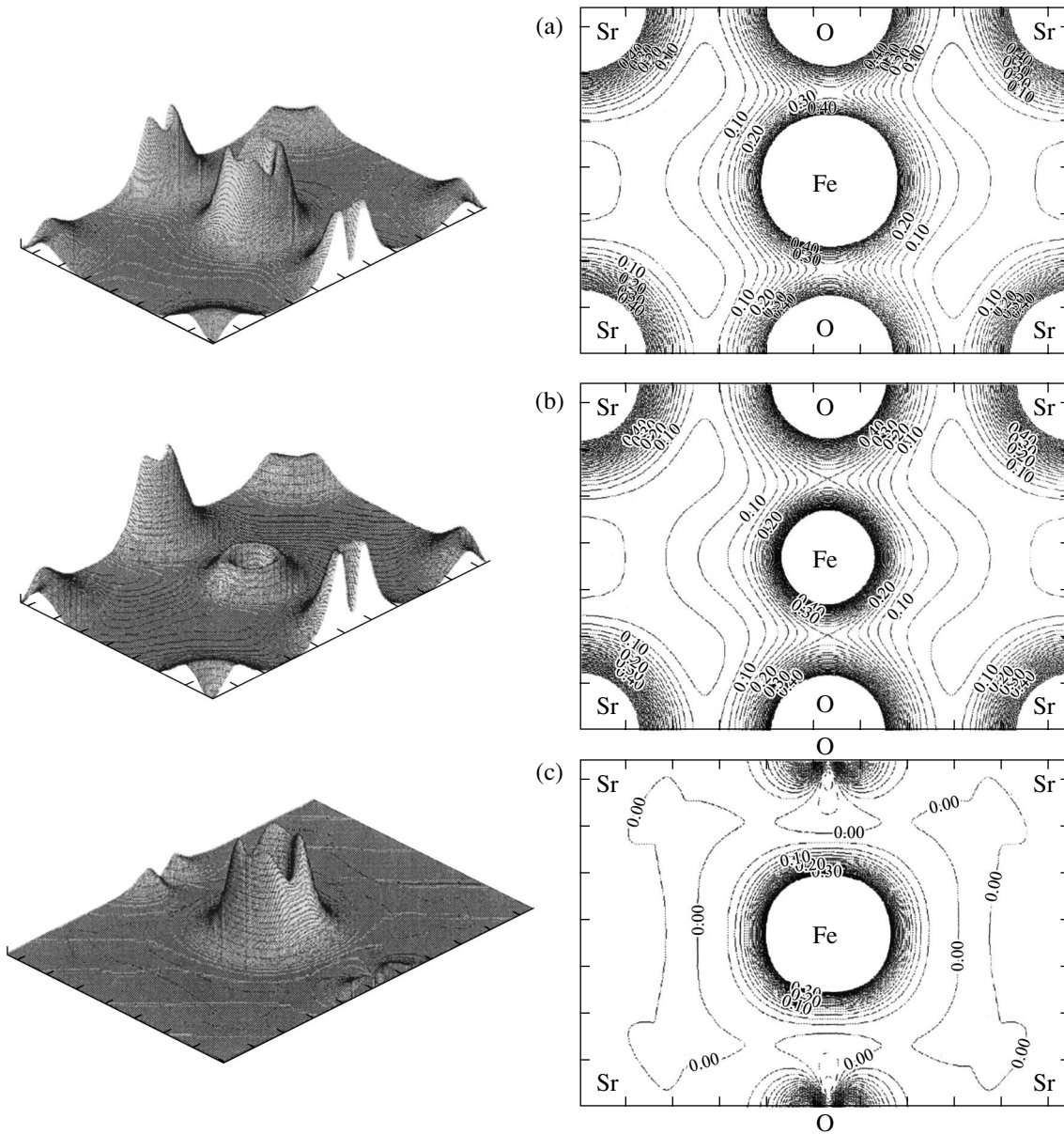


Fig. 5. Spatial configurations of spin densities and their distributions in the (110) plane for the ferromagnetic phase of the SrFeO_3 perovskite: (a) states with spin up ($\rho\uparrow$), (b) states with spin down ($\rho\downarrow$), and (c) the difference spin density map ($\Delta\rho = \rho\uparrow - \rho\downarrow$).

agreement with the neutron diffraction data for the cubic perovskite structure (space group $Pm\bar{3}m$, $a_0 = 0.3926$ nm [16]) and also with the interatomic distances in the orthorhombic (space group $Pbnm$) perovskite-like structure of the synthetic LaFeO_3 samples [28].

It can be seen from Fig. 1 and the table that, among the collinear magnetic phases of the SrFeO_3 compound, the ferromagnetic phase is most stable and the stability of the other phases decreases in the following order: $\text{FM} \rightarrow \text{AFM}(A) \rightarrow \text{AFM}(C) \rightarrow \text{AFM}(G)$.

According to neutron diffraction data [4], the SrFeO_3 compound at temperatures below $T_N = 134$ K is

a noncollinear antiferromagnet with a spiral structure. This suggests competition of the ferromagnetic and antiferromagnetic interactions between the iron atoms within the Heisenberg model. However, the small wave vector of the spiral structure ($Q = 0.135a^*$ along the $\langle 111 \rangle$ direction), the small angle of rotation of the neighboring spins ($\sim 40^\circ$), and the experimental estimates of the parameters of the exchange interactions between the nearest neighbor ($J_1 = 1.2$ meV) and more distant ($J_2 = -0.2$ meV, $J_4 = -0.3$ meV) iron atoms [4, 29, 30] indicate that the ferromagnetic interactions in the SrFeO_3 compound are considerably stronger than the antiferromagnetic interactions. This agrees with our

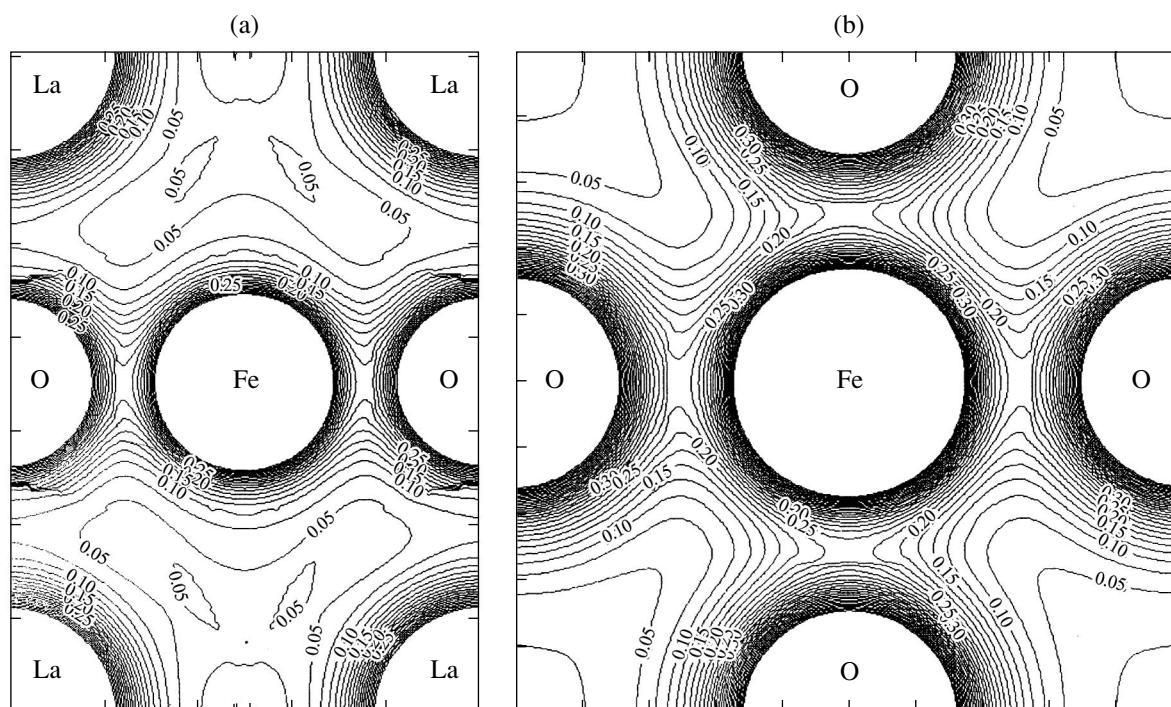


Fig. 6. Charge density maps for the LaFeO₃ perovskite in the (a) (110) and (1/2 0 0) planes (contour interval $\rho = 0.025 \text{ e}/\text{\AA}^3$).

data on the highest stability of the ferromagnetic state (among the collinear magnetic phases of the SrFeO₃ perovskite). Furthermore, the ferromagnetic phase of the SrFeO₃ compound is stabilized upon light doping with cobalt [31]. At high pressures (~ 70 GPa), the SrFeO₃ compound, according to ⁵⁷Fe Mössbauer spectroscopy, transforms into the ferromagnetic state [8, 9]. It is assumed that this transformation is associated with the decrease in the Fe–Fe distances and with the increase in the width of the Fe *d* band. As can be seen from Fig. 2, the ferromagnetic phase for all the lattice parameters remains more stable, which makes it possible to explain qualitatively the experimental data obtained in [8, 9].

A radically different situation occurs with the LaFeO₃ compound (Fig. 2). The results of the calculations (in agreement with experimental data [3]) demonstrate that, for this compound, the antiferromagnetic configuration (*G* type) is most stable and the difference between the energies of the ferromagnetic and antiferromagnetic phases ($\Delta E_{\text{tot}} = 0.318 \text{ eV}/\text{cell}$) is substantially larger than the corresponding difference for the SrFeO₃ compound.

A comparison of the calculated elastic moduli for the magnetic phases of the SrFeO₃ and LaFeO₃ compounds (see table) shows that the bulk modulus B_0 for the *G*-type antiferromagnetic phase of the LaFeO₃ compound is greater than the bulk modulus B_0 for the ferromagnetic phase of the SrFeO₃ compound.

Depending on the type of magnetic ordering, the changes in the elastic moduli $B_0(\text{FM})/B_0(\text{G-type AFM})$ for metal-like SrFeO₃ appear to be considerably larger ($\sim 16\%$) than those for the LaFeO₃ insulator (no more than 1%).

Let us consider the specific features of the band structures for the ferromagnetic phase of the SrFeO₃ compound and the antiferromagnetic phase of the LaFeO₃ compound. The total density of states for the ferromagnetic phase of the SrFeO₃ compound involves the low-energy bands of the O 2*s* and Sr 4*p* quasi-core states. The spin splittings are small ($\sim 0.4 \text{ eV}$) for the O 2*s* band and virtually absent for the Sr 4*p* states (the magnetic moment of strontium is approximately equal to $0.01 \mu_B$). The spin polarization effect most clearly manifests itself for the Fe 3*d* bands. As a result, the energy of the $d\uparrow$ band decreases, whereas the energy of the $d\downarrow$ band increases. The separation of the Fe *d* states (according to the spatial and spin symmetry) into four groups ($t_{2g}\downarrow, t_{2g}\uparrow, e_g\uparrow, e_g\downarrow$) leads to different degrees of their hybridization with the O 2*p* states in the range from -7.2 eV to E_F (Figs. 3, 4). The effects of the polarization of the states with the opposite spin orientation for different atoms become especially clear when comparing the spin density maps $\rho\uparrow$ and $\rho\downarrow$ and the difference spin density map $\Delta\rho$ (Fig. 5). It can be seen from these maps that the polarization of the oxygen states is insignificant. The magnetic moment of the oxygen atoms ($\sim 0.2 \mu_B$) is induced by the iron states due to the

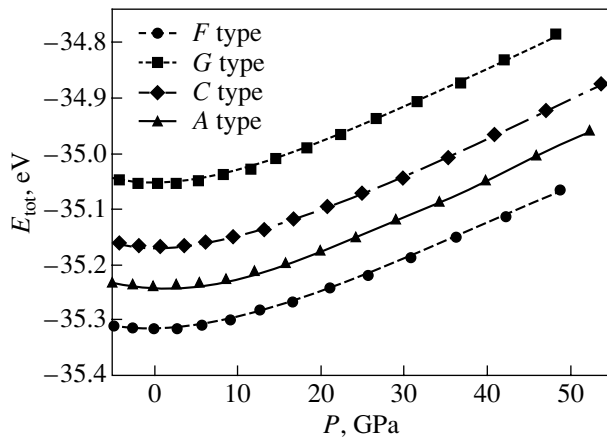


Fig. 7. Dependences of the total energy E_{tot} on the external pressure for the magnetic phases of the SrFeO_3 perovskite.

overlap of the iron–oxygen valence shells. It should be emphasized that the occupied d states with the opposite spin orientation are involved in the atomic interactions occurring in the SrFeO_3 compound in different ways. As can be seen from Fig. 5, the contours of the positive values of $\Delta\rho$ for the iron atom are substantially distorted. This suggests that the t_{2g}^{\uparrow} high-spin states dominate in the formation of the Fe–O “side” π bonds. By contrast, the low-spin states of oxygen make a significant contribution to the formation of the σ bonds.

The Fermi level E_F for the ferromagnetic phase of the SrFeO_3 compound is located in the vicinity of the t_{2g}^{\downarrow} and e_g^{\uparrow} bands, whereas the contributions of the t_{2g}^{\uparrow} and e_g^{\downarrow} bands are negligible (Fig. 3).

For the LaFeO_3 compound, the t_{2g}^{\uparrow} and e_g^{\uparrow} bands are located near the lower edge of the occupied band of the O $2p$ states (the σ band). In turn, the lower edge of the conduction band is predominantly formed by the t_{2g}^{\downarrow} states, whereas the e_g^{\downarrow} states are located ~ 0.8 eV above and are admixed to a common band of the O $2p$ –Fe $3d$ –La $5d$ free antibonding states (the σ^* band). Like the strontium ferrite, the LaFeO_3 compound is characterized by hybridization of the Fe d^{\downarrow} –O $2p$ states responsible for the covalent component of the Fe–O bond. Contrastingly, the overlap of the occupied La–O states in the σ band is insignificant. These differences are clearly seen in the charge density maps (Fig. 6). The band gap for the antiferromagnetic phase of the LaFeO_3 compound is equal to 2.52 eV, which is in good agreement with the experimental data (2.1 eV [15]), as well as with the results of the LMTO–ASA calculations in the LSDA + U approximation (2.1 eV [17]). The magnetic moments of the iron atoms are equal to $4.06 \mu_B$ (the experimental magnetic moments are $4.6 \mu_B$ [16]). According to the data obtained from other calculations, the magnetic moments of the iron atoms are equal to $3.5 \mu_B$ (LMTO–ASA [17]), $3.7 \mu_B$ (LSDA + U_2 [32]),

$4.1 \mu_B$ (LSDA + U [17]), and $4.6 \mu_B$ (the Hartree–Fock method [33]).

In conclusion, we note that the above calculations enabled us to analyze the changes observed in the energy states of the collinear magnetic phases of the SrFeO_3 and LaFeO_3 cubic perovskites under conditions of an external hydrostatic pressure. The estimates demonstrated (Fig. 7) that, in the pressure range up to 50 GPa, no magnetic phase transitions occur; i.e., the state of the ferromagnetic metal for the SrFeO_3 perovskite and the state of the G -type antiferromagnetic insulator for the LaFeO_3 perovskite remain most stable.

ACKNOWLEDGMENTS

This work was supported by the Russian Academy of Sciences within the framework of the program “Hydrogen Power Engineering and Fuel Cells.”

REFERENCES

1. R. von Helmolt, J. Wecker, B. Holzapfel, L. Schultz, and K. Samwer, *Phys. Rev. Lett.* **71** (14), 2331 (1993).
2. N. N. Oleynikov and V. A. Ketsko, *Russ. J. Inorg. Chem.* **49** (Suppl. 1), 1 (2004).
3. D. D. Sharma, N. Shanthi, S. R. Barman, N. Hamada, H. Sawada, and K. Terakura, *Phys. Rev. Lett.* **75** (6), 1126 (1995).
4. T. Takeda, Y. Yamaguchi, and H. Watanabe, *J. Phys. Soc. Jpn.* **33** (4), 967 (1972).
5. T. Akao, Y. Azuma, M. Usuda, Y. Nishihata, J. Mizuki, N. Hamada, N. Hayashi, T. Terashima, and M. Takano, *Phys. Rev. Lett.* **91** (15), 156405 (2003).
6. A. Lebon, P. Adler, C. Bernhard, A. V. Boris, A. V. Pimenov, A. Maljuk, C. T. Lin, C. Ulrich, and B. Keimer, *Phys. Rev. Lett.* **92** (3), 037202 (2004).
7. T. Kawakami, S. Nasu, T. Sasaki, K. Kuzushita, S. Morimoto, S. Endo, S. Kawasaki, and M. Takano, *J. Phys.: Condens. Matter* **14** (44), 10713 (2002).
8. S. Nasu, *Hyperfine Interact.* **128** (2), 101 (2000).
9. S. Nasu, T. Kawakami, S. Kawasaki, and M. Takano, *Hyperfine Interact.* **144** (2), 119 (2002).
10. S. Mathi Jaya, R. Jagadish, R. Rao, and R. Asokamani, *Phys. Rev. B: Condens. Matter* **43** (16), 13274 (1991).
11. S. Matar, P. Monh, and G. Demezeau, *J. Magn. Mater.* **140–144** (3), 169 (1995).
12. S. Matar, *Prog. Solid State Chem.* **31** (4), 239 (2003).
13. P. Mahadevan, N. Shanthi, and D. D. Sarma, *J. Phys.: Condens. Matter* **9** (15), 3129 (1997).
14. H. Hamada, H. Sawada, I. Solovyev, and K. Terakura, *Physica B (Amsterdam)* **237–238**, 11 (1997).
15. T. Arima, Y. Tokura, and J. B. Torrance, *Phys. Rev. B: Condens. Matter* **48** (23), 17006 (1993).
16. W. C. Koehler and E. O. Wollan, *J. Phys. Chem. Solids* **2** (2), 100 (1957).
17. Z. O. Yang, Z. Huang, L. Ye, and X. D. Xie, *Phys. Rev. B: Condens. Matter* **60** (23), 15674 (1999).
18. G. Kresse and J. Hafner, *Phys. Rev. B: Condens. Matter* **47** (1), 558 (1993).

19. G. Kresse and J. Furthmuller, *Comput. Mater. Sci.* **6** (1), 15 (1996).
20. G. Kresse and J. Furthmuller, *Phys. Rev. B: Condens. Matter* **54** (16), 11 169 (1996).
21. D. M. Ceperley and B. L. Alder, *Phys. Rev. Lett.* **45** (7), 566 (1980).
22. G. Kresse and J. Joubert, *Phys. Rev. B: Condens. Matter* **59** (3), 1758 (1999).
23. S. L. Dudarev, G. A. Botton, S. Y. Savrasov, C. J. Humphreys, and A. P. Sutton, *Phys. Rev. B: Condens. Matter* **57** (3), 1505 (1998).
24. F. Birch, *J. Geophys. Res.* **83** (8), 1257 (1978).
25. A. E. Bocquet, A. Fujimori, T. Mizokawa, T. Saitoh, H. Namatame, S. Suga, N. Kimizuka, Y. Takeda, and M. Takano, *Phys. Rev. B: Condens. Matter* **45** (4), 1561 (1992).
26. J. P. Hodges, S. Short, J. D. Jorgensen, X. Xiong, B. Dabrowski, S. M. Mini, and C. W. Kimball, *J. Solid State Chem.* **151** (2), 190 (2000).
27. A. Maljuk, J. Stremper, C. Ulrich, A. Lebon, and C. T. Lin, *J. Cryst. Growth* **257** (3), 427 (2003).
28. P. Coppens and M. Eidschutz, *Acta Crystallogr.* **19** (3), 524 (1965).
29. P. Bezdzicka, L. Fournes, A. Wattiaux, J. C. Grenier, and M. Pouchard, *Solid State Commun.* **91** (3), 501 (1994).
30. S. Kawasaki, M. Takano, and Y. Takeda, *J. Solid State Chem.* **121** (1), 174 (1996).
31. M. Abbate, G. Zampieri, J. Okamoto, A. Fujimori, S. Kawasaki, and M. Takano, *Phys. Rev. B: Condens. Matter* **65** (16), 165 120 (2002).
32. I. Solovyev, N. Hamada, and K. Terakura, *Phys. Rev. B: Condens. Matter* **53** (11), 7158 (1996).
33. T. Mizokawa and A. Fujimori, *Phys. Rev. B: Condens. Matter* **54** (8), 5368 (1996).

Translated by O. Borovik-Romanova

MAGNETISM AND FERROELECTRICITY

Frequency Dependence of the Amplitude of Domain-Wall Oscillations in an Acoustic Wave Field

V. S. Gerasimchuk* and A. A. Shitov**

* Donetsk State Technical University, ul. Artema 58, Donetsk, 83000 Ukraine

** Donbass State Architectural and Construction Academy, Makeevka, Donetsk oblast, 86123 Ukraine

e-mail: vme@dgasu.dn.ua

Received January 17, 2005

Abstract—The velocity of oscillatory motion of domain walls is investigated as a function of the parameters of a magnetic material and an external acoustic field. The dependence of the amplitude of domain-wall oscillations on the frequency of an external acoustic wave is determined. It is found that this dependence exhibits a resonant behavior. © 2005 Pleiades Publishing, Inc.

1. INTRODUCTION

In recent years, magnetic materials have been extensively used in various fields of engineering. The development of one of the promising applications of magnetic materials is associated with the use of magnetic domains as carriers in the recording and transfer of information in computer engineering [1, 2]. In films and bulk materials with a domain structure, the main process responsible for the magnetization reversal is motion of domain walls. It is this motion (velocity) of domain walls that directly limits the speed of computers in which microdomains are used as information carriers.

At present, the effect of a magnetic field on the dynamics of domain walls is well understood. Motion of domain walls can be induced by static or alternating magnetic fields [1–5]. The dynamics of domain walls in magnetic fields was experimentally investigated in [5–7]. The amplitude of displacements of a domain wall as a function of an external magnetic field was determined for weak ferromagnets [5, 6] and yttrium garnet ferrites [7]. The oscillatory motion of domain walls was theoretically studied by Bar'yakhtar *et al.* [8], who obtained the dependences of the domain-wall velocity in weak ferromagnets on the strength and frequency of the magnetic field. The dynamics of domain walls in two-sublattice ferrites in an alternating magnetic field was examined in [9]. A comprehensive review of the studies concerned with the dynamics of domain walls in the low-frequency range (0.1–10.0 kHz) was given by Kandaurova [10].

The domain structure of magnets, apart from magnetic fields, can be affected by an acoustic wave field. Investigations into the interaction of elastic waves and domain structures provide valuable information for the search for new ways of controlling magnetic carriers, the analysis of conditions favorable for the operation of magnetic recording devices, and the design of elec-

tronic elements based on the use of surface acoustic waves. A domain wall can execute oscillatory and drift motions in response to an acoustic wave [11–16]. These effects were experimentally observed in yttrium ferrites garnet [17, 18] and iron borate [19].

In this paper, the oscillatory motion of domain walls in two-sublattice garnet ferrites is theoretically analyzed within the Lagrangian formalism.

2. MODEL AND EQUATIONS OF MOTION

The dynamics of garnet ferrites with two nonequivalent sublattices in an acoustic wave field will be described on the basis of the Lagrangian density function L represented in terms of the unit antiferromagnetic vector \mathbf{I} [20]. For the description of the domain-wall dynamics, it is convenient to change over to the spherical coordinate system by parametrizing the vector \mathbf{I} with the angular variables θ and φ ; that is,

$$l_z + il_x = \sin\theta \exp(i\varphi), \quad l_y = \cos\theta. \quad (1)$$

The Lagrangian density function for a ferrimagnet in the angular variables has the form

$$\begin{aligned} L(\theta, \varphi) = & M_0^2 \left[\frac{\alpha}{2c^2} [(\dot{\theta})^2 + (\dot{\varphi})^2 \sin^2 \theta] \right. \\ & - \frac{\alpha}{2} [(\nabla\theta)^2 + (\nabla\varphi)^2 \sin^2 \theta] - \frac{\beta_1}{2} \sin^2 \theta \sin^2 \varphi - \frac{\beta_2}{2} \cos^2 \theta \\ & - B_1 [(u_{xx} \sin^2 \varphi + u_{zz} \cos^2 \varphi) \sin^2 \theta + u_{yy} \cos^2 \theta] \\ & + B_2 [\sin 2\theta (u_{zy} \cos \varphi + u_{yx} \sin \varphi) + u_{xz} \sin 2\varphi \sin^2 \theta] \\ & + \frac{\rho}{2} (\dot{\mathbf{u}})^2 + \frac{v}{gM_0} \dot{\varphi} (1 - \cos \theta) - \frac{c_{11}}{2} (u_{xx}^2 + u_{yy}^2 + u_{zz}^2) \\ & \left. - c_{12} (u_{xx} u_{yy} + u_{xx} u_{zz} + u_{yy} u_{zz}) - 2c_{44} (u_{xz}^2 + u_{xy}^2 + u_{yz}^2) \right]. \quad (2) \end{aligned}$$

Here, dots indicate the derivatives with respect to the time t ; M_0 is the magnitude of the sublattice magnetization vectors; $c = gM_0\sqrt{\alpha\delta}/2$ is the minimum phase velocity of spin waves; δ and α are the constants of the uniform and nonuniform exchange interactions, respectively; g is the gyromagnetic ratio, which is assumed to be identical for both sublattices; β_1 and β_2 are the effective orthorhombic anisotropy constants; ρ is the density of the material; \mathbf{u} is the displacement vector; u_{ik} is the elastic strain tensor; c_{ij} is the fourth-rank tensor of elastic constants, which is written in the matrix notation ($c_{11} = c_{xxxx}$, $c_{12} = c_{xyyy}$, $c_{44} = c_{yzyz}$); and B_1 and B_2 are the quantities determined through the tensor of magnetoelastic constants as $B_1 = b_{11} - b_{12} = b_{xxxx} - b_{xyyy}$ and $B_2 = b_{44} = b_{yzyz}$, respectively.

The parameter ν characterizes the conditions under which the ferrite can be treated as an effective ferromagnet with the net magnetization $M_S = \sum_i M_i$, where M_i is the magnetization of the i th sublattice. The model of an effective ferromagnet is considered to be accurate in the case when the magnitudes of the sublattice magnetization vectors differ significantly, i.e., when the net magnetization of the ferrite is sufficiently large [20]:

$$\nu = \frac{|M_1 - M_2|}{|M_{1,2}|} \gg \left(\frac{\beta}{\delta}\right)^{1/2}. \quad (3)$$

This inequality is the standard approximation used for interpreting experimental data on the dynamics of nonlinear excitations in ferrites. In the subsequent treatment, we will consider garnet ferrites with two non-equivalent sublattices whose magnetizations differ insignificantly. Below, we will make estimates for

yttrium garnet ferrite for which $\nu < \left(\frac{\beta}{\delta}\right)^{1/2}$. In this case, the ferrite cannot be considered an effective ferromagnet.

The dynamic retardation of domain walls due to magnetic dissipative processes is taken into account by the dissipative function

$$F = \frac{\lambda M_0}{2g} \dot{\mathbf{I}}^2 = \frac{\lambda M_0}{2g} (\dot{\theta}^2 + \dot{\phi}^2 \sin^2 \theta), \quad (4)$$

where λ is the Hilbert damping constant. It is assumed that the damping in the elastic subsystem is relatively weak and, hence, can be ignored.

The elastic wavelength is assumed to be considerably larger than the domain-wall thickness. We will restrict our consideration to the isotropic magnetoelastic model $\gamma = B_1 = B_2$.

In the framework of these approximations, the equations describing the magnetization dynamics (with due

regard for the relaxation terms) and the equations of elastodynamics take the form

$$\begin{aligned} & \alpha \left(\Delta \theta - \frac{1}{c^2} \ddot{\theta} \right) + \sin \theta \cos \theta \\ & \times \left[\alpha \left(\frac{1}{c^2} (\dot{\phi})^2 - (\nabla \phi)^2 \right) - \beta_1 \sin^2 \phi + \beta_2 \right] + \frac{\nu}{gM_0} \dot{\phi} \sin \theta \\ & - \gamma [\sin 2\theta (u_{zz} \cos^2 \phi + u_{xz} \sin 2\phi + u_{xx} \sin^2 \phi - u_{yy})] \\ & + 2 \cos 2\theta (u_{zy} \cos \phi + u_{yx} \sin \phi)] = \frac{\lambda}{gM_0} \dot{\theta}, \end{aligned} \quad (5)$$

$$\begin{aligned} & \alpha \nabla((\nabla \phi) \sin^2 \theta) - \frac{\alpha}{c^2} \frac{d}{dt} (\dot{\phi} \sin^2 \theta) - \beta_1 \sin^2 \theta \sin \phi \cos \phi \\ & + \gamma [\sin^2 \theta (u_{zz} \sin 2\phi - 2u_{xz} \cos 2\phi - u_{xx} \sin 2\phi) \\ & + \sin 2\theta (u_{zy} \sin \phi - u_{yx} \cos \phi)] \\ & - \frac{\nu}{gM_0} \dot{\theta} \sin \theta = \frac{\lambda}{gM_0} \dot{\phi} \sin^2 \theta, \end{aligned} \quad (6)$$

$$\rho \frac{\partial^2 u_i^{(i)}}{\partial t^2} = \frac{\partial \sigma_{ik}^{(i)}}{\partial x_k} + f_i^{(e)}. \quad (7)$$

Here, $\sigma_{ik}^{(i)}$ is the component of the internal stress tensor; and $f_i^{(e)}$ stands for the external force, i.e., the external acoustic wave. It is assumed that the strain induced by an acoustic wave ($\sim k_y u_0$, where k_y is the wave vector and u_0 is the displacement amplitude in the elastic wave) exceeds the striction strain ($\sim B_k/c_{ij}$, $k = 1, 2$).

The solutions to Eqs. (5) and (6) will be sought in terms of the perturbation theory based on the introduction of an implicit collective coordinate [9, 15, 16]. As a zeroth approximation, we use the equilibrium magnetization distribution

$$\cos \phi_0(y) = -\tanh \frac{y}{y_0}, \quad (8)$$

where $y_0 = \sqrt{\alpha/\beta_1}$ has the meaning of the thickness of the domain wall. Let us consider a monochromatic acoustic wave that has a frequency ω , propagates perpendicular to the plane of the domain wall, and is characterized by the displacement vector $\mathbf{u} = \text{Re}\{\mathbf{u}_0 \exp[i(k_y y - \omega t)]\}$. In order to analyze the motion of a domain wall in an elastic stress field induced by an acoustic wave, we use the perturbation theory scheme for solitons with a collective variable. The collective variable $Y(t)$ is introduced as the coordinate of the center of the domain wall, whose derivative determines the instantaneous velocity of the domain wall $V(t) = \dot{Y}(t)$. By assuming that the amplitude of the acoustic wave is a small parameter, the functions $\theta(y, t)$, $\phi(y, t)$, and $V(t)$

can be represented in the form of expansions in powers of the amplitude; that is,

$$\begin{cases} \theta(\xi, t) = \frac{\pi}{2} + \theta_1(\xi, t) + \theta_2(\xi, t) + \dots \\ \varphi(\xi, t) = \varphi_0(\xi) + \varphi_1(\xi, t) + \varphi_2(\xi, t) + \dots \\ V = V_1(t) + V_2(t) + \dots, \end{cases} \quad (9)$$

where $\xi = y - Y(t)$. The subscripts $n = 1, 2, \dots$ indicate the order of smallness in the acoustic wave amplitude. The function $\varphi_0(\xi)$ describes the motion of the unperturbed domain wall and has a form similar to the static solution (8). The higher order functions $\theta_n(\xi, t)$ and $\varphi_n(\xi, t)$ ($n = 1, 2, \dots$) characterize the distortion of the domain wall.

After substituting expansions (9) into Eqs. (5) and (6) and separating the terms of first order in the acoustic wave amplitude, we obtain the first-order equations of the perturbation theory

$$\begin{aligned} & \left(\hat{L} + \frac{1}{\omega_1^2} \frac{\partial^2}{\partial t^2} + \frac{\omega_r}{\omega_1^2} \frac{\partial}{\partial t} \right) \varphi_1(\xi, t) + \frac{\omega_v}{\omega_1^2} \frac{\partial}{\partial t} \theta_1(\xi, t) \\ &= -\frac{\gamma}{\beta_1} [(u_{zz} - u_{xx}) \sin 2\varphi_0(\xi) - 2u_{xz} \cos 2\varphi_0(\xi)] \quad (10) \\ & \quad + \frac{\sin \varphi_0(\xi)}{y_0 \omega_1^2} \left(\frac{\partial^2 Y_1}{\partial t^2} + \omega_r \frac{\partial Y_1}{\partial t} \right), \\ & \left(\hat{L} + \sigma + \frac{1}{\omega_1^2} \frac{\partial^2}{\partial t^2} + \frac{\omega_r}{\omega_1^2} \frac{\partial}{\partial t} \right) \theta_1(\xi, t) \\ & - \frac{\omega_v}{\omega_1^2} \frac{\partial}{\partial t} \varphi_1(\xi, t) = -\frac{\omega_v}{y_0 \omega_1^2} \frac{\partial Y_1}{\partial t} \sin \varphi_0(\xi) \quad (11) \\ & - \frac{2\gamma}{\beta_1} [(u_{zy} \cos \varphi_0(\xi) + u_{xy} \sin \varphi_0(\xi))]. \end{aligned}$$

Here, we introduced the following designations: $\sigma = (\beta_2 - \beta_1)/\beta_1$, $\omega_1 = c/y_0 = gM_0\sqrt{\beta_1}\delta/2$ is the activation frequency of the lower branch of bulk spin waves, $\omega_v = v\delta gM_0/4$, and $\omega_r = \lambda\delta gM_0/4$ is the characteristic relaxation frequency.

The operator \hat{L} has the form of the Schrödinger operator with the reflectionless potential

$$\hat{L} = -y_0^2 \frac{d^2}{d\xi^2} + 1 - \frac{2}{\cosh^2(\xi/y_0)}. \quad (12)$$

The spectrum and wave functions of the operator \hat{L} (12) are well known. This spectrum consists of one dis-

crete level with the eigenvalue $\lambda_0 = 0$ to which there corresponds the localized wave function,

$$f_0(\xi) = \frac{1}{\sqrt{2}y_0} \cosh^{-1} \frac{\xi}{y_0}, \quad (13)$$

and the continuous spectrum $\lambda_p = 1 + p^2 y_0^2$ described by the eigenfunctions

$$f_p(\xi) = \frac{1}{b_p \sqrt{L}} \left(\tanh \frac{\xi}{y_0} - ipy_0 \right) \exp(ip\xi), \quad (14)$$

where $b_p = \sqrt{1 + p^2 y_0^2}$ and L is the length of the crystal.

The eigenfunctions $f_0(\xi)$ and $f_p(\xi)$ form a complete orthonormal set of functions. Consequently, the solution to the system of equations (10) and (11) to the first order of the perturbation theory will be sought in the form of an expansion in the complete set of eigenfunctions $\{f_0(\xi), f_p(\xi)\}$. As a result, we obtain

$$\begin{aligned} & \theta_1(\xi, t) \\ &= \text{Re} \left\{ \sum_p [c_p f_p(\xi) + c_0 f_0(\xi)] \exp[i(k_y Y - \omega t)] \right\}, \quad (15) \end{aligned}$$

$$\begin{aligned} & \varphi_1(\xi, t) \\ &= \text{Re} \left\{ \sum_p [d_p f_p(\xi) + d_0 f_0(\xi)] \exp[i(k_y Y - \omega t)] \right\}. \quad (16) \end{aligned}$$

For two different positions of the sample, the domain wall executes a translational motion with an equal energy. The spatial magnetization distribution for the domain wall is described by relationship (8) with the angular variable φ . Consequently, the term describing intrawall oscillations (with the coefficient d_0) in expansion (16) corresponds to the Goldstone mode. The presence of this mode in the spectrum can lead to divergence [21]. In order to avoid divergence, we use the implicit collective coordinate method and omit this mode in expansion (16) [21] (i.e., we set $d_0 = 0$).

From the condition that the coefficient of the shear mode must vanish, we obtain the equation for the domain-wall velocity in the approximation linear in the field; that is,

$$\begin{aligned} & \dot{V}_1(t) + \left(\omega_r - \frac{i\omega_v q_3}{\sigma - q} \right) V_1(t) \\ &= \frac{\pi\gamma(ky_0)^2 \omega \omega_v}{2\beta_1(\sigma - q)} \left[\frac{i u_{0z}}{\cosh\left(\frac{\pi ky_0}{2}\right)} - \frac{u_{0x}}{\sinh\left(\frac{\pi ky_0}{2}\right)} \right] \quad (17) \\ & \quad \times \exp[i(kY - \omega t)], \end{aligned}$$

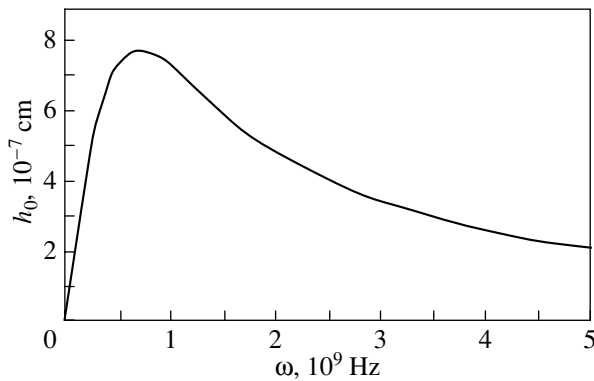


Fig. 1. Dependence of the amplitude h_0 of domain-wall oscillations on the acoustic wave frequency ω for the yttrium garnet ferrite $Y_3Fe_5O_{12}$.

where $k = k_y$, $q = q_1 + iq_2$, $q_1 = (\omega/\omega_1)^2$, $q_2 = (\omega\omega_r)/\omega_1^2$, $q_3 = (\omega\omega_v)/\omega_1^2$, and u_{0i} is the i th component of the amplitude of the displacement vector of the elastic medium.

The solution of this equation can be represented in the form

$$V_1(t) = \frac{\pi\gamma(ky_0)^2\omega\omega_v}{2\beta_1(\sigma - q)\left(\omega_r - i\omega - \frac{iq_3\omega_v}{\sigma - q}\right)} \times \left[\frac{i u_{0z}}{\cosh\left(\frac{\pi k y_0}{2}\right)} - \frac{u_{0x}}{\sinh\left(\frac{\pi k y_0}{2}\right)} \right] \exp[i(kY - \omega t)]. \quad (18)$$

When deriving relationship (18), we were interested only in forced oscillations and assumed that damped natural oscillations can be disregarded within a sufficiently long time interval $t \gg 1/\omega_r$.

3. DISCUSSION

The solution of the equations of motion to the first order of the perturbation theory describes the oscillatory motion of domain walls at a velocity V_1 . The experimentally measured quantity is the amplitude of

domain-wall oscillations $h_0 = \text{Re} \left\{ \frac{i V_1}{\omega \exp[i(kY - \omega t)]} \right\}$.

In an elastic stress field induced by an acoustic wave propagating perpendicular to the domain-wall plane in

the ferrite, the oscillation amplitude is defined by the expression

$$h_0 = \text{Re} \left\{ \frac{i\pi\gamma(ky_0)^2\omega_v}{2\beta_1(\sigma - q)\left(\omega_r - i\omega - \frac{iq_3\omega_v}{\sigma - q}\right)} \times \left[\frac{i u_{0z}}{\cosh\left(\frac{\pi k y_0}{2}\right)} - \frac{u_{0x}}{\sinh\left(\frac{\pi k y_0}{2}\right)} \right] \right\}. \quad (19)$$

In the experimental studies performed by Vlasko-Vlasov and Tikhomirov [17, 18], the strain tensor ku_{0i} was assumed to be a specified parameter of the elastic wave. In the analysis of expression (19), we also assume that the strain tensor $ku_{0i} \propto \omega$ is a specified parameter of the elastic wave and has a magnitude of the order of 10^{-5} .

In the long-wave approximation ($ky_0 \ll 1$), garnet ferrites satisfy the following relationships: $q_1 \ll 1$ and $(\omega_r^2 + \omega_v^2 - \omega^2)/\omega_1^2 \ll 1$. In this case, the frequency dependence of the amplitude of domain-wall oscillations takes the form

$$h_0(\omega) = \frac{\pi(\gamma M_0^2)y_0^2\omega_v}{2\beta_1\sigma M_0^2 s} \left[k u_{0z} \omega_r - k u_{0x} \frac{2s}{\pi y_0} \right] \frac{\omega}{\omega^2 + \omega_r^2} \sim \frac{\omega}{1 + (\omega/\omega_r)^2}, \quad (20)$$

where s is the velocity of propagation of the elastic strains induced by the acoustic wave.

The frequency dependence of the amplitude of domain-wall oscillations in the yttrium garnet ferrite is plotted in Fig. 1. This dependence exhibits a pronounced resonance at the frequency ω_r . A similar frequency dependence of the oscillation amplitude is observed for a nonlinear oscillator in a medium with damping in response to an external periodic force [22]. The asymmetry of the frequency dependence of the oscillation amplitude with respect to the extremum is associated with the external force, which leads to a distortion of the curve. Moreover, a dependence similar to that shown in Fig. 1 was obtained in our earlier work [15], in which we investigated the dynamics of domain walls in an elastic stress field induced by an acoustic wave propagating in the domain-wall plane. However, the behavior of the frequency dependence of the oscillation amplitude was not analyzed in [15].

Before proceeding to further analysis of the obtained frequency dependence of the amplitude of domain-wall oscillations, we note one important cir-

cumstance regarding the solution of the equation of domain-wall motion in weak alternating magnetic fields. It is known [23, 24] that, when the ferromagnetic resonance frequency is considerably higher than the relaxation frequency (this holds true for the classes of magnets under consideration), the frequency dependence of the amplitude of domain-wall oscillations is characterized by a relaxation decay described by the

formula
$$h_0 = \frac{\text{const}}{1 + (\omega/\omega_r)^2},$$
 where const is a parameter

independent of frequency. A similar relaxation decay of the amplitude of domain-wall oscillations in magnetic fields was revealed in [9] within the ferrite model under investigation. This dependence for the yttrium garnet ferrite is depicted in Fig. 2.

The presence of a maximum in the frequency dependence of the amplitude of domain-wall oscillations has been established for magnetic materials in an acoustic wave field. A specific feature of this effect is that the restoring force does not act on the domain wall, because, in the approximation used, the domain wall is characterized by the translational invariance. The resonant behavior of the amplitude of domain-wall oscillations is governed by the linear dependence of the strain tensor components on the acoustic wave frequency. Actually, since the strain tensor obeys the relationships $u_{ij} \sim k_i u_j \sim \omega u_j$, the numerator in the formula describing the frequency dependence of the amplitude of domain-wall oscillations includes a factor proportional to ω . As a consequence, there appears a maximum at the relaxation frequency.

The frequency dependence of the amplitude of domain-wall oscillations can be analyzed using the following numerical parameters for the yttrium garnet ferrite $\text{Y}_3\text{Fe}_5\text{O}_{12}$ [25]: $y_0 \approx 10^{-5}$ cm, $\beta_1 \approx 0.6$, $\sigma \sim 1$, $\lambda \sim 10^{-4}$, $M_0 = 140$ Oe, $\nu \approx 5 \times 10^{-3}$, $g = 1.76 \times 10^7$ (s Oe) $^{-1}$, $\omega_r = 7 \times 10^8$ s $^{-1}$, $\omega_1 \sim 10^{11}$ s $^{-1}$, $ku_{0i} \sim 10^{-5}$, $\gamma M_0^2 \approx 3.5 \times 10^6$ erg/cm 3 , and $s \sim 10^5$ cm/s. In the yttrium garnet ferrite, the maximum oscillation amplitude at frequencies close to the resonance frequency ω_r is equal to 0.8×10^{-6} cm, which is comparable to the thickness of the domain walls.

Let us compare the oscillation amplitude obtained in this study with the data available in the literature. The average magnitude of the oscillation amplitude for the yttrium orthoferrite YFeO_3 in an alternating magnetic field at the frequency $\omega = 7 \times 10^8$ s $^{-1}$ can be as large as 5×10^{-6} cm [8]. In this case, the domain-wall oscillations are induced by the magnetic field components aligned parallel to the easy magnetization axis. In the garnet ferrite in an oscillating magnetic field [9], the domain-wall oscillations are induced by the y and z components of the magnetic field, which are aligned with the hard and easy magnetization axes, respec-

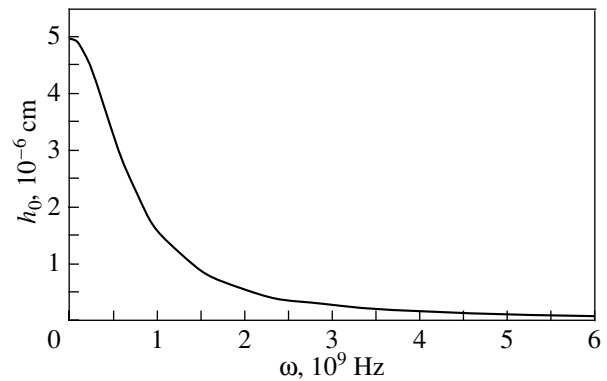


Fig. 2. Dependence of the amplitude h_0 of domain-wall oscillations on the magnetic field frequency ω for the yttrium garnet ferrite $\text{Y}_3\text{Fe}_5\text{O}_{12}$.

tively. The oscillation amplitude at the frequency ω_r is equal to 10^{-4} cm for the z component and 10^{-5} cm for the y component of the magnetic field.

REFERENCES

1. A. Hubert and R. Schöfer, *Magnetic Domains: The Analysis of Magnetic Microstructures* (Springer, Berlin, 1998).
2. V. G. Bar'yakhtar and Yu. I. Gorobets, *Cylindrical Magnetic Domains and Their Lattices* (Naukova Dumka, Kiev, 1988) [in Russian].
3. A. M. Kosevich, B. A. Ivanov, and A. S. Kovalev, *Non-linear Waves of Magnetization: Dynamical and Topological Solitons* (Naukova Dumka, Kiev, 1983) [in Russian].
4. L. P. Walker, in *Magnetism*, Ed. by G. Rado (Academic, New York, 1963), Vol. III.
5. V. G. Bar'yakhtar, B. A. Ivanov, and M. V. Chetkin, *Usp. Fiz. Nauk* **146** (3), 417 (1985) [*Sov. Phys. Usp.* **28**, 563 (1985)].
6. P. D. Kim and D. Ch. Khvan, *Fiz. Tverd. Tela (Leningrad)* **24** (8), 2300 (1982) [*Sov. Phys. Solid State* **24** (8), 1306 (1982)].
7. L. M. Dedukh and Yu. P. Kabanov, *Zh. Éksp. Teor. Fiz.* **115** (4), 1377 (1999) [*JETP* **88** (4), 761 (1999)].
8. V. G. Bar'yakhtar, B. A. Ivanov, P. D. Kim, A. L. Sukstanskiĭ, and D. Ch. Khvan, *Pis'ma Zh. Éksp. Teor. Fiz.* **37** (1), 35 (1983) [*JETP Lett.* **37** (1), 41 (1983)].
9. V. S. Gerasimchuk and A. L. Sukstanskiĭ, *J. Magn. Magn. Mater.* **146**, 323 (1995).
10. G. S. Kandaurova, *Usp. Fiz. Nauk* **172** (10), 1164 (2002) [*Phys. Usp.* **45** (10), 1051 (2002)].
11. V. G. Bar'yakhtar and B. A. Ivanov, *Fiz. Met. Metall.oved.* **39** (4), 478 (1975).
12. A. A. Lugovoiĭ and E. A. Turov, *Fiz. Tverd. Tela (Leningrad)* **24** (4), 1145 (1982) [*Sov. Phys. Solid State* **24** (4), 646 (1982)].
13. S. I. Denisov, *Fiz. Tverd. Tela (Leningrad)* **31** (11), 270 (1989) [*Sov. Phys. Solid State* **31** (11), 151 (1989)].

14. Yu. I. Gorobets and S. I. Denisov, Ukr. Fiz. Zh. (Rus. Ed.) **35** (2), 271 (1990).
15. V. S. Gerasimchuk and A. A. Shitov, Fiz. Tverd. Tela (St. Petersburg) **43** (10), 1849 (2001) [Phys. Solid State **43** (10), 1927 (2001)].
16. V. S. Gerasimchuk and A. A. Shitov, Fiz. Tverd. Tela (St. Petersburg) **45** (1), 119 (2003) [Phys. Solid State **45** (1), 124 (2003)].
17. V. K. Vlasko-Vlasov and O. A. Tikhomirov, Fiz. Tverd. Tela (Leningrad) **32** (6), 1678 (1990) [Sov. Phys. Solid State **32** (6), 978 (1990)].
18. V. K. Vlasko-Vlasov and O. A. Tikhomirov, Fiz. Tverd. Tela (Leningrad) **33** (12), 3498 (1991) [Sov. Phys. Solid State **33** (12), 1960 (1991)].
19. M. V. Chetkin, V. V. Lykov, A. A. Makovozova, and A. G. Belonogov, Fiz. Tverd. Tela (Leningrad) **33** (1), 307 (1991) [Sov. Phys. Solid State **33** (1), 177 (1991)].
20. B. A. Ivanov and A. L. Sukstanskiĭ, Zh. Éksp. Teor. Fiz. **84** (1), 370 (1983) [Sov. Phys. JETP **57**, 214 (1983)].
21. R. Radzharamam, *Solitons and Instantons: An Introduction to Solitons and Instantons in Quantum Field Theory* (North-Holland, Amsterdam, 1982; Mir, Moscow, 1985).
22. L. D. Landau and E. M. Lifshitz, *Course of Theoretical Physics, Vol. 1: Mechanics*, 3rd ed. (Pergamon, Oxford, 1976; Nauka, Moscow, 1988).
23. A. G. Gurevich, *Magnetic Resonance in Ferrites and Antiferromagnets* (Nauka, Moscow, 1973) [in Russian].
24. G. S. Krinchik, *Physics of Magnetic Phenomena* (Mosk. Gos. Univ., Moscow, 1985) [in Russian].
25. S. Krupicka, *Physik der Ferrite und der verwandten magnetischen Oxide* (Academia, Praha, 1973; Mir, Moscow, 1976).

Translated by O. Borovik-Romanova

MAGNETISM AND FERROELECTRICITY

Size Effects in Thin Antiferromagnetic Layers and “Ferromagnet–Nonmagnetic Metal” Multilayer Magnetic Structures

A. A. Berzin, A. I. Morosov, and A. S. Sigov

Moscow State Institute of Radio Engineering, Electronics, and Automation (Technical University),
pr. Vernadskogo 78, Moscow, 119454 Russia

e-mail: mor-alexandr@yandex.ru

Received January 26, 2005

Abstract—The specific features of the spin-flop and spin-flip transitions in thin antiferromagnetic layers and “ferromagnet–nonmagnetic metal” multilayer magnetic structures are considered. The dependence of the magnetic fields corresponding to these phase transitions on the thickness of the antiferromagnet or on the number of layers in the multilayer is determined. © 2005 Pleiades Publishing, Inc.

1. INTRODUCTION

Magnetic layers with a thickness of 1–10 nm and multilayer structures formed by these layers have been widely used in modern microelectronics. For these objects, the influence of the surfaces and interfaces of the layers, as well as the size effects, are clearly pronounced. In this respect, the study of their properties is an important problem. The purpose of the present work was to investigate theoretically the spin-flip and spin-flop transitions induced by an external magnetic field in a thin layer of a mirror-symmetric antiferromagnet with uncompensated surfaces.

The results obtained are completely applicable to antiferromagnetically coupled multilayer magnetic structures consisting of alternating ferromagnetic and nonmagnetic metal nanolayers. Similar structures have attracted the particular attention of researchers since the discovery of the giant magnetoresistance effect in these materials [1]. If ferromagnetic layers in such a multilayer are assumed to be uniformly magnetized, the behavior of this multilayer in an external magnetic field should be similar to the behavior of a plane-parallel antiferromagnetic layer with uncompensated boundaries. Theoretical studies of the structures under consideration have been performed using numerical methods [2–9]. However, to the best of our knowledge, attempts to investigate the size effects in these materials analytically have not been made.

In our previous work [10], we considered the distortions of the magnetic structure in response to an external magnetic field near the surface of the antiferromagnet. We analyzed the cases of both compensated and uncompensated surfaces and calculated the depth of penetration r_c of these distortions into the antiferromagnet (the correlation radius of the order parameter) over the entire range of magnetic fields up to the field at

which the magnetizations of the two sublattices of the antiferromagnet become aligned with the external magnetic field (the field of the spin-flip transition).

It has been found that, in the case of a compensated surface of the antiferromagnet, the penetration depth of surface distortions is of the order of the interatomic distances in all magnetic fields, except in the field range in the immediate vicinity of the field of the spin-flip transition in which the penetration depth r_c diverges when tending to this field.

For an uncompensated surface of the antiferromagnet, the penetration depth of surface distortions in a magnetic field weaker than that of the sublattice reorientation (or of the spin-flop transition) is equal in order of magnitude to the thickness of the domain wall in the antiferromagnet. Moreover, the penetration depth r_c in the field aligned parallel to the easy magnetization axis diverges as the bulk spin-flop transition point is approached.

In magnetic fields comparable to the field of the spin-flip transition, the behavior of the penetration depth r_c is similar to that for the compensated surface of the antiferromagnet. Thus, the size effects in the structures under consideration are clearly pronounced in magnetic fields of less than or of the order of the spin-flop transition field, as well as in the vicinity of the spin-flip transition field.

2. DESCRIPTION OF THE MODEL

Let us consider an antiferromagnet with ideally smooth boundary surfaces at temperatures $T \ll T_N$ (where T_N is the Néel temperature) with the sublattice magnetizations assumed to be constant in magnitude. We will restrict our consideration to the special case of localized spins in the approximation of the Heisenberg

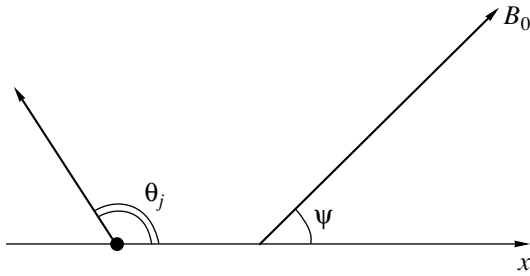


Fig. 1. Orientation of the magnetization vectors of the atomic planes in an antiferromagnetic layer with respect to the easy magnetization axis (the x axis) and the direction of an external magnetic field.

exchange interaction between nearest neighbors. The number of nearest neighbors for spins lying in the surface atomic plane is less than that for spins in the bulk. Consequently, the surface spins are more strongly affected by an external magnetic field. It is for this reason that the field of the surface spin-flop transition is weaker than the field of the bulk spin-flop transition [11–13]. We assume that the easy magnetization axis lies in the surface plane.

In the case of an uncompensated surface, all the spins lying in the surface atomic plane are collinear and belong to one sublattice. The atomic planes aligned parallel to the surface are numbered by the index j beginning from one of the surfaces. Spins in the even and odd planes correspond to different sublattices. The direction of a spin in the atomic plane is determined by the angle θ_j that the magnetic moment corresponding to this spin makes with a specified direction parallel to the easy magnetization axis (Fig. 1).

The exchange interaction energy can be written in the form

$$W_{\text{ex}} = \frac{N|J_{\text{af}}|S_{\text{af}}^2 a}{2} \sum_{j=1}^M [\cos(\theta_j - \theta_{j-1})(1 - \delta_{1,j}) + \cos(\theta_j - \theta_{j+1})(1 - \delta_{M,j})], \quad (1)$$

where N is the number of spins in the atomic plane, $J_{\text{af}} < 0$ is the exchange integral between the nearest neighbor spins, S_{af} is the average spin of the atom, a is the number of nearest neighbors of a given spin lying in the adjacent atomic plane, M is the number of atomic planes in the layer, and $\delta_{1,j}$ is the Kronecker delta. The number of nearest neighbors is $a = 4$ for the (100) section of a body-centered tetragonal lattice (with the c axis lying in the plane of the section) or an orthorhombic lattice and $a = 1$ for a multilayer magnetic structure.

The single-ion anisotropy energy and the Zeeman energy are represented in the following form:

$$W_{\text{an}} = -KN S_{\text{af}}^2 \sum_{j=1}^M \cos 2\theta_j, \quad (2)$$

$$W_B = -2\mu_B S_{\text{af}} B_0 N \sum_{j=1}^M \cos(\theta_j - \psi), \quad (3)$$

where K is the anisotropy constant, μ_B is the Bohr magneton, and B_0 is the induction of an external magnetic field aligned parallel to the surface and directed at an angle ψ to the easy magnetization axis (Fig. 1).

By minimizing the total energy $W = W_{\text{ex}} + W_{\text{an}} + W_B$ with respect to the angles θ_j , we obtain the system of equations

$$\sin(\theta_j - \theta_{j-1})(1 - \delta_{1,j}) + \sin(\theta_j - \theta_{j+1})(1 - \delta_{M,j}) = \alpha \sin 2\theta_j + \beta \sin(\theta_j - \psi), \quad (4)$$

where

$$\alpha = 2K/a|J_{\text{af}}| \ll 1, \quad (5)$$

$$\beta = 2\mu_B B_0/a|J_{\text{af}}|S_{\text{af}}. \quad (6)$$

The behaviors of thin antiferromagnetic layers (ferromagnet–nonmagnetic metal multilayers) with even and odd numbers of atomic planes (ferromagnetic layers) differ significantly. For an odd number of atomic planes, the surface atomic planes belong to one sublattice and, hence, the dependence $\theta(j)$ appears to be even with respect to the center of the structure. By contrast, this symmetry is absent in the case of an even number of atomic planes, when the surface atomic planes belong to different sublattices.

3. SPIN-FLOP TRANSITION IN A LAYER WITH AN EVEN NUMBER OF ATOMIC PLANES

In a semi-infinite antiferromagnet, when the external magnetic field is antiparallel to the magnetization vector of the uppermost atomic plane, there occurs a surface spin-flop transition in the magnetic field $\beta_s = \beta_1/\sqrt{2}$, where

$$\beta_1 = \sqrt{8\alpha} \quad (7)$$

is the field of the bulk spin-flop transition [11–13]. In this case, as was shown in our previous work [10], a 180° domain wall arises near the surface. Within this wall, the magnetizations of the second, fourth, and other successive even layers compensate for the magnetizations of the third, fifth, and other odd layers, respectively. Since the magnetization of the first atomic plane is approximately parallel to that of the last even atomic plane, the surface magnetic moment is close to $4\mu_B N S_{\text{af}}$.

The numerical solution to the system of equations (4) for layers with the numbers of atomic planes $M = 10, 16, 20, 30, 40, 60,$ and 80 and $\alpha = 0.01$ suggests that, when the magnetic field is aligned parallel to the easy magnetization axis ($\psi = 0$), the spin-flop transition occurs in the magnetic field $\beta = \beta_s$. Then, there arises a domain wall with the center located at the center of the layer.

For $\beta < \beta_s$, we have $\theta_{2n-1} = 0$ and $\theta_{2n} = \pi$. For $\beta = \beta_s + 0$, the angles at the center of the layer are given by

$$\theta_{2n-1}^{\text{mid}} = 0.75\theta_{M/2+1} + 0.25\theta_{M/2-1} \approx \pi/2,$$

$$\theta_{2n}^{\text{mid}} = 0.75\theta_{M/2} + 0.25\theta_{M/2+2} \approx -\pi/2.$$

Thus, the angles θ_j change jumpwise in the magnetic field $\beta = \beta_s$.

Let us assume that the layer thickness d exceeds the penetration depth of distortions r_c , which, in magnetic fields $\beta \approx \beta_1$, is defined by the formula [10]

$$r_c = 2b/\sqrt{|\beta^2 - \beta_1^2|}, \tag{8}$$

where b is the interplanar distance. In this case, the magnetization of the surface atomic planes is nearly parallel to the external magnetic field (Fig. 2a). At $d < r_c$, the dependence $\theta(j)$ exhibits almost linear behavior and the magnetization has not managed to rotate through an angle of $\pi/2$ from the center of the layer to the surface (Fig. 2b). The dependence $\chi = \theta_1 - \theta_{2n-1}^{\text{mid}}$ on the number M of atomic planes in a layer in the field β_s of the spin-flop transition is plotted in Fig. 3.

As the bulk spin-flop transition field β_1 is approached, the correlation radius r_c diverges in accordance with relationship (8). Therefore, the dependence $\theta(j)$ is characterized by linear behavior at all the numbers M of atomic planes in the layer under consideration.

4. SPIN-FLOP TRANSITION IN A LAYER WITH AN ODD NUMBER OF ATOMIC PLANES

In this case, both surface atomic planes belong to one antiferromagnetic sublattice. As a result, in the magnetic field aligned parallel to the magnetization of this sublattice, the spin-flop transition in a finite layer is suppressed and should occur in stronger magnetic fields $\beta_1^* > \beta_1$, because the collinear orientation of the magnetization vectors of the surface atomic planes with respect to the direction of the magnetic field is energetically favorable.

The phase transition in the magnetic field β_1^* to the spin-flop phase is a second-order transition. Unlike the first-order bulk spin-flop transition and the case of an even number of atomic planes, the rotation angle of the sublattices varies continuously with a change in the magnetic field and reaches a maximum at the center of the antiferromagnetic layer (multilayer). This situation is illustrated in Figs. 4 and 5.

The change in the field of the spin-flop transition as compared to the field of the bulk spin-flop transition can be determined from the condition $d = Cr_c(\beta_1^*)$,

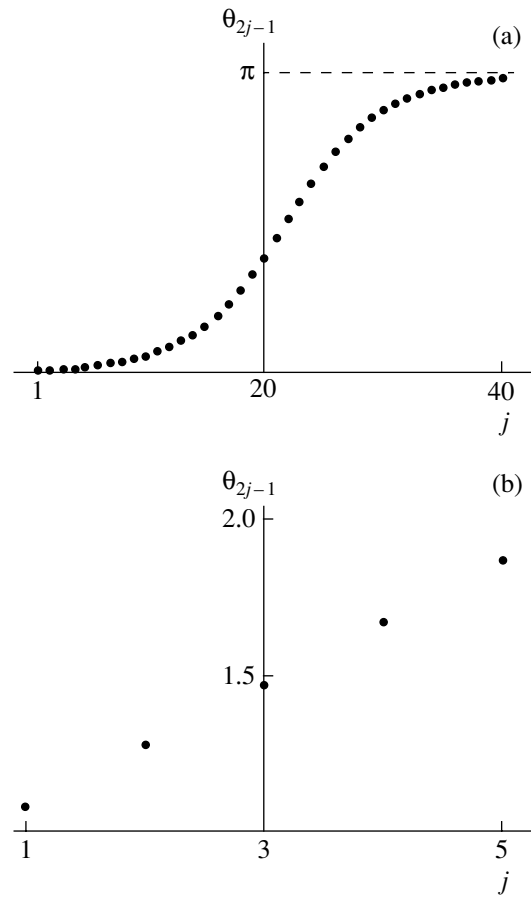


Fig. 2. Directions of the magnetization vectors of the odd atomic planes in the field of the surface spin-flop transition for $M =$ (a) 80 and (b) 10.

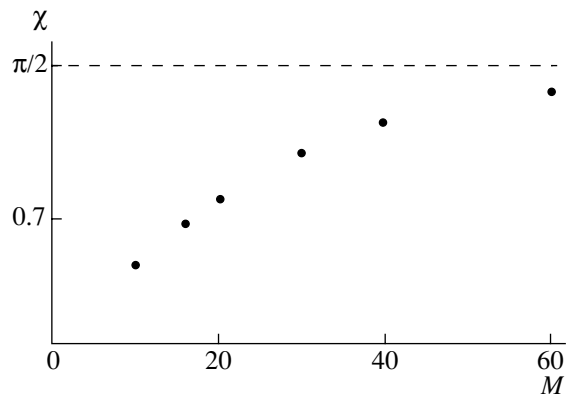


Fig. 3. Dependence of the rotation angle of the sublattice magnetization at the half-thickness of the antiferromagnetic layer on the number of atomic planes in the layer.

where C is a dimensionless constant of the order of unity. By using expression (8), we obtain

$$(\beta_1^*)^2 = \beta_1^2 + \left(\frac{2C}{M}\right)^2. \tag{9}$$

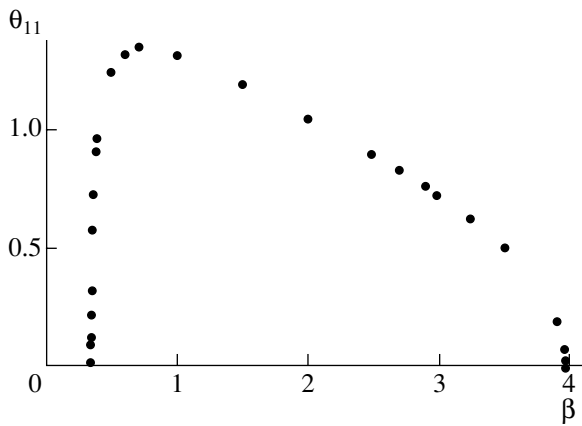


Fig. 4. Dependence of the direction of the magnetization vector of the central atomic plane on the magnetic field in the layer with $M = 21$.

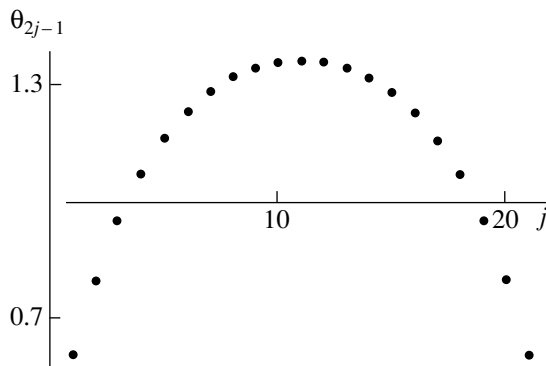


Fig. 5. Directions of the magnetization vectors of the odd atomic planes in the field $\beta = 0.4$ for the layer with $M = 41$.

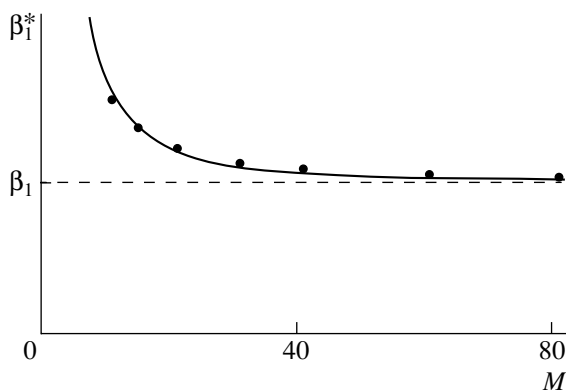


Fig. 6. Dependence of the spin-flop transition field on the number of atomic planes in the layer with a odd number of atomic planes.

A comparison of the proposed approximation with the results of calculations (Fig. 6) leads to the dimensionless constant $C \approx 2$.

5. STRONG MAGNETIC FIELDS

In the field range $\beta_1 \ll \beta < \beta_2$ [where $\beta_2 = 2(2 - \alpha) \approx 4$ is the field of the bulk spin-flip transition in the case where the external magnetic field is aligned parallel to the easy magnetization axis], the penetration depth of surface distortions is described by the relationship [10]

$$r_c = -b/\ln\left(1 - \alpha + \frac{\beta^2(2 - \alpha)}{\beta_2^2 - 2\beta^2}\right) - \sqrt{\left(1 - \alpha + \frac{\beta^2(2 - \alpha)}{\beta_2^2 - 2\beta^2}\right)^2 - 1}. \tag{10}$$

It is easy to see that the penetration depth r_c decreases with an increase in the magnetic field and vanishes at $\tilde{\beta} = \beta_2/\sqrt{2} \approx \sqrt{8}$. With a further increase in the magnetic field, the penetration depth r_c increases and exhibits a square-root divergence at $\beta \rightarrow \beta_2$.

For $\beta \sim 1$ and $|\beta_2 - \beta| \sim 1$, we have $r_c \sim b$. Therefore, at $M \gg 1$, the distortion in the vicinity of two boundaries of the layer can be independently considered, the size effect is absent, and the problem is reduced to that studied in our earlier work [10].

It should only be noted that the deviations of the canting angles of the sublattices from the bulk canting angles at $\beta < \tilde{\beta}$ are opposite in sign, whereas the corresponding deviations at $\beta > \tilde{\beta}$ are identical in sign (Fig. 7).

In the vicinity of the magnetic field β_2 , when $r_c \rightarrow \infty$, the size effects become significant. Since the antiferromagnetic layer (multilayer) has a finite thickness, the spin-flip transition occurs in a continuous manner in a magnetic field $\beta_2^* < \beta_2$. The magnetic field β_2^* determined from the condition $d = C'r_c$ is given by the formula

$$\beta_2^* = \beta_2 \left[1 - \frac{1}{8} \left(\frac{C'b}{d} \right)^2 \right]. \tag{11}$$

By comparing the calculated results with formula (11), we obtain $C' \approx 4.5$ for both even and odd numbers of atomic planes in the layer (Fig. 8).

6. SURFACE MAGNETIC MOMENT

Let us now discuss the difference between the magnetic moment induced by an external magnetic field and the magnetic moment of the same antiferromagnetic layer mentally separated in the bulk of the antifer-

romagnetic specimen (hereafter, this specimen will be referred to as the bulk analog).

In the case of layers with an even number of atomic planes, the magnetic moment is induced in the magnetic field $\beta_s = \beta_1/\sqrt{2}$; i.e., in the field range $\beta_s < \beta \leq \beta_1$, the magnetic moment of the finite antiferromagnet is nonzero (unlike the magnetic moment of the bulk analog). The magnetic moment is aligned with the magnetic field parallel to the easy magnetization axis.

In magnetic fields $\beta > \beta_1$, the magnetic moment varies almost linearly and reaches saturation in the field β_2^* (Fig. 9a). The difference between the magnetic moments of the layer and the bulk analog in strong magnetic fields $\beta \leq \beta_2^*$ is insignificant (Fig. 9b) and, hence, is difficult to determine with experimental methods.

In the case of layers with an odd number of atomic planes, the longitudinal (along the field) magnetic moment m_{\parallel} equal to the magnetic moment of an uncompensated plane occurs in a zero magnetic field. With an increase in the magnetic field, the magnetic moment m_{\parallel} increases drastically at β_1^* and then increases linearly (Fig. 10a).

Apart from the longitudinal component, in the magnetic field β_1^* , there arises a magnetic moment component m_{\perp} that is perpendicular to the magnetic field and lies in the plane of the layer (Fig. 10b). The magnetic moment component m_{\perp} is nonzero in the field range $\beta \approx \beta_1^*$, in which the sublattice magnetizations rotate continuously. In magnetic fields $\beta \gg \beta_1^*$, the rotation is completed and $m_{\perp} = 0$. In the bulk analog, the magnetic moment component

$$m_{\perp} = 2N\mu_B S_{af} \sqrt{1 - \left(\frac{\beta}{\beta_2}\right)^2}$$

differs substantially from zero over the entire field range $\beta_1 < \beta < \beta_2$ (except for magnetic fields in the vicinity of the point β_2) and has the opposite direction.

7. THE EFFECT OF ROUGHNESS

If the number of layers in multilayer magnetic structures is fixed, the presence of atomic steps on the surface of the antiferromagnet leads to a change in the number of atomic planes. On different sides of a step, the number of planes differs by unity.

In the case when the characteristic distance R between steps is considerably larger than the penetration depth r_c , the antiferromagnetic layer is separated into domains whose boundaries are perpendicular to the surface of the layer and coincide with step edges on one of the layer surfaces. The behavior of the magnetization in each domain is governed by the number of

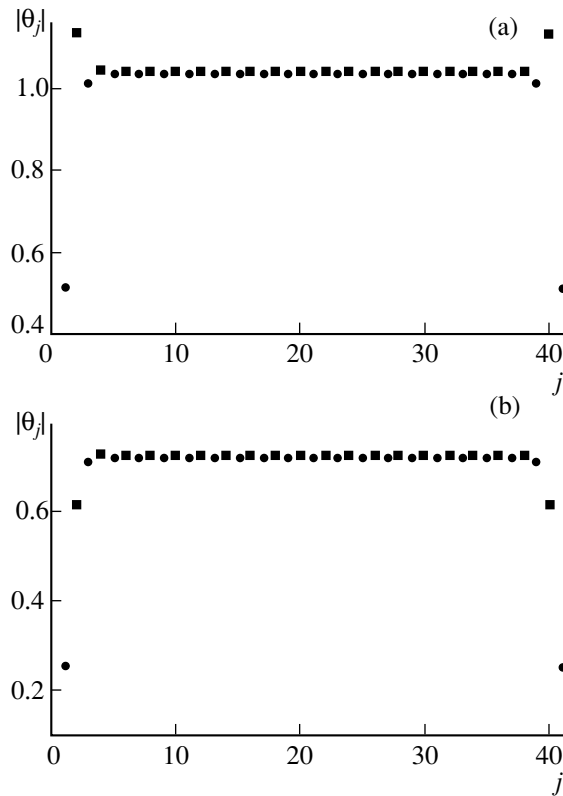


Fig. 7. Directions of the magnetization vectors of the atomic planes in magnetic fields $\beta =$ (a) 2 and (b) 3 for the layer with $M = 41$. Circles indicate odd atomic planes with an angle $\theta_j > 0$, and squares correspond to even atomic planes with an angle $\theta_j < 0$.

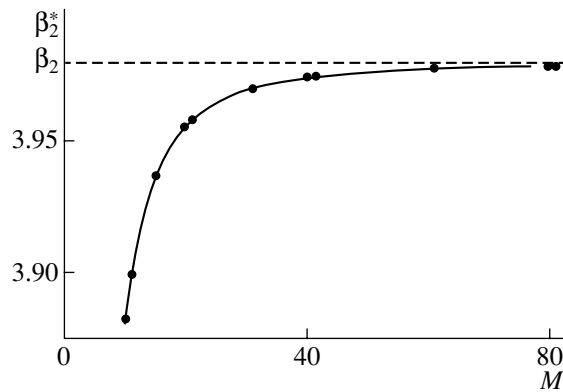


Fig. 8. Dependence of the spin-flip transition field on the number of atomic planes in the layer.

atomic planes. This number inside a domain remains unchanged. The domain type is determined by a combination of two parameters, namely, the parity of atomic planes and the number of the antiferromagnetic sublattice corresponding to the uppermost atomic plane.

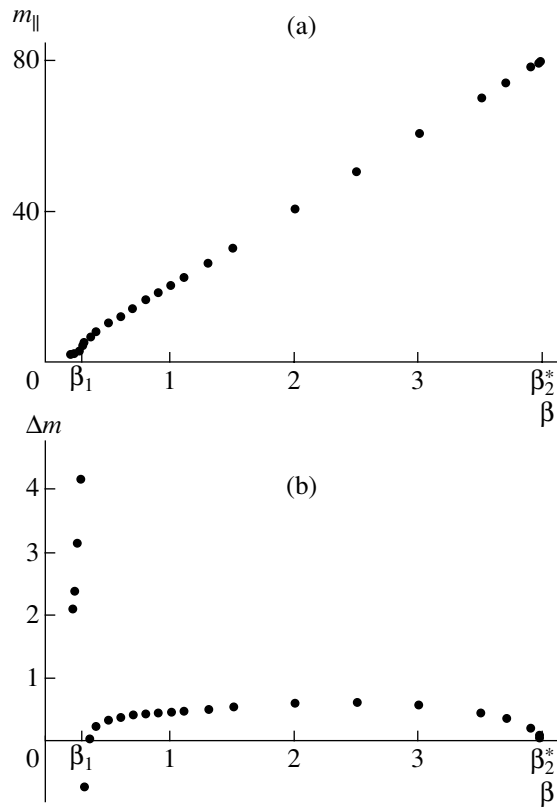


Fig. 9. Dependences of (a) the magnetic moment of the antiferromagnetic layer with $M = 80$ and (b) the difference between the magnetic moments of the layer and the bulk analog (expressed in terms of $2\mu_B N S_{af}$ on the magnetic field).

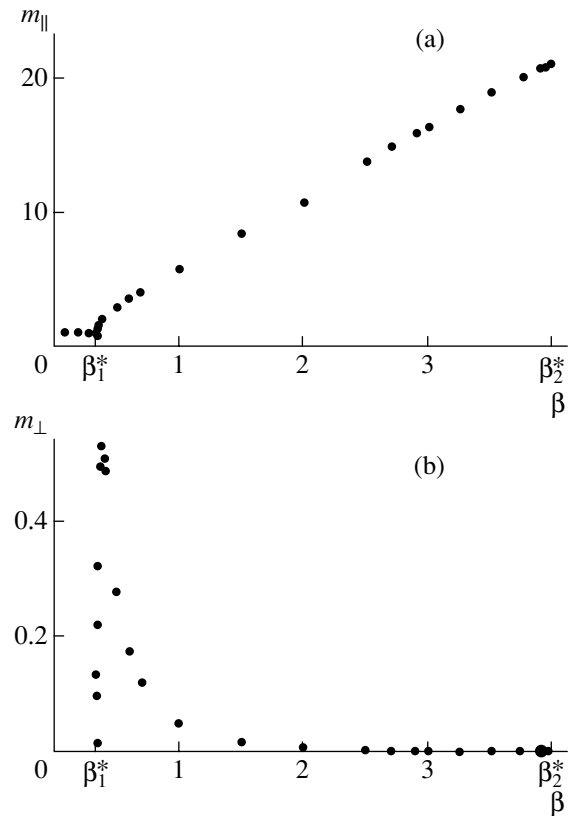


Fig. 10. Dependences of the (a) longitudinal and (b) transverse components of the magnetic moment of the antiferromagnetic layer with $M = 21$ on the magnetic field.

There are four possible combinations and, hence, four domain types. For $\beta_s < \beta < \beta_1^*$, the spin-flop phase should be observed in domains with an even number of atomic planes, whereas the collinear phase should be stable in domains with an odd number of atomic planes.

For $\beta \rightarrow \beta_1 - 0$, the correlation radius of distortions diverges. This leads to smearing of the domain structure at $r_c(\beta) > R$ due to the averaging of surface distortions.

The domain structure again becomes clearly pronounced in magnetic fields $\beta > \beta_1$, when $r_c(\beta)$ is less than the characteristic distance R between steps. As the magnetic field β_2^* is approached, the contrast between domains weakens and disappears at the point $\beta = \beta_2^*$.

8. CONCLUSIONS

The main conclusions drawn in this study can be summarized as follows.

(1) The character of the spin-flop transition in an antiferromagnetic nanolayer (“ferromagnet–nonmagnetic metal” antiferromagnetically coupled multilayer

structure) depends substantially on the parity of the number of atomic planes (ferromagnetic layers).

(2) In a layer with an even number of atomic planes, the first-order spin-flop transition occurs in the field of the surface spin-flop transition. As a result, there arises a state with a domain wall located at the center of the layer.

(3) In a layer with an odd number of atomic planes, the second-order spin-flop transition is observed in a magnetic field that is stronger than the field of the bulk spin-flop transition and depends on the thickness of the layer.

(4) The spin-flop transition in an antiferromagnet takes place in a magnetic field that is weaker than the field of the bulk spin-flop transition and depends on the thickness of the antiferromagnet.

(5) The surface roughness of the antiferromagnetic layer under specific conditions leads to its separation into domains whose boundaries are perpendicular to the surfaces of the layer and coincide with edges of atomic steps on the surfaces. The four types of domains formed differ in terms of the parity of the number of atomic planes and the number of the sublattice corresponding to the surface atomic plane.

ACKNOWLEDGMENTS

This work was supported by the US Civilian Research and Development Foundation for the New Independent States of the Former Soviet Union and the Ministry of Education and Science of the Russian Federation, project no. CRDF VZ-010-0.

REFERENCES

1. M. N. Baibich, J. M. Broto, A. Fert, Nguyen van Dau, F. Petroff, P. Etienne, G. Creuzet, A. Friederich, and J. Chazelas, *Phys. Rev. Lett.* **61** (21), 2472 (1988).
2. R. W. Wang, D. L. Mills, E. E. Fullerton, J. E. Mattson, and S. D. Bader, *Phys. Rev. Lett.* **72** (6), 920 (1994).
3. L. Trallori, *Phys. Rev. B: Condens. Matter* **57** (10), 5923 (1998).
4. N. Papanicolaou, *J. Phys.: Condens. Matter* **10** (8), L131 (1998).
5. A. L. Dantas and A. S. Carrico, *Phys. Rev. B: Condens. Matter* **59** (2), 1223 (1999).
6. S. G. E. te Velthuis, J. S. Jiang, S. D. Bader, and G. P. Felcher, *Phys. Rev. Lett.* **89**, 127203 (2002).
7. A. N. Bogdanov and U. K. Rossler, *Phys. Rev. B: Condens. Matter* **68**, 012407 (2003).
8. U. K. Rossler and A. N. Bogdanov, *Phys. Rev. B: Condens. Matter* **69**, 094405 (2004).
9. U. K. Rossler and A. N. Bogdanov, *Phys. Rev. B: Condens. Matter* **69**, 184420 (2004).
10. A. A. Berzin, A. I. Morosov, and A. S. Sigov, *Fiz. Tverd. Tela (St. Petersburg)* **47** (9), 1651 (2005) [*Phys. Solid State* **47** (9), 1714 (2005)].
11. D. L. Mills, *Phys. Rev. Lett.* **20** (1), 18 (1968).
12. D. L. Mills and W. M. Saslow, *Phys. Rev.* **171** (2), 488 (1968).
13. F. Keffer and H. Chow, *Phys. Rev. Lett.* **31** (17), 1061 (1973).

Translated by O. Borovik-Romanova

MAGNETISM AND FERROELECTRICITY

Acoustical Investigations of a $\text{La}_{0.75}\text{Sr}_{0.25}\text{MnO}_3$ Single Crystal

A. V. Goltsev¹, K. V. Dyakonov¹, N. F. Kartenko¹, L. A. Kulakova¹, V. V. Popov¹,
É. Z. Yakhkind¹, Ya. M. Mukovskii², and V. P. Dyakonov^{3,4}

¹ Ioffe Physicotechnical Institute, Russian Academy of Sciences, Politekhnikeskaya ul. 26, St. Petersburg, 194021 Russia
e-mail: k.dyakonov@mail.ioffe.ru

² Moscow Institute of Steel and Alloys, Leninskiĭ pr. 4, Moscow, 117936 Russia

³ Donetsk Physicotechnical Institute, National Academy of Sciences of Ukraine, Donetsk, 83114 Ukraine

⁴ Institute of Physics, Polish Academy of Sciences, Warsaw, 02-668 Poland

Received February 11, 2005

Abstract—The acoustical, resistive, and magnetic properties of a $\text{La}_{0.75}\text{Sr}_{0.25}\text{MnO}_3$ lanthanum manganite single crystal are investigated in the temperature range involving the second-order magnetic phase transition. The acoustical measurements are performed by the pulse-echo method in the frequency range 14–90 MHz. It is found that, as the temperature decreases, the velocity of a longitudinal acoustic wave propagating along the [111] axis in the single crystal drastically increases at temperatures below the critical point of the magnetic phase transition. No dispersion of the acoustic velocity is revealed. A sharp increase in the acoustic velocity is accompanied by the appearance of an acoustical absorption peak. The observed effects are discussed with due regard for the interaction of acoustic waves with the magnetic moments of the manganese ions. © 2005 Pleiades Publishing, Inc.

1. INTRODUCTION

Rare-earth manganites of the general formula $R_{1-x}A_x\text{MnO}_3$, where R is a rare-earth metal (La, Nd, Pr) and A is an alkaline-earth metal (Ca, Sr, Ba), have been intensively studied in recent years. These compounds have attracted a large amount of research attention owing to the unique combination of their electronic, magnetic, and structural properties, as well as to the very high sensitivity of their resistance to magnetic fields and mechanical deformations (see, for example, reviews [1, 2]). In this respect, the rare-earth manganites are convenient model objects for use in investigating the physical nature of strongly correlated systems and hold the greatest promise for practical applications (specifically in devices for the recording, storage, and processing of information).

At present, it is universally accepted that the properties of manganites are determined not only by the double-exchange mechanism [3] but also by the strong Jahn–Teller electron–phonon interaction [4]. From the standpoint of strong electron–phonon interactions, acoustical methods are the most attractive as providing a deeper insight into the physical properties of manganites and the nature of the giant magnetoresistance effect. Investigation into the acoustical characteristics of manganites (such as the absorption and velocity of sound) allows one to obtain independent information on the relaxation processes occurring in electronic, phonon, and magnetic subsystems of the objects under investigation; on the structural and magnetic phase transitions; and on the mechanisms of the electron–phonon and spin–phonon interactions [5–7].

In this work, we investigated the acoustical, resistive, and magnetic properties of a $\text{La}_{1-x}\text{Sr}_x\text{MnO}_3$ lanthanum manganite single crystal in the temperature range involving the second-order magnetic phase transition and the metal–insulator transition. The $\text{La}_{0.75}\text{Sr}_{0.25}\text{MnO}_3$ manganite is a typical representative of the compounds characterized by magnetoresistance in the vicinity of the ferromagnetic phase transition with a high critical temperature $T_c \approx 340$ K. Owing to the simple phase diagram and the possibility of growing high-quality single-crystal samples, the $\text{La}_{0.75}\text{Sr}_{0.25}\text{MnO}_3$ compound is a convenient object for use in studying the specific features and mechanisms of the interaction of acoustic waves with the electronic, phonon, and magnetic subsystems in rare-earth manganites.

2. SAMPLE PREPARATION AND EXPERIMENTAL TECHNIQUE

A single crystal of the $\text{La}_{0.75}\text{Sr}_{0.25}\text{MnO}_3$ manganite was grown by floating zone melting with radiation heating from a preliminarily sintered ceramic material [8]. X-ray diffraction analysis was performed by the Laue and rolling-crystal methods. The x-ray diffraction pattern of a powdered sample was recorded on a DRON-2 diffractometer (CuK_α radiation). The absorption and velocity of longitudinal acoustic waves were measured at temperatures of 77–420 K and frequencies of 14–90 MHz. A cylindrical sample (3 mm in diameter and 5 mm long) oriented along the [111] cubic axis was prepared by cutting in a coolant with subsequent fine

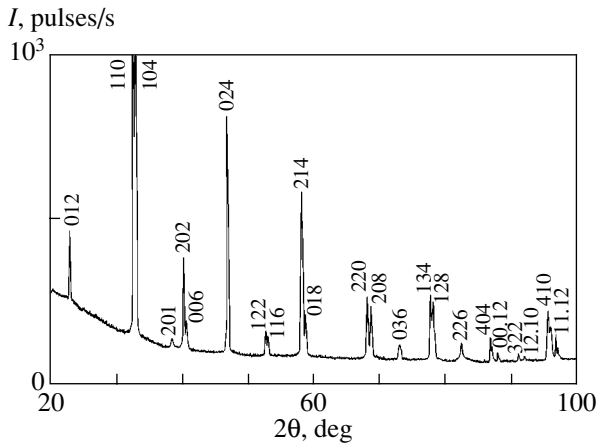


Fig. 1. X-ray diffraction pattern of the $\text{La}_{0.75}\text{Sr}_{0.25}\text{MnO}_3$ single crystal. The reflection indices correspond to a hexagonal pseudocell.

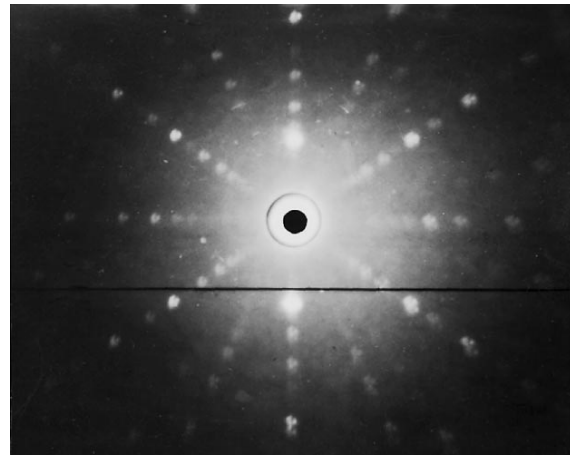


Fig. 2. Laue x-ray diffraction pattern of the $\text{La}_{0.75}\text{Sr}_{0.25}\text{MnO}_3$ single crystal along the [110] cubic axis.

grinding and optical-quality polishing of the faces. Sound was excited by resonant piezoelectric transducers made of lithium niobate and piezoelectric ceramics. The transducers were glued to the polished face of the sample with the use of Nonaq Stopcock grease. We used both the fundamental frequencies of the transducers ($f = 50, 30, 14$ MHz) and their higher harmonics.

The data on the velocity of sound were obtained by the ultrasonic pulse-echo-overlap technique (the Papadakis method [9]). The accuracy of the relative measurements was approximately equal to 0.01%.

The electrical resistance of the sample was measured by the four-point probe method in the temperature range 77–470 K. The magnetic susceptibility was determined by the induction method at a frequency of 1 kHz.

The measurements were carried out in a cryostat filled with liquid-nitrogen vapors. The temperature was controlled by a heater and measured with a thermocouple. The rate of change in the temperature in the course of the measurements was 1 K/min.

3. RESULTS AND DISCUSSION

The analysis of the experimental x-ray diffraction pattern shown in Fig. 1 revealed that the $\text{La}_{0.75}\text{Sr}_{0.25}\text{MnO}_3$ single crystal has rhombohedral symmetry. The unit cell parameters of the $\text{La}_{0.75}\text{Sr}_{0.25}\text{MnO}_3$ single crystal are presented in the table. Our results are in good agreement with the data obtained by Urushibara *et al.* [10].

The x-ray diffraction investigations demonstrated that the sample is a block single crystal in which the misorientation of the blocks does not exceed 1° . The quality of the single crystal did not permit us to reveal a rhombohedral distortion. According to our data, the $\text{La}_{0.75}\text{Sr}_{0.25}\text{MnO}_3$ crystal has a cubic pseudocell with the unit cell parameter $a = 3.91(1)$ Å. The Laue x-ray dif-

fraction pattern of the sample under investigation is displayed in Fig. 2.

At $T = 430$ K, the sample has the electrical resistivity $\rho = 6 \times 10^{-3}$ Ω cm. The temperature dependence of the electrical resistance R (Fig. 3) exhibits a behavior typical of this composition [10]: a broad maximum is observed in the temperature range 470–350 K, and the electrical resistance drastically decreases (by a factor of approximately 5) at $T = 330$ –350 K.

According to the data obtained from magnetic measurements (Fig. 3), the sample undergoes a second-order magnetic phase transition at a temperature $T_c \approx 337$ K. As the phase transition temperature is approached, the magnetoresistivity $\Delta\rho(H)/\rho(0) = [\rho(H) - \rho(0)]/\rho(0)$ increases and becomes equal to 7% in the magnetic field $H = 30$ kOe at $T = 300$ K.

The temperature dependences of the acoustical absorption coefficient α and the relative change in the velocity $\Delta V/V$ of longitudinal acoustic waves propagating in the $\text{La}_{0.75}\text{Sr}_{0.25}\text{MnO}_3$ single crystal along the [111] direction are plotted in Fig. 4. At $T = 300$ K, the magnitude of the acoustic velocity is $V = 6.41 \times 10^5$ cm/s. The dependence $\Delta V/V(T)$ involves three characteristic portions. It can be seen that the acoustic velocity increases monotonically with a decrease in the temperature in the ranges $T > 345$ K and $T < 325$ K and changes drastically ($\Delta V/V \sim 1\%$) in the temperature range of the magnetic phase transition ($T \approx 340$ K). Neither temperature hysteresis nor dispersion of the acous-

Unit cell parameters of the $\text{La}_{0.75}\text{Sr}_{0.25}\text{MnO}_3$ single crystal

Hexagonal pseudocell		Rhombohedral cell	
$a_H, \text{Å}$	$c_H, \text{Å}$	$a_R, \text{Å}$	γ, deg
5.530 (3)	13.404 (6)	5.492	60.46

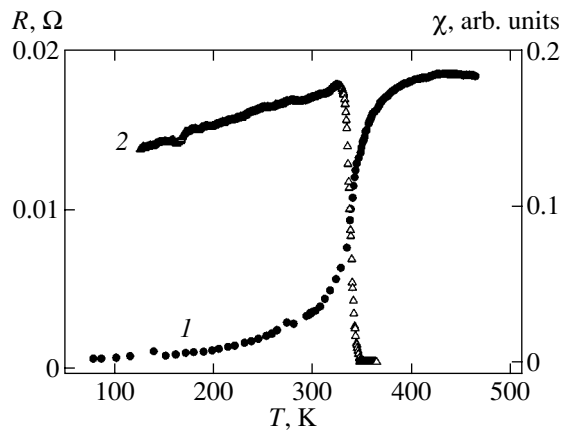


Fig. 3. Temperature dependences of (1) the electrical resistance R in a zero magnetic field and (2) the magnetic susceptibility χ for the $\text{La}_{0.75}\text{Sr}_{0.25}\text{MnO}_3$ single crystal.

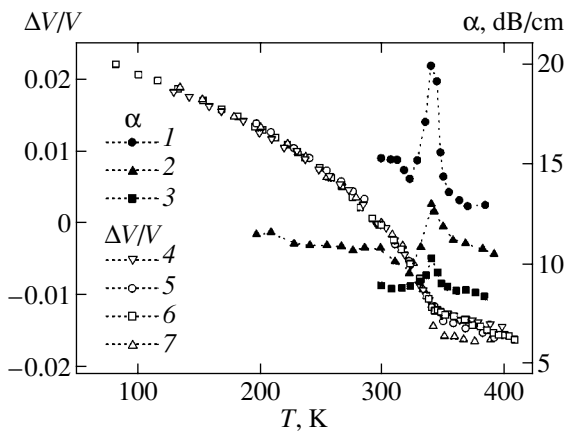


Fig. 4. Temperature dependences of (1–3) the acoustical absorption coefficient α and (4–7) the relative change in the velocity $\Delta V/V$ of longitudinal acoustic waves propagating in the $\text{La}_{0.75}\text{Sr}_{0.25}\text{MnO}_3$ single crystal at frequencies $f = (1, 4) 90, (2, 5) 50, (3, 6) 36,$ and (7) 14 MHz.

tic velocity is revealed to within the experimental error of the measurement.

The temperature dependence of the acoustical absorption coefficient α at all frequencies is relatively weak outside the temperature range corresponding to the phase transition (Fig. 4). In the phase transition range ($T \approx 340$ K), the acoustical absorption coefficient exhibits a sharp maximum. As follows from the results of the measurements, the acoustical absorption $\Delta\alpha$ at the maximum increases with an increase in the frequency. Note that, within the limits of experimental error, the temperature position of the maximum does not depend on the acoustic frequency.

The absence of additional features in the temperature dependences of the absorption coefficient and the velocity of sound indicates that no structural transfor-

mations occur in manganites of the given composition. This is confirmed by the results of x-ray and neutron diffraction investigations [11].

Our data on the absorption and velocity of sound are in qualitative agreement with the experimental temperature dependences of the velocity of longitudinal acoustic waves and the internal friction coefficient of the $\text{La}_{0.75}\text{Sr}_{0.25}\text{MnO}_3$ single crystal measured by the composite-oscillator method at a frequency of 100 kHz [12]. As in our case, Zainullina *et al.* [12] observed an increase in the acoustic velocity and the maximum of the internal friction coefficient in the range of the magnetic phase transition. Furthermore, according to [12], the internal friction coefficient at $T = 415$ K exhibits a “giant” peak, which is not accompanied by anomalies in the temperature dependence of the acoustic velocity. In the authors’ opinion [12], this peak is associated with the relaxation processes occurring in the system of point defects in the sample. The absence of a similar absorption peak in our case may suggest that either point defects are absent in the single crystal under investigation or this effect at frequencies of 14–90 MHz can be observed only in the high-temperature range (at $T \approx 570$ – 660 K according to our estimates made from the data presented in [12]).

The acoustical absorption maximum observed in the range of the magnetic phase transition at $T \approx 340$ K (Fig. 4) can be explained by the additional absorption due to the interaction of the longitudinal acoustic wave with the order parameter (the spontaneous magnetic moment). In the general case, there exist the following mechanisms of additional absorption [13–15]. First and foremost, according to the Landau–Khalatnikov theory [13, 15], the inclusion of the critical slowing-down of the order parameter relaxation in the vicinity of the second-order phase transition at $T < T_c$ leads to an additional contribution to the acoustical absorption. This contribution is a function of the frequency and has the classical form for Debye relaxation:

$$\alpha_R = \frac{AM^2}{\tau} \frac{\omega^2 t}{1 + \omega^2 t^2},$$

where A is a numerical factor, M is the spontaneous magnetic moment, $\tau = 1 - T/T_c$ is the reduced temperature, $\omega = 2\pi f$ is the circular frequency of the acoustic wave, and $t = t_0\tau^{-1}$ is the relaxation time of the spontaneous magnetic moment. The temperature dependence of the relaxation contribution α_R has the shape of an asymmetric peak with a maximum at the temperature at which the condition $\omega t = 1$ is satisfied. The characteristic time of spin relaxation t_0 for conventional magnetic materials is of the order of 10^{-9} s. Therefore, the maximum of the relaxation contribution α_R in the frequency range 14–90 MHz should be observed at temperatures close to the critical point T_c . This is in agreement with the observed position of the acoustical absorption peak.

Apart from the Landau–Khalatnikov mechanism, the additional contribution to the absorption of sound can be made by the interaction of the acoustic wave with critical fluctuations of the magnetization. The temperature dependence of this fluctuation contribution has the shape of a symmetric peak $\alpha_F \propto |\tau|^{-n}$ (where n is a critical exponent), which diverges at $T = T_c$ [14, 15]. However, this divergence can be observed only for very pure materials. In real materials, the divergence is canceled, for example, by structural defects and inhomogeneities. In some cases, the fluctuation contribution α_F can turn out to be insignificant as compared to the relaxation contribution α_R [15].

The shape of the acoustical absorption peak observed for the $\text{La}_{0.75}\text{Sr}_{0.25}\text{MnO}_3$ single crystal (Fig. 4) differs significantly from the peak corresponding to the Landau–Khalatnikov relaxation mechanism. The shape of this peak can be most adequately described by the sum of the contributions from the Landau–Khalatnikov relaxation and fluctuation mechanisms: $\alpha = \alpha_R + \alpha_F$. Unfortunately, the accuracy of the measurement does not enable us to separate these contributions and to perform a more detailed analysis.

4. CONCLUSIONS

Thus, the acoustical, resistive, and magnetic properties of a $\text{La}_{0.75}\text{Sr}_{0.25}\text{MnO}_3$ manganite single crystal were investigated over a wide temperature range, including the magnetic phase transition at $T_c \approx 340$ K. The acoustical measurements performed by the pulse-echo method in the frequency range 14–90 MHz revealed that a decrease in the temperature leads to a drastic increase in the velocity of the longitudinal acoustic wave propagating along the [111] axis of the single crystal at temperatures below the critical point T_c . The drastic increase in the velocity of sound is accompanied by the appearance of an acoustical absorption peak. These anomalies of the acoustical properties suggest that the acoustic waves strongly interact with the magnetic moments of manganese ions in the $\text{La}_{0.75}\text{Sr}_{0.25}\text{MnO}_3$ single crystal. The results obtained were analyzed theoretically. As follows from this analysis, the asymmetric shape of the acoustical absorption peak indicates that the absorption of sound in the compound under investigation is substantially affected by both the Landau–Khalatnikov relaxation and the interaction of the acoustic wave with critical fluctuations of the magnetization at temperatures in the vicinity of the second-order magnetic phase transition.

ACKNOWLEDGMENTS

This work was supported by the Russian Foundation for Basic Research (project no. 04-02-17598), the Division of Physical Sciences of the Russian Academy of Sciences, the International Research and Technical Center (project no. 1859), and the Polish Government Agency KBN (project no. 1 P03B 025 26).

REFERENCES

1. Yu. A. Izyumov and Yu. N. Skryabin, *Usp. Fiz. Nauk* **171** (2), 121 (2001) [*Phys. Usp.* **44**, 109 (2001)].
2. S. M. Dunaevskii, *Fiz. Tverd. Tela* (St. Petersburg) **46** (2), 193 (2004) [*Phys. Solid State* **46** (2), 193 (2004)].
3. C. Zener, *Phys. Rev.* **82** (3), 403 (1951).
4. A. J. Millis, P. B. Littlewood, and B. I. Schirmer, *Phys. Rev. Lett.* **74** (25), 5144 (1995).
5. R. I. Zaiñullina, N. G. Bebenin, V. V. Mashkautsan, A. M. Burkhanov, V. S. Gaviko, V. V. Ustinov, Ya. M. Mukovskii, D. A. Shulyatev, and V. G. Vasil'ev, *Zh. Éksp. Teor. Fiz.* **120** (1), 139 (2001) [*JETP* **93** (1), 121 (2001)].
6. Kh. G. Bogdanova, A. R. Bulatov, V. A. Golenishchev-Kutuzov, L. V. Blokhina, A. V. Kapralov, A. V. Korolev, É. A. Neif'el'd, and M. M. Shakirzyanov, *Fiz. Tverd. Tela* (St. Petersburg) **45** (2), 284 (2003) [*Phys. Solid State* **45** (2), 298 (2003)].
7. J. Mira, J. Rivas, A. Moreno-Gobbi, M. Perez Macho, G. Paolini, and F. Rivadulla, *Phys. Rev. B: Condens. Matter* **68** (9), 092404 (2003).
8. D. Shulyatev, S. Karabashev, A. Arsenov, and Ya. Mukovskii, *J. Cryst. Growth* **198/199**, 511 (1999).
9. E. J. Papadakis, *J. Acoust. Soc. Am.* **42** (5), 1045 (1967).
10. A. Urushibara, Y. Morimoto, T. Arima, A. Asamitsu, G. Kido, and Y. Tokura, *Phys. Rev. B: Condens. Matter* **51** (20), 14103 (1995).
11. Y. Endoh, H. Nojiri, K. Kaneko, K. Hirota, T. Fukuda, H. Kimura, Y. Murakami, S. Ishihara, S. Maekawa, S. Okamoto, and M. Motokawa, *cond-mat/9812404*.
12. R. I. Zaiñullina, N. G. Bebenin, A. M. Burkhanov, V. V. Ustinov, and Ya. M. Mukovskii, *Phys. Rev. B: Condens. Matter* **66** (6), 064421 (2002).
13. L. D. Landau and I. M. Khalatnikov, *Dokl. Akad. Nauk SSSR* **96** (3), 469 (1954).
14. F. Schwabl, *Phys. Rev. B: Solid State* **7** (5), 2038 (1973).
15. S. Zherlitsyn, G. Bruls, A. Goltsev, B. Alavi, and M. Dressel, *Phys. Rev. B: Condens. Matter* **59** (21), 13861 (1999).

Translated by O. Borovik-Romanova

**MAGNETISM
AND FERROELECTRICITY**

Magnetic Resonance in a $[\{\text{Cr}(\text{CN})_6\}\{\text{Mn}(\text{S})\text{-}pn\text{H}(\text{H}_2\text{O})\}] \cdot \text{H}_2\text{O}$ Single-Crystal Molecular Ferrimagnet

I. V. Blokhin*, A. S. Markosyan**, R. B. Morgunov*, K. Inoue***,
Y. Tanimoto***, and Y. Yoshida***

*Institute of Solid State Physics, Russian Academy of Sciences, Chernogolovka, Moscow oblast, 142432 Russia
e-mail: blokhin@issp.ac.ru

**Moscow State University, Vorob'evy gory, Moscow, 119899 Russia

***Institute for Molecular Sciences, Okazaki, Japan

Received February 22, 2005

Abstract—The variations in the magnetic resonance spectra accompanying the transition from the paramagnetic to ferrimagnetic state in $[\{\text{Cr}(\text{CN})_6\}\{\text{Mn}(\text{S})\text{-}pn\text{H}(\text{H}_2\text{O})\}] \cdot \text{H}_2\text{O}$ orthorhombic chiral molecular crystals were studied. The dependence of the EPR linewidth on temperature in the proximity of the transition point $T_C = 38$ K argues for the two-dimensional character of spin ordering. The spin resonance line was found to undergo exchange narrowing at $T > T_C$. The ferrimagnetic phase has an easy magnetization axis coinciding with the a crystallographic axis. © 2005 Pleiades Publishing, Inc.

1. INTRODUCTION

The use of hexacyanometalate complexes $[\text{M}(\text{CN})_6]^{3-}$, where M stands for a transition metal in the synthesis of new molecular magnets has lead to considerable progress in increasing magnetic ordering temperatures and to observation of the photomagnetic effect [1]. The above complexes are molecular precursors capable of being incorporated into various compounds and of controlling the number and efficiency of exchange channels among neighboring spins. This has made it possible to raise the magnetic ordering point to room temperature [2, 3] and prepare monomolecular magnets with spins of up to $27/2$ [4, 5]. The high symmetry of the $\text{M}(\text{CN})_6$ complexes makes their magnetic properties in crystals predictable, and their compatibility with metals of various types makes it possible to vary the symmetry and overlap of electronic shells. Most compounds of this type exhibit three-dimensional (3D) magnetic ordering. However, crystals whose specific structural features are capable of giving rise to magnetism of lower dimensions or helicoidal spin ordering have also attracted attention.

There have been reports [6] on the preparation of a new molecular crystal, $[\{\text{Cr}(\text{CN})_6\}\{\text{Mn}(\text{S})\text{-}pn\text{H}(\text{H}_2\text{O})\}] \cdot \text{H}_2\text{O}$, which undergoes a magnetic phase transition at $T_C = 38$ K (orthorhombic crystal structure $P2_12_12_1$ with lattice parameters $a = 7.6280(17)$, $b = 14.510(3)$, and $c = 14.935(3)$ Å). Transparent, needle-shaped, greenish crystals have been termed green needles (GNs). The atomic structure of GN crystals is shown in Fig. 1a. Their molecules are coupled to form quasi-two-dimensional wavy layers parallel to the ab plane. Within a layer, the alternating paramagnetic ions

Cr^{3+} and Mn^{2+} are covalently bonded through $-\text{CN}-$ groups to form a slightly distorted square lattice (Fig. 1b). The layers are coupled by van der Waals interaction. The local environment of the Cr^{3+} ions consists of six carbon atoms occupying the corners of an octahedron. The Mn^{2+} ions are also surrounded by six nearest neighbors, five of which are nitrogen atoms and one, an oxygen atom. In addition, as the N5–N6 long axis of the coordination octahedron is displaced along the c axis, it turns about it. In other words, the structure exhibits chirality with respect to Mn^{2+} positions and has no inversion symmetry. The chirality gives rise to circular rotation of the plane of light polarization and to asymmetry in the Faraday rotation, which depends on the strength of an external dc magnetic field [6]. The specific features of magnetic ordering of the GN molecular compound have not yet been adequately studied. In particular, the effect of chirality on the formation of the magnetic structure of this compound remains unclear. It is these features that account for the interest in GN crystals in connection with the progress made in magnetic resonance techniques as applied to chiral ferrites, chiro-FMR (see, e.g., review [7]).

The present study was aimed at determining the type of magnetic ordering and investigating the magnitude and direction of the anisotropy field in a magnetically ordered state, as well as at observing the features in the magnetic properties of GN crystals that originate from the quasi-two-dimensional character of the structure of these crystals.

It is appropriate to note also that $[\{\text{Cr}(\text{CN})_6\}\{\text{Mn}(\text{S})\text{-}pn\text{H}(\text{H}_2\text{O})\}] \cdot \text{H}_2\text{O}$ can be synthesized (depending on the actual conditions of preparation) in three different orthorhombic modifications hav-

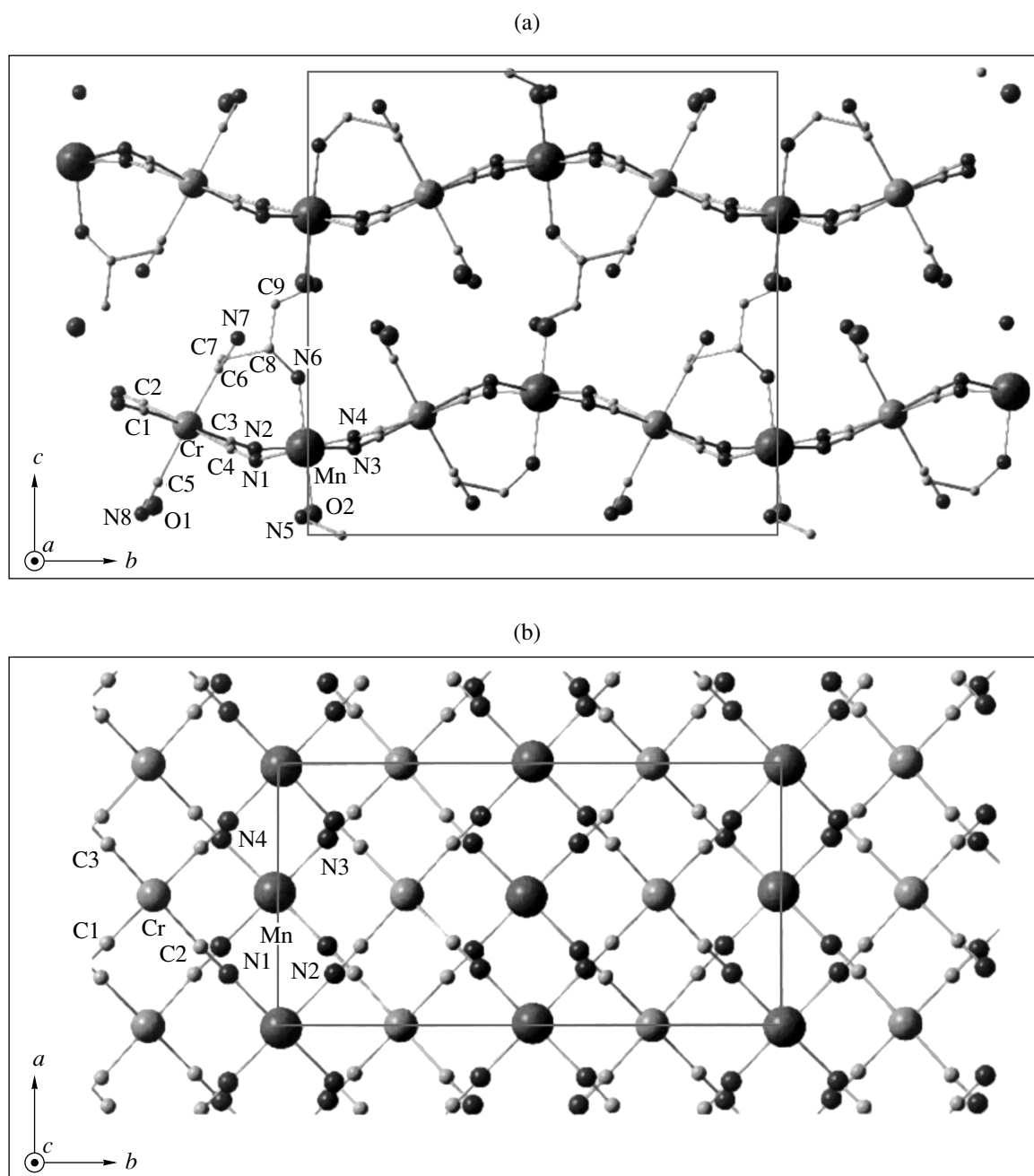


Fig. 1. Atomic structure of GN crystals as viewed (a) along the a axis and (b) along the c axis.

ing the same space group $P2_12_12_1$ to which GNs belong and chirality of the Mn^{2+} positions: GNs themselves; phase I and phase II with the same chemical formula as GNs; and phase III, the dehydrated compound $[\{\text{Cr}(\text{CN})_6\}\{\text{Mn}(\text{S})\text{-}pn\text{H}\cdot(\text{H}_2\text{O})\}]$ [6]. Here, we deal with phase I only.

2. EXPERIMENTAL TECHNIQUE

Crystals were grown as rectangular platelets measuring $\sim 0.1 \times 0.3 \times 2$ mm. Experiments were run with

X -range (~ 9.5 GHz) and Q -range (~ 32 GHz) EPR spectrometers (Bruker ESP300E and E500) with H_{102} -type rectangular resonators providing modulation frequencies of 1.56–100 kHz and a dc magnetic field sweeping range $B_0 = 0$ –1.5 T. The crystals were fixed in a node of the magnetic component of the applied microwave field. The resonator Q factor was monitored in the course of measurements. The EPR signal was proportional to the first derivative of the imaginary part of the crystal magnetic susceptibility $d\chi/dH$. The temperature was varied in the range 3.1–300 K. The sample to be

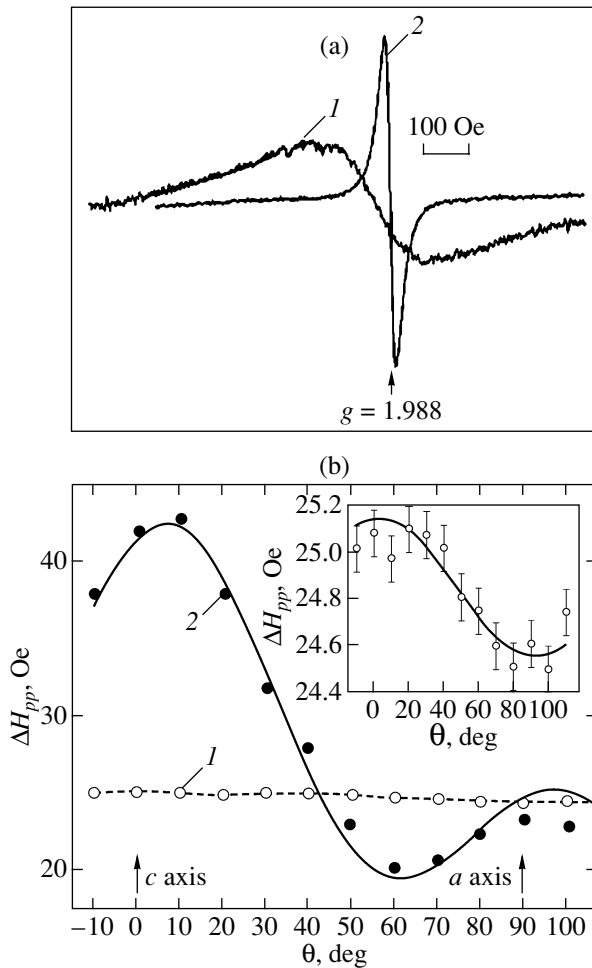


Fig. 2. (a) EPR spectra of a GN single crystal and of the $\text{K}_3\text{Cr}(\text{CN})_6$ paramagnetic salt used to prepare GN crystals at 293 K; (b) angular dependence of the linewidth ΔH_{pp} obtained with the spectrometer dc magnetic field rotated in the ac plane at 293 K. The solid line is a fitting of experimental data to the relation $\Delta H_{pp}^{\text{GN}} = \alpha + \beta(1 - 3\cos^2\theta)^2$. The inset shows the angular dependence of the linewidth ΔH_{pp} obtained under rotation of the spectrometer dc magnetic field in the ab plane. The solid line is a fitting of experimental data with a $\Delta H_{pp} = \alpha + \beta\cos^2\theta$ relation.

studied was sealed in a quartz ampoule filled with argon. $\text{CuSO}_4 \cdot 5\text{H}_2\text{O}$ single crystals exposed previously to an atmosphere saturated with water vapor were used for calibration. The magnetic susceptibility of the reference sample derived by double integration of its EPR spectrum was normalized against the value of χ obtained with a SQUID magnetometer. This permitted us to determine the deviations of the $\chi(T)$ relation in $\text{CuSO}_4 \cdot 5\text{H}_2\text{O}$ for $T < 20$ K from purely paramagnetic behavior so as to introduce the corresponding corrections into the temperature dependence of the EPR signals of the GN crystals under study.

3. EXPERIMENTAL RESULTS

At $T = 290$ K, the EPR spectrum obtained in the X range has a single line whose shape is Lorentzian to within 99% for any orientation of the spectrometer dc magnetic field \mathbf{H}_0 with respect to the crystal (Fig. 2a). Also shown for comparison is a broader line in the spectrum of the $\text{K}_3\text{Cr}(\text{CN})_6$ salt from which the crystal was prepared. The EPR line halfwidth (from the maximum to a minimum) is $\Delta H_{pp}^{\text{GN}} = 25$ Oe for \mathbf{H}_0 aligned parallel to the a axis and reveals a very weak anisotropy with the vector \mathbf{H}_0 rotated in the ab plane. By contrast, the halfwidth is notably anisotropic when \mathbf{H}_0 is rotated in the ac plane (Fig. 2b). The resonance fields vary by less than 2 Oe for rotation in any plane.

Reducing the temperature to below 40 K makes the spectrum more complex (Fig. 3). Indeed, (i) its integrated intensity in the interval from 40 to 10 K increases by 2 to 3 orders of magnitude, (ii) additional weaker lines of a smaller amplitude appear about the central maximum, and (iii) the resonance field of the strongest central line in the spectrum shifts abruptly toward higher values for the dc magnetic field \mathbf{H}_0 aligned with the b axis and becomes lower for $\mathbf{H}_0 \parallel a$ (Fig. 4a). Rotation of the crystal leaving \mathbf{H}_0 in the ab plane reveals a substantial anisotropy of the resonance magnetic field H_{res} , which is derived from the position of the strongest line in the spectrum at $T < 12$ K (Fig. 4b). Note that the value of H_{res} remains practically constant over a broad range of angles θ between \mathbf{H}_0 and the a axis. H_{res} increases strongly only when \mathbf{H}_0 deviates from the a direction by more than 45° .

The magnetic susceptibility of the crystal χ_{GN} was obtained through double integration of the spectrum and by comparing it with the magnetic susceptibility of the reference sample throughout the temperature range covered. Figure 5 shows the temperature dependence of the reciprocal magnetic susceptibility χ_{GN}^{-1} along the a axis normalized against its value at $T = 300$ K. Plotted in these coordinates, the temperature dependence of the reciprocal magnetic susceptibility is a straight line, $\chi_p^{-1} = T/C$ (C is the Curie constant). The deviation of experimental points from this line makes it possible to judge the sign of the exchange interactions and to determine the critical temperature and the type of magnetic ordering. At temperatures of 300–80 K, the $\chi_{\text{GN}}^{-1}(T)$ dependence for GN crystals is very nearly a straight line characteristic of antiferromagnets and ferrimagnets. For $T < 80$ K, experimental points start to deviate strongly from this straight line, with χ_{GN}^{-1} decreasing markedly by about two orders of magnitude in the vicinity of $T \sim 40$ K. A further decrease in temperature to below 40 K brings about only a slight decrease of χ_{GN}^{-1} in magnitude. The observed $\chi_{\text{GN}}^{-1}(T)$ relation sug-

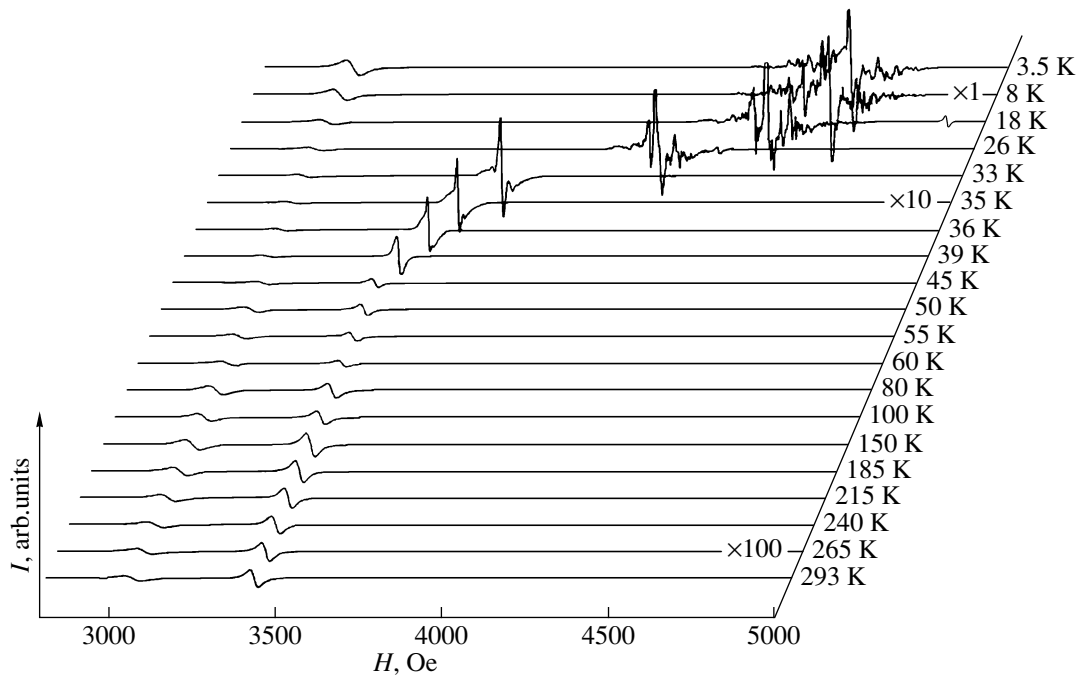


Fig. 3. EPR spectrum of a GN single crystal plotted vs temperature. The extreme left-hand point in the spectrum is the signal from the $\text{CuSO}_4 \cdot 5\text{H}_2\text{O}$ reference single crystal. The right-hand line in the spectrum is a signal from the GN sample. The dc magnetic field is directed along the b axis.

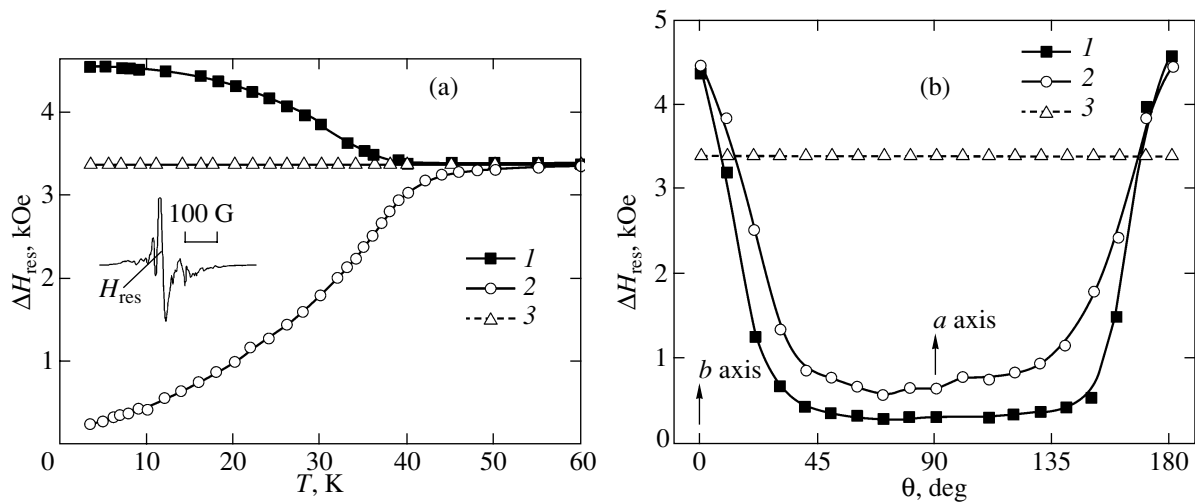


Fig. 4. (a) Temperature dependence of the resonance field H_{res} for (1) a GN crystal at $\mathbf{H}_0 \parallel b$, (2) a GN crystal at $\mathbf{H}_0 \parallel a$, and (3) a $\text{K}_3\text{Cr}(\text{CN})_6$ powder. For $T < 40$ K, the resonance field was determined for the strongest line at the center of the spectrum (see inset). (b) Dependence of the resonance field H_{res} for the GN EPR signal on the angle between the dc magnetic field \mathbf{H}_0 and the b axis, with the magnetic field swept in the ab plane: (1) $T = 3.3$, (2) 12, and (3) 293 K.

gests a ferrimagnetic character of magnetic ordering in GN crystals. For comparison, Fig. 5 presents the temperature dependence of the reciprocal susceptibility of $\text{K}_3\text{Cr}(\text{CN})_6$, which indicates typical paramagnetic behavior down to a temperature of 3.1 K.

Measurements of the temperature dependence of χ_{GN} under different sample orientations relative to \mathbf{H}_0

showed that, for the field aligned with b or c , $\chi_{\text{GN}}(T)$ increases monotonically for $T < 38$ K, whereas for the field directed along the a axis an increase is observed in the value of χ_{GN} followed by a sharp decrease normalized against its room-temperature value χ_{RT} (Fig. 6a). Variations of the modulation frequency and amplitude within approximately two orders of magnitude did not

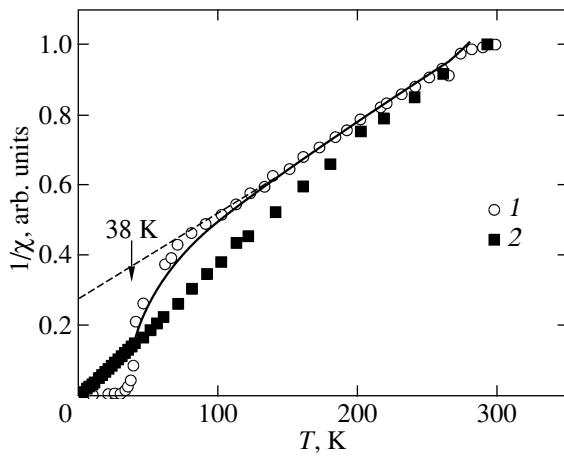


Fig. 5. Temperature dependence of the reciprocal magnetic susceptibility χ^{-1} (1) of GN single crystals along the a axis and (2) of the paramagnetic salt $K_3Cr(CN)_6$ from which the GN crystals were prepared.

affect either the pattern of the spectrum or the temperature dependence of χ to within experimental accuracy. This strongly suggests that the crystal magnetization was saturated in the magnetic field used, $H_0 \sim 3.5$ kOe.

Because the dependence of the resonance frequency ν of a magnetically ordered crystal on the magnetic field H_0 should differ from that for a crystal in the paramagnetic phase, the value of ν was measured with X- and Q-range spectrometers (Fig. 7). The resonance frequency corrected for the demagnetizing field for a plane rectangular plate (which was determined using the Kittel relations [8]) yields a negligible correction. It was established that, in the paramagnetic phase at $T > 38$ K, the straight line drawn through the experimental $\nu(H_0)$ points passes through the origin, whereas at 3.1 K this line gives an intercept of 2000 Oe on the abscissa axis. Because the spectrometer magnetic field used results in magnetization saturation, i.e., it is in excess of the anisotropy field, the intercept on the abscissa axis is the double anisotropy field $H_a \sim 1000$ Oe. By determining in this way the dependence of the anisotropy field on the angle the b axis makes with the direction of the dc magnetic field lying in the bc plane (Fig. 8), it could be verified that the anisotropy fields along the b and c axes are different. From the data obtained, it follows that the b axis is the hardest magnetization axis.

The dependence of the resonance linewidth ΔH_{pp} on temperature contains information on the mechanisms of relaxation and EPR line broadening (Fig. 9a). The smooth increase in ΔH_{pp} in the range 300–110 K is replaced by a decrease in ΔH_{pp} , and after the minimum at $T = 60$ K is reached the linewidth is seen to grow rapidly over the range up to the magnetic transition temperature. The ratio of the linewidth for the dc magnetic field aligned with the a axis, $\Delta H_{pp}(\theta = 0)$, to that for the

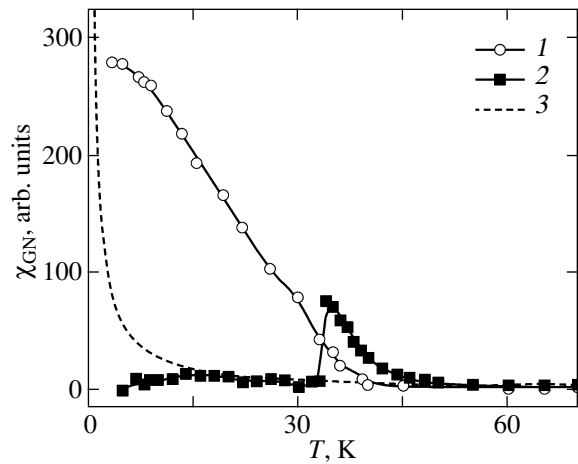


Fig. 6. Temperature dependence of the magnetic susceptibility χ of GN crystals for the dc magnetic field aligned with (1) the b axis and (2) the a axis. The susceptibility is normalized against its value at $T = 293$ K. Also shown for comparison is a plot of the Curie law for ions with spin $5/2$ (curve 3).

field oriented along the b axis, $\Delta H_{pp}(\theta = 90^\circ)$, also exhibits a minimum followed by a sharp increase as T_C is approached (Fig. 9b).

4. DISCUSSION

Because GN crystals have alternating paramagnetic ions of two types with different spins, Cr^{3+} and Mn^{2+} , the experimental dependence of the reciprocal magnetic susceptibility above the critical temperature was

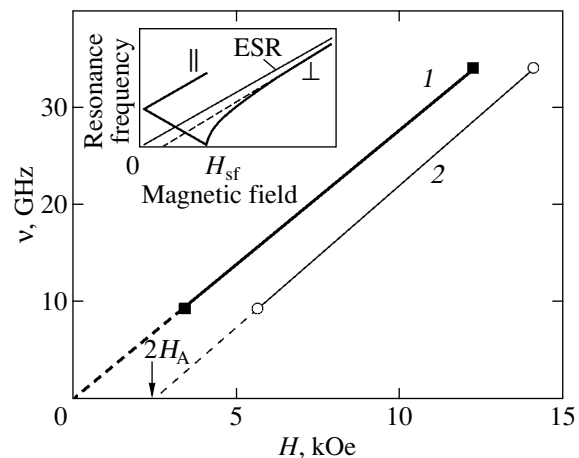


Fig. 7. Resonance frequency ν corrected for the demagnetizing field and the corresponding values of the resonance magnetic field H_{res} for (1) $T = 293$ and (2) 3.1 K. The intercept of the straight line on the H axis is twice the anisotropy field $2H_a$. The inset gives a schematic representation of the resonance frequencies plotted vs the resonance field for a typical ferromagnet for parallel and perpendicular orientations of the dc magnetic field with respect to the principal magnetization axis [12].

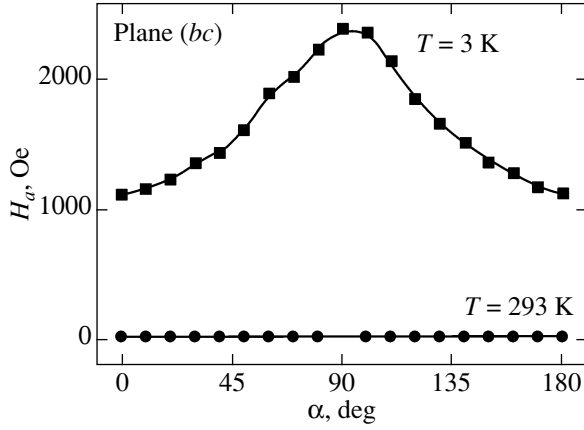


Fig. 8. Anisotropy field H_a defined as shown in Fig. 7 and plotted vs the angle between the dc magnetic field \mathbf{H}_0 and the b axis for the GN crystal rotated in the bc plane. $T = 3.1$ K.

described in terms of the model of a two-sublattice ferrimagnet using the formula [9]

$$\chi_{\text{ferri}} = \frac{(C_1 + C_2)T + 2\sqrt{C_1 C_2 T_C}}{T^2 - T_C^2}, \quad (1)$$

where C_1 and C_2 are the Curie constants for the Cr^{3+} and Mn^{2+} sublattices, respectively. As seen from Fig. 5, the theoretical (solid) curve fits fairly well the experimental points for $T > T_C$, where $T_C = 38 \pm 2$ K is the critical temperature of the transition of the GN crystal to the ferrimagnetic state. This relation suggests also that the intrasublattice Mn–Mn and Cr–Cr interactions in the GN crystal are positive, while the sublattices themselves are coupled with each other by weak negative exchange interaction (with a coupling constant $\lambda_{\text{MnCr}} \approx -0.62 \pm 0.3$ emu/mol).

Note that the resonance linewidth of GN crystals in the paramagnetic phase is substantially smaller than the EPR linewidth $\Delta H_{pp}^s = 265$ Oe of the $\text{K}_3\text{Cr}(\text{CN})_6$ salt from which they were prepared. Since the starting salt remains paramagnetic down to $T = 3.1$ K (Fig. 5), one may suggest that the narrowing of the EPR line of GN crystals is due to the interion exchange interaction averaging out local magnetic field fluctuations at the paramagnetic center induced by the dipole–dipole interaction and/or other relaxation processes. According to Anderson and Weiss [10], the width of the EPR resonance line in the presence of exchange interaction can be written as

$$\Delta H_{pp}^{\text{GN}} = \frac{(10/3)\Delta H_p^2 + \Delta H_H^2}{H_e}(T > T_C), \quad (2)$$

where H_e is the “exchange” magnetic field (the energy of exchange interaction expressed in field units), ΔH_p is the contribution to the linewidth from the dipole–dipole

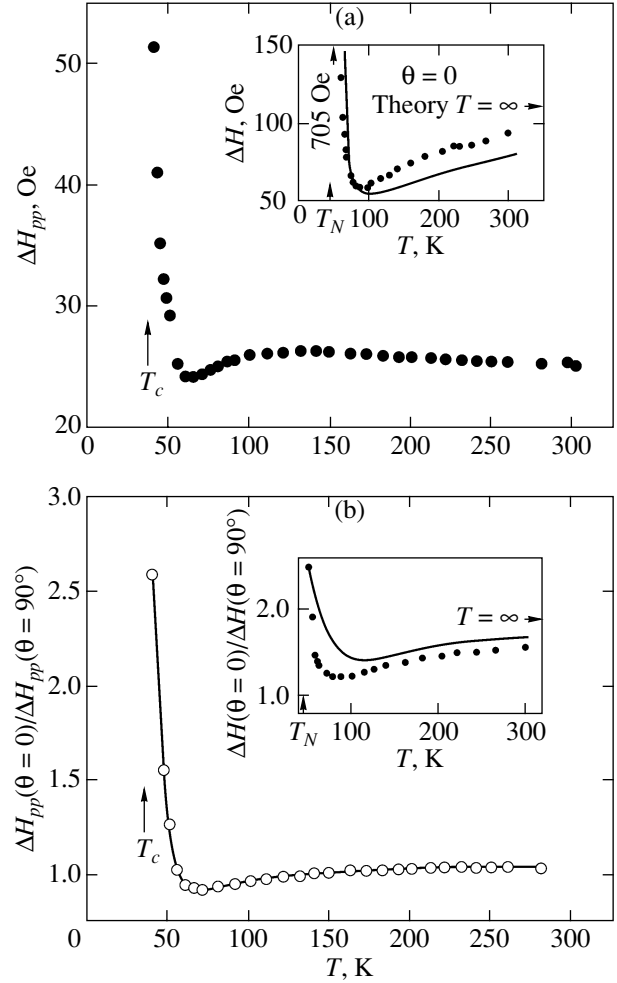


Fig. 9. (a) Temperature dependence of the linewidth ΔH_{pp} of GN crystals plotted for $T > T_C = 38$ K. The dc magnetic field is aligned with the easy magnetization axis (the a axis). For comparison, the inset shows the temperature dependence of the EPR line halfwidth for a two-dimensional uniaxial antiferromagnet K_2MnF_4 with an easy magnetization axis (data from [11]). (b) Temperature dependence of the ratio of the EPR line halfwidth of GN crystals along the easy magnetization axis, $\Delta H_{pp}(\theta = 0^\circ)$, to that obtained in the transverse orientation, $\Delta H_{pp}(\theta = 90^\circ)$. The inset shows an analogous plot drawn for K_2MnF_4 crystals [11].

interaction, and ΔH_H is the contribution to the linewidth from relaxation processes not related to exchange interaction (hyperfine interaction, zero-field splitting, etc.).

We accept $\Delta H_H = 0$ to estimate the part played by exchange interaction. According to [10], $\Delta H_p^2 = 5.1(g\mu_B n)^2 S(S+1)$. Here, S is the spin of paramagnetic ions; n is their volume concentration; g is the g factor derived from the EPR condition $h\nu = g\mu_B H_{\text{res}}$; ν is the microwave frequency; h is the Planck constant; μ_B is the Bohr magneton; H_{res} is the resonance field; and $H_e =$

$2.83 \frac{J}{g\mu_B} \sqrt{S(S+1)}$, where J is the exchange integral, which in the Weiss molecular field theory (accounting only for the exchange among nearest neighbors) is related to the critical ordering temperature through the relation $3k_B T_C = 2zJS(S+1)$, with z being the number of nearest neighbors and k_B being the Boltzmann constant [1]. Thus, the Anderson–Weiss theory makes it possible to estimate the critical temperature of magnetic ordering from the magnitude of line narrowing. It appears appropriate to note here, however, that this theory was developed for magnets with paramagnetic ions of one type only. In our case, there are two such ions, Cr^{3+} and Mn^{2+} ; therefore, the above expressions for H_e and ΔH_p should be modified by replacing $S(S+1) \rightarrow \sqrt{S_{\text{Cr}}(S_{\text{Cr}}+1)S_{\text{Mn}}(S_{\text{Mn}}+1)}$, where $S_{\text{Cr}} = 3/2$ and $S_{\text{Mn}} = 5/2$ [9], and by considering the exchange integral J to be an effective parameter including the inter- and intrasublattice exchange integrals. After these modifications, we estimate the critical temperature for GN crystals using the following parameter values: $g \approx 2$, $n = 4.84 \times 10^{21} \text{ cm}^{-3}$, $z = 6$, $\Delta H_H = \Delta H_{pp}^s = 265 \text{ Oe}$, and $\Delta H_{pp}^{\text{GN}} = 25 \text{ Oe}$ (Fig. 2a). Assuming the contributions to the linewidth that are not related to exchange factors to be small, we arrive at $T_C \approx 30 \text{ K}$, which compares well with the measured value $T_C = 38 \text{ K}$ and means that the exchange interaction dominates the linewidth (and is responsible for its substantial narrowing) in the paramagnetic region.

The literature abounds with data on the magnetic properties of crystals based on hexacyanometalate complexes, so it seems appropriate to compare this experimental value of T_C with the values found for this parameter in other compounds. It was shown in [1] that the value of T_C is readily predictable and is determined by two factors, namely, (i) the relative number of ferromagnetic and antiferromagnetic exchange channels for metallic ions, as well as the symmetry of their wave functions, and (ii) the number of nearest magnetic neighbors z . In GN crystals, the Mn^{2+} ions with a $3d^5$ shell contain three electrons with wave-function symmetry t_{2g} and two electrons of e_g symmetry. The $3d^3$ Cr^{3+} ions have three electrons with wave-function symmetry t_{2g} . It is known that indirect exchange interaction in a pair of ions coupled by the CN bond is ferromagnetic if the wave functions of two unpaired electrons belonging to different ions are of symmetry t_{2g} and this interaction is antiferromagnetic if the symmetry of one wave function is t_{2g} and that of the other is e_g . Therefore, the crystals under study have six ferromagnetic and nine antiferromagnetic exchange channels. As a result, the net intersublattice exchange is antiferromagnetic, which, on account of the Mn^{2+} and Cr^{3+} spins being different, results in ferrimagnetism. The value of T_C in known compounds of this kind with $z_1 = 6$ is close to 60 K [1].

In GN crystals, $z_2 = 4$. The simple model mentioned above yields therefore $T_C = 60z_2/z_1 = 40 \text{ K}$, a figure which is in good agreement with the experimental value $T_C = 38 \text{ K}$. The fact that data on the crystal stoichiometry permit a good guess of T_C suggests that the approximation of independent exchange channels and d -electron pair interactions offers a correct description of the interrelation between the electronic and magnetic properties of the crystals under study.

Consider the angular dependences of the linewidth. The classical theory of exchange narrowing in three dimensions predicts the angular dependence of the halfwidth to be $\Delta H_{pp} = \alpha + \beta \cos^2 \theta$, where α and β are constants and θ is the angle between \mathbf{H}_0 and the plane. The small variations of the EPR line halfwidth in GN crystals observed with \mathbf{H}_0 rotated in the ab plane, to which layers of exchange coupled ions are stacked in parallel, do indeed fit with the above relation (solid line in the inset to Fig. 2b). In the ac plane, however, the line halfwidth scales as $\Delta H_{pp}^{\text{GN}} = \alpha + \beta(1 - 3\cos^2 \theta)^2$ (Fig. 2b). The factors accounting for the relation of the type $(1 - 3\cos^2 \theta)^2$ were studied in considerable detail by Richards and Salamon and reported in a number of publications [11] on the magnetic resonance in 1D and 2D antiferromagnets for $T > T_C$. These factors basically consist in that, because the exchange interaction is localized in an atomic chain or plane, the interaction cannot effectively average the local magnetic field fluctuations initiated by dipole–dipole interactions in the direction perpendicular to the line or plane of exchange. This fact accounts for the appearance of the EPR linewidth contribution $\sim (1 - 3\cos^2 \theta)^2$ characteristic of dipole–dipole interaction. The only exception is the magic angle $\theta \approx 55^\circ$, at which $1 - 3\cos^2 \theta = 0$; in this case, the dipole–dipole correlations are nonexistent and the linewidth is minimal (Fig. 9b). Thus, one is led to the conclusion that, in GN crystals, exchange interaction among Cr^{3+} and Mn^{2+} ions for $T > T_C$, as well as ferrimagnetic spin ordering for $T < T_C$, occurs in the ab plane. This conclusion is consistent with the fact that the covalently bonded Cr^{3+} and Mn^{2+} layers are arranged along the ab plane and that there are no covalent bonds coupling the layers (Fig. 1).

5. CONCLUSIONS

$\{[\text{Cr}(\text{CN})_6]\{\text{Mn}(\text{S})\text{-pnH}-(\text{H}_2\text{O})\}\} \cdot \text{H}_2\text{O}$ crystals undergo a magnetic phase transition from the paramagnetic to ferrimagnetic state at $T = 38 \text{ K}$. The easy magnetization axis is aligned with the a axis.

Exchange narrowing of the spin resonance line has been found to occur for $T > T_C$. The critical magnetic ordering temperature as estimated from the linewidth, $T_C \sim 30 \text{ K}$, compares with $T_C = 38 \text{ K}$, the figure derived from magnetic susceptibility measurements, and is consistent with theoretical predictions based on data on

the filling of metal ion electronic shells and crystal stoichiometry.

It has been established that, when the dc magnetic field rotates in the *ab* plane, in which complexes of paramagnetic ions are coupled by covalent CN bonds, the resonance linewidth is very nearly isotropic, while when the rotation occurs in the *ac* plane the resonance linewidth obeys the Richards relation. This behavior of the linewidth argues for two-dimensional spin ordering in the *ab* plane.

ACKNOWLEDGMENTS

The support of the Russian Foundation for Basic Research (project no. 04-02-17576), the state program "Spintronics" of the Russian Academy of Sciences, and the Science Support Foundation is gratefully acknowledged.

REFERENCES

1. M. Verdaguer, A. Bleuzen, V. Marvaud, J. Vaissermann, M. Seuleiman, C. Desplanches, A. Scuille, C. Train, R. Garde, G. Gelly, C. Lomenech, I. Rosenman, P. Veillet, C. Cartier, and F. Villain, *Coord. Chem. Rev.* **190–192**, 1023 (1999).
2. T. Mallah, S. Thiebaut, M. Verdaguer, and P. Veillet, *Science (Washington)* **262**, 1554 (1993).
3. S. Ferlay, T. Mallah, R. Ouahes, P. Veillet, and M. Verdaguer, *Nature (London)* **378**, 701 (1995).
4. T. Mallah, C. Auberger, M. Verdaguer, and P. Veillet, *J. Chem. Soc., Chem. Commun.*, No. 61 (1995).
5. A. Scuille, T. Mallah, A. Nivorozhkin, M. Verdaguer, and P. Veillet, *New J. Chem.* **20**, 1 (1996).
6. K. Inoue, K. Kikuchi, and M. Ohba, *Angew. Chem. Int. Ed. Engl.* **42/39**, D3461 (2003).
7. G. A. Kraftmakher, *Radiotekh. Elektron. (Moscow)* **48** (2), 183 (2003).
8. Ch. Kittel, *Phys. Rev.* **73** (2), 155 (1948).
9. S. Chikasumi, *Physics of Ferromagnetism: Magnetic Characteristics and Engineering Application* (Syokabo, Tokyo, 1984; Mir, Moscow, 1987), Vol. 1.
10. P. W. Anderson and P. R. Weiss, *Rev. Mod. Phys.* **25** (1), 269 (1953).
11. P. M. Richards and M. B. Salamon, *Phys. Rev. B: Solid State* **9** (1), 32 (1974).
12. A. G. Gurevich, *Magnetic Resonance in Ferrites and Antiferromagnets* (Nauka, Moscow, 1973) [in Russian].

Translated by G. Skrebtsov

MAGNETISM
AND FERROELECTRICITY

Synthesis and Properties of Barium Ferrigermanate $\text{Ba}_2\text{Fe}_2\text{GeO}_7$

G. A. Petrakovskii*, L. N. Bezmaternykh*, I. A. Gudim*, D. Sheptyakov**, O. A. Bayukov*,
A. M. Vorotynov*, D. A. Velikanov*, and A. F. Bovina*

* Kirensky Institute of Physics, Siberian Division, Russian Academy of Sciences,
Akademgorodok, Krasnoyarsk, 660036 Russia

e-mail: sasa@iph.krasn.ru

** Paul Scherrer Institute, Villigen PSI, 5232 Switzerland

Received March 2, 2005

Abstract—The magnetic susceptibility and specific heat of single crystals of the $\text{Ba}_2\text{Fe}_2\text{GeO}_7$ barium ferrigermanate are investigated. It is revealed that the temperature dependence of the magnetic susceptibility exhibits a kink at a temperature $T = 8.5$ K. The number of nonequivalent positions of Fe^{3+} ions and their occupancies are determined using Mössbauer spectroscopy. It is shown that the Fe^{3+} ions located in tetrahedral positions $T2$ are ordered incompletely, which is inconsistent with the results obtained previously. An assumption is made regarding the possible ground magnetic state of the $\text{Ba}_2\text{Fe}_2\text{GeO}_7$ compound. © 2005 Pleiades Publishing, Inc.

1. INTRODUCTION

Magnetic systems whose structure contains tetragonal layers with antiferromagnetic exchange interactions can exhibit interesting properties, such as order by disorder (with complete frustration of the exchange interactions in the layer) [1] and a spin-singlet state due to the modification of the structure through magnetoelastic coupling [2]. It is worth noting that an important role in this case is played by quantum magnetic fluctuations. The situation is complicated when the system is characterized by a considerable covalency of bonding, i.e., when different spin states of paramagnetic ions become possible due to the violation of the Hund rule. Similar effects can be observed, for example, in a melilite structure [3] with paramagnetic ions.

It should be noted that, in the physics of polyfunctional materials, single crystals with a combination of different magnetic and electrical properties have particularly attracted the attention of researchers. For example, tetragonal copper metaborate, which is of interest from the standpoint of the nontrivial type of magnetic ordering [4], exhibits a piezoelectric effect comparable in magnitude to that of quartz [5]. Similar properties can be expected for other magnetically ordered crystals. In the present work, we synthesized and investigated the properties of single crystals of tetragonal barium ferrigermanate $\text{Ba}_2\text{Fe}_2\text{GeO}_7$ [3]. The barium ferrigermanate undergoes melting with decomposition, and single crystals of this compound have not been grown to date.

In this work, we grew barium ferrigermanate single crystals using the solution–melt method and analyzed the first results of an experimental investigation into its

magnetic properties, specific heat, and Mössbauer effect.

2. CRYSTAL STRUCTURE OF BARIUM FERRIGERMANATE

Tetragonal barium ferrigermanate $\text{Ba}_2\text{Fe}_2\text{GeO}_7$ is a representative of the family of compounds that have a structure of the melilite ($\text{Ca}_2\text{Al}_2\text{SiO}_7$) type and crystallize in the space group $P\bar{4}2_1m$ ($Z = 2$) [3, 6]. Polycrystals of this compound were first synthesized by the solid-phase reaction at a temperature $T = 1200^\circ\text{C}$ [3]. The structure of the barium ferrigermanate is built up of layers that alternate along the c tetragonal axis and consist of polyhedra containing barium ions (Thomson cubes) and two types of oxygen tetrahedra joined into five-membered rings (Fig. 1). Larger sized relatively regular tetrahedra $T1$, which have symmetry $\bar{4}$ and are located at vertices and at the center of the bases of the tetragonal cell, are predominantly occupied by Fe^{3+} ions. Less regular tetrahedra $T2$, which form diortho groups [$M_2\text{O}_7$] with symmetry $mm2$, are statistically occupied by Fe^{3+} and Ge^{4+} ions approximately in a 1 : 1 ratio. The structural formula, which accounts for the distribution of cations over crystallographic positions $T1$ and $T2$, can be approximately written in the form $\text{Ba}_2(\text{Fe}^{3+})_{T1}(\text{Fe}^{3+}\text{Ge}^{4+})_{T2}\text{O}_7$. This distribution of Fe^{3+} cations over tetrahedral positions $T1$ and $T2$ was determined using Mössbauer spectroscopy for polycrystalline samples [3]. Among the compounds synthesized to date in the melilite family and belonging to the same structural type, the $\text{Ba}_2\text{Fe}_2\text{GeO}_7$ barium ferrigermanate is characterized by the highest iron content and is most

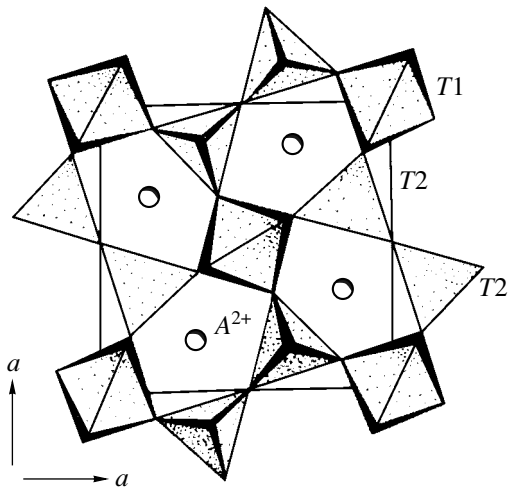


Fig. 1 Structure of the melilite crystal as projected onto the (001) plane. $A^{2+} = Ba^{2+}$ or Sr^{2+} .

attractive for use in magnetic investigations. As regards the magnetic properties, it is important to note that Fe^{3+} ions form square planes perpendicular to the c crystallographic axis in such a way that the Fe^{3+} ion is located at the center of each square formed by the Fe^{3+} ions. In the case when the exchange interactions in each plane are antiferromagnetic in nature, they are frustrated completely. This prevents manifestation of a long-range antiferromagnetic order. Consequently, the exchange interactions between far neighbors play an important role. Moreover, the so-called mechanism of attainment of order by disorder due to the nonlinear interaction of magnetic excitations in the frustrated spin system [1] can also make a significant contribution.

3. EXPERIMENTAL TECHNIQUE, RESULTS, AND DISCUSSION

3.1. Crystal Synthesis

This paper reports on the results of the first investigations into the crystal structure and the magnetic, thermal, and electrical properties of barium ferrigermanate single crystals. The crystals were grown by the solution–melt method with the use of a PbF_2 – B_2O_3 -based solution melt containing 68 wt % ($PbF_2 + 0.62B_2O_3 + 1.09BaO + 0.45GeO_2$) and 32 wt % $Ba_2Fe_2GeO_7$. In this system, $Ba_2Fe_2GeO_7$ is the high-temperature phase ($T_{sat} = 940^\circ C$) and, in the range of its stability, is represented in a binary form. The density of the solution melt is higher than that of the barium ferrigermanate, and the growth was performed in a weakly nonuniform temperature field at $dT/dh < 0$ ($|dT/dh| \leq 2$ K/cm) according to the Kyropoulos method. Black single crystals of the compound had the shape of rectangular plates ($4 \times 6 \times 2$ mm).

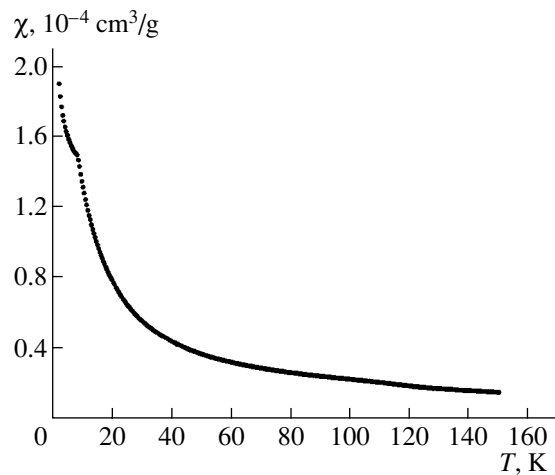


Fig. 2. Temperature dependence of the real part of the magnetic susceptibility at a frequency of 1000 Hz in a magnetic field of 10 Oe.

The X-ray diffraction investigations confirmed that the crystal grown has a helenite structure with the tetragonal unit cell parameters $a = 8.33$ Å and $c = 5.59$ Å. The lattice parameters of the crystals grown and the polycrystals synthesized by the solid-phase reaction [3] are in good agreement. This indicates that partial substitution of Pb^{2+} for Ba^{2+} due to the ion exchange $PbF_2 + BaO \rightleftharpoons PbO + BaF_2$ does not occur under the above conditions of crystal growth.

3.2. Magnetic Susceptibility and Specific Heat

The magnetic and thermal measurements were performed on a PPMS setup and a SQUID magnetometer. The complex magnetic susceptibility was measured in the temperature range 2–150 K at a frequency of 1 kHz in a magnetic field of 10 Oe, which was directed both perpendicular and parallel to the c axis. The results of the measurements are presented in Fig. 2.

It can be seen from Fig. 2 that, at a temperature of approximately 8.5 K, the temperature dependence of the magnetic susceptibility exhibits a kink, which is characteristic of transitions to a magnetically ordered state. The anisotropy of the magnetic susceptibility manifests itself at temperatures below 30 K. It should be noted that the temperature dependence of the reciprocal of the magnetic susceptibility can be separated into three linear portions (13 K $< T < 45$ K, 60 K $< T < 100$ K, 120 K $< T < 150$ K) with different slopes and, hence, with different Curie–Weiss temperatures. This can be associated with the retention of exchange-coupled fragments of the magnetic structure at intermediate temperatures. The fitting at temperatures higher than 120 K results in the Curie–Weiss temperature $\theta = -6.7$ K and the effective magnetic moment $\mu_{eff} = 2.3\mu_B$, where μ_B is the Bohr magneton. This magnetic moment differs substantially from the theoretical value of the

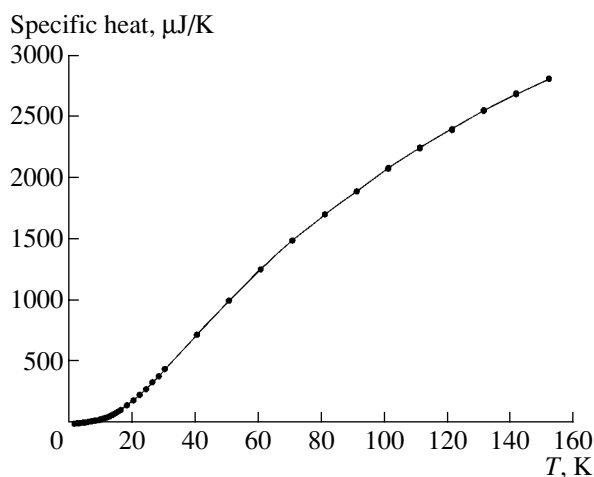


Fig. 3. Temperature dependence of the specific heat for the $\text{Ba}_2\text{Fe}_2\text{GeO}_7$ crystal.

magnetic moment ($5.92 \mu_B$) for Fe^{3+} ions. The Curie–Weiss temperature is negative and, hence, the antiferromagnetic exchange interactions are dominant in the studied compound. Under the assumption that the Curie–Weiss temperature θ is determined by the exchange interaction J of the nearest neighbors $z = 4$, the exchange interaction between the nearest neighbors of the Fe^{3+} ions (i.e., $J = -0.6 \text{ K}$) is determined from the relationship $\theta = -zJS(S + 1)/3k_B$. It should be emphasized that the obtained value corresponds to the average exchange interaction in the system. Since all the exchange interactions in the plane are antiferromagnetic and frustrated, the calculated exchange integral can appear to be considerably underestimated.

The experimental temperature dependence of the specific heat in the temperature range 2–14 K is plotted in Fig. 3. Note that this dependence does not exhibit a noticeable feature at temperatures close to 9 K. A similar situation was also observed for the $\text{Ca}_3\text{CoRhO}_6$ compound and was explained by the smearing of the magnetic phase transition [7]. However, this effect is still not clearly understood.

The $\text{Ba}_2\text{Fe}_2\text{GeO}_7$ crystal is a good insulator.

3.3. Mössbauer Investigation

The analysis of the crystal structure of the ferrihelenite revealed that the spacing between layers containing structure-forming tetrahedra is rather large. The distance between the nearest anions of the adjacent layers is greater than 3 Å. The Ba–O distance is approximately equal to 2.5 Å. These large distances allow us to ignore the exchange interaction between cations of the adjacent layers. Within this approximation, the ferrihelenite lattice can be considered a two-dimensional lattice from the standpoint of magnetism.

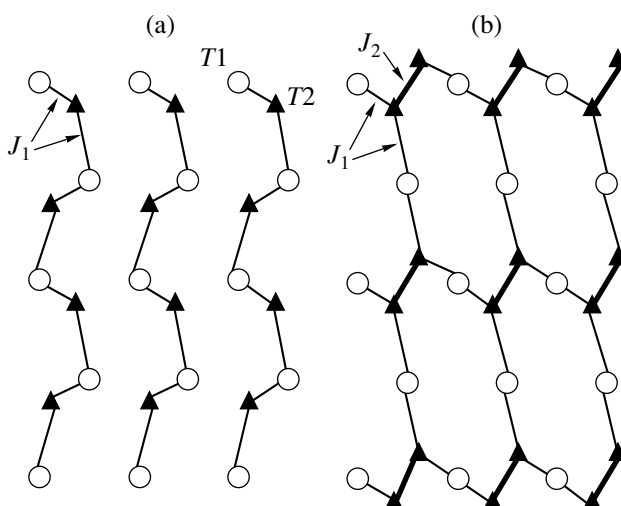


Fig. 4. Ordering of Fe^{3+} and Ge^{4+} ions over the $T2$ positions of helenite.

Large-sized weakly distorted tetrahedra $T1$ form two simple tetragonal lattices inserted into each other. More strongly distorted tetrahedra $T2$ are joined in pairs. These pairs also form two simple tetragonal lattices inserted into each other. One lattice is located above and the other lattice is positioned below the plane formed by $T1$ tetrahedra. In the ferrihelenite structure, the $T1$ tetrahedra are occupied only by Fe^{3+} cations, whereas the $T2$ tetrahedra are occupied by Fe^{3+} and Ge^{4+} cations in a 1 : 1 ratio.

From analyzing the cation–cation exchange interactions in the framework of the simple model of indirect coupling [8, 9], we obtained the following relationships:

$$\begin{aligned} J_1(\text{Fe}^{3+}(T1) - \text{Fe}^{3+}(T2)) &= -6a^2U \cos 45^\circ/25, \\ J_2(\text{Fe}^{3+}(T2) - \text{Fe}^{3+}(T2)) &= -24a^2U/75, \end{aligned} \quad (1)$$

where a is the parameter of ligand–cation electronic transfer, which is equal to the square of the coefficient characterizing the admixture of the ligand wave function to the cation wave function; U is the energy of cation–ligand electronic excitation; and the cosine roughly describes the angular dependence of the transfer integral. It follows from relationships (1) that the exchange interaction J_2 is nearly twice as strong as the exchange interaction J_1 .

The distribution of Fe^{3+} and Ge^{4+} cations over the $T2$ tetrahedral positions plays an important role in the formation of the magnetic structure of ferrihelenite layers. By assuming that cations of different types are ordered in the $T2$ tetrahedral positions, we can consider two possible variants.

(i) A pair of $T2$ cations is formed by cations of different types (Fe^{3+} , Ge^{4+}). In this case, we obtain zigzag chains along one of the a axes, as is shown in Fig. 4a,

where circles indicate Fe^{3+} cations in the $T1$ tetrahedral positions and triangles represent Fe^{3+} cations in the $T2$ tetrahedral positions. Since the exchanges for each cation to the right and to the left along the chain are equivalent, the chains are magnetically homogeneous. For this type of ordering, the (a, a, c) lattice should transform into the (a, b, c) lattice due to the difference between the radii of the Fe^{3+} and Ge^{4+} cations.

(ii) A pair of $T2$ cations is formed by cations of the same type (layer-by-layer ordering). In this case, we have antiferromagnetic pairs of Fe^{3+} cations. These pairs are coupled with each other in two directions through the interaction with $T1$ cations, thus forming a two-dimensional lattice. This type of ordering is illustrated in Fig. 4b. Since $J_2 > J_1$, we can expect the formation of antiferromagnetic dimers, which are in a singlet state and, hence, cannot be magnetically coupled with the surrounding matrix. The matrix is the sublattice of Fe^{3+} cations ($T1$) that are not bonded to each other. Consequently, this sublattice is in a quasi-paramagnetic state. Therefore, in the case of ordering of the second type, we have an ensemble of antiferromagnetic dimers Fe^{3+} ($T2$) in the paramagnetic lattice of Fe^{3+} ions ($T1$). In this situation, the helenite lattice can undergo an orthorhombic distortion.

The above analysis clearly demonstrates that, in the case when the Fe^{3+} and Ge^{4+} cations are statistically distributed over the $T2$ positions, the helenite layer involves a set of magnetically different objects, namely, single paramagnetic cations, singlet pairs, finite homogeneous chains, and two-dimensional regions.

The Mössbauer spectrum measured for a powder of the single crystal is fairly well approximated by two doublets. The doublet parameters listed in Table 1 (where IS is the isomer shift with respect to $\alpha\text{-Fe}$, QS is the quadrupole splitting, W is the absorption line width at half-maximum, and S is the fractional occupancy of the cation position) are in qualitative agreement with the results obtained for polycrystalline samples in [3]. The considerably larger values of the isomer shift and quadrupole splitting in [3] are most likely associated with the defect structure of polycrystals. The isomer shift is characteristic of Fe^{3+} ions in the tetrahedral environment, and the large value of the quadrupole splitting indicates a strong distortion of this environment.

In order to reveal the possible ordering of cations over the $T2$ positions in the ferrihelenite structure, the Mössbauer spectra were identified in two stages. At the first stage, we determined the distribution functions of the quadrupole splitting $P(QS)$ for two valence states of iron. For this purpose, the Mössbauer spectrum was represented as the sum of two groups of doublets with the isomer shifts given in Table 1 and natural width of the absorption line. The quadrupole splitting was varied in steps of 0.05 mm/s. The distribution functions $P(QS)$ were determined by varying the amplitudes of doublets

Table 1. Parameters of the Mössbauer spectrum of barium ferrigermanate

Position	IS , mm/s	QS , mm/s	W , mm/s	S
$T1$	0.205	1.117	0.413	0.497
$T2$	0.187	1.525	0.337	0.503

and the isomer shifts that were identical for each group of doublets. The distribution functions $P(QS)$ thus obtained are presented in Fig. 5.

The maxima in the distribution functions $P(QS)$ indicate that the helenite structure can involve additional iron positions that are nonequivalent in terms of the degree of local distortion. The information obtained from the distribution functions $P(QS)$ is qualitative in character, because these functions were determined using identical isomer shifts for each group of doublets. In the general case, this can lead to the appearance of false maxima.

At the second stage of the identification of the Mössbauer spectra, we constructed a model spectrum on the basis of the number and approximate values of the parameters estimated for the nonequivalent positions from the distribution functions $P(QS)$. The model spectrum was fitted to the experimental spectrum by varying the entire set of hyperfine parameters with the use of the least-squares procedure in the linear approximation. In the course of this fitting, the desired parameters are refined and the occupancies of positions that are responsible for the doublets corresponding to the false maxima become negligible. The results of the two-stage identification of the Mössbauer spectra are presented in Table 2.

The revealed nonequivalent positions, namely, three $T1$ and two $T2$ positions, can be assigned to the positions with different numbers of nearest cations of a particular type. In the case when the $T2$ positions are half occupied, the most probable configuration of the four

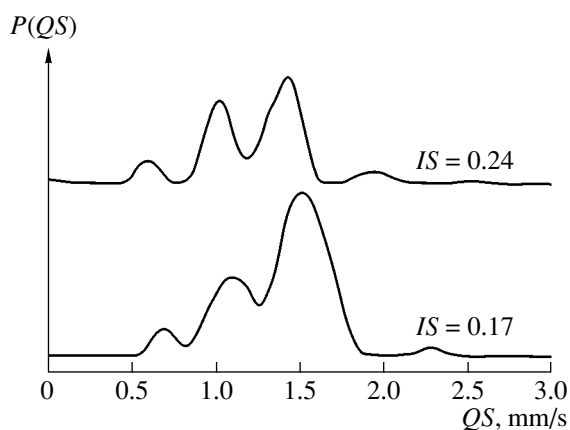


Fig. 5. Distribution functions of the quadrupole splitting $P(QS)$ for two valence states of iron ions in barium ferrigermanate.

Table 2. Mössbauer parameters of the nonequivalent positions of iron ions in barium ferrigermanate

Position	IS , mm/s	QS , mm/s	W , mm/s	S	Nearest neighbor configuration	Occupation probability for a random distribution
$T1$	0.204	0.711	0.251	0.060	3Fe1Ge	0.125
	0.223	1.038	0.268	0.065	1Fe3Ge	0.125
	0.230	1.403	0.361	0.355	2Fe2Ge	0.1875
$T2$	0.163	1.201	0.432	0.253	3Fe	0.25
	0.159	1.571	0.312	0.267	2Fe1Ge	0.25

nearest neighbors for the $T1$ position is the 2Fe2Ge configuration. This is the sole configuration when the cations are ordered over the $T2$ positions. The appearance of the 3Fe1Ge and 1Fe3Ge configurations indicates a random distribution of Fe^{3+} and Ge^{4+} cations over the $T2$ positions.

Of the three neighbors of the $T2$ position, two are always represented by Fe^{3+} cations occupying the $T1$ positions. The third neighbor is a Ge^{4+} cation in the case of ordering. For a random distribution, the Fe^{3+} or Ge^{4+} cation can equiprobably serve as the third neighbor; i.e., the presence of nonequivalent positions $T2$ counts in favor of the random distribution. Therefore, the structure of the barium ferrigermanate can be treated from the standpoint of magnetism as built up of magnetically different objects (from isolated paramagnetic cations to two-dimensional regions). It is worth noting that the occupancies of the cation positions with the revealed configurations differ significantly from their occupation probabilities for the actual random distribution of cations (see the last column in Table 2). These differences are larger than the experimental error and may suggest a partial ordering of Fe^{3+} and Ge^{4+} cations over the $T2$ positions.

4. CONCLUSIONS

A tetragonal crystal of the $Ba_2Fe_2GeO_7$ melilite was grown for the first time. The distribution of Fe^{3+} cations over nonequivalent tetrahedral positions in the crystal lattice was determined using Mössbauer spectroscopy. The temperature dependence of the magnetic susceptibility was measured. The presence of three linear portions in the temperature dependence of the reciprocal of the magnetic susceptibility and the small effective magnetic moment can serve as indirect evidence that the magnetic structure of the $Ba_2Fe_2GeO_7$ compound involves singlet pairs, finite homogeneous chains, and two-dimensional regions, which are characterized by specific effective exchange interactions and are sequentially ordered with a decrease in the temperature. The observed feature in the temperature dependence of the magnetic susceptibility at $T = 8.5$ K can be associated with the manifestation of a long-range magnetic order in the system.

The temperature dependence of the specific heat does not exhibit an anomalous behavior at the point of the magnetic phase transition. This finding is not clearly understood. Possibly, this can be explained by the specific features of the transition to the magnetically ordered state.

At present, we intend to perform experiments on inelastic neutron scattering in order to elucidate the type of magnetic ordering in the $Ba_2Fe_2GeO_7$ compound.

ACKNOWLEDGMENTS

This work was supported by the Division of Physical Sciences of the Russian Academy of Sciences, project no. 2.1.1.2.

REFERENCES

1. R. Singh, W. Zheng, J. Oitmaa, O. Sushkov, and C. Hamer, *Phys. Rev. Lett.* **91**, 017 201 (2003).
2. V. V. Val'kov, V. A. Mitskan, and G. A. Petrakovskii, in *Proceedings of the Second Euro-Asian Symposium "Trends in Magnetism," EASTMAG-2004, Krasnoyarsk, Russia, 2004* (Krasnoyarsk, 2004), p. 74.
3. I. S. Lyubutin, B. V. Mill', V. G. Terziev, and A. V. Butashin, *Kristallografiya* **33** (1), 136 (1988) [*Sov. Phys. Crystallogr.* **33**, 78 (1988)].
4. B. Roessli, J. Schefer, G. Petrakovskii, B. Ouladdiaf, M. Boehm, U. Staub, A. Vorotinov, and L. Bezmaternykh, *Phys. Rev. Lett.* **86** (9), 1885 (2001).
5. K. S. Aleksandrov, B. P. Sorokin, D. A. Glushkov, L. N. Bezmaternykh, S. I. Burkov, and S. V. Belushchenko, *Fiz. Tverd. Tela* (St. Petersburg) **45** (1), 42 (2003) [*Phys. Solid State* **45** (1), 41 (2003)].
6. Yu. Sigalovskaya, P. Sandomirskii, and V. Urusov, *Mineral. Zh.* **6** (2), 3 (1984).
7. V. Hardy, M. Lees, A. Maignan, S. Hebert, D. Flahaut, C. Martin, and D. McK Paul, *J. Phys.: Condens. Matter* **15**, 5737 (2003).
8. O. Bajukov and A. Savitskii, *Phys. Status Solidi B* **155** (2), 249 (1989).
9. O. A. Bayukov and A. F. Savitskiĭ, *Fiz. Tverd. Tela* (St. Petersburg) **36** (7), 1923 (1994) [*Phys. Solid State* **36** (7), 1049 (1994)].

Translated by O. Borovik-Romanova

MAGNETISM AND FERROELECTRICITY

On the Nature of the Phase Transitions in Cadmium Pyroniobate

V. A. Isupov

Ioffe Physicotechnical Institute, Russian Academy of Sciences, Politekhnicheskaya ul. 26, St. Petersburg, 194021 Russia

Received October 25, 2004

Abstract—The existing, doubtful interpretations of the numerous phase transitions in cadmium pyroniobate $\text{Cd}_2\text{Nb}_2\text{O}_7$, which is a ferroelectric with a pyrochlore-type structure and a Curie temperature lying near 200 K, are critically analyzed. The manifestations of all phase transitions in cadmium pyroniobate, the mechanisms proposed for these transitions, and doubts about their validity are discussed. Various dielectric anomalies observed near 200 K are related to three phase transitions in this temperature range. The causes of the large number of phase transitions observed in this material, the dislocation structure of the crystal, the diffuseness of the ferroelectric phase transition, and the relaxor properties of the crystal are also explained. © 2005 Pleiades Publishing, Inc.

1. INTRODUCTION

When the ferroelectric (FE) properties of cadmium pyroniobate $\text{Cd}_2\text{Nb}_2\text{O}_7$ (which has a pyrochlore-type structure and a maximum permittivity at $T_m = 173$ K and exhibits dielectric hysteresis below T_m [1, 2]) were discovered, the behavior of this compound seemed usual. Its peculiarities were discovered later.

It was found in [3] that, at a certain temperature higher than T_m , the third harmonic suddenly appears in an electric current passing through a sample; moreover, a step was also observed in the $\epsilon(T)$ curve (Fig. 1a). Below T_m , triple dielectric hysteresis loops were detected (Fig. 2a), which had not been observed earlier in any known ferroelectric [4]. The loops are characterized by primary and secondary saturation, which can be used to determine the spontaneous polarizations P'_s and $P''_s > P'_s$. The fields under which secondary growth and saturation of polarization occur increase upon cooling; so, when cooled in an actual field, the triple loops transform into ordinary FE loops in a certain temperature range. As a result, the total polarization P_t passes through a maximum (Fig. 2b) caused by the transition from a state with P''_s to a state with P'_s . The authors of [5, 6] found a sharp change in the slope of the $\epsilon(T)$ and $1/\epsilon(T)$ curves at temperatures well above T_m (Fig. 1b). This change is equivalent to a jumplike change in the constants C and θ in the Curie–Weiss law $\epsilon = C(T - \theta)^{-1}$. Moreover, an extremely sharp, narrow peak in $\epsilon(T)$ was later discovered slightly above T_m (Fig. 1c) [7, 8]. Very strong dielectric dispersion was found in the region of the maximum ϵ at T_m : as the frequency of the measuring field E_{ac} increases, this maximum shifts rapidly toward high temperatures and almost merges with the sharp peak in ϵ (Fig. 1c) [9]. Strong dielectric dispersion is

characteristic of classic FE relaxors, where different-type ions randomly occupy the same sublattice (e.g., like in PMN). However, in cadmium pyroniobate, cadmium ions occupy one sublattice and niobium ions occupy another sublattice.

A substantial specific feature of cadmium pyroniobate is the large number of phase transitions (PTs), which are spaced close to each other in temperature and can affect each other. The most interesting temperature range is that near 200 K, where various dielectric anomalies are observed in most cases. Sometimes, these anomalies overlap and it is difficult to relate them to a certain PT. Nevertheless, we will attempt to do so.

As is seen from Fig. 1, the most important dielectric anomalies observed near 200 K are a diffuse maximum at $T_{DM} (=T_m)$, a break in slope in the $\epsilon(T)$ and $1/\epsilon(T)$ curves at T_B , steps at T_{St1} and T_{St2} , and a sharp maximum in $\epsilon(T)$ at T_{SM} . Sometimes, an St3 step is also observed; however, its presence can be explained by a certain difference in the temperature T_{DM} between the surface and the volume of the crystal. PTs have also been detected at lower temperatures: T_{LN} , T'_{LN} (which are close to liquid-nitrogen temperature), T_x , T_y , T_z . Moreover, there are signs of PTs at $T > T_m$ (at temperatures τ_1 , τ_2 , τ_3 , τ_4 , τ_5). Each of these PTs is characterized by a certain mechanism. In this work, we describe the most important characteristics of these PTs and their nature and discuss possible interpretations of them. Moreover, we try to explain the large number of PTs, the causes of the diffuseness of the FE PTs, the complex dislocation structure, and the relaxor properties of cadmium pyroniobate.

Figure 3 shows some actual $\epsilon(T)$ curves (upper curves) and an idealized dependence (curve f). The designations of the PT temperatures, which are used here-

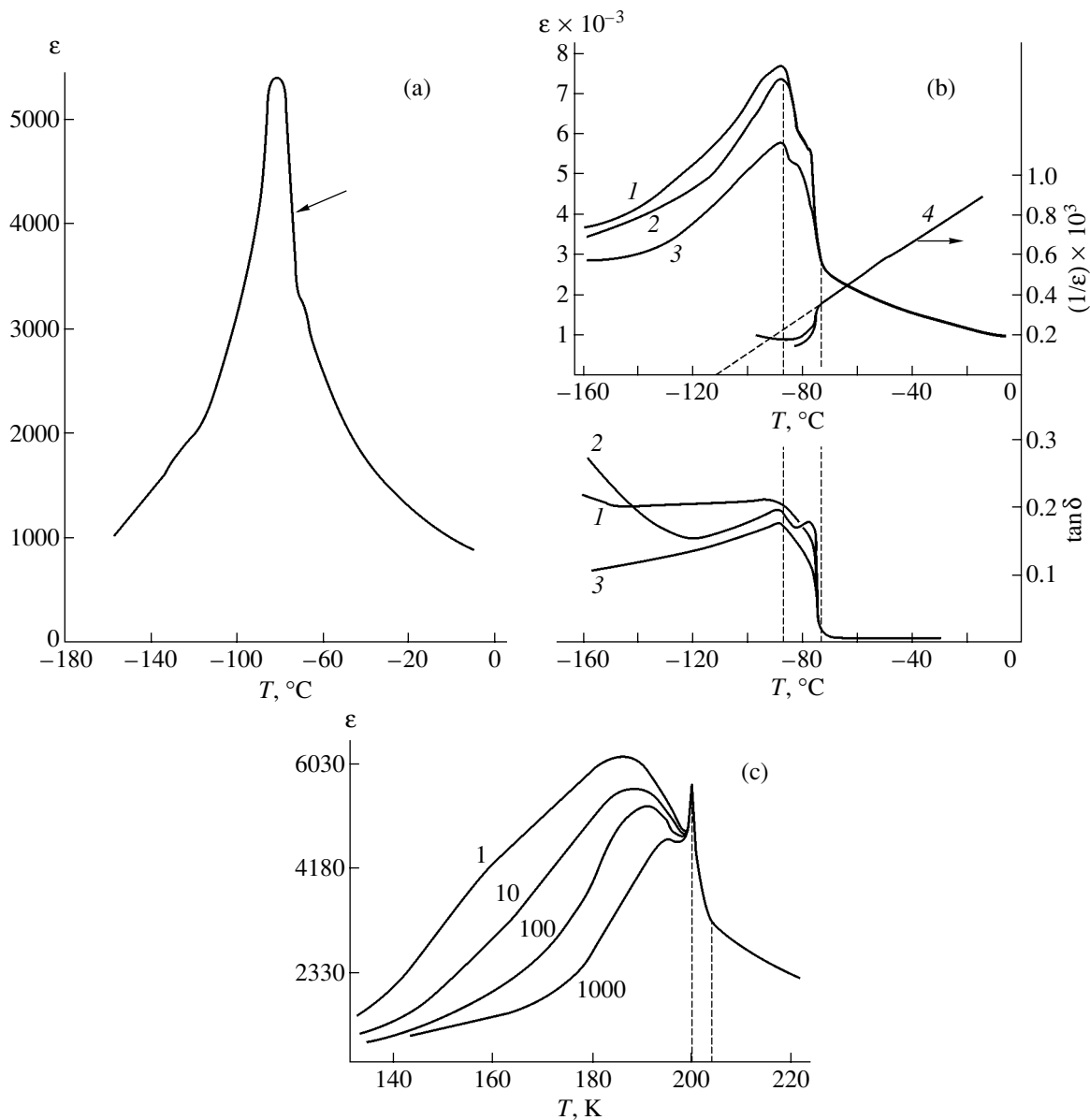


Fig. 1. Some unusual properties of cadmium pyroniobate (the temperature dependence of its permittivity). (a) Hot-pressed ceramics [3] (the arrow shows the temperature of appearance of the third harmonic). (b) Single crystal [4]: ϵ , $1/\epsilon$, and $\tan \delta$ measured at 1 kHz along (1) [110], (2) [111], and (3) [100]; (4) $1/\epsilon$. (c) Single crystal: $\epsilon(T)$ measured at various frequencies [8]; the frequencies (in kilohertz) are indicated on the curves.

after, are also given in Fig. 3. The PT from the cubic paraelectric (PE) to a pseudocubic phase occurring at T_{PE} is assumed to be characterized by a jump in the $\epsilon(T)$ curve. This PT can also manifest itself as an inflection point or a step in this curve (i.e., we state that $T_{PE} = T_B = T_{St1}$). We assume that the PT at T_{SM} can also manifest itself in the form of a step (i.e., we assume that $T_{SM} = T_{St2}$). Thus, we state that, in the vicinity of 200 K, there occur only three PTs (at T_{PE} , T_{SM} , T_{DM}), which can manifest themselves differently. The grounds for this statement will be given below.

Let us consider each of the PTs separately.

2. PHASE TRANSITION AT T_{PE}

According to [5, 6], the PT to the pseudocubic phase occurs at $T_{PE} = T_B = 205$ K. The Curie–Weiss law is obeyed both below and above T_B : $C = (1.13\text{--}1.30) \times 10^5$ K above T_B [6, 10] and $C = (3.3 \pm 0.3) \times 10^4$ K below T_B [7]. Thus, the constant C decreases four to five times at T_B . Below T_B , $\tan \delta$ increases sharply and a domain structure appears [6]. According to [11], the temperature T_{PE} corresponds to the St1 step and the constant C below and above this step has different values.

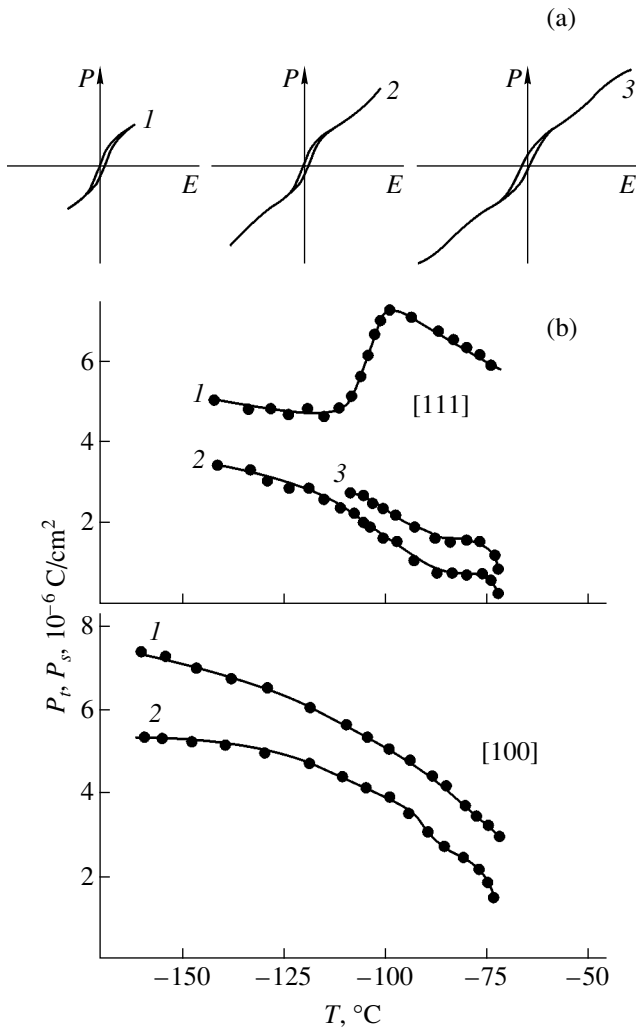


Fig. 2. Some unusual properties of cadmium pyroniobate (polarization in a strong field E_{ac}). (a) Dielectric hysteresis loops at E_{ac} equal to (1) 22.4, (2) 44.6, and (3) 60 kV/cm. (b) The temperature dependences of (1) the total polarization P_r , (2) spontaneous polarization P'_s , and (3) spontaneous polarization P''_s as determined from hysteresis loops recorded at $E_{ac} = 25$ kV/cm along [111] and at 15 kV/cm along [100] [4, 5].

The PT at T_{PE} is sometimes considered an improper FE PT [12] or an improper ferroelastic PT [13]. The question arises as to whether spontaneous polarization appears at T_{PE} . Our results [6] indicate that it does appear. The same conclusion follows from [9, 12], where a clear peak in the pyroelectric current was observed at $T_{PE} = 205$ K (Fig. 4). After appearing, the spontaneous polarization P_s increases upon cooling. In the range between T_{PE} and T_{SM} , i.e., in the improper phase, P_s is very low (about 0.02×10^{-6} C/cm²). The value of P_s measured in the [001] direction is higher than that in the [011] and [111] directions, which means that P_s in the improper phase is directed along [001]

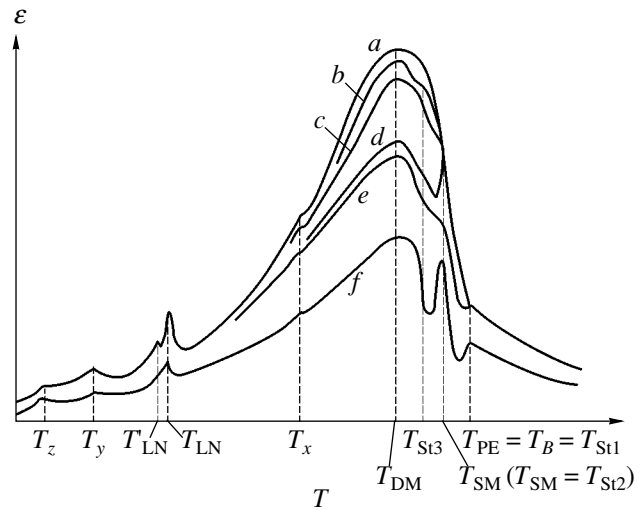


Fig. 3. Temperature dependence of the permittivities of different cadmium pyroniobate samples (schematic): (a–e) real cases and (f) a hypothetical idealized curve.

[12]. (For ceramics, P_s was also found to occur in the improper phase [14].) However, the authors of [15] attributed the improper phase to a nonpolar space group (of the mmm type), which excludes the presence of spontaneous polarization (i.e., the phase is assumed to be purely ferroelastic).

An increase in the measuring-field frequency does not shift T_{PE} (Fig. 1c), and dielectric dispersion is absent up to 200 kHz [8, 12]. Dilatometric studies of ceramics [5] have shown that the appearance of P_s and pseudocubic distortions is accompanied by a weak decrease in volume (which differentiates $Cd_2Nb_2O_7$ from FE perovskites). Below T_{PE} , the spontaneous birefringence is low and positive (Fig. 5) [12].

Under the action of a strong dc bias field ($E_{dc} = 8$ kV/cm), only the anomaly with a maximum value of ϵ at T_{PE} is retained instead of the three dielectric anomalies (at T_{PE} , T_{SM} , T_{DM}) near 200 K [4, 5, 16]. When the field increases further, this maximum shifts toward low temperatures (Fig. 6b). This maximum is likely to correspond to the transition from the PE to FE state; therefore, the behavior mentioned just above is unusual, since an E_{dc} field in all known ferroelectrics shifts the maximum of ϵ at the Curie point toward high temperatures.

According to [8, 17], compression of the crystal shifts $T_{PE} = T_{St1}$ toward high temperatures and the step St1 changes into a small maximum (jump). That is why the idealized $\epsilon(T)$ curve (Fig. 3, curve f) contains a jump at $T = T_{PE}$ that looks like a small maximum.

The authors of [18] concluded that the PT at T_{PE} is associated with a three-component order parameter that transforms according to the F_{2u} representation at the center of the Brillouin zone of the cubic phase; this behavior corresponds to improper ferroelectricity.

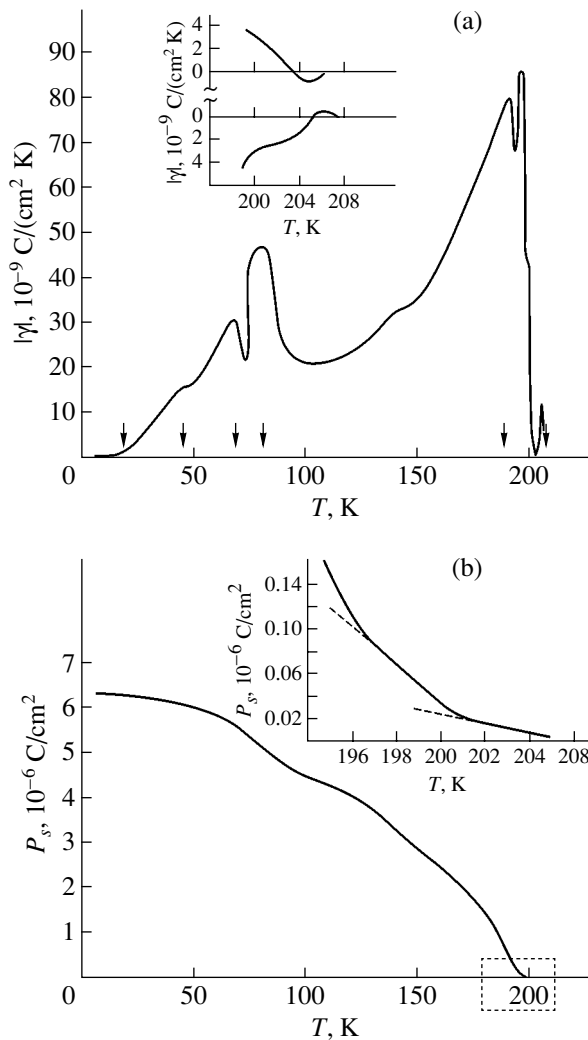


Fig. 4. Temperature dependence of (a) the pyroelectric coefficient γ and (b) the spontaneous polarization P_s of single-crystal cadmium pyroniobate measured along [110] [12].

However, the fact that multiplication of the unit cell has not been observed below T_{PE} is confusing. At the same time, it is unclear whether this multiplication should exist in the case of a unit cell as large as a pyrochlore unit cell. Maybe “improper” displacements can occur inside the unit cell without its multiplication. However, this problem is for theorists to solve.

3. PHASE TRANSITION AT T_{SM}

At $T_{SM} = T_{St2} = 201$ K, there is either a sharp maximum of ϵ or an St2 step. The curves in Fig. 3 show that the step is observed when the maximum at T_{DM} is sufficiently high to conceal the sharp maximum (SM) and only the St2 step is visible. Thus, the presence or absence of the sharp maximum at T_{SM} is determined not by the transformation at T_{SM} but rather by the next PT (at T_{DM}). The authors of [10] found that the Fe^{3+} accep-

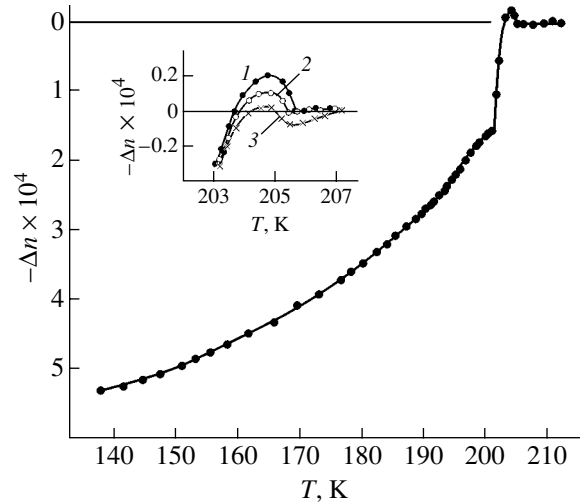


Fig. 5. Spontaneous birefringence of single-crystal cadmium pyroniobate at a bias field E_{dc} . In the inset, E_{dc} is equal to (1) 0, (2) 1, and (3) 2 kV/cm [12].

tor impurity causes the peak in ϵ to become clearly defined and that the Gd^{3+} donor impurity (which is located on the Cd sublattice) makes this peak invisible. In other words, impurities affect the dielectric polarization at T_{DM} .

The Curie–Weiss law is obeyed with constant $C = (3.3 \pm 0.3) \times 10^4$ K above the sharp peak in ϵ and with $C = (5 \pm 1) \times 10^4$ K below this peak (over a range 1 K wide) [7]. The temperature T_{SM} is independent of the measuring-field frequency [8, 12].

According to [9, 19], a pyroelectric-current peak is detected near 201 K (Fig. 4) and P_s increases faster below 201 K. At T_{SM} , the spontaneous birefringence changes sign and becomes negative in all low-temperature phases (Fig. 5) [6, 7]. Twin (domain) boundaries below T_{SM} become clearer [6, 7].

The application of a static electric field shifts T_{SM} toward T_{PE} and, as noted above, changes the dielectric anomalies into a single maximum of ϵ near T_{PE} . As the field increases (at $E_{dc} > 8$ kV/cm), the maximum shifts toward low temperatures [5, 6]. A field applied along [001] suppresses the sharp peak in ϵ . On the contrary, a field applied along [111] makes the peak well defined [8]. What causes this phenomenon is still unclear.

The PT at T_{SM} is commonly considered to be a proper FE PT. Perhaps this is true. However, its specific features, such as the sharpness of the peak in ϵ , the validity of the Curie–Weiss law above and below T_{SM} with very low values of the constant C (33000 above and 50000 K below the peak), and, most importantly, the finite value of the peak at the phase transition point, which is far from temperatures where $\epsilon \rightarrow \infty$, raise doubts in the ordinary nature of this FE transition.

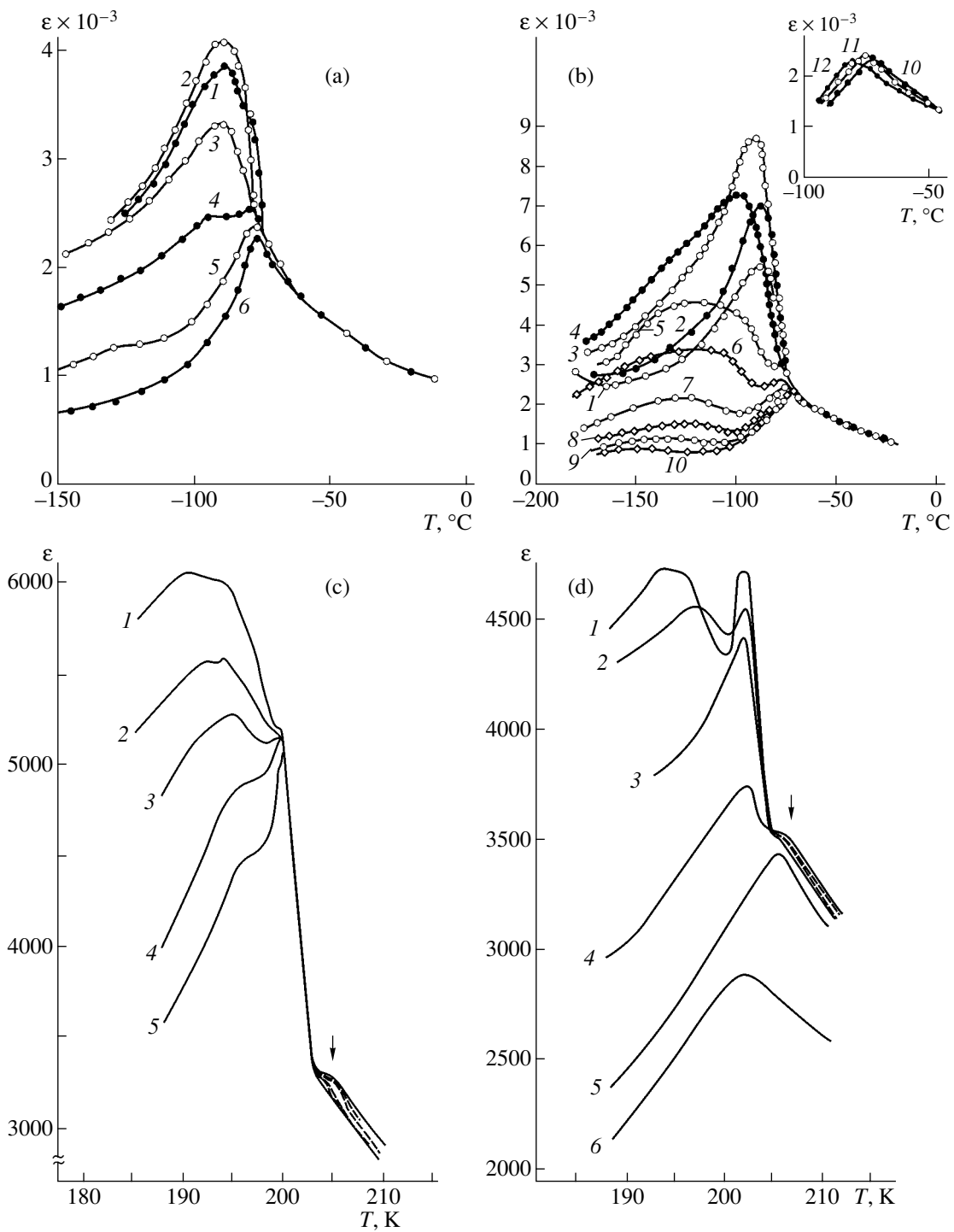


Fig. 6. Temperature dependences of the permittivity of single-crystal cadmium pyroniobate at various bias fields E_{dc} along (a, c) [001] and (b, d) [111]. The data are taken from (a, b) [5] and (c, d) [10]. E_{dc} is equal to (a) (1) 0, (2) 0.18, (3) 0.6, (4) 1.0, (5) 2.0, and (6) 5.3 kV/cm; (b) (1) 0, (2) 0.1, (3) 0.2, (4) 0.4, (5) 0.6, (6) 1.0, (7) 1.6, (8) 3.0, (9) 4.0, (10) 6.0, (11) 10.0, and (12) 15.0 kV/cm; (c) (1) 0, (2) 0.2, (3) 0.25, (4) 0.3, and (5) 0.4 kV/cm; and (d) (1) 0, (2) 0.2, (3) 0.35, (4) 0.85, (5) 5.0, and (6) 17.0 kV/cm.

According to [20, 21], a phase transition from a symmetric phase to an incommensurate FE phase is sharp (in a certain approximation) and obeys the Curie–Weiss law above and below the transition point, but ϵ at

the PT point is finite. The assumption that T_{SM} corresponds to a PT to an incommensurate phase is quite reasonable. (The requirement that the constant C in the Curie–Weiss law be the same above and below T_{PT} can

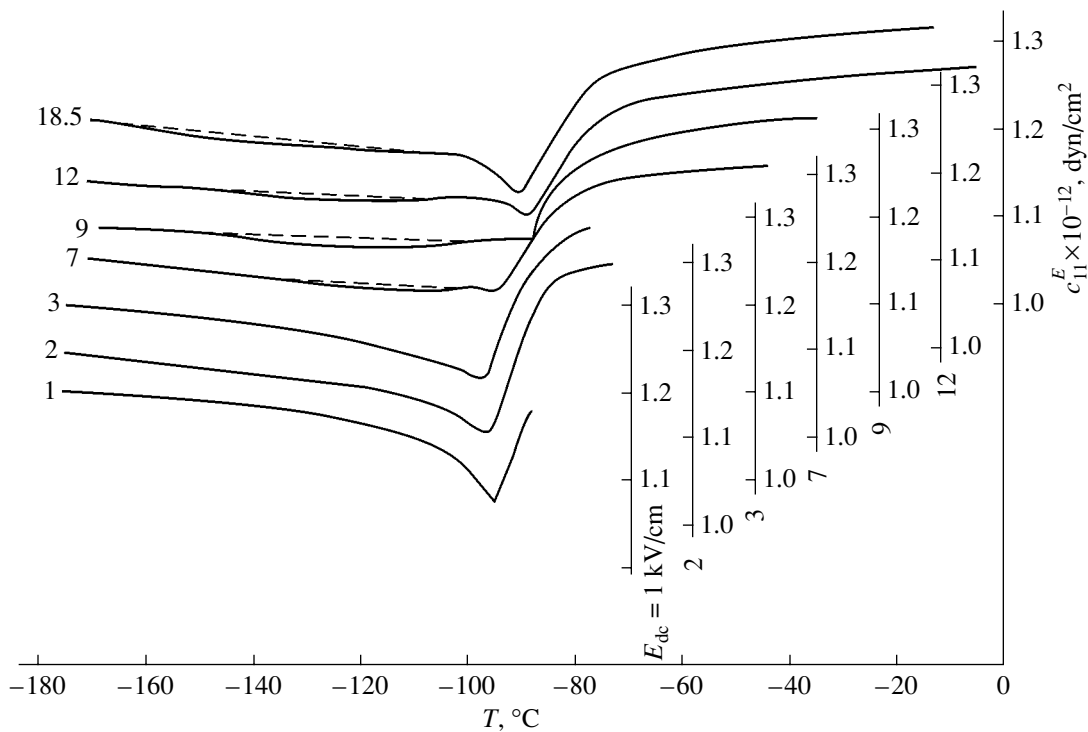


Fig. 7. Temperature dependence of the elastic modulus c_{11}^E of ceramic cadmium pyroniobate at various values of E_{dc} [23].

be the result of the rough approximations used in the theory.) However, if the phase below T_{SM} is incommensurate, there is obviously no modulation in P_s (since P_s neither disappears nor decreases below T_{SM} (Fig. 4)). However, the present author states nothing and would only like to show that the conclusion that the transition at T_{SM} is an ordinary proper FE PT should not be considered final.

4. PHASE TRANSITIONS AT T_{DM} AND T_x

In the case of classic FE relaxors (e.g., PMN), where the temperature of a maximum in $\epsilon(T)$ depends on the frequency of the measuring field E_{ac} , the average temperature of the diffuse FE PT is usually taken to be the temperature of the maximum in ϵ at a frequency of 1 kHz (although it is more correct to take the temperature of the maximum of static ϵ). In this work, we also defined the temperature in this way and found that $T_{DM} \cong 188$ K for cadmium pyroniobate. (Note that the position of the corresponding maximum of ϵ depends not only on the frequency but also on E_{ac} ; it shifts toward T_{SM} but does not reach it with decreasing E_{ac} [5, 6].)

As already noted, below T_{DM} , very narrow triple dielectric hysteresis loops (Fig. 2a) with a ratio P_s''/P_s' higher than 2.7 were observed at 155 K in [17]. Upon cooling, the total polarization P_t passes through a maximum due to an increase in the secondary polarization

growth field (Fig. 2b). In a high field E_{ac} , this maximum was observed at a lower temperature. (Although triple loops were also detected between T_{PE} and T_{DM} , they were less pronounced and extremely narrow.)

The data on the effect of a strong static field on the PT at T_{DM} are very conflicting. Our results [5, 16] indicate that the corresponding maximum of ϵ is shifted by a field E_{dc} toward low temperatures (Figs. 6a, 6b), whereas the results from [10] demonstrate that this maximum shifts toward high temperatures (Figs. 6c, 6d). The causes of this discrepancy are unknown.

In a weak bias field, the elastic modulus passes through a sharp minimum near T_{DM} (Fig. 7) [22]. At $E_{dc} \geq 7$ kV/cm, a flat minimum splits off from it and shifts toward low temperatures (this fact supports the shift in the temperature of the maximum of ϵ noted above).

The existence of triple hysteresis loops can be explained by the presence of two types of domains with different pinning energies or by the occurrence of a PT from the state with P_s' to the state with P_s'' under the action of a field (as is supposed in [4]) or of a forced PT from the FE phase with a low ϵ and a very low P_s to a PE phase with a high ϵ (as is supposed in [6]). It is obvious that, in the last case, the change in the thermodynamic potential due to the application of a field E ($-\epsilon_{PE}E^2$ in the PE phase and $-\epsilon_{FE}E^2 - (1/2)P_sE$ in the FE phase) is greater in the PE phase. This fact can also

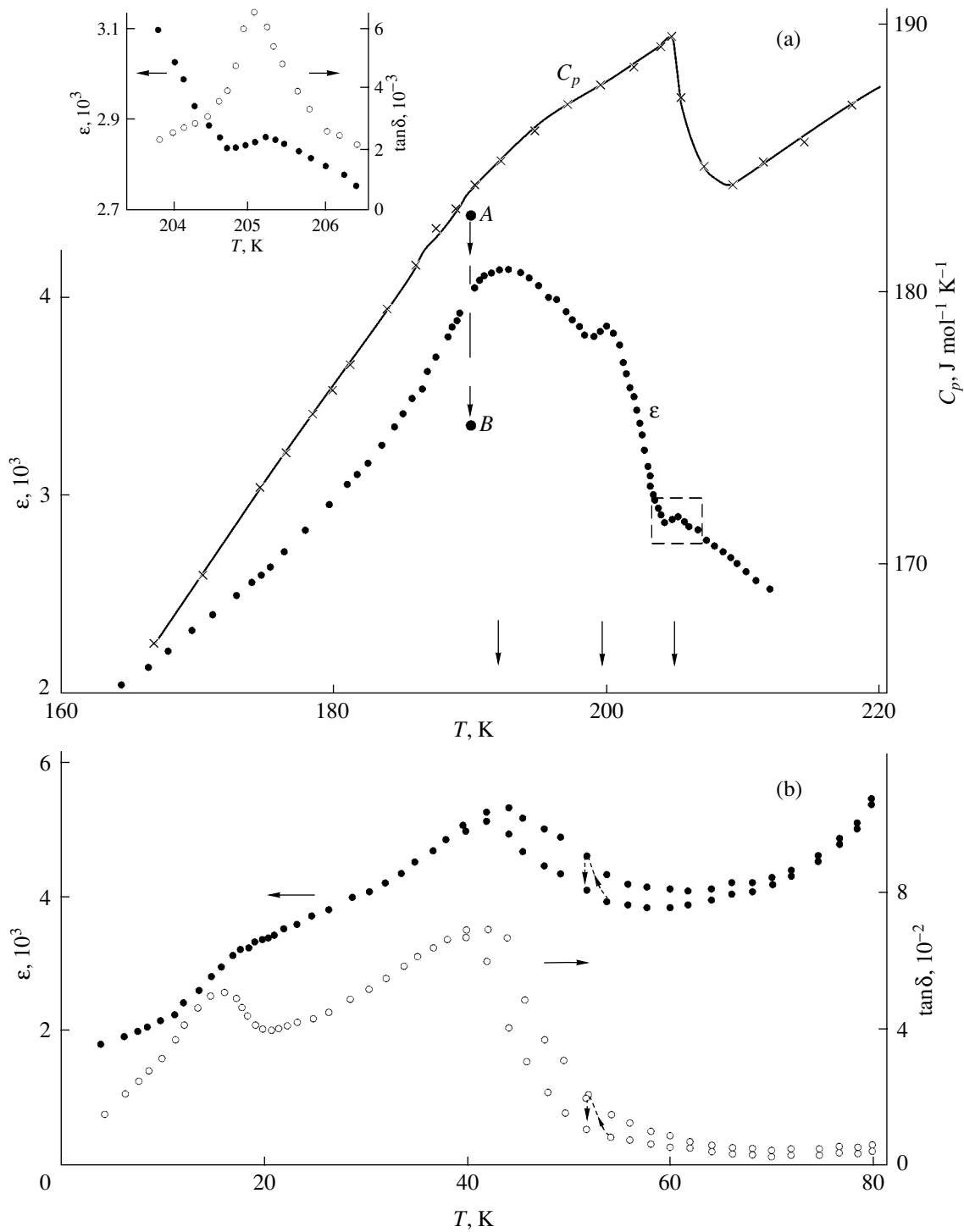


Fig. 8. Temperature dependences of (a, b) ϵ and $\tan \delta$ along [100] for different temperature ranges and (a) the specific heat C_p [24]. Point A in (a) corresponds to the instant at which a temperature T is reached, and point B is recorded after 3 h. The inset in (a) shows the region confined by the rectangle. The upper curve in (b) corresponds to a time after 40-min temperature fixation.

account for the decrease in the temperature of the single ϵ maximum near T_{PE} at $E_{dc} > 8$ kV/cm that occurs with an increase in field. (However, it should be noted that this is only an assumption.)

Upon cooling below T_{DM} , the permittivity begins to decrease in time when a certain temperature T is reached, and the decrease is significant (Fig. 8, points A, B). (The inset to Fig. 8 clearly shows the jump (max-

imum) in $\epsilon(T)$ at T_{PE} that was discussed above.) Figure 8 also shows that the specific-heat maxima associated with the three phase transitions merge into one diffuse maximum extending toward low temperatures down to 140 K (i.e., to T_x) [9, 23]. Kolpakova and coworkers (see, e.g., [17, 24, 25]) studied the relaxation dielectric polarization of single crystals and ceramics [26] and revealed two relaxation mechanisms. One mechanism is related to the motion of domain walls, and the other is related to jumps of cadmium ions in potential wells, which are assumed to exist inside the CdO_8 polyhedra. Unfortunately, the great body of experimental results obtained cannot explain the nature of numerous PTs in cadmium pyroniobate.

As is seen from Fig. 3, a weak dielectric anomaly occurs near $T_x = 140\text{--}150$ K [11, 12]. The phase below T_x is still ferroelectric. (For ceramics, it was found that $P_s = 1.8 \times 10^{-6}$ C/cm² at 100 K [2] and $P_s = 2.7 \times 10^{-6}$ C/cm² at 125 K [14].) At 140–150 K, there exists a hump in the temperature dependence of the pyroelectric current (Fig. 4) [9, 12, 19]. According to [8], domains cease to change in number upon cooling below 140 K.

The temperature $T_x = 140$ K is considered in [12] to be the lower boundary of the range where the improper FE phase undergoing the diffuse PT exists. It should be noted that PTs in classic FE relaxors do not have a well-defined lower boundary. It is significant that, near T_x , the relaxation time distribution parameters are virtually unchanged [25] and that the EPR spectrum has no anomalies [27]. Apparently, it is still too early to discuss the nature of the phenomena occurring at 140–150 K, since one has to reveal first whether these phenomena are associated with PTs.

5. PHASE TRANSITIONS AT T_{LN} (T'_{LN}) AND T_y

In $\text{Cd}_2\text{Nb}_2\text{O}_7$ ceramics, a PT with an ϵ maximum at 80–86 K was detected in [2]. Later, two closely spaced ϵ maxima (at 80 and 83 K) were detected in its single crystals [13] and the authors of [8, 9] observed two pyroelectric-effect maxima at 69 and 82 K (Fig. 4). Since only one PT (at T_{LN}) was observed in most studies, the presence of two ϵ maxima in single crystals can be assumed to be caused by their inhomogeneity (i.e., by a difference in T_{LN} between the bulk and surface layers of the single crystals).

According to [24], the PT at T_{LN} is of the first order. However, weak broadening of the x-ray (622) reflection (which is likely related to rhombohedral distortions) begins at 115 K and, while increasing upon cooling, does not undergo a jump near 80 K [28]. According to [15], the symmetry below 86 K is likely to be monoclinic.

Taking into account the small value of $\tan \delta$ (which is 0.002), the unstable behavior of ϵ in time, and the character of the temperature hysteresis of ϵ below T_{LN} ,

the authors of [29, 30] concluded that the PT at T_{LN} is to an incommensurate phase. Moreover, based on the fact that the intensity of the soft mode appearing below T_{LN} decreases jumpwise upon cooling below $T_y = 46$ K, those authors assumed that a PT into a normal (unmodulated) FE phase occurs at 46 K.

It is obvious that P_s modulation should result in the disappearance of or, at least, a decrease in the macroscopic spontaneous polarization. However, according to [12], P_s actually slightly increases rather than decreases below 80 K (Fig. 4). According to [23], this increase is strong. Therefore, in the range from T_{LN} to T_y , the phase has no P_s modulation. The behavior of a crystal modulated in a parameter other than P_s (but in the presence of P_s) has not been studied. However, it is clear that, if modulation occurs that is not in P_s , a low value of $\tan \delta$ does not guarantee incommensurability. As for the time dependence of ϵ , it is also observed above T_{LN} (Fig. 6, points A, B). Thus, the assumption that the phase between T_{LN} and T_y is incommensurate is insufficiently grounded. Moreover, an analysis of the damping of modes appearing below 80 K does not support the opinion that this phase is incommensurate [31].

6. TRANSITION AT T_z

Below $T_z = 18\text{--}19$ K, where a maximum in $\epsilon(T)$ is observed (Fig. 8), the crystal remains ferroelectric [21, 25, 29, 30]. (According to [2], dielectric hysteresis loops are detected down to 1.2 K.) The authors of [25, 26, 31] assume that a glassy state exists below $T_z = 18\text{--}19$ K. Indeed, Lawless *et al.* [32] showed that $\text{Cd}_2\text{Nb}_2\text{O}_7$ exhibits signs of a glassy state at low temperatures; namely, c_p/T^3 passes through a maximum at 17 K, its thermal conductivity is proportional to T^2 in the range 0.7–5.0 K, and $\Delta\epsilon/\epsilon$ passes through a minimum at 0.47 K. However, does this mean that the PT to a glassy state occurs at T_z ? For example, BaTiO_3 also exhibits signs of a glassy state at low temperatures [32]; however, this does not mean that the low-temperature PT (into the rhombohedral phase) in barium titanate is a transition to a glassy state. We agree with [33], where the signs of a glassy state in cadmium pyroniobate were observed at high temperatures and were found to be caused by various lattice defects and domain walls. In this case, it is beyond reason to believe that T_z is the glass transition temperature and to designate it as T_{gl} . This transition is most likely an ordinary phase transition associated with a change in crystal symmetry.

7. TRANSITIONS AT $T > T_{PE}$

The occurrence of phase transitions at $\tau_1 = 218$ K, $\tau_2 = 230$ K, and $\tau_3 = 261$ K needs to be checked, since data on them are scarce and have not been confirmed. There are data on DTA effects at τ_2 and τ_3 [34]. Kraňnik *et al.* [11] observed jumps in $\epsilon(T)$ and $1/\epsilon(T)$ in a strong

bias field ($E_{dc} = 8$ kV/cm) at τ_1 and τ_2 , and the jumps were absent in a zero field. These jumps were attributed to phase transitions. It should be noted that a hump in the temperature dependence of the electrooptic coefficient was observed at τ_1 in the case of $E_{dc} = 0$ and a hysteresis in $\Delta n(E)$ appeared at $E_{dc} > 10$ kV/cm [7]. However, no anomalies in the resonance frequencies of piezoelectric vibrations (which are very sensitive to phase transitions) have been detected at τ_1 , τ_2 , and τ_3 (Fig. 7) [22].

The authors of [24, 35] reported on the occurrence of $O_h^1-O_h^7$ PTs (i.e., without a change in cubic symmetry) at $\tau_4 = 319$ K and $\tau_5 = 512$ K, where ϵ , the ionic conduction, and the lattice parameter changed only slightly ($\Delta a/a = 0.00002$). However, those authors also detected a white hoarfrost-like deposit on the crystal heated above 512 K, which unambiguously indicates chemical changes [35]. They assumed a loss of water or of another impurity at $\tau_4 = 319$ K. Thus, the temperatures τ_4 and τ_5 most likely do not correspond to phase transitions.

8. DISCUSSION

Obviously, the cause of the specific features of $Cd_2Nb_2O_7$ consists in its crystal structure. A cubic pyrochlore-type structure with space group $Fd\bar{3}m$ and $a = 10.4$ Å is usually derived from a cubic fluorite-type (CaF_2 or AO_2) structure with space group $Fm\bar{3}m$ and $a = 5.4$ Å constructed from CaF_8 cubes (or AO_8 cubes). In the case of a compound $A_2B_2O_7 = 2(A_{0.5}B_{0.5})(O_{0.875}\square_{0.125})_2$, a pyrochlore rather than fluorite lattice forms if the B ions are smaller than the A ions: the A and B ions become ordered. The regular BO_8 and AO_8 cubes change into BO_6 octahedra and strongly distorted $AO_8 = AO_6'O_2''$ cubes compressed along the body diagonal of the cube. A pyrochlore-type structure (Fig. 9) is characterized by an extremely rigid network of octahedra $(B_2O_6)_\infty$ and a very flexible sublattice $(OA_2)_\infty$ (Fig. 9b) (which corresponds to a β -cristobalite-type structure) inserted into this network. (The A ions enter the “windows” between the octahedra, and the spaces between the octahedra are occupied by $O(A_{0.5})_4$ tetrahedra (Fig. 9b).) Thus, a very compliant sublattice, where the OA_4 tetrahedra are connected via “hinges,” is inserted into the very rigid network of octahedra.

The presence of these two sublattices can explain a large number of the PTs in cadmium pyroniobate induced by vibration modes characteristic of both the $(B_2O_6)_\infty$ network and the β -cristobalite sublattice and by their relative-vibration modes. According to [31], the pyrochlore lattice is characterized by 66 vibration modes, 38 of which are infrared-active modes. Therefore, it is not surprising that $Cd_2Nb_2O_7$ undergoes many PTs. It is obvious that finding a relation between the PTs and the vibration modes requires knowledge of the

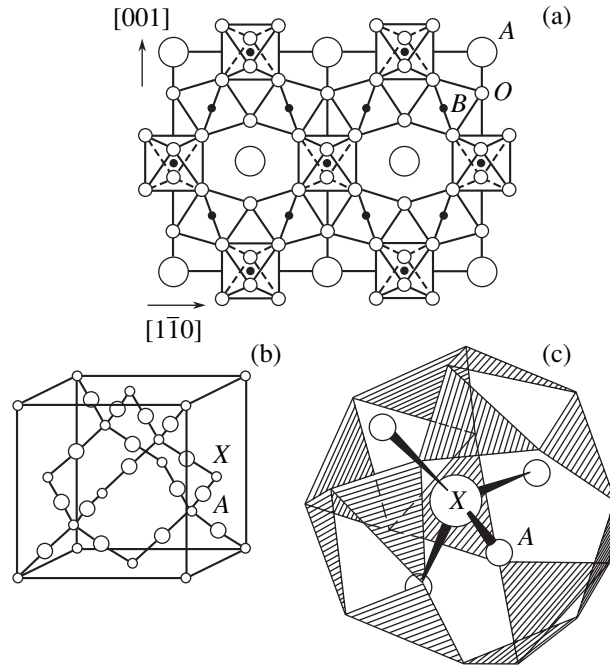


Fig. 9. (a) Pyrochlore-type crystal structure (the projection on the (110) plane); (b) cubic structure of the β -cristobalite type, XA_2 ; and (c) the location of an XA_4 tetrahedron in the space between octahedra (only the octahedron faces adjacent to the ion X are shown).

symmetries of various phases; unfortunately, they are either unknown or have been determined unreliably.

Now, let us discuss relaxor properties. In classic FE relaxors (e.g., PMN or $Ba(Ti,Sn)O_3$), the PTs are diffuse due to inhomogeneities (frozen composition fluctuations) induced by a random distribution of two cation types in one of the sublattices. However, in $Cd_2Nb_2O_7$, one of the cation sublattices contains only cadmium ions and the other contains only niobium ions. Therefore, this mechanism of diffuse PTs is invalid in this case. The fact that the diffuse character of the FE PT is different is also supported by the presence of a domain structure, which is clearly visible in the absence of an electric field. (In classic FE relaxors, a domain structure is invisible until a strong field is applied.)

The causes of the diffuse FE PT in $Cd_2Nb_2O_7$ can be explained if we pay attention to the similarity of the pyrochlore and fluorite structures. We assume that, when a pyrochlore lattice forms, numerous fluorite atomic groups embedded into the pyrochlore lattice appear. (They can arise if the A and B ions randomly change their polyhedra. The sizes of the fluorite and pyrochlore cells make this possible.) In principle, these groups can contain excess oxygen ions and can have the $(Cd_2Nb_2O_8)_m^{2-}$ composition, or, rather, $(Cd_2Nb_2O_{8-x}\square_x)_m^{2(1-x)}$ with $x < 1$. (This situation is possible for small atomic groups.)

These groups would have a negative charge, whereas their environment would have a positive charge due to an oxygen deficiency. It is known that randomly directed nonuniform electric fields can make an FE PT diffuse [36]. It is clear that the crystal fields acting on the fluorite groups should be nonuniform and random.

Here, we would like to mention the results from [37], where the (111) surfaces of plates were studied by x-ray diffraction. All the crystals had peculiar (dislocation) defects. Colorless crystals and weakly colored crystals were found to be most imperfect. Strongly colored and doped crystals were most perfect. Undoped crystals had a homogeneous netlike dislocation distribution with a linear cell size of 10–50 μm . The dislocation density ranged from 10^4 cm^{-2} for strongly colored crystals to $5 \times 10^5 \text{ cm}^{-2}$ for colorless or weakly colored crystals.

This raises the following question: Why does cadmium pyroniobate have such a high dislocation density? It is likely that dislocations are generated by the fluorite groups. The additions of Zn, Ni, Cu, Fe^{3+} , and Gd^{3+} ions used in [37] most likely hindered the formation of fluorite groups and thereby decreased the number of dislocations.

According to [33], the strongest dielectric dispersion near T_{DM} was observed in colorless or weakly colored crystals, where the number of dislocations was maximum. It is clear that the larger the number of sources of random fields, the stronger the diffuseness of an FE PT.

It is obvious that, because of their gradients, random fields acting on fluorite groups affect the Curie temperatures of different pyrochlore regions differently (on a microscopic rather than nanoscopic scale). As a result, boundaries arise between PE and FE regions. The displacement of these boundaries due to thermal motion or an applied alternating field would result in dielectric relaxation. Domain walls can also take part in dielectric relaxation. Obviously, it is beyond reason to suppose that in $\text{Cd}_2\text{Nb}_2\text{O}_7$ there are relaxing polar nanoscopic regions characteristic of classic relaxors.

It is unlikely that cadmium-ion jumps in the potential barriers of $\text{CdO}_6\text{O}_2''$ polyhedra are responsible for the FE PT and dielectric relaxation. The point is that similar cadmium-ion displacements (or even larger) have been found in $\text{Cd}_2\text{Ta}_2\text{O}_7$ [38], which is not a ferroelectric. Moreover, the cadmium-ion displacements decrease as the temperature decreases.

9. CONCLUSIONS

Thus, we have discussed the phenomena accompanying all PTs in cadmium pyroniobate and various opinions regarding the nature of these PTs. As a result, a number of doubts have arisen: (1) Is the PT at T_{PE} ferroelectric or only ferroelastic? (2) Is the FE transition at T_{SM} improper (without multiplication of the unit cell) or

incommensurate? (3) Is the relaxor FE transition at T_{DM} classic or of another nature? By analyzing the available data, we have drawn the following conclusions: (i) The presence of a PT at T_x is not proved. (ii) The existence of an incommensurate modulated phase seems to be unlikely in the range from T_{LN} to T_y . (iii) The transition at T_z is most likely an ordinary PT with a change in symmetry. (iv) The occurrence of phase transitions at τ_1 , τ_2 , and τ_3 needs to be checked, and the phenomena observed at temperatures τ_4 and τ_5 are likely to be unrelated to phase transitions.

We have tried to explain the large number of PTs, the dislocation structure, the diffuseness of the ferroelectric phase transition, and the dielectric relaxation of cadmium pyroniobate. However, our conclusions need to be verified.

Thus, we have critically analyzed the generally accepted concepts of the nature of phase transitions in cadmium pyroniobate, which, in our opinion, erroneously explain the nature of these transitions.

The author hopes that the doubts described in this work will stimulate further investigations.

REFERENCES

1. W. R. Cook and H. Jaffe, *Phys. Rev.* **88**, 1426 (1952); *Phys. Rev.* **89**, 1297 (1953).
2. G. Shirane, R. Pepinsky, and J. K. Hulm, *Phys. Rev.* **92**, 504 (1953).
3. A. de Bretteville, F. A. Holden, T. Vasilos, and L. Reed, *J. Am. Ceram. Soc.* **40**, 86 (1957).
4. V. A. Isupov and O. K. Khomutetskiĭ, *Zh. Tekh. Fiz.* **27** (12), 2704 (1957) [*Sov. Phys. Tech. Phys.* **2**, 2513 (1957)].
5. V. A. Isupov and G. I. Tarasova, *Fiz. Tverd. Tela (Leningrad)* **25** (4), 1013 (1983) [*Sov. Phys. Solid State* **25** (4), 584 (1983)]; *Fiz. Tverd. Tela (Leningrad)* **25** (4), 1018 (1983) [*Sov. Phys. Solid State* **25** (4), 587 (1983)].
6. V. A. Isupov, G. I. Golovshchikova, and I. E. Mylnikova, *Ferroelectrics* **8**, 507 (1974).
7. G. A. Smolenskiĭ, F. M. Salaev, L. S. Kamzina, N. N. Kraĭnik, and S. N. Dorogovtsev, *Pis'ma Zh. Ėksp. Teor. Fiz.* **37** (6), 257 (1983) [*JETP Lett.* **37** (6), 303 (1983)].
8. F. M. Salaev, L. S. Kamzina, N. N. Krainik, and V. M. Egorov, *Ferroelectrics* **98**, 75 (1989).
9. F. M. Salaev, L. S. Kamzina, N. N. Kraĭnik, A. L. Kholkin, and V. M. Egorov, *Pis'ma Zh. Tekh. Fiz.* **10** (10), 600 (1984) [*Sov. Tech. Phys. Lett.* **10** (10), 253 (1984)].
10. L. S. Kamzina, F. M. Salaev, N. N. Kraĭnik, S. N. Dorogovtsev, and G. A. Smolenskiĭ, *Fiz. Tverd. Tela (Leningrad)* **25** (9), 2846 (1983) [*Sov. Phys. Solid State* **25** (9), 1645 (1983)].
11. N. N. Kraĭnik, L. S. Kamzina, F. M. Salaev, I. E. Mylnikova, and E. S. Sher, *Fiz. Tverd. Tela (Leningrad)* **24** (6), 1701 (1982) [*Sov. Phys. Solid State* **24** (6), 970 (1982)].
12. F. M. Salaev, L. S. Kamzina, N. N. Kraĭnik, E. S. Sher, and G. A. Smolenskiĭ, *Fiz. Tverd. Tela (Leningrad)* **25** (1), 164 (1983) [*Sov. Phys. Solid State* **25** (1), 89

- (1983)]; *Fiz. Tverd. Tela* (Leningrad) **26** (10), 2997 (1984) [*Sov. Phys. Solid State* **26** (10), 1808 (1984)]; *Fiz. Tverd. Tela* (Leningrad) **27** (4), 1252 (1985) [*Sov. Phys. Solid State* **27** (4), 758 (1985)].
13. N. N. Kolpakova, I. G. Siniĭ, M. Polomska, and R. Margraf, *Fiz. Tverd. Tela* (Leningrad) **24** (6), 1729 (1982) [*Sov. Phys. Solid State* **24** (6), 985 (1982)].
 14. S. L. Swartz, C. A. Randall, and A. S. Bhalla, *J. Am. Ceram. Soc.* **72** (4), 637 (1989).
 15. Z. G. Ye, N. N. Kolpakova, J. P. Rivera, and H. Schmid, *Ferroelectrics* **124**, 275 (1991).
 16. G. I. Golovshchikova, L. S. Pogaĭdash, and V. A. Isupov, in *Solid State Physics and Chemistry*, Ed. by Yu. N. Venetsev (NIFKhI, Moscow, 1973), No. 4, p. 27.
 17. N. N. Kolpakova, R. Margraf, and M. Polomska, *J. Phys.: Condens. Matter* **6** (14), 2787 (1994).
 18. F. M. Salaev, L. S. Kamzina, and N. N. Kraĭnik, *Fiz. Tverd. Tela* (Leningrad) **34** (6), 1843 (1992) [*Sov. Phys. Solid State* **34** (6), 982 (1992)].
 19. I. P. Raevskii, M. A. Malitskaya, P. F. Tarasenko, O. I. Prokopalo, and Ya. E. Cherner, *Fiz. Tverd. Tela* (Leningrad) **25** (11), 3468 (1983) [*Sov. Phys. Solid State* **25** (11), 1997 (1983)]; *Zh. Tekh. Fiz.* **29** (7), 1325 (1984) [*Sov. Phys. Tech. Phys.* **29** (7), 763 (1984)].
 20. B. A. Strukov and A. P. Levanyuk, *Ferroelectric Phenomena in Crystals* (Nauka, Moscow, 1995; Springer, Berlin, 1998).
 21. I. K. Kamilov and S. N. Kallaev, *Phase Transitions in Ferroelectrics with an Incommensurate Structure* (Dagestan. NTs RAN, Makhachkala, 2002) [in Russian].
 22. V. A. Isupov and V. N. Skubitskii, *Fiz. Tverd. Tela* (Leningrad) **5** (3), 957 (1963) [*Sov. Phys. Solid State* **5** (3), 701 (1963)].
 23. G. A. Smolenskii, N. N. Kolpakova, S. A. Kizhaev, I. G. Siniĭ, V. V. Tikhonov, M. Polomska, R. Margraf, and E. S. Sher, *Fiz. Tverd. Tela* (Leningrad) **26** (4), 989 (1984) [*Sov. Phys. Solid State* **26** (4), 604 (1984)].
 24. N. N. Kolpakova, I. L. Shulpina, M. S. Shcheglov, S. Waplak, W. Bednarski, and M. Wiesner, *Ferroelectrics* **240**, 265 (2000).
 25. N. N. Kolpakova, *Ferroelectrics* **251**, 65 (2003).
 26. C. Ang, A. S. Bhalla, R. Guo, and L. E. Cross, *J. Appl. Phys.* **87**, 7452 (2000); **90**, 2465 (2001).
 27. I. N. Geifman, I. N. Kravtsova, and E. S. Sher, *Fiz. Tverd. Tela* (Leningrad) **28** (7), 2057 (1986) [*Sov. Phys. Solid State* **28** (7), 1150 (1986)].
 28. D. G. Demurov and Yu. N. Venetsev, *Fiz. Tverd. Tela* (Leningrad) **12** (8), 2460 (1970) [*Sov. Phys. Solid State* **12** (8), 1968 (1970)].
 29. G. A. Smolenskii, N. N. Kolpakova, and S. A. Kizhaev, *Pis'ma Zh. Éksp. Teor. Fiz.* **36** (8), 295 (1982) [*JETP Lett.* **36** (8), 361 (1982)].
 30. G. A. Smolensky, N. N. Kolpakova, and S. A. Kizhaev, *Ferroelectrics* **73**, 161 (1987).
 31. E. Buixaderos, S. Kamba, J. Petzelt, M. Savinov, and N. N. Kolpakova, *Eur. Phys. J. B* **19** (1), 9 (2001).
 32. N. N. Lawless, A. C. Anderson, and F. Walker, *Ferroelectrics* **37**, 627 (1981); **43**, 223 (1982).
 33. N. N. Kolpakova, *Zh. Éksp. Teor. Fiz.* **123** (3), 607 (2003) [*JETP* **96**, 538 (2003)].
 34. A. de Bretteville and R. M. Oman, *Bull. Am. Phys. Soc.* **4**, 62 (1959).
 35. N. N. Kolpakova, A. Pietraszko, S. Waplak, and L. Szczepanska, *Solid State Commun.* **79** (9), 707 (1991).
 36. B. E. Vugmeister and M. D. Glinchuk, *Rev. Mod. Phys.* **62** (4), 993 (1990).
 37. I. L. Shul'pina, N. N. Kolpakova, M. P. Shcheglov, and A. O. Lebedev, *Pis'ma Zh. Tekh. Fiz.* **25** (14), 26 (1999) [*Tech. Phys. Lett.* **25** (7), 561 (1999)].
 38. K. Lukaszewicz, A. Pietraszko, J. Stepień-Damm, and N. N. Kolpakova, *Mater. Res. Bull.* **29** (9), 987 (1994).

Translated by K. Shakhlevich

MAGNETISM AND FERROELECTRICITY

Comparative Analysis of the Phonon Modes in AgNbO₃ and NaNbO₃

S. A. Prosdandeev

Rostov State University, ul. Zorge 5, Rostov-on-Don, 344090 Russia

e-mail: pros@aaanet.ru

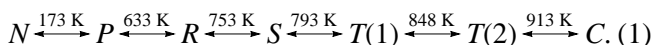
Received February 22, 2005

Abstract—The lattice dynamics of silver niobate AgNbO₃ and sodium niobate NaNbO₃ is calculated from first principles. The unstable modes (i.e., tilting of oxygen octahedra and ferroelectric atomic displacements) in silver and sodium niobates are analyzed. It is shown that the existence of ferroelectric modes is associated primarily with the instability of the atomic positions of silver and sodium in the crystal lattice. The dynamic charges in the structure of silver and sodium niobates are determined. According to the first-principles calculations, both silver and sodium niobates in the ground state ($T = 0$) are characterized by ferroelectric atomic displacements and frozen tilting of oxygen octahedra, with the only difference being that the tilting modes of the oxygen octahedra in silver niobate correspond to the M point of the Brillouin zone, whereas those in sodium niobate are attributed to the R point of the Brillouin zone. The results of these calculations are in good agreement with experimental data. © 2005 Pleiades Publishing, Inc.

1. INTRODUCTION

Silver niobate AgNbO₃ and sodium niobate NaNbO₃ [1–5] are promising materials for use in radio-telephone engineering. Upon doping, crystals of these compounds acquire properties inherent in relaxors, which, in turn, can also have extensive applications in various devices. The phase diagrams of silver and sodium niobates are complicated by the formation of a large number of phases due to tilting of the oxygen octahedra and ferroelectric atomic displacements. Both crystals at low temperatures are ferroelectrics. Moreover, these crystals exhibit ferroelectric properties in response to an electric field. At low temperatures, tilting of oxygen octahedra in the structure of silver and sodium niobates is accompanied by ferroelectric atomic displacements.

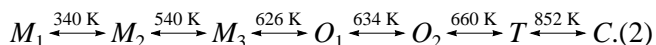
As the temperature increases, sodium niobate undergoes the following sequence of phase transitions (see [4] and references therein):



Here, the ground state N corresponds to the rhombohedral ferroelectric phase. This phase is characterized by both frozen tilting of oxygen octahedra of the $a^-a^-a^-$ type in the Megaw notation [2] and frozen rhombohedral ferroelectric atomic displacements. The above sequence of phase transitions was discussed earlier when solving the problem associated with the determination of the sequence of phase transitions in the high-temperature range [4, 5]. Note that the ground state of sodium niobate was beyond question.

As the temperature increases, silver niobate undergoes a somewhat different sequence of phase transi-

tions than that revealed for sodium niobate (see [4] and references therein):



Silver niobate in the ground state M_1 is characterized by both frozen displacements of oxygen octahedra of the $a^+a^+b^0$ type in the Megaw notation and frozen rhombohedral ferroelectric atomic displacements.

In this paper, we call attention to the fact that the ground states of silver and sodium niobates differ from each other. This fact has been reliably established, even though the above difference is observed only in the cryogenic temperature range. However, it should be noted that the thermodynamics of excited states (stabilized at relatively high temperatures), as a rule, is governed by the structure of the compound in the ground state. In this respect, the nature and structure of the ground state are of special interest.

The structure of a crystal in the ground state ($T = 0$) is governed by the atomic interaction constants, which, in turn, determine the frequencies of atomic vibrations. Thus, the structure and atomic vibrations correlate with each other. Indeed, it is known that the phase transition to the low-symmetry phase leads to the disappearance of the vibrational mode corresponding to the symmetry of this phase. This fact has been used in first-principles calculations, i.e., calculations that do not include fitting parameters, are based on the fundamental laws of quantum mechanics, and, as a rule, are performed within the density functional approximation.

The symmetry of the low-symmetry phase can be determined from *ab initio* calculations of the unstable modes in the high-symmetry phase. The unstable

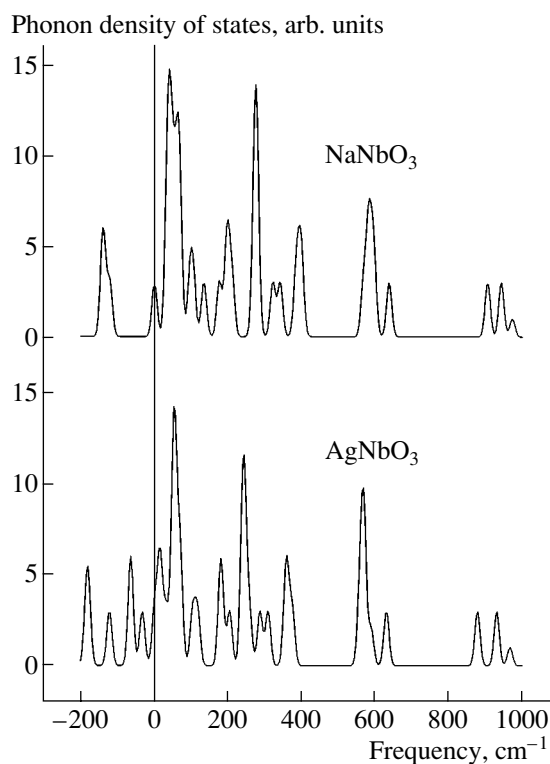
modes in the high-symmetry phase have a complex frequency, and their eigenvector indicates the direction and relative magnitudes of the atomic displacements in the low-symmetry phase (provided these displacements are sufficiently small, i.e., nonlinear effects do not substantially affect the results of the calculations). Calculations of the unstable modes (with complex frequencies) entail relatively low computational costs, and the results obtained make it possible to reveal crystal distortions that reduce the energy of the system. In order to refine these results, it is necessary to perform self-consistent calculations of the atomic coordinates in the low-symmetry phase.

This paper reports on the results of comparative *ab initio* calculations of the lattice dynamics in the cubic phases of sodium and silver niobates at $T = 0$. The purpose of these calculations is to determine the unstable modes and their eigenvectors for both crystals. We will discuss the nature of the ferroelectric and tilting modes in sodium and silver niobates (tilting of octahedra). This paper does not seek to calculate equilibrium atomic coordinates and frequencies of atomic vibrations in the ground state, because these calculations would require considerably more computer time. All the calculations are performed for cubic symmetry. This does not permit us to compare directly the obtained equilibrium (within the given symmetry) atomic coordinates and the frequencies of atomic vibrations with experimental data but does provide the fastest way of revealing the unstable modes.

2. CALCULATION TECHNIQUE AND RESULTS

The calculations were performed with the Vienna Ab Initio Simulation Package (VASP) [6, 7]. This program package provides a means for performing self-consistent quantum-mechanical calculations of the electronic structure on the basis of ultrasoft atomic potentials and the calculations of equilibrium atomic coordinates in crystal structures. The VASP code does not use any parameters. The electron wave functions and forces exerted on individual nuclei by electrons and ions are calculated for each set of atomic coordinates. The forces are minimized according to an efficient scheme.

In order to solve the formulated problem, the equilibrium parameters of the crystal structures were calculated with the cubic symmetry retained. A supercell composed of 40 atoms was used in both cases (silver and sodium niobates). This supercell is eight times larger than the primitive cell of the ABO_3 crystals. In the reciprocal space, we used an $8 \times 8 \times 8$ Monkhorst–Pack Grid. After complete relaxation of the lattice with retention of the cubic symmetry, we obtained the parameters $a = 7.9088 \text{ \AA}$ for silver niobate and $a = 7.9033 \text{ \AA}$ for sodium niobate. It should be noted that it is incorrect to compare these data with the experimental data directly, because the structures of both oxides in



Phonon densities of states for silver and sodium niobates. The phonon densities of states at negative frequencies correspond to the complex frequencies and are plotted along one vertical axis for the sake of clarity.

the ground state are strongly distorted by tilting of the oxygen octahedra.

Then, each atom was displaced in three possible directions by 0.01 \AA and the self-consistent quantum-mechanical calculations were again performed with a high degree of accuracy. The interatomic forces thus obtained were used to calculate the interatomic force constants and to construct the dynamic matrices for sodium and silver niobates. Let us now analyze the results of diagonalizing these matrices.

The calculated phonon densities of states are presented in the figure. It can be seen from this figure that both curves are similar to each other in the range of stable states. However, in the range of complex frequencies (for the sake of clarity, the density of complex frequencies is plotted in the range of negative frequencies with the same magnitudes), there are substantial differences. These differences can be analyzed using the detailed information on the modes presented in Tables 1 and 2. The analysis of these data revealed that a^+a^0 and a^-a^- are the dominant unstable modes in silver niobate and sodium niobate, respectively. Therefore, the instability in silver niobate corresponds to the M point of the Brillouin zone, whereas the instability in sodium niobate is attributed to the R point of the Brillouin zone. This can be associated with the somewhat

Table 1. Analysis of the instability of the phonon modes in silver niobate

Crystal	Frequency, cm^{-1}	Atoms	Point in the Brillouin zone	Designation	Type	Degeneracy
Silver niobate	184 <i>i</i>	O	<i>M</i>	$a^+a^+a^0$	$(\pi/a, \pi/a, 0)$	3
	178 <i>i</i>	O	<i>R</i>	$a^-a^-a^-$	$(\pi/a, \pi/a, \pi/a)$	3
	122 <i>i</i>	Ag, Nb, O	Γ		T_{1u}	3
	65 <i>i</i>	Nb, O	Σ		$(\pi/2a, \pi/2a, 0)$	6
	34 <i>i</i>	Nb	<i>M</i>		$(\pi/a, \pi/a, 0)$	3
Sodium niobate	140 <i>i</i>	O	<i>R</i>	$a^-a^-a^-$	$(\pi/a, \pi/a, \pi/a)$	3
	138 <i>i</i>	O	<i>M</i>	$a^+a^+a^0$	$(\pi/a, \pi/a, 0)$	3
	121 <i>i</i>	Na, Nb, O	Γ		T_{1u}	3

smaller size of sodium atoms as compared to silver atoms.

In sodium niobate, the difference between the ground state and the first excited state ($a^+a^+a^0$) is very small (Table 1). Consequently, the stable phase of sodium niobate in a “sodium niobate–silver niobate” solid solution should disappear even at a very low concentration of sodium niobate.

Apart from the tilting modes, the ferroelectric modes are also unstable in both cases. The frequencies of these modes in sodium and silver niobates are nearly identical (121 cm^{-1}). However, the ferroelectric mode along the [110] direction in silver niobate is predominantly unstable, whereas the vibrational mode at the Brillouin zone boundary along the [110] direction in sodium niobate is stable.

The analysis of the eigenvector of the ferroelectric mode demonstrates that both atoms *A* (Na, Ag) and *B* (Nb) move out of phase with oxygen atoms. Taking into account that the atomic mass of sodium is considerably smaller than the atomic mass of niobium, we can infer that the niobium atomic displacements corresponding to the ferroelectric mode are relatively small in sodium niobate (the relative displacements are determined by dividing the eigenvector into the square root of the mass). The atomic masses of silver and niobium are close to each other. As a consequence, in silver niobate, the niobium atoms make a significant contribution to the displacements, even though the displacements of the silver atoms are dominant. Therefore, the ferroelectric instability in silver niobate and, especially, in

sodium niobate is primarily determined by the instability of the centrosymmetric atom *A* (silver and sodium, respectively) rather than by the strong Lorentz field at the niobium atoms (as is the case with classical ferroelectrics of the potassium niobate type).

The ferroelectric instability in oxides, as a rule, is explained by the large dynamic charges. The dynamic charge is defined as the derivative of the polarization **P** with respect to the displacement \mathbf{r}_i of the *i*th atom [8]:

$$Z_{i\alpha\beta} = \frac{\partial P_\alpha}{\partial r_{i\beta}}. \quad (3)$$

In modern first-principles calculations, the polarization has been determined in the framework of the strictly quantum-mechanical approach with due regard for charge transfer between atoms upon their displacement and for the difference between the local field and the mean field. For this purpose, it is common practice to use the Berry phase approach. The VASP code enables one to calculate the Berry phases. We used this code in our calculations of the dynamic charges for sodium and silver niobates. The results of the calculations are presented in Table 3. It can be seen from this table that the dynamic charges of niobium and oxygen in silver niobate somewhat exceed those in sodium niobate. Hence, the inference can be made that the polarization in silver niobate should exceed the polarization in sodium niobate for identical displacements of niobium and oxygen atoms. To the best of our knowledge, data on the polarization in the low-temperature phases of these crystals are not available in the literature.

Table 4 lists the selected force constants obtained by dividing the force acting on the atom in its displacement by the atomic displacement. It is worth noting that these force constants correspond to the interaction between the atomic sublattices rather than to the interaction between individual atoms. As follows from analyzing these data, the inclusion of the interaction between the atoms leads to relatively large diagonal elements of the dynamic matrix. For sodium and silver niobates, we obtained the following results: 79, 197, 248, and 695 cm^{-1} (sodium niobate) and 76, 182, 214,

Table 2. Characteristics of the eigenvector of the unstable mode T_{1u} for sodium and silver niobates

Atom	Sodium niobate	Silver niobate
Ag	0.106	0.082
Nb	0.063	0.109
O _{par}	-0.087	-0.113
O _{perp}	-0.144	-0.194

Table 3. Results of calculating the dynamic charges Z_{zz} in the cubic structures of sodium and silver niobates

Atom	Sodium niobate	Silver niobate
A = Na, Ag	1.102	1.044
Nb	9.718	10.055
O _x	-2.270	-2.387
O _y	-2.270	-2.387
O _z	-6.280	-6.325

and 681 cm⁻¹ (silver niobate) for atoms Na (Ag), Nb, O (displacement perpendicular to the chemical bond), and O (displacement along the chemical bond), respectively. It can be seen from these data that the smallest values are obtained for atoms Na (Ag), which are responsible for the lattice dynamics. This is consistent with the results presented in Table 2. Moreover, the large off-diagonal elements of the force constants correspond to tilting of the oxygen octahedra. The complex values of the collective frequencies of polar atomic

Table 4. Selected force constants (eV/Å²) according to the calculations for sodium and silver niobates

Atom (displacement)	x	y	z	Atom (displacement)	x	y	z	Sodium niobate	Silver niobate
Nb(z)	0	0	0	O(z)	1/2	0	0	1.053	0.607
					0	0	1/2	2.746	3.157
					1	0	1/2	-0.171	-0.196
					1/2	1	0	0.084	0.112
					1/2	0	1	-2.027	-1.792
					1/2	1	1	-0.063	-0.140
					1	1	1/2	0.006	0.011
A(z)	1/2	1/2	1/2	Nb(z)	0	0	0	0.176	0.133
					O(z)	1/2	0	0	-0.182
Nb(z)	0	0	0	Nb(z)	0	0	1/2	0.496	0.315
					0	0	1	23.180	20.154
					1	0	0	-0.358	-0.393
					1	1	0	-0.191	-0.409
					1	0	1	0.482	0.483
					1	1	1	0.179	0.410
					1/2	1/2	1/2	0.360	0.390
A(z)	1/2	1/2	1/2	A(z)	1/2	1/2	1/2	0.360	0.390
					1 1/2	1/2	1/2	-0.121	-0.171
					1 1/2	1 1/2	1/2	-0.064	-0.111
					1 1/2	1/2	1 1/2	0.113	0.183
					1 1/2	1 1/2	1 1/2	0.063	0.102
					0	0	1/4	-1.308	-1.248
					1	0	1 1/2	10.544	10.369
O(z)	1/2	0	0	O(z)	1/2	0	1	1.447	1.304
					0	1/2	1	-0.003	-0.003
					0	0	1/2	-1.715	-1.343
					0	1	1/2	-0.530	-0.310
					0	1	1 1/2	0.537	0.396
					0	0	1 1/2	2.177	1.948
					0	1/2	0	-0.393	-0.458
					1/2	1	0	-0.061	-0.058
					1 1/2	1	0	0.027	0.021
					1 1/2	0	0	0.623	0.545
					1/2	0	1	0.322	0.273
					1 1/2	0	1	0.502	0.484
					1/2	1	1	0.044	0.053
					1	1/2	1	0.124	0.136

Note: The atomic coordinates are given in terms of the lattice constant of the primitive lattice.

vibrations and the tilting of the oxygen octahedra suggest that both types of motion are unstable at $T = 0$.

3. CONCLUSIONS

The results of the first-principles calculations performed in this work are in agreement with the experimental data available in the literature according to which the ground state of sodium niobate differs from that of silver niobate [3]. Both silver and sodium niobates in the ground state are characterized by rhombohedral ferroelectric displacements and frozen tilting of the oxygen octahedra; however, the tilting of the oxygen octahedra in sodium niobate corresponds to the R point of the Brillouin zone, whereas the tilting of the oxygen octahedra in silver niobate is related to the M point of the Brillouin zone. The new data obtained provide an explanation of the difference between the ground states of sodium and silver niobates at $T = 0$ and allow one to perform the calculations for solid solutions according to a similar scheme. Information on the nature of the unstable modes and their frequencies can be used in further investigation into solid solutions of these crystals.

ACKNOWLEDGMENTS

This work was supported by the Russian Foundation for Basic Research, project no. 04-02-16103.

REFERENCES

1. G. A. Smolenskii, V. A. Bokov, V. A. Isupov, N. N. Kraïnik, R. E. Pasynkov, A. I. Sokolov, and N. K. Yushin, in *Physics of Ferroelectric Phenomena* (Nauka, Leningrad, 1985) [in Russian].
2. H. D. Megaw, *Ferroelectrics* **7**, 87 (1974).
3. M. Ahtee and A. W. Hewat, *Acta Crystallogr., Sect. A: Cryst. Phys., Diffr., Theor. Gen. Crystallogr.* **34**, 309 (1978); *Acta Crystallogr. Sect. B: Struct. Crystallogr. Cryst. Chem.* **29**, 2171 (1973).
4. A. Kania and J. Kwapulinski, *J. Phys.: Condens. Matter* **11**, 8933 (1999).
5. C. N. W. Darlington and K. Knight, *Physica B (Amsterdam)* **266**, 368 (1999).
6. G. Kresse and J. Hafner, *Phys. Rev. B: Condens. Matter* **47**, 558 (1993).
7. G. Kresse and J. Furthmüller, *Phys. Rev. B: Condens. Matter* **54**, 11 169 (1996).
8. R. Resta, *Rev. Mod. Phys.* **66**, 899 (1994).

Translated by O. Borovik-Romanova

MAGNETISM AND FERROELECTRICITY

Pyroelectric Properties of Some Compounds Based on Protein Aminoacids

V. K. Yarmarkin*, S. G. Shul'man*, G. A. Pankova**, and V. V. Lemanov*

*Ioffe Physicotechnical Institute, Russian Academy of Sciences, ul. Politekhnikeskaya 26, St. Petersburg, 194021 Russia
e-mail: lemanov@mail.ioffe.ru

**Institute of Macromolecular Compounds, Russian Academy of Sciences, Bol'shoi' proezd 31, St. Petersburg, 119004 Russia
Received December 29, 2004; in final form, March 1, 2005

Abstract—Protein aminoacid-based compounds were synthesized, and their single crystals were grown. The dielectric and pyroelectric properties of the crystals were studied in the temperature ranges 80–340 and 140–340 K, respectively. It was established that three of the compounds studied (*L*-His(H₃PO₄)₂, *L*-TyrHCl, *L*-Ala₂H₃PO₃ · H₂O) are linear pyroelectrics, with their room-temperature pyroelectric figures of merit being close to those of ferroelectric triglycine sulfate crystals. © 2005 Pleiades Publishing, Inc.

1. INTRODUCTION

Investigation of the physical properties and crystal structure of compounds based on protein aminoacids has been attracting considerable interest (see, e.g., [1]). The present study deals with the dielectric and pyroelectric properties of some of these materials. The piezoelectric properties of these compounds were studied previously in [2].

2. EXPERIMENTAL TECHNIQUES

The crystals to be studied were grown from saturated aqueous solutions of the appropriate aminoacids and inorganic substances by slow cooling from 25 to 8°C at a rate of 1 K/day. The chemical composition of the compounds under study was obtained by elemental analysis. The crystal symmetry and orientation of the crystallographic axes were derived from x-ray diffraction measurements. The crystals studied have monoclinic or orthorhombic symmetry; i.e., they belong to the C_{2h} or D_{2h} diffraction classes.

The samples intended for study were cut from single crystals in the form of 0.1- to 0.2-mm-thick platelets 5–10 mm² in area, with the major plane oriented perpendicular to the C_2 symmetry axes. Conducting electrodes were deposited from a suspension of finely dispersed silver. Measurements were conducted in vacuum at a pressure of 10⁻⁴ bar.

The pyroelectric response of the crystals was measured through stepwise illumination with infrared light. In this method, the kinetics of variation of the temperature of the crystals, ΔT , and of the pyroelectric voltage U induced across them by the radiation are described by the differential equations [3]

$$C_T \frac{d(\Delta T)}{dt} + G_T \Delta T = AF_0, \quad (1)$$

$$C \frac{dU}{dt} + \frac{U}{R} = Ap \frac{dT}{dt}, \quad (2)$$

where C_T is the heat capacity of the sample measured in J/K; G_T is a coefficient in units of W/K characterizing heat exchange between the sample and its environment; A is the sample area in m²; F_0 is the radiation power absorbed by a unit area of the crystal under illumination in units of W/m²; C and R are the capacitance and the resistance of the crystal with the amplifier capacitance and load resistance connected parallel to it, respectively; and p is the pyroelectric coefficient. As follows from these equations, the shape of a pyroelectric signal is determined by two time constants, namely, the electronic time $\tau_e = RC$, characterizing the rise of the pyroelectric response of the sample after the switching on of illumination, and the thermal time $\tau_T = C_T/G_T$, characterizing the attainment of thermal equilibrium under constant illumination intensity.

In our experiments, the relation $\tau_e \ll \tau_T$ held ($\tau_e \leq 1$ s, $\tau_T \geq 5$ s). In accordance with the conclusions reached in [3], the peak pyroelectric response voltage under illumination of a crystal is given by

$$U_p = pAF_0R/c_pL, \quad (3)$$

where c_p and L are the specific heat and the thickness of the crystal, respectively.

In the present study, we used techniques that included either single illumination on-off cycles about 1 min long in intervals of a few minutes or periodic trains with illumination pulses 1 s long in intervals of 10 s. Figure 1 presents the voltage diagrams corresponding to these techniques, with the voltage proportional to the light intensity incident on the crystal (top diagrams in Figs. 1a, 1b) and the pyroelectric response (bottom diagrams). The source of radiation was an

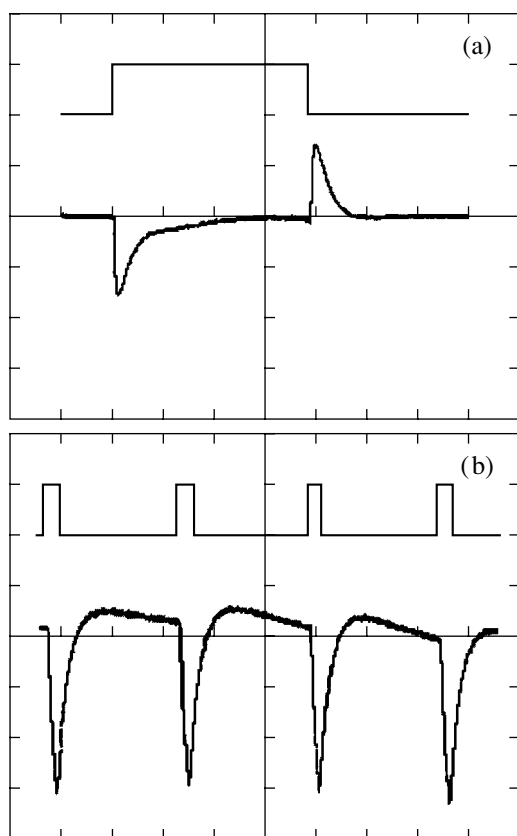


Fig. 1. Voltages across a load resistance of the photodiode (top curves) and a load resistance of the pyroelectric detector (bottom curves) obtained under (a) single and (b) cyclic illumination of the crystal under study. The illumination pulse length is (a) 1 min and (b) 1 s.

incandescent lamp with a 0.2-mm-thick filter of undoped silicon; the heat flux incident on a crystal was varied in the range 1–100 mW/cm². The illumination intensity was monitored with an FD-1 photodiode placed in the measurement chamber in the immediate proximity of the crystal and connected in the photodiode mode (i.e., with a voltage of ~1 V applied in the blocking direction).

As is evident from Fig. 1a, the pyroelectric response signals generated immediately after the illumination was switched on and off are practically identical, which indicates the absence of any noticeable contribution to

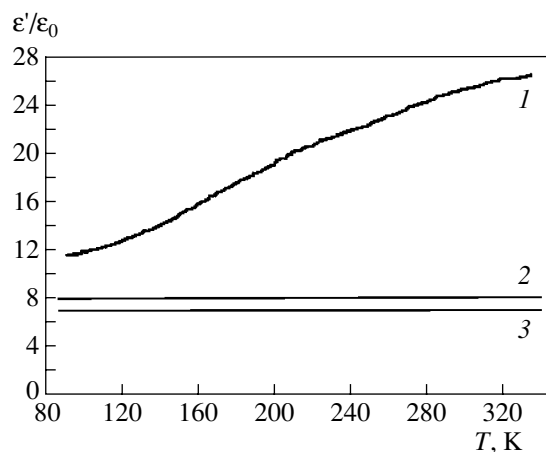


Fig. 2. Temperature dependences of the dielectric permittivity of (1) *L*-His(H₃PO₄)₂, (2) *L*-TyrHCl, and (3) *L*-Ala₂H₃PO₃ · H₂O.

the pyroelectric response due to a possible temperature difference between the illuminated and nonilluminated crystal surfaces. The specific shape of the pyroelectric response voltage pulses observed under periodic illumination (Fig. 1b) is accounted for by the superposition of the signals of opposite polarity generated after the application and termination of the illumination pulses. However, as follows from Eqs. (1) and (2) and is supported by direct measurements, the peak voltage in this case is also proportional to the pyroelectric coefficient of the crystal studied. Periodic illumination permits one to obtain continuous recording of U_p under a variation in crystal temperature.

The voltage drop across the load resistance of 100 MΩ was fed into an operational amplifier based on a KR544-UD-1A chip with a voltage gain of unity and, thereafter, into an electronic recorder. The load resistance was chosen so as to provide a high enough pyroelectric current measurement accuracy (of about 10⁻¹² A), on the one hand, while reducing the crystal resistance (to values of about 10⁹ Ω at the upper limit of the temperature range covered), on the other.

The dielectric permittivity and the loss tangent were measured with an E7-12 bridge at a frequency of 1 MHz and a voltage amplitude of 100 mV.

Symmetry and room-temperature pyroelectric figure-of-merit coefficients ($\epsilon_0 = 8.85 \times 10^{-12}$ F/m is the permittivity of vacuum)

Compound	Symmetry	p_i , nC/cm ² K	ϵ'/ϵ_0	ϵ''/ϵ_0	$F_i = p_i/c_p$, nA cm/W	$F_u = p_i/\epsilon'c_p$, V cm ² /J	$F_D = p_i/c_p(\epsilon'')^{1/2}$, (cm ³ /J) ^{1/2}
TGS	C_2	30	50	0.16	17.8	4000	0.149
<i>L</i> -His(H ₃ PO ₄) ₂	C_2	6	25	0.20	3.5	1600	0.04
<i>L</i> -TyrHCl	C_{2v}	3	8	0.02	1.5	2500	0.06
<i>L</i> -Ala ₂ H ₃ PO ₃ · H ₂ O	C_2	2.7	7	0.02	1.6	3200	0.07

3. EXPERIMENTAL RESULTS AND DISCUSSION

The table lists the measured dielectric permittivity and pyroelectric coefficients of *L*-histidine phosphate (*L*-His(H₃PO₄)₂) [5], *L*-tyrosine hydrochloride (*L*-TyrHCl), and di(*L*-alanine) phosphite monohydrate (*L*-Ala₂H₃PO₃ · H₂O) [6], which exhibited the highest pyroelectric activity over the temperature interval covered, and analogous data for triglycine phosphate (TGS) [4], which was chosen for comparison. (Taking into account the small size of the crystals studied and the limited accuracy of measurement of their capacitance, the error with which the reduced real (ϵ'/ϵ_0) and imaginary (ϵ''/ϵ_0) parts of the dielectric permittivity were determined is about 10%.) The table also specifies the crystal symmetry derived in this study from the diffraction class of symmetry accounting for the results of pyroelectric measurements. The symmetry group of the *L*-His(H₃PO₄)₂ and *L*-Ala₂H₃PO₃ · H₂O crystals is consistent with the available literature data [5, 6].

The values of the pyroelectric response of other crystalline compounds based on protein aminoacids differ by more than three orders of magnitude. The pyroelectric response of some crystals with a diffraction class of symmetry D_{2h} , such as *L*-asparagine, *L*-arginine hydrochloride, and *L*-tyrosine hydrochloride, measured along one of the three orthogonal C_2 axes substantially exceeds (by one to two orders of magnitude) the values obtained along the two other axes, thus giving one grounds to assign these crystals to the C_{2v} symmetry group, which is a subgroup of the group of diffraction symmetry D_{2h} .

The temperature dependences of the dielectric permittivity and pyroelectric response of the crystals did not reveal any features in the temperature interval studied (Figs. 2, 3). Note that the pyroelectric response of the crystals, as well as their dielectric permittivity, was not affected by prepolarization of the crystals by applying a dc electric field of ± 10 kV/cm within the interval from room temperature to 80 K and that no dielectric hysteresis was observed, which implies that these crystals are not ferroelectrics.

Since experimental data on the piezoelectric moduli e_{ikl} and thermal expansion coefficients α_{kl} of these crystals are lacking, we cannot separate the primary, p_i^I , and secondary, $p_i^{II} = e_{ikl}\alpha_{kl}$, components of the total pyroelectric coefficient, which determines the polarization variation of the crystals $\Delta P_i = (p_i^I + p_i^{II})\Delta T$.

In view of the relatively large pyroelectric coefficients of the *L*-His(H₃PO₄)₂, *L*-TyrHCl, and *L*-Ala₂H₃PO₃ · H₂O crystals and their relatively low dielectric permittivity, it is of interest to compare these crystals with TGS in terms of their pyroelectric figure-of-merit coefficients [4]. Estimates of these coefficients for the current sensitivity (F_i), voltage sensitivity (F_u),

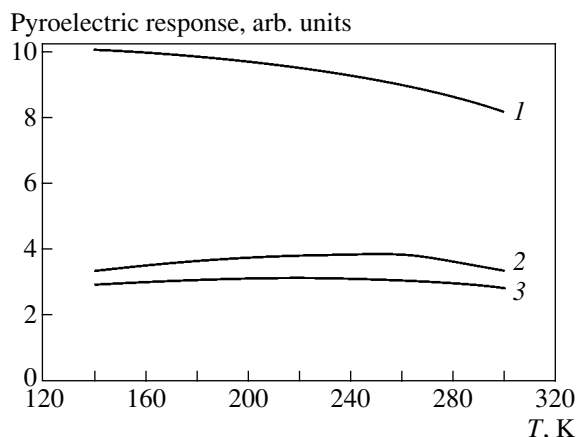


Fig. 3. Temperature dependences of the pyroelectric response of (1) *L*-His(H₃PO₄)₂, (2) *L*-TyrHCl, and (3) *L*-Ala₂H₃PO₃ · H₂O.

and detectability (F_D) are listed in the table. Because of the lack of experimental data on the specific heat c_p of the crystals under study, their figure-of-merit coefficients were calculated using the value $c_p = 1.7$ J/cm³ K for TGS crystals. From examining the table, it becomes evident that some of the figure-of-merit coefficients of the crystals studied here are comparable to those of the TGS crystals.

ACKNOWLEDGMENTS

The authors are indebted to N.V. Zaitseva for carrying out the x-ray diffraction measurements.

This study was supported in part by the Russian Foundation for Basic Research (project no. 02-02-17666), the Russian Foundation for Support of Leading Scientific Schools (project no. NSh-2168.2003.2), and the Department of Physical Sciences of the Russian Academy of Sciences.

REFERENCES

1. V. V. Lemanov, *Ferroelectrics* **238**, 211 (2000).
2. V. V. Lemanov, S. N. Popov, and G. A. Pankova, *Fiz. Tverd. Tela (St. Petersburg)* **44** (10), 1840 (2002) [*Phys. Solid State* **44** (10), 1929 (2002)].
3. M. Simhony and A. Shaulov, *J. Appl. Phys.* **42**, 3741 (1971).
4. M. E. Lines and A. M. Glass, *Principles and Applications of Ferroelectrics and Related Materials* (Clarendon, Oxford, 1977; Mir, Moscow, 1981).
5. R. H. Blessing, *Acta Crystallogr., Sect. B: Struct. Sci.* **42**, 613 (1986).
6. Yu. I. Smolin, A. E. Lapshin, and G. A. Pankova, *Zh. Strukt. Khim.* **44**, 564 (2003).

Translated by G. Skrebtsov

LATTICE DYNAMICS
AND PHASE TRANSITIONS

Effect of γ Irradiation on the Thermochromic Phase Transition in $[(C_2H_5)_2NH_2]_2CuCl_4$ Crystals (as Derived From Heat Capacity Measurements)

A. U. Sheleg, T. I. Dekola, and N. P. Tekhanovich

*Institute of Solid State Physics and Semiconductors, National Academy of Sciences of Belarus,
ul. P. Brovki 17, Minsk, 220072 Belarus*

e-mail: sheleg@iftp.bas-net.by

Received November 15, 2004

Abstract—The heat capacity of $[(C_2H_5)_2NH_2]_2CuCl_4$ crystals, both nonirradiated and γ -irradiated to a dose of 10^7 R, was studied in the temperature interval 90–330 K by adiabatic calorimetry. The temperature dependence of $C_p(T)$ was found to have a peak-shaped anomaly in the region of the thermochromic phase transition (PT) at $T = 322.7$ K. Smoothed experimental heat capacity data were used to calculate the changes in the thermodynamic functions. The changes in the entropy and enthalpy of the thermochromic PT were determined to be $\Delta S = 42$ J K⁻¹ mol⁻¹ and $\Delta H = 13653$ J mol⁻¹ for the nonirradiated crystals and $\Delta S = 39$ J K⁻¹ mol⁻¹ and $\Delta H = 12120$ J mol⁻¹ for the irradiated crystals, respectively. Irradiation of a $[(C_2H_5)_2NH_2]_2CuCl_4$ crystal by γ rays to a dose of 10^7 R was shown to shift the PT point toward lower temperatures by $\Delta T \approx 1.7$ K. © 2005 Pleiades Publishing, Inc.

1. INTRODUCTION

The $[(C_2H_5)_2NH_2]_2CuCl_4$ compound belongs to a large family of A_2BX_4 crystals most of which feature a sequence of temperature-driven phase transitions (PTs). The structure of the various phases of these crystals is determined by a balance of hydrogen bonds coupling the structural components, namely, molecular cations and metal–halogen complexes. This accounts for the PT parameters in these crystals being very sensitive to external factors of various types, including γ irradiation.

The A_2BCl_4 compounds [where A stands for $(C_2H_5)_2NH_2$ and B stands for (Cu, Co)] represent a new class of thermochromic materials, which are known to have application potential in optoelectronics. The $[(C_2H_5)_2NH_2]_2CuCl_4$ crystal undergoes a thermochromic PT at $T = 323$ K, which changes the crystal color from green to yellow with increasing temperature [1]. The nature of this phenomenon is still very poorly understood. It should be pointed out, however, that the manifestation of the thermochromic effect is dominated in this case by hydrogen bonds, which account for the deformation of structural blocks in the crystal lattice. Studies of the nature of the PT in $[(C_2H_5)_2NH_2]_2CuCl_4$ have revealed [1, 2] that the thermochromic transition in this crystal is driven by a change in the coordination geometry of the Cu^{2+} ion from plane square to tetrahedral, which is reflected in a change in the absorption spectra.

Since this promising crystal has remained practically unstudied (with only a few publications avail-

able), it appeared worthwhile to measure its heat capacity in the low-temperature domain, including the PT region, and to investigate the effect of γ irradiation on the parameters of this PT.

2. EXPERIMENTAL TECHNIQUE

Crystals of $[(C_2H_5)_2NH_2]_2CuCl_4$ were grown from an aqueous solution of a stoichiometric mixture of $CuCl_2 \cdot 2H_2O$ and $[(C_2H_5)_2NH_2]Cl$ by slow evaporation at a temperature $T \approx 300$ K. Bulk green crystals grew in 3 to 4 weeks to a size $\sim 10 \times 6 \times 3$ mm.

The heat capacity was measured in the temperature interval 90–330 K using a setup with automatic temperature control in a vacuum adiabatic calorimeter with discrete heat injection in steps of 1–1.5 K. The sample 5.8233 g in weight was placed in the calorimeter 10 cm³ in volume, which was sealed in a helium atmosphere.

In the PT region, the measurements were conducted in temperature steps of 0.2–0.5 K. The sample was heated at a rate of 0.07–0.10 K/min. The error in the heat capacity measurements as estimated against a KV-grade quartz reference did not exceed 0.3% in the temperature interval covered. In the region near the PT, the accuracy of measurement was lower, because thermal equilibrium was reached in this region in 2.5–4.0 h, whereas both above and below the PT the equilibration time was 7–10 min. The experimental heat capacity data were least squares fitted with a cubic-power law.

The sample was irradiated at room temperature with Co^{60} γ rays at dose rates of ~ 80 R/s in the irradiation region.

3. EXPERIMENTAL RESULTS AND DISCUSSION

Figure 1 illustrates heat capacity measurements performed on a nonirradiated $[(\text{C}_2\text{H}_5)_2\text{NH}_2]_2\text{CuCl}_4$ crystal. The $C_p(T)$ curve reveals a clearly pronounced anomaly in the form of a fairly high symmetric peak at a temperature $T = 322.7$ K. The sharp anomaly in the heat capacity, as well as the increase in the thermal equilibration time in the PT region observed in the course of the experiment, strongly suggests that the PT at $T = 322.7$ K is a first-order transition. In order to avoid the merge of points, not all experimental data obtained were used to construct the $C_p(T)$ curve. The PT temperature determined by us almost coincides with the value $T = 323$ K quoted in [1] while slightly exceeding $T = 311$ K, the value derived from optical measurements [2].

Using numerical integration, the changes in the entropy and enthalpy due to this PT were determined to be $\Delta S = 42 \text{ J K}^{-1} \text{ mol}^{-1}$ and $\Delta H = 13653 \text{ J mol}^{-1}$, respectively. The smoothed values of the heat capacity and the changes in the thermodynamic functions (entropy S , enthalpy H , Gibbs free energy Φ) as derived from these values for the $[(\text{C}_2\text{H}_5)_2\text{NH}_2]_2\text{CuCl}_4$ crystal are listed in the table.

Note the large values of ΔS and ΔH . As pointed out in [1], the reason for this lies in the fact that the PT in this crystal not only entails disorder in individual blocks but also gives rise to a radical structural rearrangement of the lattice.

Our experimental values $\Delta S = 42 \text{ J K}^{-1} \text{ mol}^{-1}$ and $\Delta H = 13653 \text{ J mol}^{-1}$ for the PT in $[(\text{C}_2\text{H}_5)_2\text{NH}_2]_2\text{CuCl}_4$

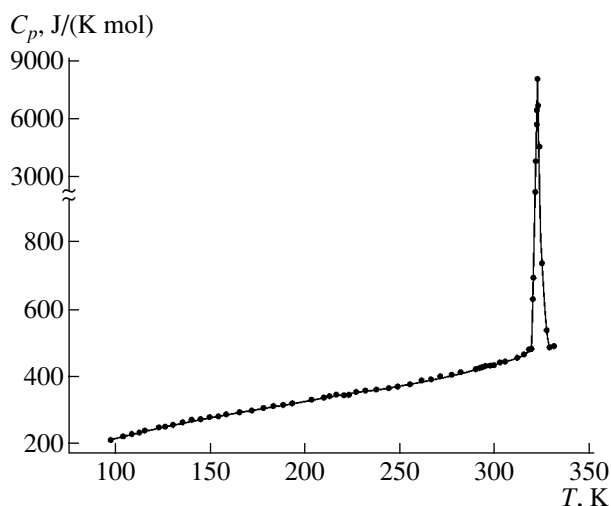


Fig. 1. Temperature dependence of the heat capacity of $[(\text{C}_2\text{H}_5)_2\text{NH}_2]_2\text{CuCl}_4$.

at $T = 322.7$ K are consistent with the values $\Delta S = 45(3) \text{ J K}^{-1} \text{ mol}^{-1}$ and $\Delta H = 14.6(9) \text{ kJ mol}^{-1}$ obtained by differential scanning calorimetry in [1].

Figure 2 presents the experimental temperature dependences of the heat capacity in the region of the phase transition for $[(\text{C}_2\text{H}_5)_2\text{NH}_2]_2\text{CuCl}_4$ crystals both nonirradiated and γ -irradiated to a dose of 10^7 R. We readily see that γ irradiation shifts the anomaly in the $C_p(T)$ curve at $T = 322.7$ K toward lower temperatures by $\Delta T \approx 1.7$ K. The calculated changes in the entropy and enthalpy due to the PT at $T' = 321.0$ K for the irradiated $[(\text{C}_2\text{H}_5)_2\text{NH}_2]_2\text{CuCl}_4$ sample are $\Delta S = 39 \text{ J K}^{-1} \text{ mol}^{-1}$ and $\Delta H = 12120 \text{ J mol}^{-1}$. Irradiation of $[(\text{C}_2\text{H}_5)_2\text{NH}_2]_2\text{CuCl}_4$ crystals ruptures hydrogen bonds. Heating of irradiated $[(\text{C}_2\text{H}_5)_2\text{NH}_2]_2\text{CuCl}_4$ samples with broken hydrogen

Smoothed heat capacity data and changes in the thermodynamic functions of $[(\text{C}_2\text{H}_5)_2\text{NH}_2]_2\text{CuCl}_4$

$T, \text{ K}$	$C_p(T)$	$S(T) - S(80 \text{ K})$	$\Phi(T) - \Phi(80 \text{ K})$	$H(T) - H(80 \text{ K}), \text{ J/mol}$
	J/(K mol)			
80	199.7	0.000	0.000	0.0
100	221.5	47.11	10.8	4212
120	243.5	89.54	25.8	8860
140	265.1	128.7	4.6	13944
160	286.9	165.6	60.1	19464
180	308.7	200.7	77.9	25420
200	330.5	234.4	95.7	31812
220	352.3	266.9	113	38640
240	374.1	298.5	130	45904
260	395.9	329.3	148	53604
280	417.7	359.5	165	61740
300	439.5	389.0	182	70312

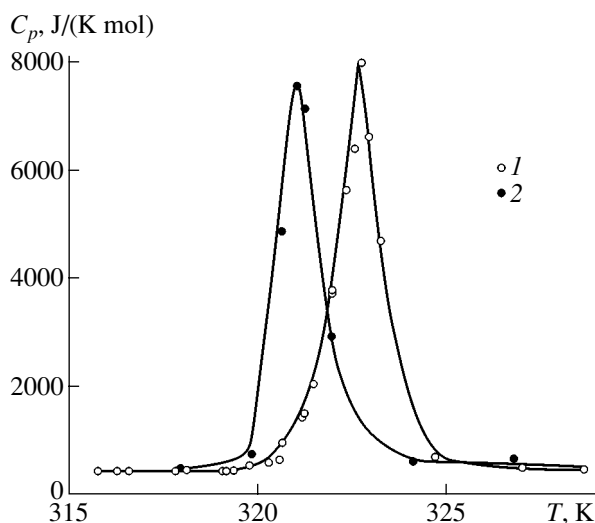


Fig. 2. Temperature dependence of the heat capacity of $[(C_2H_5)_2NH_2]_2CuCl_4$ in the region of the thermochromic phase transition for (1) a nonirradiated sample and (2) a sample irradiated to a dose of 10^7 R.

bonds brings about not only intensified ion thermal motion but also rearrangement of the crystal structure. As a result of this rearrangement, the high-temperature phase stabilizes at a temperature $T' = 321.0$ K, which is lower than that of the thermochromic PT in a nonirradiated sample. We thus see that the thermochromic PT in

$[(C_2H_5)_2NH_2]_2CuCl_4$ crystals is sensitive to ionizing radiation. Analogous results were obtained in [2] when studying the absorption spectra of nonirradiated $[(C_2H_5)_2NH_2]_2CuCl_4$ samples and samples irradiated with Co^{60} and Ra^{226} isotopes. The shift of the PT temperature in $[(C_2H_5)_2NH_2]_2CuCl_4$ under low irradiation doses was shown to be reversible [2]. In view of the clearly pronounced thermochromic effect and the high sensitivity of the thermochromic PT temperature to radiation, these materials may have application potential in sensors of ionizing radiation.

ACKNOWLEDGMENTS

The authors are indebted to N.F. Kurilovich for his assistance in the sample irradiation.

The support of the Belarus Basic Research Foundation (project no. F04-005) is gratefully acknowledged.

REFERENCES

1. D. R. Bloomquist, M. R. Pressprich, and R. D. Willet, *J. Am. Chem. Soc.* **110**, 7391 (1988).
2. V. B. Kapustyanyk and Yu. M. Korchak, *Zh. Prikl. Fiz.* **67** (6), 759 (2000).

Translated by G. Skrebtsov

**LATTICE DYNAMICS
AND PHASE TRANSITIONS**

Ultrafast Semiconductor–Metal Phase Transition in Vanadium Dioxide Induced by a Femtosecond Laser Pulse

A. L. Semenov

Ul'yanovsk State University, Ul'yanovsk, 432970 Russia

e-mail: smnv@mail.ru

Received December 21, 2004

Abstract—A model is proposed for a photoinduced Peierls-type semiconductor–metal phase transition that makes it possible to determine the time dependence of the bandgap width in the electronic spectrum of vanadium dioxide subjected to a light field and the dependence of the time at which a photoinduced semiconductor–metal phase transition occurs on the laser pulse duration. The theoretical results obtained are consistent with experimental data on the illumination of a VO₂ film with an intense laser pulse. © 2005 Pleiades Publishing, Inc.

1. INTRODUCTION

Experiments have shown [1] that an intense laser pulse incident on a vanadium dioxide film on a substrate transfers the film from the semiconducting to metallic state while heating it by less than 10 K [2]. This phase transition cannot be interpreted in terms of the thermal model because the onset of thermal instability would require heating of a VO₂ film by about 50 K (up to 340 K) [3]. The nonthermal (for times $t < 1$ ps) and thermal (for $t \approx 3$ –15 ps) stages in the development of a photoinduced semiconductor–metal phase transition have been observed experimentally to occur in VO₂ subjected to a laser pulse $\tau_p \approx 50$ fs long [4]. In [5], a vanadium dioxide film was illuminated with a laser pulse of energy density $W \approx 50$ mJ/cm² and photon energy $\hbar\omega \approx 1.6$ eV. The dependence of the time τ to the onset of the photoinduced semiconductor–metal phase transition on the laser pulse duration τ_p was found in [5] for τ_p swept from 15 to 1000 fs. As far as we are aware, the measured experimental relation has thus far not been interpreted theoretically.

We report on a theoretical investigation of the dynamics of the photoinduced semiconductor–metal phase transition in vanadium dioxide. The nonthermal mechanism of the onset of instability is considered. An equation for the order parameter ξ of the metal–semiconductor phase transition in a light field is derived. The time dependence of the bandgap width in the electronic spectrum is found. The time τ at which a photoinduced phase transition occurs is calculated as a function of the duration τ_p of the incident laser pulse. The theory developed is used to interpret the experimental data from [5] on the illumination of a vanadium dioxide film on a substrate by an intense laser pulse.

2. BASIC EQUATIONS

The electronic spectrum of vanadium dioxide has a quasi-one-dimensional band deriving from the overlap of the 3*d* electronic wave functions of vanadium atoms arranged in parallel chains [3]. The wave-function overlap along the chains is substantially larger than that in a perpendicular direction, thus permitting one to treat this system within a one-dimensional model.

Consider a chain of atoms bearing one outer electron each. It is known that, at a temperature T below a certain critical value T_0 , the equidistant arrangement of atoms in a chain becomes unstable with respect to their pairwise approach [6]. As a result, a bandgap appears in the electronic spectrum at the Fermi level.

The coordinate x_n of the n th vanadium atom in a chain can be written as

$$x_n = na + \frac{(-1)^n R \xi}{2}, \quad (1)$$

where a is the atomic separation in the metallic phase, ξ is a parameter characterizing the pairwise approach of atoms in the chain (the order parameter of the metal–semiconductor phase transition), and R is the effective radius of the electron wave function in an atom. The evolution of the order parameter ξ with time is described by the Lagrange equation:

$$\frac{d}{dt} \frac{\partial L}{\partial \dot{\xi}} - \frac{\partial L}{\partial \xi} = Q, \quad (2)$$

where Q is the generalized dissipative force corresponding to the generalized coordinate ξ ; L is the Lagrangian

$$L = \sum_n \frac{m \dot{x}_n^2}{2} - F_1 - F_2 - F_c, \quad (3)$$

m is the atomic mass;

$$F_c = \frac{A\xi^2}{2} \quad (4)$$

is the free energy of the crystal lattice written in the harmonic approximation, which takes into account only the first nonvanishing term in the Taylor expansion in the order parameter ξ (A is the expansion coefficient); F_j are the free energies corresponding to the valence ($j = 1$) and conduction ($j = 2$) bands of the electronic subsystem,

$$F_j = \mu_j N_j - 2k_B T \sum_k \ln \left(1 + \exp \left(\frac{\mu_j - \varepsilon_j(k)}{k_B T} \right) \right), \quad (5)$$

μ_j , N_j , and $\varepsilon_j(k)$ are the quasi-Fermi level, the number of electrons, and the j th-band dispersion law, respectively; T is the temperature; and k_B is the Boltzmann constant. The factor of 2 before the summation sign in Eq. (5) accounts for spin degeneracy. The dispersion law $\varepsilon_j(k)$ of d -band electrons for a vanadium atom chain in vanadium dioxide described by Eq. (1) can be cast in the form [7]

$$\varepsilon_{1,2}(k) = \mp 2b \sqrt{\cos^2 k + \sinh^2 \xi}. \quad (6)$$

Here, $4b$ is the conduction band width in the metallic phase (for $\xi = 0$) and $k = -\pi + 2\pi s/N_0$, where $s = 1, 2, \dots, N_0$ and N_0 is the number of atoms in the chain.

Substituting Eq. (3) into Eq. (2) and taking into account Eqs. (1) and (4)–(6), we arrive at

$$\ddot{\xi} = \frac{4}{N_0 m R^2} \left(Q N_0 - A \xi - 2 \sum_{k,j} \frac{\partial \varepsilon_j(k)}{\partial \xi} n_j(k) \right), \quad (7)$$

where

$$n_j(k) = 1 + \exp \left(\frac{\varepsilon_j(k) - \mu_j}{k_B T} \right) \quad (8)$$

is the electron occupation number of the k th level in the j th band.

Accepting the relaxation time approximation ($Q \sim \dot{\xi}$), we calculate roughly the sum in Eq. (7) for $\xi < 1$ to find

$$\begin{aligned} \ddot{\xi} + \gamma \dot{\xi} = & -\frac{4}{N_0 m R^2} \\ & \times \left(\frac{4bN_0}{\pi} \xi \ln \xi + 2b(N_0 - N_1 + N_2) + A \xi \right), \end{aligned} \quad (9)$$

where γ^{-1} is the characteristic phonon relaxation time. At $T = 0$, all electrons in the absence of illumination are in the valence band ($N_1 = N_0$, $N_2 = 0$) and the order

parameter for the metal–semiconductor phase transition is $\xi = \xi_0$. In this case, we obtain from Eq. (9)

$$A = -\frac{4bN_0}{\pi} \ln \xi_0, \quad (10)$$

$$\ddot{\xi} + \gamma \dot{\xi} = \frac{4b}{\pi m R^2} \left(\xi \ln \frac{\xi_0}{\xi} - \frac{\pi}{2N} (n + p) \right), \quad (11)$$

where N , n , and p are the concentrations of vanadium atoms, of electrons in the conduction d band, and of holes in the valence d band, respectively.

The time dependence of the hole concentration is described by the rate equation [8]

$$\dot{p} = \frac{(1-r)\alpha I}{\hbar \omega} - \frac{p}{\tau_1}, \quad (12)$$

where α and r are the optical absorption and reflection coefficients, respectively; ω and I are the frequency and intensity of the light field, respectively; and $\tau_1(p, \xi)$ is the recombination time. The film thickness is assumed to be much smaller than the optical radiation attenuation length $1/\alpha$.

3. RESULTS OF NUMERICAL ANALYSIS

Equations (11) and (12) were numerically solved for the following parameter values [3, 9]: vanadium atom concentration $N \cong 3 \times 10^{22} \text{ cm}^{-3}$, conduction d -band width in the metallic phase $4b \cong 1.1 \text{ eV}$, bandgap width in electronic spectrum (6) in the low-temperature semiconductor phase $\varepsilon_0 = 4b \sinh \xi_0 \cong 0.6 \text{ eV}$, vanadium atomic mass $m \cong 8.5 \times 10^{-23} \text{ g}$, and effective electron wave-function radius in the $3d$ state $R \cong 4.1 \times 10^{-9} \text{ cm}$. For a photon energy $\hbar \omega \cong 1.6 \text{ eV}$, the optical reflectance is $r \cong 0.2$ [5] and the optical absorbance is $\alpha \cong 2.3 \times 10^4 \text{ cm}^{-1}$. The characteristic room-temperature phonon relaxation time is $\gamma^{-1} \approx 5 \times 10^{-13} \text{ s}$ [10].

In the experiment described in [5], photons of energy $\hbar \omega \cong 1.6 \text{ eV}$ excited electrons from the valence d band into the conduction π band. The effective lifetime of nonequilibrium electrons present in a concentration $n_\pi \sim 10^{20} \text{ cm}^{-3}$ [2] in the conduction π band is $\sim 10^{-9} \text{ s}$ [1]. Therefore, for $n_\pi \sim 10^{21} \text{ cm}^{-3}$ and $t < 10^{-12} \text{ s}$, the second term on the right-hand side of Eq. (12) may be neglected. In Eq. (11), the electron concentration in the conduction d band satisfies the inequality $n \ll p$.

The dependence of the light field intensity I on time t was chosen to be a Gaussian pulse,

$$I(t) = \frac{2W}{\sqrt{\pi}\tau_p} \exp[-(2t/\tau_p)^2], \quad (13)$$

where W and τ_p are the energy density and pulse duration, respectively. The numerical analysis of Eqs. (11)–(13) was performed for the initial conditions

$$p(t = -2\tau_p) = 0, \quad \varepsilon(t = -2\tau_p) = 0.6 \text{ eV}. \quad (14)$$

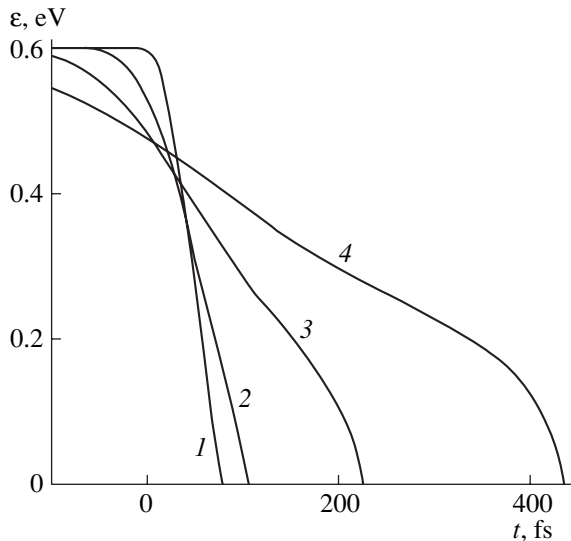


Fig. 1. Bandgap width of the electronic spectrum ε plotted vs time t in the case of illumination of the system with a light pulse of intensity (13); energy density $W = 50 \text{ mJ/cm}^2$; and duration τ_p equal to (1) 20, (2) 100, (3) 200, and (4) 400 fs.

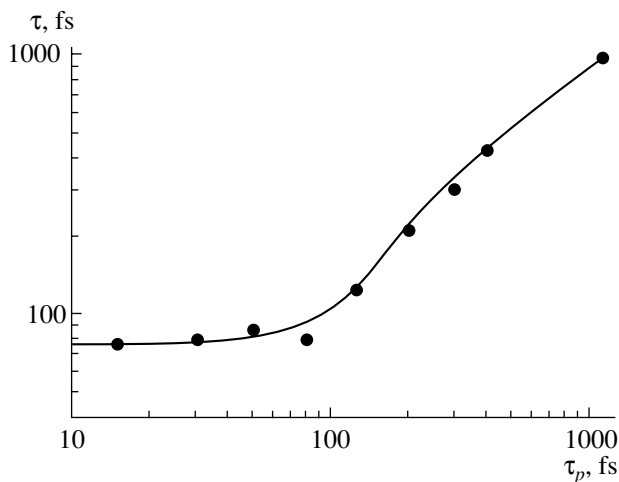


Fig. 2. Time τ at which a photoinduced semiconductor–metal phase transition occurs in vanadium dioxide plotted vs the duration τ_p of a laser pulse of energy density $W = 50 \text{ mJ/cm}^2$. The line refers to calculations using Eqs. (11)–(13), and points are experimental data from [5].

Figure 1 plots the bandgap width $\varepsilon = 4b \sinh \xi$ in the electronic spectrum (6) of vanadium dioxide versus the time t as obtained from Eqs. (11) and (12) for the case where the light field intensity is described by Eq. (13)

and the initial conditions are given by Eq. (14). We readily see that the bandgap width ε decreases with time down to zero. The vanishing of ε corresponds to a photoinduced semiconductor–metal phase transition. The time τ to the onset of the phase transition increases with τ_p . The $\tau(\tau_p)$ dependence as calculated from Eqs. (11)–(13) is shown graphically in Fig. 2, with points referring to the experimental data from [5]. The results obtained in terms of the proposed model are seen to agree quite well with the experimental data.

In conclusion, we note that ultrafast ($t \sim 10^{-13} \text{ s}$) photoinduced phase transitions to a new crystalline or amorphous state have been observed experimentally to occur in Si and GaAs. The mechanism underlying these transitions involves electron–phonon coupling [8, 11], which suggests their commonality with the photoinduced semiconductor–metal phase transition in vanadium dioxide considered here.

REFERENCES

1. A. A. Bugaev, V. V. Gudyalis, B. P. Zakharchenya, and F. A. Chudnovskii, *Pis'ma Zh. Éksp. Teor. Fiz.* **34** (8), 452 (1981) [*JETP Lett.* **34** (8), 430 (1981)].
2. A. L. Semenov, *Fiz. Tverd. Tela* (St. Petersburg) **40** (11), 2113 (1998) [*Phys. Solid State* **40** (11), 1915 (1998)].
3. A. A. Bugaev, B. P. Zakharchenya, and F. A. Chudnovskii, *The Metal–Semiconductor Phase Transition and Its Applications* (Nauka, Leningrad, 1979) [in Russian].
4. A. Cavalleri, Cs. Toth, C. W. Siders, J. A. Squier, F. Raksi, P. Forget, and J. C. Kieffer, *Phys. Rev. Lett.* **87** (23), 237401 (2001).
5. A. Cavalleri, Th. Dekorsy, H. H. Chong, J. C. Kieffer, and R. W. Schoenlein, cond-mat/0403214; *Phys. Rev. B: Condens. Matter* **70** (12), 161102 (2004).
6. L. N. Bulaevskii, *Usp. Fiz. Nauk* **115** (2), 263 (1975) [*Sov. Phys. Usp.* **115**, 131 (1975)].
7. A. L. Semenov, *Zh. Éksp. Teor. Fiz.* **111** (4), 1398 (1997) [*JETP* **84** (4), 774 (1997)].
8. V. I. Emel'yanov and D. V. Babak, *Fiz. Tverd. Tela* (St. Petersburg) **41** (8), 1462 (1999) [*Phys. Solid State* **41** (8), 1338 (1999)].
9. A. L. Semenov, *Zh. Éksp. Teor. Fiz.* **117** (6), 1175 (2000) [*JETP* **90** (6), 1022 (2000)].
10. C. Kittel, *Introduction to Solid State Physics*, 5th ed. (Wiley, New York, 1976; Nauka, Moscow, 1978).
11. V. I. Emel'yanov and D. V. Babak, *Laser Phys.* **7** (2), 514 (1997).

Translated by G. Skrebtsov

**LATTICE DYNAMICS
AND PHASE TRANSITIONS**

Pseudo- ϵ -Expansion and the Two-Dimensional Ising Model

A. I. Sokolov

St. Petersburg State Electrotechnical University, ul. Professora Popova 5, St. Petersburg, 197376 Russia

e-mail: ais2002@mail.ru

Received January 14, 2005

Abstract—The pseudo- ϵ -expansions for the coordinate of the fixed point g^* , the critical exponents, and the sextic effective coupling constant g_6 are determined for the two-dimensional Ising model on the basis of the five-loop renormalization group series. It is found that the pseudo- ϵ -expansions for the coordinate of the fixed point g^* , the inverse exponent γ^{-1} , and the constant g_6 possess a remarkable property, namely, the higher terms of these series are so small that reliable numerical results can be obtained without invoking Borel summation.
© 2005 Pleiades Publishing, Inc.

1. INTRODUCTION

The two-dimensional Ising model, for which Onsager obtained the exact solution 60 years ago, has been widely used as a proving ground for testing approximate methods [1–10]. Recently [7, 10], the five-loop contributions to the renormalization group (RG) functions were determined for a theoretical-field version of this model, namely, the two-dimensional scalar Euclidean theory $\lambda\phi^4$. These results, together with known four-loop expansions [4], made it possible to obtain renormalization group series of record-value length. However, resummation of these series demonstrated [7] that the high order of perturbation theory does not ensure a sufficient accuracy in determining numerical values. For example, the coordinate of the Wilson fixed point specified by a five-loop series for the β function is 5% greater than the known value of high accuracy [11],

$$g^* = 1.7543637(25), \quad (1)$$

and the renormalization group estimate of the critical exponent η differs almost twofold from $1/4$ [7]. This situation contrasts sharply with the case of three-dimensional systems [4–6, 12].

Does there exist any method for improving numerical estimates obtained from two-dimensional renormalization group expansions? Below, it will be demonstrated that such a method exists. This method consists in transforming the renormalization group expansions into alternative power series with the coefficients exhibiting a more favorable behavior. The case in point is the implementation of the pseudo- ϵ -expansion technique proposed by B. Nickel (see reference [19] in the paper by Le Guillou and Zinn-Justin [5]). The idea put forward by Nickel is that the coefficient of the linear term in the expansion of the β function should be replaced by a fictitious small parameter τ and that the coordinate of a nontrivial fixed point g^* should be sought in the form of a power series in the parameter τ

in order to obtain the τ expansions for the critical exponents. Actually, this technique has already been employed for calculating the critical exponents in two dimensions [5]; however, the relatively short series used in these calculations have made demonstrating the advantages of the method impossible.

2. CALCULATION TECHNIQUE

We will operate with a two-dimensional massive theory of the $\lambda\phi^4$ type, which is normalized to zero external momenta. In this case, the five-loop renormalization group expansions for the β function and the critical exponents γ and η have the following form [7]:

$$\frac{\beta(g)}{2} = -g + g^2 - 0.716173621g^3 + 0.930766443g^4 - 1.58238834g^5 + 3.26042g^6, \quad (2)$$

$$\gamma^{-1} = 1 - \frac{1}{3}g + 0.125023295g^2 - 0.122455138g^3 + 0.164004651g^4 - 0.288554g^5, \quad (3)$$

$$\eta = 0.033966147g^2 - 0.002022555g^3 + 0.011393097g^4 - 0.0137362g^5. \quad (4)$$

Here, the refined value of the five-loop contribution to the inverse exponent γ^{-1} is taken from [10]. Let us substitute $-\tau g$ for the first term on the right-hand side of relationship (2) and implement the algorithm described above. As a result, we obtain the expressions

$$g^* = \tau + 0.716173621\tau^2 + 0.095042867\tau^3 + 0.086080396\tau^4 - 0.204139\tau^5, \quad (5)$$

$$\gamma^{-1} = 1 - \frac{1}{3}\tau - 0.113701246\tau^2 + 0.024940678\tau^3 - 0.039896059\tau^4 + 0.0645212\tau^5, \quad (6)$$

$$\eta = 0.033966147\tau^2 + 0.046628762\tau^3 + 0.030925471\tau^4 + 0.0256843\tau^5. \quad (7)$$

It can be seen that the power series in τ for g^* and γ^{-1} compare favorably with the renormalization group expansions in the space of physical dimension, because their higher coefficients, even if irregular in sign, are small in magnitude. The smallness of these coefficients allows one to obtain reliable numerical estimates from relationships (5) and (6) without invoking popular summation techniques based on the Borel transform.

This can be easily verified by constructing the Padé approximants $[L/M]$ with a parameter $\tau = 1$ for g^* and γ^{-1} .

3. RESULTS AND DISCUSSION

The results obtained for g^* and γ^{-1} are presented in Tables 1 and 2, respectively. Since the τ expansion for the coordinate of the fixed point g^* begins with the linear term, the maximum rank of the approximants $L + M$ in this case is actually equal to 4, whereas for the inverse exponent γ^{-1} , we have $(L + M)_{\max} = 5$. For this reason, the numbers of rows and columns in Table 2 exceed those in Table 1 by unity. The subscripts on the numbers in the tables indicate the coordinates of those poles of the Padé approximants which lie on the real positive τ semiaxis. The best approximation properties are exhibited by the diagonal Padé approximants $[L/L]$ and those close to them which do not have poles at a parameter $\tau > 0$. Therefore, the most reliable estimates of the coordinate g^* should be the numbers 1.751 and 1.837 from Table 1. Averaging over these values, we obtain $g^* = 1.794$, which differs from the exact value (1) by only 2%. As can be seen from Table 1, it is this five-loop approximation that gives such a good estimate; almost all the Padé approximants have “dangerous” poles in lower orders, which leads to a considerable scatter in the numerical values. It seems likely that it is this scatter that led to pessimism in earlier calculations with four-loop series [5].

A similar situation occurs when calculating the critical exponent γ . It can be seen from Table 2 that, in this case also, reliable estimates are obtained only in the five-loop approximation. Indeed, the numbers specified by the main working approximants $[2/3]$ and $[3/2]$, as well as by the approximant $[4/1]$, almost coincide with each other and are close to the exact value $\gamma = 1.75$. In contrast, the approximants $[2/2]$ and $[1/3]$, which corre-

Table 1. Coordinate of the Wilson fixed point g^* according to calculations from pseudo- ϵ -expansion (5) with the use of the Padé approximants $[L/M]$

M/L	1	2	3	4	5
0	1.000	1.716	1.811	1.897	1.693
1	3.523 _{1,4}	1.826 _{7,5}	2.724 _{1,1}	1.837	
2	1.425	1.918 _{3,0}	1.850 _{6,1}		
3	2.601 _{1,4}	1.751			
4	1.194				

Note: In Tables 1–4, the subscripts on the numbers indicate the coordinates of the dangerous poles of the corresponding approximants, i.e., the poles lying on the real positive semiaxis.

Table 2. Critical exponent γ calculated by the Padé summation of expansion (6) for γ^{-1}

M/L	0	1	2	3	4	5
0	1.000	1.500	1.808	1.730	1.859	1.660
1	1.333	2.024 _{2,9}	1.744	1.778	1.777	
2	1.558	1.702	1.800 _{5,2}	1.777		
3	1.646	6.871 _{1,1}	1.772			
4	1.732	1.718				
5	1.714 _{6,1}					

spond to the four-loop approximation, have dangerous poles. It is worth noting that the pole of the second approximant is located in the vicinity of the physical value $\tau = 1$, which substantially affects the result obtained.

Now, we calculate the Fisher exponent η . From the comparison of series (4) and (7), we can conclude that, in this case, the pseudo- ϵ -expansion does not lead to any advantages. Furthermore, upon changing over to the expansion in terms of the parameter τ , we obtain not an alternating series but a series of constant signs in which the coefficients are approximately equal in magnitude. By adding four terms of this series at $\tau = 1$, we obtain the Fisher exponent $\eta = 0.137$, whereas the only working Padé approximant $[2/2]$ (all the other approximants have dangerous poles) gives $\eta = 0.0565$. Both of these estimates differ significantly from the exact value $\eta = 0.25$, as well as the result of the processing of the renormalization group expansion (4) using the Padé–Borel–Leroy technique, i.e., $\eta = 0.146$ [7].

We made an attempt to improve the situation. For this purpose, instead of series (7) for the “small” exponent η , we processed series for the “large” exponents ν and $\eta^{(2)}$, which are related to the exponent η through the

Table 3. Padé triangle for the critical exponent ν calculated by the summation of pseudo- ϵ -expansion (9) for ν^{-1}

M/L	0	1	2	3	4	5
0	0.500	0.750	0.933	0.920	1.005	0.898
1	0.667	1.107 _{2,6}	0.921	0.931	0.955	
2	0.788	0.901	0.971 _{3,6}	0.959 _{5,2}		
3	0.846	2.999 _{1,1}	0.959			
4	0.903	0.907				
5	0.907					

Table 4. Padé triangle for the universal ratio R_6 specified by pseudo- ϵ -expansion (12)

M/L	1	2	3	4
0	4.000	2.364	3.587	1.837
1	2.839	3.064	2.867	
2	3.148 _{4,5}	2.940		
3	2.621			

standard expression. To accomplish this, we find the following expansions in terms of τ for ν and ν^{-1} :

$$\nu = \frac{\gamma}{2-\eta} = \frac{1}{2} + \frac{1}{6}\tau + 0.1208977\tau^2 + 0.0584363\tau^3 + 0.0568918\tau^4 + 0.0037987\tau^5, \quad (8)$$

$$\frac{1}{\nu} = 2 - \frac{2}{3}\tau - 0.2613686\tau^2 + 0.0145746\tau^3 - 0.0913127\tau^4 + 0.118121\tau^5. \quad (9)$$

It turned out that the first of these expansions is of little use for obtaining numerical estimates: all the Padé approximants generated by this expansion, except for the approximants [5/0] and [0/5], have dangerous poles located in the vicinity of the physical value $\tau = 1$. Therefore, the series for ν admits only direct summation and also summation of the corresponding inverse series. These operations lead to almost coinciding results, namely, $\nu = 0.907$ and $\nu = 0.898$, which, however, differ from the exact value $\nu = 1$.

The expansion of the inverse exponent ν^{-1} , on the contrary, has a favorable structure for the Padé summation. As follows from the results given in Table 3, all except one of the higher (the fifth order) approximants are free from dangerous poles. Moreover, the approximants [2/3], [3/2], and [4/1] lead to very close values. Nonetheless, assuming that the values of $\gamma = 1.78$ and $\nu = 0.96$, which follow from the results presented in Tables 2 and 3, are the most reliable estimates, we obtain the critical exponent $\eta = 0.156$, which is only scarcely better than the direct estimate $\eta = 0.137$.

Unfortunately, the calculations with the critical exponent $\eta^{(2)} = (2 - \eta)(\gamma^{-1} - 1)$ are also ineffective. Although the pseudo- ϵ -expansion for this exponent can be efficiently summed using the Padé technique, because all the higher approximants do not have poles at $\tau > 0$ and the most symmetric of these approximants give close values of $\eta^{(2)}$ (-0.851 , -0.854 , -0.837), the final estimate of the exponent differs significantly from the exact value $\eta^{(2)} = -0.75$.

Apart from the critical exponents, some other quantities also take on universal values at a temperature $T \rightarrow T_c$. In particular, these are the higher effective coupling constants g_6, g_8, \dots , which enter into the equation of state and determine the nonlinear susceptibilities χ_{2n} of the system (see, for example, [13–17]). These constants can be represented in the form of power series in the renormalized charge g . At present, the renormalization group expansion for the constant g_6 of the two-dimensional scalar theory $\lambda\phi^4$ is known in the four-loop approximation [16]:

$$g_6 = \frac{4\pi^2}{81}g^3(1 - 1.125210g + 1.822531g^2 - 3.64849g^3). \quad (10)$$

By substituting expansion (5) into this series, we can readily obtain the pseudo- ϵ -expansion for the sextic effective coupling constant:

$$g_6 = \frac{4\pi^2}{81}(\tau^3 + 1.023311\tau^4 + 0.422991\tau^5 + 0.021201\tau^6). \quad (11)$$

The coefficients of series (11) decrease rapidly in magnitude. However, attempting to sum this series with the use of the Padé approximants leads to the problem of dangerous poles. Only one of the approximants corresponding to the four-loop approximation, namely, the approximant [4/2], is free from dangerous poles; the calculation with this approximant gives the coupling constant $g_6 = 1.122$. This estimate agrees well with the result of the summation of the renormalization group expansion (10) using the Padé–Borel–Leroy technique, i.e., $g_6 = 1.10$ [16].

On the other hand, it is known that the equation of state and the expression for the nonlinear susceptibility χ_6 involve not the vertex g_6 itself but the ratio $R_6 = g_6/g_4^2$ [13–17], where $g_4 = g\pi/9$ [16]. Hence, it would be interesting to obtain a power series in τ for the above ratio. Such a series has the form

$$R_6 = 4\tau(1 - 0.409036\tau + 0.305883\tau^2 - 0.437676\tau^3). \quad (12)$$

The higher coefficients of this expansion do not exhibit a pronounced tendency toward a decrease. Nonetheless, even in this case, the use of the Padé approximants turns

out to be efficient. As can be seen from Table 4, only the approximant $[1/2]$ has a pole at $\tau > 0$ and the numbers specified by the working approximants $[2/2]$ and $[3/1]$ are very close to each other. By averaging these values, we obtain $R_6 = 2.90$. This estimate differs by only 1.5% from the results of analyzing the multiloop renormalization group series ($R_6 = 2.94$ [16], $R_6 = 2.95 \pm 0.03$ [18]) and the high-temperature expansions ($R_6 = 2.943 \pm 0.007$ [19]), as well as from recently obtained values of high accuracy ($R_6 = 2.94294$ [11], $R_6 = 2.94238$ [9, 20]).

The computational potential of the pseudo- ϵ -expansion as applied to the ratio R_6 is not exhausted by the above estimate. This ratio can be refined by resumming series (12) using the Padé–Borel technique. The calculations demonstrate that the approximants $[2/2]$ and $[3/1]$ constructed for the Borel transform of R_6 do not have dangerous poles, and their processing leads to the values $R_6 = 2.970$ and 2.909 , respectively. Averaging these values, we obtain the ratio $R_6 = 2.94$, which coincides with the results of the calculations performed in [11, 16, 19, 20].

In conclusion, we should note that the Ising model is not a unique system for which the higher coefficients of the pseudo- ϵ -expansions are small as compared to the coefficients of the renormalization group series in ϵ and g . A similar feature was revealed recently for the three-dimensional cubic model [21], the three-dimensional chiral model [22], and the two-dimensional MN model [10]. This made it possible, in particular, to obtain alternative numerical estimates for the marginal dimensions of the order parameter, i.e., those values of M and N which separate the regions with different regimes of the critical behavior [10, 21, 22].

ACKNOWLEDGMENTS

The author would like to thank E.V. Orlov for performing some of the control calculations.

This work was supported by the Russian Foundation for Basic Research, project no. 04-02-16189.

REFERENCES

1. Th. Neimeyer and J. M. J. van Leeuwen, *Physica (Amsterdam)* **71** (1), 17 (1974).
2. L. P. Kadanoff and A. Houghton, *Phys. Rev. B: Solid State* **11** (1), 377 (1975).
3. B. Nienhuis and M. Nauenberg, *Phys. Rev. B: Solid State* **11** (11), 4152 (1975).
4. G. A. Baker, Jr., B. G. Nickel, and D. I. Meiron, *Phys. Rev. B: Solid State* **17** (3), 1365 (1978).
5. J. C. Le Guillou and J. Zinn-Justin, *Phys. Rev. B: Condens. Matter* **21** (9), 3976 (1980).
6. J. C. Le Guillou and J. Zinn-Justin, *J. Phys., Lett.* **46**, L131 (1985); *J. Phys. (Paris)* **48**, 19 (1987); *J. Phys. (Paris)* **50**, 1365 (1989).
7. E. V. Orlov and A. I. Sokolov, *Fiz. Tverd. Tela (St. Petersburg)* **42** (11), 2087 (2000) [*Phys. Solid State* **42** (11), 2151 (2000)].
8. B. N. Shalaev, *Teor. Mat. Fiz.* **131** (2), 206 (2002).
9. A. Pelissetto and E. Vicari, *Phys. Rep.* **368** (6), 549 (2002).
10. P. Calabrese, E. V. Orlov, D. V. Pakhnin, and A. I. Sokolov, *Phys. Rev. B: Condens. Matter* **70** (9), 094425 (2004).
11. M. Caselle, M. Hasenbusch, A. Pelissetto, and E. Vicari, *J. Phys. A: Math. Gen.* **33** (46), 8171 (2000); *J. Phys. A: Math. Gen.* **34** (14), 2923 (2001).
12. S. A. Antonenko and A. I. Sokolov, *Phys. Rev. E: Stat. Phys., Plasmas, Fluids, Relat. Interdiscip. Top.* **51** (3), 1894 (1995).
13. A. I. Sokolov, E. V. Orlov, and V. A. Ul'kov, *Phys. Lett. A* **227** (3–4), 255 (1997).
14. R. Guida and J. Zinn-Justin, *Nucl. Phys. B* **489** (3), 626 (1997).
15. A. I. Sokolov, *Fiz. Tverd. Tela (St. Petersburg)* **40** (7), 1284 (1998) [*Phys. Solid State* **40** (7), 1169 (1998)].
16. A. I. Sokolov and E. V. Orlov, *Phys. Rev. B: Condens. Matter* **58** (5), 2395 (1998).
17. A. I. Sokolov, E. V. Orlov, V. A. Ul'kov, and S. S. Kashanov, *Phys. Rev. E: Stat. Phys., Plasmas, Fluids, Relat. Interdiscip. Top.* **60** (2), 1344 (1999).
18. A. Pelissetto and E. Vicari, *Nucl. Phys. B* **522** (3), 605 (1998).
19. S. L. Zinn, S. N. Lai, and M. E. Fisher, *Phys. Rev. E: Stat. Phys., Plasmas, Fluids, Relat. Interdiscip. Top.* **54** (2), 1176 (1996).
20. P. Fonseca and A. Zamolodchikov, hep-th/0112167 (2001).
21. R. Folk, Yu. Holovatch, and T. Yavors'kii, *Phys. Rev. B: Condens. Matter* **62** (18), 12195 (2000).
22. Yu. Holovatch, D. Ivaneyko, and B. Delamotte, *J. Phys. A: Math. Gen.* **37** (11), 3569 (2004).

Translated by O. Moskalev

LATTICE DYNAMICS AND PHASE TRANSITIONS

Formation and Growth of CuCl Phase Nuclei in Glass

P. M. Valov and V. I. Leiman

*St. Petersburg State Technological University of Plant Polymers,
ul. Ivana Chernykh 4, St. Petersburg, 198095 Russia*

e-mail: leiman@inbox.ru

Received February 15, 2005

Abstract—In glass, the CuCl phase starts to form a certain time after the onset of supersaturation. As the temperature is increased, the transient period (stage of formation of critical nuclei) shortens and the growth kinetics of the CuCl phase switches from the first to second stage. The observed pattern of the CuCl phase growth kinetics is fully consistent with the Zel'dovich–Frenkel classical theory of new-phase formation. The delay time is determined by the radius of the critical nucleus (CuCl nanomelt) and the diffusion coefficient of the limiting component, the Cu^+ ions. The radius of the critical nucleus is about 1 nm and does not vary within a broad temperature range. The activation energy for the CuCl phase growth process does not change in the transition from the formation of critical nuclei to the first and, subsequently, second stage. © 2005 Pleiades Publishing, Inc.

1. INTRODUCTION

As seen from a recent review [1], the existing theoretical models of nucleation of a new phase are extremely diverse. This imparts considerable significance to experimental studies, which should facilitate correct selection and refinement of theoretical models.

One of the key issues in the formation of a new phase is its nonstationary stage and the determination of the incubation (delay) time in the onset of intense growth of the new phase. The classical studies by Zel'dovich [2] and Frenkel [3] were followed by theoretical investigations of the nonstationary stage in the formation of a new phase (see, e.g., [4–8] and references therein). The relevant publications deal with studies of the nonstationary nucleation of AgCl clusters in glass [6], the electrical conductivity in supercooled melts [7], the crystal nucleation on the surface [8] and in the bulk [9] of glass, and the electrically conducting layer of copper oxide on the surface of various glasses [10, 11]. Most of those studies, both experimental and theoretical, paid, however, little attention, if any, to the part played by temperature and the size of the critical nucleus in the growth kinetics of the new phase.

The present communication reports on a study of the initial stages in the formation of a new phase in solid solutions of the CuCl phase components in glasses, where nucleation of a new phase is limited by diffusion of one component, the Cu^+ ions [12]. The kinetics of the phase formation and the growth of CuCl particles in size were studied experimentally within a broad temperature range. The experimental results are shown to be in good agreement with the Zel'dovich–Frenkel classical theory of new-phase formation.

2. INITIAL STAGE IN THE CuCl PHASE GROWTH KINETICS IN GLASS

Glass with additions of NaCl (1.5 wt %) and CuO (0.7 wt %) heated to 500°C and higher reveals the formation of nuclei of a new phase, a nanomelt (NM), which contains CuCl and possibly a certain amount of NaCl [12, 13]. Cooling the sample stops growth of the new phase, after which the eutectic melt of the new phase first detaches from the glass (because of their thermal expansion coefficients being different) and subsequently undergoes crystallization with segregation into CuCl and NaCl nanocrystals (NCs) [13]. (Reference book information [14]: above 500°C, the thermal expansion coefficient of the CuCl and NaCl melt is about 100×10^{-6} , while for glass it is substantially smaller, about 6×10^{-6} .)

The formation of the CuCl crystalline phase is accompanied by the appearance of optical absorption in the transparency window of the glass matrix. The optical absorption spectrum of the initial glass exhibits a smooth falloff in the wavelength region from 300 to 370 nm, which is associated with the Cu^+ ions distributed in the glass. After the sample has been subjected to a temperature of 500°C or higher, absorption starts to grow throughout the above spectral region. As the time of holding is increased, the main absorption band of the $Z_{1,2}$ exciton in CuCl NCs peaking in the range 350–370 nm appears. The absorption value at the band maximum was used to determine the amount of the CuCl crystalline phase precipitated in glass, which yields the number of CuCl molecules in the NM of the new-phase nucleus. The energy position of the maximum of the $Z_{1,2}$ exciton absorption band offered the possibility of deriving the average radius of a CuCl NC.

Note that, due to the presence of NaCl (up to 30% [13]), the radius of a nucleus in the growing new phase

(nanomelt) may be slightly larger than that of the CuCl NC obtained experimentally.

To study the growth kinetics of the CuCl phase, three samples (0.65, 0.64, 0.63 mm thick) were prepared from a starting glass not subjected to thermal treatment. Each glass sample was heated repeatedly at one of three temperatures (500, 615, or 707°C). After holding at this temperature, the sample was quickly taken out of the furnace and the absorption spectrum was measured (at 300 K) in the wavelength region 310–400 nm. After this, the sample was again held for a certain time in the furnace at the same temperature and then removed for the next absorption measurement.

Figure 1 illustrates the changes that occur in the CuCl NC absorption spectra of glass as the total time of holding of a sample in the furnace at 500°C increases. Curve 0 is the absorption spectrum of Cu⁺ ions distributed in the starting glass. After heat treatment for 4 h at 500°C, the absorption spectrum (curve 1) exhibits an increase in $Z_{1,2}$ exciton and CuCl NC interband edge absorption [the spectrum is given in units of optical density $\alpha(E) = \log(I_0/I)$, where I_0 and I are the light intensities incident on and transmitted through the sample, respectively].

An increase in the time of holding brings about an increase in interband absorption and a more clearly pronounced isolation of the $Z_{1,2}$ exciton absorption band. The energy position E_{ex} of the $Z_{1,2}$ exciton band was derived from the second derivative (see the bars on the corresponding curves in Fig. 1). The absorption at the maximum of the absorption band may be considered, in a first approximation, to be proportional to the total amount of the CuCl phase precipitated in the glass. Similar changes in the absorption spectra of CuCl NCs were observed to occur after heat treatment of the glass at 615 and 707°C.

Figure 2 shows experimental data (points) obtained in the case where the absorbance in the region of the $Z_{1,2}$ exciton band maximum increased with the time of holding at three different temperatures. The increase in the absorbance $K(t) = \ln(I_0/I)/d$ with time (d is the glass sample thickness) is shown on a semilogarithmic scale.

The growth kinetics of the CuCl crystalline phase permits the isolation of two regions, namely, delay region I and a linear region where $K(t)$ increases at a constant rate (region II). The linear part of the $K(t)$ curves can be extrapolated to give an intercept on the abscissa axis, which is equal to the delay time τ . At 500°C, the time τ is longer than 4 h; at 615°C, it is 0.5 h; and at 707°C, 7.7 min. The slope of the curves in region II is practically the same for all temperatures of CuCl phase formation.

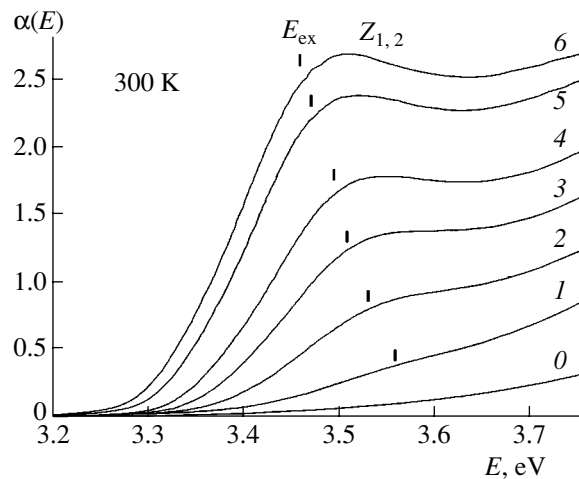


Fig. 1. Absorption spectra of CuCl nanocrystals in a glass sample measured after heat treatment at 500°C over various times t : (0) 0, (1) 4.0, (2) 5.8, (3) 7.7, (4) 9.5, (5) 11.3, and (6) 13.2 h. Sample thickness, 0.63 mm.

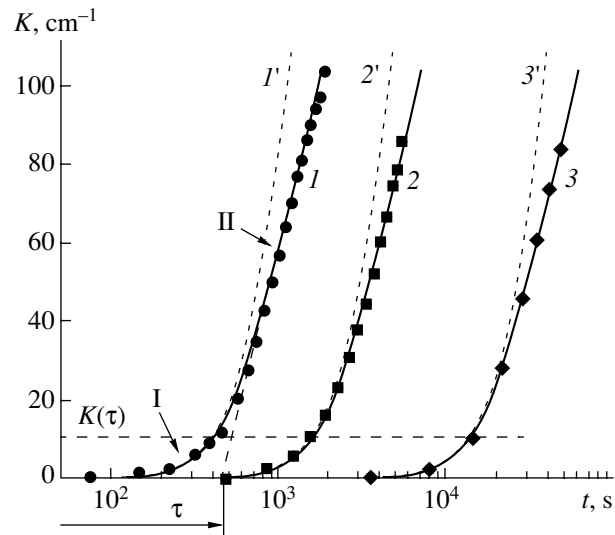


Fig. 2. Kinetics of absorption growth at the maximum of the CuCl NC $Z_{1,2}$ exciton band measured at a glass heat treatment temperature of (1) 707, (2) 615, and (3) 500°C. Points are experimental data. Curves 1'–3' are plots of Eq. (7), and solid curves 1–3 were obtained with inclusion of the decrease in supersaturation given by Eq. (10). I indicates the transition region, and II indicates the region of growth of the new phase at a steady rate. $K(\tau)$ is proportional to the amount of the CuCl phase precipitated in time τ .

3. VARIATION OF THE CuCl PHASE IN SIZE IN THE COURSE OF GROWTH

As the content of the CuCl crystalline phase increases, the spectra exhibit an energy shift of the $Z_{1,2}$ exciton band maximum to longer wavelengths (Fig. 1), which is associated with the growth of the average radius of CuCl NCs. This shift is a signature of the

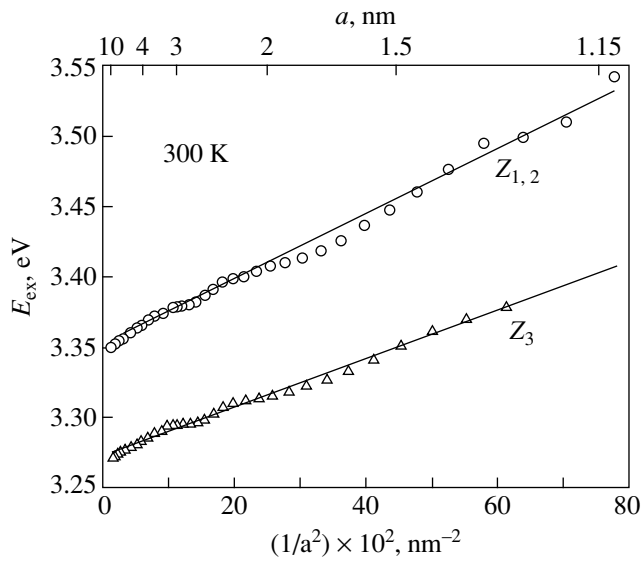


Fig. 3. Energy positions of the $Z_{1,2}$ and Z_3 excitons plotted vs the inverse square of the average CuCl NC radius.

quantum confinement effect in exciton energy states [15]:

$$E_{\text{ex}} = E_{\infty} + 0.67 \frac{\hbar^2 \pi^2}{2ma^2}, \quad (1)$$

where E_{∞} is the position of the exciton level for an NC radius $a = \infty$ and m is the exciton effective mass.

The confinement shift in E_{ex} for the $Z_{1,2}$ exciton in CuCl NCs is shown in Fig. 3 for room temperature. The data presented in Fig. 3 were extracted from an analysis of experimental data [16, 17] on the variation of the CuCl NC melting temperature induced by quantum confinement. Extrapolation of the data in Fig. 3 makes it possible to determine the parameters in Eq. (1) determining the confinement shift of exciton energy in CuCl NCs at 300 K. For the $Z_{1,2}$ exciton, we find that $E_{\infty} = 3.353$ eV (which corresponds to the position of the excitonic level in a bulk sample at 300 K, $a = \infty$) and the effective mass is $m = 1.07m_0$ (m_0 is the electron mass). For the Z_3 exciton (see [15]), the corresponding values are found to be $E_{\infty} = 3.274$ eV and $m = 1.5m_0$. These values of the effective masses and energy of excitonic states in CuCl NCs differ from those reported in [15] for 4 K. The increased value of E_{∞} is most likely a result of thermal expansion of the CuCl NC lattice heated to 300 K [18].

The values of the quantum confinement parameters found for the $Z_{1,2}$ exciton energy were used to determine the variation of the average CuCl NC nucleus radius from the shift of the maximum in the exciton absorption spectra undergoes during growth of the CuCl phase. The data on the variation in the NC size at different growth temperatures are presented in Fig. 4.

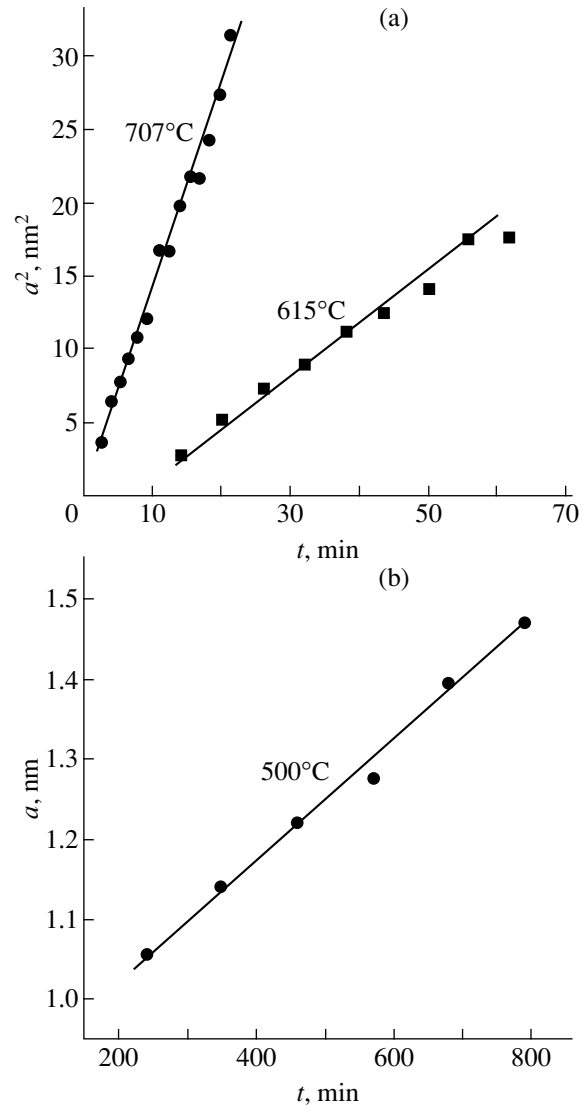


Fig. 4. (a) Square of the average radius and (b) radius of CuCl NCs in glass as a function of growth time.

4. DISCUSSION OF THE RESULTS

The radius of CuCl NCs at the beginning of the curve presented in Fig. 4b is slightly above 1 nm. This implies that the critical radius of CuCl NCs in glass is not above this value. Note that the critical CuCl crystalline nucleus in the melt of the same composition is 12 nm in size [17]. On the other hand, free-surface CuCl NCs less than 1.3 nm in size crystallize without supercooling, because the formation of the crystal surface does not require any expenditure of work in this case [17] (in other words, the surface energy of CuCl particles of such size with a free surface is zero).

As follows from Fig. 4a, the average volume of CuCl phase nuclei increases by a factor 6.13 at 707°C. The total amount of the CuCl phase increases in the same time by a factor of 8.22 (see curve 1 in Fig. 2, the seventh point in which corresponds to the first point in

Fig. 4a). The fact that absorption of the CuCl phase exceeds only by a factor of 1.34 the increase in the volume of the nuclei (which can be assigned to an increase in the exciton absorption oscillator strength) suggests that the conditions of growth of a new phase at 707°C are characteristic of the second stage, in which nuclei grow in size without a noticeable increase in their number.

A similar analysis of data obtained at 615°C showed the increase in absorption to exceed that of the nucleus volume only insignificantly (by 1.24 times). Therefore, accounting for the increase in the oscillator strength of absorption, one may assume that the CuCl phase passes through the second stage of growth at 615°C as well.

The situation is different at 500°C. During observation, the CuCl phase particles grew fairly little in size (Fig. 4b), only by a factor of 1.4. However, absorption increases by 7.78 times (curve 3 in Fig. 2). This means that the number of particles increases nearly threefold. Hence, the growth of the CuCl phase at 500°C passes through the first stage (in which an increase in the number of nuclei is accompanied by only a small increase in their size).

Thus, at 500°C (curve 3 in Fig. 2), one observes the first stage of CuCl phase growth in glass. As the temperature increases to 615°C or higher under the same supersaturation (the beginning of the linear parts), the new phase crosses over to the second stage of its growth kinetics. This is possibly due to an increase in the Cu⁺ diffusion coefficient and, accordingly, in the mean diffusion path of the components of the new phase.

Next, we consider the possibility of interpreting the experimental data in terms of the theory accounting for the existence of a transient period of growth of the new phase [2, 3], during which critical nuclei form. The growth of $K(t)$ in the region of the CuCl NC exciton absorption band is proportional to the number $N(t)$ of CuCl molecules in the new phase that have precipitated in the glass in time t :

$$K(t) = \gamma N(t), \quad (2)$$

where γ is the effective oscillator strength of optical absorption per CuCl molecule.

According to the nucleus formation theory (see [2, Sect. 6]), $N(t)$ is given by

$$N(t) = \int_0^t J_s \exp(-\tau/t') dt'. \quad (3)$$

Here, J_s is the steady diffusion flux of CuCl molecules penetrating into all critical nuclei, which is described by the Zel'dovich–Frenkel equation:

$$J_s = B(g_*) f_0(g_*) Z(g_*), \quad (4)$$

where $B(g_*)$ is the diffusion coefficient in size space, $f_0(g_*)$ is the equilibrium number of molecules in the critical nuclei, and $Z(g_*)$ is the Zel'dovich factor

$$f_0(g_*) = C \exp\left(-\frac{\Phi(g_*)}{kT}\right), \quad (5)$$

$$Z(g_*) = \sqrt{\frac{1}{2\pi kT} \left(\frac{\partial^2 \Phi(g)}{\partial g^2}\right)_*}.$$

In Eqs. (5), C is the concentration of the limiting component of the new phase in solution (glass), $\Phi(g)$ is the minimum work expended in the formation of a new-phase nucleus, g_* is the number of molecules in the critical nucleus, k is the Boltzmann constant, and T is the temperature. According to [2], the time τ is determined by the following relation containing the initial (a_1) and critical (a_*) radii of the nucleus and the diffusion coefficient $D = D_0 \exp(-\epsilon/kT)$ (where D_0 is the prefactor and ϵ is the diffusion activation energy):

$$\tau = \frac{(a_* - a_1)^2}{4D}, \quad a \sim g^{1/3}. \quad (6)$$

In the case of vapor condensation, the coefficient $B(g_*)$ is determined by the vapor pressure and temperature [3, 4], and for cavitation, by the temperature and viscosity of the liquid [2]. In the particular case of weak solutions, $B(g_*)$ is proportional to D and C (see [19, problem in Sect. 100]).

Substituting Eq. (3) into Eq. (2) and taking into account Eqs. (4)–(6), we obtain the following relation for the initial stage of CuCl phase nucleation:

$$K(t) = \gamma \int_0^t D C(t')^2 \exp\left(-\frac{\Phi(g_*)}{kT}\right) \sqrt{\frac{1}{2\pi kT} \left(\frac{\partial^2 \Phi}{\partial g^2}\right)_*} \times \exp\left(-\frac{(a_* - a_1)^2}{4Dt'}\right) dt'. \quad (7)$$

As the starting components of the CuCl phase become expended, the equilibrium concentration C decreases. It is believed [19, 20] that, in the case of weak solutions, supersaturation near supercritical nuclei is compensated from the bulk. In these conditions, the variation $C(t)$ can be written as the difference between C_0 (the initial concentration of the components of the new phase) and the number of molecules $N(t)$ already incorporated in the nuclei:

$$C(t) = C_0 - N(t). \quad (8)$$

Multiplying both sides by γ , we obtain

$$\gamma C(t) = \gamma C_0 - \gamma N(t). \quad (9)$$

The product $\gamma C_0 = K_0$ is hypothetical absorption in the case of total precipitation of the CuCl phase. Using

Eqs. (2) and (9), we can make the following substitution into Eq. (7):

$$\gamma C(t)^2 = (K_0 - K(t))^2 / \gamma. \quad (10)$$

Equation (7) can be used in combination with Eq. (10) to numerically calculate the absorption $K(t + dt)$ at time $t + dt$ from the known absorption $K(t)$ at time t .

Without considering the decrease in supersaturation, Eq. (7) correctly describes the phase growth kinetics within initial part I (for $t \leq \tau$), i.e., in the stage of formation of critical nuclei (curves 1'-3' in Fig. 2). The calculation is carried out with the following parameter values: in the exponent of the second exponential function in Eq. (7), we put $a_*^2 / 4D_0 = 0.9 \times 10^{-3}$ s (parameter a_1 in this exponent is set to zero, because at the beginning of the experiment there are no nuclei at any temperature), the diffusion activation energy is $\varepsilon = 1.10$ eV, the quantity $\Phi(g_*)$ does not exceed 0.05 eV, and

$$\gamma D_0 C_0^2 \sqrt{-(\partial^2 \Phi / \partial g^2)_*} = 1.178 \times 10^5 \text{ cm}^{-1}.$$

The time τ is calculated to be 460, 1.8×10^3 , and 15.54×10^3 s at temperatures of 707, 615, and 500°C, respectively. These results practically coincide with the values derived earlier graphically from Fig. 2.

By substituting Eq. (10) into Eq. (7), one can account for the decrease in $C(t)$ in region II as the starting components of the CuCl phase are being expended. Numerical calculations (solid line 3 in Fig. 2) fit well the experimental data obtained for the first stage of phase growth. The parameter values are $K_0 = 355 \text{ cm}^{-1}$

and $D_0 \sqrt{-(\partial^2 \Phi / \partial g^2)_*} / \gamma = 0.885 \text{ cm}^{-1}$. In the course of CuCl phase growth, supersaturation falls off in the same way (by 30%) for all temperatures.

Although relation (4) for the diffusion flux J_s cannot be used to calculate $K(t)$ for the temperatures 707 and 615°C (second stage), the agreement between the calculated curves and experimental data (see solid curves 1, 2 in Fig. 2) does not seem accidental. We believe this to be due to the fact that the diffusion flux in the second stage is dominated by the contributions from the diffusion coefficient D and supersaturation $C(t)$, while the effect of the parameters associated with the variation of $\Phi(g)$ is small.

Calculations showed that $K(\tau)$, which is proportional to the amount of the CuCl phase precipitated in time τ (the time taken for the formation of the critical nuclei), is the same at all temperatures and equals 10.9 cm^{-1} (horizontal dashed line in Fig. 2). The radii of the nuclei are 1.05, 1.67, and 1.84 nm for temperatures of 500, 615, and 707°C, respectively. It follows that, at 615 and 707°C, the first nuclei to appear undergo accelerated growth because of the large mean diffusion length of the CuCl phase components.

Note that the constancy of the factor $a_*^2 / 4D_0$ determining the behavior of τ with temperature may indicate

that the size of the critical nucleus pushing out the glass during its growth is independent of temperature. In accordance with the classical theory of formation of new-phase nuclei, we have

$$a_* = \frac{2\sigma v'}{\mu - \mu'}, \quad (11)$$

where σ is the specific surface energy of the interface between the critical nucleus and glass; v' is the average volume of molecules of the nucleus; and μ and μ' are the chemical potentials of the separated components of the new phase in the glass and of their compounds in the nucleus melt, respectively. According to Eq. (11), the independence of a_* from temperature during the formation of a new phase may imply that the surface energy σ decreases with increasing temperature just as the denominator does.

As is evident from Fig. 4a, the square of the radius a grows linearly with time at temperatures of 707 and 615°C. The data obtained can be approximated by a relation describing the growth of the CuCl phase in the second stage [20]. To obtain a better match with experiment, we introduced a delay time τ_1 into the relation proposed in [20] to describe the variation of a in the second stage:

$$a^2(t) = 2Dv'C(t - \tau_1) + a_1^2, \quad (12)$$

where v' is the molar volume of the new phase.

The parameters providing the best fit of Eq. (12) to the experimental data at temperatures of 707 and 615°C are the same: $D_0 v' / C = 1.2 \times 10^4 \text{ nm}^2/\text{s}$, $a_1 = 1 \text{ nm}$, and $\varepsilon = 1.10$ eV. Only the delay time τ_1 is different: for 707°C, $\tau_1 = 40$ s, and for 615°C $\tau_1 = 600$ s.

The situation changes radically at 500°C. CuCl nanocrystals increase in size much more slowly. In view of such a small increase (1.5 times), the data from Fig. 4b can be fitted by a linear time dependence,

$$a(t) = 1.27 \times 10^{-5}(t - \tau_1) + a_1. \quad (13)$$

Assuming that $a_1 = 1 \text{ nm}$, the delay time is found to be $\tau_1 = 10.2 \times 10^3$ s. For a zero delay time, the initial radius will be $a_1 = 0.87 \text{ nm}$.

5. CONCLUSIONS

The kinetics of CuCl growth in glass in the first stage is in agreement with classical theory for the non-stationary case if the decrease in supersaturation is included. For the CuCl phase growth in glass, the delay time needed for the formation of critical nuclei may range from a few hours to a few minutes. The delay time is determined by the size of the critical nucleus and the diffusion coefficient of the components of the new phase. The size of the critical nucleus (CuCl nanomelt) is practically independent of the temperature of formation and does not exceed 1 nm.

For the same supersaturation, the CuCl phase growth kinetics in glass transfers from the first to second stage with increasing temperature, which may imply a substantial influence of the temperature-induced variation of the mean diffusion length characterizing the new-phase components on the growth kinetics. The growth kinetics of the amount of the CuCl phase in the first and second stages can be described with one relation taking into account the stage of formation of the critical nuclei.

ACKNOWLEDGMENTS

This study was supported by the Russian Foundation for Support of Leading Scientific Schools, project no. NSh-2223.2003.02.

REFERENCES

1. M. P. Anisimov, *Usp. Khim.* **72** (7), 664 (2003).
2. Ya. B. Zel'dovich, *Zh. Éksp. Teor. Fiz.* **12** (11–12), 525 (1942).
3. Ya. I. Frenkel', *Collection of Selected Works* (Akad. Nauk SSSR, Moscow, 1958), Vol. 2 [in Russian].
4. Z. Kozisek, K. Sato, P. Demo, and A. M. Sveshnikov, *J. Chem. Phys.* **120** (14), 6660 (2004).
5. V. A. Shneidman, *J. Chem. Phys.* **115** (17), 8141 (2001).
6. J. Schmelzer, Jr., U. Lembke, and R. Kranold, *J. Chem. Phys.* **113** (3), 1268 (2000).
7. P. Demo, A. M. Sveshnikov, K. Nitsch, M. Rodova, and Z. Kozisek, *Mater. Phys. Mech.* **6** (1), 43 (2003).
8. V. Filipovich, V. Fokin, N. Yuristin, and A. Kalinina, *Thermochim. Acta* **280/281**, 205 (1996).
9. P. M. Valov, V. I. Leĭman, and K. S. Semenov, *Fiz. Tverd. Tela* (St. Petersburg) **43** (9), 1698 (2001) [*Phys. Solid State* **43** (9), 1770 (2001)].
10. O. S. Shchavelev, V. N. Polukhin, V. I. Leĭman, P. M. Valov, and K. O. Shchavelev, *Fiz. Khim. Stekla* **22** (5), 614 (1996).
11. O. S. Shchavelev, V. N. Polukhin, V. I. Leĭman, P. M. Valov, and K. O. Shchavelev, *Fiz. Khim. Stekla* **22** (6), 739 (1996).
12. V. V. Golubkov, A. I. Ekimov, A. A. Onushchenko, and V. A. Tsekhomskii, *Fiz. Khim. Stekla* **7** (4), 397 (1981).
13. V. V. Golubkov and V. A. Tsekhomskii, *Fiz. Khim. Stekla* **12** (2), 206 (1986).
14. *A Handbook on Molten Salts* (Khimiya, Leningrad, 1971), Vol. 1 [in Russian].
15. A. I. Ekimov, A. A. Onushchenko, A. G. Plyukhin, and Al. L. Éfros, *Zh. Éksp. Teor. Fiz.* **88** (4), 1490 (1985) [*Sov. Phys. JETP* **61**, 891 (1985)].
16. P. M. Valov and V. I. Leĭman, *Fiz. Tverd. Tela* (St. Petersburg) **41** (2), 310 (1999) [*Phys. Solid State* **41** (2), 278 (1999)].
17. P. M. Valov and V. I. Leĭman, *Pis'ma Zh. Éksp. Teor. Fiz.* **66** (7), 481 (1997) [*JETP Lett.* **66** (7), 510 (1997)].
18. P. M. Valov, L. V. Gracheva, V. I. Leĭman, and T. A. Negovorova, *Fiz. Tverd. Tela* (St. Petersburg) **36** (6), 1743 (1994) [*Phys. Solid State* **36**, 954 (1994)].
19. L. D. Landau and E. M. Lifshitz, *Course on Theoretical Physics*, Vol. 10: *Physical Kinetics* (Nauka, Moscow, 1979; Pergamon, New York, 1981).
20. V. I. Marchenko, *Pis'ma Zh. Éksp. Teor. Fiz.* **64** (1), 61 (1996) [*JETP Lett.* **64** (1), 66 (1996)].

Translated by G. Skrebtsov

LOW-DIMENSIONAL SYSTEMS
AND SURFACE PHYSICS

Effect of an Electric Field on the Carrier Collection Efficiency of InAs Quantum Dots¹

E. S. Moskalenko^{1,2}, K. F. Karlsson¹, V. Donchev³, P. O. Holtz¹,
W. V. Schoenfeld⁴, and P. M. Petroff⁴

¹ Department of Physics and Measurement Technology, Linköping University, Linköping, S-58183 Sweden
e-mail: evgenii.moskalenko@mail.ioffe.ru

² Ioffe Physicotechnical Institute, Russian Academy of Sciences, St. Petersburg, 194021 Russia

³ Faculty of Physics, Sofia University, Sofia, 1164 Bulgaria

⁴ Department of Materials, University of California, Santa Barbara, California, 93106 United States

Received January 17, 2005

Abstract—Individual and multi-quantum dots of InAs are studied by means of microphotoluminescence in the case where, in addition to the principal laser exciting photoluminescence, second infrared laser is used. It is demonstrated that the absorption of the infrared photons effectively creates free holes in the sample, which leads to both a change in the charge state of a quantum dot and to a considerable reduction of their photoluminescence signal. The latter effect is explained in terms of effective screening of the internal electric field, facilitating carrier transport along the plane of a wetting layer, by the surplus holes from the infrared laser. It is shown that the effect of quenching of quantum dot photoluminescence gradually disappears at increased sample temperature (T) and/or dot density. This fact is due to the essentially increased value of quantum dot collection efficiency, which could be achieved at elevated sample temperatures for individual quantum dots or even at low T for the case of multi-quantum dots. It is suggested that the observed phenomena can be widely used in practice to effectively manipulate the collection efficiency and the charge state of quantum-dot-based optical devices.
© 2005 Pleiades Publishing, Inc.

1. INTRODUCTION

Semiconductor quantum dots (QDs) effectively confine electrons (e 's) and holes (h 's) on the nanometer length scale in all three dimensions and, hence, may be considered as “artificial atoms” [1]. Unlike real atoms, QDs can be manipulated in different ways, which opens the possibility of tailoring their shape, size, and composition [2] in order to achieve desired properties. Consequently, QDs are potential candidates for various optoelectronic (electronic) applications, such as QD lasers [3], QD infrared detectors [4], QD memory devices [5], and single-electron transistors [6].

For the majority of these devices, the QDs become populated with carriers, which are primarily created outside the QDs somewhere in the sample (in the barriers or in the wetting layer (WL), on which QDs are normally grown [7]) by means of electrical or optical excitation. Consequently, excited carriers undergo transport in the WL/barriers prior to capture into the QDs. This circumstance highlights the crucial role of the carrier capture processes into the QD for the performance and operation of QD-based devices.

The carrier capture mechanisms intensively studied in the last decade reveal optical-phonon-assisted [8, 9], Auger-like [10], shakeup [11] processes and carrier

relaxation through the band tail states of the WL with a subsequent emission of localized phonons [12]. The lateral carrier transport (in the plane of the WL) could be affected by carrier hopping between QDs [13] or by trapping of migrating particles into localized states of the WL [14] or into nonradiative centers [15] in the surrounding media. A more efficient carrier transfer from the WL into the QDs via radiation-induced defects in the WL has been reported [16]. A magnetic field directed perpendicular to the plane of the structure was observed to limit the lateral transport of carriers [17].

It has also been suggested [8] that the carrier drift could be considerably influenced by a long-range attractive potential caused by the strain field surrounding the QD. On the other hand, strain-induced potential barriers in the barrier-QD [18] and in the WL-QD interface [19] were considered to limit the carrier capture into the QD. The important role of an electric field directed in the growth direction of the sample on the carrier capture into and escape out of the QD has been demonstrated by studies of the electric current passing through QDs [20].

In our previous study [21], we pointed out another mechanism of carrier transfer from the WL into the QDs which had not been previously considered. A built-in electric field (F) was directed in the plane of a WL to facilitate the lateral carrier transport. However,

¹ This article was submitted by the authors in English.

in these measurements, individual QDs were studied only at a fixed sample temperature (T) of 5 K. In the present paper, the suggested mechanism of carrier capture into the QDs is investigated at increased sample temperatures (up to 70 K), as well as at an increased dot density.

In our experiments, we use an additional infrared (IR) laser to influence the field F . The excitation energy of the IR laser, $h\nu_{\text{IR}} = 1.240$ eV, is considerably less than the lowest transition energy of the sample studied and, accordingly, cannot simultaneously excite both electrons (e 's) and holes (h 's); however, it can generate solely either e 's or h 's through the excitation of deep level (DL) defects positioned in the band gap of the CaAs barriers [22]. According to our model, these extra carriers, excited by the IR laser, will effectively screen the field F and will consequently slow down the carrier transport in the plane of the WL. Due to this effect, a considerable reduction (up to 10 times) of the QD photoluminescence (PL) signal (I_{QD}) is experimentally observed when the sample is exposed to dual excitation of an IR laser and a main laser.

To the best of our knowledge, there are very few earlier publications [23, 24] on the study of the IR-laser-induced changes in I_{QD} . In contrast to our findings, it was found in [23] that the IR laser induces an increase in the PL from the QDs by up to 40%. This phenomenon was explained in terms of an IR-laser-induced release of carriers that were trapped into deep defects from the QDs. Considerable changes in the fluctuations of the I_{QD} during the time interval of the measurement were detected when the sample was illuminated with an additional near-IR laser irradiation [24]. Carriers trapped at deep localized centers in the vicinity of the QDs were suggested to be responsible for the observed phenomenon [24].

Our present results demonstrate that the strength of the observed quenching effect of I_{QD} progressively decreases as the temperature, as well as dot density, increases. This is explained in terms of an essentially increased QD collection efficiency (α), i.e., the ability of QDs to collect photoexcited carriers from an illuminated area. Under these experimental conditions, the role of F , which facilitates carrier transport at lower values of α , becomes diminishing.

2. SAMPLE AND EXPERIMENTAL SETUP

The sample studied was grown by molecular beam epitaxy on a GaAs(100) substrate. It consisted of lens-shaped InAs QDs developed on an InAs WL from about 1.7-monolayer InAs deposited in the Stranski–Krastanov growth mode. The WL–dot layer was sandwiched between two 100-nm-thick GaAs barriers. The sample was grown without rotation of the substrate, resulting in a gradual variation of the In flux across the wafer and, consequently, in a gradient in the QD density. The QDs were studied by means of a diffraction-limited micro-

PL (μPL) setup (a detailed description of the setup and the sample growth procedure is given in [25]). The μPL technique employed in the present experiments allowed us to excite and study a single QD (SQD).

To excite the sample, we used two Ti–Sp lasers, whose beams were focused on the same position of the sample surface down to a spot diameter of 2 μm . The main laser (L_0) was used to excite the PL of the WL and the QDs. The excitation energy ($h\nu_{\text{ex}}$) was tuned in the range from 1.410 to 1.480 eV with a maximum excitation power (P_0) of 20 μW . The other laser, L_{IR} , operating at a fixed excitation energy, $h\nu_{\text{IR}} = 1.240$ eV, had a maximum output power (P_{IR}) of 100 μW . It is important to note that the $h\nu_{\text{IR}}$ is well below the value of the QD-related emission and, accordingly, no signal from either the WL or the QDs was detected with excitation solely with L_{IR} . The sample was positioned inside a continuous-flow cryostat operating in the temperature (T) range 5–70 K.

To find the particular QD to study, a laser beam was scanned across the sample surface. Once the desired QD was found, special marks (grids) were burnt into the sample surface around the QD with a high-power laser beam. The average distance between the adjacent QDs in the low dot density area of the sample was around 10 μm . To control the exact position of the laser spot on the sample surface, an image of the region of interest was projected with a video camera, which made it easy to find the desired QD marked by the grid. In addition, this arrangement allowed us to effectively correct the laser position on the sample in cases where the sample had moved due to thermal drift. It should be noted that the method of locating the exact QD position by using the above-described grids is favorable in several respects over alternative methods, e.g., employing a metal mask with small holes deposited on top of the sample, which may produce an electric field in the near-surface region and, consequently, may influence the carrier transport in the plane of the WL. In addition, the metal mask may act as a stressor, which could spoil the quality of the QDs.

Eight SQDs located at different spatial positions of the sample, all with analogous behavior with respect to the L_{IR} , were examined in this study. In this report, we present data measured on a low-density structure with one SQD within the laser spot together with a high dot density area with a varying number of QDs within the area of the laser spot.

3. EXPERIMENTAL RESULTS AND DISCUSSION

The low-temperature μPL spectrum of a sample spot with only one QD (SQD) within the laser illumination area obtained under excitation with a single laser L_0 at an excitation energy $h\nu_{\text{ex}} = 1.471$ eV is shown in Fig. 1 (dotted lines). The μPL spectrum of the sample is dominated by the WL emission at an energy of

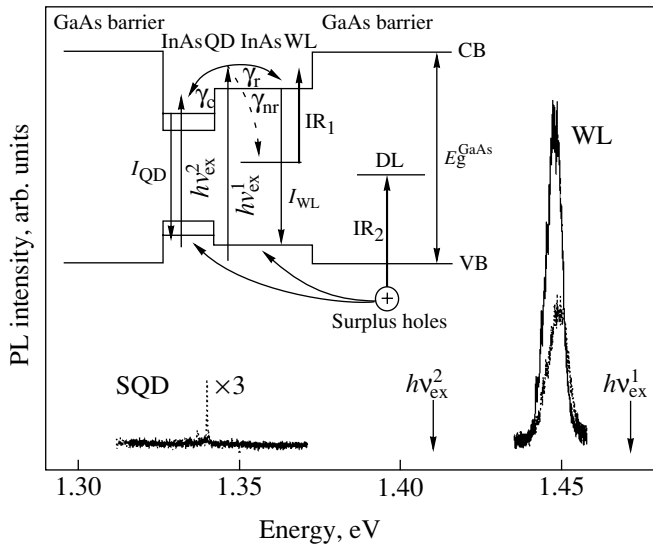


Fig. 1. μ PL spectra of a SQD and the WL measured at $T = 5$ K and $h\nu_{\text{ex}} = 1.471$ eV with single (dotted lines) and dual (solid lines) laser excitation, respectively, at an excitation power of $P_0 = 200$ nW and $P_{\text{IR}} = 100$ μ W. The vertical solid arrows show the excitation energies of L_0 used in the experiment. The inset shows the principle transitions involved in the energy scheme of the sample together with the positions of the GaAs conduction band (CB), valence band (VB), and deep level (DL). The vertical and curved arrows are explained in the text.

around 1.445 eV. A weak emission line peaking at around 1.340 eV is attributed to the PL from a SQD. The spectrally integrated PL signal from a SQD (I_{QD}) is approximately 1% with respect to the corresponding PL intensity of the WL (I_{WL}). This ratio is much higher than the corresponding volume ratio ($\approx 10^{-3}$) of the SQD versus the excited WL volume. This fact is direct evidence that the PL signal from a SQD is not entirely determined by the number of carriers excited in the SQD as a result of the absorption of photons in the dot volume but rather to a significant extent by carriers excited in the WL. In other words, the WL serves as a reservoir that supplies the QD with carriers. Indeed, carriers excited in the WL ($h\nu_{\text{ex}}^1$ in the inset to Fig. 1) can undergo alternative trapping processes: (a) relaxation down to the localized WL states, followed by radiative recombination; (b) trapping at centers of non-radiative recombination (CNRs); or (c) capture into a SQD (these processes are shown by arrows γ_r , γ_{nr} , and γ_c , respectively, in the inset to Fig. 1). The interplay between these processes determines the values of I_{QD} and I_{WL} measured in the experiment.

We have solved a simple set of rate equations under steady-state conditions (not shown here), which resulted in $I_{\text{QD}}/I_{\text{WL}} = \gamma_c/\gamma_r = \alpha$ at any value of γ_{nr} , where the parameter α is the collection efficiency of the SQD. The physical meaning of the introduced parameter α can be explained using the following example. If the

capture probability γ_c were to exceed the value of γ_r , the PL of the SQD would dominate the PL spectrum of the sample at the expense of the WL PL; i.e., the dot would efficiently collect a majority of carriers created by the laser absorption within the laser spot.

A spectacular effect was observed when, in addition to the excitation of L_0 at $h\nu_{\text{ex}} = 1.471$ eV, the sample was illuminated with an infrared laser, L_{IR} . Indeed, the μ PL spectrum of the sample (solid lines in Fig. 1) undergoes a dramatic change in this case: while I_{WL} increases by a factor of 2.5, the SQD emission almost completely vanishes. The increase in the I_{WL} could be explained in terms of a release of carriers from the centers of nonradiative recombination as a result of the infrared absorption by L_{IR} (arrow IR_1 in the inset to Fig. 1). Such an enhancement of the radiative efficiency, induced by an additional below-band-gap excitation, has been reported earlier (see, e.g., [26]). If this were the only operating mechanism caused by L_{IR} , an increase in I_{QD} would also be expected, since the WL serves as a reservoir of carriers which could be trapped into the SQD, as explained above. Consequently, a different mechanism of the L_{IR} influence on the sample has to be considered in order to explain the observed decrease in I_{QD} .

To understand the origin of the effect of the infrared laser on the PL intensity, we studied the temperature (T) dependence of the observed effect. Figure 2a shows a number of pairs of SQD μ PL spectra recorded with single-laser L_0 excitation (dotted lines) and dual laser excitation (solid lines) at different T . The two emission lines marked as X and X^- were earlier interpreted [25] as excitonic lines with different charge configurations. The neutral and single negatively charged excitons, i.e., the $1e1h$ and $2e1h$ charge states, respectively, could be detected. The progressive redistribution of the μ PL spectra in favor of the X^- line, detected with single laser L_0 excitation with increasing T (dotted lines in Fig. 2a), was explained in [27] in terms of a temperature-induced increased electron diffusivity in the WL plane. This leads to faster diffusion and, hence, capture of e^- 's into the dot with respect to the capture of h^+ 's. The μ PL spectra measured with dual laser excitation (solid lines in Fig. 2a) reveal both a redistribution of the emission lines in favor of the X line and a progressively vanishing quenching effect with increasing T .

The redistribution effect in favor of X at elevated temperatures is clearly illustrated in Fig. 2a. This fact clearly demonstrates that L_{IR} supplies the sample with extra h^+ 's, which can be captured by the QD and, accordingly effectively "neutralize" its charge configuration. The generation of extra h^+ 's is assumed to take place in the GaAs barriers as a result of an IR-laser-induced electron excitation from the GaAs valence band into the DLs always present in the GaAs band gap [22] (arrow IR_2 in the inset to Fig. 1). It is interesting to note that the PL spectrum measured under dual-laser excitation at

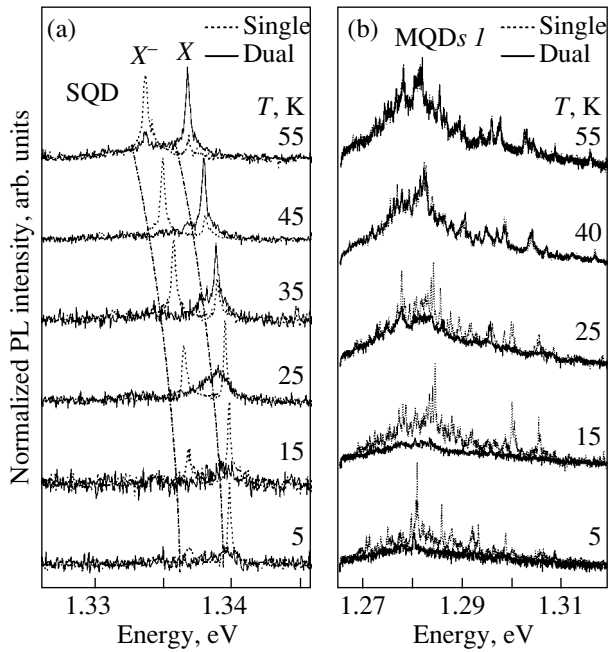


Fig. 2. μ PL spectra of (a) SQD and (b) MQDs 1 measured at $h\nu_{\text{ex}} = 1.471$ eV and $h\nu_{\text{IR}} = 1.240$ eV for a number of temperatures as indicated in the figure and at excitation with a single (dotted lines) and double (solid lines) laser, respectively, at an excitation power of $P_0 = 200$ nW and $P_{\text{IR}} = 100$ μ W. The curved dash-dotted lines in (a) are given to guide the eye.

$T = 25$ K is very broad and a peak appears between the X and X^- lines (Fig. 2a). This experimental finding is unclear, and further studies are needed to reveal its nature. However, some insight that can help elucidate the situation may be gained from spectral diffusion, a phenomenon previously observed in single self-assembled quantum dots [28, 29]. In particular, it was found that the electric field induced by the charges located in close vicinity to a QD initiated an energy shift of the QD spectral lines, which were quasiperiodic in time [28, 29]. Consequently, the widths of the spectral lines registered in the time-integrated regime (as in the present paper) are expected to broaden in the case where there are quasiperiodic (in time) local electric fields around the SQD under study [29]. That is why the experimentally observed broadening of the QD PL line and its energy shift detected in the temperature range around $T = 25$ K (Fig. 2a) could be regarded as evidence of the presence of a local electric field around the QD.

The effect of the change in I_{QD} induced by the IR laser could quantitatively be described in terms of a “quenching rate,” R_{QD} , which is defined as the ratio of I_{QD} measured with dual laser excitation ($I_{\text{QD}}^{\text{dual}}$) to the corresponding single-laser excitation PL intensity ($I_{\text{QD}}^{\text{single}}$). R_{QD} values measured for a SQD are shown by solid squares in Fig. 3a. It is seen that an R_{QD} value of

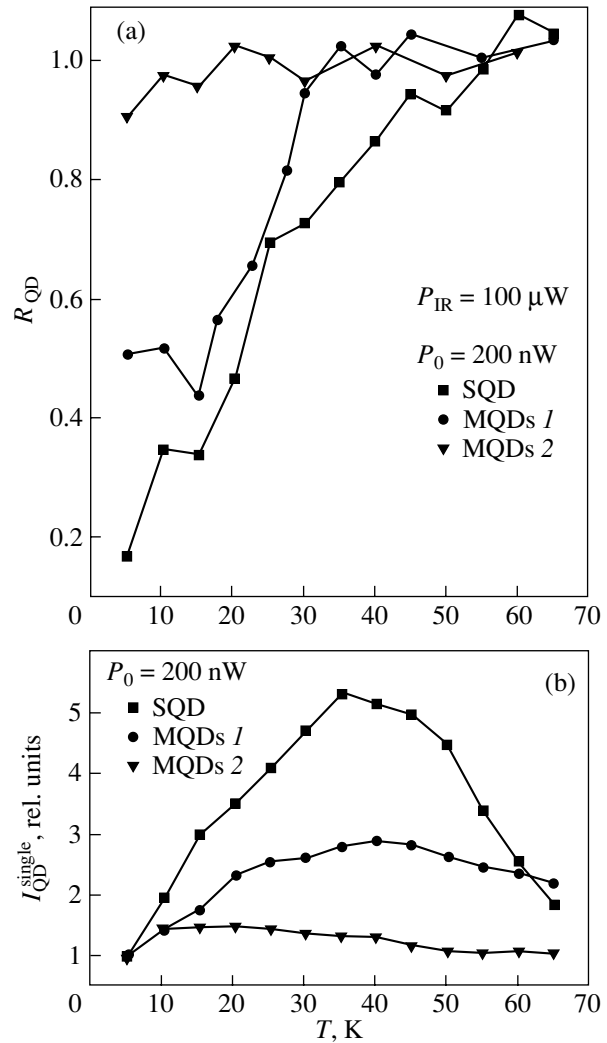


Fig. 3. (a) R_{QD} for $h\nu_{\text{IR}} = 1.240$ eV and $P_{\text{IR}} = 100$ μ W and (b) normalized values of $I_{\text{QD}}^{\text{single}}$ for SQD, MQDs 1, and MQDs 2 measured for a number of T 's at $h\nu_{\text{ex}} = 1.471$ eV and $P_0 = 200$ nW and shown by solid squares, circles, and triangles, respectively.

low as 0.1 at $T = 5$ K progressively increases to reach a value of 1 at $T \approx 60$ K; i.e., the quenching effect gradually disappears with increasing T .

A qualitatively similar behavior could be recorded for another sample spot with a higher dot density (MQDs 1). In this case, the μ PL spectra consist of a number of sharp lines superimposed on a broad PL band in the spectral range 1.27–1.31 eV (Fig. 2b). It is clearly seen that the IR laser also induces a quenching of the PL signal at low temperatures. The quenching rate is found to increase from $R_{\text{QD}} \approx 0.5$ at $T = 5$ K with increasing temperature to reach $R_{\text{QD}} \approx 1$ already at $T \approx 30$ K (solid circles in Fig. 3a). This T is essentially lower than the temperature needed to completely cancel the quenching for the SQD (60 K) (Fig. 3a).

In sharp contrast to these observations, practically no such quenching effects were registered at a sample position with an even higher dot density (MQDs 2). In fact, $R_{\text{QD}} \approx 0.9$ already at $T = 5$ K (solid triangles in Fig. 3a) and remains at a value of around 1 for $T > 5$ K. In the following, we will present a qualitative model which explains the quenching phenomenon, as well as its disappearance at increased temperature and dot density.

To explain the quenching effect, we note first that, at an excitation energy of $h\nu_{\text{ex}} = 1.410$ eV of the principal laser L_0 (vertical solid arrow $h\nu_{\text{ex}}^2$ in the inset to Fig. 1), the IR laser had no effect on I_{QD} (results not shown here). This means that L_{IR} cannot influence the number of e - h pairs which have already been captured into the QD (under these experimental conditions, e 's and h 's are not subjected to transport along the plane of the WL prior to capture into the QD). Consequently, the reason for the observed decrease in I_{QD} registered for an excitation energy of $h\nu_{\text{ex}}^2 = 1.471$ eV is the influence of the L_{IR} on the transport properties of the carriers in the WL plane. Secondly, I_{QD} is proportional to the collection efficiency α , as explained above. Accordingly, the observed decrease in I_{QD} means a considerable reduction in α measured under dual laser excitation (α^{dual}) with respect to the corresponding single-laser excitation conditions (α^{single}). Thirdly, as was stated above, L_{IR} supplies the sample with excess h 's. Consequently, the model suggested should explain how the appearance of the surplus h 's can affect the carrier transport in the WL plane.

We propose the following model to explain the influence of the extra charge on the collection efficiency of the photocreated carriers from the WL into the QD. The existence of an electric field F in the plane of the WL is assumed. Photoexcited e 's and h 's, generated at arbitrary spots within the laser illumination, move along the plane of the WL for a certain time (τ) while decreasing in kinetic energy until they bind together and recombine as excitons, contributing to I_{WL} . The QD can capture carriers/excitons only for the case when the capture time from the WL into the QD is less than τ . Accordingly, a rather high velocity is needed to have a nonvanishing probability for carrier transport and capture into a QD. The carriers are assumed to achieve a rather high velocity with respect to the thermal velocity when their transport is influenced by the field F .

The origin of the built-in field is at present not known, and further studies are needed to reveal its nature. The origin is believed to be due to donors and acceptors positioned in the vicinity of the QD [15, 16]. An e from the donor atom can be captured by an acceptor, thus giving rise to a built-in field F with a component along the WL plane as a result of the charge separation. When the surplus h 's, photoexcited by the L_{IR} ,

appear in the WL, the carriers will move along the direction of the built-in field. If these extra h 's are localized at the interface potential fluctuations, they could stay there for a rather long time (until an e to recombine with approaches), providing an effective screening of the field F . (A more detailed discussion of the screening mechanism is given in [21].) Consequently, the transport of e 's and h 's excited in the WL by L_0 and L_{IR} will be determined by the thermal velocity, which is assumed to be essentially lower than the drift velocity under the unscreened field conditions, and, accordingly, a decrease in I_{QD} ($R_{\text{QD}} < 1$) is expected.

It is important to note that the absolute value of R_{QD} measured under the given experimental conditions (with respect to P_0 , P_{IR} , T) for other individual SQDs was found to exhibit variations depending on the particular SQD under study. This is reasonable since the concentration and space distribution of impurity atoms in close vicinity to a given SQD, which determines the value of F , should vary depending on their exact location in the sample.

The experimentally measured R_{QD} can be expressed in terms of the collection efficiencies in the following way:

$$R_{\text{QD}} = \frac{\alpha^{\text{dual}}}{\alpha^{\text{single}}} R_{\text{WL}}, \quad (1a)$$

where

$$R_{\text{WL}} = \frac{I_{\text{WL}}^{\text{dual}}}{I_{\text{WL}}^{\text{single}}}, \quad (1b)$$

$I_{\text{WL}}^{\text{single}}$ ($I_{\text{WL}}^{\text{dual}}$) is the WL PL intensity with single (dual) laser excitation. To explain the observed increase in R_{QD} with increasing T (Fig. 3a), we need, according to Eq. (1a), information on the temperature evolution of both R_{WL} and $\alpha^{\text{dual}}/\alpha^{\text{single}}$.

Figure 4a shows R_{WL} for a SQD measured as a function of temperature. It is seen that its value progressively reduces down to $R_{\text{WL}} \approx 1$ at elevated T 's. Consequently, according to Eq. (1a), the only reason for the observed increase in R_{QD} (Fig. 3a) is the increase in $\alpha^{\text{dual}}/\alpha^{\text{single}}$ as T becomes higher. Obviously, there could be two basically different reasons for the increase in $\alpha^{\text{dual}}/\alpha^{\text{single}}$: α^{single} reduces down to α^{dual} as T increases or, on the contrary, α^{dual} could increase significantly to reach a value of α^{single} at elevated temperatures. The first possibility would imply a temperature-induced screening of the built-in electric field, which facilitates carrier capture into the QD. The second possibility would correspond to the experimental situation where the carrier capture into the QD at high T 's becomes so effective that the role of the field F for the carrier transport progressively diminishes with temperature.

To distinguish between these two possibilities, we have studied the temperature evolution of $I_{\text{QD}}^{\text{single}}$ and $I_{\text{WL}}^{\text{single}}$ (Fig. 4b). It is seen that, with increasing T , $I_{\text{WL}}^{\text{single}}$ progressively reduces (by more than two orders of magnitude for the total T range studied), while $I_{\text{QD}}^{\text{single}}$ reveals an essential increase (>5 times) when T changes from 5 up to 40 K and then dominates the μPL spectrum of a sample for $T > 40$ K. The considerable decrease in $I_{\text{WL}}^{\text{single}}$ (Fig. 4b) could be explained in the following way. At low T 's, photoexcited carriers are captured into localized states of the WL (processes shown by arrow γ_r in the inset to Fig. 1) and stay there until they recombine radiatively, contributing to the PL signal of the WL (arrow I_{WL} in the inset to Fig. 1). The existence of such localized states in the WL is evidenced by the observation of a number of sharp peaks (separated from each other by <1 meV) superimposed on the low-energy tail of the WL emission band (Fig. 1). As T increases, carriers become delocalized and their thermal velocity increases. These two effects result in a more efficient transport of carriers along the plane of the WL. Consequently, the probability of a carrier approaching a QD (proportional to γ_c) or, alternatively, a CNR (proportional to γ_{nr}) is considerably increased at elevated T 's. This eventually results in both processes. The increased probability of capture at a CNR will contribute to the quenching of the WL PL, while the increased probability of becoming trapped in a QD will contribute to the enhancement of the SQD PL signal (Fig. 4b). The crucial role of the carrier transport prior to the trapping into the CNR has been described elsewhere [30].

The observed temperature dependence of the R_{WL} (Fig. 4a) can be qualitatively explained in terms of an essentially increased value of γ_{nr} at elevated T 's. Indeed, at low T 's, i.e., low values of γ_{nr} , carriers which are released from the CNRs (as a result of the influence of L_{IR}) were captured into localized states of the WL prior to capture back to the CNRs. This resulted in an increase in I_{WL} ($R_{\text{WL}} > 1$). At elevated T 's, the capture to the CNRs becomes more efficient, as explained above. Consequently, the L_{IR} -induced effect of carrier release from the CNRs (arrow IR_1 in the inset to Fig. 1), which initiates an essential increase in the I_{WL} at low T 's, starts to play a minor role at elevated T 's. This explains the gradual decrease in R_{WL} with increasing T (Fig. 4a).

We thus conclude that the observed increase in I_{QD} is entirely determined by T -induced changes in the transport of carriers. This conclusion is justified by the following experimental observation. At a principal laser excitation energy of $h\nu_{\text{ex}} = 1.410$ eV (shown by the vertical solid arrow $h\nu_{\text{ex}}^2$ in the inset to Fig. 1), i.e., at excitation directly into the dot, when no transport of carriers along the plane of the WL is needed prior to capture into the dot, the SQD PL signal does not change

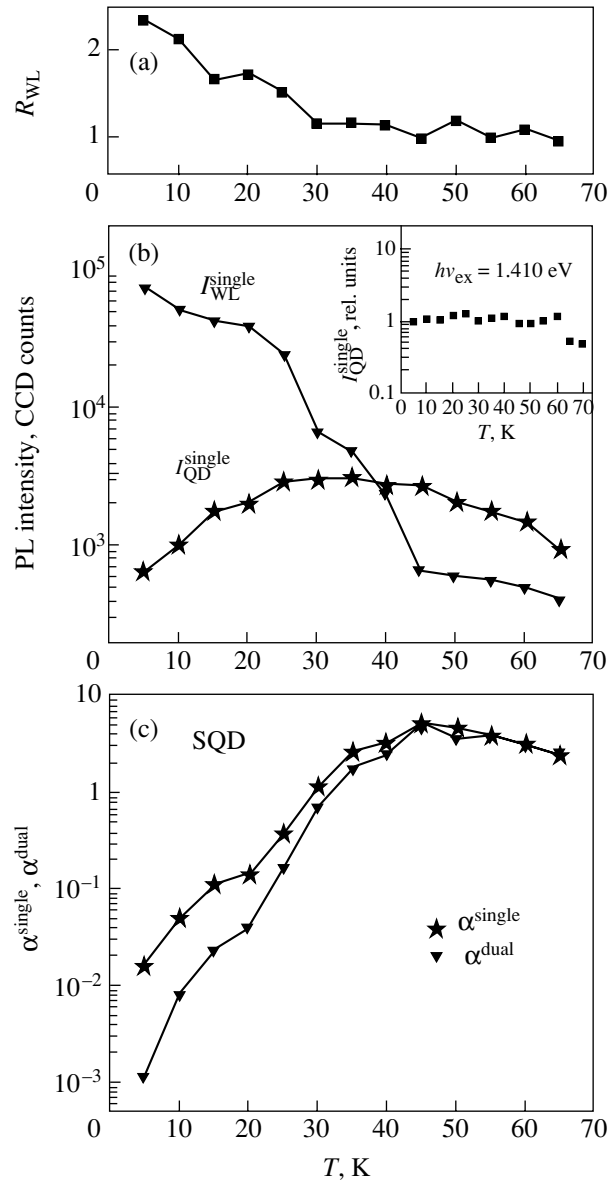


Fig. 4. (a) R_{WL} measured for SQD at $h\nu_{\text{IR}} = 1.240$ eV, $h\nu_{\text{ex}} = 1.471$ eV, $P_0 = 200$ nW, and $P_{\text{IR}} = 100$ μW for a number of T 's. (b) $I_{\text{WL}}^{\text{single}}$ and $I_{\text{QD}}^{\text{single}}$ measured for SQD at $h\nu_{\text{ex}} = 1.471$ eV and $P_0 = 200$ nW at different T 's. (c) α^{single} and α^{dual} measured for SQD at $h\nu_{\text{IR}} = 1.240$ eV, $h\nu_{\text{ex}} = 1.471$ eV, $P_0 = 200$ nW, and $P_{\text{IR}} = 100$ μW for a number of T 's. The inset to (b) shows $I_{\text{QD}}^{\text{single}}$ measured for SQD at $h\nu_{\text{ex}} = 1.410$ eV and $P_0 = 17$ μW at different T 's.

in the temperature range $5 < T < 60$ K (see inset to Fig. 4b).

Figure 4c shows the experimentally derived values of α^{dual} and α^{single} measured for a SQD as a function of temperature. It is seen that both α^{dual} and α^{single} progressively increase with increasing T , with $\alpha^{\text{dual}} \approx \alpha^{\text{single}}$ at elevated temperatures, which in turn results in the dis-

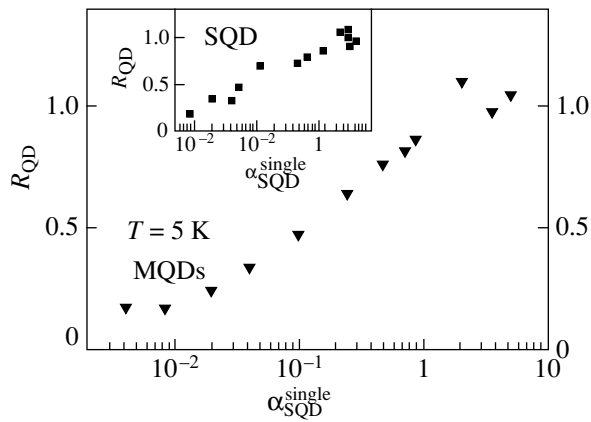


Fig. 5. R_{QD} measured for sample spots with different dot density at $T = 5$ K, $h\nu_{\text{IR}} = 1.240$ eV, $h\nu_{\text{ex}} = 1.471$ eV, $P_0 = 200$ nW, and $P_{\text{IR}} = 100$ μ W plotted for a number of $\alpha_{\text{MQDs}}^{\text{single}}$. The inset shows R_{QD} for SQD plotted for a number of $\alpha_{\text{SQD}}^{\text{single}}$ measured at different T 's (taken from Fig. 4c).

appearance of the I_{QD} quenching effect. Consequently, we explain the experimentally observed fact of the progressive increase in R_{QD} up to 1 at elevated T 's (Fig. 3a) in terms of a considerable increase in the QD collection efficiency rather than by a decrease in α^{single} down to α^{dual} . In other words, at increased temperatures, the SQD collects carriers so effectively that the role of the internal field, which improves the carrier transport at low T 's, becomes negligible.

It is interesting to note that the increase in T results in a qualitatively similar behavior of I_{QD} and I_{WL} measured on high dot density spots. Typical examples of the temperature evolution of $I_{\text{QD}}^{\text{single}}$ measured for the MQDs 1 and MQDs 2 and compared with the SQD are shown in Fig. 3b. An increase in the $I_{\text{QD}}^{\text{single}}$ by approximately 2.7 times was recorded for MQDs 1, which is essentially less than the corresponding value of 5.5 measured for the SQD (Fig. 3b). In contrast to these observations, only a small increase (up to 50%) in the $I_{\text{QD}}^{\text{single}}$ was revealed for MQDs 2. The observed behavior (Fig. 3b) is consistent with the idea of a temperature-improved transport of carriers in the plane of the WL. In fact, the different sample positions reveal different values of α^{single} at $T = 5$ K, namely, 0.01, 0.1, and 2.3 for the SQD, MQDs 1, and MQDs 2, respectively. We note here that, in the upper limit of the value of collection efficiency ($\alpha^{\text{single}} \rightarrow \infty$), all the carriers generated are able to be captured into the quantum dots even at low T . Accordingly, the increase in T is not expected to give any further increase in I_{QD} . Consequently, the higher the value of α^{single} at low T , the less the predicted T -induced increase in I_{QD} , which is nicely confirmed by the data shown in Fig. 3b. These experimental findings are con-

sistent with the temperature-induced behavior of the $I_{\text{QD}}^{\text{single}}$ revealed in ordinary (macro)-PL measurements: $I_{\text{QD}}^{\text{single}}$ for low dot density revealed an increase by two times as T was increased from 20 to 90 K, while no increase was registered for the case of high dot density structures [14].

The changes in the temperature evolution of the R_{QD} registered for the case of MQDs 1 and MQDs 2 with respect to the case of SQD (Fig. 3a) can also be explained satisfactorily within the model proposed. In fact, with increasing collection efficiency, the role of the internal field becomes less important. This explains the essentially higher values of R_{QD} 's of 0.5 and 0.9 measured at $T = 5$ K for MQDs 1 and MQDs 2, respectively, as compared to that of 0.1 for the case of SQD (Fig. 3a). In addition, the higher the collection efficiency at $T = 5$ K, the lower the temperature needed to increase its value even further up to the value at which the role of F on the carrier transport diminishes. This satisfactorily explains the T values of 30 and 10 K at which R_{QD} becomes equal to 1 for MQDs 1 and MQDs 2, respectively (Fig. 3a).

We finally note that the increase in R_{QD} up to 1 measured for the SQD at different T 's was interpreted in terms of a temperature-induced increase in the parameter $\alpha^{\text{single}}(\alpha^{\text{dual}})$. To verify this interpretation, we performed another experiment with the aim of increasing the QD collection efficiency even at low T , namely, by selecting sample positions with different dot densities. If the suggested model is correct, a similar effect of $\alpha^{\text{single}}(\alpha^{\text{dual}})$ on R_{QD} should also be detected in the latter case. Figure 5 shows the ratio R_{QD} plotted as a function of α^{single} for different dot density spots of the structure ($\alpha_{\text{MQDs}}^{\text{single}}$) and for the SQD ($\alpha_{\text{SQD}}^{\text{single}}$) (inset to Fig. 5). The different values of $\alpha_{\text{SQD}}^{\text{single}}$ were evaluated for different T (from Fig. 4c), as explained above. The two dependences behave in a similar way. A progressive increase in R_{QD} with increasing $\alpha_{\text{MQDs}}^{\text{single}}$ or $\alpha_{\text{SQD}}^{\text{single}}$ is recorded (Fig. 5 or inset to Fig. 5, respectively), a fact which strongly supports the model proposed.

4. CONCLUSIONS

An additional IR laser considerably quenches the QD PL signal. This is explained in terms of the screening of the internal electric field by the extra holes created in the sample as a result of the IR excitation. The quenching effect progressively vanishes with increasing temperature, as well as dot density. These observations are due to a considerably improved QD collection efficiency, at which the effect of an electric field on the carrier transport in the plane of the WL becomes less important. The observed effects could be widely used in practice to effectively tune the QD collection effi-

ciency and manipulate the light emission intensity in QD-based optoelectronic devices.

ACKNOWLEDGMENTS

E.S.M. gratefully acknowledges financial support from the Wenner–Gren Foundations and partial support from the program “Low-Dimensional Quantum Structures” of the Russian Academy of Sciences. V.D. is thankful to the Swedish Foundation for International Cooperation in Research and Higher Education (STINT) for their financial support.

REFERENCES

- L. Jacak, P. Hawrylak, and A. Wojs, *Quantum Dots* (Springer, Berlin, 1998).
- D. Gammon and D. G. Steel, *Phys. Today* **55** (10), 36 (2002).
- L. Harris, D. J. Mowbray, M. S. Skolnick, M. Hopkinson, and G. Hill, *Appl. Phys. Lett.* **73** (7), 969 (1998).
- S. Maimon, E. Finkman, G. Bahir, S. E. Schacham, J. M. Garcia, and P. M. Petroff, *Appl. Phys. Lett.* **73** (14), 2003 (1998).
- J. J. Finley, M. Skalitz, M. Arzberger, A. Zrenner, G. Böhm, and G. Abstreiter, *Appl. Phys. Lett.* **73** (18), 2618 (1998).
- D. Bimberg, M. Grundmann, and N. N. Ledentsov, *Quantum Dot Heterostructures* (Wiley, London, 1999).
- K. H. Schmidt, G. Medeiros-Ribeiro, J. M. Garcia, and P. M. Petroff, *Appl. Phys. Lett.* **70** (13), 1727 (1997); J. M. Garcia, T. Mankad, P. O. Holtz, P. J. Wellman, and P. M. Petroff, *Appl. Phys. Lett.* **72** (24), 3172 (1998); J. M. Garcia, G. Medeiros-Ribeiro, K. Schmidt, T. Ngo, J. L. Feng, A. Lorke, J. Kotthaus, and P. M. Petroff, *Appl. Phys. Lett.* **71** (14), 2014 (1997).
- R. Heitz, M. Veit, N. N. Ledentsov, A. Hoffmann, D. Bimberg, V. M. Ustinov, P. S. Kop'ev, and Zh. I. Alferov, *Phys. Rev. B: Condens. Matter* **56** (16), 10435 (1997).
- A. W. E. Minnaert, A. Yu. Silov, W. van der Vleuten, J. E. M. Haverkort, and J. H. Wolter, *Phys. Rev. B: Condens. Matter* **63** (7), 075 303 (2001); F. Findeis, A. Zrenner, G. Böhm, and G. Abstreiter, *Phys. Rev. B: Condens. Matter* **61** (16), R10 579 (2000); R. Heitz, I. Mukhametzhanov, O. Stier, A. Madhukar, and D. Bimberg, *Phys. Rev. Lett.* **83** (22), 4654 (1999).
- B. Ohnesorge, M. Albrecht, J. Oshinowo, A. Forchel, and Y. Arakawa, *Phys. Rev. B: Condens. Matter* **54** (16), 11 532 (1996); U. Bockelmann and T. Egeler, *Phys. Rev. B: Condens. Matter* **46** (23), 15 574 (1992); A. Rack, R. Wetzler, A. Wacker, and E. Schöll, *Phys. Rev. B: Condens. Matter* **66** (16), 165 429 (2002); S. Raymond, K. Hinzer, S. Fafard, and J. L. Merz, *Phys. Rev. B: Condens. Matter* **61** (24), R 16331 (2000).
- P. P. Paskov, P. O. Holtz, B. Monemar, J. M. Garcia, W. V. Schoenfeld, and P. M. Petroff, *Appl. Phys. Lett.* **77** (6), 812 (2000).
- Y. Toda, O. Moriwaki, M. Nishioka, and Y. Arakawa, *Phys. Rev. Lett.* **82** (20), 4114 (1999).
- A. F. G. Monte, J. J. Finley, A. D. Ashmore, A. M. Fox, D. J. Mowbray, M. S. Skolnick, and M. Hopkinson, *J. Appl. Phys.* **93** (6), 3524 (2003).
- C. Lobo, R. Leon, S. Marcinkevičius, W. Yang, P. Sercel, X. Z. Liao, J. Zou, and D. J. H. Cockayne, *Phys. Rev. B: Condens. Matter* **60** (24), 16 647 (1999).
- M. M. Sobolev, A. R. Kovsh, V. M. Ustinov, A. Yu. Egorov, A. E. Zhukov, M. V. Maksimov, and N. N. Ledentsov, *Semiconductors* **31** (10), 1074 (1997).
- S. Marcinkevičius, J. Siegert, R. Leon, B. Čechavičius, B. Magness, W. Taylor, and C. Lobo, *Phys. Rev. B: Condens. Matter* **66** (23), 235 314 (2002).
- S. Ménard, J. Beerens, D. Morris, V. Aimez, J. Beauvais, and S. Fafard, *J. Vac. Sci. Technol.* **20** (4), 1501 (2002).
- S. Marcinkevičius, A. Gaarder, and R. Leon, *Phys. Rev. B: Condens. Matter* **64** (11), 115 307 (2001).
- S. Marcinkevičius and R. Leon, *Appl. Phys. Lett.* **76** (17), 2406 (2000).
- P. W. Fry, J. J. Finley, L. R. Wilson, A. Lemaître, D. J. Mowbray, M. S. Skolnick, M. Hopkinson, G. Hill, and J. C. Clark, *Appl. Phys. Lett.* **77** (26), 4344 (2000).
- E. S. Moskalkenko, V. Donchev, K. F. Karlsson, P. O. Holtz, B. Monemar, W. V. Schoenfeld, J. M. Garcia, and P. M. Petroff, *Phys. Rev. B: Condens. Matter* **68** (15), 155 317 (2003).
- P. Silverberg, P. Omling, and L. Samuelson, *Appl. Phys. Lett.* **52** (20), 1689 (1988).
- D. A. Mazurenko, A. V. Scherbakov, A. V. Akimov, A. J. Kent, and M. Henini, *Semicond. Sci. Technol.* **14** (12), 1132 (1999).
- M. Sugisaki, H. W. Ren, K. Nishi, and Y. Masumoto, *Phys. Rev. Lett.* **86** (21), 4883 (2001).
- E. S. Moskalkenko, K. F. Karlsson, P. O. Holtz, B. Monemar, W. V. Schoenfeld, J. M. Garcia, and P. M. Petroff, *Phys. Rev. B: Condens. Matter* **64** (8), 085 302 (2001).
- A. V. Akimov, V. V. Krivolapchuk, N. K. Poletaev, and V. G. Shofman, *Semiconductors* **27** (2), 171 (1993).
- K. F. Karlsson, E. S. Moskalkenko, P. O. Holtz, B. Monemar, W. V. Schoenfeld, J. M. Garcia, and P. M. Petroff, *Appl. Phys. Lett.* **78** (19), 2952 (2001).
- H. D. Robinson and B. B. Goldberg, *Phys. Rev. B: Condens. Matter* **61** (8), R5086 (2000).
- J. Seufert, R. Weigand, G. Bacher, T. Kummell, A. Forchel, K. Leonardi, and D. Hommel, *Appl. Phys. Lett.* **76** (14), 1872 (2000).
- V. N. Abakumov, V. I. Perel, and I. N. Yassievich, *Non-radiative Recombination in Semiconductors* (North-Holland, Amsterdam, 1991).

LOW-DIMENSIONAL SYSTEMS
AND SURFACE PHYSICS

Exciton and Intracenter Luminescence in $\text{Cd}_{0.6}\text{Mn}_{0.4}\text{Te}/\text{Cd}_{0.5}\text{Mg}_{0.5}\text{Te}$ Quantum-Well Structures

V. F. Agekyan*, N. N. Vasil'ev*, A. Yu. Serov*, N. G. Filosofov*, and G. Karczewski**

*Fock Institute of Physics, St. Petersburg State University, ul. Ul'yanovskaya 1, Petrodvorets, St. Petersburg, 198504 Russia
e-mail: avf@VA4678.spb.edu

**Institute of Physics, Polish Academy of Sciences, Warsaw, 02-668 Poland

Received February 1, 2005

Abstract—Exciton luminescence and intracenter luminescence (IL) of Mn^{2+} ions in $\text{Cd}_{0.6}\text{Mn}_{0.4}\text{Te}/\text{Cd}_{0.5}\text{Mg}_{0.5}\text{Te}$ structures with quantum wells (QWs) 7, 13, and 26 monolayers thick were studied. It was established that in QWs the intensity of exciton luminescence with respect to that of IL is a few orders of magnitude higher than that in bulk crystals. The spectral position of manganese IL profile changes noticeably in going from a bulk crystal to a QW of the same composition. The nonexponential parts of the IL decay curves are determined by excitation migration and the cooperative upconversion process, whose contribution is high under strong excitation and efficient migration. At 77 K, the IL decay constant τ within the exponential region increases with decreasing QW thickness. The decay constant τ in a QW, unlike in a bulk $\text{Cd}_{0.5}\text{Mn}_{0.5}\text{Te}$ crystal, decreases substantially under cooling from 77 to 4 K. © 2005 Pleiades Publishing, Inc.

1. INTRODUCTION

The II–VI crystals part of whose cations are replaced by iron group elements make up the best known family of dilute magnetic semiconductors (DMS). The specific properties of DMSs, which are responsible, for instance, for the giant magneto-optical effects and magnetic polaron formation, are accounted for by the large magnetic moment of the unfilled $3d$ shells. This explains the existence of strong exchange interaction between magnetic atoms and between magnetic atoms and electrons [1, 2]. Another remarkable property of DMSs is the intracenter optical transitions connecting electronic levels of the $3d$ shell of iron group ions, which contribute to the absorption and luminescence. The bright intracenter photo- and electroluminescence of Mn^{2+} ions is observed in the visible spectral region. This makes manganese-based DMSs an attractive subject for basic and applied research. The decrease in the quantum yield of intracenter luminescence (IL) observed at high manganese concentrations is due to excitation migration. Hence, partial or total suppression of this migration in structures with lowered dimensionality can substantially change the dependence of the IL parameters on the temperature, Mn^{2+} ion concentration, and optical excitation level (or electric current in the case of electroluminescence). The IL parameters can also be strongly affected by quantum confinement effects. One of the most popular DMSs is $\text{Cd}_{1-x}\text{Mn}_x\text{Te}$, where intracenter transitions between the 6A_1 and 4T_1 levels are observed for $x > 0.4$ [1, 3–5]. The 6A_1 ground state is insensitive to the magnitude of the crystal field, whereas the radiating 4T_1 level lowers with

an increase in the field, so the excitation threshold and the Mn^{2+} IL band shift toward lower energies [6].

Bulk crystals and nanocrystals of manganese-containing DMSs have been fairly well studied. In the particular case of doped nanostructures, the Mn^{2+} IL has been investigated in broad-bandgap II–VI nanocrystals [7–18]. Considerable attention has been focused on exciton emission from $\text{Cd}_{1-x}\text{Mn}_x\text{Te}$ quantum wells (QWs) with a low manganese content, as well as on the Mn^{2+} IL from the wide barriers in $\text{CdTe}/\text{Cd}_{0.4}\text{Mn}_{0.6}\text{Te}$ [19, 20]. There was an increase in interest in low-dimensional structures containing optically active ions after the publication of theoretical studies [21, 22], which provided an explanation for the strong variation of intracenter transition parameters in the $3d$ and $4f$ shells of iron and rare-earth group ions under the conditions of spatial and quantum constraints characteristic of low-dimensional systems. The factors underlying these changes are the enhancement of $sp-d$ and $sp-f$ hybridization (caused by quantum confinement), reduced excitation migration over the ions, and faster energy transfer from matrix band states (excitons) to the $3d$ or $4f$ shells. The IL characteristics in nanostructures should also be affected by changes in the crystal field and electron–phonon coupling. Some studies seem to suggest that the predictions made in [21, 22], in particular, a decrease in the Mn^{2+} IL decay time in nanocrystals by a few orders of magnitude, find experimental support [16–18, 22]. However, there is another point of view, namely, that the fast luminescence component observed in nanocrystals is not related in any way to intracenter transitions in manganese [9, 18]. It was shown in [7, 23] that the IL quantum yield of man-

ganese can be raised markedly if the nanocrystal surface is well passivated.

The radiative time τ_0 for the 4T_1 level also depends on the matrix refractive index n . According to [24, 25]

$$\tau_0 = f^{-1} \lambda_0 / [(n+2)^2 n],$$

where f is the transition oscillator strength, λ_0 is the wavelength in vacuum, and the value of n is determined in a volume around the radiating center that is substantially smaller than λ_0^3 . In the superlattices studied by us, the magnitude of n is affected by the replacement of manganese by magnesium as one goes from the quantum well to the barrier. An important factor is the dependence of n in the Mn^{2+} IL spectral region on the energy separation between the intracenter excitation threshold and the exciton level, which can be varied. In a bulk $\text{Cd}_{1-x}\text{Mn}_x\text{Te}$ crystal, this separation is determined by the value of x , and in nanostructures, by x and the quantum-confinement shift of the exciton level.

We report here on the Mn^{2+} IL and exciton luminescence in $\text{Cd}_{1-x}\text{Mn}_x\text{Te}$ QWs of different thickness and with a high manganese content and on a comparison of the IL kinetics in bulk crystals and QWs.

2. EXPERIMENTAL TECHNIQUES

A series of $\text{Cd}_{1-x}\text{Mn}_x\text{Te}/\text{Cd}_{0.5}\text{Mg}_{0.5}\text{Te}$ superlattices (SL) 100 or 80 periods long were MBE grown. In samples 1–3 ($x = 0.4$), the QW thicknesses L_z are 7, 13, and 26 monolayers (ML), respectively, and in sample 4 ($x < 0.4$), $L_z = 13$ ML. In all SLs, the $\text{Cd}_{0.5}\text{Mg}_{0.5}\text{Te}$ barriers are 46 ML thick. The structures are type I, and the barrier height is about 100 meV in the conduction band and 60 meV in the valence band. The SLs were grown on (100) GaAs substrates with CdTe (4.2 μm) and $\text{Cd}_{0.5}\text{Mg}_{0.5}\text{Te}$ (0.4 μm) buffer layers and capped by a 40-nm-thick $\text{Cd}_{0.5}\text{Mg}_{0.5}\text{Te}$ layer. The luminescence was excited at 4 and 77 K with a cw argon ion laser and the second harmonic of a YAG : Nd^{3+} laser operating with pulses about 10^{-8} s long at a repetition rate of 1 kHz; so the pulse separation was substantially in excess of the Mn^{2+} IL decay time.

3. RESULTS AND DISCUSSION

3.1. Luminescence Spectra

All samples exhibit exciton emission bands from the QWs and barriers, with the relative intensity of these bands varying little in the temperature interval 4–77 K. When measured in identical excitation conditions, the spectra of samples 2 ($L_z = 13$ ML) and 3 ($L_z = 26$ ML) are dominated by the QW exciton, whereas in sample 1 ($L_z = 7$ ML) the barrier exciton is much stronger (Fig. 1). In the latter case, the relaxation of free carriers and excitons into the narrow QW occurs slowly; so, on the one hand, the barrier exciton luminescence is

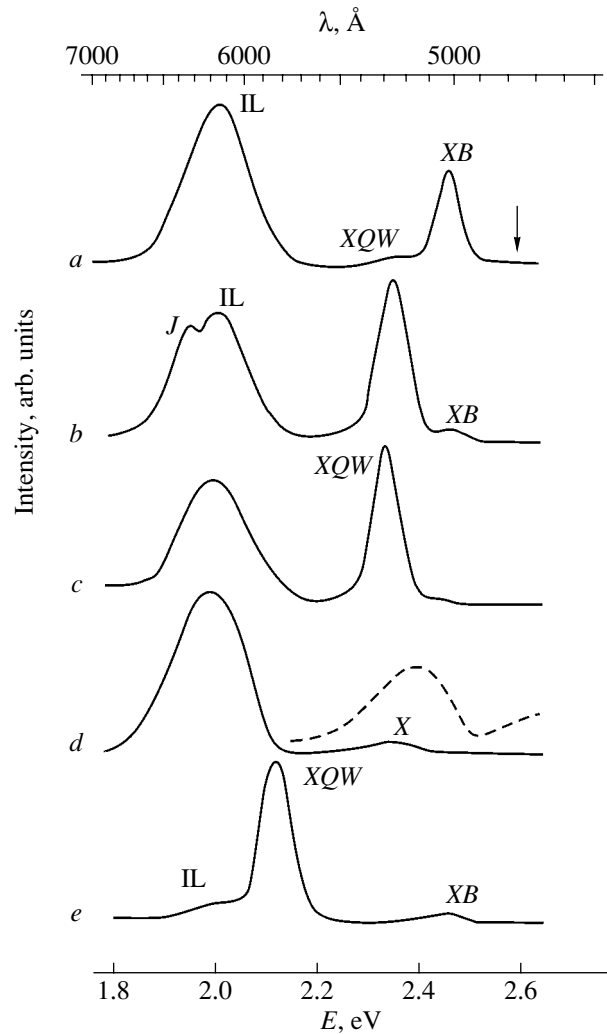


Fig. 1. Luminescence spectra of $\text{Cd}_{1-x}\text{Mn}_x\text{Te}/\text{Cd}_{0.5}\text{Mg}_{0.5}\text{Te}$ QW structures obtained under cw excitation with $I_E = 10 \text{ W cm}^{-2}$ at $T = 77 \text{ K}$ for (a) sample 1 (with 7-ML-thick QWs), (b) sample 2 (13 ML), (c) sample 3 (26 ML), (d) bulk $\text{Cd}_{0.5}\text{Mn}_{0.5}\text{Te}$ crystal, and (e) sample 4 (13 ML). IL indicates Mn^{2+} intracenter luminescence; XQW and XB stand for quantum-well and barrier excitons, respectively; indicates a line of unknown origin; and stands for the bulk-crystal exciton. The dashed line is a reflectance spectrum of bulk $\text{Cd}_{0.5}\text{Mn}_{0.5}\text{Te}$.

strong, but, on the other hand, practically all excitons in a QW have enough time to transfer their energy nonradiatively into the $3d$ shell of the manganese ions. In sample 4, where the exciton level lies below the Mn^{2+} intracenter excitation threshold, the Mn^{2+} IL is weaker than that in the other samples.

The QWs contain Mn^{2+} ions located on the interface and inside the QWs. The crystal field acting on a Mn^{2+} ion is determined primarily by the nearest anion environment. It was shown, however, that the position of the IL maximum is noticeably affected by the relative cation concentrations, because the average interatomic

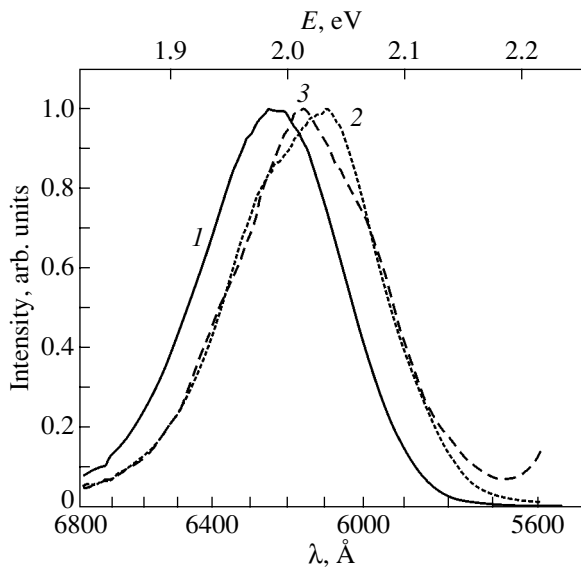


Fig. 2. Mn^{2+} intracenter luminescence normalized to the maximum intensity under cw excitation at $I_E = 10 \text{ W cm}^{-2}$ and $T = 77 \text{ K}$ for (1) bulk $\text{Cd}_{0.5}\text{Mn}_{0.5}\text{Te}$, (2) sample 1 (with 7-ML-thick QWs), and (3) sample 3 (26 ML). The IL profiles in the superlattice are distorted by interference in the thick buffer layer.

distances depend on the cation type. The IL maximum can be shifted either due to a change in manganese concentration (in $\text{Cd}_{1-x}\text{Mn}_x\text{Te}$), which may be partially assigned to $d-d$ interaction, or at a fixed manganese concentration (e.g., in $\text{Cd}_{1-x-y}\text{Mn}_x\text{Mg}_y\text{Te}$, due to a change in magnesium content [26, 27]). In our SLs, the interface manganese ions are acted upon by a weaker crystal field. In sample 1, which has a narrow QW that is dominated by interface ions, one should expect the IL shift to higher energies to be maximum. Moreover, the crystal field acting on an interface Mn^{2+} ion has a lowered symmetry, which should initiate enhancement of the oscillator strength of the forbidden $d-d$ transition as compared to transitions in ions residing inside a QW and, thus, make the high-energy wing of the IL profile stronger. Figure 2 demonstrates a considerable high-energy shift of the SL IL band as compared to that in a bulk $\text{Cd}_{0.5}\text{Mn}_{0.5}\text{Te}$ crystal (a change of x from 0.4 to 0.5 does not markedly displace the IL band), but the emission band profiles of samples 1 and 3 do not differ noticeably. A change in the electron-phonon coupling (which is dependent on the QW thickness and elemental composition of the barrier) may provide a certain contribution to the SL IL shift. The SL IL profiles are superposed upon by buffer-layer interference bands, whose separations are several times smaller than the IL profile width.

The homogeneous and inhomogeneous broadenings of the IL band are close in magnitude for a high manganese concentration; in bulk $\text{Cd}_{0.4}\text{Mn}_{0.6}\text{Te}$, they are 85 and 70 meV at 15 K, respectively [28]. The inhomoge-

neous broadening originates from the influence of defects and static fluctuations in the solid-solution composition on the crystal field. The quality of MBE-grown layers should be much higher than that of a bulk crystal prepared by the Bridgman technique. Inhomogeneous broadening, however, is determined primarily by the intrinsic properties of the solid solution; therefore, one can hardly expect a noticeable narrowing of the Mn^{2+} IL band in MBE-grown layers, even less so since the crystal field in QWs is not homogeneous for the above reasons. The $d-d$ interaction among the manganese ions also contributes to inhomogeneous broadening. Experiment argues for the IL band half-widths in an SL and a bulk crystal being very nearly equal.

The relative intensities of Mn^{2+} IL and exciton luminescence in a bulk crystal and a QW differ strongly (Fig. 1). A comparison between a bulk crystal and a QW having the same energy separations between the Mn^{2+} excitation threshold and the exciton level reveals that exciton luminescence in a QW is a few orders of magnitude stronger than the Mn^{2+} IL.

The 1.4-eV region contains a broad band with a decay time of about 100 μs , whose intensity with respect to the 2.0-eV Mn^{2+} band varies from one sample to another both in SLs and bulk $\text{Cd}_{1-x}\text{Mn}_x\text{Te}$ crystals. This band probably derives from structural defects, which are responsible for some manganese ions residing in a region with rock-salt or NiAs structure. In both cases, the crystal field exerted on a cation becomes strongly enhanced as compared to that in a zinc-blende structure; so the fluorescing 4T_1 level of the Mn^{2+} ion shifts toward lower energies. The 1.4-eV band is not observed in SLs with thin QWs (sample 1), implying that, in very thin $\text{Cd}_{1-x}\text{Mn}_x\text{Te}$ layers, structural defects do not form.

3.2. Kinetic Properties of the Mn^{2+} Intracenter Luminescence

The Mn^{2+} IL kinetics depends substantially on external conditions and the parameters of the structure under study. Among them are the temperature, optical excitation level, method of IL excitation (directly into the Mn^{2+} 3d absorption bands or through the band exciton states), manganese concentration, elemental composition of the crystal matrices [4, 28–31], and the design of the structure. We present below data on the IL decay in SLs with narrow and wide $\text{Cd}_{0.6}\text{Mn}_{0.4}\text{Te}$ QWs (samples 1, 3) and in a bulk $\text{Cd}_{0.5}\text{Mn}_{0.5}\text{Te}$ crystal. Taking into account the quantum-confinement exciton-level shift in a QW, one should take for comparison a bulk $\text{Cd}_{0.5}\text{Mn}_{0.5}\text{Te}$ crystal with the same energy distance between the Mn^{2+} excitation threshold and the excitonic level as in the QWs under study. It is essential that the SL barriers be thick enough to suppress intracenter excitation transfer among the QWs.

The Mn^{2+} intracenter emission band derives primarily from the phonon wings of the zero-phonon band, whose half-width is governed by inhomogeneous broadening. Even in the case of selective monochromatic excitation of a zero-phonon state, various zero-phonon states contribute to the kinetics at the point of the IL profile chosen for measurements, because at manganese concentrations above 1% of the total number of cation positions there is spectral diffusion over an inhomogeneously broadened profile. The Mn^{2+} absorption and luminescence bands shown schematically in Fig. 3 for the low-temperature case provide insight into the real situation, which is dependent on the actual position of the IL excitation and measurement points. At high temperatures, emission involving both generation and annihilation of phonons becomes possible, thus complicating the situation. Energy transfer into the 3d shell via band excitons excites the whole Mn^{2+} system. The necessity of taking into account a variety of factors creates difficulties in the quantitative determination of the relative concentration of excited ions for different excitation methods and excitation levels. This aspect requires separate study.

Mn^{2+} IL saturates under strong optical pumping (Fig. 4) not only as a result of a high excited-ion concentration comparable to the total manganese content but also because of upconversion (a cooperative effect) [32], an effect favoring nonradiative relaxation of intracenter excitation. In this particular case, the cooperative effect is a consequence of intracenter excitation transfer to an already excited ion. The upconversion process is essential in the initial stage of the IL decay profile, as long as the excited ion concentration is high. In our case, this process is the energy transfer from one ion to another (already excited) ion, as a result of which part of the energy of the doubly excited ion does not contribute to the 2.0-eV manganese emission band. For this mechanism to be efficient, strong optical pumping should be combined with excitation migration. Migration also favors excitation transfer to lower states of the inhomogeneously broadened profile. Thus, the fast IL decay should become enhanced with increasing temperature and be particularly manifested on the high-energy wing of the Mn^{2+} emission profile. The essential part played by upconversion is indicated, in particular, by the behavior of the IL saturation, which is faster at 77 K than at lower temperatures, where migration becomes weaker. Figure 5 displays the Mn^{2+} IL decay measured in different structures at a high temperature under weak and strong pumping. We readily see that, in the initial nonexponential part of the decay curve, the decay becomes stronger with increasing excitation. With other external conditions being equal, the deviation from an exponential decay is strongest in sample 3. In this structure, the high quality of the crystal layers is combined with efficient in-plane intracenter excitation migration in the thick QW, whereas in sample 1, which

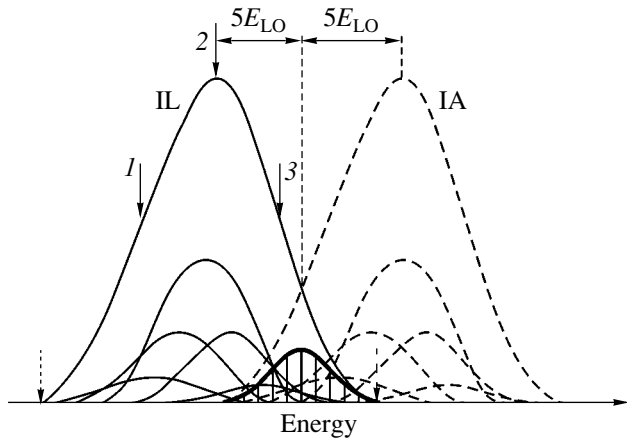


Fig. 3. Intracenter luminescence (IL) and intracenter absorption (IA) bands in $\text{Cd}_{1-x}\text{Mn}_x\text{Te}$ produced at low temperatures in the ${}^6A_1-{}^1T_4$ transition in Mn^{2+} , which become observable for $x > 0.4$ (schematic). The bold profile at the center combines inhomogeneously broadened zero-phonon transitions, and the solid and dashed profiles refer to IL and IA involving phonons. Solid arrows 1–3 identify points in the IL profile at which the radiation kinetics is usually measured, and the extreme points in the IL profile are specified by dashed arrows. E_{LO} is the longitudinal optical phonon energy.

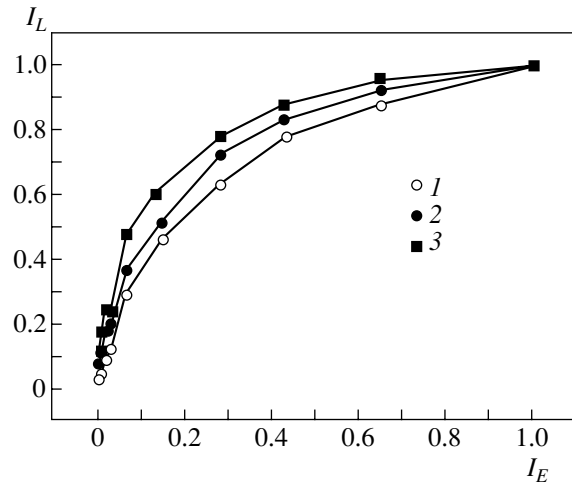


Fig. 4. Mn^{2+} intracenter luminescence intensity I_L in sample 3 (26 ML) measured vs the excitation level I_E with time delays of (1) 0, (2) 1, and (3) 20 μs at $T = 77$ K. The values of I_L are normalized to the level $I_E = 3 \times 10^5 \text{ W cm}^{-2}$ accepted as unity.

has narrow QWs, the migration is limited by the two-dimensional topology of the manganese cluster.

We consider now the exponential part of the IL decay profile, which is described by the $I_L = I_{0L} \exp(-t/\tau)$ relation and corresponds to long delay times, where the cooperative effect is no longer essential. At high manganese concentrations, the homogeneous and inhomogeneous

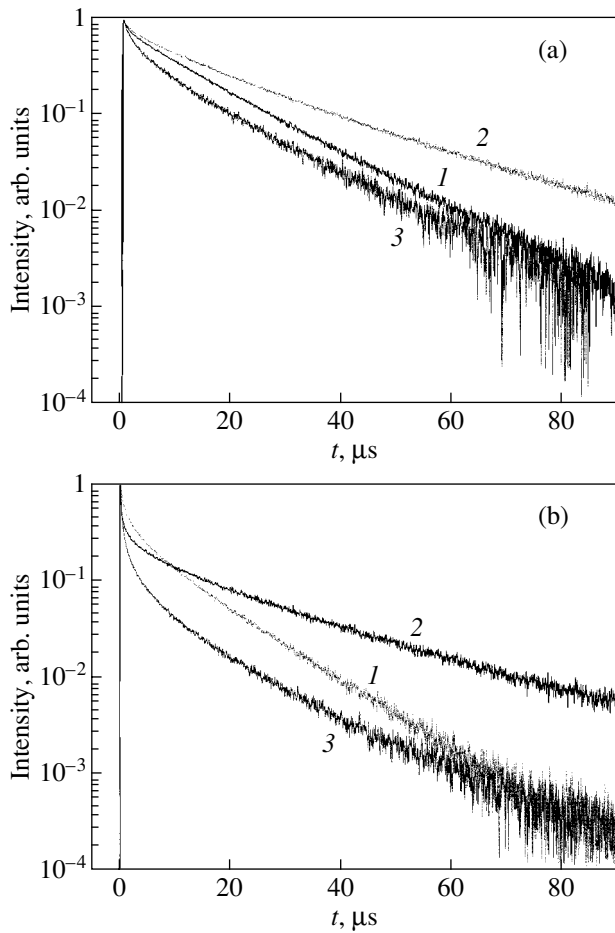


Fig. 5. Mn^{2+} intracenter luminescence decay at the band maximum measured at excitation levels I_E equal to (a) 1×10^2 and (b) $3 \times 10^5 \text{ W cm}^{-2}$ for (1) bulk $\text{Cd}_{0.5}\text{Mn}_{0.5}\text{Te}$, (2) sample 1 (7 ML), and (3) sample 3 (26 ML) at $T = 77 \text{ K}$.

geneous IL band broadenings are not spectrally resolvable; therefore, as already mentioned, the value of τ measured at a point of the profile is actually a superposition of the decay times corresponding to different states within an inhomogeneous zero-phonon profile. The solid arrows in Fig. 3 identify the points at which kinetic measurements are usually performed. “Pure” measurements are seen to be possible only at the extreme IL profile points specified by dashed arrows. Within the other parts of the profile, the dependence of τ on phonon energy offers only a qualitative idea of the lifetime variation over inhomogeneously broadened zero-phonon states. The IL decay profiles in a QW and a bulk crystal at 77 K are shown in Fig. 5. The values of τ at the IL band maximum measured at 77 K and at excitation $I_E = 3 \times 10^5 \text{ W cm}^{-2}$ are 21, 15, and 14 μs for samples 1 and 3 and a bulk $\text{Cd}_{0.5}\text{Mn}_{0.5}\text{Te}$ crystal, respectively. The large value of τ obtained for the structure with thin QWs implies a limited migration of intraionic excitation over a two-dimensional manganese cluster in the QW plane and a high quality of the

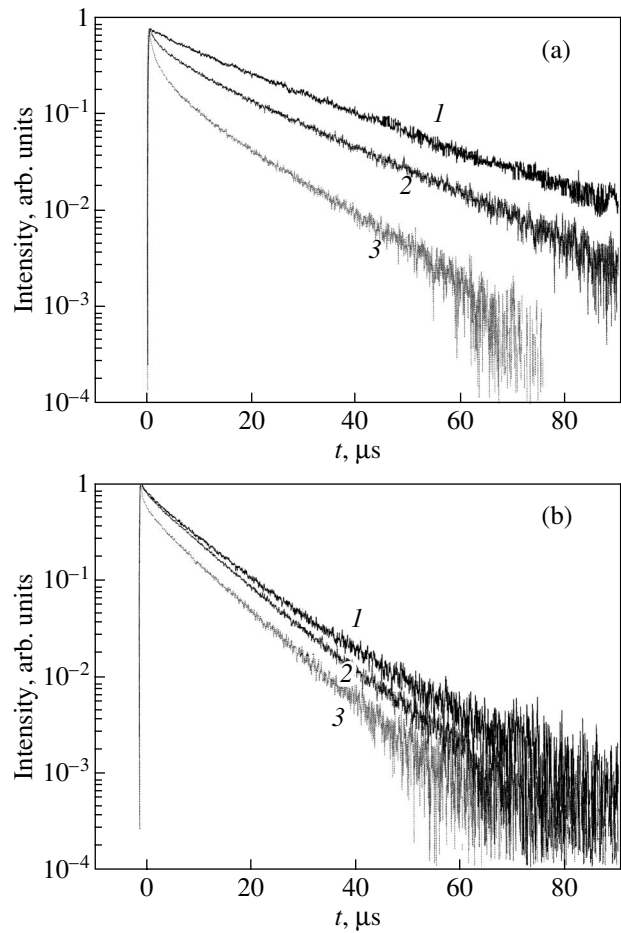


Fig. 6. Mn^{2+} intracenter luminescence decay at a high excitation level $I_E = 3 \times 10^5 \text{ W cm}^{-2}$ for (a) bulk $\text{Cd}_{0.5}\text{Mn}_{0.5}\text{Te}$ and (b) sample 3 (26 ML) at $T = 4 \text{ K}$. Curves 1–3 refer to the three IL profile points identified by solid arrows in Fig. 3.

$\text{Cd}_{0.6}\text{Mn}_{0.4}\text{Te}$ epitaxial layers. The comparatively short τ in sample 3 with wide QWs and in the bulk crystal can be assigned to efficient migration in the QW plane, which results in a higher probability of nonradiative relaxation at defects.

At low temperatures, the nonexponential pattern of decay becomes significant only in the high-energy wing of the IL band, whereas at the band center and particularly on its low-energy wing the decay is close to exponential, irrespective of the excitation level (Figs. 6, 7). In an SL, the decay kinetics is seen to vary over the IL profile much more weakly than it does in a bulk crystal (Fig. 6). This attests to a strong effect of the suppression of intracenter excitation migration in a QW on the low-temperature IL kinetics even in the case of very high manganese concentrations. Note that differences become pronounced already in thick QWs (26-ML thick), which apparently indicates excitation transfer over manganese ions to large distances.

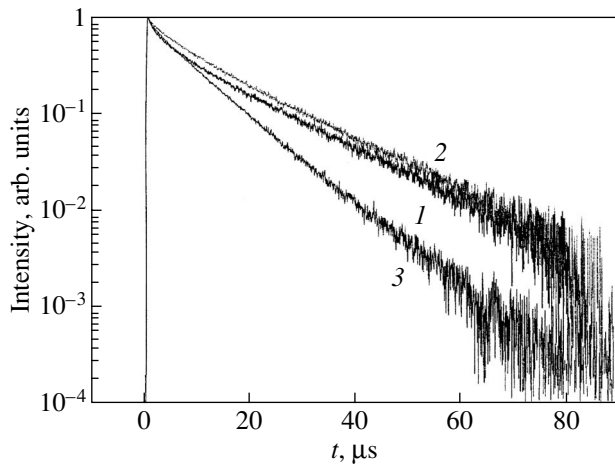


Fig. 7. Mn^{2+} intracenter luminescence decay at the band maximum measured at a high excitation level $I_E = 3 \times 10^5 \text{ W cm}^{-2}$ for (1) bulk $\text{Cd}_{0.5}\text{Mn}_{0.5}\text{Te}$, (2) sample 1 (7 ML), and (3) sample 3 (26 ML) at $T = 4 \text{ K}$.

The values of τ at the IL band maximum obtained at 4 K and at $I_E = 3 \times 10^5 \text{ W cm}^{-2}$ are 12.5, 9, and 16 μs for samples 1 and 3 and a bulk $\text{Cd}_{0.5}\text{Mn}_{0.5}\text{Te}$ crystal, respectively (Fig. 7). Thus, cooling a sample to 4 K drastically cuts the IL exponential decay time in QWs while hardly affecting it in the bulk sample. A possible reason for the decrease in τ in QWs is the considerable increase in the probability of nonradiative relaxation under conditions favoring low-temperature localization of excitations in the interface region, where defects can cluster.

The value of τ within the exponential part of the IL kinetics curves depends on I_E ; indeed, in sample 3, τ decreases from 17 to 14.5 μs as I_E increases from 10^4 to 10^5 W cm^{-2} (at $T = 77 \text{ K}$). This may originate from long-lived optical recharging of interface defects, which changes the nonradiative recombination rate. The values of τ at three points of the IL profile (Fig. 3) listed in the table for sample 3 were obtained at $I_E = 10^4 \text{ W cm}^{-2}$. We readily see that, between points 2 and 3, the decay at 77 K varies slowly, because at high temperatures excitation migration can be accompanied by both a decrease and an increase in energy and the density of states decreases from point 2 to point 3. At 4 K,

Decay times τ at three Mn^{2+} IL profile points (Fig. 3) for sample 3 obtained at $I_E = 10^4 \text{ W cm}^{-2}$

Point	$\tau, \mu\text{s}$	
	77 K	4 K
1	13	9
2	14.5	10
3	15	12.5

where migration of intracenter excitation occurs only with a decrease in energy, τ varies more uniformly over the IL profile.

4. CONCLUSIONS

We have studied exciton and Mn^{2+} IL emission spectra in $\text{Cd}_{1-x}\text{Mn}_x\text{Te}/\text{Cd}_{0.5}\text{Mg}_{0.5}\text{Te}$ SLs with QW widths of 7, 13, and 26 ML at different temperatures and optical pumping levels. The luminescence spectra of excitons and of the Mn^{2+} 3d shell and the kinetics of the manganese 3d shell luminescence are substantially dependent on external conditions and the QW width. The initial nonexponential part of the IL decay profiles is determined by excitation migration and cooperative upconversion, whose contribution depends on the pumping level, temperature, and sample parameters. The IL spectral response and kinetics can be used in describing II–VI semiconductor QW structures containing optically active iron-group ions, for instance, Mn^{2+} and Cr^{2+} .

ACKNOWLEDGMENTS

This study was supported in part by the Ministry of Education of the Russian Federation, project no. E02-3.4-426.

REFERENCES

1. J. K. Furdyna, *J. Appl. Phys.* **64**, R29 (1988).
2. O. Goede and W. Heimbrodt, *Phys. Status Solidi B* **146**, 11 (1988).
3. V. F. Agekyan, Fan Zung, and S. V. Pogarev, *Fiz. Tverd. Tela (Leningrad)* **29**, 3312 (1987) [*Sov. Phys. Solid State* **29**, 1900 (1987)].
4. L. D. Park, S. Yamamoto, J. Watanabe, K. Takamura, and J. Nakahara, *J. Phys. Soc. Jpn.* **66**, 3289 (1997).
5. M. Katiar and A. N. Kitai, *J. Lumin.* **46**, 227 (1990).
6. J. N. Murrell, S. F. A. Kettle, and J. M. Tedder, *Valence Theory* (Wiley, London, 1965).
7. Wei Chen, R. Sammynaiken, and Y. Huang, *J. Appl. Phys.* **88**, 5188 (2000).
8. Wei Chen, F. Su, G. Li, A. L. Joly, J.-O. Malm, and J.-O. Bovin, *J. Appl. Phys.* **92**, 1950 (2002).
9. A. A. Bol and A. Meijerink, *J. Lumin.* **87/89**, 315 (2000).
10. W. Park, T. C. Jones, S. Schon, W. Tong, M. Chaichimansur, B. K. Wagner, and C. J. Sommers, *J. Cryst. Growth* **184/185**, 1123 (1998).
11. D. Adachi, S. Hasui, T. Toyama, and H. Okamoto, *Appl. Phys. Lett.* **77**, 1301 (2000).
12. J. Zhou, Y. Zhou, S. Buddhudu, S. L. Ng, Y. L. Lam, and H. Kam, *Appl. Phys. Lett.* **76**, 3513 (2000).
13. A. D. Dinsmore, D. S. Hsu, S. B. Qadri, J. O. Cross, T. A. Kennedy, H. F. Grey, and B. R. Ratna, *J. Appl. Phys.* **88**, 4985 (2000).
14. T. Toyoda, J. Matsuzawa, and Q. Chen, *Jpn. J. Appl. Phys.* **41**, 3383 (2002).

15. M. Tanaka and Y. Masumoto, *Solid State Commun.* **120**, 7 (2001).
16. J. Yu, H. Liu, Y. Wang, and W. Jia, *J. Lumin.* **79**, 191 (1998).
17. F. G. Anderson, W. M. Dennis, and G. F. Imbush, *J. Lumin.* **90**, 27 (2000).
18. C. de Mello Donega, A. A. Bol, and A. Meijerink, *J. Lumin.* **96**, 87 (2002).
19. J. Nakamura, K. Takamura, and S. Yamamoto, *Phys. Status Solidi B* **211**, 223 (1999).
20. P. Perlin, S. Shilo, T. Sosin, Y. Tyagur, T. Suski, W. Trzeciakowski, G. Karczewski, T. Wojtowicz, E. Janik, A. Zakrzewski, M. Kutrowski, and J. Kossut, *J. Phys. Chem. Solids* **56**, 415 (1995).
21. R. N. Bhargava, D. Gallagher, X. Hong, and A. Nurmikko, *Phys. Rev. Lett.* **72**, 416 (1994).
22. R. N. Bhargava, *J. Cryst. Growth* **214/215**, 926 (2000).
23. L. M. Gan, B. Lui, C. H. Chew, S. J. Xu, S. J. Chua, G. L. Loy, and G. Q. Xu, *Langmuir* **13**, 6427 (1997).
24. F. Schuurmans, D. de Lang, G. Wegdam, R. Sprik, and A. Lagendijk, *Phys. Rev. Lett.* **80**, 5077 (1998).
25. E. Yablonovitch, T. J. Gmitter, and R. Bhat, *Phys. Rev. Lett.* **61**, 2546 (1988).
26. S. Biernacki, M. Kutrowski, G. Karczewski, T. Wojtowicz, and J. Kossut, *Semicond. Sci. Technol.* **11**, 48 (1996).
27. V. F. Agekian, N. N. Vasil'ev, A. Yu. Serov, and N. G. Filosofov, *J. Cryst. Growth* **214/215**, 391 (2000).
28. J. Gregus, J. Watanabe, and J. Nakahara, *J. Phys. Soc. Jpn.* **66**, 1810 (1997).
29. V. F. Agekyan and Fan Zung, *Fiz. Tverd. Tela (Leningrad)* **30**, 3150 (1988) [*Sov. Phys. Solid State* **30**, 1812 (1988)].
30. V. F. Agekyan, N. N. Vasil'ev, V. I. Konstantinov, A. Yu. Serov, N. G. Filosofov, and V. N. Yakimovich, *Fiz. Tverd. Tela (St. Petersburg)* **45**, 1369 (2003) [*Phys. Solid State* **45**, 1435 (2003)].
31. V. F. Agekyan, N. N. Vasil'ev, and A. Yu. Serov, *Fiz. Tverd. Tela (St. Petersburg)* **41**, 49 (1999) [*Phys. Solid State* **41**, 41 (1999)].
32. V. V. Ovsyankin and P. P. Feofilov, *Opt. Spektrosk.* **37**, 262 (1973).

Translated by G. Skrebtsov

LOW-DIMENSIONAL SYSTEMS
AND SURFACE PHYSICS

Properties of Nanogranular Metal–Dielectric Composites in Strong Electric Fields and the Cluster Electronic States

L. V. Lutsev*, M. N. Kopytin**, A. V. Sitnikov**, and O. V. Stogneĭ**

*Ferrit-Domen Research Institute, St. Petersburg, 196084 Russia

e-mail: lutsev@domen.ru

**Voronezh State Technical University, Moskovskii pr. 14, Voronezh, 394026 Russia

e-mail: michaelkopytin@mail.ru

Received December 6, 2004; in final form, March 9, 2005

Abstract—The electrical resistance of granular structures with ferromagnetic and nonferromagnetic metal nanoparticles embedded in concentrations below the percolation threshold was studied in strong electric fields. More specifically, amorphous silicon dioxide containing nanoparticles of a $\text{Co}_{41}\text{Fe}_{39}\text{B}_{20}$ alloy [$(a\text{-SiO}_2)_{100-x}(\text{Co}_{41}\text{Fe}_{39}\text{B}_{20})_x$ structure] and amorphous hydrogenated carbon with embedded copper nanoparticles, $a\text{-C} : \text{H}(\text{Cu})$, were investigated. The $(a\text{-SiO}_2)_{100-x}(\text{Co}_{41}\text{Fe}_{39}\text{B}_{20})_x$ structures revealed changes in the electrical resistance and magnetoresistance after being subjected to a strong electric field. The changes could have reversible or irreversible character and depended on the electrical prehistory of the sample. A strong electric field caused not only a decrease in the electrical resistance but also a decrease in the magnetoresistance, although the magnetization of the sample remained unchanged. The temperature dependences of the current in $a\text{-C} : \text{H}(\text{Cu})$ films exhibited conductivity peaks under a decrease in temperature in strong electric fields and transitions from the insulating to conducting state; after the field was removed, there occurred reverse transitions and conductivity relaxation, as well as pronounced changes in the dielectric permittivity and an increase in dielectric losses with increasing temperature. A model of cluster electronic states (CESs) is proposed to account for the experimental findings. These states are created by electrons of the metal grains and matrix defects near the Fermi surface. The observed features find explanation in a change in the CES structure. A strong electric field does not bring about d -electron delocalization, and the fraction of d electron wave functions in a CES is small. © 2005 Pleiades Publishing, Inc.

1. INTRODUCTION

Granular structures with nanosized metal grains embedded in an insulating matrix possess electronic properties which distinguish them markedly from bulk crystalline and amorphous materials. The differences in these properties stem from the small size of mutually isolated nanoparticles and electron tunneling among them. The small size of metal nanoparticles gives rise to macroscopic charge quantization effects and Coulomb blockade [1–3]. Tunneling between ferromagnetic nanoparticles in granular structures produces specific features in the magnetoresistance and an anomalous Hall effect [4–6]. These phenomena were observed in weak electric fields. However, electron transport in strong electric fields have not been sufficiently studied. High electric fields are capable of significantly modifying the effects seen to occur in weak fields.

The present study deals with electron transport in granular structures with ferromagnetic and nonferromagnetic metal nanoparticles in strong electric fields, as well as looks for an interpretation of the observed features in terms of the model of cluster electronic states (CES). These states form when the tunneling barriers separating metal grains are highly transparent and the wave function of an electron in the Fermi level of a

grain spreads out to become localized on a group (cluster) of grains [7–9]. Below the percolation threshold, CESs are of a limited size and determine conduction regions in a granular structure. Above the percolation threshold, the CES size grows without limit, with the CESs forming an infinite conducting cluster. CESs affect small-angle x-ray scattering spectra and dielectric permittivity [8, 9]. A granular structure containing ferromagnetic grains of a d metal poses a problem of paramount importance, that of how a strong electric field acts on spin-polarized transport; namely, whether d electrons become delocalized and what the fraction of the d electron wave functions in CESs is.

These issues motivated our study of the behavior of electrical resistance in granular structures with embedded ferromagnetic and nonferromagnetic metal nanoparticles in strong electric fields, more specifically, in amorphous silicon dioxide with nanoparticles of a $\text{Co}_{41}\text{Fe}_{39}\text{B}_{20}$ alloy (we denote it by $(a\text{-SiO}_2)_{100-x}(\text{Co}_{41}\text{Fe}_{39}\text{B}_{20})_x$) and amorphous hydrogenated carbon loaded with copper nanoparticles, $a\text{-C} : \text{H}(\text{Cu})$. The field and temperature dependences of electrical resistance are explained in terms of the CES model. Dielectric permittivity measurements permitted estimation of the CES size. Studies of the magnetization and magnetoresistance per-

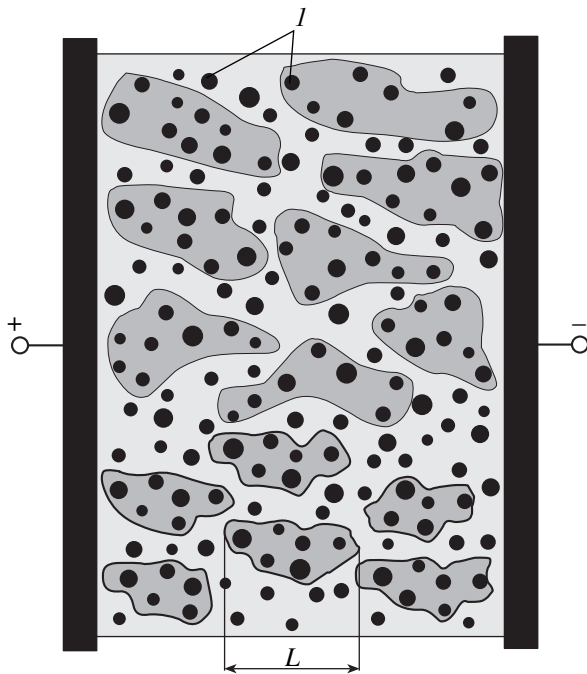


Fig. 1. Granular structure with regions of high conductivity on which CES wave functions are localized. (*I*) Metal grains; *L* is the CES localization size.

formed on $(a\text{-SiO}_2)_{100-x}(\text{Co}_{41}\text{Fe}_{39}\text{B}_{20})_x$ structures offered the possibility of evaluating the extent to which strong electric fields affect spin-polarized transport and *d*-electron delocalization.

2. CLUSTER ELECTRONIC STATES

Consider a granular structure consisting of nanoparticles (grains) of a metal and an amorphous matrix. The amorphous matrix typically has a large number of structural defects and impurities; in addition, there are defects at grain boundaries. The defects and impurities give rise to the formation of localized electronic states in the matrix. The presence of localized states results, in turn, in a sharp increase in the probability of electron tunneling between metal grains [10, 11]; so electrons residing in metal grains near the Fermi level may partially delocalize with the formation of CESs on a group of grains. In general, the CES wave function $\Psi_\alpha(\mathbf{r})$ of such an electron derives from the wave functions $\psi_\lambda^{(n)}(\mathbf{r})$ of electrons belonging to the metal grains of this group and from the wave functions $\phi_v^{(i)}(\mathbf{r})$ of electrons in localized states *i* in the matrix that are located near the grains [9]:

$$\Psi_\alpha(\mathbf{r}) = \sum_{n,\lambda} a_{\alpha\lambda}^{(n)} \psi_\lambda^{(n)}(\mathbf{r}) + \sum_{i,v} b_{\alpha v}^{(i)} \phi_v^{(i)}(\mathbf{r}). \quad (1)$$

The indices α , λ , and *v* in Eq. (1) label the eigenfunctions of the CES, of the electrons in the *n*th grain, and

of the *i*th localized state in the matrix, respectively. Therefore, we understand a group of metal grains on which the CES (1) is localized to be a cluster in what follows.

The CES localization length *L* depends on the depth distribution of potential wells formed by the metal grains, on the distribution of electron tunneling coefficients among the grains, and on the defect and impurity density in intergrain space in the matrix. In the case where the grain size is a random parameter, CES localization can be described by the Anderson localization model [12, 13]. The random character of grain size results in a random pattern of the electrical capacitance of the grains and of the Coulomb energy shift for electrons residing on grains. For granular structures below the percolation threshold, this model yields the following relation for the CES localization size [9] in the first approximation:

$$L = Ax^{-4/3} \exp\left[-\frac{d_0}{\xi} \left(\frac{v_m}{v_g}\right)^{1/3} \left(\frac{x}{100}\right)^{-1/3}\right], \quad (2)$$

where *A* is a coefficient; *x* is the metal phase concentration (in atomic percent); *d*₀ is the average size of metal grains; *v*_{*m*} and *v*_{*g*} are the average atom volumes in the matrix and a grain, respectively; and ξ is the tunneling barrier transparency, related to the tunneling coefficient *I* through the relation $I = I_0 \exp(-I/\xi)$ (*l* is the average grain separation). The coefficient ξ depends on the density of localized states in the matrix (i.e., on the density of defects and impurities in intergrain space) and is determined by inelastic resonance tunneling of electrons via localized electronic states of defects and impurities [10, 11]. Besides a sharp increase in barrier tunneling transparency, localized states of defects and impurities in the matrix bring about an increase in transparency ξ with temperature because of the inelastic character of tunneling via defects and impurities, with the result that the CES localization length *L* (2) increases.

The CES formation breaks up the granular structure into regions with a high conductivity [in which electrons with CES wave functions (1) are localized] and low-conductivity regions (Fig. 1). Below the percolation threshold, the high-conductivity regions, on which the CESs are localized, are of a limited size. Since the conductivity of these regions is substantially higher than the tunneling conductivity over impurity channels in regions with a low conductivity, the total conductivity will be determined by the average number $\langle n \rangle$ of localized states of defects and impurities in tunneling channels between the high-conductivity regions. Because of the inelastic character of tunneling, an increase in $\langle n \rangle$ will produce a sharper temperature dependence of transparency ξ and of the total conductivity of the granular structure. Therefore, the average number $\langle n \rangle$ of localized states of defects and impurities in intercluster space can be derived from the temperature dependences of conductivity [14–16]. Above the

percolation threshold, the CES grows in size without limit to become an infinite conducting region and forms a conduction band. A further increase of the metallic phase content in the granular structure transforms the CES conduction band to the conduction band of the metal.

The formation of CESs gives rise to several observable effects.

2.1. Specific Features of Conduction in Strong Electric Fields

An external electric field acts on electrons in a CES and may change their localization by changing the CES wave function (1) of each localized electron: this function can be combined with the wave functions $\psi_{\lambda}^{(n)}(\mathbf{r})$ of electrons of the metal grains that did not belong earlier to the cluster and with the wave functions $\phi_{\nu}^{(i)}(\mathbf{r})$ of electrons from localized states of other defects and impurities in the matrix. The localization length L and the spatial structure of the CES may change. On removal of the external field, the electrons in the CES may occupy energy levels different from the original ones. If the energy level of an electron in the new electronic state lies higher than that of the original or another state, this electron may return to the original state or transfer to another state characterized by another CES wave function. The transition time, which may be called the relaxation time, will be determined by the activation energy necessary for the electron to transfer from one energy state to another. Depending on the actual electric field, these changes of the state may be reversible or irreversible. This should give rise to features and a hysteresis in the field dependences of the conductivity.

2.2. Specific Features of the Temperature Dependence of the Conductivity

The inelastic character of tunneling via defects and impurities increases the barrier tunneling transparency among high conductivity regions and the CES localization length (2) with increasing temperature. Therefore, when the temperature increases so fast that the CES structure is left in a nonequilibrium state, one may observe conductivity relaxation to equilibrium. In these conditions, the electronic wave functions $\psi_{\lambda}^{(n)}(\mathbf{r})$ and $\phi_{\nu}^{(i)}(\mathbf{r})$ of particles and defects may either be involved in a CES (1) or be excluded from it. If the distance between contacts is comparable to the CES size L and the conductivity of a granular structure is determined by one conducting channel only, the involvement of wave functions in a CES or their exclusion from it should bring about conductivity jumps with changes in the temperature.

2.3. Additional Peaks in Small-Angle X-ray Scattering Spectra

It was found in [8] that small-angle x-ray scattering spectra of granular films of amorphous hydrogenated carbon with embedded cobalt nanoparticles, $a\text{-C} : \text{H}(\text{Co})$, are produced by scatterers of two types, cobalt grains and objects larger than the nanoparticles. The observed objects were identified as CESs.

2.4. Specific Features of the Field and Temperature Dependences of Dielectric Permittivity

The formation of CESs gives rise to changes in the dielectric permittivity ϵ . The dielectric permittivity depends linearly on the electric dipole moments of the components (atoms, molecules, clusters) making up a substance [17]. Clusters have the largest dipole moment in a granular structure, and their polarization should provide the largest contribution to dielectric permittivity. Therefore, measurements of ϵ yield information on changes in the size L of the conducting clusters. In strong electric fields, clusters should expand along the field direction, thus increasing ϵ . Because the CES localization length L increases with temperature, heating should increase the dielectric permittivity of a granular structure.

2.5. Decrease in Dielectric Permittivity with Decreasing Number of Defects in the Matrix

A decrease in the number of defects entails a decrease in the tunneling transparency of the barriers between the metal grains and in the CES localization length (2). This accounts for the annealing-induced falloff of the imaginary part of the dielectric permittivity in granular $(a\text{-SiO}_2)_{100-x}(\text{Co}_{41}\text{Fe}_{39}\text{B}_{20})_x$ composites observed in the 4.8- to 16.6-GHz frequency range [9].

3. SAMPLE PREPARATION

The experiment was performed on films of silicon dioxide with embedded nanoparticles of the $\text{Co}_{41}\text{Fe}_{39}\text{B}_{20}$ alloy (the $(a\text{-SiO}_2)_{100-x}(\text{Co}_{41}\text{Fe}_{39}\text{B}_{20})_x$ structure) and on films of amorphous hydrogenated carbon loaded with copper nanoparticles, $a\text{-C} : \text{H}(\text{Cu})$. The thin-film nanogranular $(a\text{-SiO}_2)_{100-x}(\text{Co}_{41}\text{Fe}_{39}\text{B}_{20})_x$ composites were prepared by ion-beam sputtering of a $\text{Co}_{41}\text{Fe}_{39}\text{B}_{20}$ composite alloyed target with SiO_2 additions in an argon–oxygen environment at a pressure $P = 30 \mu\text{Torr}$. The material was deposited on polished glass ceramic substrates. The film thickness was, on the average, $5 \mu\text{m}$. The films used in transmission electron microscopy (TEM) studies were thinner ($\sim 500 \text{ \AA}$) and were deposited on a NaCl substrate. TEM images show the composites to be complex systems consisting of metal grains 2–5 nm in size (Fig. 2) arranged randomly in the dielectric matrix. The current–voltage dependences and magnetoresistance of the composites were

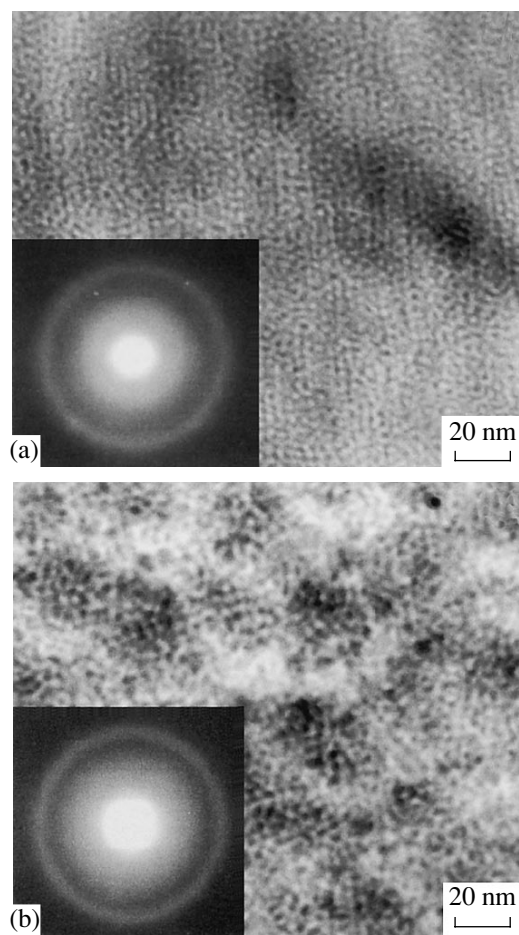


Fig. 2. TEM image of the microstructure of amorphous $(a\text{-SiO}_2)_{100-x}(\text{Co}_{41}\text{Fe}_{39}\text{B}_{20})_x$ composites with x equal to (a) 30 and (b) 44 at. %.

measured on a special contact structure. Metal layers (Cr–Cu–Cr) were deposited consecutively on a glass ceramic substrate, followed by application of the composite material proper, on top of which contact pads were applied through the repeated deposition of Cr–Cu–Cr metal layers through a template (Fig. 3a). The electric contact to the composite was effected through the bottom metal layer and upper contact pads. The granular composite samples prepared for the study had compositions below the percolation threshold.

$(a\text{-C} : \text{H})_{100-x}\text{Cu}_x$ granular films were grown on quartz substrates by cosputtering of a graphite and a copper target in an argon–hydrogen plasma (80% Ar + 20% H_2). Contacts were evaporated on the substrate and the film surface (Fig. 3b). The contact pad width was 0.5 mm. The film thickness D varied from 1.0 to 1.73 μm . Conductivity measurements revealed that films with $x = 16$ at. % lie below the percolation threshold and that the size of the conducting clusters is smaller than the contact separation. The size of the conducting clusters in $(a\text{-C} : \text{H})_{100-x}\text{Cu}_x$ films with $x > 16$ at. % is equal to or larger than the distance between

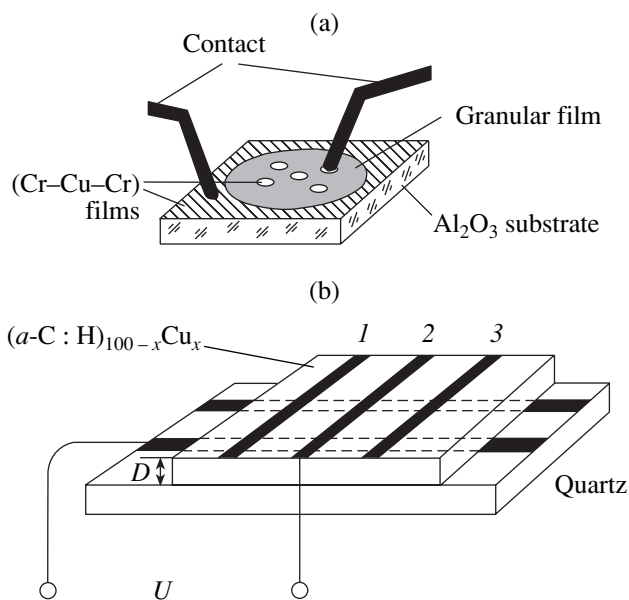


Fig. 3. Geometry of contacts of the granular structures under study: (a) $(a\text{-SiO}_2)_{100-x}(\text{Co}_{41}\text{Fe}_{39}\text{B}_{20})_x$ and (b) $(a\text{-C} : \text{H})_{100-x}\text{Cu}_x$.

the contacts, which accounts for the metallic type of conduction observed in these structures. The average size d_0 of copper grains in $(a\text{-C} : \text{H})_{84}\text{Cu}_{16}$ films as derived from optical spectra, small-angle x-ray scattering, and electron microscopy data is 4 nm [18–20]. The scatter in grain size is $\Delta d = 1.7$ nm. Amorphous hydrogenated carbon $a\text{-C} : \text{H}$ in the evaporated $(a\text{-C} : \text{H})_{100-x}\text{Cu}_x$ granular films acts as an organic amorphous semiconductor and plays the part of an insulating matrix loaded by copper grains [21]. The activation barrier Δ , which is equal to the energy difference between the Fermi level of copper grains and the mobility edge of the $a\text{-C} : \text{H}$ π^* conduction band, was derived from the temperature dependences of conductivity in weak electric fields ($< 6 \times 10^2$ V/cm). In granular $(a\text{-C} : \text{H})_{100-x}\text{Cu}_x$ structures, the barrier height Δ varied in the range 0.46–0.54 eV [7].

4. ELECTRICAL RESISTANCE IN STRONG ELECTRIC FIELDS

In accordance with the CES model, the resistance R of a granular structure is determined by a multiplicity of channels i , which include conducting regions with CES and high-resistance regions. Obviously, $R^{-1} = \sum_i R_i^{-1}$. The channel with the lowest resistance provides the major contribution to the structure conductivity and determines the resistance R . A strong electric field affects the degree of CES localization and transforms the channel network. The resistance variation of a granular structure will be determined, however, by that of the channel with the lowest resistance. In this sense,

study of the resistance of a granular structure may be considered to have local character. The granular films studied by us in strong fields differed somewhat from one another in terms of their conduction pattern. Because of the substantial activation-barrier height Δ in $(a\text{-SiO}_2)_{100-x}(\text{Co}_{41}\text{Fe}_{39}\text{B}_{20})_x$ structures, their conduction is determined by resonance tunneling over localized states in dielectric spacers. In $(a\text{-C} : \text{H})_{100-x}\text{Cu}_x$ structures, the activation barrier Δ is lower and resonance tunneling among conducting clusters is complemented by conduction effected by electrons thermally activated from conducting clusters into the π^* conduction band of $a\text{-C} : \text{H}$ [7]. In addition, the $a\text{-C} : \text{H}$ structure contains graphite-like nanoclusters, which may contribute to the formation of conduction channels [22]. In the presence of graphite-like nanoclusters, the CES wave functions (1) should include not only the wave functions of electrons in metal grains and localized states in the matrix but also the wave functions of the sp^2 phase of graphite-like nanoclusters.

The resistance and I - V curves of granular $(a\text{-SiO}_2)_{100-x}(\text{Co}_{41}\text{Fe}_{39}\text{B}_{20})_x$ structures were investigated at voltages providing an electric field strength between contacts of up to 2.5×10^4 V/cm. The I - V characteristics of the $(a\text{-SiO}_2)_{100-x}(\text{Co}_{41}\text{Fe}_{39}\text{B}_{20})_x$ composites revealed the following features. First, the I - V curves are asymmetric; i.e., the currents measured at the same voltages but of opposite polarity are different (see Fig. 4; the numerals indicate the sequence of I - V measurements). Second, in the high-voltage region, a hysteresis is observed in the I - V curves; this hysteresis, according to the CES model, should be assigned to a variation in the CES localization size in the channel of lowest resistance. Third, it was established that the pattern of the I - V curve depends on the electrical prehistory of the sample, i.e., on the magnitude and sign of the voltage previously applied to the sample (Figs. 4a, 4b; the order in which the I - V curves were measured is different).

Remarkable results were obtained in measurements of the I - V characteristics of $(a\text{-SiO}_2)_{100-x}(\text{Co}_{41}\text{Fe}_{39}\text{B}_{20})_x$ films performed in the mode where each step of voltage increase was followed by a resistance measurement at a fixed low voltage (0.14 V in our case) (Fig. 5). This voltage was chosen because, in samples of the given composition, the point on the I - V curve corresponding to 0.14 V lies within a linear portion and the application of this voltage does not entail irreversible changes in the electrical resistance. This mode permits study of the variation of composite resistance after subjection of the composite to a high electric field. Because the subsequent measurement of the resistance was carried out in a low field, the result obtained directly reflects the changes induced by a strong external electric field. One of the relations obtained in the course of these measurements is presented graphically in Fig. 5. The arrows specify the sequence in which the characteristics were measured. An analysis of the experimental data shows

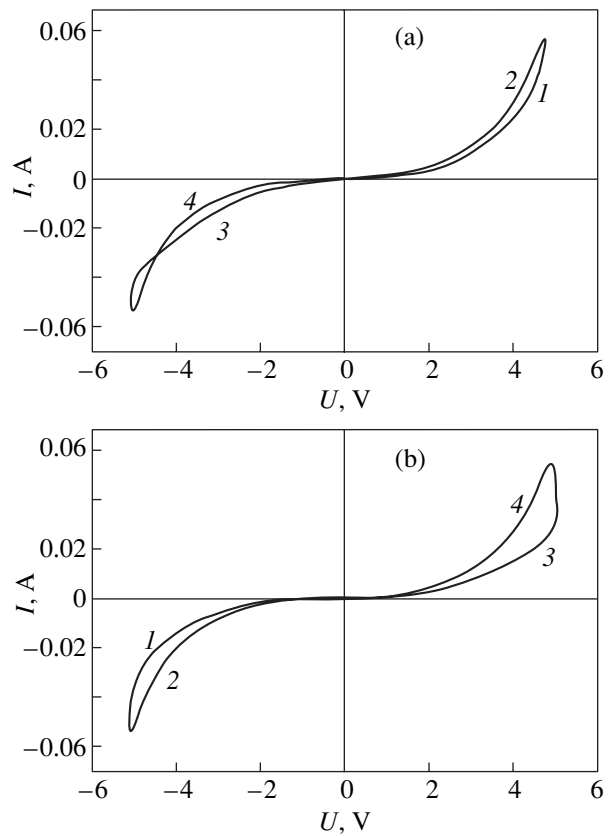


Fig. 4. I - V curves of the $(a\text{-SiO}_2)_{59}(\text{Co}_{41}\text{Fe}_{39}\text{B}_{20})_{41}$ composite obtained in a different order of measurements (1-4 specify the sequence of measurements).

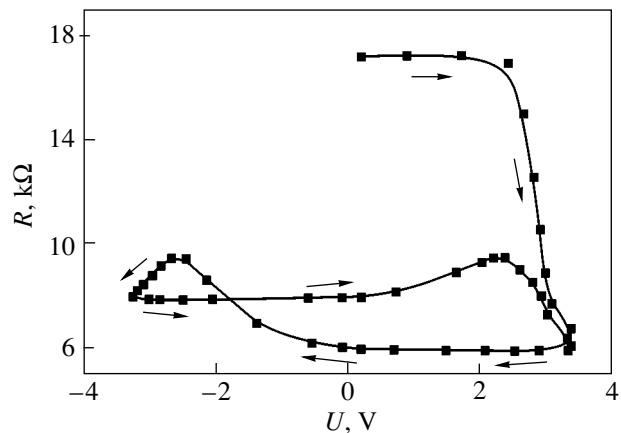


Fig. 5. Electrical resistance R (measured at a voltage of 0.14 V across the sample) of the $(a\text{-SiO}_2)_{59}(\text{Co}_{41}\text{Fe}_{39}\text{B}_{20})_{41}$ composite plotted vs applied voltage (arrows specify the sequence of measurements).

that the electrical resistance of the composite measured at a low fixed voltage depends on the magnitude and sign of the voltage previously applied to the sample, i.e., on the electrical prehistory of the sample. The

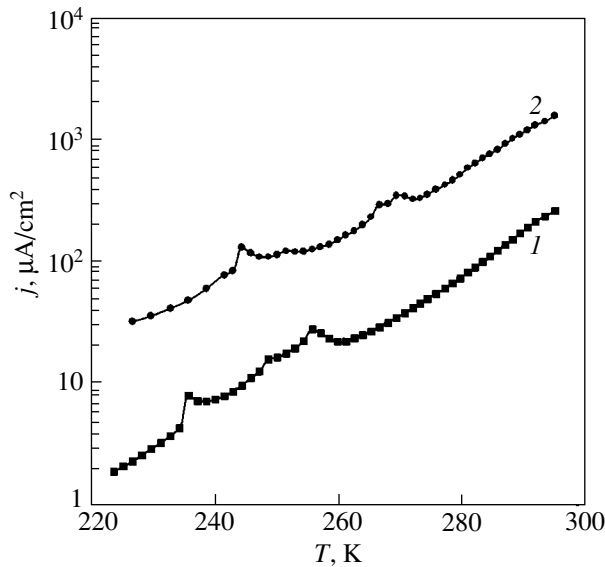


Fig. 6. Temperature dependence of current density j and the conductivity peaks at contacts (1) $a3$ and (2) $a1$ observed in an $(a\text{-C:H})_{84}\text{Cu}_{16}$ film. The applied voltage is 20 V.

resistance measured before the application of a strong electric field exceeds that measured after the removal of a strong field by a factor of 1.8–2.9. In accordance with the CES model, resistance variation is connected with a variation of the localization length L of the conducting regions making up the CES and with a decrease of the gap between conducting regions in the channel of lowest resistance. The resistance variation measured after the sample was subjected to a strong electric field can be either reversible or irreversible. The irreversibility of the resistance variation may mean that field removal initiates the formation of a new CES structure different from the previous one.

The $(a\text{-C:H})_{84}\text{Cu}_{16}$ granular structures were used to study the temperature dependences of the current in strong electric fields, the transition from the insulating to conducting state, and the resistance relaxation. The electric field strengths were in excess of 2.0×10^5 V/cm. Figure 6 plots the temperature dependence of current density j measured at a voltage $U = 20$ V at contacts $a1$ and $a3$ of the film (Fig. 3b). The cluster structure between the contacts was in the insulating state. Conduction is governed by electrons thermally activated from the Fermi level of copper grains into the $a\text{-C:H}$ π^* conduction band and overcoming the activation barrier Δ and by electrons tunneling among clusters. We observed conductivity peaks on the temperature dependence of the current as the temperature decreased. The position and magnitude of the peaks on the temperature dependence curve varied from one experiment to another. At low voltages ($U = 0.1$ V), no conductivity peaks were observed. The CES model offers the following explanation for the peaks. The current is determined by the channel of lowest resistance. In this channel, the

number of thermally activated electrons in the π^* conduction band of $a\text{-C:H}$ and, accordingly, the current decrease with decreasing temperature as

$$j \propto \exp[-(\Delta - W_c)/kT], \quad (3)$$

where W_c is the average Coulomb energy shift for electrons on clusters involved in the channel of lowest resistance. The CES localization length L decreases with decreasing temperature. The decrease of the CES localization length to a size corresponding to an equilibrium state can proceed through either detachment of peripheral cluster grains or rupture of an internal cluster bond. In the latter case, an electron becomes localized in one of the broken off cluster parts. Cluster decomposition favored by a strong electric field gives rise to an abrupt increase of the Coulomb energy shift W_c of the part of clusters on which electrons are localized. In granular structures where conduction is due to electrons thermally activated into the conduction band, an increase in the energy W_c results in an increase in the number of activated electrons in the conduction band in the proximity of the decomposed clusters and, according to Eq. (3), accounts for the increase in current j . This becomes manifest as a peak in the temperature dependence curve.

Another effect observed in $(a\text{-C:H})_{84}\text{Cu}_{16}$ films was the transition from the insulating to conducting state (and the reverse transition from the conducting to insulating state). According to the CES model, a transition between two states with two different electrical resistivities can be accounted for by rearrangement of the cluster structure. For $U > 20$ V, a group of isolated clusters on which electrons with CES wave functions (1) were localized transformed into one conducting cluster. This may be initiated by small changes in clusters in which insulating spacers disappear. As a result of this transition, the resistance between the contacts decreased by five orders of magnitude. During a certain period of time (several days), relaxation occurred and the conducting cluster transferred to the initial state transforming into a group of isolated clusters. As long as the granular film between the contacts remained in the state of conducting cluster, the temperature dependence of resistance was metallic in character with a large residual resistance [7]. The value of the residual resistance was used to derive the electron mean free path. It was found to be 20 nm, which is substantially less than the mean free path in pure copper.

The resistance relaxation observed following fast heating of a $(a\text{-C:H})_{84}\text{Cu}_{16}$ film is shown in Fig. 7 for the $a3$ contact. The granular film between the contacts resided in the state of a group of isolated clusters. The film was cooled to $T = 77$ K and maintained at this temperature for 45 min. The resistance between the contacts exceeded 1.2 G Ω . After the cooling, the film was heated rapidly to 297 K. The beginning of the relaxation curve ($t = 0$) is the time at which the film temperature reached 297 ± 1 K. Thereafter, the temperature

did not change. The smallest resistance was at $t = 0$. Over the time interval 1.5–5.5 min, the resistance is seen to grow linearly. At $t = 5.5$ min, resistance relaxation changes pattern. For $t > 5.5$ min, the resistance does not vary noticeably. In accordance with the CES model, resistance relaxation can be accounted for in the following way. At low temperatures ($T = 77$ K), the CES localization length L given by Eq. (2) and, accordingly, the cluster capacitance are smaller than those at higher temperatures. If heating is performed fast enough, L cannot grow noticeably in this time. As a result, in the given nonequilibrium state, the Coulomb energy shift W_c in Eq. (3) at $T = 297$ K in the channel of lowest resistance turns out to be larger than the energy shift $W_c^{(eq)}$ for the equilibrium CES characteristic of this temperature. The increase in the Coulomb shift gives rise to an increase in the number of thermally activated electrons in the a -C : H π^* conduction band and to a lower resistance in the nonequilibrium state at $t = 0$. The ratio of the resistances between contacts in the equilibrium ($t > 5.5$ min) and nonequilibrium ($t = 0$) states is determined by the ratio of currents (3) with Coulomb energy shifts $W_c^{(eq)}$ and W_c , respectively:

$$\frac{R^{(eq)}}{R} = \exp[(W_c - W_c^{(eq)})/kT].$$

At 297 K, clusters grow in size and W_c relaxes to its equilibrium value $W_c^{(eq)}$. This brings about a decrease in the number of thermally activated electrons in the π^* conduction band of a -C : H and an increase in the resistance between contacts.

5. VARIATION OF THE DIELECTRIC PERMITTIVITY

Variations of the dielectric permittivity were studied on $(a$ -C : H) $_{84}$ Cu $_{16}$ structures at a frequency of 1 MHz. In contrast to the case of resistance, where the major contribution to the total resistance of the structure is provided by the channel with the lowest resistance, the dielectric permittivity $\epsilon = \epsilon' + \epsilon''$ is determined by the polarization of all CESs and is essentially a sum of individual effects. Because variations of the dielectric permittivity are proportional to those of the CES localization length L (2) along the applied electric field (Fig. 1), measurements of ϵ provide information on the variation of conducting clusters in size. The dielectric permittivity was studied by the capacity–voltage technique in an ac electric field of 1 MHz. The electric capacitances C were formed by a granular film and the top (I –3) and bottom (a , b) contacts (Fig. 3b). The real part of the dielectric permittivity was extracted from the electrical capacitance using the relation $\epsilon' = 4\pi DC/S$, where D is the film thickness and S is the contact area. The relative variation of ϵ' as derived from the capacitance dependences for contact $a3$ of an $(a$ -C : H) $_{84}$ Cu $_{16}$ film is

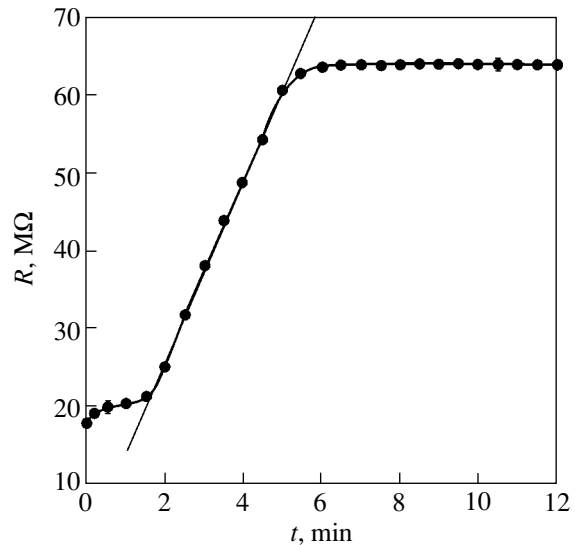


Fig. 7. Relaxation of resistance R at contact $a3$ for an $(a$ -C : H) $_{84}$ Cu $_{16}$ film.

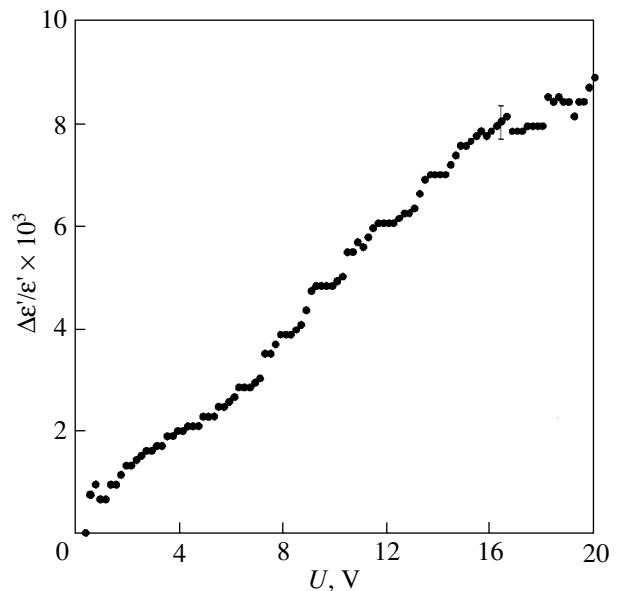


Fig. 8. Relative variation of the real part of the dielectric permittivity, $\Delta\epsilon'/\epsilon'$, with increasing voltage U applied to an $(a$ -C : H) $_{84}$ Cu $_{16}$ film.

shown graphically in Figs. 8 and 9. The real part of the dielectric permittivity was found to grow with the voltage U applied across the contacts (Fig. 8). At 20 V, the electric field strength was as high as 2.0×10^5 V/cm. If a sample did not contain metal nanoparticles, i.e., was a conventional a -C : H film, no increase in ϵ' with voltage was observed. Figure 9 displays the growth of ϵ' with increasing temperature. The observed growth is consistent with the CES model. The temperature

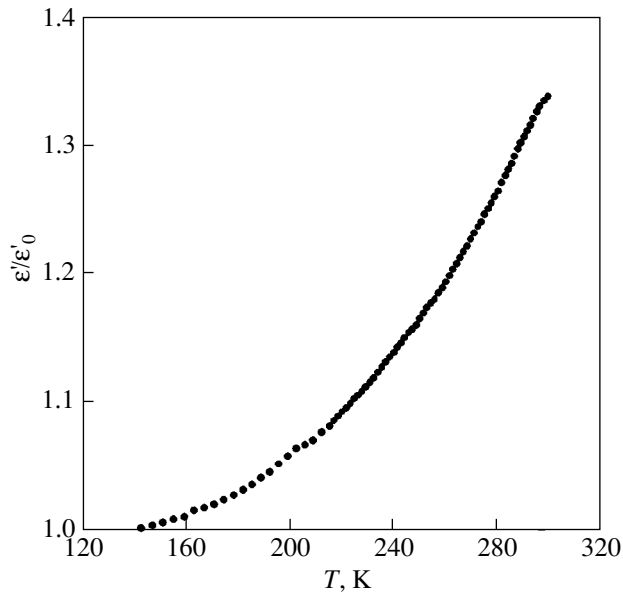


Fig. 9. Relative temperature-induced variation of the dielectric permittivity ϵ'/ϵ_0 of an $(a\text{-C}:\text{H})_{84}\text{Cu}_{16}$ film biased by a voltage $U = 0.25\text{ V}$ (ϵ_0 is the real part of the dielectric permittivity at $T = 142\text{ K}$).

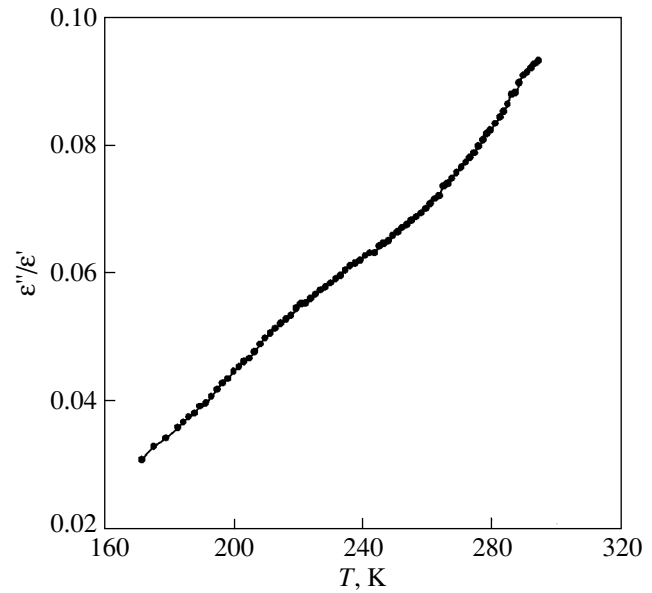


Fig. 10. Temperature dependence of the ratio of the imaginary part to the real part of the dielectric permittivity, ϵ''/ϵ' (the loss tangent), measured in an ac electric field of frequency 1 MHz on an $(a\text{-C}:\text{H})_{84}\text{Cu}_{16}$ film.

dependences measured under decreasing and increasing temperature were identical. Similar experiments carried out on an $a\text{-C}:\text{H}$ film without metal nanoparticles reveal insignificant temperature-induced variations of the real part of the dielectric permittivity ϵ' . Thus, a comparison of the capacity–voltage dependences and the temperature dependences of ϵ' obtained on both granular and bulk films suggests that the major contribution to dielectric permittivity variation is due to variation of the conducting clusters of the structure in size. In our experiments, the increase of conducting clusters in size L in strong fields did not exceed 1%. The increase of the conducting clusters in size with temperature was substantially more pronounced and reached as high as 34%.

Figure 10 plots a temperature dependence of the ratio of the imaginary part to the real part of the dielectric permittivity, ϵ''/ϵ' (loss tangent), measured on an $(a\text{-C}:\text{H})_{84}\text{Cu}_{16}$ film in an ac electric field of 1 MHz. The losses determined by the imaginary part ϵ'' grow linearly with increasing temperature. According to the CES model, the growth of electric losses is determined by that of the cluster dipole moments and by the increase in the number of thermally activated electrons in the conduction band of the $a\text{-C}:\text{H}$ matrix. When an $a\text{-C}:\text{H}$ film had no metal inclusions, the ϵ''/ϵ' ratio was 0.0085 and the temperature-induced variations were very small.

6. MAGNETORESISTANCE AND MAGNETIZATION

As follows from the capacity–voltage dependences of the real part of the dielectric permittivity of granular structures, the size of the conducting regions on which the CESs are localized grows with increasing electric field. A study of the variation of the composite resistance after the sample was subjected to a strong electric field leads one to conclude that an increase of the field is accompanied by a decrease in the extent of high-resistance regions between clusters. If a granular structure is loaded by ferromagnetic metal grains, e.g., grains of a d metal, one may reasonably ask the following questions.

(i) How does a strong electric field act on magnetoresistance; in other words, to what extent are the s -, p -, and d -electron systems of grains involved in the conduction effects observed in strong electric fields?

(ii) Does an electric field affect the magnetization of a granular structure, or, said otherwise, do the wave functions of d electrons of metal atoms delocalize, and, if so, what is the fraction of these functions in a CES?

In a search of answers to these questions, we studied the magnetoresistance and magnetization of $(a\text{-SiO}_2)_{100-x}(\text{Co}_{41}\text{Fe}_{39}\text{B}_{20})_x$ films. The magnetoresistance and magnetization curves of a sample were measured in the initial state (before the application of a strong electric field), with magnetization performed with the film fixed either along the magnetic field lines or perpendicular to them. Next, after applying a strong electric field to the sample for 2 min, measurements of

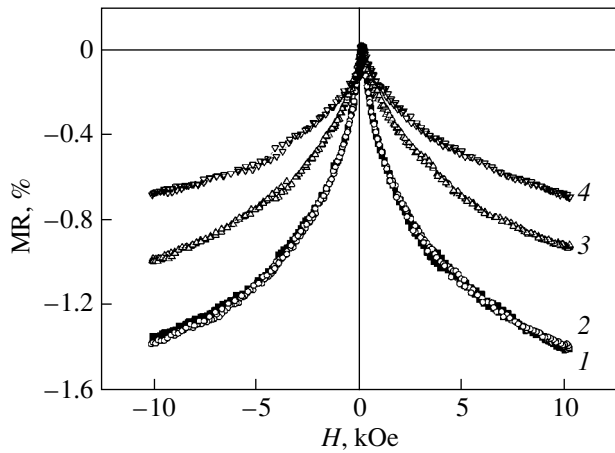


Fig. 11. Magnetoresistance (MR) of the $(a\text{-SiO}_2)_{54}(\text{Co}_{41}\text{Fe}_{39}\text{B}_{20})_{46}$ composite (1) before the application and (2–4) after the removal of an electric field with the voltage across the contacts U equal to (2) 0.8, (3) 0.94, and (4) 1.13 V.

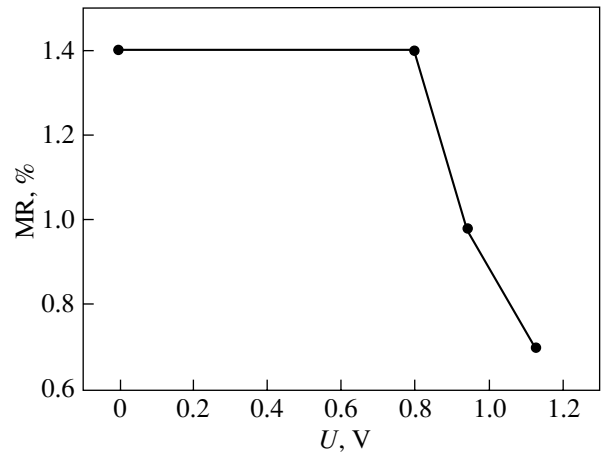


Fig. 12. Magnetoresistance (MR) of the $(a\text{-SiO}_2)_{54}(\text{Co}_{41}\text{Fe}_{39}\text{B}_{20})_{46}$ composite measured in a magnetic field $H = 10$ kOe (after the sample was subjected to a strong electric field) and plotted vs the voltage U across the contacts.

the magnetoresistance (at 0.14 V) and magnetization were repeated. These measurements were repeated under ever higher electric fields, but the magnetoresistance was always measured at 0.14 V. The results obtained for the $(a\text{-SiO}_2)_{54}(\text{Co}_{41}\text{Fe}_{39}\text{B}_{20})_{46}$ composite are presented in Figs. 11–13. It was established that the electrical resistance of the composite decreased from 40.7 to 7.44 Ω and the magnetoresistance decreased from the initial value of 1.38% to 0.71%. Interestingly, at comparatively low applied voltages (below 0.8 V; see Fig. 12), there is almost no variation in the magnetoresistance. The application of a higher voltage, however, substantially reduces the MR, which indicates the existence of a threshold electric field. Unlike the magnetoresistance of the composite, its magnetization and, accordingly, the magnetization curves are not affected by strong electric fields (Fig. 13).

The CES model permits the following interpretation of the data obtained in the study. The magnitude of magnetoresistance is governed by spin-dependent tunneling between conducting clusters in the channel of lowest resistance. The tunneling-barrier transparency is determined by overlap of the metal outer-shell s -, p -, and d -electron wave functions involved in the $\Psi_\alpha(\mathbf{r})$ CES wave functions (1) of two neighboring clusters and by the number of localized electronic states of defects and impurities in the tunneling channel connecting the clusters. The overlap integrals of wave functions composed of s orbitals of metal atoms provide the major contribution to the tunneling barrier transparency (s – s tunneling) [23, 24]. The role of d electrons reduces to polarization of the spin of tunneling s electrons. The tunneling barrier may have split localized electronic states, which become involved in spin-dependent resonance tunneling. In this case, an increase in the number of localized states between clus-

ters over which an electron tunnels gives rise to an increase in magnetoresistance [15]. The $(a\text{-SiO}_2)_{54}(\text{Co}_{41}\text{Fe}_{39}\text{B}_{20})_{46}$ composite under study here revealed a decrease in MR in a strong electric field. This may be attributed to a decrease in the number of localized states between conducting clusters, which occurs because electron localization in CESs changes through transfer of the wave functions of a part of the localized states belonging to the matrix intercluster regions to a CES.

The magnetization of a sample is intimately related to the spin polarization of d electrons in the outer shells of metal atoms. The fact that magnetization curves of

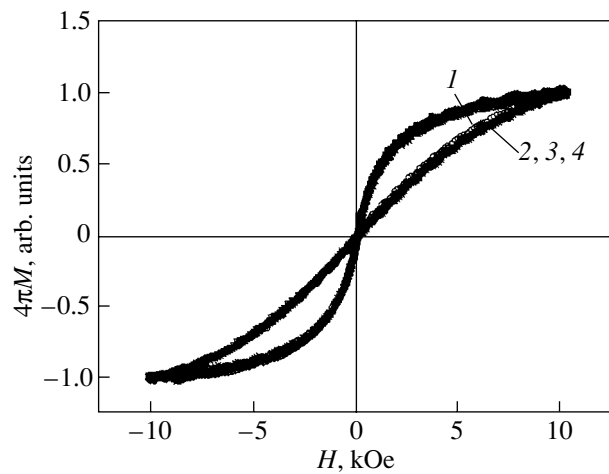


Fig. 13. Magnetization $4\pi M$ of the $(a\text{-SiO}_2)_{54}(\text{Co}_{41}\text{Fe}_{39}\text{B}_{20})_{46}$ composite measured (1) before the application and (2–4) after the removal of an electric field with the voltage across the contacts U equal to (2) 0.8, (3) 0.94, and (4) 1.13 V.

the composite are not affected by a strong electric field changing the CES structure suggests that d electrons of metal grains are only weakly coupled with the CES electrons. Hence, while d electrons polarize the CES electrons to some extent, the former electrons remain localized in the outer shells of metal atoms and are only insignificantly involved in the CES wave function $\Psi_{\alpha}(\mathbf{r})$ (1).

7. CONCLUSIONS

The main results of this study can be summarized as follows.

(1) Specific features have been observed in the I - V curves and in the behavior of the resistance of granular structures of amorphous silicon dioxide loaded with nanoparticles of a $\text{Co}_{41}\text{Fe}_{39}\text{B}_{20}$ alloy ($(a\text{-SiO}_2)_{100-x}(\text{Co}_{41}\text{Fe}_{39}\text{B}_{20})_x$ structure) and of amorphous hydrogenated carbon with embedded copper nanoparticles, $a\text{-C} : \text{H}(\text{Cu})$, subjected to strong electric fields. The $(a\text{-SiO}_2)_{100-x}(\text{Co}_{41}\text{Fe}_{39}\text{B}_{20})_x$ structures revealed an I - V hysteresis whose pattern depends on the electrical prehistory of the sample. Note that the resistance measured before the application of a strong electric field is substantially higher than that after the removal of a strong field. The resistance of a sample subjected to a strong electric field may change by as high as 70% in both a reversible and an irreversible manner. The $a\text{-C} : \text{H}(\text{Cu})$ structures revealed conductivity peaks in the temperature dependence of current under a decrease in temperature in strong electric fields and transitions from the insulating to conducting state; after the field was removed, there occurred reverse transitions and conductivity relaxation. A CES model was proposed to account for the experimental data obtained. These states are created by electrons of metal grains and matrix defects near the Fermi surface of metal grains and form a conducting cluster structure. According to the CES model, the change in resistance is connected with the change in size of the localization length of conducting clusters and the decrease in the intercluster separation in the channel of lowest resistance. The irreversibility of a change in resistance can be assigned to the formation, after removal of the field, of a new CES structure different from the previous one.

(2) Voltage-capacitance measurements made on $a\text{-C} : \text{H}(\text{Cu})$ structures offered an estimate of the changes in dielectric permittivity associated with variation of the degree of CES localization in strong electric fields and under temperature variation. The increase of conducting clusters in size in strong fields did not exceed 1%. The increase in conducting cluster size with increasing temperature was substantially larger and could be as high as 34%.

(3) The effect of a strong electric field on the d -electron system of metal grains in granular structures loaded with $3d$ -metal grains has been studied. It was found that subjecting $(a\text{-SiO}_2)_{100-x}(\text{Co}_{41}\text{Fe}_{39}\text{B}_{20})_x$ sam-

ples to a strong electric field brings about not only a decrease in electrical resistance but also a decrease in magnetoresistance. Note that this did not entail a change in the shape of the magnetization curves. According to the CES model, the decrease in magnetoresistance is connected with the decrease in the number of localized intercluster states over which electrons tunnel. The constancy of the composite magnetization curves under a strong electric field that changes the CES structure leads to the conclusion that d electrons of metal grains do not delocalize and are only weakly coupled with the CES electrons. The CESs derive primarily from the wave functions of s and p electrons of atoms of the metal grains.

ACKNOWLEDGMENTS

The authors are indebted to T.K. Zvonareva, L.V. Sharonova, and V.I. Ivanov-Omskiĭ for preparation of and providing experimental samples of amorphous hydrogenated carbon loaded with copper nanoparticles, $a\text{-C} : \text{H}(\text{Cu})$.

Support of the Russian Foundation for Basic Research (project nos. 05-02-16713, 02-02-12102, and 03-02-96486) and of the Ministry of Education of the Russian Federation within the program of support of leading scientific schools is gratefully acknowledged.

REFERENCES

1. S. V. Vyshenski, Pis'ma Zh. Éksp. Teor. Fiz. **61** (1–2), 105 (1995) [JETP Lett. **61**, 111 (1995)].
2. S. V. Vyshenski, Pis'ma Zh. Éksp. Teor. Fiz. **64** (7–8), 543 (1996) [JETP Lett. **64**, 592 (1996)].
3. S. A. Gurevich, V. V. Horenko, T. A. Zarayskaya, L. Yu. Kupriyanov, M. Yu. Kupriyanov, T. N. Vasilevskaya, and S. V. Vyshenski, Pis'ma Zh. Éksp. Teor. Fiz. **64** (9–10), 684 (1996) [JETP Lett. **64**, 736 (1996)].
4. S. Mitani, K. Takanashi, K. Yakushiji, and H. Fujimori, J. Appl. Phys. **83** (11), 6524 (1998).
5. B. A. Aronzon, A. B. Granovskii, D. Yu. Kovalev, E. Z. Meĭlikhov, V. V. Ryl'kov, and M. V. Sedova, Pis'ma Zh. Éksp. Teor. Fiz. **71** (11), 687 (2000) [JETP Lett. **71** (11), 469 (2000)].
6. B. A. Aronzon, D. Yu. Kovalev, A. N. Logar'kov, E. Z. Meĭlikhov, V. V. Ryl'kov, M. A. Sedova, N. Negre, M. Goïran, and J. Leotin, Pis'ma Zh. Éksp. Teor. Fiz. **70** (2), 87 (1999) [JETP Lett. **70** (2), 90 (1999)].
7. L. V. Lutsev, S. V. Yakovlev, and V. I. Siklitskiĭ, Fiz. Tverd. Tela (St. Petersburg) **42** (6), 1105 (2000) [Phys. Solid State **42** (6), 1139 (2000)].
8. V. I. Siklitskiĭ, L. V. Lutsev, and M. V. Baĭdakova, Pis'ma Zh. Tekh. Fiz. **28** (7), 46 (2002) [Tech. Phys. Lett. **28** (7), 283 (2002)].
9. L. V. Lutsev, N. E. Kazantseva, I. A. Tchmutin, N. G. Ryvkina, Yu. E. Kalinin, and A. V. Sitnikoff, J. Phys.: Condens. Matter **15** (22), 3665 (2003).
10. L. I. Glazman and K. A. Matveev, Zh. Éksp. Teor. Fiz. **94** (6), 332 (1988) [Sov. Phys. JETP **67**, 1276 (1988)].

11. L. I. Glazman and R. I. Shekhter, *Zh. Éksp. Teor. Fiz.* **94** (1), 292 (1988) [*Sov. Phys. JETP* **67**, 163 (1988)].
12. P. W. Anderson, *Phys. Rev.* **109** (5), 1492 (1958).
13. N. Mott and E. Davis, *Electronic Processes in Non-Crystalline Materials* (Oxford University Press, Oxford, 1979; Mir, Moscow, 1982), Vols. 1, 2.
14. L. V. Lutsev, T. K. Zvonareva, and V. M. Lebedev, *Pis'ma Zh. Tekh. Fiz.* **27** (15), 84 (2001) [*Tech. Phys. Lett.* **27**, 659 (2001)].
15. L. V. Lutsev, Yu. E. Kalinin, A. V. Sitnikov, and O. V. Stogneĭ, *Fiz. Tverd. Tela (St. Petersburg)* **44** (10), 1802 (2002) [*Phys. Solid State* **44** (10), 1889 (2002)].
16. Yu. E. Kalinin, A. N. Remizov, and A. V. Sitnikov, *Fiz. Tverd. Tela (St. Petersburg)* **46** (11), 2076 (2004) [*Phys. Solid State* **46** (11), 2146 (2004)].
17. L. D. Landau and E. M. Lifshitz, *Electrodynamics of Continuous Media* (Nauka, Moscow, 1982; Pergamon, Oxford, 1984), Vol. 8.
18. V. I. Ivanov-Omskii, A. V. Tolmachev, and S. G. Yastrebov, *Philos. Mag. B* **73** (4), 715 (1996).
19. V. I. Siklitsky, S. G. Yastrebov, and A. B. Lodygin, *Chaos, Solitons, Fractals* **10** (12), 2067 (1999).
20. V. I. Ivanov-Omskiĭ, V. I. Siklitskiĭ, and S. G. Yastrebov, *Fiz. Tverd. Tela (St. Petersburg)* **40** (3), 568 (1998) [*Phys. Solid State* **40** (3), 524 (1998)].
21. J. Robertson, *Adv. Phys.* **35** (4), 317 (1986).
22. T. K. Zvonareva, V. M. Lebedev, T. A. Polyanskaya, L. V. Sharonova, and V. I. Ivanov-Omskiĭ, *Fiz. Tekh. Poluprovodn. (St. Petersburg)* **34** (9), 1135 (2000) [*Semiconductors* **34** (9), 1094 (2000)].
23. J. Mathon, *Phys. Rev. B: Condens. Matter* **56** (18), 11810 (1997).
24. J. S. Moodera and G. Mathon, *J. Magn. Magn. Mater.* **200**, 248 (1999).

Translated by G. Skrebtsov

LOW-DIMENSIONAL SYSTEMS
AND SURFACE PHYSICS

Field-Desorption Microscopy Study of the Deformation of a Tungsten Tip Subjected to Thermal Treatment in an Electric Field

V. G. Pavlov

Ioffe Physicotechnical Institute, Russian Academy of Sciences, Politekhnicheskaya ul. 26, St. Petersburg 194021 Russia
e-mail: vpavlov@ms.ioffe.rssi.ru

Received November 10, 2004; in final form, December 14, 2004

Abstract—Deformation of a tungsten tip 500 to 1000 nm in radius subjected to heating in an electric field is studied using field-emission microscopy and continuous-mode field-desorption microscopy. Measurements are performed immediately after the thermal field treatment without any smoothing of the tip by either heating or field evaporation. The edges of the tip (which is shaped into a polyhedron) are found to consist of monatomic steps about 1 nm wide and about 100 nm long. Microscopic protrusions about 10 nm in size are shaped like pyramids or wedges with single-atom apexes or monatomic edges and facets that are a continuation of the facets of the reconstructed tip or an outgrowth on which the protrusions are situated. The outgrowths are shaped like stepped truncated pyramids with monatomic edges. The observed phenomena are explained in terms of competing processes of surface diffusion, crystal growth in an electric field, and field evaporation. © 2005 Pleiades Publishing, Inc.

1. INTRODUCTION

Deformations of metal crystals subjected to heating in an electric field (thermal field treatment) have been studied using field electron emission microscopy, field ion emission microscopy, transmission electron microscopy, and high-temperature field evaporation microscopy. Usually, metal tips are studied; after a high-temperature heat treatment, the apex of a tip becomes a single crystal with flat facets and rounded transient regions. The main types of deformation have been found and investigated: reconstruction of the tip into a polyhedron consisting of close-packed planes, the formation of outgrowths on the close-packed faces, and the creation of nanosized protrusions on apexes and edges of the crystal and outgrowths [1–5].

The field-emission microscopy techniques applied make it possible to observe surface regions with the highest electric field intensity, i.e., with sharp protruding parts. If a sample has nanosized protrusions, they would be the only observable feature [1, 3–5]. In a transmission electron microscope, the profile of a crystal becomes visible [2, 6]. In both cases, surface regions in between the protruding parts remain unobservable. In order to study these regions, microscopic protrusions and sharp edges are dulled by heating [3, 5] and the field-emission microscopy images obtained after the heating are used to judge the original tip shape after the thermal field treatment but before the heating. In field ion-emission microscopy, protruding parts are removed by low-temperature field evaporation [4].

Additional information about inadequately explored surface regions that form under thermal field treatment

and about the processes occurring in them can be obtained using continuous-mode field-desorption microscopy [7–9]. This method can also provide more accurate data on the actual shape of outgrowths and protrusions immediately after a thermal field treatment and about the shape and surface structure of the reconstructed tip.

In the present paper, we attempt to study the state of a surface immediately after thermal treatment in an electric field using continuous-mode field-desorption microscopy. We took tungsten as the material to be studied because its deformation under thermal field treatment is the most explored. Potassium and cesium are taken as adsorbates for imaging of the surface, since they make it possible to obtain field-desorption images at the lowest possible field strength and temperature and, accordingly, with the least impact on the surface under study.

2. CONTINUOUS-MODE FIELD-DESORPTION MICROSCOPY

In continuous-mode field-desorption microscopy, ions of substances that are easily ionized and weakly linked to the surface under study (for example, ions of alkali or alkaline-earth metals) are used for imaging. An alkali metal coating about one monolayer thick is deposited onto the tip surface, and then a positive voltage is applied to the tip to create a desorption field. Desorbed alkali metal ions, which move along radial trajectories, project an enlarged image of the tip surface onto the screen of a field-emission microscope. The tip has

to be maintained at a relatively high temperature in order to facilitate surface diffusion of adsorbed atoms and renew their supply in the desorption area. A common technique of imaging is as follows: initially, the applied voltage is set high to remove all adsorbed atoms from the tip point, and then the voltage is lowered and the image formed by ions that diffuse from the side surface of the tip to its point and are desorbed there is observed.

The image obtained is affected by many factors: the applied voltage, the temperature, the surface density of adsorbed atoms in the region that is imaged and around it, and the work function, shape, and atomic structure of the surface. For our purpose, the possibility of observing different parts of the surface achieved by varying the applied voltage is the most important. As the voltage is gradually decreased after all adsorbed atoms are removed from the tip point, peripheral parts of the tip (where the field strength is the lowest) appear in the image first, since desorption prevents adsorbed atoms from reaching parts with a higher field strength. As the voltage is lowered further, regions with a higher field strength become visible in the image. Thus, unlike other field-emission microscopy techniques, surface regions with a field strength less than its maximum value can be observed here. If the tip shape is irregular, the image pattern can be more complicated, since the variation of the field strength is not monotonic in the paths along which adsorbed atoms diffuse to the region being imaged. The tip shape can be determined by observing the evolution of the image during an increase and a decrease in the applied voltage.

3. EXPERIMENTAL TECHNIQUE

Measurements were carried out in the metallic ultra-high-vacuum chamber of a field-emission microscope with a residual gas pressure below 10^{-10} mm Hg. Field-emission and desorption images were formed by a detector consisting of two microchannel plates and a fluorescent screen. The images were recorded with a video camera and digitized. The electric field strength F was determined from the Fowler–Nordheim current–voltage characteristics using the average field-emission work function of pure tungsten equal to 4.44 eV. A tungsten tip was preliminarily heated at 2800 K for several tens of minutes in order to clean it and produce a close-to-equilibrium shape of the microcrystal.

The experiment was conducted as follows. The tip is heated up to the target temperature T , and then a positive voltage is applied. If field-desorption occurs, the image created by tungsten ions is recorded on video. After the thermal field treatment is finished, the tip is cooled and then the high voltage is removed. Thereafter, the current–voltage characteristics of the field-electron emission are measured and field electron emission images are recorded. Next, cesium and potassium are deposited on the tip and field-desorption images are obtained for various values of the electric field strength

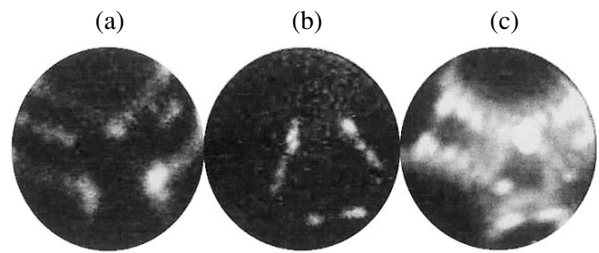


Fig. 1. Field-desorption images of the edges of a reconstructed tip for the cases when (a) there is no field evaporation during the thermal field treatment and (b, c) the field evaporation occurs from the apex of the $\langle 111 \rangle$ angle.

and for the tip temperature gradually increasing from room temperature. When the temperature of the thermal desorption of the adsorbed atoms is reached and desorption images disappear, the field electron emission parameters and field electron emission images are recorded again.

4. EXPERIMENTAL RESULTS

The field-desorption images of a surface obtained immediately after the thermal field treatment of the tip confirm, for the most part, the general character of the tip deformations as derived from field electron and field ion images obtained after smoothing of the treated tip by heating or low-temperature field evaporation. Yet, significant new insight is obtained into the deformation processes and resulting shapes.

During the reconstruction and after its completion (at high T and low F), we observed not only expansion of close-packed facets but also the formation of new atomic layers on their surface, i.e., the process of layer-by-layer crystal growth. In the field-desorption images, these layers appear as outlines of steps that do not cross the edges of the facet. The steps are not visible in field electron emission images, which consist of bright spots corresponding to apexes of the reconstructed tip regardless of whether there are steps or not. The layer-by-layer crystal growth at this stage of the thermal field treatment does not give rise to any outgrowths or protrusions.

Using field-desorption images (Fig. 1), we managed to study the structure of the edges separating facets at the stage of complete reconstruction, when electron field images show only trihedral $\langle 111 \rangle$ angles formed by crossings of (011) planes and the tip point is confined by either close-packed (011) facets or (011) and (001) facets. The facets turn out to be separated either by monatomic edges or by edges of more complex structure (Fig. 2). The edges that separate (011) facets are found to be formed as steps in the (112) crystal plane.

The width of the steps across the edge is from one to several atomic rows. The edge shown in Fig. 1c is about 500 nm long and is divided into six steps; so in this case

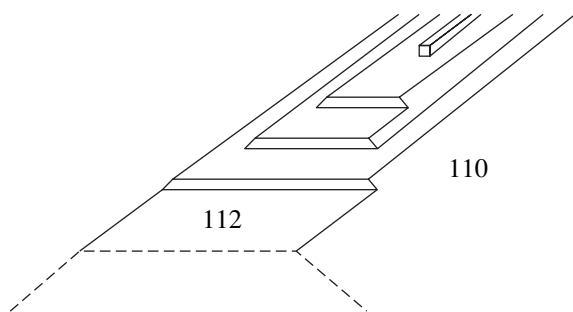


Fig. 2. A sketch of the edge of a reconstructed tip with steps in the (112) plane.

the length of a step along the edge is about 100 nm. Since the magnification of the projecting field-emission microscope across the edge is much larger than that along the edge, a step ~ 100 nm long and 1 nm wide appears with the opposite dimension ratio in the field-desorption image: its width across the edge is larger than its length.

The edge structure is not resolved in electron field images. Only trihedral $\langle 111 \rangle$ angles are visible as bright spots, blurred triangles, or three-point stars. Steps across the edge (Fig. 1b) usually arise when field evaporation occurs from the apex of the trihedral $\langle 111 \rangle$ angle during a thermal field treatment. If there is no evaporation, the edge either is a monatomic row or consists of mainly longitudinal steps (Fig. 1a).

At low T and high F , no faceting takes place; instead, steps of different height and width dependent on T and F form. The higher the value of T , the wider and higher the steps and the smaller their number. When viewed in the direction normal to their plane, the steps are polyhedra surrounding (100), (110), and (112) facets of the original tip. At the step angles, nanosized protrusions arise and become centers of field evaporation, which results in protrusion images on the screen. When F is increased, the images of the protrusions, which are arranged in circles, move toward the centers of the facets and disappear, forming a “collapsing-ring” pattern [10]. The central steps decrease in width and disappear, and new steps arise at the outskirts of the facets.

Buildups on (100) and (110) close-packed facets appear at higher T and F than during the reconstruction. The field desorption images confirm that the outgrowths are shaped like truncated pyramids or stepped truncated pyramids (Fig. 3f).

The upper face of such a pyramid [a square or rectangle in the case of outgrowths on (100) facets]. There are protrusions on the edge of each step of an outgrowth.

At this stage (beginning of the formation of outgrowths), oscillations in the field evaporation current originating from a protrusion are often observed: a protrusion in the field evaporation image disappears and

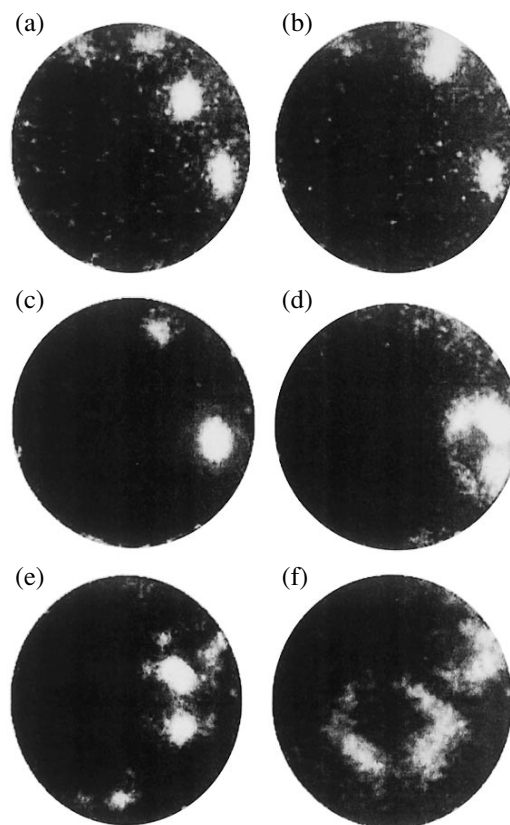


Fig. 3. Images of nanosized protrusions and outgrowths formed (a, b) via field evaporation at (a) $T = 2400$ and (b) 1550 K and (c–f) via field desorption of cesium.

reappears again at the same place. Another remarkable fact is that the field evaporation from nanosized protrusions at the same applied voltage can occur over a very wide temperature range, ~ 1000 K wide (Figs. 3a, 3b). As F increases, the number of protrusions grows and their positions in the field-evaporation images change. The collapsing-ring effect is observed, as is the case with the formation and destruction of steps at low T and high F . The point of the tip is dulled in this case. The increase in the tip radius was measured after outgrowths were smoothed away by heating.

Field-desorption images of nanosized protrusions are shown in Figs. 3c–3e, and the shape of the protrusions is shown schematically in Fig. 4. As the applied voltage gradually grows, first there appear bright spots, which are images of the protrusion apices (Fig. 3c). Then, the spots are enlarged both smoothly and in steps and facets and edges of the protrusions show up (Figs. 3d, 3e). The enlargement can occur uniformly in all directions around the tip point or be predominantly directed (Figs. 3c, 3d). Sometimes the image of a protrusion apex bifurcates (Fig. 3e).

5. DISCUSSION

We derived conclusions about the shapes of formations created during thermal treatment of a tip in an electric field by analyzing dynamic changes in the field-desorption images under variation of the desorbing field rather than on the basis of the separate frames of video recordings shown here. For example, in Fig. 1b, only one step in each edge of the reconstructed tip is visible; when the field is varied, the image jumps from one step to another. It is possible to capture all steps in one frame by increasing the field sharply (Fig. 1c).

The general character of the tip deformation as derived from the field-emission microscopy studies is confirmed. However, continuous-mode desorption microscopy made it possible to detect further fine details of the deformation process and of the shape of tips that cannot be observed by other means, such as the structure of edges and apexes of the reconstructed tip and outgrowths, as well as the shape of nanosized protrusions.

All observed protrusions have pointed apexes probably ending with a single atom or with a monatomic crest. However, these observations were made after cooling of the tip. Cooling takes some time due to the thermal inertia; therefore, surface diffusion, crystal growth, and field evaporation continue to proceed during the cooling period. If the field evaporation stops earlier than the diffusion, a protrusion can be completed into a pyramid even in the case where its growth is limited by the field evaporation, which causes its apex to be rounded.

Therefore, during the thermal field treatment itself, when there are shape modifications and field evaporation from the protrusion, the nanosized protrusion can have a shape other than that of a pyramid. This assumption is confirmed by the field-evaporation images where images of apexes of nanosized protrusions are sufficiently large. Thus, during their growth and thermal field evaporation, the nanosized protrusions are shaped like a pyramid or a wedge with a truncated (Figs. 4c, 4d) or rounded top, but after cooling they are shaped like a regular pyramid or a wedge with a pointed top made of a single atom or of a monatomic crest (Figs. 4a–4c).

Desorption images show that the layered growth on close-packed facets can also occur at the stage of reconstruction, where shape variations are limited to the transition from a partially rounded tip to a polyhedron and there are no outgrowths or protrusions. If this is the case, the reasons for the transition from the layer-by-layer growth preserving the polyhedron shape of the tip point up to the formation of outgrowths are unclear. It is also difficult to understand the wide temperature range in which the field evaporation from the nanosized protrusions occurs at the initial stage of formation of the outgrowths. Since both the field evaporation and surface self-diffusion (which provides a renewal of evaporating material at the protrusion apex) depend

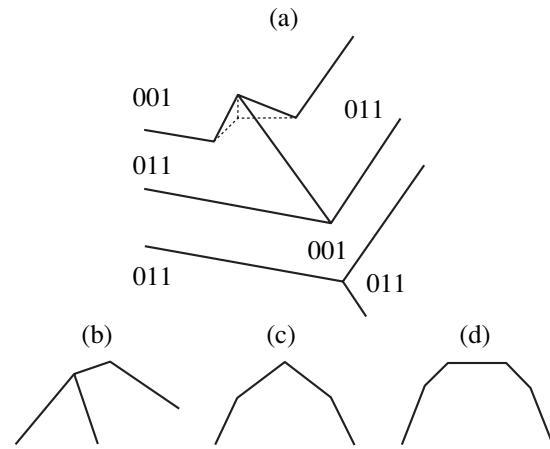


Fig. 4. Sketches of different kinds of nanosized protrusions: (a) a pyramid-shaped protrusion on the edge of an outgrowth on the (001) facet, (b) a wedge-shaped protrusion, (c) a pyramid- or wedge-shaped protrusion on top of a truncated pyramid, and (d) a protrusion in the form of a truncated pyramid on top of a truncated pyramid.

drastically on temperature, the field evaporation from the protrusion apex should have been stopped after a minor drop in temperature regardless of the cause of the limitation of the field-evaporation rate (field evaporation itself or the diffusion feed of the material). Another unexplained phenomenon is the termination of the field evaporation from a nanosized protrusion and its resumption some time later at the same place. We tried to cool a tip down at the moment when field evaporation from the protrusion ceased and to study the tip using field electron emission microscopy and field-desorption microscopy. The nanosized protrusion was observed at the same place at all times, and no differences in its properties were noticed in relation to the moment at which the tip was cooled down (whether field evaporation did or did not occur at that moment). Also, the motions of the protrusions during the thermal field treatment are not completely understood yet. Only some of them are related to the modifications of the shape of the underlying surface.

To explain the observations, we propose a model of the processes that occur during high-temperature heating of the tip in an electric field. The model is based on competition between the surface diffusion, layered crystal growth, and field evaporation. We use the Herring theory [11] and ideas developed in [1–5, 12–14]. At high temperatures, the following processes occur: destruction of atomic layers when atoms on the tip surface break out of atomic planes of steps and become adsorbed on the surface, migration of adsorbed atoms (surface diffusion), and growth of atomic layers when adsorbed atoms are attached to steps. The resulting transfer of matter is governed by the gradient of the chemical potential of surface atoms. In the absence of an external electric field, the chemical potential gradient and the matter flow are directed from the tip point

toward its side surface (where the surface curvature is lower). Therefore, atomic layers are destroyed at the tip point and grow on the side surface; so the tip is dulled. After prolonged heating in the absence of an electric field, the processes of destruction and growth become balanced and the tip assumes a quasi-equilibrium shape.

An electric field disturbs this equilibrium. It contributes the term $-F^2/8\pi$ to the surface free energy of the metal and to the chemical potential of atoms adsorbed on the surface [11]. Since the local field strength at the tip point and near edges of flat facets is higher than that on the side surface and in the central parts of flat facets, the electric field can counterbalance the influence of the curvature, turn back the mass transfer, stop dulling of the tip, and induce faceting of the tip by close-packed planes. The tip becomes faceted because the growth rate on loose planes is higher and because the nucleation of new atomic layers on close-packed surfaces is impeded.

When faceting of the tip is completed, the diffusion flow keeps bringing atoms to the tip point and flat facets and can induce a sufficiently high surface supersaturation (an excess over the equilibrium density that balances the processes of atoms joining and breaking away from a two-dimensional island); so a two-dimensional nucleus forms and a new layer starts growing. If new layers grow successively over the entire facet, the tip point preserves its polyhedral shape. The supersaturation near the edges of facets is higher than that in the central parts, since the field strength is higher near the edges and since atoms flow in through the facet edges. Therefore, the nucleation and growth rates are higher near the edges. This situation is similar to the conditions when dendrite crystals are grown from a solution without agitation. A new layer can be nucleated earlier than the previous layer finishes growing. Then, the growth of the underlying layer is slowed down, since part of the migrating atoms is captured by the new layer and since the field is partially screened. The upper layer can catch up with the lower one and create a double-height step. In this case, the field strength increases at the upper edge of the step and decreases at the lower edge. Therefore, with a high probability, an atom that is attached to the step edge will come to the upper surface before the next atoms arrive and form a nucleus of the next atomic row. So, the growth of the step width will be slowed down or come to a halt.

This process can also result in the formation of a nanosized protrusion at the step edge if the nucleation of the new layers occurs significantly ahead of their growth. The growth can become avalanche-like due to the boost to the field strength with an increase in the protrusion height. Some of the atoms arriving at the outgrowth from the side surface of the tip (Fig. 4a) come to the close-packed plane of the side surface of the outgrowth and then diffuse over it toward the nanosized protrusion and are field-evaporated from its apex.

This process reduces the atomic density on the lower plane and near the edge of the outgrowth and precludes growth of a new layer on the lower plane.

So, we propose two reasons that can limit the growth of a layer before it fills the entire facet of the reconstructed tip and thereby can cause a transition from faceting of the tip to the formation of outgrowths.

(i) The formation of steps of more than monatomic height (with a close-packed side surface) on the facets due to upper growing layers catching up with lower ones; these steps reduce the probability of nucleation for new atomic rows on the facet because atoms flow out to the top plane of the step.

(ii) The formation of a nanosized protrusion on the step edge (not on the facet edge) and the field evaporation of atoms from its apex (these atoms would have completed the step to the facet edge in the absence of evaporation).

Probably, both mechanisms are effective. Experimentally, however, each outgrowth always had protrusions on all of its steps. Therefore, the second mechanism prevails and it can be the field evaporation that governs the transition to the formation of outgrowths.

The growth of a protrusion and field evaporation from its apex, on the one hand, and nucleation and the growth of atomic layers, on the other hand, are competing processes, since both reduce the density of adsorbed atoms on the facet and outgrowth surfaces. The field evaporation from a protrusion reduces the nucleation and growth rates of an atomic layer. However, the growing layer takes in some of the atoms arriving at the facets and reduces the rate of field evaporation from the protrusion (we assume that the rate is limited by the supply of atoms to the protrusion).

This model can explain the oscillations of the field evaporation and the wide temperature range in which the field evaporation from nanosized protrusions is observed under constant conditions. Indeed, if a new layer does not grow, the diffusion flow creates a large density of atoms on the facet, which can only be removed through field evaporation from a protrusion. When nucleation occurs and a new layer grows, the density of atoms reduces; accordingly, the rate of field evaporation also reduces. After completion of the new layer and before the next nucleation, the field-evaporation rate is restored. Therefore, the field-evaporation current oscillates. A decrease in temperature causes a decrease in the rate of nucleation of atomic layers (a process which competes with the field evaporation). Due to this decrease, under certain conditions, the rate of the field evaporation can remain unchanged even after a considerable drop in temperature. Oscillations in the field-evaporation current with a lower amplitude but at a higher frequency can also be related to nucleation and growth of new atomic rows on the edge of the growing layer.

An increase in the voltage applied to the tip boosts the rate of field evaporation from protrusions, which

can reduce the atomic density on the plane to below its critical value for the nucleation of new atomic layers, thereby causing the outgrowth formation to terminate. When the field strength is increased even higher, the evaporation exceeds the diffusion flow, the dynamic balance between the growth and destruction of atomic layers shifts toward destruction, atomic layers are dissolved, and atoms of destructed layers are removed by the field evaporation from the protrusions. The tip point retreats, preserving the polyhedral shape with stepped outgrowths on the facets and with nanosized protrusions on the edges. During this process, the number of protrusions grows and the protrusions move in the field-evaporation images. The processes of destruction of a step of an outgrowth and a gradual decrease in its width manifest themselves in the images as the collapsing-ring effect.

6. CONCLUSIONS

The application of continuous-mode field-desorption microscopy for studying deformations of a tip, which occur when the tip is heated in a strong electric field, has made it possible to more accurately determine the shapes of the formations that arise. The edges of a tip 500 to 1000 nm in radius that is reconstructed into a polyhedron are formed by monatomic steps about 1 nm wide and 100 nm long. Bumps about 10 nm in size are shaped like a pyramid or a wedge with a single-atom apex or a monatomic crest on the top and with side facets that are a continuation of the facets of the reconstructed tip or the outgrowth where the protrusion is situated. We confirm that, immediately after thermal field treatment, outgrowths are shaped like stepped truncated pyramids with monatomic edges.

The author dedicates this work to the memory of Vladimir Nikolaevich Shrednik.

REFERENCES

1. M. Benjamen and R. O. Jenkins, Proc. R. Soc. London, Ser. A **176**, 262 (1940).
2. P. C. Bettler and F. M. Charbonnier, Phys. Rev. **119**, 85 (1960).
3. V. G. Pavlov, A. A. Rabinovich, and V. N. Shrednik, Pis'ma Zh. Eksp. Teor. Fiz. **17**, 247 (1973) [JETP Lett. **17**, 177 (1973)].
4. V. N. Shrednik, V. G. Pavlov, A. A. Rabinovich, and B. M. Shaikhin, Izv. Akad. Nauk SSSR, Ser. Fiz. **38**, 296 (1974).
5. V. G. Pavlov, A. A. Rabinovich, and V. N. Shrednik, Fiz. Tverd. Tela (Leningrad) **17**, 2045 (1975) [Sov. Phys. Solid State **17**, 1335 (1975)].
6. V. M. Zhukov and S. A. Polezhaev, Zh. Tekh. Fiz. **57**, 1133 (1987) [Sov. Phys. Tech. Phys. **32**, 659 (1987)].
7. D. P. Bernatskiĭ, Yu. A. Vlasov, and V. G. Pavlov, Zh. Tekh. Fiz. **57**, 2257 (1987) [Sov. Phys. Tech. Phys. **32**, 1366 (1987)].
8. D. P. Bernatskiĭ and V. G. Pavlov, in *Proceedings of the 9th International Conference on Vacuum Microelectronics, St. Petersburg, 1996* (St. Petersburg, 1996), p. 47.
9. V. G. Pavlov, in *Field-Ion and Field-Emission Microscopy and Spectroscopy: History, Achievements, the Current State of the Art, and Prospects*, Ed. by A. L. Suvorov (Akademprint, Moscow, 2003), p. 315 [in Russian].
10. V. G. Butenko, O. L. Golubev, E. L. Kontorovich, and V. N. Shrednik, Pis'ma Zh. Tekh. Fiz. **18**, 86 (1992) [Sov. Tech. Phys. Lett. **18**, 275 (1992)].
11. C. Herring, in *Structure and Properties of Solid Surfaces*, Ed. by R. Gomer and C. S. Smith (Chicago University Press, Chicago, 1953), p. 5.
12. M. Drechsler, Z. Elektrochem. **61**, 48 (1957).
13. J. P. Barbour, F. M. Charbonnier, W. W. Dolan, W. P. Dyke, E. E. Martin, and J. K. Trolan, Phys. Rev. **117**, 1452 (1960).
14. Yu. A. Vlasov, O. L. Golubev, and V. N. Shrednik, Rost Krist. **19**, 5 (1991).

Translated by G. Tsydynzhapov

LOW-DIMENSIONAL SYSTEMS
AND SURFACE PHYSICS

Vibrational Spectra of 2-Cyclooctylamino-5-Nitropyridine and Its Mixtures with C₆₀ and C₇₀ Fullerenes

A. Leyderman[†]*, E. I. Radovanova**, S. S. Sarkisov***, and V. S. Vikhnin**

* Department of Physics, University of Puerto-Rico, Mayaguez, Puerto-Rico, 00680 United States

** Ioffe Physicotechnical Institute, Russian Academy of Sciences, Politeknicheskaya ul. 26, St. Petersburg, 194021 Russia
e-mail: radeli@mail.ioffe.ru

*** Department of Physics, Alabama Agricultural and Mechanical University, Normal, Alabama, 35762-1268 United States

Received November 25, 2004

Abstract—The vibrational spectra of 2-cyclooctylamino-5-nitropyridine (COANP) solutions and the evolution of the spectra upon changing over from the solutions to solid-phase COANP are investigated. The bands observed in the spectra are assigned to the corresponding vibrational modes. The nature of the interaction of COANP with C₆₀ and C₇₀ fullerenes is elucidated by analyzing the transmission spectra of these compounds. No interaction of the COANP compound with C₆₀ and C₇₀ fullerenes is revealed under the studied conditions. It is assumed that the physical nature of this phenomenon can be associated with the formation of liquid-crystal clusters consisting of fullerene molecules. © 2005 Pleiades Publishing, Inc.

1. INTRODUCTION

2-Cyclooctylamino-5-nitropyridine (COANP) is a known organic material characterized by large electro-optical coefficients. The optical and nonlinear optical properties of this compound were investigated in [1–5]. The structural formula of COANP is presented in Fig. 1. The large dipole moment of the molecule is associated with the charge transfer from the donor NH group to the acceptor NO₂ group [6].

2-Cyclooctylamino-5-nitropyridine molecules form noncentrosymmetric orthorhombic crystals (point group *mm2*, space group *Pca2₁*). The methods used to grow the crystals were described in [7–10].

In the crystal structure, the COANP molecules are linked by hydrogen bonds formed between the oxygen atoms of the nitro groups and the nitrogen atoms of the amino groups. These oxygen and nitrogen atoms are separated by a distance of 2.9 Å. The other interactions between the oxygen atoms and nitrogen atoms of the pyridine rings (separated by a distance of 3.9 Å) are considerably weaker [1]. The crystal structure and molecular mechanics calculations of COANP were described in [11].

It is well known that fullerenes in different liquid and solid matrices exhibit remarkable nonlinear optical properties, in particular, optical limiting at low thresholds of incoming laser radiation [12–15]. The combination of nonlinear optical properties of fullerenes and COANP seems to be very attractive from the practical standpoint, especially because COANP can be prepared in the form of bulk crystals, thin single-crystal films [4], and amorphous glassy films of high optical quality [2,

16, 17]. However, the mixing of these compounds can lead to unpredictable changes in their properties that can prove to be desirable and undesirable. For example, according to Kamanina *et al.* [18], the possible formation of a complex with charge transfer from the donor moiety of the COANP molecule to the fullerene molecule is considered a desirable interaction. It is also known that the primary and secondary amines (including the COANP compound) can form covalent bonds with fullerene molecules [19–21].

In order to reveal the bonding between COANP and fullerene molecules, we thoroughly investigated the vibrational spectra of COANP and the IR transmission spectra of COANP solutions with C₆₀ and C₇₀ fullerenes. This study is a continuation of the spectroscopic investigations performed in our previous work [5].

2. VIBRATIONAL SPECTRA OF 2-CYCLOOCTYLAMINO-5-NITROPYRIDINE

The transmission spectra were measured using 2-cyclooctylamino-5-nitropyridine synthesized and purified at the Department of Chemistry of the New Mexico Highlands University (Las Vegas, New Mex-

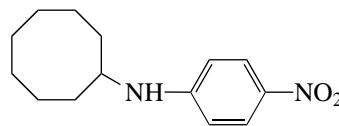


Fig. 1. Structural formula of 2-cyclooctylamino-5-nitropyridine.

[†] Deceased.

ico, United States). Carbon tetrachloride CCl_4 and carbon disulfide CS_2 served as solvents, because the IR spectra of these compounds contain regions free of intense absorption bands in the spectral range of interest. The transmission spectra of the solutions (in layers 10 μm thick) were recorded on the Perkin-Elmer System 2000 GS-IR and Bruker Tensor 27 Fourier-Transform spectrophotometers in KBr or NaCl cells. The concentrations of the COANP solutions were equal to 3, 4, 7, 20, and 60 mg/ml.

The IR transmission spectra of the COANP solutions in carbon tetrachloride in the frequency range 500–1400 cm^{-1} and those in carbon disulfide in the range 1200–3500 cm^{-1} are shown in Figs. 2a and 2b, respectively. The frequency range 1650–2500 cm^{-1} in Fig. 2b is omitted because, in this range, no absorption bands of COANP are observed. The frequencies of the absorption bands attributed to COANP in the solutions are listed in the table (columns 1, 2). Considering the purpose of this study, it is necessary to assign the observed absorption bands to the corresponding vibrations.

The vibrational spectra of COANP in the solid phase were studied earlier by Petzelt *et al.* [22]. The Raman spectra were measured for samples in the form of crystal plates. The absorption spectra were recorded using crystal plates and COANP powders pressed into KBr pellets for measurements in the frequency ranges in which the crystal plates exhibited a very small transmittance. For comparison, the table (columns 6–9) presents the vibrational frequencies observed in [22] and the proposed approximate assignment of the bands to particular modes of vibration in the COANP molecule.

It can be seen from the table that, for the most part, the frequencies of the bands observed in the transmission spectra of the solutions are in good agreement (to within a few inverse centimeters) with those obtained in [22] for the solid-phase samples. The considerable differences are observed only in the frequency range $\nu > 3300 \text{ cm}^{-1}$, in which the spectrum of the solid sample contains one intense band with the maximum at a frequency $\nu = 3340 \text{ cm}^{-1}$ [22], whereas the absorption spectrum of the solution in this range exhibits a fine structure and is shifted by almost 100 cm^{-1} toward the high-energy range (see table, Fig. 2b). For this reason, we also measured the transmission spectra of COANP in the solid phase with the use of thin films deposited from the CS_2 solution. In order to prepare these films, a drop of the solution was applied to special windows (transparent in the IR range) from AgCl or poly(ethylene) (St-IR Card), followed by the evaporation of the solvent.

Figure 3 shows the IR transmission spectra of the deposited films and the COANP solutions (in CCl_4 and CS_2) at two concentrations in the frequency range 3200–3500 cm^{-1} . For the solid phase (Fig. 3, curve 6), the position of the absorption band ($\nu_{\text{max}} = 3341 \text{ cm}^{-1}$)

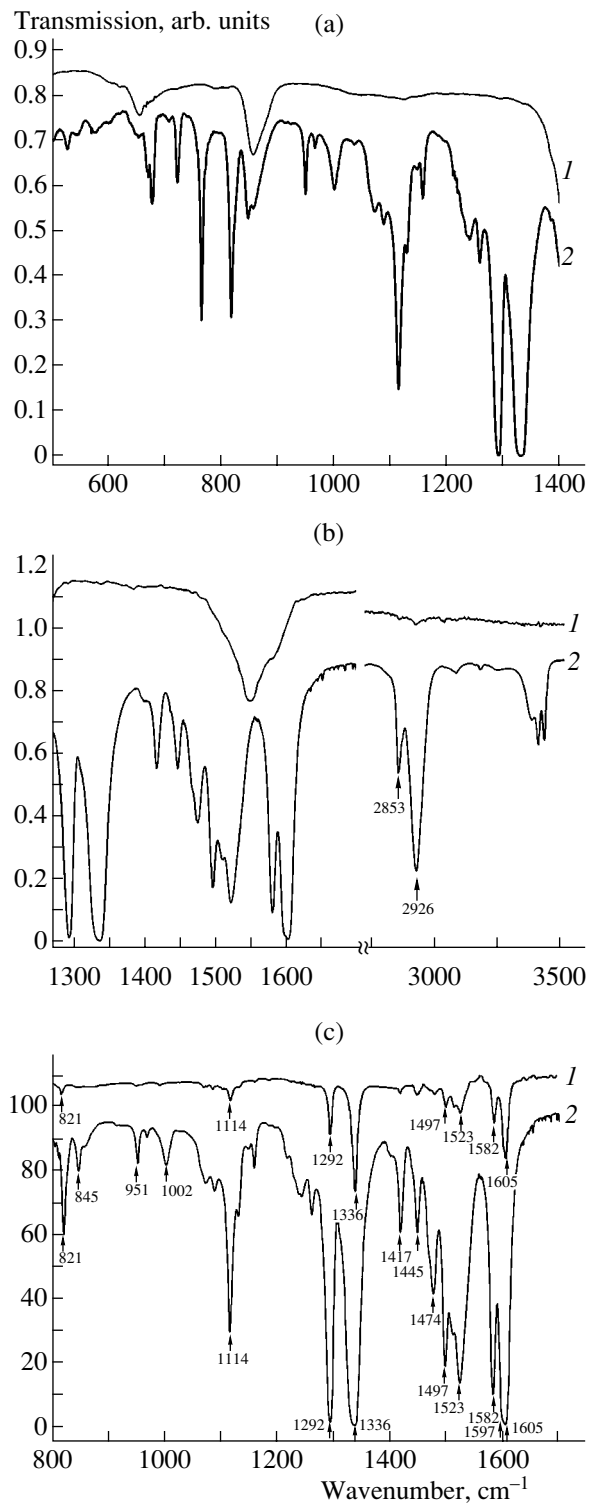


Fig. 2. (a) IR transmission spectra of (1) the CS_2 solvent and (2) the COANP solution (60 mg/ml) in CS_2 , (b) IR transmission spectra of (1) the CCl_4 solvent and (2) the COANP solution (60 mg/ml) in CCl_4 , and (c) IR transmission spectra of the COANP solutions in CCl_4 (with the one-hundred-percent line represented by the spectrum of a cell with CCl_4) at concentrations of (1) 3 and (2) 60 mg/ml.

Absorption bands in the vibrational spectra of COANP

COANP solution in CCl ₄ , cm ⁻¹	COANP solution in CS ₂ , cm ⁻¹	Solid-phase COANP on AgCl, cm ⁻¹	Solid-phase COANP on poly(ethylene), cm ⁻¹	Characteristic vibrations	Crystalline COANP (according to the data taken from [22])				
					Raman spectra, cm ⁻¹	Absorption spectra		Characteristic vibrations	
						single crystals, cm ⁻¹	pow- ders, cm ⁻¹		
1	2	3	4	5	6	7	8	9	
Strong absorption in solvent	502 w	503 vw	503 vw	β (Py ring)	505	495	500	C-C in-plane bending	
	527 w	528 w	530 w		550	520	523		
	546 w	547 w	547 m		573		545		
		577 vw	576 w	580 w	584		576		
		618 w		~616 w			614		
	678 m	677 w	678 m	677 m	674	679	677		
	723 m	722 m	726 m	Bands of poly(ethylene)	727	730	727		CH ₂ rocking
		765 w	766 m	766 m	770	764	765		
				797 vw	797				
				809 w	801				
	820 m	818 m	825 m	831 m	} γ(CH) in Py v(CN) in Py-NO ₂	841		845	CH out-of-plane bending
	847 m	847 w	~846 m	846 w		843			
					850				
	860 vw	858 vw		864 vw	866				
			873 vw	872 vw					
			913 vw	912 vw		915			
	951 m	949 w	948 w	945 w	γ(CH) in Py	951	946	945	
	968 vw	965 vw	~970 vw	973 vw		974			
	1001 m	1001 m	1000 m	~999 m ~1011 m	} v(ring), Py(1)	1010			
						1015			
1071 m	1071 w	1069 m	1062 vw	v(CN) in Oct-NH	1065		1063		
1088 vw		1088 vw	1088 vw		1090				
1114 s	1114 s	1114 s	1114 s	β(CH), Py (18a, 18b)	1115		1112	CH, ON in-plane bending	
1130 m	1129 w	~1130 w	1125 m		1124				
1148 vw	1147 vw	1146 vw	1144 w		1140				
					1151				
1158 w	1157 w	1159 w	1164 w		1165				
					1190				
1240 w	1239 w	1243 vw	1231 m	v(CN) in Py-NH	1231				
1258 vw	1258 m	1260 w	1248 w						
			1282 vs	} β(CH) Py (3, 9a, 9b)	1282			} CH ₂ twist C-C stretching CH ₂ wagging	
1293 vs	1292 vs	1292 vs	1293 vs		1286		1292		
					1292				
					1296				
				1323					
1337 vs	1332 vs	1332 vs	1324	} v(NO ₂) symmetric	1329		1325		
			1341 m		1342				
			1361 m		1362				
				CH ₂ wagging					

Table (Contd.)

COANP solution in CCl_4 , cm^{-1}	COANP solution in CS_2 , cm^{-1}	Solid-phase COANP on AgCl, cm^{-1}	Solid-phase COANP on poly(ethylene), cm^{-1}	Characteristic vibrations	Crystalline COANP (according to the data taken from [22])			Characteristic vibrations
					Raman spectra, cm^{-1}	Absorption spec- tra		
						single crys- tals, cm^{-1}	pow- ders, cm^{-1}	
1417 m	1417 m	1420 m	1409 w	$\nu(\text{ring})$, Py(14)	1459			
1448 m		1447 m	1442 m	$\nu(\text{ring})$, Py(19b)				
1475 m		1474 s	Bands of PE card	CH_2 deformation in Oct	1498	1498	} CH_2 deformation NO stretching C-N stretching	
1497 s		1497 m		1498 m				$\nu(\text{ring})$, Py(19a)
1510 m				$\beta(\text{N-H})$ free				
1523 s				$\beta(\text{N-H}\cdots\text{O})$ bound				
		1529 s	1531 s	$\beta(\text{N-H}\cdots\text{O})$ bound				
1582 m		1578 s	1578 s	$\nu(\text{ring})$, Py(8b)	1581		}	
	1597 vs			$\nu(\text{ring})$, Py(8a)	1597			
1603 vs	1604 vs	1604 vs	1601 vs ~1616 m	$\nu(\text{NO}_2)$ asymmetric	1602	1603	C=C stretching	
					1626		}	
					1806			C=N stretching
1897 vw	1896 vw			} Overtones and com- bination bands in Py ring	1890	1886		
1931 vw	1931 vw		1943 vw					
2448 vw	2449 vw	2447 vw	2437 vw					
2492 vw	2486 vw	2485 vw						
					2580			
2698 vw	2694 vw	2694 vw	Strong absorption in poly(ethylene)	$\nu(\text{CH}_2)$ asymmetric in Oct		2692	2691	
2855 m	2850 m	2854 s				2862		2865
						2917		
2926 s	2923 s	2923 s				2921		2922
				$\nu(\text{CH}_2)$ symmetric in Oct	3059		} CH stretching	
					3066	3068		3067
3084 vw	3084 vw	3084 vw	~3080 vw	$\nu(\text{CH})$ in Py				
3181 vw	3181 vw	3181 vw	3182 vw	$\nu(\text{CH})$ in Py				
3252 vw	3252 vw	3258 vw						
			3341 m	} $\nu(\text{N-H}\cdots\text{O})$ coupled	3344	3340	NH, OH stretching	
		3374 m						
3386 m	3383 m			} $\nu(\text{NH})$ free				
3415 m	3404 m							
3440 m	3427 m							

Note: Py is pyridine, Oct is cyclooctyl, ν is the stretching vibration, β is the in-plane bending vibration, and γ is the out-of-plane bending vibration. The number notation for pyridine vibrations is given according to [26]. Abbreviations for the relative intensities of the absorption bands are as follows: s = strong, vs = very strong, m = medium, w = weak, and vw = very weak.

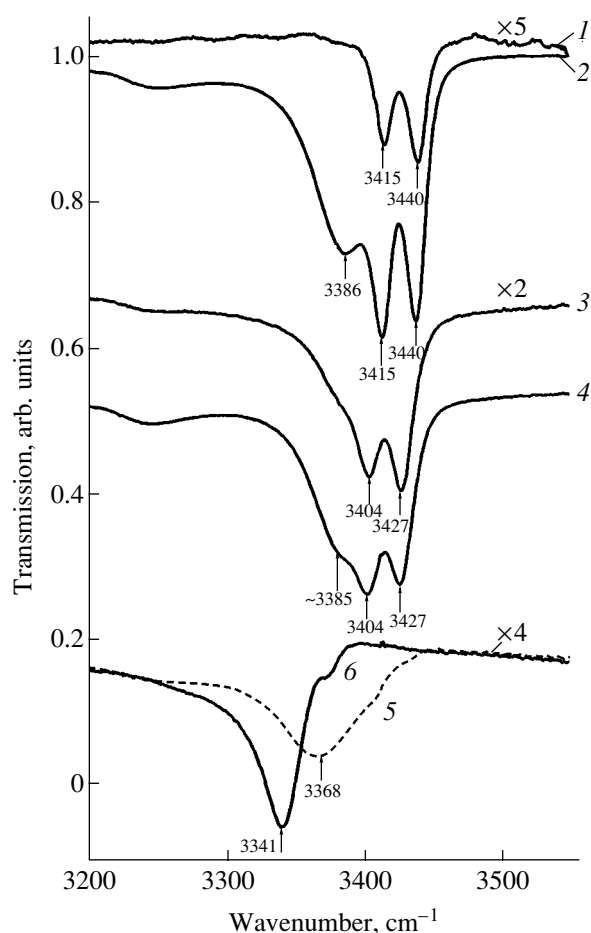


Fig. 3. IR transmission spectra of the COANP solutions in CCl_4 at concentrations of (1) 4 and (2) 60 mg/ml, the COANP solutions in CS_2 at concentrations of (3) 2 and (4) 60 mg/ml, and (5, 6) the COANP thin film deposited from the solution in CS_2 on the poly(ethylene) window within (5) ten minutes and (6) two days after the deposition of the film.

coincides (accurate to within 1 cm^{-1}) with the position of the band observed for the powder sample in [22] (see table, column 8). For the solutions at low COANP concentrations (Fig. 3, curves 1, 3), the spectra involve two narrow bands separated by $\Delta\nu = 25 \text{ cm}^{-1}$. An increase in the COANP concentration in the solution leads to an increase in the intensity of these bands; moreover, there appears a third broader band (Fig. 3, curves 2, 4).

In our opinion, the strong effect of the solvent on the absorption in this frequency range can be explained as follows. According to [22], the band with the maximum at a frequency $\nu = 3340 \text{ cm}^{-1}$ corresponds to the stretching vibrations of the NH and OH groups, i.e., the vibrations of the NH group involved in the intermolecular hydrogen bond with the oxygen atom of the nitro group of the neighboring molecule in the crystal (in other words, this band is attributed to the stretching vibrations of the $\text{N-H}\cdots\text{O}$ bonds).

It is known that the formation of hydrogen bonds, as a rule, is accompanied by a decrease in the frequency of stretching vibrations and an increase in the frequency of bending vibrations [23]. The shorter the distance between the corresponding atoms (in our case, between the nitrogen atom of the amino group and the oxygen atom of the nitro group of the neighboring molecule), the larger the change in the vibrational energy [24]. Moreover, it is also known that the band of bound vibrations in amines is always broad [25]. Since the average distances between molecules in the solutions are considerably larger than those in the solid phase, the N–H vibrations of unbound molecules occur at low concentrations. As is known, the band of the N–H vibrations in the spectra of solutions of the primary and secondary amines often has a fine structure due to the intramolecular hydrogen bonds [25]. In our spectra (Fig. 3, curves 1, 3), the fine structure of the band associated with the N–H vibrations (the band splitting) can be associated with the intramolecular hydrogen bonds in the COANP molecule. An increase in the concentration of molecules in the solutions results in a decrease in the average distance between the molecules. As a consequence, the third (broad) band associated with the $\text{N-H}\cdots\text{O}$ bonds of the molecules separated by distances greater than those in the crystal appears in the spectrum of the COANP solution (Fig. 3, curves 2, 4).

It should be noted that, after the evaporation of the solvent, two narrow bands disappear almost immediately and the broad band initially occupies an intermediate position (Fig. 3, curve 5), and, only after a time, it is located at the same position as in the spectrum of the crystal (Fig. 3, curve 6).

Let us now determine the position of the absorption band attributed to the stretching vibrations of the NH groups. For this purpose, we analyze the evolution of the vibrational spectrum of the COANP compound in the other spectral range upon changing over from the solution to the solid phase (Fig. 4). The transmission spectrum of the COANP film on the AgCl window (Fig. 4, curve 2) was recorded almost immediately (within ten minutes) after the evaporation of the solution, whereas the spectrum of the COANP film on the poly(ethylene) window (Fig. 4, curve 3) was measured within two days after the evaporation of the solution. It can be seen from Fig. 4c that, in the frequency range $1510\text{--}1530 \text{ cm}^{-1}$, the changes in the spectrum are qualitatively similar to those observed for the stretching vibrations of the NH bonds (in the range $3300\text{--}3500 \text{ cm}^{-1}$): immediately after the evaporation of the solution, the band structure observed in the spectrum of the solution (curve 1) disappears and the band shifts initially from 1523 to 1529 cm^{-1} (curve 2) and then from 1529 to 1531 cm^{-1} (curve 3). Unlike the band of the stretching vibrations, the band under consideration shifts toward higher frequencies, which is characteristic of bending vibrations during the formation of hydrogen bonds. This evolution of the bands, their energy posi-

tion, and the large half-width of the band in the spectrum of the solid phase ($\Delta\nu = 33 \text{ cm}^{-1}$) give grounds to assign the bands observed at frequencies $\nu = 1510$ and 1523 cm^{-1} (in the spectrum of the solution) to the free vibrations of the N–H bonds and the band revealed at a frequency $\nu = 1531 \text{ cm}^{-1}$ (in the spectrum of the solid phase) to the bound vibrations of the N–H...O bonds.

According to Brown *et al.* [27], the spectra of nitro compounds exhibit intense absorption bands at approximately 1300 and 1600 cm^{-1} due to the symmetric and asymmetric stretching vibrations of the NO_2 groups, respectively. It can be seen from Fig. 2 that the bands observed at frequencies of 1336 and 1603 cm^{-1} are most intense in the spectrum of COANP. Indeed, the comparison of the spectra of the solutions at low (3 mg/ml) and high (60 mg/ml) concentrations in Fig. 2c clearly demonstrates that the intensities of these bands are considerably higher than those of the other bands in the spectra. The above bands are most intense in the spectrum of the solution at a low concentration, whereas many bands (which are well pronounced in the spectrum of the solution at a high concentration) are hardly seen in the spectrum of the solution at a low concentration. We believe that the bands observed at frequencies of 1336 and 1603 cm^{-1} correspond to the symmetric and asymmetric stretching vibrations of the NO_2 groups, respectively.

A close examination of the band observed at approximately 1600 cm^{-1} revealed that this band consists of two overlapping bands with maxima at 1603 and $\sim 1597 \text{ cm}^{-1}$. The latter of these bands is most likely attributed to the stretching vibrations of the pyridine rings. As is known [26], the spectra of pyridines involve bands of the skeletal vibrations, which are subdivided into the stretching vibrations (the corresponding bands are located in the range ~ 1300 – 1600 cm^{-1}), the in-plane bending vibrations (600 – 700 cm^{-1}), and the out-of-plane bending vibrations (300 – 700 cm^{-1}) of the rings. The vibrations of the CH groups of the rings are also separated into the stretching (in the range of 3000 cm^{-1}), in-plane bending (1000 – 1300 cm^{-1}), and out-of-plane bending (700 – 1000 cm^{-1}) vibrations. Furthermore, as follows from the data available in the literature, the intense band observed in the range 860 – 840 cm^{-1} due to the stretching vibrations of the C–N bonds is characteristic of aromatic nitro compounds. In our spectra, the frequencies of the band at $\nu = 817 \text{ cm}^{-1}$ in the spectrum of the solution (Fig. 4a, curve 1) and the corresponding band at $\nu = 831 \text{ cm}^{-1}$ in the spectrum of the solid phase (Fig. 4a, curve 3) are closest to the frequency range 860 – 840 cm^{-1} . However, the evolution of this band (its high-frequency shift and the appearance of new closely spaced bands upon changing over to the solid phase) suggests that, in our case, there occurs a coupling of vibrations. Possibly, this can be associated with the coupling of the stretching vibrations of the CN bonds and the out-of-plane bending vibrations of the CH

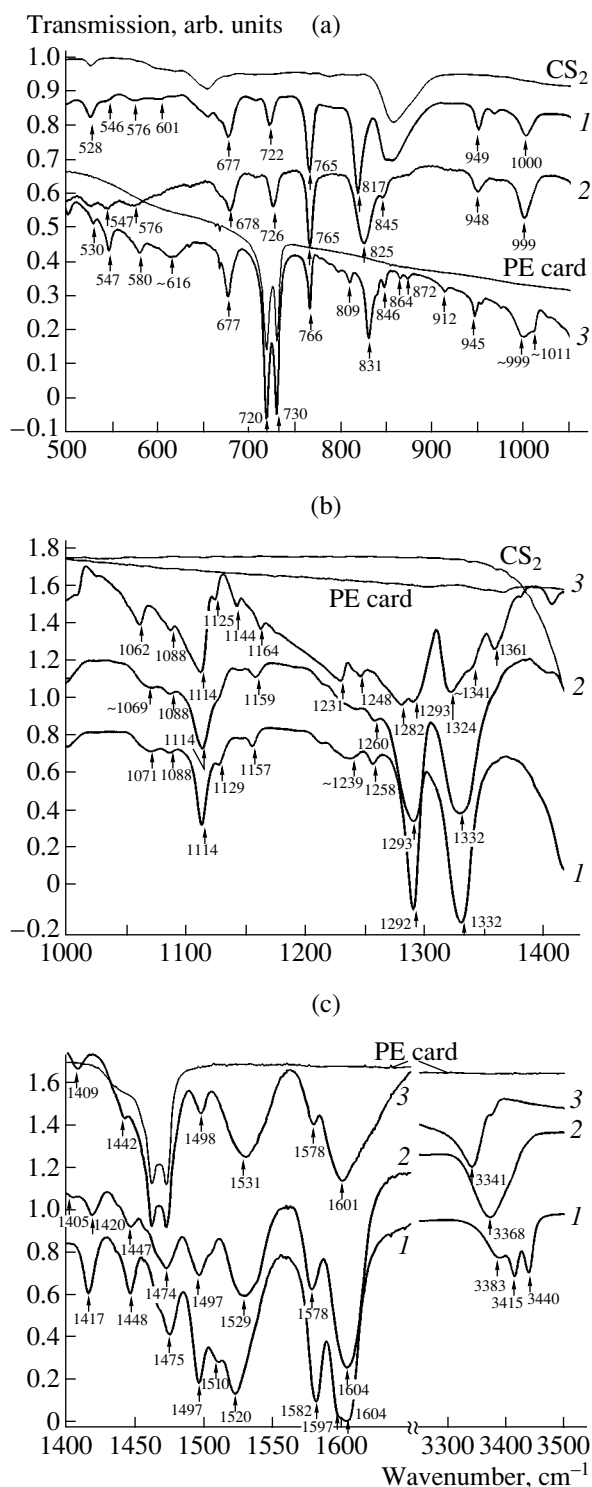


Fig. 4. Evolution of the IR transmission spectra of COANP upon changing over from the solution to the solid phase: (1) the COANP solutions in (a, b) CS_2 and (c) CCl_4 , (2) the COANP thin film deposited from the solution in CS_2 on the AgCl window within ten minutes after the deposition of the film, and (3) the COANP thin film deposited from the solution in CS_2 on the poly(ethylene) window within two days after the deposition of the film.

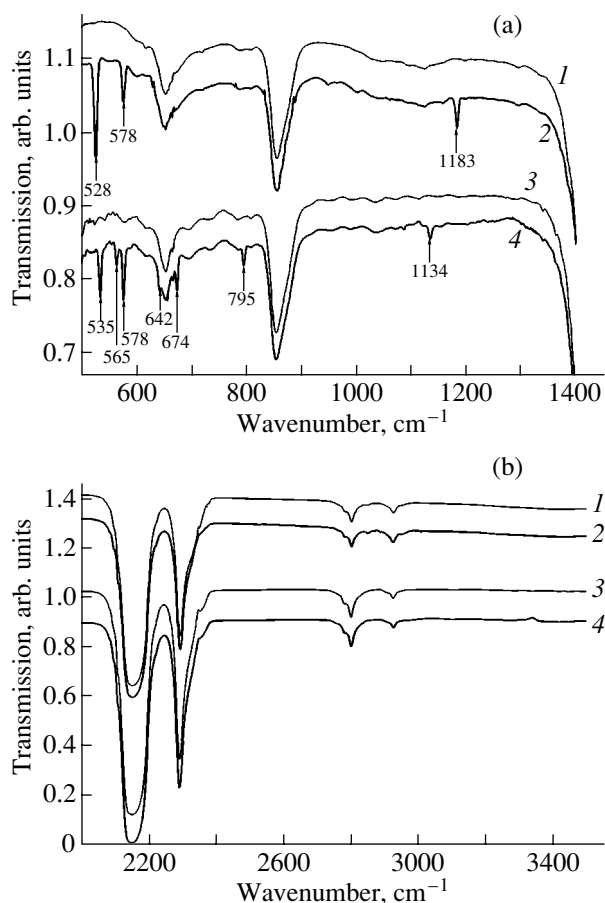


Fig. 5. IR transmission spectra of (1, 3) the CS₂ solvent, (2) the CS₂ solution of the C₆₀ fullerene (7 mg/ml), and (4) the CS₂ solution of the C₇₀ fullerene (7 mg/ml).

groups, whose energies also fall in the aforementioned range.

The nitrogen atom of the amino group forms two CN bonds with the carbon atoms of the cyclooctyl and pyridine rings. Their wide range of possible frequencies of vibrations [27] complicates assignment of the bands. The analysis of the evolution of the transmission spectra demonstrates that the frequencies $\nu = 1062 \text{ cm}^{-1}$ for vibrations of the CN bonds with carbon atoms of the cyclooctyl rings and $\nu = 1231 \text{ cm}^{-1}$ for vibrations of the CN bonds with carbon atoms of the pyridine rings are most probable.

The cyclooctyl fragment of the COANP molecule contains CH₂ groups whose vibrations can be easily identified. The frequencies of the intense bands at $\nu = 2853$ and 2925 cm^{-1} in the spectrum of the solution in CCl₄ (Fig. 2b) are very close to the frequencies of the symmetric and asymmetric stretching vibrations of the CH₂ groups in poly(ethylene). In the frequency ranges 720–730 and 1460–1475 cm⁻¹ corresponding to the rocking and deformation vibrations of poly(ethylene),

the spectra of the COANP solutions also contain absorption bands (Figs. 4a, 4b) that can be undeniably assigned to the bending vibrations of the CH₂ groups.

By considering the evolution of the other bands in the spectra shown in Fig. 4 and using the ranges of possible energies for the CH and skeletal vibrations in the pyridine ring [23, 26, 27], we determined the bands in the observed spectra that can be assigned to these vibrations with the highest probability.

The characteristic vibrations thus determined for the COANP molecule are presented in the table (column 5). A comparison of the data in columns 5 and 9 shows that our assignment differs significantly from the assignment proposed in [22].

3. ABSORPTION IN COANP SOLUTIONS WITH C₆₀ AND C₇₀ FULLERENES

Since the solubility of fullerenes in CCl₄ is relatively low (0.35 mg/ml for the C₆₀ fullerene [28]), this solvent is inappropriate for studying the vibrational spectra of COANP–fullerene solutions because of the low intensity of the bands in the spectra of the solutions at these concentrations. In this respect, the measurements were performed both with solutions in the CS₂ solvent (in which the solubility of fullerenes is approximately equal to 7 mg/ml [29]) and with films deposited from these solutions onto the AgCl window in the frequency range where the transparency of CS₂ is relatively low.

The transmission spectra of the C₆₀ and C₇₀ fullerene solutions in CS₂ and the spectra of the solvent recorded in the same cell are depicted in Fig. 5. The IR-active vibrations in fullerene molecules manifest themselves in the spectra of the solutions in the form of narrow lines, whose energies coincide with those determined earlier by Bethune *et al.* [30]: 528, 578, and 1183 cm⁻¹ for the C₆₀ fullerene and 535, 565, 678, 642, 674, 795, and 1134 cm⁻¹ for the C₇₀ fullerene. For comparison, Figs. 6a and 6b show the transmission spectra of the solutions of the C₆₀ fullerene, COANP, and the C₆₀ fullerene together with COANP, as well as the spectra of the solvent. The transmission spectra of the COANP and COANP–C₆₀ films deposited on the AgCl windows in the frequency range of intense absorption bands of the solvent are presented in Fig. 6c. Similar spectra for the C₇₀ fullerene are depicted in Fig. 7. The fullerene concentration in the solutions was maximum (approximately 7 mg/ml), and the COANP concentration was 20 mg/ml.

In the case when COANP and fullerene molecules chemically interact in solutions, we should expect changes primarily in the frequency range of the bands attributed to the vibrations of the NH groups and N–H...O bonds and then in the range of the bands assigned to the CN and ON vibrations (see frequencies in the table) or the appearance of new bands. As is seen from Figs. 6 and 7, the spectra of the COANP–fullerene sys-

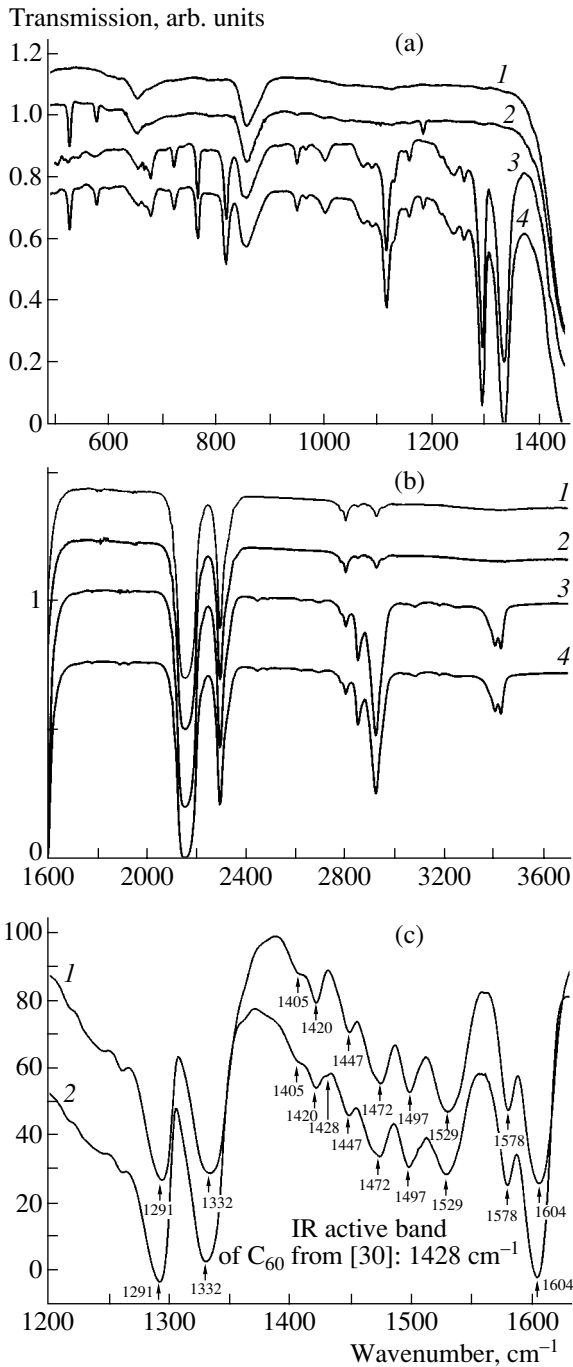


Fig. 6. (a, b) IR transmission spectra of (1) the CS₂ solvent and (2–4) CS₂ solutions of (2) C₆₀ fullerene (7 mg/ml), (3) COANP (20 mg/ml), and (4) C₆₀ fullerene (7 mg/ml) together with COANP (20 mg/ml). (c) IR transmission spectra of the thin films deposited from CS₂ solutions of (1) COANP (20 mg/ml) and (2) C₆₀ fullerene (7 mg/ml) together with COANP (20 mg/ml) on AgCl windows.

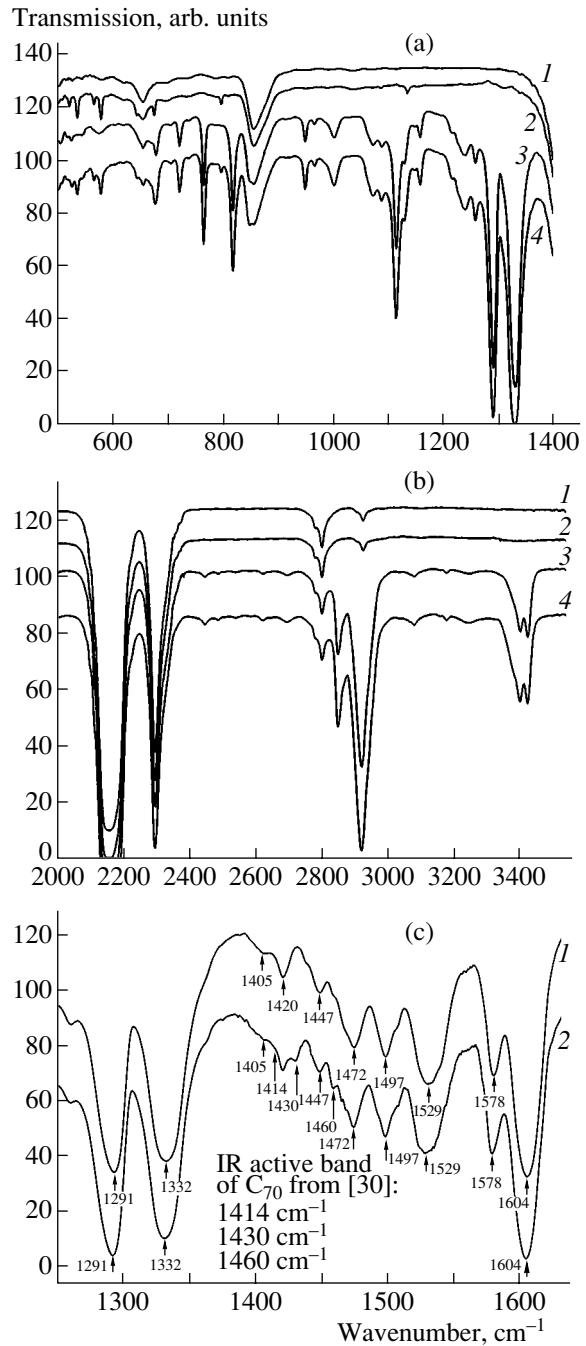


Fig. 7. (a, b) IR transmission spectra of (1) the CS₂ solvent and (2–4) CS₂ solutions of (2) C₇₀ fullerene (7 mg/ml), (3) COANP (20 mg/ml), and (4) C₇₀ fullerene (7 mg/ml) together with COANP (20 mg/ml). (c) IR transmission spectra of the thin films deposited from the CS₂ solutions of (1) COANP (20 mg/ml) and (2) C₇₀ fullerene (7 mg/ml) together with COANP (20 mg/ml) on AgCl windows.

tems can be considered a simple superposition of the spectra of the individual components.

The difference between the spectra of the COANP and COANP–fullerene systems in our experiments lies

only in the rate at which the band corresponding to the stretching vibrations of the N–H...O bonds shifts after the evaporation of the solvent from the position in the spectrum of the solution to the position in the spectrum

of the crystal (Fig. 3). Actually, the films were deposited on poly(ethylene) windows from the solution of pure COANP and the solutions of COANP with fullerenes in weight ratios $C_{60} : \text{COANP} = 1 : 10, 1 : 5,$ and $2 : 5$. The spectra of these samples were recorded immediately after the deposition and within one, four, and ten days after the deposition, respectively. It was found that the initial (i.e., after deposition) positions of the band attributed to the vibrations of the N–H...O bonds coincide for all the samples ($\nu_0 = 3368 \text{ cm}^{-1}$). Moreover, the final position (after ten days) is also identical ($\nu_1 = 3340 \text{ cm}^{-1}$) for all the samples studied. However, within one and four days after the deposition, the band is observed at frequencies intermediate between ν_0 and ν_1 . In this case, the higher the fullerene content, the larger the difference between the frequency ν and the frequency ν_1 of the band in the spectrum of the crystal. This retardation of the crystallization rate in the presence of fullerenes can be explained by steric factors: the higher the fullerene concentration, the longer the time it takes for COANP molecules to approach one another closely enough to form a crystal lattice.

4. POSSIBLE ORIGIN OF THE OBSERVED INDEPENDENCE OF OPTICAL CONTRIBUTIONS

The results of the investigation into the IR transmission spectra of the solutions and thin films of COANP and fullerenes allow the conclusion that no chemical interaction between the components with the formation of chemical bonds or charge-transfer molecular complexes occurs in the COANP–fullerene system under the experimental conditions used. This circumstance, which takes place even though there exists a considerably high probability of COANP and fullerene (C_{60}, C_{70}) molecules colliding under conditions providing a random distribution, seems rather unusual. A possible explanation could be a substantial deviation from a random distribution, in particular, due to clustering effects.

Indeed, the absence of the influence of fullerene (C_{60}, C_{70}) molecules on the optical spectra of COANP molecules can be primarily associated with the clustering of more mobile fullerene (C_{60}, C_{70}) molecules around single COANP molecules. In this case, the latter molecules play the role of nuclei of these clusters. It is assumed that, in the region of a COANP nucleus, the $C_{60} (C_{70})$ molecules move as though around the core of a liquid-crystal cluster composed of $C_{60} (C_{70})$ molecules but do not interact with this COANP molecule. The latter circumstance stems both from a weak hybridization of the electronic states of the fullerene and COANP molecules and from the effect of the potential barrier to the $C_{60} (C_{70}) \rightleftharpoons \text{COANP}$ charge transfer.

However, in the cluster under consideration, the $C_{60} (C_{70})$ molecules are attracted to each other and to the COANP core molecule. This effect is caused by two

factors. First, the COANP molecule has a large electric dipole moment. Second, the $C_{60} (C_{70})$ molecules are strongly polarizable due to the closely spaced energy levels HOMO and LUMO. As a consequence, the $C_{60} (C_{70})$ molecules located close to the core dipole molecule COANP turn out to be strongly polarized and are attracted to the core. This results in the formation of a potential well for the $C_{60} (C_{70})$ molecules in the vicinity of the COANP molecule. Furthermore, the electric dipole moments induced in the $C_{60} (C_{70})$ molecules are oriented so that there arises mutual attraction between them. Consequently, the aforementioned potential well for the $C_{60} (C_{70})$ molecules in the vicinity of the COANP core molecule becomes deeper due to the cooperative effect in the system of the $C_{60} (C_{70})$ molecules clustering around the COANP molecule. Thus, we assume that the structure of the COANP– $C_{60} (C_{70})$ fullerene solution is characterized by “nonrigid” dynamic clustering of the $C_{60} (C_{70})$ molecules around the core dipole molecule COANP. This situation can correspond to the formation of small-sized liquid-crystal clusters consisting of the $C_{60} (C_{70})$ molecules arranged around the COANP molecule. It is this clustering of the $C_{60} (C_{70})$ molecules with induced electric dipole moments around the COANP molecules (having an electric dipole) that is responsible (on average over the sample) for the substantial weakening of the effect of $C_{60} (C_{70})$ molecules on the physical (primarily, optical) properties of the COANP molecules. Actually, the $C_{60} (C_{70})$ molecules appear to be concentrated in the regions of cluster formation around individual core molecules COANP and have an effect only on the COANP molecules that are located in these regions and make up only an insignificant fraction of the total COANP molecules.

ACKNOWLEDGMENTS

We would like to thank A. Cardona and S. Ramos (Department of Chemistry, University of Puerto-Rico, Mayaguez, Puerto-Rico, United States) for their assistance in measuring the spectra of the solutions used in this study.

This work was performed at the Alabama Agricultural and Mechanical University (Normal, Alabama, United States) and the University of Puerto-Rico (Mayaguez, Puerto-Rico, United States) and was supported by the NASA-funded Alliance for Nonlinear Optics and the grant AFOSR F49620-01-1-0561.

REFERENCES

1. Ch. Bosshard, K. Sutter, P. Gunter, and G. Chapuis, *J. Opt. Soc. Am. B* **6**, 721 (1989).
2. M. Eich, H. Looser, Do Y. Yoon, R. Twieg, G. Bjorklund, and J. C. Baumert, *J. Opt. Soc. Am. B* **6**, 1590 (1989).
3. A. Leyderman and Y. Cui, *Opt. Lett.* **23**, 909 (1998).

4. R. Quantero-Torres and M. Thakur, *Opt. Lett.* **19** (2), 87 (1994).
5. S. S. Sarkisov, E. I. Radovanova, B. H. Peterson, A. Leyderman, M. Curley, and P. A. Fleitz, *J. Nonlinear Opt. Phys. Mater.* **13** (1), 113 (2004).
6. J. F. Nicoud and R. J. Twieg, in *Nonlinear Optical Properties of Organic Molecules and Crystals*, Ed. by D. S. Chemla and J. Zyss (Academic, Orlando, 1987), p. 229.
7. J. Hulliger, B. Brezina, and M. Ehrensperger, *J. Cryst. Growth* **106**, 605 (1990).
8. B. Brezina and J. Hulliger, *Cryst. Res. Technol.* **26** (12), 155 (1991).
9. J. Hulliger, K. Sutter, Y. Schumacher, B. Brezina, and V. A. Ivanshin, *J. Cryst. Growth* **128**, 886 (1993).
10. J. Hulliger, Y. Schumacher, K. Sutter, B. Brezina, and H. Amman, *Mater. Res. Bull.* **26**, 887 (1991).
11. M. Yu. Antipin, T. V. Timofeeva, R. O. Clark, V. N. Nesterov, F. M. Dolgushin, J. Wu, and A. Leyderman, *J. Mater. Chem.* **11**, 351 (2001).
12. Lee W. Tutt and Alan Kost, *Nature (London)* **335**, 225 (1992).
13. S. Couris, E. Koudoumas, A. A. Ruth, and S. Leach, *J. Phys. B: At., Mol. Opt. Phys.* **28**, 4537 (1995).
14. V. P. Belousov, I. M. Belousova, V. G. Bespalov, V. P. Budtov, V. M. Volynkin, V. A. Grigor'ev, O. B. Danilov, A. P. Zhevlakov, A. G. Kalintsev, A. N. Ponomarev, S. T. Tul'skiĭ, and E. Yu. Yutanova, *Opt. Zh.* **64** (9), 82 (1997).
15. V. P. Belousov, I. M. Belousova, V. P. Budtov, O. B. Danilov, A. G. Kalintsev, and A. A. Mak, *Opt. Zh.* **64** (12), 3 (1997).
16. S.-X. Qu, H. Zheng, A. Barrientos, and A. Leyderman, *Phys. Lett. A* **268**, 360 (2000).
17. A. Leyderman and S.-X. Qu, *Phys. Rev. E: Stat. Phys., Plasmas, Fluids, Relat. Interdiscip. Top.* **62**, 3293 (2000).
18. N. V. Kamanina, L. N. Kaporskiĭ, A. Leyderman, and A. Barrientos, *Pis'ma Zh. Tekh. Fiz.* **26** (7), 24 (2000) [*Tech. Phys. Lett.* **26**, 279 (2000)].
19. F. Wudl, A. Hirsh, K.S. Khemani, T. Suzuki, P.-M. Allemand, A. Koch, H. Eskert, G. Sradnov, and H. M. Webb, in *Fullerenes: Synthesis, Properties, and Chemistry of Large Carbon Clusters*, Ed. by G. S. Hammond and V. J. Kuck (American Chemical Society, Washington, 1992), p. 161.
20. Y. Chen, Z.-E. Huang, R.-F. Cai, and B.-C. Yu, *Eur. Polym. J.* **34**, 137 (1998).
21. L. Dai, *J. Macromol. Sci., Rev. Macromol. Chem. C* **39**, 273 (1999).
22. J. Petzelt, J. Hrabovska, S. Kamba, I. Gregora, V. Vorliceck, K. Kokesova, Brezina, and J. Hulliger, *Nonlinear Opt.* **7**, 7 (1994).
23. L. Bellami, *The Infrared Spectra of Complex Molecules* (Wiley, New York, 1961; Inostrannaya Literatura, Moscow, 1963).
24. L. M. Babkov, G. A. Puchkovskaya, S. P. Makarenko, and T. A. Gavrilko, *Spectroscopy of Molecular Crystals with Hydrogen Bonds* (Naukova Dumka, Kiev, 1989), p. 14 [in Russian].
25. A. Gordon and R. Ford, *The Chemist's Companion: A Handbook of Practical Data, Techniques, and References* (Wiley, New York, 1972; Mir, Moscow, 1976).
26. A. R. Katritskiĭ, *Physical Methods in Chemistry of Heterocyclic Compounds* (Khimiya, Moscow, 1966), p. 576 [in Russian].
27. D. Brown, A. Floyd, and M. Sainsburi, *Organic Spectroscopy* (Wiley, New York, 1988; Mir, Moscow, 1992).
28. A. V. Eletskiĭ and B. M. Smirnov, *Usp. Fiz. Nauk* **165** (9), 977 (1995) [*Phys. Usp.* **38**, 935 (1995)].
29. M. V. Korobov and A. L. Smith, in *Fullerenes (Chemistry, Physics, and Technology)* Ed. by K. M. Kadish and R. S. Ruoff (Wiley & Sons, New York, 2000), p. 54.
30. D. S. Bethune, G. Meijer, W. C. Tang, H. J. Rosen, W. G. Golden, H. Seki, Ch. A. Brown, and M. S. de Vries, *Chem. Phys. Lett.* **179**, 181 (1991).

Translated by O. Borovik-Romanova

FULLERENES AND ATOMIC CLUSTERS

Optimization of the Calculations of the Electronic Structure of Carbon Nanotubes

A. S. Fedorov and P. B. Sorokin

Kirensky Institute of Physics, Siberian Division, Russian Academy of Sciences,
Akademgorodok, Krasnoyarsk, 660036 Russia

e-mail: alex99@akadem.ru

Received November 22, 2004

Abstract—A method is proposed for calculating the electronic structure and physical properties (in particular, Young's modulus) of nanotubes, including single-walled carbon nanotubes. This method explicitly accounts for the periodic boundary conditions for the geometric structure of nanotubes and makes it possible to decrease considerably (by a factor of 10 – 10^3) the time needed to calculate the electronic structure with minimum error. In essence, the proposed method consists in changing the geometry of the structure by partitioning nanotubes into sectors with the introduction of the appropriate boundary conditions. As a result, it becomes possible to reduce substantially the size of the unit cell of the nanotube in two dimensions, so that the number of atoms in a new unit cell of the modified nanotube is smaller than the number of atoms in the initial unit cell by a factor equal to an integral number. A decrease in the unit cell size and the corresponding decrease in the number of atoms provide a means for drastically reducing the computational time, which, in turn, substantially decreases with an increase in the degree of partition, especially for nanotubes with large diameters. The results of the calculations performed for carbon and non-carbon (boron nitride) nanotubes demonstrate that the electronic structures, densities of states, and Young's moduli determined within the proposed approach differ insignificantly from those obtained by conventional computational methods. © 2005 Pleiades Publishing, Inc.

1. INTRODUCTION

The experimental discovery of carbon nanotubes in 1991 [1] has opened up new fields in applied and fundamental physics. Owing to their sizes (the transverse size is of the order of nanometers) and one-dimensional structure, carbon nanotubes exhibit unique mechanical, chemical, and electrical properties [2] and, already at present, have found wide applications in many areas of engineering. For example, since the invention of field-effect transistors based on carbon nanotubes in 1998, these devices have been fabricated in many laboratories and subjected to experimental tests [3, 4]. The unique combination of mechanical, elastic, and electrical (conductivity) properties of carbon nanotubes has allowed their use in tunneling and atomic-force microscopy. High hopes have been pinned on the design of ultrastrong fibers from carbon nanotubes (in particular, for practical implementation of the space elevator idea). Any technical application should be based on a detailed theoretical analysis. In this respect, theoretical investigations into the electrical and mechanical properties of nanotubes, the formation of defects in nanotube structures, and nanotube functionalization (i.e., the formation of chemical bonds between nanotubes and modifying molecules) are very important problems. Unfortunately, theoretical quantum-chemical investigations of nanotubes involve rather time-consuming procedures, primarily, because of the long time required for calculating the electronic structure of nanotubes with large

diameters (which are most frequently encountered in experiments). For example, a unit cell of typical single-walled carbon nanotubes (SWCNTs), as a rule, contains from 10^1 to 10^2 atoms. However, in order to elucidate how defects of different types (adsorbed molecules, vacancies) affect the properties of single-walled carbon nanotubes, it is necessary to examine several unit cells; in this case, the minimum length of the region of the single-walled carbon nanotube under consideration is approximately equal to 10 Å. For this length, it is possible to avoid the undesirable effect exerted by defects in adjacent unit cells on each other; i.e., these defects are assumed to be isolated. Therefore, the study of any defects inside single-walled carbon nanotubes necessitates analysis of the structures in which the number of atoms ($\sim 10^2$ – 10^3) is one order of magnitude larger than that contained in the unit cell. The calculation of the electronic structure of these objects involves an extremely cumbersome procedure for any quantum-chemical (especially, *ab initio*) method, even for those that explicitly account for the periodic Bloch conditions, such as the methods based on the muffin-tin approximation (LMTO, FPLMTO, LAPW, etc.), the pseudopotential formalism, and other approaches. The computational time needed to calculate the electronic structure with these methods is proportional to N^2 – N^4 (Hartree–Fock LCAO method), where N is the number of atoms in the unit cell in the structure under consideration. According to [5], one of

the fastest computational algorithms is provided by the pseudopotential method operating with the Vanderbilt ultrasoft pseudopotential [6], the plane-wave basis set, and the iterative diagonalization of the Hamiltonian in the framework of the density functional theory. In [5], it was demonstrated that, for systems containing up to 1000 electrons, the computational time of the algorithm is proportional to $\sim N^2$. However, we can assume that, even in the calculations performed with the above method for nanotubes having large diameters, the considerable decrease in the size of the computational cell and in the number of atoms in it is of crucial importance in the case when this does not lead to substantial errors due to the transformation of the cell.

2. COMPUTATIONAL TECHNIQUE

In this paper, we propose a technique that makes it possible to reduce considerably the time needed to calculate the electronic structure of nanotubes. This approximation is based on a change in the nanotube geometry and allows one to decrease substantially the size of the unit cell of the nanotube and the number of atoms in the cell. By assuming that the method is used to perform calculations in a plane-wave basis set in which the wave function is calculated in different spatial regions, including those with an almost zero value, the proposed algorithm enables one to avoid calculations of the electron density in the vicinity of the nanotube axis where the electron density is virtually zero ($\rho \approx 0$) and, thus, to additionally increase the computational speed. The applicability of the method is illustrated by calculating a number of single-walled carbon nanotubes and a (10, 10) single-walled boron nitride nanotube.

The key idea underlying this method is that the electronic structures of a single-walled carbon nanotube and a graphite sheet are similar to each other. Only for single-walled carbon nanotubes with very small diameters ($D \leq 6 \text{ \AA}$) are the electronic structures of graphite and single-walled carbon nanotubes somewhat different. A comparison of the geometric structures of the graphite sheet and the single-walled carbon nanotube shows that the fundamental difference between them lies in the boundary conditions. The graphite sheet is treated as an infinite plane, and the boundary conditions for the electron wave functions are specified using the Bloch theorem. The electron wave function depends on the two-dimensional wave vector $k = \{k_x, k_y\}$ aligned parallel to the graphite sheet. For a single-walled carbon nanotube, the boundary conditions are similar to those for graphite only along the nanotube axis (the Z axis).

Let us consider the wave vector k_x along the rolled graphite sheet perpendicular to the nanotube axis. It is evident that, in this case, the wave vector changes discretely as a result of the periodicity when tracing around the circumference of the nanotube.

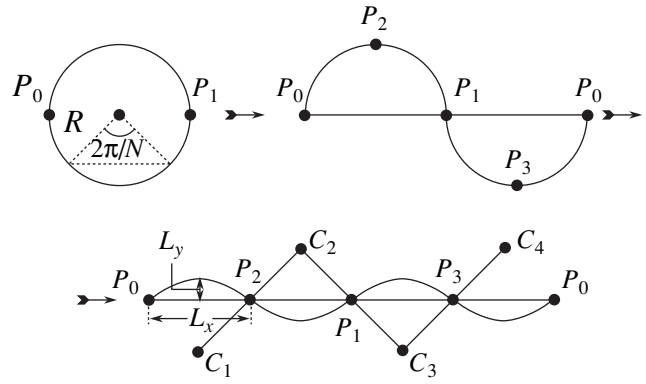


Fig. 1. Sequential transformation of a nanotube sector into a corrugated surface.

The symmetry group of the (n, n) and $(n, 0)$ nanotubes contains the rotation axes [7, 8]:

$$\begin{cases} D_{nh} : N = 2m \\ D_{nd} : n = 2m + 1, \quad m = 1, 2, \dots \end{cases}$$

Hence, the nanotube can be separated into n equivalent sectors [9].

Chiral nanotubes of the (n, m) type are characterized by the symmetry group $G = C_d \otimes C'_{Nd/\Omega}$, where $C_d = \{C_d, C_d^2, \dots, C_d^d = E\}$ and d is determined by the following conditions:

$$\begin{cases} mp - nq = d \\ q < m/d \\ p < n/d. \end{cases}$$

Owing to the screw axes, the chiral nanotube can be separated into d equivalent sectors with the corresponding increase in their period along the Z axis.

The periodicity of the nanotube geometry enables us to change the geometry of the calculated structure by separating the structure of the nanotube into equivalent sectors and reflecting each subsequent sector with respect to the plane tangential to the adjacent sectors along the line of their contact. Figure 1 illustrates this sequential transformation of the single-walled carbon nanotube into corrugated surfaces consisting of two and then four sectors with the exact same curvature as that of the initial geometric structure of the single-walled carbon nanotube. The projections of the nanotube and two corrugated surfaces onto the plane perpendicular to the nanotube axis are also depicted in Fig. 1. The $C_i - C_{i+1}$ lines are perpendicular to the reflection planes of the sectors whose reflection provides the formation of the corrugated surface. The points P_i are the projections of the contact lines of sequential sectors. At the first stage of the nanotube transformation, the initial single-

walled carbon nanotube is transformed into the simplest corrugated surface by reflecting the half-sector of the nanotube with respect to the plane passing through the line of contact (with the projection P_1). Then, this structure is transformed into the next corrugated surface by reflecting the previous corrugated surface with respect to two planes (passing through the lines with the projections P_2 and P_3). The partition of the corrugated surfaces can be repeated. In this case, if the number of reflection planes is equal to M , the number N of equivalent sectors of the corresponding corrugated surface formed from the nanotube structure is $N = M + 1$.

Since the single-walled carbon nanotube is partitioned into a number of periodically repeated sectors located along the X axis, it is possible to calculate the electronic structure only for one sector of the corrugated surface. An increase in the degree of partition of the nanotube leads to a decrease in the unit cell of the corrugated surface. This results in an increase in the computational speed. Proper allowance must be made for the fact that the periodicity of the corrugated surface along the X axis leads to a dependence of the electron wave function $\psi^v(r)$ (where $v = \{k_x, k_z, n\}$ and n is the number of the band) on the wave vector component k_x . The wave vector k of the nanotube has only one component (along the nanotube axis), whereas the wave vector k of the corrugated surface has two components (k_x, k_z). Note that the inclusion of the boundary conditions (periodicity) for the wave function when tracing around the circumference of the nanotube leads to the sole possible set $k_{xi} = \{2\pi i/L_x N, i = 0 \dots (N - 1)\}$ (where L_x is the period of the corrugated surface along the x direction).

The structure of the corrugated surface differs from the structure of the single-walled carbon nanotube only in that the curvature of the corrugated surface changes jumpwise (only in sign) along a small number of lines with the projections P_i . Therefore, it can be expected that any wave eigenfunction $\psi^v(r)$ ($v = \{k_x, k_z, n\}$) of an electron traveling along the corrugated surface should be similar to a wave function of an electron traveling along the surface corresponding to the single-walled carbon nanotube.

It should be noted that the number of atoms in the unit cell of the corrugated surface is smaller than the number of atoms in the unit cell of the single-walled carbon nanotube by a factor of N . In this case, an increase in the set of possible values of the quasi-momentum k_x by a factor of N restores the total number of possible electron eigenstates in the nanotube.

It is interesting to estimate the gain in the computational speed that can be achieved with the use of the proposed approximation as compared to the conventional calculation of nanotubes. We assume that, in the case of single-walled carbon nanotubes with large radii R , the chosen unit cell size determined by the periods L_x and L_y is considerably larger than the vacuum gap between the adjacent nanotubes. Under this assumption

with due regard for the schematic diagram depicted in Fig. 1, it is easy to derive the relationships $L_x = 2R \sin(\pi/N)$ and $L_y = R(1 - \cos(\pi/N))$. Taking into account that, in the proposed method, the computational speed V is proportional to $O(N_{\text{at}}^{-2})$ (where N_{at} is the number of atoms in the unit cell) and the number of atoms in the unit cell depends linearly on the unit cell volume, we obtain the formula

$$\begin{aligned} \frac{V_{\text{tube}}}{V_{\text{CSS}}} &\sim \left(\frac{\Omega_{\text{tube}}}{\Omega_{\text{CSS}}} \right)^2 = \left(\frac{(2R)^2 L_z}{L_x L_y L_z} \right)^2 \\ &= \left(\frac{2}{\sin(\pi/N)(1 - \cos(\pi/N))} \right)^2. \end{aligned}$$

For $N \gg \pi$, the computational speed is proportional to $V_{\text{tube}}/V_{\text{CSS}} \sim 2N/\pi$. The increase in the number of wave vector components k_x in the corrugated surface is compensated for by the decrease in the number of atoms in its unit cell.

3. THE ORIGIN OF POSSIBLE ERRORS OF THE METHOD

It is very important to reveal the origin of possible errors in the calculation of the electronic structure after the transformation of the carbon nanotube into a corrugated surface. It is clear that possible errors are associated with the change in the curvature of the structure under consideration. It is this curvature of the rolled graphite sheet that is responsible for the small differences between the electronic structures of the nanotube and the graphite sheet. The analysis of the corrugated surface in the cylindrical coordinates relative to the rotation axes (see the projections of the C_i axes in Fig. 1) demonstrates that the first derivative of the coordinates of the point on the corrugated surface with respect to the rotation angle is continuous and that the curvature determined by the second derivative of the coordinates vanishes along the lines whose projections in Fig. 1 are represented by the points P_i . At other points of the corrugated surface, the curvature coincides in magnitude with the curvature of the single-walled carbon nanotube. To put it differently, the transformation of the geometric structure of the nanotube into the corrugated surface in terms of the solutions to the Schrödinger equation is a correct procedure at all points except for the points of the contact lines of the sectors (with the projections P_i), which simultaneously belong to two different sectors of the corrugated surface and in which the curvature vanishes.

The origin of the errors can be revealed directly from analyzing the differential Schrödinger equation

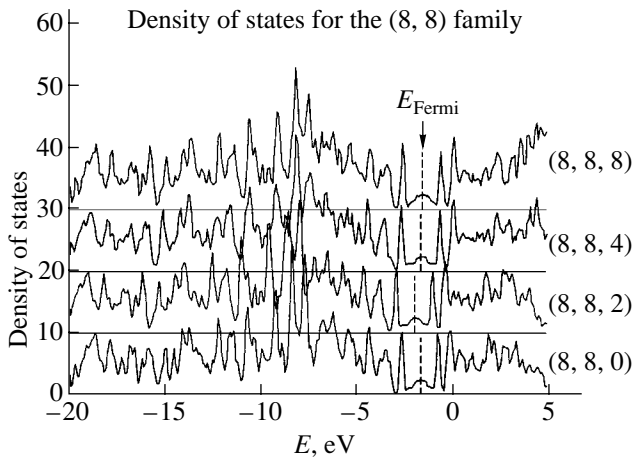


Fig. 2. Densities of states for the $(8, 8, i)$ structures at $i = \{0, 2, 4, 8\}$.

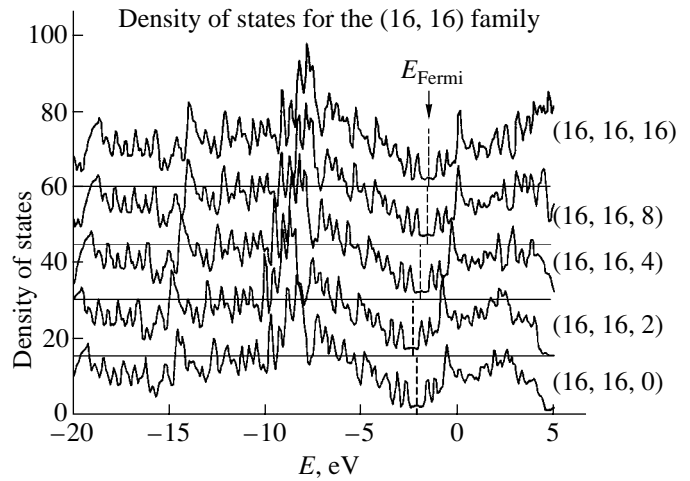


Fig. 3. Densities of states for the $(16, 16, i)$ structures at $i = \{0, 2, 4, 8, 16\}$.

by writing the Laplacian in the cylindrical coordinates:

$$-\left[\frac{\nabla^2}{2m} + \hat{V}(r)\right]\Psi^v(r) = \varepsilon^v\Psi^v(r), \quad v = \{k, n\}, \quad (1)$$

$$\nabla^2 = \frac{\partial^2}{\partial \rho^2} + \frac{1}{\rho}\frac{\partial}{\partial \rho} + \frac{1}{\rho^2}\frac{\partial^2}{\partial \phi^2} + \frac{\partial^2}{\partial z^2}.$$

Now, we take into account that $C_3P_1 = -C_2P_1$ and that the first and second derivatives in the Laplacian have the difference approximations $\partial y_i/\partial \rho \approx 1/2h(-y_{i-1} + y_{i+1})$ and $\partial^2 y_i/\partial \rho^2 \approx (1/h^2)(16y_{i-1} - 2y_i + y_{i+1})$. Then, it becomes clear that all the terms in the Laplacian are continuous functions of the arguments (ρ, ϕ) , except for the term $(1/\rho)\partial/\partial \rho$ that changes the sign along the contact lines P_i . This term is the sole factor responsible for the possible change in the Laplacian upon transformation of the single-walled carbon nanotube into the corrugated surface. Fortunately, it follows from relationship (1) that this term decreases in proportion to the increase in the nanotube radius. Consequently, when the diameter of the initial nanotube is sufficiently large and the number of points P_i is small, we can expect that the electronic structure of the corrugated surface will virtually coincide with the electronic structure of the single-walled carbon nanotube.

4. CALCULATIONS OF THE ELECTRONIC STRUCTURE OF CORRUGATED SURFACES

As an example, we calculated the electronic structures of single-walled carbon nanotubes with different diameters and chiralities and also the electronic structures of the corresponding corrugated surfaces. The band structures, densities of states, and binding energies were calculated for the $(20, 0)$ zigzag single-walled carbon nanotube (according to the notations proposed

in [10]) and the $(8, 8)$ and $(16, 16)$ armchair single-walled carbon nanotubes.

All the calculations were performed with the Vienna Ab Initio Simulation Package (VASP) [5, 11, 12]. This program package makes it possible to perform *ab initio* calculations based on the pseudopotential method and a plane-wave basis set in the framework of the local density functional formalism [13, 14]. The use of the Vanderbilt pseudopotentials in the calculations led to a substantial decrease (to 287 eV) in the maximum kinetic energy E_{cutoff} of the plane-wave basis set without a significant loss of accuracy. The electron–electron exchange and correlation interactions were described by the functional density theory method with the Ceperley–Alder exchange–correlation functional [15], which has worked well in similar calculations.

All the geometric structures of the nanotubes and the corresponding corrugated surfaces were constructed on the basis of the graphite sheet (with an interatomic distance of 1.42 Å) curved in a specific manner. The densities of states for all the structures under investigation are shown in Figs. 2–4. In these figures, the corrugated surfaces are designated by the indices (i, j, k) , where k is the number of sectors into which the nanotube is partitioned upon transformation into a corrugated surface and (i, j) are the chirality indices. For example, the designation $(8, 8, 0)$ corresponds to the initial $(8, 8)$ single-walled carbon nanotube and the designation $(8, 8, 4)$ refers to the corrugated surface obtained by partitioning the initial nanotube into four sectors. It can be seen from Figs. 2–4 that the densities of states for all the corrugated surfaces almost coincide with the density of states for the initial nanotube. This indicates an insignificant contribution from a finite number of lines in which the curvature of the geometric structures of the single-walled carbon nanotube and the corrugated surfaces differ from each other.

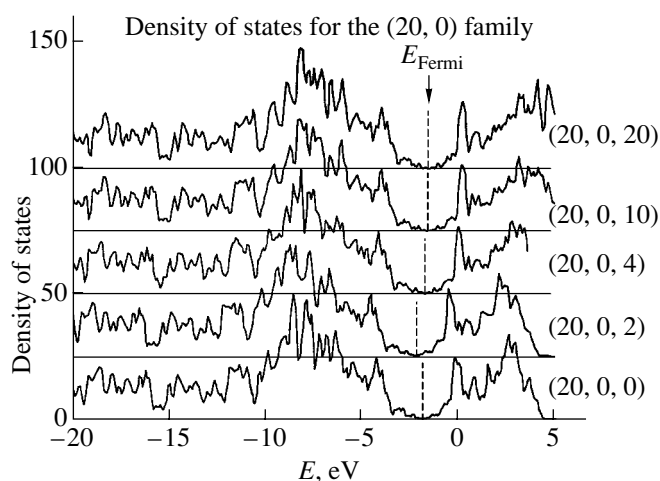


Fig. 4. Densities of states for the $(20, 0, i)$ structures at $i = \{0, 2, 4, 10, 20\}$.

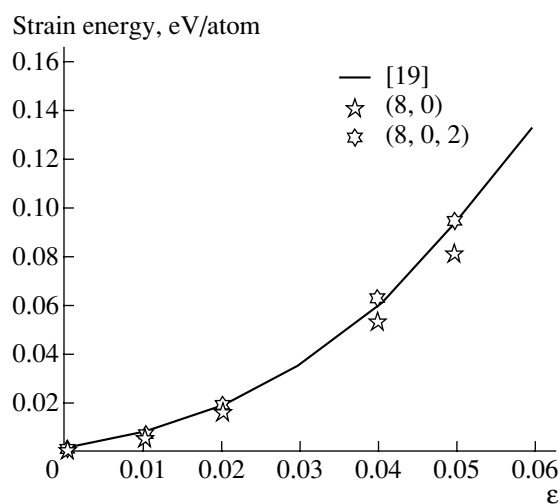


Fig. 5. Dependences of the strain energy on the strain for the $(8, 0)$ single-walled carbon nanotube and the $(8, 0, 2)$ corrugated surface.

Moreover, we investigated how the optimization of the geometry structure affects the electronic structures of all the objects. For this purpose, the electronic characteristics were calculated for the structures with optimized and unoptimized geometries. All the degrees of freedom of atomic coordinates could be varied in the course of optimization. The optimization was carried out by the conjugate-gradient method. The structure was treated as optimized when the magnitude of the force acting on any atom was less than 0.02 eV/\AA . The calculations demonstrated that the densities of states for the optimized structures are in close agreement with the densities of states for the corresponding unoptimized structures. For this reason, these densities of states are not presented in the figures.

The total binding energies (per atom) for all the structures (optimized and unoptimized) are listed in Table 1. The computational times of one iteration (over all k points), the numbers of k points, and the numbers of plane waves (averaged over the k points) are also presented in Table 1. The calculations were carried out on a PIII-860 personal computer. As can be seen from Table 1, the binding energies for the corrugated surfaces are very close to the binding energies for the corresponding single-walled carbon nanotubes. Note that the difference between these energies increases with an increase in the degree of partition of the nanotubes. It can also be seen from these data that, in all cases, the binding energy depends very weakly on the optimization of the structure.

5. APPLICATION OF THE CORRUGATED-SURFACE METHOD FOR CALCULATING THE ELASTIC PROPERTIES OF NANOTUBES

The proposed method was also used to calculate the elastic properties of carbon and non-carbon structures. The Young's moduli Y were calculated for the $(6, 6)$ and $(10, 10)$ single-walled carbon nanotubes. The Young's moduli of the nanotubes, as a rule, have been calculated from the standard formula $Y = (1/V_0)(\partial^2 E/\partial \epsilon^2)$, where $V_0 = 2\pi LR\delta R$ is the volume of the unstrained structure and δR is the thickness of the nanotube wall. However, there is arbitrariness in choosing the thickness of the nanotube wall δR . For example, Lu [16] determined the thickness of the nanotube wall δR as the distance between the graphite sheets, whereas Yakobson *et al.* [17], reasoning from the atomic radius of carbon, assumed that the thickness δR is equal to 0.66 \AA . This problem was solved by Hernandez *et al.* [18], who introduced the modified Young's modulus $Y_s = (1/S_0)(\partial^2 E/\partial \epsilon^2)$, where $S_0 = 2\pi LR$. It is this relationship that was used in the present work.

The calculated Young's moduli Y_s are given in Table 2. It can be seen from this table that, in the case of the $(6, 6)$ single-walled carbon nanotube with a small diameter, the error in the calculation of the Young's moduli Y_s for the corrugated structure is rather large. However, as the nanotube diameter increases, the accuracy of the calculation increases in accordance with the predictions made in Section 2. In addition to the calculations of the elastic properties of the armchair carbon nanotubes, we calculated the strain energy (i.e., the energy associated with the bending of the graphite sheet upon formation of the nanotube) for the $(8, 0)$ zigzag single-walled carbon nanotube and the corresponding $(8, 0, 2)$ corrugated surface. The results obtained are presented in Fig. 5 (the dependence shown by the solid line is taken from [19]).

It can be seen from Fig. 5 that the strain energies of the initial single-walled carbon nanotube and the corresponding corrugated surface are very close to each other (at moderate strains). This indicates that the pro-

Table 1. Binding energies per atom (eV) for the (8, 8, i), (16, 16, i), and (20, 0, i) structures; numbers of k points; numbers of plane waves; and times of one iteration for the calculation of the (20, 0, i) structures

(8, 8, i) $i = 0, 2, 4, 8$	9.340	9.356	9.375	9.390	–
(optimized/unoptimized)	9.331	9.340	9.347	9.364	–
(16, 16, i) $i = 0, 2, 4, 8, 16$	9.390	9.392	9.393	9.406	9.405
(optimized/unoptimized)	9.381	9.348	9.381	9.385	9.389
(20, 0, i) $i = 0, 2, 4, 10, 20$	9.304	9.308	9.318	9.336	9.336
(optimized/unoptimized)	9.304	9.307	9.310	9.321	9.331
Number of k points	14	28	42	84	154
Number of plane waves	26290	15216	6290	2350	1158
Time of one iteration (s)	88517	40037	12340	2500	890

Table 2. Young's moduli Y_S (TPa nm) calculated for the carbon and non-carbon structures

SWCNT	Y_S	SWCNT	Y_S	SWCNT	Y_S	BN nanotube	Y_S
(6, 6)	0.463	(8, 0)	0.437	(10, 10)	0.423	(10, 10)	0.316
(6, 6, 2)	0.546	(8, 0, 2)	0.455	(10, 10, 2)	0.439	(10, 10, 2)	0.329
[14]	0.415	[14]	–	[14]	0.423	[14]	0.306

posed method can be used for calculating not only the electronic structure but also the elastic properties of carbon nanotubes.

Apart from the calculations of the properties of the single-walled carbon nanotubes, we calculated some properties for a number of boron nitride (BN) nanotubes. In particular, we calculated the binding energies for the (10, 10) nanotube and the (10, 10, 2) corrugated surface, as well as the Young's moduli for these structures (Table 2). The results obtained demonstrate that, within the proposed approach, the properties of non-carbon structures are described with a high accuracy.

6. CONCLUSIONS

Thus, we proposed a method for calculating the electronic structure and elastic properties of nanotubes, including single-walled carbon nanotubes. This method makes it possible to accelerate the calculations significantly. The proposed approach is based on modification of the geometry of the calculated nanotube through a local piecewise change in its curvature and on the introduction of additional boundary conditions. This provides a means for calculating the corrugated surface with a unit cell having considerably smaller transverse sizes. Moreover, the number of atoms in the unit cell of the new corrugated surface is N times smaller than that in the nanotube. The applicability of the method was illustrated by calculating the electronic structure for a number of carbon and non-carbon (boron nitride) single-walled nanotubes. It was shown that the time it takes for the nanotube properties to be calculated decreases considerably (by a factor of 10 – 10^3 depending on the diameter) as the degree of partition of the sin-

gle-walled carbon nanotube increases, especially for nanotubes with large diameters. A detailed analysis of the Hamiltonian along the lines of the piecewise change in the nanotube curvature demonstrated that the proposed approach leads to an insignificant difference between the calculated structures of the nanotube and the corresponding corrugated structure. This difference decreases in proportion to the increase in the radius of the carbon nanotube.

ACKNOWLEDGMENTS

We would like to thank the Institute of Computer Modeling (Siberian Division, Russian Academy of Sciences, Russia) for providing the opportunity to use a cluster computer for performing the quantum-chemical calculations.

This work was supported in part by the Russian federal program "Integration," project nos. B0017 and Ya0007.

REFERENCES

1. S. Iijima, *Nature (London)* **354**, 56 (1991).
2. P. M. Ajayan and T. W. Ebbesen, *Rep. Prog. Phys.* **60**, 1025 (1997).
3. S. J. Tans, A. R. M. Verschueren, and C. Dekeer, *Nature (London)* **393**, 49 (1998).
4. Ph. Avouris, R. Martel, S. Heinze, M. Radosavljevec, S. Wind, V. Derycke, J. Appenzeller, and J. Terso, in *Proceedings of the XVI International Winter School on Electronic Properties of Novel Materials, Kirchberg Winter School, Tyrol, Austria, 2002*, Ed. by H. Kuzmany, J. Fink, M. Mehring, and S. Roth (AIP, Melville, NY, 2002).

5. G. Kresse and J. Furthmüller, Phys. Rev. B: Condens. Matter **54** (16), 11 169 (1996).
6. D. Vanderbilt, Phys. Rev. B: Condens. Matter **41** (11), 7892 (1990).
7. R. A. Jishi, L. Venkataraman, M. S. Dresselhaus, and G. Dresselhaus, Chem. Phys. Lett. **209**, 77 (1993).
8. R. A. Jishi, M. S. Dresselhaus, and G. Dresselhaus, Phys. Rev. B: Condens. Matter **47** (24), 16671 (1993).
9. G. Ya. Lyubarskii, *The Application of Group Theory in Physics* (GITTL, Moscow, 1957; Pergamon, New York, 1960).
10. C. T. White, D. H. Robertson, and J. W. Mintmire, Phys. Rev. B: Condens. Matter **47** (9), 5485 (1993).
11. G. Kresse and J. Hafner, Phys. Rev. B: Condens. Matter **47** (1), 558 (1993).
12. G. Kresse and J. Hafner, Phys. Rev. B: Condens. Matter **49** (20), 14251 (1994).
13. P. Hohenberg and W. Kohn, Phys. Rev. **136** (3B), B864 (1964).
14. W. Kohn and L. J. Sham, Phys. Rev. **140** (4A), A1133 (1965).
15. D. M. Ceperley and B. J. Alder, Phys. Rev. Lett. **45** (14), 566 (1980).
16. J. P. Lu, Phys. Rev. Lett. **79** (7), 1297 (1997).
17. B. I. Yakobson, C. J. Brabec, and J. Bernholc, Phys. Rev. Lett. **76** (14), 2511 (1996).
18. E. Hernandez, C. Goze, and P. Bernier, Appl. Phys. A: Mater. Sci. Process. **68** (24), 287 (1999).
19. D. Srivastava, M. Menon, and K. Cho, Phys. Rev. Lett. **83** (15), 2973 (1999).

Translated by O. Borovik-Romanova

Erratum: “VUV-Luminescence and Excitation Spectra of the Heavy Trivalent Rare-Earth Ions in Fluoride Matrices”

[Physics of the Solid State 47, 1416 (2005)]

M. Kirm, V. N. Makhov, M. True, S. Vielhauer, and G. Zimmerer

The correct version of Fig. 2 is given below.

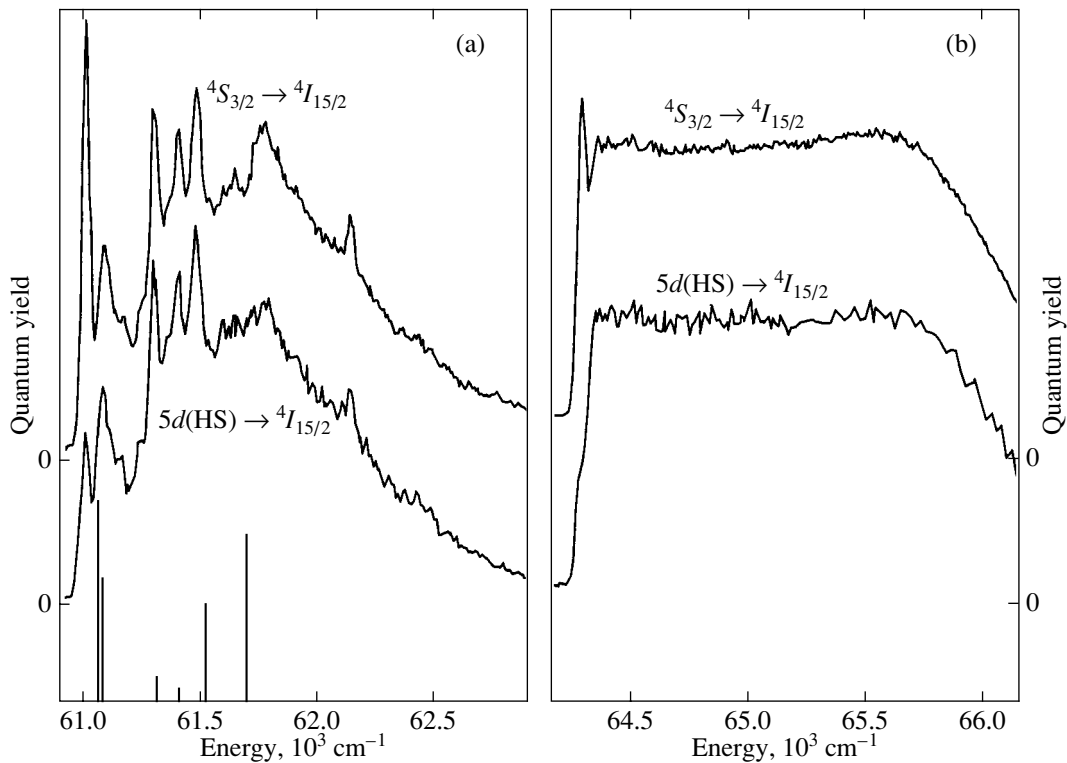


Fig. 2. Excitation spectra of the spin-forbidden $\text{LiYF}_4 : \text{Er}^{3+} (1\%)$ $d \rightarrow f$ and ${}^4S_{3/2} \rightarrow {}^4I_{15/2}$ emission at the onset of (a) spin-forbidden and (b) spin-allowed $f \rightarrow d$ excitation. $T = 9 \text{ K}$, $\Delta\lambda_{\text{ex}} = 0.6 \text{ \AA}$.